LLE 2006 Annual Report

UR
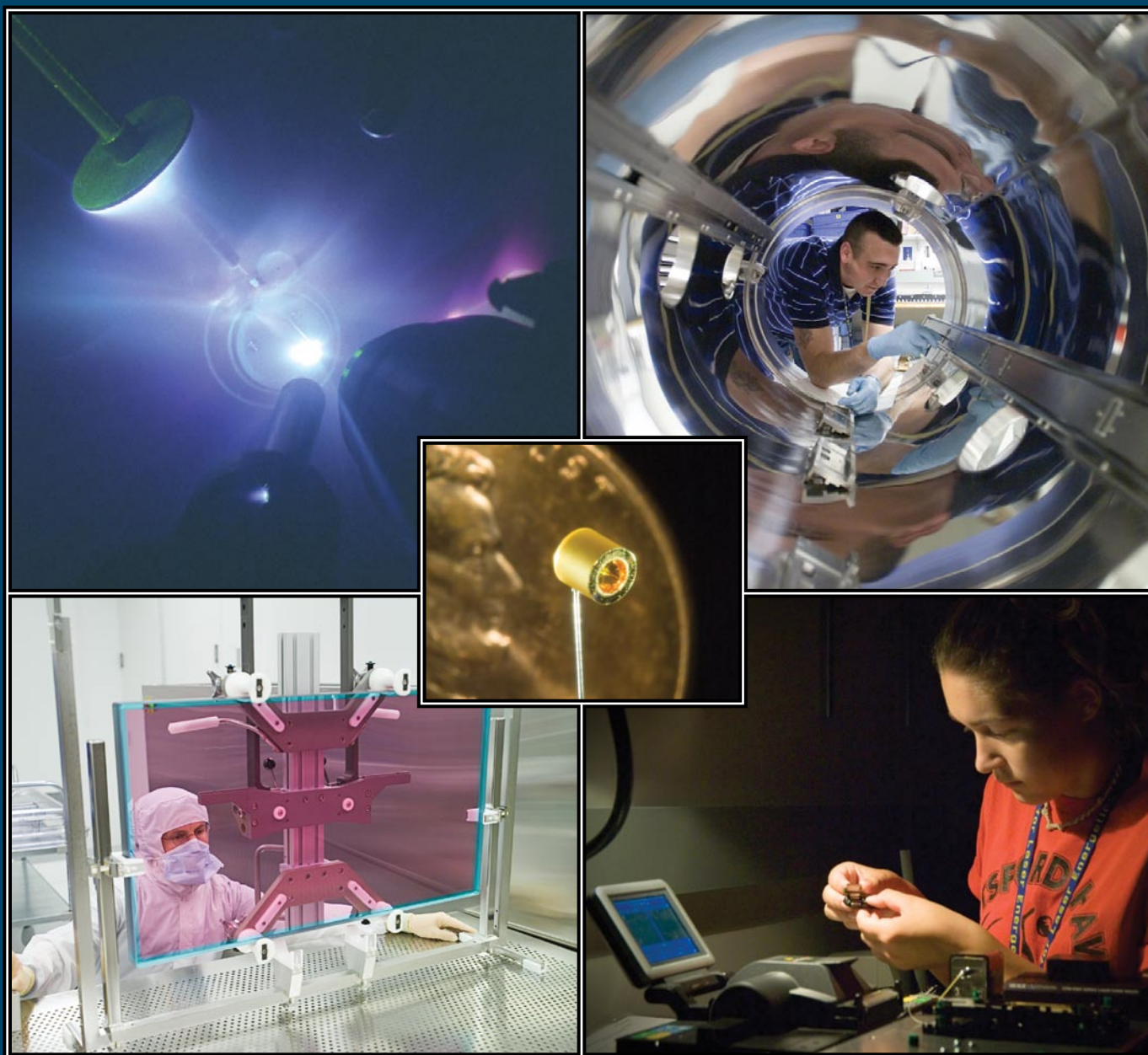LLE

October 2005 – September 2006

Cover Photos

Upper Left: Image of the inside of the OMEGA target chamber during a shot taken as part of a collaborative National Ignition Campaign (NIC) experiment to develop an experimental platform for measuring shock timing in ICF capsules.

Lower Left: Gary Mitchell, Senior Manufacturing Engineer, is shown examining a finished Nd:glass slab to be used on one of the OMEGA EP power amplifiers.

Upper Right: Lee Shepler, a contract assembler, is shown assembling the off-axis parabola inserter (OAPI), which will be used to focus the OMEGA EP short-pulse beams onto targets placed in the OMEGA target chamber.

Center: A half-hohlraum target used on an LLE-directed indirect-drive experiment in support of the National Ignition Campaign.

Lower Right: Elizabeth Gregg, an LLE summer high school intern from Naples Central High School, is shown working on her project: optimization of fiber slicing.

For questions or comments, Laboratory for Laser Energetics, 250 East River Road, Rochester, NY 14623-1299, (585) 275-5286. Worldwide-Web Home Page: http://www.lle.rochester.edu/

University of Rochester
Laboratory for Laser Energetics

DOE/SF/19460-723
January 2007

LLE 2006 Annual Report

October 2005 – September 2006

UR
LLE

Inertial Fusion Program and
National Laser Users' Facility Program

Contents

Executive Summary

The fiscal year ending in September 2006 concluded the fourth year of the five-year renewal of Cooperative Agreement DE-FC52-92F19460 with the U.S. Department of Energy. This report summarizes progress in laser-fusion research at the Laboratory for Laser Energetics (LLE) during the past fiscal year; LLE progress on laser, optical materials, and advanced technology development; work on the OMEGA Extended Performance (EP) laser project, operation of OMEGA for the National Laser Users' Facility (NLUF) and other external users; and programs focusing on the education of high school, undergraduate, and graduate students during the year.

Progress in Laser Fusion Research

The laser-fusion research program at the University of Rochester's Laboratory for Laser Energetics (LLE) is focused on Campaign-10 inertial confinement fusion (ICF) ignition and experimental support technology, operation of facilities (OMEGA), and the construction of OMEGA EP—a high-energy petawatt laser system. LLE is the lead laboratory for research into the direct-drive approach to ICF ignition and is taking a lead role in some indirect-drive tasks within the National Ignition Campaign.

Progress in the laser-fusion research program during this past year was made in three principal areas: OMEGA direct-drive and indirect-drive experiments and targets; development of diagnostics for experiments on OMEGA, OMEGA EP, and the National Ignition Facility (NIF); and theoretical analysis and design efforts aimed at improved direct-drive-ignition capsule design.

1. OMEGA Direct-Drive Targets and Experiments

Virtually all ignition target designs for the NIF are based on a spherical low-Z ablator containing a solid, cryogenic-fuel layer of deuterium and tritium. Techniques refined at LLE have produced targets with an inner D_2- or DT-ice surface that meets the surface-smoothness requirements for ignition (≤ 1-μm rms in all modes meeting an FY07 Level-2 milestone). The first of a series of direct-drive, ignition-scaled cryogenic capsule implosions containing tritium occured in 2006. A DOE milestone was achieved in March by imploding two β-layered capsules

containing tritium. The first high-yield, direct-drive, ignition-scaled β-layered 50:50 DT cryogenic implosion was carried out in June 2006—the first time such a target has been imploded in an ICF facility. We report (p. 167) on the historical development and the significant progress made recently in cryogenic D_2 and DT capsule fabrication and characterization technology and present results from the most recent cryogenic-capsule implosions. Simulations of these experiments suggest that values for peak areal density (ρR_{peak}) as high as 190 ± 20 mg/cm^2 may have been achieved.

The results of OMEGA direct-drive implosions of capsules filled with different mixtures of D_2 and ^{3}He gas are reported (p. 90). At temperatures above a few electron volts, D_2 and ^{3}He gases are fully ionized, and hydrodynamically equivalent fuels with different ratios of D_2 and ^{3}He can be chosen to have the same mass density, total particle density, and equation of state. Implosions with a 50:50 mixture of D^3He by atom consistently result in measured nuclear yields half of that anticipated by scaling from measured yields of implosions with pure D_2 and nearly pure ^{3}He. This observation is seen over a wide range of experimental configurations, including targets with a variety of shell thicknesses and fill pressures, simultaneously for two different nuclear yields (D-D and D^3He), as well as for shock and compression yields. A number of possible mechanisms that may cause this scaling are considered, but no dominant mechanism has yet been identified.

In a collaborative effort with the Massachussetts Institute of Technology (MIT) Plasma Science and Fusion Center (PSFC), measurements of the dependence of the nuclear burn region size on implosion parameters in OMEGA experiments were carried out (p. 1). Radial profiles of nuclear burn in directly driven implosions were systematically studied for the first time using a proton emission imaging system on OMEGA. The system is sensitive to energetic 14.7-MeV protons from the D^3He fusion reaction. Clear relationships were identified between variations in the size of the burn region and variations in such experimental parameters as capsule size, shell composition and thickness, gas-fill pressure, and laser energy.

Measurements of the Rayleigh–Taylor hydrodynamic instability growth rate in the non linear regime are presented on p. 17. The measured modulation Fourier spectra and nonlinear growth velocities are in excellent agreement with Haan's model. In real-space analysis, the bubble merger was quantified by a self-similar evolution of bubble-size distributions, in agreement with the Alon–Oron–Shvarts theoretical predictions.

Detailed studies of the displacement of cryogenic targets from their optimum position [at target chamber center (TCC)] are presented (p. 179). While beam smoothing and power balancing can ensure highly uniform illumination of capsules, target displacement greater than 5 μm or more from TCC can lead to significant drive nonuniformity and reduce the capsule performance. Correlation between target vibration at TCC and the response characteristics obtained in this study indicate that the modes of spider silk are the primary cause of the displacement.

Results of studies of isotopic fractionation during solidification of H_2-HD-D_2 mixtures are reported on p. 26. Isotopic fractionation could reduce the efficiency of the fusion reaction in future crogenic D-T targets. It is found that frozen H–D mixtures have spatial concentration gradients of the order of 0.02 to 0.05 molecular fraction per millimeter, well below the level that would compromise cryogenic target performance (p. 35).

The development of methods and techniques for the decontamination of metals and alloys from tritium is presented (p. 70). The efficacy of tritium removal from stainless steel using two different approaches was studied: thermal desorption in an inert gas purge containing hydrogen peroxide, and radio-frequency–driven argon plasma irradiation. This study indicates that reducing the activity in metals below 0.5 μCi/g is feasible without generating secondary active waste by-products other than water.

2. Target Diagnostics for OMEGA, OMEGA EP, and the NIF

The time interval from the beginning of the laser pulse to the peak of neutron emission (bang time) is an important parameter in inertial confinement fusion experiments. The NTD streak camera previously deployed on OMEGA was saturated by neutron yields in excess of 3×10^{13}, whereas the latest OMEGA experiments and the planned fast-ignition experiments using OMEGA EP are expected to produce neutron yields above 10^{14}. The new detector described on p. 147 will support these experiments plus high-yield experiments on the NIF.

A collaboration including MIT-PSFC, LLE, and LLNL led to a novel imaging technology for measuring E and B fields in laser-produced plasmas using monoenergetic proton radiography (p. 189). The generation of electromagnetic fields by the interaction of laser light with matter is a process of fundamental interest in high-energy-density physics. This article presents high-resolution, time-gated radiographic images of a plastic foil driven by a 10^{14}-W/cm^2 laser that imply B fields of ~0.5 MG and E fields ~1.5×10^8 V/m. Furthermore, these measurements demonstrate the beneficial focal-smoothing effects produced by distributed phase plates for substantially reducing medium-scale chaotic field structures.

Sensitive electronic detectors are difficult to operate in petawatt laser–target interaction experiments. The laser–plasma interaction at relativistic intensitites (>10^{18} W/cm^2) creates large amounts of relativistic electrons ($E > 1$ MeV), hard x rays, and charged particles. The article starting on p. 153 presents strategies to minimize the impact of electromagnetic pulses on diagnostics inside the OMEGA EP target chamber.

X-ray film is still commonly used for recording the absolute x-ray fluence in high-temperature plasma experiments. Absolute calibration of Kodak Biomax-MS film response to x rays in the 1.5- to 8-keV range has been carried out at LLE and is presented starting on p. 138. This calibration was performed using an e-beam–generated x-ray source, a crystal/multilayer monochrometer, a film pack, and an absolutely calibrated x-ray photon detector. The results agree with predictions from a theoretical model presented in a companion article beginning on p. 142. The response model starts with simple mathematical models and extends them to T-grain–type film such as Biomax-MS.

3. Theoretical Analysis and Design

A review of the basic concepts of laser-driven ICF ignition is presented (p. 83) with emphasis on the direct-drive-ignition target designs, requirements for the temporal shape of the laser pulse, and considerations of stability issues.

Polar-direct-drive (PDD) simulations and experiments on the OMEGA Laser System are discussed beginning on p. 41. Forty OMEGA beams were arranged in six rings to emulate the NIF x-ray-drive configuration and used to perform direct-drive implosions of CH shells filled with D_2 gas. Simulations performed with the *DRACO* code are in good agreement with the experimental x-ray radiographs. Simulations of NIF-scale capsules achieve ignition with a gain of ~20 and show the development of a 40-μm-radius, 10-keV region with a neutron-averaged ρR ~ 1.27 g/cm^2 near stagnation.

Implication of hydrogen fractionation in ICF ignition designs is discussed beginning on p. 35. A numerical investigation of the effects of fractionation on hot-spot formation, ignition, and burn in ICF target designs indicates that small levels of fractionation (~10%) are acceptable for ignition performance on the NIF.

Lasers, Optical Materials, and Advanced Technology

The design and analysis of binary beam shapers for high-power laser systems are described (p. 202). In a manner similar to NIF, OMEGA EP uses square beams with high-order super-Gaussian spatial profiles to maximize the fill factor of the power amplifiers without exceeding the damage fluence of the laser components. The spatially dependent gain of the amplifiers can be, to a large extent, precompensated by attenuating regions of the input beam inversely with the gain they receive in the amplifiers. An error diffusion algorithm is applied to the design of binary beam shapers consisting of a uniform array of 10-mm-sq pixels that can be produced using standard lithographic techniques on high damage threshold, metal-on-glass substrates. Simulations show that this technique can produce beam shapers with the correct profile to precompensate the spatially dependent gain of the OMEGA EP's amplifiers with low rms error.

The characteristics and performance of the high-contrast plasma-electrode Pockels cell (PEPC) are discussed beginning on p. 129. This device was developed as a prototype for OMEGA EP and demonstrated high-switching contrasts exceeding 500:1 throughout the clear aperture. The key to producing this level of performance was the reduction of stress birefringence by using circular windows. In addition to the usual function of holding the pulse in the amplifier cavity for four passes, the OMEGA EP PEPC will be used to provide isolation from target retroreflections. Most existing multipass high-energy laser systems use frequency conversion to direct second- or third-harmonic light onto the target. This is not the case for the short-pulse part of OMEGA EP; therefore, any light reflected by the target can experience gain in the unsaturated amplifiers as it propagates back up the system, posing a significant damage threat to the system.

A description of the characteristics and performance of a high-gain, polarization-preserving, Yb-doped fiber amplifier for low-duty-cycle pulse amplification begins on p. 63. A high-gain, low-noise, double-pass, ytterbium-doped amplifier for which amplified spontaneous emission (ASE)–suppression techniques were used to fabricate a double-pass amplifier with the noise properties of a single-pass amplifier has been demonstrated. A double-pass configuration allows for significantly higher gains to be obtained in a fiber amplifier than can be achieved in a single-pass configuration. Simulations based on a rate-equation model were used to analyze the ASE and the impact of the suppression techniques. These techniques were implemented in an alignment-free, double-pass fiber amplifier with 26-dB gain at a wavelength 23 nm off the gain peak and a −48-dB noise floor, while amplifying linearly polarized optical pulses with a low duty cycle.

In single-photon sources (SPS's) based on single-emitter fluorescence, a laser beam is focused into an area containing a low concentration of single emitters so that only one emitter becomes excited. A report on p. 102 shows the advantages of using liquid crystals as the hosts for SPS's. Deterministically polarized fluorescence from single emitters (dye molecules) was demonstrated for the first time at room temperature. In this experiment, a planar-aligned, nematic liquid crystal host provides uniaxial alignment of single-dye molecules in a preferred direction. As a result, fluorescence of these single emitters is deterministically polarized, which allows one to consider such systems for applications in photonic quantum information.

The performance of the fiber-coupled single-photon detectors based on NbN superconducting nanostructures for practical quantum cryptography and photon-correlation studies is described beginning on p. 108. Several two-channel, single-photon detector systems based on two fiber-coupled, superconducting, single-photon detectors were built and characterized. The best device reached the system quantum efficiency of 0.3% in the 1540-nm telecommunication wavelength with a fiber-to-detector coupling factor of about 30%.

Results from the design and synthesis of transition-metal dithiolene near-IR dyes are presented on p. 112. Transition-metal complexes based on nickel, palladium, or platinum dithiolene cores show substantial promise for guest–host liquid crystal (LC) devices operating in the near- to mid-IR region. Some specific application examples for these materials in LC electro-optical devices are presented and the most recent results in the computational modeling of physical and optical properties of this interesting class of organometallic optical materials are discussed.

Surface features of tungsten carbide composites processed by bound-abrasive microgrinding and magnetorheological finishing (MRF) were analyzed (p. 51). It was found that the peak-to-valley microroughness of the surface gives a measure of the deformed-layer depth. MRF spots revealed the true depth of the grinding-induced deformed surface layer.

Results of simulation for gain apodization in highly doped distributed-feedback (DFB) fiber lasers are presented on p. 160. DFB lasers can be designed with an internal grating structure to provide high output power (up to 60 mW), single frequency, single polarization, and high optical signal-to-noise ratio. The effects of gain apodization on threshold behavior along with the impact on output power and mode discrimination are investigated. Apodization of the longitudinal gain profile is found to lower the laser threshold by 21% without degrading mode discrimination.

Status and Progress of OMEGA EP

The OMEGA EP (extended performance) project was in its fourth year in FY06. In FY06 congressional funding allowed the project to move forward with the full four-beam project. In February 2006 a baseline change was adopted that includes two additional long-pulse beams that were in the original project conceptual design and UV conversion for all four beams. With these additions, the OMEGA EP total estimated cost increased from $67 million to $89 million. A total of $87 million was appropriated through FY06. The project will be complete in April 2008.

The first quarter of FY06 was highlighted by the installation of the major structural assemblies. The largest of the structure installations was the grating compressor chamber. This 350,000-lb vacuum vessel was assembled and tested at vacuum, completing one of the largest single acquisition items for the project. Adjacent to this structure, the target-area structure took form and in November the target chamber was delivered and installed. By the end of December 2005, the entire Laser Bay structure installation was complete, marking the end of heavy construction.

In the second quarter of FY06 the OMEGA EP bay was re-certified at class-1000 cleanliness and optical assembly deployment began. Beam equipment such as spatial-filter tubes and alignment tables were installed, and laser light began to traverse the optical path of the beamline. After one diffraction-grating vendor failed to perform, a second vendor demonstrated the ability to manufacture all gratings and deliver them by the end of 2006. During this quarter, acquisition of the grating compressor's internal structure became the controlling critical path item on the short-pulse-laser project path. Contamination issues drove a design revision that delayed the start of manufacturing and made the fabrication task substantially more complex.

During the third and fourth quarters of FY06, the Beam-1 laser source, amplifier, and power conditioning subsystems completed major assembly phases. The first beam assembly was completed to the output of the transport spatial filter, and four-pass alignment was accomplished. The completion of integration and alignment of the first beam included firing all of the amplifiers at full operational charge voltages. The successful activation of the amplifiers completed preparations for propagating beam tests to be carried out in FY07. Continued incremental delay in the manufacture of the grating compressor chamber's internal structures stimulated a change in schedule that advanced the UV activation of all four beams ahead of short-pulse activation.

Overall, the project achieved all objectives for FY06 and continued to make excellent progress toward project completion. With the baseline change to the full four-beam OMEGA EP system, the project scope, budget, and schedule are fixed. The initial highest-risk element of the project was overcome: diffraction gratings of large aperture, high efficiency, and high damage threshold. Other technically challenging elements such as adaptive optics, plasma-electrode Pockels cells, and optical parametric chirped-pulse amplification were completed through production and subsystem tests. At the end of the fiscal year the completion of these systems allowed the integrated operational testing phase to begin.

National Laser Users' Facility (NLUF) and External Users' Programs

Nearly half of the OMEGA shots in FY06 were dedicated to external users including the NLUF programs, LLNL, LANL, SNL, and CEA.

FY06 NLUF Experiments

Fiscal year 2006 was the second of a two-year period of performance for the NLUF projects approved for FY05–FY06 funding and OMEGA shots. A total of 122 OMEGA shots were dedicated to seven NLUF projects. Beginning on p. 215, their progress is detailed in the following reports:

- *Isentropic Compression Experiments (ICE) for Measuring EOS on OMEGA*
  (J. R. Asay, Washington State University)

- *Laser–Plasma Interactions in High-Energy-Density Plasmas*
  (H. Baldis, University of California, Davis)

- *Experimental Astrophysics on the OMEGA Laser*
  (R. P. Drake, University of Michigan)

- *Astrophysical Jets and HED Laboratory Astrophysics*
  (P. Hartigan, Rice University)

- *Recreating Planetary Core Conditions on OMEGA*
  (R. Jeanloz, University of California, Berkeley)

- *Three-Dimensional Study of the Spatial Structure of Direct-Drive Implosion Cores on OMEGA*
  (R. Mancini, University of Nevada, Reno)

- *Implosion Dynamics and Symmetry from Proton Imaging, Spectrometry, and Temporal Measurements*
  (R. D. Petrasso and C. K. Li, MIT)

FY07–FY08 NLUF Experiments

During this past year, DOE issued a solicitation for NLUF grants for the period FY07–FY08. Twelve proposals were submitted in response to this solicitation and an independent DOE Technical Evaluation Panel was convened to review the proposals. The following six proposals were approved for DOE funding and OMEGA shots:

- *Experimental Astrophysics on the OMEGA Laser*
  (R. P. Drake, University of Michigan)

- *X-Ray Compton Scattering on Compressed Matter*
  (R. Falcone, University of California, Berkeley)

- *Laboratory Experiments on Supersonic Astrophysical Flows Interacting with Clumpy Environments*
  (P. Hartigan, Rice University)

- *Recreating Planetary Core Conditions on OMEGA: Techniques to Produce Dense States of Matter*
  (R. Jeanloz, University of California, Berkeley)

- *Multiview Tomographic Study of OMEGA Direct-Drive Implosions*
  (R. Mancini, University of Nevada, Reno)

- *Monoergetic Proton Radiography of Laser/Plasma-Generated Fields and ICF Implosions*
  (R. D. Petrasso and C. K. Li, Massachusetts Institute of Technology)

FY06 LLNL–OMEGA Experimental Programs

In FY06, LLNL led 354 shots on the OMEGA Laser System for the National Ignition Campaign (NIC), for high-energy-density sciences (HEDS) experiments, and for the NWET program. The LLNL-led experiments included the following:

- *Foam-ball hohlraum symmetry studies*

- *Collective x-ray scattering from plasmons in warm dense matter*

- *Laser–plasma interaction studies*

- *"Cocktail" hohlraum albedo studies*

- *X-ray conversion measurements on spherical targets (with CEA)*

- *Rayleigh–Taylor experimental platform development*

- *Hohlraum window x-ray preheat studies*

- *NIF fill-tube simulations*

- *NIF x-ray backlighter development*

- *Hot hohlraum radiation sources*

- *Double-shell experiments*

- *Study of the radiative effects of high-Z dopants on implosions*

- *Opacity platform development*

- *Dynamic hohlraum experiments (double shell driven by radiative shock wave)*

- *Isentropic compression equation-of-state experiments*

- *Shock–sphere interaction experiment*

- *Jet generation and propagation into low-density background material*

FY06 LANL–OMEGA Experimental Programs

LANL teams led 125 OMEGA shots in FY06 for the following NIC and HEDS experiments:

- *Off-Hugoniot heated hydrodynamics*

- *Inhomogeneous radiation flow*

- *Beryllium fill-tube defect studies*

- *High-Z shell implosions*

- *High-Z dopant impact in stimulated Raman scattering (SRS)*

- *Gas Cherenkov detector development*

FY06 SNL OMEGA Experimental Programs

SNL carried out 30 shots on OMEGA in FY06 including the following experiments:

- *Beryllium ablation-rate measurements in planar geometry*

- *Beryllium x-ray burnthrough and ablation-rate measurements in convergent geometry*

- *VISAR determination of hohlraum radiation temperature*

- *Development of a NIF shock-timing diagnostic*

FY06 CEA OMEGA Experimental Programs

In FY06, CEA carried out 49 target shots on OMEGA including the following experiments:

- *Rayleigh–Taylor instabilities in indirect-drive, mode-coupling experiments*

- *Implementation of a high-resolution x-ray imaging diagnostic (HXRI)*

FY06 Laser Facility Report

During FY06 the OMEGA Laser Facility conducted 1394 target shots for a variety of users as illustrated in Fig. 1. During this period, the system availability and experimental effectiveness averaged 93.3% and 95.3%, respectively. Major highlights of the facility operations in FY06 were as follows:

- *First implosions of beta-layered ignition-scaled DT capsules*

- *A full set (42) of new indirect-drive distributed phase plates designed and fabricated*

- *Low-adiabat, high-contrast pulse shapes developed and implemented for the OMEGA ignition-scaled cryogenic DT implosion experiments*

- *Upgrade of the active-shock-breakout (ASBO) diagnostic completed*

- *OMEGA EP short-pulse beam-transport tube installed*

The detailed facility report may be found on p. 213.
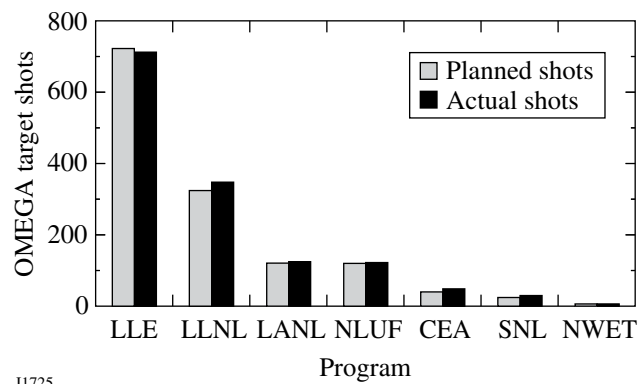
I1725

Figure 1
FY06 OMEGA usage.

Education at LLE

As the only major university participant in the National ICF Program, education continues to be an important mission for the Laboratory. A report on this year's summer high school research program is described in detail on p. 211. Thirteen students participated in this year's program. The William D. Ryan Inspirational Teacher Award was given to Mr. Thomas Lewis, a former Earth Science teacher (currently retired) at Greece Arcadia High School.

Graduate students are using the OMEGA laser for fusion research and other facilities for HED research and technology development. They are making significant contributions to LLE's research activities. Thirty faculty from five departments collaborate with LLE's scientists and engineers. Presently, 93 graduate students are involved in research projects at LLE, and LLE directly sponsors 48 students pursuing Ph.D. degrees. Their research includes theoretical and experimental plasma physics, high-energy-density physics, x-ray and atomic physics, nuclear fusion, ultrafast optoelectronics, high-power-laser development and applications, nonlinear optics, optical materials and optical fabrications technology, and target fabrication.

A total of 183 University of Rochester students have earned Ph.D. degrees at LLE since its founding. An additional 90 graduate students and 25 postdoctoral fellows from other universities have been funded by NLUF grants. The most-recent University of Rochester Ph.D. graduates and their thesis titles include the following:

Anderson, K.   *"Adiabat Shaping in Direct-Drive Inertial Confinement Fusion Implosions"*

Culligan, S.   *"Organic Blue Light–Emitting Diodes and Field-Effect Transistors Based on Monodisperse Conjugated Oligomers"*

Gotchev, O.   *"Experiments on Dynamic Overpressure Stabilization of the Ablative Richtmyer–Meshkov Instability in ICF Targets"*

Guazzotto, L.   *"Equilibrium and Stability of Tokamak Plasmas with Arbitrary Flow"*

Park, J.-R.   *"Time-Resolved Imaging Using Non-Collinear Parametric Down-Conversion"*

Pearlman, A.   *"Ultrafast NbN Single-Photon Optical Detectors for Quantum Communications"*

Teng, X.   *"Synthesis of Metal, Metal Oxide, and Alloy Nanostructures for Magnetic and Catalytic Implications"*

Trajkovska, A.   *"Chiroptical Properties and Photoalignment of Monodisperse Glassy Liquid Crystalling Oligofluorences"*

Zheng, L.   *"UV-Laser–Induced Densification of Fused Silica: A Molecular Dynamics Study"*

Approximately 42 University of Rochester undergraduate students participated in work or research projects at LLE this past year. Student projects include operational maintenance of the OMEGA Laser System; work in laser development, materials, and optical-thin-film–coating laboratories; and programming, image processing, and diagnostic development. This is a unique opportunity for students, many of whom will go on to pursue a higher degree in the area in which they gained experience at the Laboratory.

In addition, LLE directly funds research programs within the MIT Plasma Science and Fusion Center, the State University of New York (SUNY) at Geneseo, the University of Nevada, Reno, and the University of Wisconsin. These programs involve a total of approximately 16 graduate students, 27 undergraduate students, and 7 faculty members.

Robert L. McCrory
Director, Laboratory for Laser Energetics
Vice Provost, University of Rochester

Measured Dependence of Nuclear Burn Region Size on Implosion Parameters in Inertial Confinement Fusion Experiments

Introduction

Images of the nuclear burn regions in inertial confinement fusion (ICF) capsules are important for fully assessing the combined results of all the complicated processes that affect capsule implosion dynamics; these processes, including drive, preheat, instabilities, and mix, must be understood and controlled to achieve ignition and energy generation.[1–3] In the direct-drive approach to ICF, a spherical capsule containing fuel is compressed and heated by direct illumination of laser beams focused on the capsule surface in a nominally uniform fashion.[2] Hydrodynamic instabilities affect the performance of these implosions,[2–10] ultimately determining the size, symmetry, and yield of the nuclear burn region. This article, the third in a series about proton emission imaging,[11–13] presents the first comprehensive studies of D^3He burn region sizes in nominally symmetric direct-drive implosions with diverse capsule and drive conditions. Radial burn profiles and total yields are obtained from measurements of energetic 14.7-MeV protons from the fusion of deuterium (D) and 3-helium (^{3}He) using methods described in Refs. 11 and 12 and in the appendix (see p. 10) of this article. Complementary data from x-ray images,[14–17] proton spectrometers,[18–23] and clean 1-D simulations[24,25] are used in interpreting the burn region sizes and their implications. Asymmetric burn distributions and their relationships to capsule and drive parameters are described in Refs. 11 and 13, and tests of the fidelity of the reconstructed images are discussed in Refs. 11 and 12. Burn images have previously been made of deuterium–tritium-filled capsules using 14.1-MeV neutrons,[8,26–29] 3-MeV protons,[30–32] or 3.5-MeV alpha particles,[32] but for a more limited range of implosion types (see also other papers cited in Ref. 11).

Experimental Conditions (p. 1) describes the drive and capsule parameters studied along with general information about the proton emission imaging cameras and the other diagnostics used. **Data Analysis** (p. 2) provides an overview of the analysis of proton imaging data with examples from two implosions that have dramatically different burn regions. Similarities and differences between nuclear burn images and x-ray images are discussed and important connections between burn profiles, areal density (ρR), and clean 1-D simulations are made. **The Dependence of R_{burn} on Laser and Capsule Parameters** (p. 5) summarizes the results obtained when capsule and drive conditions were systematically varied. The dependence of the burn radius on shell thickness, gas pressure, laser energy, and shell type is investigated for a large set of implosions and evidence of the presence of mix is discussed. **Summary and Discussion** (p. 9) details the results and future work, and the appendix (p. 10) provides detailed information about methods of calculating radial burn profiles from penumbral images (including neutron images).

Experimental Conditions

To explore the range of burn region sizes associated with different kinds of symmetrically driven implosions, and to reveal effects of complicated physics such as preheat, mix, drive efficiency, and core distortions, a wide variety of implosions were examined on the OMEGA Laser System.[33] OMEGA is a 60-beam, frequency-tripled, UV (0.35-μm) laser capable of delivering up to 30 kJ of laser energy in a variety of pulse shapes. The individual laser beams were smoothed with distributed phase plates (DPP's),[34] 2-D smoothing by spectral dispersion with a bandwidth of 1.0 THz,[35,36] and polarization smoothing using birefringent wedges.[37] Two types of DPP's (SG3 and SG4) were used in the experiments described here, producing different beam-intensity profiles.[38] Only 1-ns square laser pulses were used to directly illuminate the capsule. The beam-to-beam energy imbalance was typically less than 4% rms.

The capsules used either 1.8- to 2.3-μm-thick glass (SiO_2) shells filled with 18-atm D^3He gas or 17- to 24-μm-thick plastic (CH) shells filled with 3.6- or 18-atm D^3He gas. The glass-shell implosions used SG3 DPP's while the thick plastic-shell implosions used SG4 DPP's, except where noted. Initial capsule radii were nominally 470 μm for the SG3 DPP's and 430 μm for SG4 DPP's.

Proton core imaging system (PCIS) cameras[11–13] imaged the time-integrated D^3He proton emission distribution from

up to three nearly orthogonal directions simultaneously. These are penumbral imaging cameras, each consisting of a round imaging aperture that is significantly larger than the size of the D^3He burn region and a detector pack comprised of several ranging filters and CR-39 charged-particle detectors.[12,19] The distances from the implosion to the imaging aperture and from the imaging aperture to the detector pack (L_1 and L_2, respectively) determine the geometric magnification $M \equiv L_2/L_1$. Aperture diameters of 600 μm and 2000 μm were used; L_1 was typically 3 cm and M varied from 8 to 20. The energetic protons that pass through the aperture are detected with 100% efficiency in the CR-39 as long as the detector has filtering that slows incoming protons down to the CR-39 sensitivity range of about 0.5 to 8 MeV.

X-ray framing cameras were used to obtain 4- to 5-keV x-ray emission images[14–16] at 58-ps time intervals using 12× magnification and 40-ps integration times. At the time of peak proton production, the x-ray images represent primarily continuum emission from the heated inner portion of the shell material and can be used to estimate the radius of the fuel–shell interface, as described in Ref. 14.

Up to five proton spectrometers[19] were used simultaneously to obtain time-integrated measurements of the D^3He proton spectrum. These spectra are used to determine the total areal density $\langle \rho R \rangle$[19,23,39] using the downshift from the 14.7-MeV birth energy.[18–22,39] In these experiments the measured total ρR comprises both the shell ρR and the fuel ρR, but is usually dominated by the shell.[19,23,39] For given capsule shell and laser conditions, ρR provides a measure of shell convergence since, all else being equal, ρR scales as the inverse of the square of the shell radius at the time of burn. The PCIS and spectrometers typically give the same D^3He yield to within the observed proton-yield asymmetry of 15% to 20% rms.[19]

Data Analysis

1. Finding the Nuclear Burn Radius R_{burn}

The proton emission imaging cameras produce time-integrated penumbral images that are processed to produce either a 2-D image of the burn region surface brightness in D^3He reactions per unit area, $B(r,\phi)$, or a 1-D radial profile of the local number of D^3He reactions per unit volume, $S(r)$, which corresponds to an average over angles. The 2-D analysis technique is extremely useful for studying low-mode deviations from spherical symmetry, and simultaneous views of the burn region from three orthogonal directions can provide measurements of a 3-D structure; this approach has been used to study the important effects of asymmetric laser drive and asymmetric

shell structure on implosion symmetry.[13] A disadvantage of 2-D image reconstruction is that it always requires significant smoothing for control of statistical noise, as described in detail in Ref. 11. For the types of implosions studied at OMEGA, D^3He burn region sizes and yields typically require smoothing that limits the 2-D spatial resolution to the range of 15 to 30 μm. If it is desired to make an accurate measurement of characteristic burn region size for nearly symmetric implosions, it is advantageous to use the 1-D approach; it avoids smoothing errors and typically results in statistical measurement uncertainties of a few microns. Since the object of this article is to study burn region size, we will use 1-D analysis here and discuss 2-D results elsewhere.[13]

The 1-D reconstruction approach utilizes the relationship between $S(r)$ and the radial derivative dN/dR of the penumbral image values N (proton tracks per unit area on the detector); dN/dR is equivalent to a set of line integrals through the surface brightness of the D^3He burn region, as discussed in detail in Ref. 11 and in the appendix (p. 10). Of the two 1-D methods described in the appendix, we will use the method of fitting dN/dR with a family of functions that correspond either analytically or numerically to a family of local burn profile shapes.[11] The radial profile $S(r)$ of the proton source in reactions per unit volume is represented by a member of the family of super-Gaussians and sub-Gaussians

$$S(r) = S_0 e^{-(r/r_0)^{2/p}}, \tag{1}$$

where p is a "peakedness" shape parameter and r_0 is a measure of burn radius. The median radius R_{burn} containing half of the total local emission is actually used rather than r_0 to characterize the burn region size because it can be determined much more accurately and is nearly independent of the emission profile shape (see the appendix on p. 10). The burn profile parameters and geometric parameters are then varied to generate the best fit between the measured and predicted dN/dR.

Figure 105.1 shows sample data from two very different implosions involving capsules whose shells are 2-μm-thick glass [Fig. 105.1(a)] and 20-μm-thick plastic [Fig. 105.1(e)]. The plotted data show dN/dR from the azimuthally averaged penumbral images with error bars representing statistical uncertainties. For each data set, a best fit (solid line) was found and used to determine the absolute radial profile of the burn [Figs. 105.1(c) and 105.1(g)] and its characteristic radius R_{burn} as well as the absolute radial profile of surface brightness $B(r)$ [Figs. 105.1(d) and 105.1(h)]. The values of R_{burn} were 29±2.5 μm for the plastic-shell implosion and 54±2 μm for
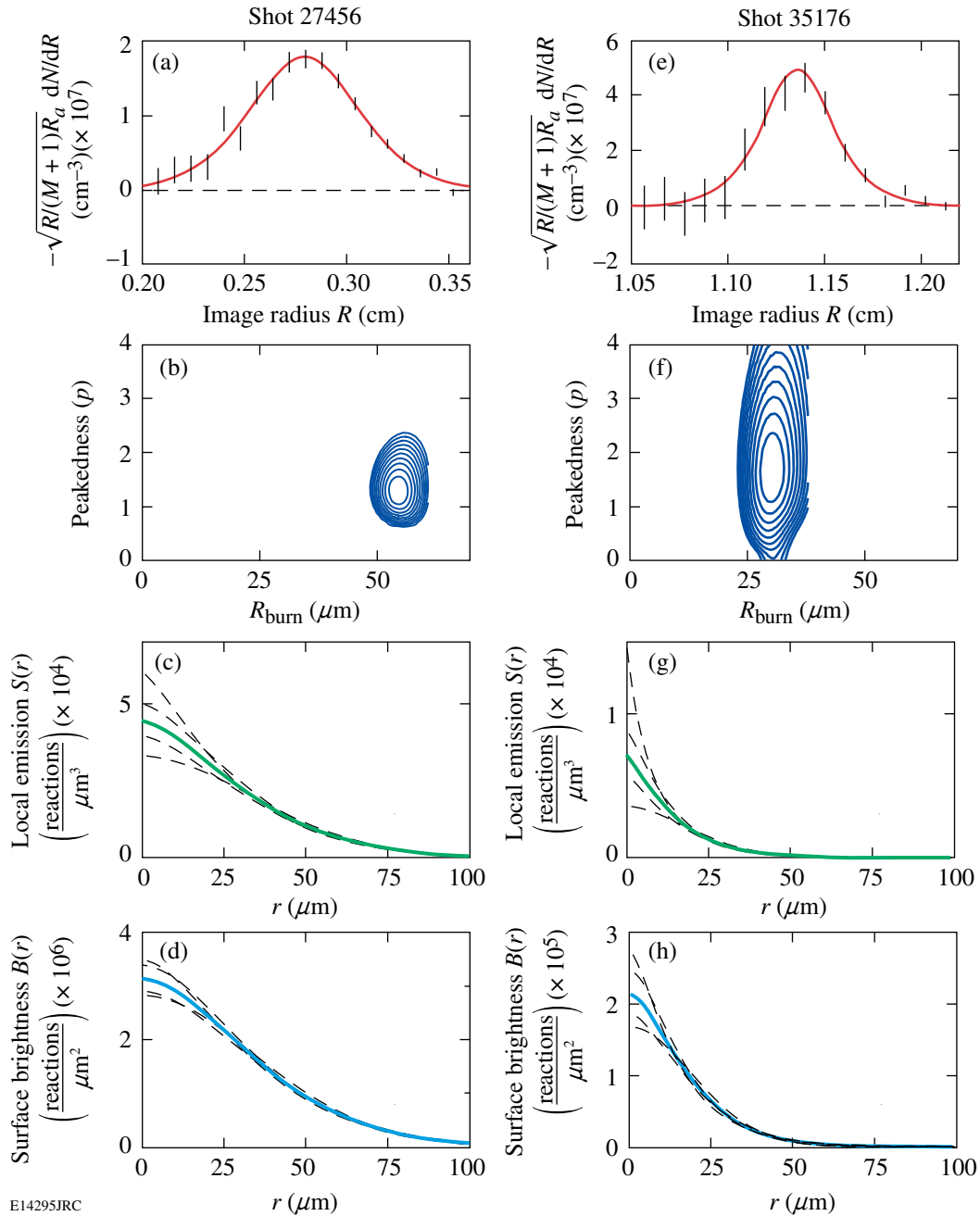
Figure 105.1

Data illustrating the burn region analysis of two very different implosions on OMEGA. The left-hand column corresponds to shot 27456 (2-μm-thick, glass-shell capsule), while the right-hand column corresponds to shot 35176 (20-μm-thick, plastic-shell capsule); each capsule was filled with 18-atm D^{3}He and irradiated with a 23-kJ, 1-ns laser pulse. The vertical lines in (a) and (e) represent statistical error bars for measured values of dN/dR; the locations of all individual proton tracks on the penumbral image detector are measured to a fraction of a micron, but $N(R)$ needs to be binned with a finite interval in R to achieve acceptable statistics. Note that the significance of the square root appearing as a coefficient dN/dR in the vertical axis labels is discussed in the appendix (p. 10) in connection with Eq. (14); this slowly varying coefficient is very close to 1.0 for the data shown here. The thick lines in (a) and (e) are best fits to the data using the approach described in **Data Analysis** (p. 2) and in the appendix (p. 10). Contour plots showing the total χ^2 as a function of R_{burn} and peakedness p are shown in (b) and (f); the contour levels correspond to $\chi^2_{minimum} + 1, \chi^2_{minimum} + 2, \ldots$. In (c) and (g) the inferred radial distributions $S(r)$ of D^{3}He reactions in the burn regions are shown; each thick line corresponds to a best fit while the thin dashed lines show alternate fits resulting in the total χ^2 being larger than the minimum value by 1 (indicating an approximate error envelope for the best-fit profile). The corresponding surface brightness distributions $B(r)$ are shown in (d) and (h). The parameters describing the profiles $S(r)$ are $R_{burn} = 54\pm2$ μm and $p = 1.35\pm0.25$ (shot 27456) and $R_{burn} = 29\pm2.5$ μm and $p = 1.7\pm0.6$ (shot 35176).

the glass-shell implosion (where the errors quoted here and throughout reflect statistical uncertainties). As discussed in the appendix (p. 10), the shapes of the radial profiles have their largest uncertainties at $r = 0$ and the values of R_{burn} are determined much more accurately than the shape parameter.

While multiple imaging cameras are generally used to study implosion asymmetry, a single camera provides enough information to calculate a 1-D emission profile of a nominally symmetric capsule implosion. When data from more than one camera were available for an individual implosion studied in this article, the images were analyzed separately and the values of R_{burn} were averaged.

2. Comparing Nuclear Burn Data with X-Ray Data

Since x-ray imaging has been a standard diagnostic technique for decades, it is important to compare x-ray and fusion-burn profiles even though they have very different sensitivities to plasma processes and parameters. They provide valuable and complementary spatial information. The fusion burn profile $S(r)$ represents the time-integrated spatial distribution of the nuclear reaction rate

$$RR = N_D N_{3_{He}} \langle \sigma v \rangle_{D^3He}, \tag{2}$$

where N_D and $H_{3_{He}}$ are the D and ^{3}He ion number densities and $\langle \sigma v \rangle$ is the reaction rate for the D^{3}He reaction. In contrast, x-ray images primarily record emissions from heated CH near the fuel–shell interface.[14] In addition, the burn data are time integrated while the x-ray images are gated with a 40-ps window[16] (and show slightly decreasing size during the ~150-ps burn interval). Figure 105.2 provides a comparison between burn data and an x-ray image taken approximately at peak burn time for shot 35176 (analyzed in Fig. 105.1). Although the image of x-ray surface brightness itself [Fig. 105.2(b)] isn't quite symmetric, its azimuthally averaged radial profile allows us to estimate that the fuel–shell interface was located approximately at the radius $R_{xray} = 32\pm5$ μm where the brightness peaks before decreasing with increasing radius.[14] The value of R_{burn} was 29 ± 2.5 μm; considering the different nature of the two kinds of data and the ambiguities as to exactly how they should be compared, the two measurements appear approximately consistent with each other. We will see in **The Dependence of R_{burn} on Laser and Capsule Parameters** (p. 5) that the x-ray and nuclear burn profile data respond in a similar fashion to changes in the experimental conditions for a variety of implosions.
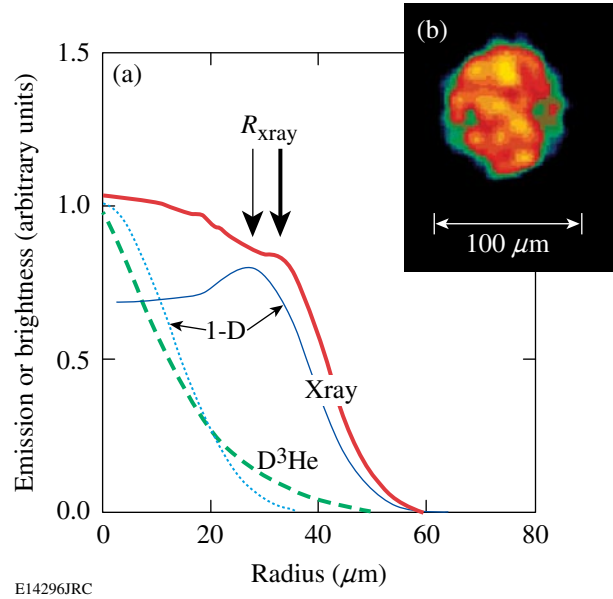

Figure 105.2
Comparison of the measured local D^{3}He emission profile, the measured x-ray surface brightness profile, and 1-D simulations for shot 35176. A 4- to 5-keV x-ray image taken at the peak nuclear burn time (a 40-ps exposure) is shown in (b), and its radial profile is shown in (a) along with a 1-D simulation (solid lines). The D^{3}He burn profile [from Fig. 105.1(g)] is also shown in (a) along with a 1-D simulation (broken lines). In all cases, the measured profiles are thick lines and the 1-D profiles are thin lines. The D^{3}He profiles are arbitrarily normalized to have the same value at $r = 0$.

3. Comparing Nuclear Burn Data and X-Ray Data with 1-D Simulations

The burn data and x-ray data can also be compared to clean 1-D simulations,[24,25] keeping in mind the fact that these simulations don't properly model such important physical processes as fuel–shell mix, preheat, or any type of implosion asymmetry and that they nearly always overestimate the nuclear burn yield.[4] In Fig. 105.2 the measured local burn profile and the measured x-ray surface brightness profile for the plastic-shell implosion 35176 are compared to simulations. The predicted value of R_{xray} is slightly smaller than the measured value (by about 15%). The predicted profile of the D^{3}He burn is quite similar in shape to the measured profile in the core [although the measured shape uncertainty is large there, as shown in Fig. 105.1(g)], but the measured emission values are considerably higher than predicted at larger radii where they contribute heavily to the yield-weighted R_{burn}: the predicted R_{burn} is about 25% smaller than the measured value. On the other hand, there are other indications that the 1-D predictions aren't exactly right: the predicted yield is about 150% higher than the measured value, while the predicted shell

areal density is 26% larger than the measured value (indicating that the shell did not converge radially as much as predicted). It will be seen in **The Dependence of R_{burn} on Laser and Capsule Parameters** (p. 5) that measured values of R_{burn} are uniformly larger than simulated values for the CH-shell implosions studied here but that the measured and predicted values agree fairly well for a wide range of glass-shell implosions (which have different implosion dynamics[40]). Possible explanations of this measurement/simulation discrepancy in terms of either systematic measurement errors (of which we have no evidence[41]) or effects not included in 1-D simulations (mix, preheat, and hydrodynamic instabilities) are considered in **Summary and Discussion** (p. 9).

The Dependence of R_{burn} on Laser and Capsule Parameters

Correlations between R_{burn} and the capsule and drive conditions allow an elucidation of some basic implosion dynamics. Systematic studies that examine the dependence of R_{burn} on laser drive energy, capsule shell material and thicknesses, capsule fill pressure, and DPP type are presented here. These external parameters are often strongly correlated with one or more fundamental quantities or processes such as ion tempera-

ture, capsule convergence, fuel density, and fuel–shell mix. For that reason, attempts were made to change only one external parameter at a time in experiments whenever possible.

1. Laser Energy

Figure 105.3(a) shows the effect of increasing laser energy for 1-ns square pulses when irradiating thin glass-shell capsules. As the energy was increased from 6 kJ to 23 kJ, R_{burn} increased from about 35 μm to 80 μm. For capsules with 19- to 20-μm CH shells and 18-atm D^{3}He fills, R_{burn} was about 30 μm; data are not yet available for illustrating variations with laser energy. The change in yield-weighted ion temperature $\langle T_{ion} \rangle$[42] probably dominates the change in R_{burn} for the glass-shell capsules, as illustrated in Fig. 105.3(b) where the data of Fig. 105.3(a) are replotted as a function of $\langle T_{ion} \rangle$. Increases in $\langle T_{ion} \rangle$ should result in a larger R_{burn} since the D^{3}He reactivity is extremely sensitive to the ion temperature. Figure 105.3(c) replots the data of Fig. 105.3(a) with the corresponding R_{burn} values from 1-D simulations. For the glass shells, 1-D simulations agree fairly well with R_{burn} measurements and show the same variation with laser energy; for the plastic shells, the 1-D values are uniformly lower than the measured R_{burn} values.

E14297JRC
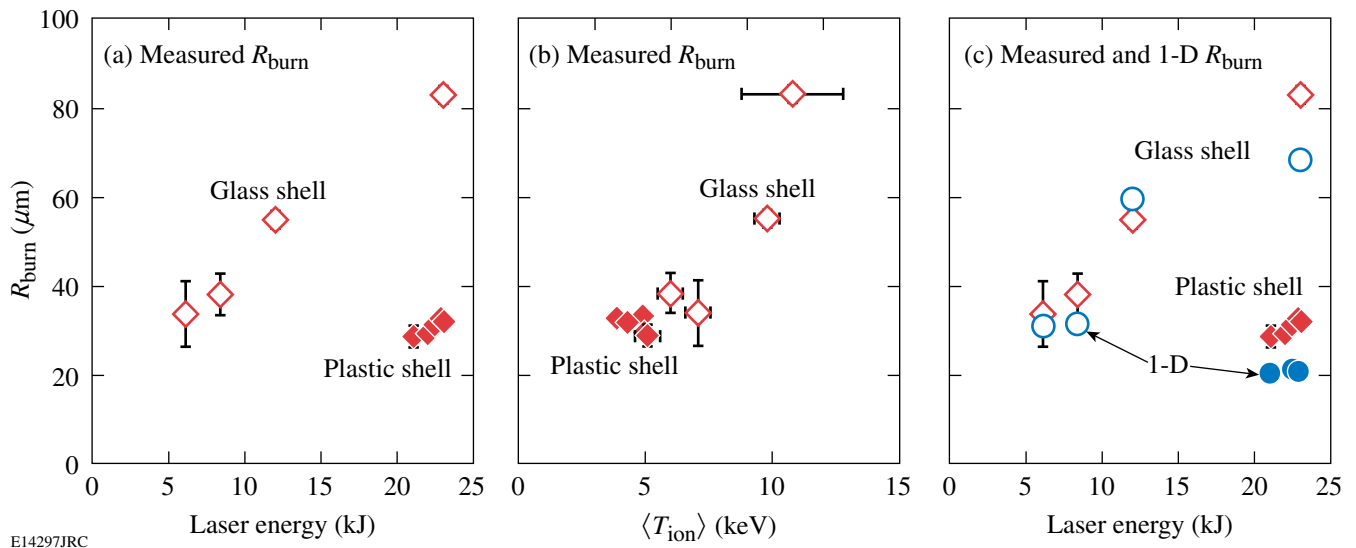
Figure 105.3
(a) Data showing the relationship of burn region size to laser energy for implosions of capsules with an 18-atm D^{3}He fill and either 20-μm plastic or 2-μm glass shells. For the thin-glass-shell, exploding-pusher implosions (open diamonds), increasing the laser energy results in a dramatically larger D^{3}He burn region radius. For the thick-CH-shell, compressive implosions, $R_{burn} \approx 30$ μm for 23-kJ laser energy (solid diamonds), but data are not currently available for lower laser energies. The ion temperature was strongly correlated with R_{burn}, as shown in (b) where R_{burn} has been plotted versus the burn-averaged ion temperature $\langle T_{ion} \rangle$ obtained with neutron time-of-flight systems. (c) Comparison of R_{burn} measurements with values from 1-D simulations (circles).

2. Capsule Fill Pressure

The effects of fill pressure changes on R_{burn} for CH-shell implosions were studied systematically. Figure 105.4(a) shows R_{burn} plotted as a function of measured $\langle \rho R \rangle$ for fill pressures of 3.6 atm and 18 atm. R_{burn} is consistently larger for the higher fill pressure. Figure 105.4(b) shows the averages of the measured values[43] for all implosions of each fill pressure in Fig. 105.4(a); the plotted values are

$$\langle R_{burn}(18\text{ atm})\rangle = 30.6 \pm 0.3 \text{ } \mu\text{m} \tag{3}$$

and

$$\langle R_{burn}(3.6\text{ atm})\rangle = 24.8 \pm 0.8 \text{ } \mu\text{m}, \tag{4}$$

where the quoted errors reflect only the statistical uncertainties and do not include any other possible systematic errors. Figure 105.4(b) also shows corresponding values of R_{xray} for which we have data. The same trend is seen in both R_{burn} and R_{xray}. Figure 105.4(c) compares values of R_{burn} and $\langle \rho R \rangle$ from 1-D simulations (solid circles for 18 atm and open circles for 3.6 atm) to the data. While the measured R_{burn} values are all larger than predicted (as for all other plastic-shell implosions studied here), there are other important differences between simulations and measurements. The 1-D simulations predict

that a reduction in fill pressure from 18 atm to 3.6 atm should result in a large increase in ρR (by ~93%) due to increased radial convergence of the shell material accompanied by a substantial decrease in R_{burn} (by ~40%) largely due to a corresponding decrease in the core size. In contrast, the data indicate a much smaller increase in ρR (by ~13%), implying little change in radial convergence of the bulk of the shell material and a moderate decrease in R_{burn} (by ~20%).

These results agree quite well with data and interpretations published by C. K. Li et al.[4] for implosions of plastic-shell capsules with DT fills of various pressures. For laser conditions and shell thicknesses similar to those examined here, it was concluded that the experimental radial convergence increased only slightly when the pressure was reduced from ~18 to 3 atm, in distinct contrast to 1-D calculations, exactly as seen here; it was suggested that the failure to achieve higher radial shell convergence with a low fill pressure was probably due to the fuel–shell mix, which converts some of the kinetic energy of radial shell movement to lateral motion. This is also consistent with the present data, which show a significant reduction in measured R_{burn} when the pressure was decreased in spite of little change in the compressed shell radius; if the radius of most of the shell is held fixed, cooling and dilution of the outer fuel region due to the mixing in of a small amount of cooler shell

E14298JRC
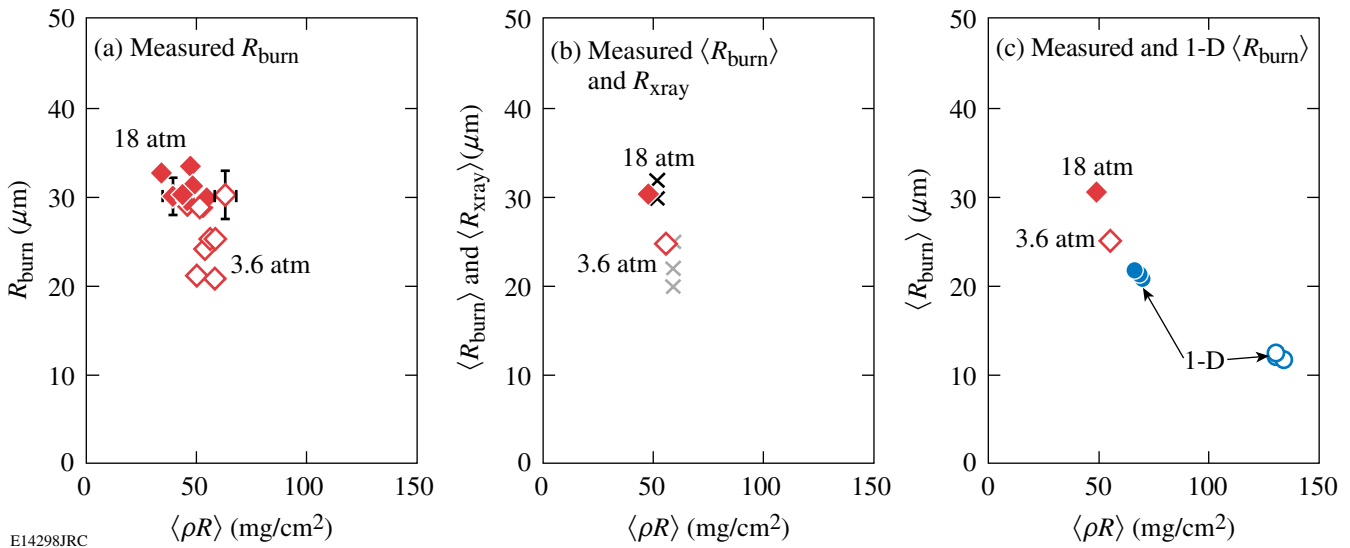
Figure 105.4
(a) A significant difference in the D³He burn size is shown for 18-atm (solid diamonds) and 3.6-atm (open diamonds) fill pressures in implosions of D³He-filled capsules with 19- to 20-μm plastic shells. R_{burn} is plotted as a function of the areal density $\langle \rho R \rangle$ measured from proton energy downshifts. (b) The averages of data in (a) are displayed with fuel–shell interface estimates (R_{xray}) for 18-atm (black ×'s) and 3.6-atm (gray ×'s) implosions, demonstrating agreement in the trends of both R_{burn} and R_{xray}. (c) When the average data are displayed with the 1-D calculated R_{burn} (circles), the same trend is present but the simulations predict lower R_{burn} values overall and a much larger increase in ρR with decreased fill pressure.

material would reduce the number of D³He reactions there and reduce R_{burn}. The 1-D simulations predict a much larger decrease in R_{burn} at a lower fill pressure without invoking mix, but this is because they predict a much larger increase in radial convergence than is measured.

Finally, it seems plausible that the increased scatter of R_{burn} at lower pressures may reflect decreased stability for those implosions. As shown in Fig. 105.4(a), the standard deviation in the 3.6-atm data is larger than that for the 18-atm data (by the ratio of 3.6 μm to 1.4 μm).

3. Distributed Phase Plates

An important goal of the OMEGA program is to improve the single and overlapping beam uniformity of the laser. As a step in that direction, the older SG3 DPP's were recently replaced with SG4 DPP's that result in a flatter on-target beam intensity [$\propto e^{-(r/353\ \mu m)^{4.1}}$, where r is radius from beam center, rather than $e^{-(r/308\ \mu m)^{2.2}}$ with the SG3 DPP].[38] To adjust for a reduction in the new spot size, the capsule radii were also reduced from ~470 to 430 μm. Figure 105.5 shows the effect of these changes on R_{burn} for several shots, plotted as a function of ρR. R_{burn} is larger for the SG3 data than for the SG4 data.

The average measurement values[43] of all implosions shown in Fig. 105.5(a) are

$$\langle R_{burn}\ (SG3)\rangle = 37.1 \pm 0.8\ \mu m \tag{5}$$

and

$$\langle R_{burn}\ (SG4)\rangle = 30.5 \pm 0.3\ \mu m \tag{6}$$

and are plotted in Fig. 105.5(b). The fact that convergence, determined from ρR,[4] is about the same for the SG3 and SG4 implosions, suggests that the reduction in R_{burn} for the SG4 DPP is largely a consequence of the smaller initial capsule radius (this is consistent with other measurements,[44] indicating that changing from SG3 DPP's to SG4 DPP's brought no significant improvement in overall implosion performance for capsules with 20-μm CH shells and 18-atm fills). The values of R_{xray} show the same kind of variation with DPP type as the values of R_{burn}, as shown in Fig. 105.5(b).[45] The 1-D R_{burn} simulations [Fig. 105.5(c), open circles for SG3 and solid circles for SG4] don't show as large a change with DPP type as the measured R_{burn} or R_{xray}. An interesting question to address would be whether the SG4 DPP reduces the scatter in 3.6-atm

E14299JRC
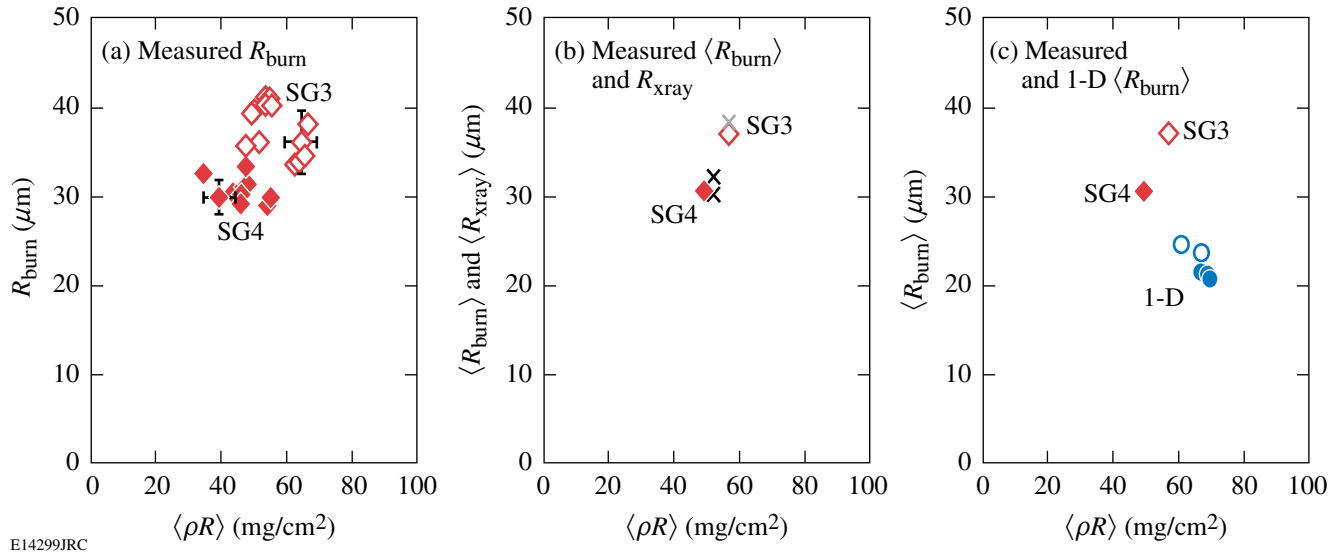
Figure 105.5
(a) Consistently smaller burn radii are produced with SG4 phase plates and targets (solid diamonds) than with SG3 DPP's (open diamonds). R_{burn} is plotted as a function of the measured areal density ρR for implosions of capsules with 19- to 20-μm-thick plastic shells and 18-atm D³He fill. (b) The averages of burn radii data in (a) are displayed with fuel–shell interface estimates (R_{xray}) from SG3 (gray ×) and SG4 (black ×) implosions,[44] demonstrating agreement in the trends of R_{burn} and R_{xray}. (c) When the average R_{burn} data are displayed with the 1-D values (circles) the same trend is present but the simulations predict lower R_{burn} values and a smaller change in R_{burn} with the change in phase plates. The reduction in R_{burn} with the change from SG3 to SG4 DPP's seems largely dominated by the reduction in initial capsule radius from ~470 to 430 μm.

capsule performance that was discussed in connection with Fig. 105.4, but comparative data are currently unavailable.

4. Capsule Shell Thickness

The shell thickness is known to have an effect upon mix and convergence.[4–9,10] Figure 105.6(a) shows the effect on R_{burn} (diamonds). The trend of these data is more fully revealed by averaging the data over capsules with similar shell thicknesses [Fig. 105.6(b)]. As illustrated, R_{burn} increases slowly as the shell thickness increases from 17 to 24 μm with the values

$$\langle R_{burn}(17\ \mu m)\rangle = 29.1\pm0.4\ \mu m, \tag{7}$$

$$\langle R_{burn}(20\ \mu m)\rangle = 30.5\pm0.5\ \mu m,\ and \tag{8}$$

$$\langle R_{burn}(24\ \mu m)\rangle = 32.8\pm1.1\ \mu m. \tag{9}$$

The convergence for the thicker-shell capsules was slightly smaller, as reflected in the fact that the ρR's of those capsules are about the same [Fig. 105.6(c)];[4] the larger burn radii for the thicker 24-μm capsules reflect the smaller convergence. R_{xray}, also plotted in Fig. 105.6(b), shows a similar trend. R_{burn} for 1-D simulations shows the same trend [triangles, Fig. 105.6(d)], but the absolute value, as remarked earlier, is significantly smaller.
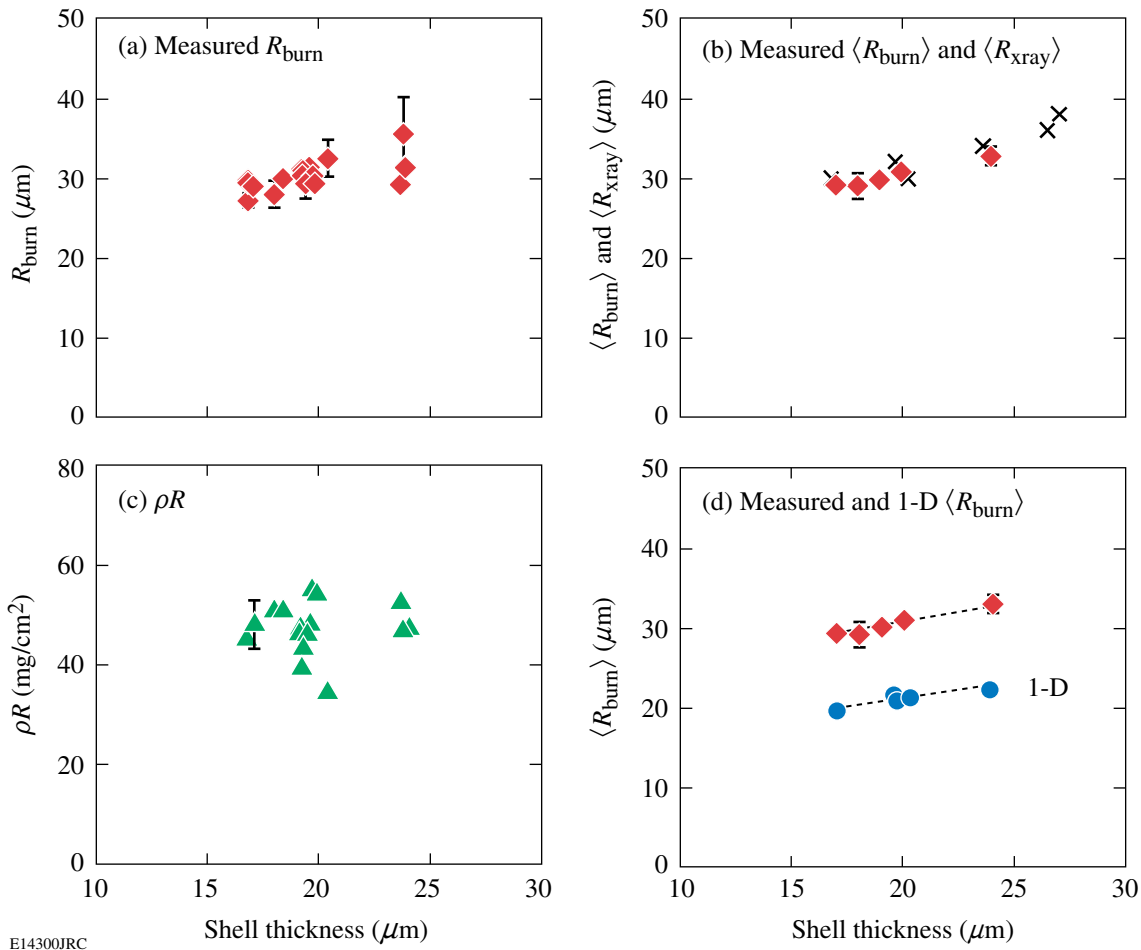
Figure 105.6

(a) The dependence of R_{burn} on plastic shell thickness provides information about mix and convergence.[2–10] (b) The trend is more obvious when the R_{burn} data for similar capsule thicknesses are averaged (diamonds). The fuel–shell interface estimates [R_{xray} (×'s)] for these implosions and others demonstrate virtually the same trend. (c) The areal densities ρR measured for the same implosions were only weakly dependent on shell thickness. (d) Predicted values of R_{burn} from 1-D simulations (circles) show the same trend as the measurements but lower values.

Summary and Discussion

In summary, we have described methods for measuring nuclear burn region sizes and presented the first measurements for a wide range of direct-drive implosion conditions, identifying systematic changes in burn region size due to changes in laser conditions and fuel capsule parameters. These measurements complement our related studies demonstrating systematic relationships between drive asymmetry, shell asymmetry, and burn asymmetry.[11,13] Collectively, this work demonstrates the practicality and usefulness of emission imaging of nuclear burn, which directly reveals the spatial distributions of the fusion reactions that are the end result of all physical processes affecting capsule implosions.

Starting with laser drive conditions, it was shown that the burn radius in capsules with thin (~2-μm) glass shells and 18-atm fills varies strongly with total laser energy, going from ~35 μm at 6 kJ to 80 μm at 23 kJ (all with 1-ns square pulses). Most measurements to date for capsules with plastic shells have been at 23 kJ, so no conclusions were drawn here about energy variations (but future experiments may investigate this). Measurements also indicated that changing from the SG3 DPP's to the SG4 DPP's for 20-μm CH shells and 18-atm fills didn't significantly change shell convergence but did result in a somewhat smaller R_{burn} that may simply reflect the smaller initial shell radius; this is consistent with other measurements,[44] indicating that changing from SG3 DPP's to SG4 DPP's brought no significant improvement in overall implosion performance for such capsules. Data for comparing R_{burn} for SG3 DPP's and SG4 DPP's with 3.6-atm fill pressures are currently unavailable.

Looking next at capsule structure, it was seen that increasing the CH shell thickness from 17 to 24 μm for 18-atm fills resulted in the burn radius increasing from 30 μm to 33 μm, a modest change largely attributed to the slightly smaller convergence of the more massive, thicker shell capsules. Measurements have not yet been made for glass capsules with different shell thicknesses, but capsules with 2-μm glass shells have burn radii 2.5 times larger than capsules with 20-μm CH shells with equal laser energy (23 kJ) and fill pressures (18 atm). It was also demonstrated that reducing the D^{3}He fill pressure from 18 to 3.6 atm in 20-μm CH shells resulted in little change in shell convergence but a significant change in burn radius (from 31 μm to 25 μm), a reduction largely attributed to increased fuel–shell mix for the more unstable 3.6-atm implosions. These data and interpretations are consistent with previous measurements of fuel ρR versus gas pressure in implosions of DT-filled capsules,[4] and we anticipate that more experiments

and comparisons with simulations will be devoted to studying and quantifying the effects of mix.

The burn data were compared with x-ray images, which have a long history with ICF and therefore provide a very important point of comparison. As discussed in the text, x-ray images and burn images reflect different aspects of the compressed capsules and there is considerable ambiguity about how they should be compared and interpreted; the x-rays are most sensitive to CH from the inner part of the shell that is in contact with, or mixed into, the hot fuel. What was found is that the characteristic radius R_{xray}, calculated as described in Ref. 14 and thought to be an indication of the inner boundary of hot CH, is usually comparable to the characteristic burn radius R_{burn}, which represents the median burn radius. There is, therefore, usually a radial overlap between the apparent burn region and the apparent inner CH location. This overlap may represent a region of atomic mix or a region where fingers of shell material extend into the fuel region, although interpretation of the x-ray images in the presence of mix is beyond the scope of this article. A crucial fact about all of the data displayed here is that wherever R_{xray} and R_{burn} measurements are available for comparison [Figs. 105.4(b), 105.5(b), and 105.6(b)], they are comparable to each other and changes in one are tracked almost precisely by changes in the other. This is a strong independent confirmation that changes in burn region size measurements reflect true changes in the compressed capsule structure.

The burn data and x-ray data were both compared with predictions of 1-D simulations. It was found that while the 1-D burn radii were similar to the measured radii for capsules with thin glass shells [Fig. 105.3(c)], the predicted burn radii for capsules with 20-μm CH shells are smaller than the measured values by about 30% for an 18-atm fill and 50% for a 3.6-atm fill (and the measured R_{xray} was also larger than predicted for the 18-atm fill). These discrepancies are qualitatively consistent with the discrepancies between predicted and measured values of areal density, which show that shell convergence is lower than predicted for all CH-shell capsules studied. The dependence on fill pressure suggests that mix or instabilities could be a contributing factor. For a given amount of radial shell convergence, mix would be expected to make the burn region smaller by cooling the outer fuel regions, but we saw in **Capsule Fill Pressure** (p. 6) that the convergence is very much smaller than predicted for lower fill pressures, probably because of mix. In addition, mix is known to truncate the burn in time, leading to a higher-than-predicted average radius during the burn interval. Another possible explanation for the simulation/measurement difference is preheat, which

results in reduced compression due to increased pressure. For the glass-shell implosions, on the other hand, the roles of mix, hydrodynamic instabilities, and preheat are expected to be substantially smaller at burn time in glass-shell implosions than in CH-shell implosions,[40] and this could account for the closer agreement between simulation and data found in all such cases. In the future we hope to see if 2-D and 3-D simulations come closer to predicting the measured average shell convergence and measured burn region size. A thorough search for systematic errors that could lead to artificially broadened burn image data has been made, but no sources of error that could be large enough to account for the discrepancy in burn radii for CH shells have yet been identified.[12,41]

Comparisons of our D^{3}He burn profiles with DT and DD burn profiles now being obtained by Disdier *et al.* on OMEGA with important new neutron imaging techniques[46] for hydrodynamically similar DT- and D$_2$-filled capsules are now being pursued and will be reported in the future. These comparisons could provide a test of consistency of the different burn imaging methods and could potentially provide information about ion temperature profiles (through the local ratios of reaction rates).

Appendix: Notes on Determining Radial Burn Profiles from Penumbral Images

As described in Ref. 11, it is possible to determine the radial profile $S(r)$ of nuclear reactions in a burn region assumed spherically symmetric by analyzing a penumbral image made using reaction products. The details of the approach used in this article are slightly different from what is described in Ref. 11, and we discuss them here, along with alternative approaches and sample analyses. We start with the idealized assumption that the imaging aperture has a perfectly defined hard edge; a penumbral image of a point source would be uniform within a circular area and zero outside. This assumption is not warranted for the imaging of DT burn with DT neutrons, but it was shown in Ref. 12 that it should be sufficiently accurate for imaging D^{3}He burn with D^{3}He protons. A few protons will scatter off the edge of the aperture, but their scattering angle is sufficiently

large that they contribute only a small, relatively flat penumbral image background that disappears when the radial derivative is taken for analysis. In **Generalization to Apertures Without "Hard Edges" and Neutron Imaging** (p. 14), we discuss how this limitation can be removed either for neutron images or for small corrections with proton images if the effects of the aperture edge can be characterized.

1. The Problem

The surface brightness of the spherically symmetric burn region is

$$B(r) = \int_{-\infty}^{\infty} S\left(\sqrt{r^2 + \ell^2}\right) d\ell. \qquad (10)$$

A penumbral image made with a hard-edged, round aperture of radius R_a is azimuthally symmetric with a radial profile $N(R)$ of detected protons per unit area, where R is the radius measured with respect to the center of the image. The radial derivative of this image can be written

$$\left.\frac{dN}{dR}\right|_{R = R_d + Mx} = -\frac{1}{4\pi M\left(L_1 + L_2\right)^2} P_c(x), \qquad (11)$$

where

$$P_c(x) = R_d \int_{-\pi}^{\pi} B\left[\sqrt{x^2 + 2R_c\left(R_c + x\right)(1 - \cos\theta)}\right]\cos\theta \, d\theta. \qquad (12)$$

In Eq. (11), L_1 and L_2 are the source–aperture and aperture–detector distances, $M = L_2/L_1$ is the geometric magnification of the penumbral camera, and $R_d \equiv (M + 1)R_a$ is the radius of the aperture image at the detector. In Eq. (12), $R_c = R_a(M + 1)/M$ is the radius of the aperture's projection at the location of the burn region, as seen from the detector, and the angle θ is measured relative to the center of this projection. As discussed in Ref. 11, $P_c(x)$ is a set of integrals through the surface brightness of the burn region along parallel paths that are curved but become straight in the limit $R_{\text{burn}}/R_c \ll 1$;

$$P_c(x) \xrightarrow{R_{\text{burn}}/R_a \to 0} P(x) = \int_{-\infty}^{\infty} B\left(\sqrt{x^2 + \ell^2}\right) d\ell. \qquad (13)$$

$P_c(x)$ can be thought of as a 1-D projection of the surface brightness $B(r)$.

$P_c(x)$ can be obtained experimentally from dN/dR through Eq. (11) and, if $R_{\text{burn}}/R_c \ll 1$, it can be used to obtain $B(r)$

through Abel inversion. Similarly, $B(r)$ can be Abel inverted to obtain the source profile $S(r)$. If R_{burn}/R_c is not negligible, then the straight-line integral $P(x)$ can be calculated approximately from $P_c(x)$ before the Abel inversion process;[47]

$$
\begin{aligned}
P(x) &\cong \sqrt{1 + x/R_c}\, P_c(x) \\
&= -4\pi M (L_1 + L_2)^2 \sqrt{\frac{R}{R_d}} \frac{dN}{dR}\bigg|_{R=R_d+Mx}.
\end{aligned}
\tag{14}
$$

A simple analytic solution for direct calculation of the double Abel inversion relating $S(r)$ to $P(x)$ was described in Ref. 48 in connection with a different application (imaging of a spherically symmetric source with a linear slit aperture);

$$
S(r) = -\frac{1}{2\pi r} \frac{dP(x)}{dx}\bigg|_{x=r}.
\tag{15}
$$

Equation (15) works well for perfect data (no noise or other distortions, infinitesimal sampling width, and $R_{\text{burn}}/R_c \ll 1$), but it isn't ideal for the data discussed in this article, even though the data generally satisfy the condition $R_{\text{burn}}/R_c \ll 1$ for several reasons. First, the statistics aren't good enough even after the data are binned [see the caption of Fig. 105.1(a)] except for the high-yield glass-shell capsules. Second, it becomes inaccurate when the data are binned, since this is equivalent to imposing a finite sampling width and results in artificial broadening of the inferred $S(r)$ and smoothing of any feature that is not much larger than the sampling width.[49] Finally, it has a problem at $r = 0$ where, even if $P(0) \equiv 0$, any noise or measurement uncertainty in the data near $r = 0$ translates into uncertainties in S that become infinite as $r \to 0$ [this is not a defect in Eq. (15), but a consequence of the fact that the central emissivity value applies to a small volume and has very little effect on line integrals through the surface brightness]. Nevertheless, the direct method works away from $r = 0$ if statistics allow and its application to the current data are illustrated in **Direct Calculation of $S(r)$** (p. 13).

2. Inferring $S(r)$ from Least-Squares Fits

As with many Abel inversion applications, the statistics issue can be improved by fitting the raw data with analytic functions that automatically smooth out some of the statistical fluctuations in $P(x)$ and simultaneously enforce reasonable behavior at the singular point $r = 0$. In Ref. 11, we proposed the use of powers of parabolas to represent $S(r)$ because these map analytically to other powers of parabolas for $P(x)$; the experimental $P(x)$ can be fit to powers of a parabola and $S(r)$ found analytically. This makes possible a range of profile shapes for $S(r)$

varying from hollow to peaked, with the limiting peaked shape being a Gaussian when the power goes to infinity, and works well because many of the data sets analyzed are statistically consistent with a Gaussian shape for $S(r)$. With many data sets there were indications that slightly better fits might be achieved with a profile more peaked than Gaussian, however, so here we take a different approach that has several advantages.

Instead of using a set of functions to fit to $P(x)$ and analytically deducing $S(r)$ using Eq. (15), we start by representing $S(r)$ by the family of super- and sub-Gaussians

$$
S(r) = S_0 e^{-(r/r_0)^{2/p}},
\tag{16}
$$

where r_0 is the "$1/e$" radius and p is the "peakedness" of the emission profile ($p = 0$ is flat, $p = 1$ is Gaussian, and $p > 1$ is more centrally peaked than Gaussian). From a given trial function $S(r)$, the functions $B(r)$, $P_c(x)$, and dN/dR can be calculated numerically using Eqs. (10), (12), and (11). For comparison with experimental data, the predicted dN/dR must then be convolved with a boxcar function to model the actual binning used in tabulating the measured data. To determine the most probable profile $S(r)$, the parameters R_d, S_0, p, and r_0 are varied and the values leading to a minimum χ^2 fit of predicted to measured dN/dR are determined along with their statistical uncertainties.[50] The deduced $S(r)$ can then be described by S_0 (or by the total yield), p, and r_0 though, as shown below, it turns out to be more useful to parameterize the radial size by the mean yield-weighted burn radius $\langle r \rangle_s = \int r S(r) r^2 dr \big/ \int S(r) r^2 dr$ or by the median burn radius $r_{S,\text{median}}$ containing half the yield rather than by r_0.

Figure 105.7 illustrates sample shapes of $S(r)$ with corresponding functions $B(r)$ and $P(x)$. We see immediately that small differences in the shape of $P(x)$ translate into much larger differences in the shape of $S(r)$, which is characteristic of inversion procedures. This means that finite errors in the raw data are amplified into much larger errors in the shape of $S(r)$, particularly for small r, though it will turn out that errors in the characteristic radius are not amplified by the inversion process.

Figure 105.8 illustrates what happens when this technique is applied to the measured dN/dR data shown in Figs. 105.1(a) and 105.1(e). Figures 105.8(a) and 105.8(d) show contour plots of total χ^2 versus p and r_0 (using the values of R_c and S_0 that minimize χ^2 at every point). In each case there is a well-defined location

E14301JRC
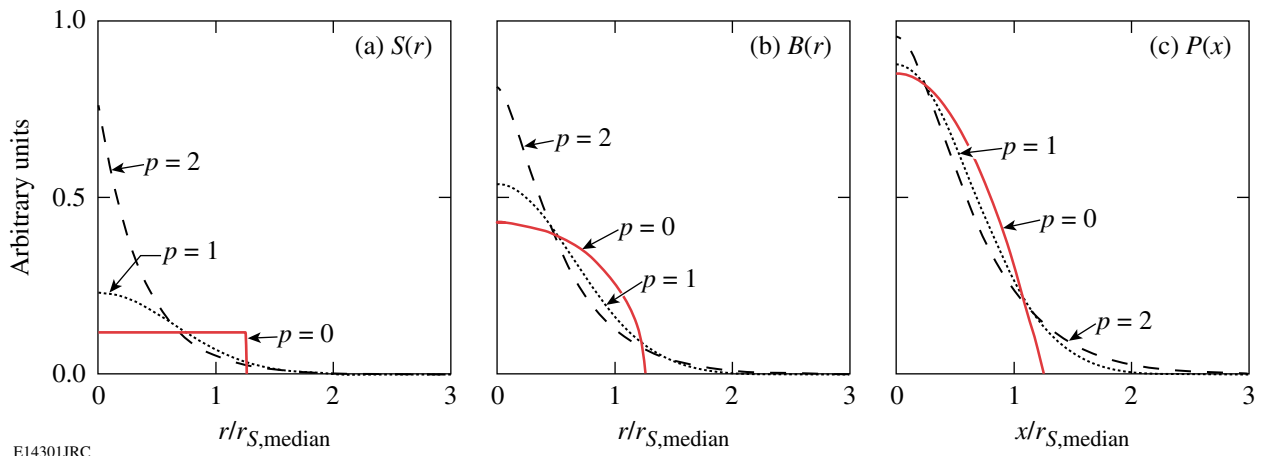
Figure 105.7

(a) $S(r)$ from Eq. (11) for $p = 0$, 1, and 2, normalized so that each curve has the same total yield. As discussed in the text, $r_{S,median}$ is the median radius (containing half the yield). (b) The corresponding curve for $B(r)$. (c) $P(x)$ for the case of no data binning. Note that hollow profiles of $S(r)$ can easily be added to this family of functions.

E14302JRC
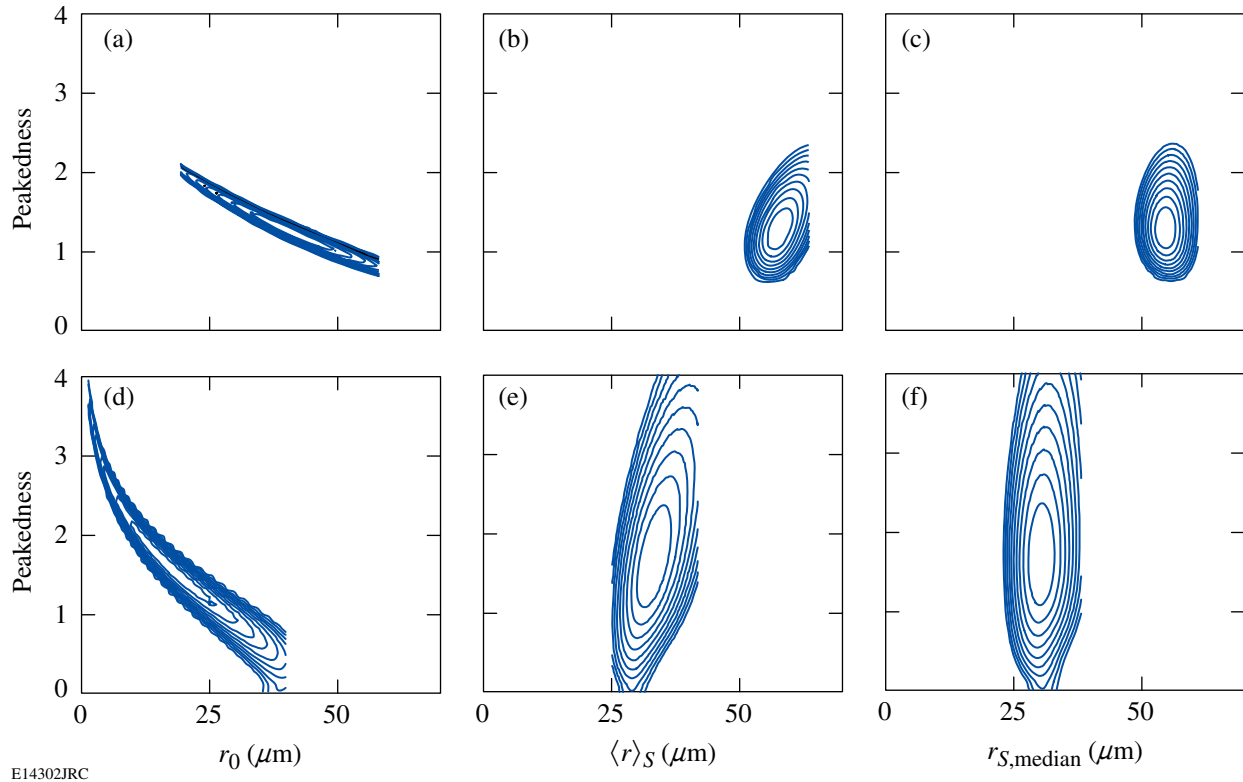
Figure 105.8

Contours of total χ^2 for fits to two real data sets as a function of the shape parameter p and either the $1/e$ radius r_0, $\langle r \rangle_S$, or $r_{S,median}$. The upper three plots correspond to shot 27456, while the lower plots correspond to shot 35176. In each case, the contour levels correspond to $\chi^2_{minimum} + 1, \chi^2_{minimum} + 2, \ldots$.

corresponding to the best fit (lowest χ^2). Figures 105.8(b) and 105.8(e) show the same contours parameterized by $\langle r \rangle_S$ rather than r_0, and Figs. 105.8(c) and 105.8(f) show parameterization by $r_{S,\text{median}}$. Notice that either $\langle r \rangle_S$ or $r_{S,\text{median}}$ is much more independent of the peakedness parameter p than r_0; the same conclusion has been reached using a wide range of functional forms for $S(r)$ and a wide range of data sets. The problem with r_0 is that a change in the central value of $S(r)$ changes the $1/e$ radius but has little effect on $P(x)$. In general, $r_{S,\text{median}}$ seems slightly better than $\langle r \rangle_S$, so henceforth we will define the characteristic burn radius R_{burn} to be $r_{S,\text{median}}$. Notice also that the percent statistical uncertainty in p is much larger than the uncertainty in R_{burn}. This is because errors in radial size do not get amplified in the inversion process, as can be shown analytically using Eq. (15) for the case $R_{\text{burn}}/R_a \ll 1$. The mean burn radius $\langle r \rangle_S$ is always exactly twice the average radius of $P(x)$; $\langle r \rangle_P \equiv \int x P(x) dx / \int P(x) dx = 0.5 \langle r \rangle_S$, regardless of the shape of $S(r)$. This means that a fractional error in $\langle r \rangle_P$ results in the same fractional error in $\langle r \rangle_S$. A similar result holds for the median radius ($r_{P,\text{median}} = 0.44 \, r_{S,\text{median}}$).

Figures 105.1(c), 105.1(g), 105.1(d), and 105.1(h) show the radial profiles of $S(r)$ and $B(r)$ corresponding to the same data and fits with uncertainties deduced from the fitting procedure. The largest uncertainties in $S(r)$ and $B(r)$ are at the center, and the uncertainties get larger with each level of inversion. The

large uncertainties at $r = 0$ simply reflect the fact that the central emissivity has very little effect on penumbral images.

The family of functions represented by Eq. (16) doesn't extend to hollow profiles, but can easily be extended in that direction through the use of different functions. In addition, more complicated radial profiles using series expansions (e.g., of Chebyshev polynomials) can be used if statistics allow. But if yields are high enough, the direct calculation of $S(r)$ becomes practical.

3. Direct Calculation of $S(r)$

Subject to the conditions discussed in **The Problem** (p. 10), Eq. (15) allows direct calculation of $S(r)$ from $P(x)$ calculated with Eq. (14). Figure 105.9 shows how this works out for the two implosions analyzed above. This approach requires knowledge of R_d; for the calculations illustrated in Fig. 105.9, the values of R_d inferred from the fitting method were used. In each case the binning width was made as small as possible, consistent with the counting statistics. Shot 27456 has a high enough proton yield ($\sim 2 \times 10^{10}$) to make this method work for $r \gtrsim R_{\text{burn}}/3$; as r is reduced, the calculated values start to fall because of the effects of binning near the central peak, and as r approaches 0 the result is completely unreliable because of the singularity in Eq. (15). The yield is much lower for shot 37156 ($\sim 4 \times 10^8$), so the statistical errors on the calculated values of $S(r)$
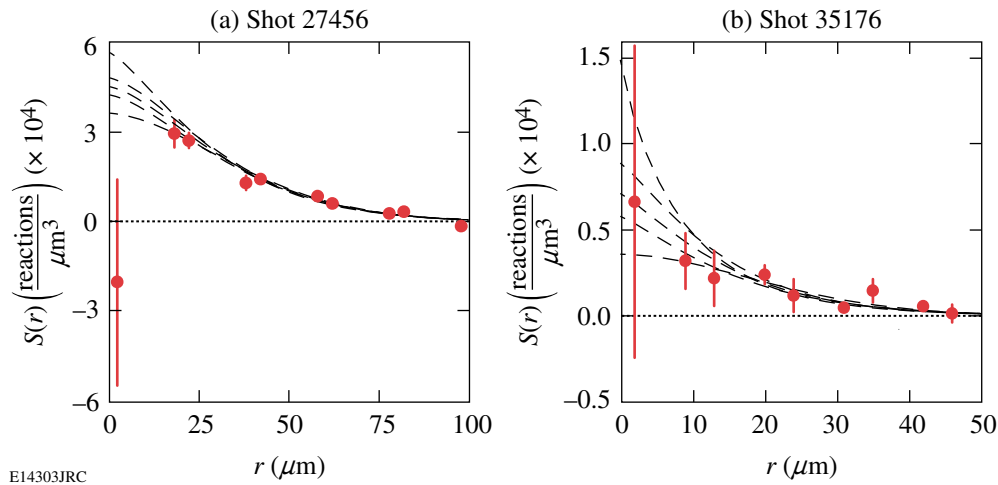
Figure 105.9

Results of applying the direct inversion method to data from shots (a) 27456 and (b) 35176. The plotted data points with error bars result from the application of Eq. (14) to the dN/dR data shown in Figs. 105.1(a) and 105.1(e); the data were binned slightly differently [with radial bins at the detector equivalent to bins in the burn region of 20 μm for (a) and 11 μm for (b), the effective ratios of bin width to R_{burn} were 0.37 and 0.41, respectively]. The uneven spacing of the data points reflects the fact that values of $S(r)$ were calculated from $P(x)$ for both positive and negative x, and S values at negative r values were reflected to positive r. The thin dashed lines correspond to the profiles shown in Figs. 105.1(d) and 105.1(h), including the error envelope.

are much larger and the shape of $S(r)$ is somewhat ill defined. The calculated value near $r = 0$ happened to be about right, but this was partly a matter of luck; changing the binning resulted in erratic values.

4. Generalization to Apertures Without "Hard Edges" and Neutron Imaging

If a penumbral-imaging aperture has a perfect, opaque edge, then the radial derivative dN/dR of a penumbral image of a point source will be a delta function. If not, and if dN/dR for a point source can be either calculated or measured, then it can be incorporated directly into the method described in **Inferring $S(r)$ from Least-Squares Fits** (p. 11). Before comparison with measured values of dN/dR, each predicted function calculated from a trial function $S(r)$ through Eqs. (10), (12), and (11) need only be convolved by an appropriate smearing function F before being convolved by the boxcar function that models the data binning. $F(R')$ is simply dN/dR for a point source evaluated at $R = R_d + R'$ and normalized to have unit integral. If the direct-calculation method is to be used instead of the least-squares fitting method, then the data must be deconvolved to remove the effect of F.

REFERENCES

1. J. Nuckolls *et al.*, Nature **239**, 139 (1972).

2. J. D. Lindl, *Inertial Confinement Fusion: The Quest for Ignition and Energy Gain Using Indirect Drive* (Springer-Verlag, New York, 1998).

3. S. Atzeni and J. Meyer-ter-Vehn, *The Physics of Inertial Fusion: Beam Plasma Interaction, Hydrodynamics, Hot Dense Matter*, International Series of Monographs on Physics (Clarendon Press, Oxford, 2004).

4. C. K. Li, F. H. Séguin, J. A. Frenje, S. Kurebayashi, R. D. Petrasso, D. D. Meyerhofer, J. M. Soures, J. A. Delettrez, V. Yu. Glebov, P. B. Radha, F. J. Marshall, S. P. Regan, S. Roberts, T. C. Sangster, and C. Stoeckl, Phys. Rev. Lett. **89**, 165002 (2002).

5. D. D. Meyerhofer, J. A. Delettrez, R. Epstein, V. Yu. Glebov, V. N. Goncharov, R. L. Keck, R. L. McCrory, P. W. McKenty, F. J. Marshall, P. B. Radha, S. P. Regan, S. Roberts, W. Seka, S. Skupsky, V. A. Smalyuk, C. Sorce, C. Stoeckl, J. M. Soures, R. P. J. Town, B. Yaakobi, J. D. Zuegel, J. Frenje, C. K. Li, R. D. Petrasso, D. G. Hicks, F. H. Séguin, K. Fletcher, S. Padalino, M. R. Freeman, N. Izumi, R. Lerche, T. W. Phillips, and T. C. Sangster, Phys. Plasmas **8**, 2251 (2001).

6. P. B. Radha, J. Delettrez, R. Epstein, V. Yu. Glebov, R. Keck, R. L. McCrory, P. McKenty, D. D. Meyerhofer, F. Marshall, S. P. Regan, S. Roberts, T. C. Sangster, W. Seka, S. Skupsky, V. Smalyuk, C. Sorce, C. Stoeckl, J. Soures, R. P. J. Town, B. Yaakobi, J. Frenje, C. K. Li, R. Petrasso, F. Séguin, K. Fletcher, S. Padalino, C. Freeman, N. Izumi, R. Lerche, and T. W. Phillips, Phys. Plasmas **9**, 2208 (2002).

7. S. P. Regan, J. A. Delettrez, F. J. Marshall, J. M. Soures, V. A. Smalyuk, B. Yaakobi, V. Yu. Glebov, P. A. Jaanimagi, D. D. Meyerhofer, P. B. Radha, W. Seka, S. Skupsky, C. Stoeckl, R. P. J. Town, D. A. Haynes, Jr., I. E. Golovkin, C. F. Hooper, Jr., J. A. Frenje, C. K. Li, R. D. Petrasso, and F. H. Séguin, Phys. Rev. Lett. **89**, 085003 (2002).

8. C. R. Christensen, D. C. Wilson, C. W. Barnes, G. P. Grim, G. L. Morgan, M. D. Wilke, F. J. Marshall, V. Yu. Glebov, and C. Stoeckl, Phys. Plasmas **11**, 2771 (2004).

9. D. C. Wilson, C. W. Cranfill, C. Christensen, R. A. Forster, R. R. Peterson, H. M. Hoffman, G. D. Pollak, C. K. Li, F. H. Séguin, J. A. Frenje, R. D. Petrasso, P. W. McKenty, F. J. Marshall, V. Yu. Glebov, C. Stoeckl, G. J. Schmid, N. Izumi, and P. Amendt, Phys. Plasmas **11**, 2723 (2004).

10. P. B. Radha, V. N. Goncharov, T. J. B. Collins, J. A. Delettrez, Y. Elbaz, V. Yu. Glebov, R. L. Keck, D. E. Keller, J. P. Knauer, J. A. Marozas, F. J. Marshall, P. W. McKenty, D. D. Meyerhofer, S. P. Regan, T. C. Sangster, D. Shvarts, S. Skupsky, Y. Srebro, R. P. J. Town, and C. Stoeckl, Phys. Plasmas **12**, 032702 (2005).

11. F. H. Séguin, J. L. DeCiantis, J. A. Frenje, S. Kurebayashi, C. K. Li, J. R. Rygg, C. Chen, V. Berube, B. E. Schwartz, R. D. Petrasso, V. A. Smalyuk, F. J. Marshall, J. P. Knauer, J. A. Delettrez, P. W. McKenty, D. D. Meyerhofer, S. Roberts, T. C. Sangster, K. Mikaelian, and H. S. Park, Rev. Sci. Instrum. **75**, 3520 (2004).

12. J. L. DeCiantis, F. H. Séguin, J. A. Frenje, V. Berube, M. J. Canavan, C. D. Chen, S. Kurebayashi, C. K. Li, J. R. Rygg, B. E. Schwartz, R. D. Petrasso, J. A. Delettrez, S. P. Regan, V. A. Smalyuk, J. P. Knauer, F. J. Marshall, D. D. Meyerhofer, S. Roberts, T. C. Sangster, C. Stoeckl, K. Mikaelian, H. S. Park, and H. F. Robey, "Proton Core Imaging of the Nuclear Burn in Inertial Confinement Fusion Implosions," to be published in Review of Scientific Instruments (see also LLE Review Quarterly Report **104**, p. 197).

13. F. H. Séguin, J. L. DeCiantis, J. A. Frenje, C. K. Li, J. R. Rygg, C. D. Chen, R. D. Petrasso, V. A. Smalyuk, F. J. Marshall, J. A. Delettrez, J. P. Knauer, P. W. McKenty, D. D. Meyerhofer, S. Roberts, T. C. Sangster, H. S. Mikaelian, and H. S. Park, Bull. Am. Phys. Soc. **49**, 63 (2004); *ibid.* "Measured Effects of Drive Asymmetry and Shell Asymmetry on Nuclear Burn Region Symmetry in Direct-Drive ICF implosions," to be submitted to Physics of Plasmas.

14. S. P. Regan, J. A. Delettrez, R. Epstein, P. A. Jaanimagi, B. Yaakobi, V. A. Smalyuk, F. J. Marshall, D. D. Meyerhofer, W. Seka, D. A. Haynes, Jr., I. E. Golovkin, and C. F. Hooper, Jr., Phys. Plasmas **9**, 1357 (2002).

15. D. Ress *et al.*, Rev. Sci. Instrum. **66**, 579 (1995).

16. V. A. Smalyuk, T. R. Boehly, L. S. Iwan, T. J. Kessler, J. P. Knauer, F. J. Marshall, D. D. Meyerhofer, C. Stoeckl, B. Yaakobi, and D. K. Bradley, Rev. Sci. Instrum. **72**, 635 (2001).

17. F. J. Marshall, J. A. Delettrez, R. Epstein, V. Yu. Glebov, D. R. Harding, P. W. McKenty, D. D. Meyerhofer, P. B. Radha, W. Seka, S. Skupsky,

V. A. Smalyuk, J. M. Soures, C. Stoeckl, R. P. Town, B. Yaakobi, C. K. Li, F. H. Séguin, D. G. Hicks, and R. D. Petrasso, Phys. Plasmas **7**, 2108 (2000).

18. F. H. Séguin, C. K. Li, J. A. Frenje, S. Kurebayashi, R. D. Petrasso, F. J. Marshall, D. D. Meyerhofer, J. M. Soures, T. C. Sangster, C. Stoeckl, J. A. Delettrez, P. B. Radha, V. A. Smalyuk, and S. Roberts, Phys. Plasmas **9**, 3558 (2002).

19. F. H. Séguin, J. A. Frenje, C. K. Li, D. G. Hicks, S. Kurebayashi, J. R. Rygg, B.-E. Schwartz, R. D. Petrasso, S. Roberts, J. M. Soures, D. D. Meyerhofer, T. C. Sangster, J. P. Knauer, C. Sorce, V. Yu. Glebov, C. Stoeckl, T. W. Phillips, R. J. Leeper, K. Fletcher, and S. Padalino, Rev. Sci. Instrum. **74**, 975 (2003).

20. F. H. Séguin, C. K. Li, D. G. Hicks, J. A. Frenje, K. M. Green, R. D. Petrasso, J. M. Soures, D. D. Meyerhofer, V. Yu. Glebov, C. Stoeckl, P. B. Radha, S. Roberts, C. Sorce, T. C. Sangster, M. D. Cable, S. Padalino, and K. Fletcher, Phys. Plasmas **9**, 2725 (2002).

21. C. K. Li, F. H. Séguin, J. A. Frenje, R. D. Petrasso, R. Rygg, S. Kurebayashi, B. Schwartz, R. L. Keck, J. A. Delettrez, J. M. Soures, P. W. McKenty, V. N. Goncharov, J. P. Knauer, F. J. Marshall, D. D. Meyerhofer, P. B. Radha, S. P. Regan, T. C. Sangster, W. Seka, and C. Stoeckl, Phys. Plasmas **10**, 1919 (2003).

22. R. D. Petrasso, J. A. Frenje, C. K. Li, F. H. Séguin, J. R. Rygg, B. E. Schwartz, S. Kurebayashi, P. B. Radha, C. Stoeckl, J. M. Soures, J. Delettrez, V. Yu. Glebov, D. D. Meyerhofer, and T. C. Sangster, Phys. Rev. Lett. **90**, 095002 (2003).

23. C. K. Li, D. G. Hicks, F. H. Séguin, J. A. Frenje, R. D. Petrasso, J. M. Soures, P. B. Radha, V. Yu. Glebov, C. Stoeckl, D. R. Harding, J. P. Knauer, R. L. Kremens, F. J. Marshall, D. D. Meyerhofer, S. Skupsky, S. Roberts, C. Sorce, T. C. Sangster, T. W. Phillips, M. D. Cable, and R. J. Leeper, Phys. Plasmas **7**, 2578 (2000).

24. M. C. Richardson, P. W. McKenty, F. J. Marshall, C. P. Verdon, J. M. Soures, R. L. McCrory, O. Barnouin, R. S. Craxton, J. Delettrez, R. L. Hutchison, P. A. Jaanimagi, R. Keck, T. Kessler, H. Kim, S. A. Letzring, D. M. Roback, W. Seka, S. Skupsky, B. Yaakobi, S. M. Lane, and S. Prussin, in *Laser Interaction and Related Plasma Phenomena*, edited by H. Hora and G. H. Miley (Plenum Publishing, New York, 1986), Vol. 7, pp. 421–448.

25. J. Delettrez, R. Epstein, M. C. Richardson, P. A. Jaanimagi, and B. L. Henke, Phys. Rev. A **36**, 3926 (1987).

26. K. A. Nugent and B. Luther-Davies, J. Appl. Phys. **58**, 2508 (1985).

27. D. Ress *et al.*, Rev. Sci. Instrum. **59**, 1694 (1988).

28. R. A. Lerche *et al.*, Laser Part. Beams **9**, 99 (1991).

29. L. Disdier, R. A. Lerche, J. L. Bourgade, and V. Yu. Glebov, Rev. Sci. Instrum. **75**, 2134 (2004).

30. Y.-W. Chen *et al.*, Opt. Commun. **73**, 337 (1989).

31. M. Nakai *et al.*, Rev. Sci. Instrum. **61**, 3235 (1990).

32. A. P. Fews *et al.*, Phys. Rev. Lett. **73**, 1801 (1994).

33. T. R. Boehly, D. L. Brown, R. S. Craxton, R. L. Keck, J. P. Knauer, J. H. Kelly, T. J. Kessler, S. A. Kumpan, S. J. Loucks, S. A. Letzring, F. J. Marshall, R. L. McCrory, S. F. B. Morse, W. Seka, J. M. Soures, and C. P. Verdon, Opt. Commun. **133**, 495 (1997).

34. Y. Lin, T. J. Kessler, and G. N. Lawrence, Opt. Lett. **20**, 764 (1995).

35. S. Skupsky, R. W. Short, T. Kessler, R. S. Craxton, S. Letzring, and J. M. Soures, J. Appl. Phys. **66**, 3456 (1989).

36. S. P. Regan, J. A. Marozas, R. S. Craxton, J. H. Kelly, W. R. Donaldson, P. A. Jaanimagi, D. Jacobs-Perkins, R. L. Keck, T. J. Kessler, D. D. Meyerhofer, T. C. Sangster, W. Seka, V. A. Smalyuk, S. Skupsky, and J. D. Zuegel, J. Opt. Soc. Am. B **22**, 998 (2005).

37. T. R. Boehly, V. A. Smalyuk, D. D. Meyerhofer, J. P. Knauer, D. K. Bradley, R. S. Craxton, M. J. Guardalben, S. Skupsky, and T. J. Kessler, J. Appl. Phys. **85**, 3444 (1999).

38. R. A. Forties and F. J. Marshall, Rev. Sci. Instrum. **76**, 073505 (2005).

39. C. K. Li, F. H. Séguin, D. G. Hicks, J. A. Frenje, K. M. Green, S. Kurebayashi, R. D. Petrasso, D. D. Meyerhofer, J. M. Soures, V. Yu. Glebov, R. L. Keck, P. B. Radha, S. Roberts, W. Seka, S. Skupsky, C. Stoeckl, and T. C. Sangster, Phys. Plasmas **8**, 4902 (2001).

40. M. D. Rosen and J. H. Nuckolls, Phys. Fluids **22**, 1393 (1979).

41. Calculations showed insignificant image broadening associated with proton scattering in the capsule, aperture, and detector filters, while experiments showed no indication of different results with different aperture size or magnification. Neither experiments nor simulations revealed any serious field effects.[12]

42. V. Yu. Glebov, C. Stoeckl, T. C. Sangster, S. Roberts, G. J. Schmid, R. A. Lerche, and M. J. Moran, Rev. Sci. Instrum. **75**, 3559 (2004).

43. The plotted R_{burn} and $\langle \rho R \rangle$ results for individual implosions already represent a mean value of the measurements obtained from that implosion; there were as many as six measurements of R_{burn}[12] and five of ρR for each implosion. When the mean value is calculated for an implosion type, all these measurements are weighted equally.

44. S. P. Regan, J. A. Delettrez, V. Yu. Glebov, V. N. Goncharov, J. A. Marozas, F. J. Marshall, P. W. McKenty, D. D. Meyerhofer, P. B. Radha, T. C. Sangster, V. A. Smalyuk, C. Stoeckl, J. A. Frenje, C. K. Li, R. D. Petrasso, and F. H. Séguin, Bull. Am. Phys. Soc **49**, 62 (2004).

45. The SG3 R_{xray} data point was taken from a hydrodynamically equivalent 15-atm, D_2 gas-fill implosion (shot 22546).[7] The substitution is reasonable; similar R_{xray} results are obtained from D_2 and D^3He gas implosions (J. L. DeCiantis, "Proton Emission Imaging of the Nuclear Burn in Inertial Confinement Fusion Experiments," M.S. thesis, Massachusetts Institute of Technology, 2005).

46. L. Disdier, A. Rouyer, I. Lantuejoul, O. Landuas, J. L. Bourgade, T. C. Sangster, V. Yu. Glebov, and R. A. Lerche, "Inertial Confinement Fusion Neutron Images," to be published in Physics of Plasmas.

47. The correction factor $\sqrt{1 + x/R_c} = \sqrt{R/R_d}$ in Eq. (14) can be found by calculating the integrals for a circular disk with uniform surface brightness and keeping the lowest-order terms. Since any radial profile of surface brightness can be made up from a superposition of disks, the result is independent of radial profile. This is a better correction than that shown in Eq. (7) of Ref. 11, which was found empirically. In any case, the correction is too small to be important for the data considered here.

48. C. M. Vest and D. G. Steel, Opt. Lett. **3**, 54 (1978).

49. M. M. Mueller, Opt. Lett. **4**, 351 (1979).

50. The parameter R_d is the radius on the detector corresponding to the center of the penumbra. In principle, this value is known in advance from the dimensions of the imaging system, but it must be known very accurately, and including it as a fit parameter allows for the possibility of small errors in camera positioning. Two more parameters that need to be known are the coordinates of the center of the penumbral image. This is found by doing a simplified version of the analysis described in the text, but varying the assumed center coordinates and finding the values that give the smallest burn radius (since any displacement from the true center broadens the average penumbra and the inferred burn radius).

Rayleigh–Taylor Growth Measurements of 3-D Modulations in a Nonlinear Regime

Introduction

Rayleigh–Taylor (RT)[1,2] instability is of critical importance in inertial confinement fusion (ICF)[3] and astrophysics.[4] In ICF, the RT instability leads to shell disruption and performance degradation of spherically imploding targets.[3] In astrophysics, when a star becomes a supernova, the outer shell is pushed by the inner exploding core and heavy material from the inner core appears in the outer shell because of the RT mixing process.[4] In the linear regime of classical RT instability,[3,5] small initial modulations grow exponentially in time with the growth rate $\gamma = (Akg)^{0.5}$, where k is the modulation wave number, g is the target acceleration, and A is the Atwood number defined as $A = (\rho_h - \rho_l)/(\rho_h + \rho_l)$, where ρ_h and ρ_l are the densities of heavy and light fluids, respectively. Most ICF-related cases involve ablative drive in which the growth rate $\gamma = \alpha(kg)^{0.5} - \beta k V_a$ is stabilized by the ablation term $\beta k V_a$, where V_a is the ablation velocity and α and β are constants.[6,7] This growth rate is an approximation of a more exact formula in Ref. 7. The growth rates of linear RT instability have been measured in both classical[5] and ablative regimes.[8–12] The indication of nonlinearity in RT growth in real space is that the modulations develop into bubbles (penetration of the lighter fluid into the heavier) and spikes (penetration of the heavier fluid into the lighter).[13] In Fourier space, this is equivalent to the harmonics generation of initial fundamental spatial modes. As the RT instability further progresses, the two fluids mix in turbulent and chaotic regimes.[14–17] There are two modeling approaches for nonlinear RT instability: a modal one[18–20] that describes the evolution in Fourier space and a bubble competition and merger that describes instability in real space.[17,21–24] In Fourier space, Haan's model[18] [see Fig. 105.10(a)] predicts that the spectral amplitudes of 3-D, broadband modulations grow exponentially with the RT growth rates of $\gamma(k)$ until they reach the saturation levels[18,25] $S_k = 2/Lk^2$ (L is the size of the analysis
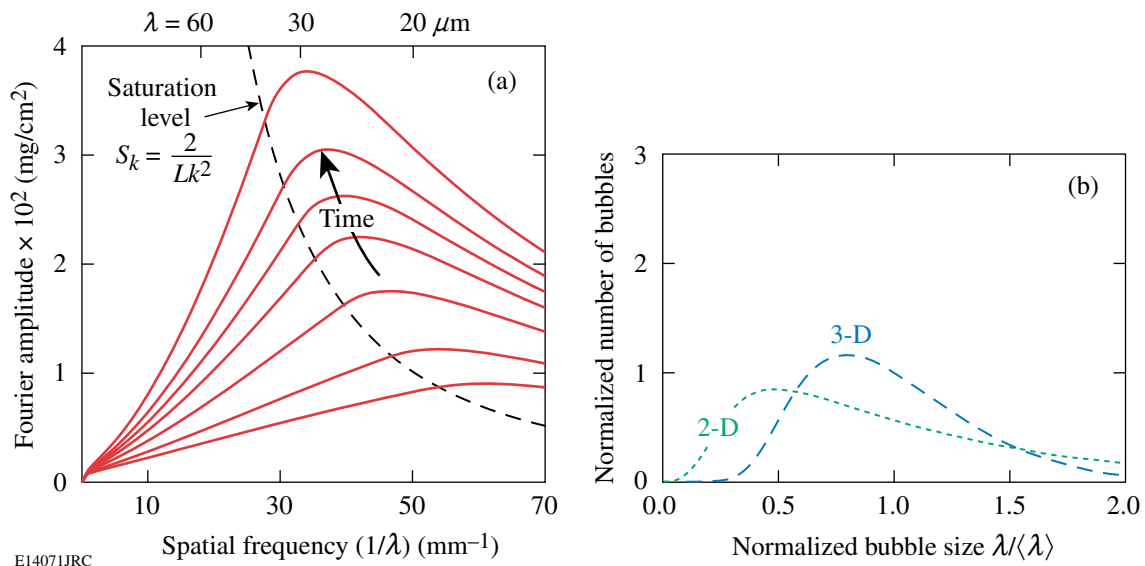

Figure 105.10
(a) Fourier spectra of target areal-density modulations driven by Rayleigh–Taylor instability, as predicted by Haan's model.[18] The dashed line is Haan's saturation level $S_k = 2/Lk^2$ ($L = 400$ μm is the size of analysis box) multiplied by the calculated target density to be converted to areal density.[25] (b) Bubble size distributions as a function of the bubble size normalized to the average bubble size $\lambda/\langle\lambda\rangle$ as predicted by 2-D (dotted curve) and 3-D (dashed curve) bubble competition models in a self-similar regime.[27]

box), after which they grow linearly in time with the saturation velocities[18,26] $V_s(k) = S_k\gamma(k)$. The short-wavelength modes grow initially most rapidly and quickly saturate at levels S_k while very long-wavelength modes grow more slowly. As a result, the midwavelength modes have the largest growth factors, producing a peak in the spectrum. As the evolution continues, this peak moves to longer wavelengths, as shown in Fig. 105.10(a). Haan's model applies in the weakly nonlinear regime for broadband modulation amplitudes around the saturation levels.[25] In real space, bubble competition models predict that smaller bubbles (with smaller nonlinear velocities) are taken over by larger bubbles (with higher nonlinear velocities) through bubble competition and the bubble merger processes.[17,21–24] As a result, the average size of the modulations shifts to longer wavelengths as the modulations grow. The real-space models predict that the bubble sizes and amplitudes evolve with a self-similar behavior in an advanced nonlinear regime.[24,27,28] The self-similar behavior predicts that the distribution function $f(\lambda/\langle\lambda\rangle)$ of the bubble size normalized to the average bubble size $\lambda/\langle\lambda\rangle$ is constant as the modulation average size and average amplitude grow.[24,27,28] Figure 105.10(b) shows self-similar bubble size distributions predicted by 2-D and 3-D bubble competition models.[24,27] It should be noted here that Haan's model is applicable for broadband initial spectra, which can contain both long and short wavelengths. The bubble competition model is mainly applicable for initial spectra dominated by short wavelengths, whereas long wavelengths are mainly produced by bubble merger processes.[27] This article presents results of nonlinear RT experiments[25,26,28,29] performed over several years on the OMEGA Laser System[30] and shows new results in which planar targets were directly driven by laser light and 3-D broadband modulation growth was measured near nonlinear saturation levels. The initial broadband modulations

were dominated by short wavelengths in these experiments; therefore, both real-space (bubble) and Fourier-space models can be used for comparison with experimental data. This article compares measured RT evolution with that predicted by both Fourier- and real-space nonlinear RT models. The experiments with initial broadband modulations dominated by long-wavelengths modes are described elsewhere.[26]

In this article, **Experimental Configuration** (p. 18) describes the experimental configuration and measurement technique. **Experimental Results** are discussed on p. 19 and **Conclusions** are presented on p. 24.

Experimental Configuration

In the experiments, initially smooth, 1-mm-diam CH targets with thicknesses ranging from 20 to 50 μm were driven with 12-ns and 3-ns square pulses at laser intensities of ~5 $\times$ 10^{13} W/cm^2 and ~2 $\times$ 10^{14} W/cm^2, respectively, on the OMEGA Laser System.[30] The modulation growth was measured with through-foil, x-ray radiography.[29] The backlighter x rays that probe target modulations were imaged by an 8-μm pinhole array onto a framing camera, allowing up to eight images with a temporal resolution of ~80 ps and a spatial resolution of ~10 μm to be captured at different times in each shot.[29] The initial target modulations, used for RT growth measurements, were imprinted by laser-beam nonuniformities created by using standard distributed phase plates[31] (SG8 DPP's) during the first several hundred picoseconds of the drive. Figure 105.11 shows a measured equivalent-target-plane image of the laser beam with the DPP [Fig. 105.11(a)] along with its Fourier spectrum [Fig. 105.11(b)]. The beam with DPP has broadband modulations with spatial frequencies up to ~320 mm^{-1}, corresponding to the smallest spatial size of ~3 μm and an intensity
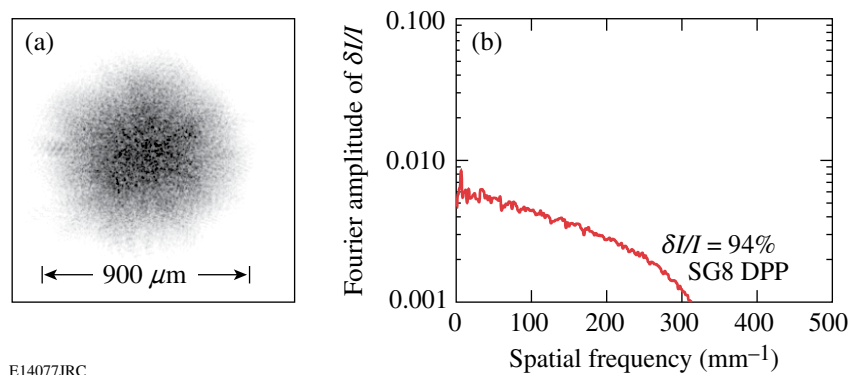

E14077JRC

Figure 105.11

(a) The equivalent-target-plane image of the laser beam with a distributed phase plate (SG8 DPP). (b) Fourier spectrum of relative intensity [$\delta I/I$] modulations of the laser beam with a SG8 DPP. The smallest size of intensity modulations in the beam is ~3 μm and it has an intensity modulation σ_{rms} of ~94%.

modulation σ_{rms} of ~94%. The amplitudes of target modulations $a_t(k)$ are proportional to the amplitudes of relative laser modulations[32,33] $a_l(k)$, $a_t(k) = E(k)a_l(k)$, where $E(k) \sim 1/k$ is the imprint efficiency.[33–35] Some experiments used smoothing by spectral dispersion (SSD)[36] and polarization smoothing (PS)[37] to vary the spectrum of target modulations to study the dependence of the RT growth on the initial conditions. Polarization smoothing reduces the modulations of most laser spatial frequencies by a factor[37] of $\sqrt{2}$, while SSD reduces high-spatial frequency modulations more strongly than the low-spatial frequency modulations.[36]

The typical optical-depth (OD) images (obtained by taking a natural logarithm of intensity-converted, framing-camera images) of x-ray radiographs are shown in Fig. 105.12 for an experiment with a 20-μm-thick target driven with a 3-ns square pulse shape.[29] A Weiner filter (based on measured system resolution and noise) was applied to these images to remove noise and deconvolve the system's modulation transfer function to recover target OD modulations.[29] The measured target OD variations are proportional to the variations of target areal density $\delta[\rho R]$; $\delta[\mathrm{OD}(t)] = \mu_{CH}(E)\delta[\rho R(t)]$, where $\mu_{CH}(E)$ is the CH target mass absorption rate at x-ray energy E used
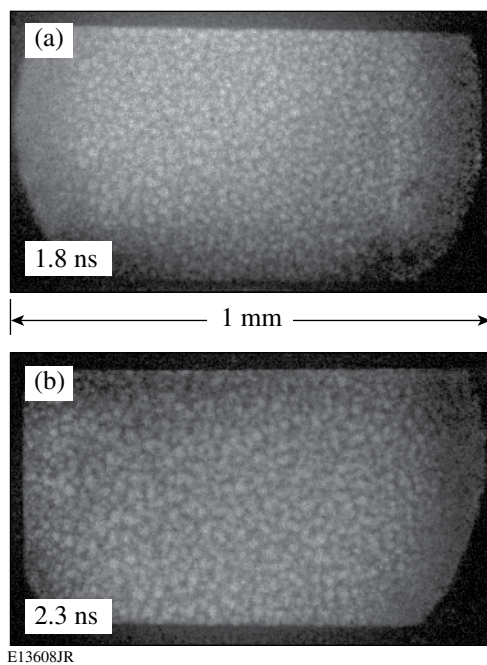

Figure 105.12
X-ray framing-camera images of RT growth modulations measured at (a) 1.8 and (b) 2.3 ns in a 20-μm-thick target driven by a 3-ns laser pulse at an intensity of ~2×10^{14} W/cm^2. Central, 400-μm-square parts of the images were taken for analysis.

for backlighting and t is the time of the measurement. The areal-density $\delta[\rho R(t)]$ modulations were obtained by dividing measured OD modulations by target mass absorption rates. The RT growth of the initial nonuniformities was analyzed in the central parts (with a box size of up to 400 μm) of these images where the average drive is uniform.

As laser light is applied to the target, the pressure created by the target ablation launches a shock wave that compresses the target.[35] Any nonuniformities in the laser drive are imprinted into the target modulations at this time.[32–35] When the shock front reaches the rear surface of the target, it sends the rarefaction wave back to the ablation surface; shortly thereafter, the target begins to accelerate (in these experiments after around 0.5 to 1 ns, depending on target thickness). During the acceleration phase, the ablation-surface modulations grow exponentially because of Rayleigh–Taylor instability.[1–3] At later times these modulations become detectable with our diagnostics as their evolution enters the nonlinear regime. [25,26,28,29]

Experimental Results
Figure 105.13 shows the Fourier spectra of growing target areal-density modulations $\delta[\rho R(t)]$ measured in 20-μm-thick targets [Figs. 105.13(a) and 105.13(b)] and a 40-μm-thick target [Fig. 105.13(c)] driven with a 3-ns square laser drive pulse at an intensity of ~2×10^{14} W/cm^2 (Refs. 25 and 29). The smoothing conditions included DDP's, SSD, and PS on a shot shown in Fig. 105.13(a) and DPP's only on shots in Figs. 105.13(b) and 105.13(c). The dashed lines show Haan's saturation levels[18] (as described in the **Introduction** on p. 17). The smoothing conditions were varied to determine whether the shapes of modulation Fourier spectra in the nonlinear regime depend on the initial conditions. The target thickness was varied to measure the sensitivity of modulation Fourier spectra to drive conditions since target acceleration and growth rates depend on the target thickness. The shapes of the measured spectra are very similar to Haan's model predictions in all shots[25,29] (compare with Fig. 105.10). These shapes are insensitive to initial and drive conditions, as predicted by Haan's model. In the shot with more laser smoothing [Fig. 105.13(a)], the modulations are detected later than in the shot with less smoothing [Fig. 105.13(b)], and the growth is shifted by ~1 ns. In the shot with a 40-μm-thick target [Fig. 105.13(c)], the growth is detected later than with a 20-μm-thick target because of the reduced growth in the thicker target [compare Figs. 105.13(b) and 105.13(c)]. At later times, the measured modulation level becomes comparable with the target thickness and the effects of finite target thickness significantly slow the growth,[29] as shown in Fig. 105.14(a). The amplitudes of short-scale modulations

even decrease toward the end of the drive (~2.8 ns) because of this effect.[29] The measured target images [see Figs. 105.14(b) and 105.14(c)] show that smaller bubbles start to merge as larger bubbles grow during this time. In these earlier 1999 experiments, two questions still remained: (1) Do the bubble-merger processes happen around saturation levels or do they begin in a more deeply nonlinear regime (as it was considered in bubble-competition models)? (2) Is the bubble competition accompanied by a reduction of the short-wavelength modula-

tions [as shown in Fig. 105.14(a)], or is this reduction because of the finite target thickness effects?

To address these questions and to make a connection between Fourier-space and real-space models, new experiments were conducted[26] with thicker targets driven to much higher amplitudes with longer pulses in a deeper nonlinear regime. Figure 105.15 shows examples of the measured images[26] for a shot with a 50-μm-thick target driven by a 12-ns square pulse
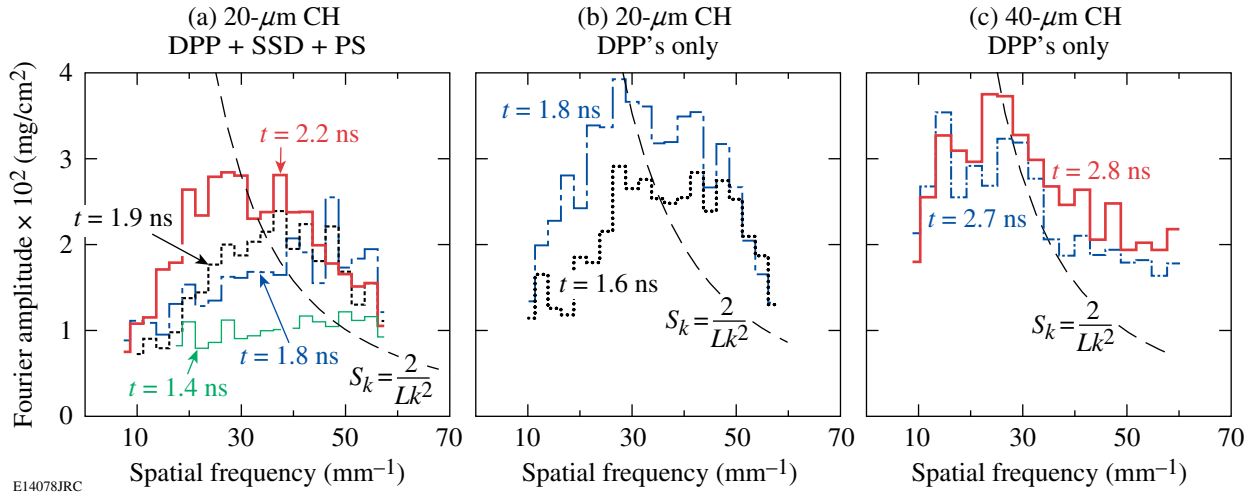

Figure 105.13
Evolution of the azimuthally averaged, areal-density modulation Fourier amplitudes as a function of spatial frequency for shots with 20-μm-thick [(a) and (b)] and 40-μm-thick (c) targets driven by a 3-ns laser pulse at an intensity of ~2 × 10^{14} W/cm^2 and with beam-smoothing conditions that include DDP's, SSD, and PS (a) and DPP's only [(b) and (c)]. The dashed line is Haan's saturation level $S_k = 2/Lk^2$ ($L = 400$ μm is the size of analysis box) multiplied by the calculated target density to be converted to areal density. The spectral shapes of measured modulations are similar to those predicted by Haan's model and are insensitive to initial and drive conditions.

Figure 105.14
(a) Evolution of the azimuthally averaged, areal-density modulation Fourier amplitudes as a function of spatial frequency for the shot with a 20-μm-thick target driven by a 3-ns laser pulse at an intensity of ~2 × 10^{14} W/cm^2 and with beam-smoothing conditions including DDP's, SSD, and PS measured at 2.5 and 2.8 ns. As the level of target modulations becomes comparable to the target thickness, the modulation growth slows down and is later reversed (at 2.8 ns). The bubble-merger processes are evident from the images measured at (b) 2.5 ns and (c) 2.8 ns.

shape at an intensity of $\sim 5 \times 10^{13}$ W/cm^2. The beam-smoothing conditions in these experiments included DPP's and PS. As the modulations grow, the average bubble size shifts to longer wavelengths, big bubbles become bigger, and small bubbles disappear, as is evident from the images in Fig. 105.15. Two to three generations of bubbles change (by coalescence events) in these images, allowing clear observations of the bubble competition and merger processes. One can claim that the bubble competition and merger processes occur around saturation levels (and not only in a more advanced, turbulent regime).

Figure 105.16(a) shows examples of Fourier amplitude evolution of areal-density modulations, typical for these experiments.[26] The spectral shapes are very similar to Haan's model predictions; the amplitudes grow to much higher values than those achieved in the 1999 experiments[29] because thicker targets do not limit RT growth at the times of these measurements. The fact that in the 2005 experiments [see Fig. 105.16(a)] there is no reduction in short-wavelength modulations allows one to conclude that the bubble competition is not accompanied by a reduction of the short-wavelength modulations [as shown in

E13702aJR

Figure 105.15
Central parts (with the analysis box size of 333 μm) of the x-ray framing-camera images measured at (a) 4 ns, (b) 6 ns, and (c) 10 ns in a 50-μm-thick target driven by a 12-ns laser pulse at an intensity of $\sim 5 \times 10^{13}$ W/cm^2 from Ref. 26. The bubble merger is evident in the images showing more advanced nonlinear RT evolution measured in thicker targets driven by longer pulses.
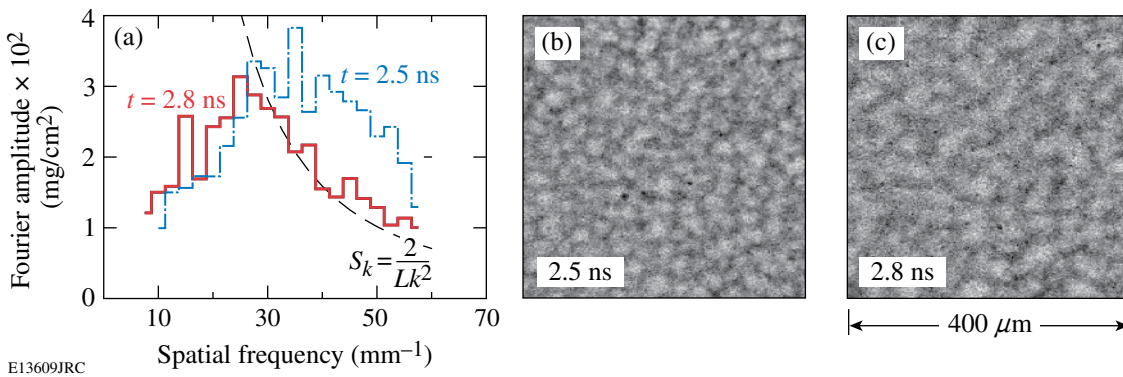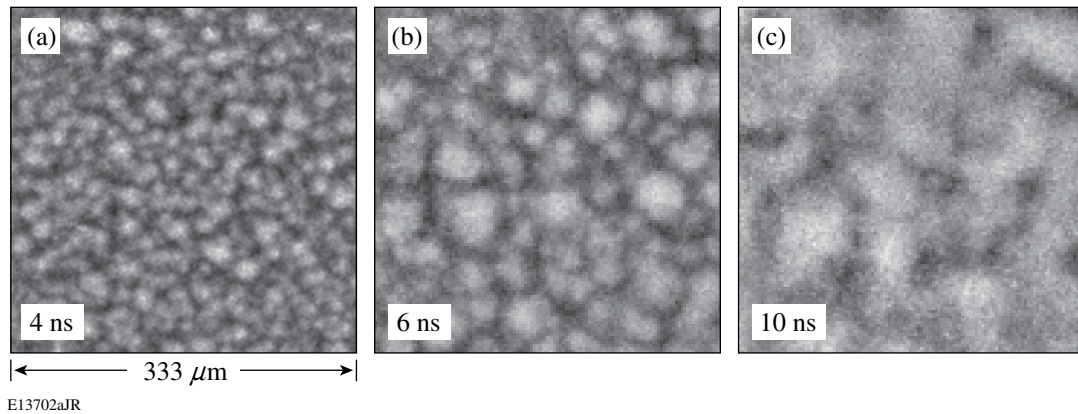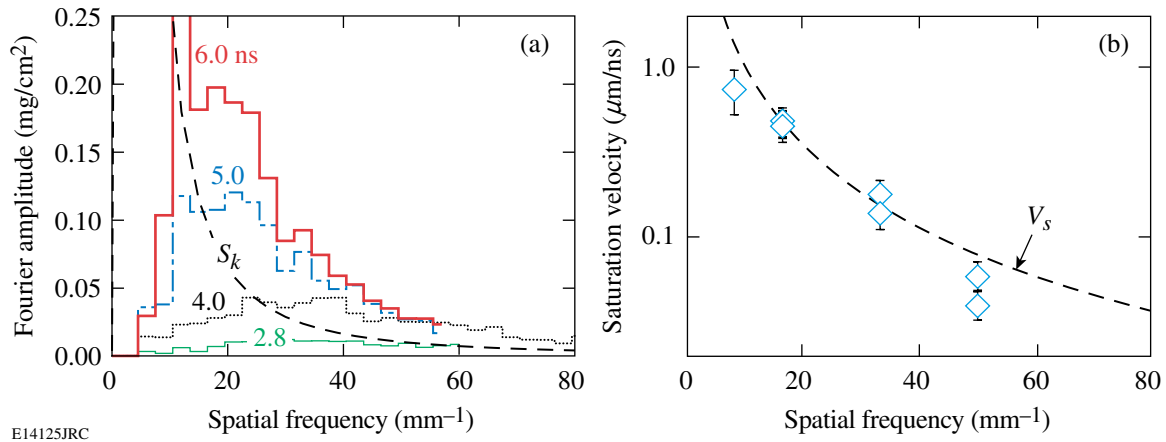

E14125JRC

Figure 105.16
(a) Evolution of the azimuthally averaged, areal-density modulation Fourier amplitudes as a function of spatial frequency for shots with 50-μm-thick targets driven by a 12-ns laser pulse at an intensity of $\sim 5 \times 10^{13}$ W/cm^2 from Ref. 26. The dashed line is Haan's saturation level $S_k = 2/Lk^2$ ($L = 333$ μm is the analysis box size) multiplied by the calculated target density to be converted to areal density. The spectral shapes of the measured modulations are similar to those predicted by Haan's model. (b) Saturation velocities of target modulations measured at spatial frequencies of 8, 17, 33, and 50 mm^{-1} corresponding to spatial wavelengths of 120, 60, 30, and 20 μm from Ref. 26. The dashed line is Haan's saturation velocity $V_s(k) = S_k \gamma(k)$. The measured nonlinear velocities are in excellent agreement with Haan's model predictions.

Fig. 105.14(a)]—this reduction is because of the finite target thickness effects that limited RT growth and prevented clear observation of the bubble competition in the 1999 experiments. Additionally, the fact that the RT growth in the 2005 experiments is not limited by target thickness allows a direct comparison of the measured nonlinear velocities $V_s(k)$ with those predicted by Haan's model,[26] and excellent agreement between the experiments and the model was observed[26] [as shown in Fig. 105.16(b)]. We find it remarkable that this simple model predicts such complicated phenomenon as the nonlinear saturation and the postsaturation growth of the RT instability so accurately in terms of the spectral shapes and nonlinear velocities.

The real-space analysis of the 2005 experiments was based on evolution distributions of the bubble sizes and amplitudes along with the evolution of average bubble size and amplitude.[28] Figure 105.17 shows an example of the measured image with bubble edges superimposed on top of it. The bubble edges were determined using a watershed algorithm.[38] The bubble size λ was calculated using $\lambda = 2(S/\pi)^{0.5}$, where S is the bubble area. The evolution of the distributions of bubble sizes λ [corresponding to images in Figs. 105.14(a) and 105.14(b)] is shown in Fig. 105.18(a). As modulations grow, the number of bubbles decreases while their average size and amplitude increase and the distributions become broader. The measured distributions of bubble sizes were fitted with the normal distributions from which average sizes $\langle \lambda \rangle$ were

determined. Figure 105.18(b) shows the normalized distributions [from Fig. 105.18(a)] as functions of normalized bubble size $\lambda/\langle \lambda \rangle$. Bubble size distributions are in the self-similar regime because the normalized distributions do not change in time. The self-similarity of RT growth is explicitly measured in these experiments using the evolution of bubble size distributions, while in earlier simulations and experiments[16,17] the self-similarity was inferred from the growth of the mixing-zone size. The dashed line in Fig. 105.18(b) represents the fit to the experimental data using the normal distribution
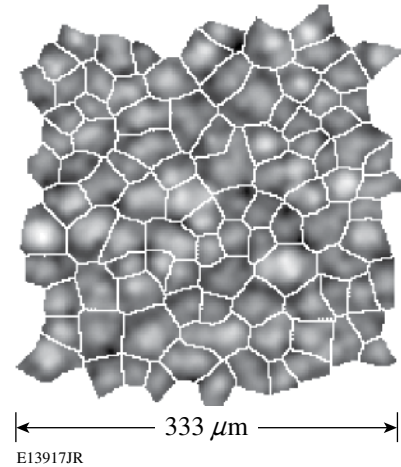

E13917JR

Figure 105.17
An example of the measured image with bubble edges (determined using watershed algorithm[38]) superimposed on top of it.

E14079JRC
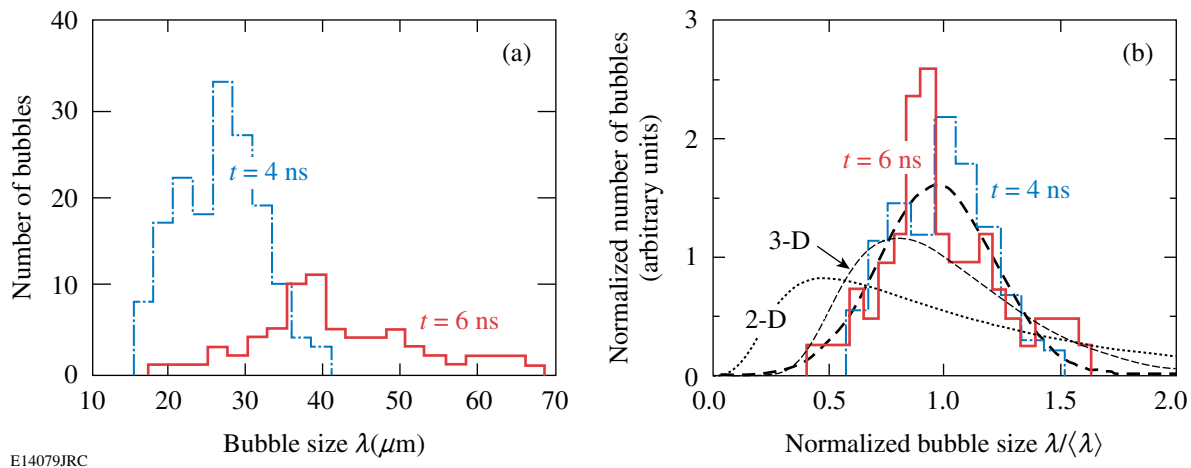
Figure 105.18
(a) Examples of the measured bubble size distributions in the images taken at 4 and 6 ns [images in Figs. 105.15(a), and 105.15(b), respectively] with a 50-μm-thick target driven by a 12-ns laser pulse at an intensity of ~5×10^{13} W/cm². (b) Bubble-size distributions, normalized to the total number of bubbles, as a function of the bubble size normalized to the averaged bubble size $\lambda/\langle \lambda \rangle$ for the same 4- and 6-ns images as in (a). The measured bubble distributions are in a self-similar regime because their normalized distributions do not change in time. The thicker dashed line represents a normal distribution fit to the data.

$f_\sigma(\lambda/\langle\lambda\rangle) = \exp\left[-(\lambda/\langle\lambda\rangle - 1)^2\big/2C_\lambda^2\right]\big/\sqrt{2\pi} \cdot C_\lambda$, where $C_\lambda =$ 0.24±0.01 is the constant determined from the fit. The dotted and dot–dashed lines in Fig. 105.18(b) are the distributions predicted from the 2-D and 3-D models, respectively (presented in Ref. 27). The 3-D model prediction is in better agreement with the experimental results, as expected. It was shown[28] that the modulation σ_{rms} grows as $\alpha_\sigma g t^2$, as expected in a self-similar regime, where g is the foil acceleration, t is the time, and $\alpha_\sigma =$ 0.027±0.003 is a measured constant. The bubble-front amplitude h_b can be estimated[18] as $h_b \sim \sqrt{2}\,\sigma_{rms}$, which yields $h_b \sim$ 0.04 gt^2. It was shown in Refs. 20 and 39 that Haan's saturation at amplitudes $S_k = 2/Lk^2$ in Fourier space is equivalent to self-similar growth $h_b = 0.04\ gt^2$ in real space. Therefore, experimentally measured growth is in agreement with what was predicted.[20,39] The weak, logarithmic dependence of the α_σ on the initial conditions[17] still requires experimental verification for ablative acceleration.

The experimental results presented above show the behavior of "average" modulation characteristics. The evolution of the average amplitude (calculated by the azimuthal average of the 2-D Fourier image) was compared with Haan's model predictions in Fourier space. The analysis in real space was presented in terms of bubble size distributions. The measured data, however, can also be used to quantitatively describe what happens to an individual bubble (in real space) and individual Fourier mode (in Fourier space). Figure 105.19 shows images of the modulation growth at the same area of the target measured at 2.7, 3.5, and 4.3 ns in the shot with a 35-μm-thick target driven at an intensity of ~5 × 10^{13} W/cm^2.

Figure 105.20 shows overlapped bubble contours of the 2.7- (gray lines) and 4.3-ns (black lines) images. As evident from this figure, some bubbles coalesce with others to form larger bubbles. Some bubbles disappear and other bubbles expand to take their place, while some bubbles stay in their original place without changing sizes. As for the Fourier-space analysis, if all modes at any wavelength grow uniformly according to Haan's model prediction for the average modulation growth, there could not be a bubble merger in real space. Therefore, to be consistent with the bubble-merger picture of real-space evolution, the individual Fourier modes at a given

E14081JR
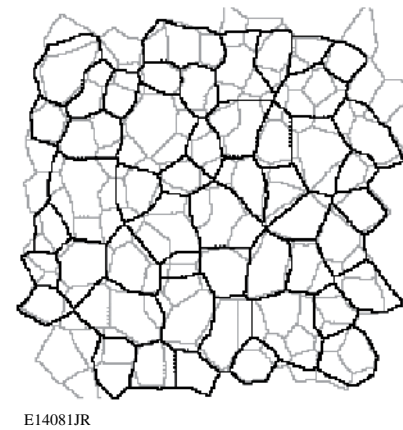
Figure 105.20
Bubble edge contours of the 2.7-ns (gray contours) and (c) 4.3-ns (black contours) images from Fig. 105.19. Some of the bubbles do not change their size while most bubbles merge into bigger bubbles and some bubbles disappear during evolution.

(a)   2.7 ns   (b)   3.5 ns   (c)   4.3 ns
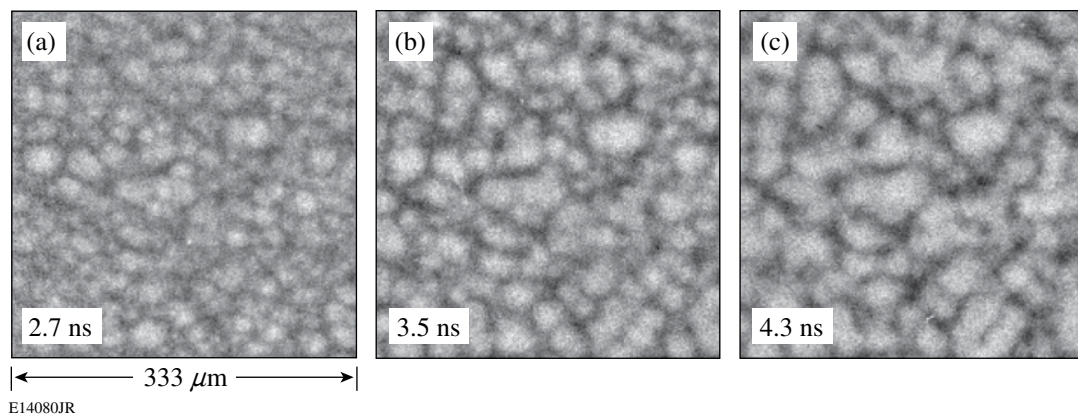
|←   333 μm →|

E14080JR

Figure 105.19
The evolution of the same target area as shown by the central parts (with a 333-μm analysis box size) of the x-ray framing-camera images measured at (a) 2.7 ns, (b) 3.5 ns, and (c) 4.3 ns in a 35-μm-thick target driven by a 12-ns laser pulse at an intensity of ~5 × 10^{13} W/cm^2. The evolution of each modulation feature can be tracked in these images.

(mainly short) wavelength should have a different growth than their average amplitude. Figure 105.21(a) shows the Fourier image with typical "spiky" amplitudes, characteristic to "noise-like" 3-D modulations. The azimuthal lineout of data at a 60-μm wavelength is shown in Fig. 105.21(b). There are

(a) Fourier image

(b) Fourier lineout at $\lambda = 60~\mu$m

(c) $\lambda = 60~\mu$m

(d) $\lambda = 20~\mu$m

(e)
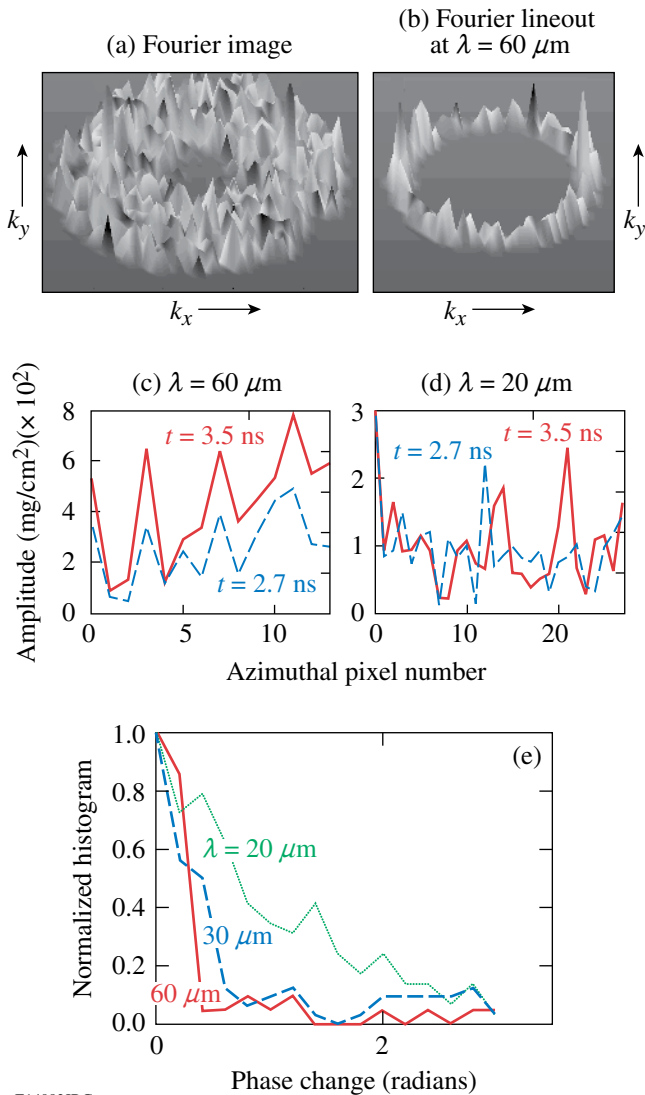
Figure 105.21

(a) An example of the typical measured Fourier-space image (shown in terms of the absolute value). (b) The azimuthal lineout of this image at a spatial wavelength of 60 μm. The azimuthal lineouts of absolute values of Fourier modes at a (c) 60-μm wavelength and a (d) 20-μm wavelength measured at 2.7 and 3.5 ns. (e) Normalized (to the value at zero phase change) histograms of the absolute phase change of the modes at spatial wavelengths of 20, 30, and 60 μm calculated from the difference of the 2.7- and 3.5-ns images. The bubble merger in Fourier space corresponds to the short-wavelength modes growing nonuniformly (with many modes changing their phases significantly), while longer-wavelength modes do not change their phases.

many modes in this lineout and their average amplitude grows according to Haan's model prediction, as shown above. Is the growth of each individual mode in this lineout the same as the growth of the average amplitude? If it is the same, then the phase of each mode (related to the ratio of the real and imaginary parts of the mode's complex amplitude) does not change in time. Figure 105.21(c) shows the evolution of the absolute values of modes in a 60-μm wavelength lineout from 2.7 to 3.5 ns, while the evolution of the modes in a 20-μm wavelength lineout is presented in Fig. 105.21(d). These data show that all 60-μm wavelength modes grow similarly, while modes at a 20-μm wavelength do not all grow the same way and many phase changes are seen during the growth of these short-wavelength modes. Figure 105.21(e) shows the histograms of the absolute values of the phase changes of all modes at spatial wavelengths of 20, 30, and 60 μm measured between 3.5- and 2.7-ns images. At wavelengths of 30 and 60 μm, most of the modes do not change phases, while most of the modes at wavelengths of 20 μm change their phases significantly. As a result, the bubble merger in Fourier space corresponds to short-wavelength modes growing nonuniformly (with many modes changing their phases significantly), while longer-wavelength modes do not change their phases, meaning that the images keep their long-wavelength structure unchanged.

Conclusions

The nonlinear Rayleigh–Taylor growth of 3-D nonuniformities was measured near saturation levels using x-ray radiography in laser-driven planar foils. The initial target modulations were seeded by laser nonuniformities. The measured modulation Fourier spectra and nonlinear growth velocities are in excellent agreement with Haan's model[18] predictions in Fourier space.[25,26] These spectra and growth velocities are insensitive to initial conditions. Bubble competition and merger was quantified by the evolution of bubble size distributions in real space. A self-similar evolution of these distributions was observed.[28]

REFERENCES

1. Lord Rayleigh, Proc. London Math Soc. **XIV**, 170 (1883).

2. G. Taylor, Proc. R. Soc. London Ser. A **201**, 192 (1950).

3. J. D. Lindl, Phys. Plasmas **2**, 3933 (1995).

E14082JRC

4. B. A. Remington *et al.*, Phys. Plasmas **4**, 1994 (1997).

5. K. S. Budil *et al.*, Phys. Rev. Lett. **76**, 4536 (1996).

6. H. Takabe *et al.*, Phys. Fluids **28**, 3676 (1985).

7. R. Betti, V. N. Goncharov, R. L. McCrory, P. Sorotokin, and C. P. Verdon, Phys. Plasmas **3**, 2122 (1996).

8. K. Shigemori *et al.*, Phys. Rev. Lett. **78**, 250 (1997).

9. S. G. Glendinning, S. N. Dixit, B. A. Hammel, D. H. Kalantar, M. H. Key, J. D. Kilkenny, J. P. Knauer, D. M. Pennington, B. A. Remington, R. J. Wallace, and S. V. Weber, Phys. Rev. Lett. **78**, 3318 (1997).

10. C. J. Pawley *et al.*, Phys. Plasmas **6**, 565 (1999).

11. J. P. Knauer, R. Betti, D. K. Bradley, T. R. Boehly, T. J. B. Collins, V. N. Goncharov, P. W. McKenty, D. D. Meyerhofer, V. A. Smalyuk, C. P. Verdon, S. G. Glendinning, D. H. Kalantar, and R. G. Watt, Phys. Plasmas **7**, 338 (2000).

12. T. Sakaiya *et al.*, Phys. Rev. Lett. **88**, 145003 (2002).

13. B. A. Remington *et al.*, Phys. Fluids B **5**, 2589 (1993).

14. K. I. Read, Physica **12D**, 45 (1984).

15. D. H. Sharp, Physica **12D**, 3 (1984).

16. M. B. Schneider, G. Dimonte, and B. Remington, Phys. Rev. Lett. **80**, 3507 (1998).

17. G. Dimonte, Phys. Rev. E **69**, 056305 (2004).

18. S. W. Haan, Phys. Rev. A, Gen. Phys. **39**, 5812 (1989).

19. S. W. Haan, Phys. Fluids B **3**, 2349 (1991).

20. D. Ofer, U. Alon, D. Shvarts, R. L. McCrory, and C. P. Verdon, Phys. Plasmas **3**, 3073 (1996).

21. C. L. Gardner *et al.*, Phys. Fluids **31**, 447 (1988).

22. Q. Zhang, Phys. Lett. A **151**, 18 (1990).

23. J. Glimm and X. L. Li, Phys. Fluids **31**, 2077 (1988).

24. U. Alon *et al.*, Phys. Rev. Lett. **74**, 534 (1995).

25. V. A. Smalyuk, T. R. Boehly, D. K. Bradley, V. N. Goncharov, J. A. Delettrez, J. P. Knauer, D. D. Meyerhofer, D. Oron, and D. Shvarts, Phys. Rev. Lett. **81**, 5342 (1998).

26. V. A. Smalyuk, O. Sadot, J. A. Delettrez, D. D. Meyerhofer, S. P. Regan, and T. C. Sangster, Phys. Rev. Lett. **95**, 215001 (2005).

27. D. Oron *et al.*, Phys. Plasmas **8**, 2883 (2001).

28. O. Sadot, V. A. Smalyuk, J. A. Delettrez, D. D. Meyerhofer, T. C. Sangster, R. Betti, V. N. Goncharov, and D. Shvarts, Phys. Rev. Lett. **95**, 265001 (2005).

29. V. A. Smalyuk, T. R. Boehly, D. K. Bradley, V. N. Goncharov, J. A. Delettrez, J. P. Knauer, D. D. Meyerhofer, D. Oron, D. Shvarts, Y. Srebro, and R. P. J. Town, Phys. Plasmas **6**, 4022 (1999).

30. T. R. Boehly, D. L. Brown, R. S. Craxton, R. L. Keck, J. P. Knauer, J. H. Kelly, T. J. Kessler, S. A. Kumpan, S. J. Loucks, S. A. Letzring, F. J. Marshall, R. L. McCrory, S. F. B. Morse, W. Seka, J. M. Soures, and C. P. Verdon, Opt. Commun. **133**, 495 (1997).

31. Y. Lin, T. J. Kessler, and G. N. Lawrence, Opt. Lett. **20**, 764 (1995).

32. V. A. Smalyuk, V. N. Goncharov, T. R. Boehly, D. Y. Li, J. A. Marozas, D. D. Meyerhofer, S. P. Regan, and T. C. Sangster, Phys. Plasmas **12**, 040702 (2004).

33. V. A. Smalyuk, V. N. Goncharov, T. R. Boehly, J. A. Delettrez, D. Y. Li, J. A. Marozas, A. V. Maximov, D. D. Meyerhofer, S. P. Regan, and T. C. Sangster, Phys. Plasmas **12**, 072703 (2005).

34. S. V. Weber, S. G. Glendinning, D. H. Kalantar, M. H. Key, B. A. Remington, J. E. Rothenberg, E. Wolfrum, C. P. Verdon, and J. P. Knauer, Phys. Plasmas **4**, 1978 (1997).

35. V. N. Goncharov, S. Skupsky, T. R. Boehly, J. P. Knauer, P. McKenty, V. A. Smalyuk, R. P. J. Town, O. V. Gotchev, R. Betti, and D. D. Meyerhofer, Phys. Plasmas **7**, 2062 (2000).

36. S. P. Regan, J. A. Marozas, J. H. Kelly, T. R. Boehly, W. R. Donaldson, P. A. Jaanimagi, R. L. Keck, T. J. Kessler, D. D. Meyerhofer, W. Seka, S. Skupsky, and V. A. Smalyuk, J. Opt. Soc. Am. B **17**, 1483 (2000).

37. T. R. Boehly, V. A. Smalyuk, D. D. Meyerhofer, J. P. Knauer, D. K. Bradley, R. S. Craxton, M. J. Guardalben, S. Skupsky, and T. J. Kessler, J. Appl. Phys. **85**, 3444 (1999).

38. L. Vincent and P. Soille, IEEE Trans. Pattern Anal. Mach. Intell. **13**, 583 (1991).

39. M. J. Dunning and S. W. Haan, Phys. Plasmas **2**, 1669 (1995).

Isotopic Fractionation During Solidification of H_2–HD–D_2 Mixtures

Introduction

In inertial fusion experiments, it is energetically advantageous to form the fuel into a solid shell before compression.[1] Current cryogenic target experiments on OMEGA are being performed with pure deuterium (D_2) as the fuel.[2] Future cryogenic target experiments will be performed with an equimolar solid mixture of deuterium and tritium (D-T). An equilibrium D-T mixture consists of D_2, DT, and T_2 molecules in a 25:50:25% ratio. Each molecular species has a different triple point, which may lead to fractionation of the isotopes during fuel-layer formation. Spatial separation of the D and T nuclei due to isotopic fractionation during the cryogenic target layering process reduces the efficiency of the fusion reaction.[3]

Complete isotopic fractionation has long been predicted for hydrogen isotopes for temperatures approaching absolute zero—well below the triple point of the mixture.[4] It has been observed for ^{3}He-^{4}He mixtures but not for bulk solid hydrogen isotope mixtures. Partial fractionation of hydrogen–deuterium mixtures has been observed in monolayers adsorbed onto graphite substrates using neutron scattering and x-ray diffraction.[5] The separation is mainly limited to the formation of local molecular clusters of one isotope versus the other as the monolayer is completed. It was speculated that no long-range ordering was observed because of the limited mobility of the molecules at temperatures approaching 3 K.

We have examined the possibility of fractionation in cryogenic targets using a 25:50:25% mixture of H_2, HD, and D_2 (H-D). The use of nonradioactive hydrogen isotopes allows a simpler experimental system to be constructed without the radiological controls necessary for using tritium. Although nonradiological experiments are easier to perform, less fractionation may occur in samples containing tritium. Molecular diffusion in the bulk may be enhanced for D-T mixtures because of the large amount of energy deposited locally from β decay, which raises the neighboring solid's temperature and disassociates nearby molecular bonds. This study investigates fractionation that occurs during the liquid-to-solid phase transition near the triple point. Possible fractionation during solid-to-vapor-to-solid mass transfer during β-layering or IR-enhanced β-layering as a result of sublimation and refreezing will be investigated in a future study.

For the liquid-to-solid phase transition, there was little separation of the isotopes during the solidification process. The maximum spatial concentration gradients are of the order of 0.02 to 0.05 molecular fraction per millimeter. The average D_2 concentration gradient (percentage) is greatest for the lowest D_2 concentrations. The absorption coefficient's gradient was also measured and appears to be less for the longer cooling times, which may be indicative of solid diffusion. Thermodynamically, the mixtures form a completely soluble isomorphous system since the mixture solidifies over a finite temperature range for all concentrations.

Experimental Details

By scanning a focused infrared (IR) laser probe tuned to the major absorption band of D_2 at $\tilde{\nu} = 3162$ cm^{-1} ($\lambda = 3.162$ μm) across a thin, slowly frozen solid sample of the mixture, the D_2 concentration as a function of position can be determined. The infrared absorption spectrum of pure deuterium is shown in Fig. 105.22. The major absorption peak of solid D_2 is from an induced dipole interaction between adjacent D_2 molecules in the crystal.[7] Solid hydrogen forms a hexagonal close-packed crystal at its vapor pressure. Therefore, each molecule has 12 nearest neighbors in the crystal, as shown in Fig. 105.23. Substitution of H_2 or HD into these sites will reduce the D_2–D_2 dipole interaction and increase the local IR transmission.

A schematic of the commercially available[8] infrared Pb:salt laser system is shown in Fig. 105.24. The IR laser diode is housed in a liquid-nitrogen (LN$_2$) dewar and is operated at ~125 K and ~650 mA to produce an optical power approaching 1 mW at 3162 cm^{-1}. The laser source is a PbSe double-hetero-structure, single-mode diode laser for high-resolution spectroscopy. It has a typical line width of 6.7×10^{-4} cm^{-1}, a current tuning rate of 0.09 cm^{-1}/mA, and a temperature tuning rate of 4 cm^{-1}/K. This gives a wave number tuning range of ~3.140 to 3.190 cm^{-1} over the operable temperature/current range. Even though the line

width is very narrow, by coarsely tuning the temperature and finely tuning the current, any wave number within the specified range can be achieved.

The light is collimated using an off-axis parabolic mirror which can be positioned in three dimensions. The light is sent through a grating monochrometer that has been precalibrated to transmit only 3.162 ± 0.003-μm light. The wavelength emitted by the laser diode is adjusted by varying its current at a fixed temperature until maximum transmission through the monochrometer is obtained. The dual-detector photodiode is also housed in a LN_2 dewar. A small fraction (~10%) of the beam is split off and focused onto one detector to monitor the stability of the laser source during data acquisition (refer to this as the reference beam).

The remainder of the beam is transported through the sample. The light is focused to a 0.3-mm × 0.6-mm spot on the sample using an off-axis parabolic mirror mounted on a five-axis positioner. It is recollimated on the other side of the
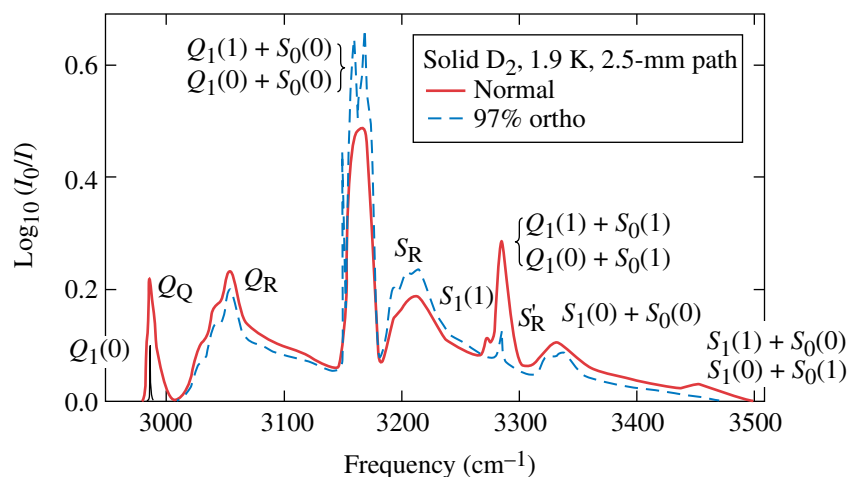
T2067aJR1C

Figure 105.22
The absorption spectrum of solid D_2 at 1.9 K for a 2.5-mm-thick sample. (Figure courtesy of the Canadian Journal of Physics.)[6]
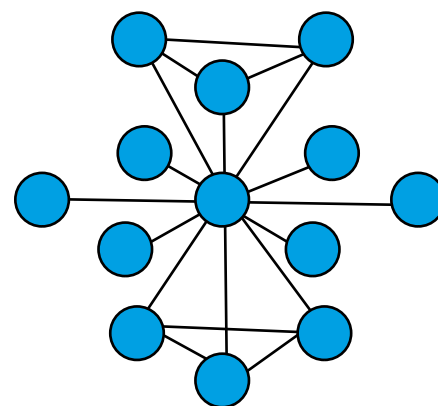
T2067aJR2C

Figure 105.23
Each molecule in the hexagonal close-packed structure of solid hydrogen is neighbored by 12 other molecules. Substitution of non-D_2 molecules into these sites will interfere with adjoining D_2–D_2 dipole interactions and greatly reduce the absorption coefficient of the solid.
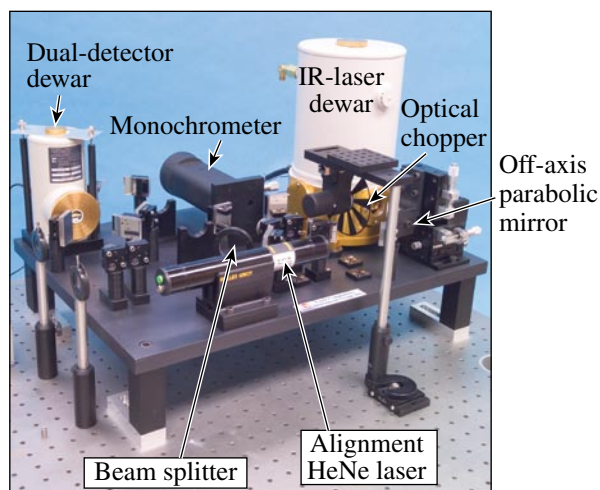
T2069JRC
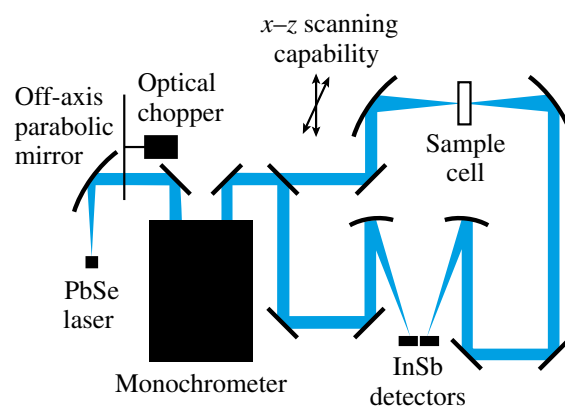
Figure 105.24
The optical layout and a schematic of the infrared Pb:salt laser system.

sample with an identical mirror and positioner. The mirrors are mounted on a stage that can be positioned with micrometer screws vertically and horizontally with respect to the fixed sample without causing the beam to "walk off" in the remainder of the optical system. This beam is subsequently focused onto the other detector (refer to this as the sample beam). The output of the IR laser is chopped at 790 Hz and the signals from each detector are sent to a chopper-synchronized lock-in amplifier with a 30-ms integration period.
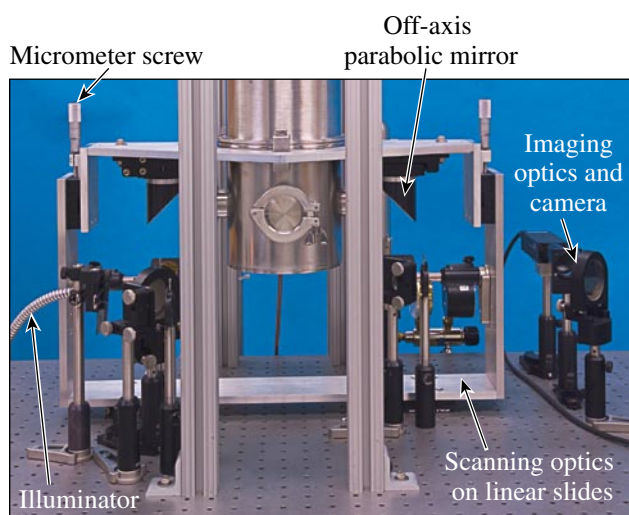
A sketch of the sample cell used to form the H-D crystal is shown in Fig. 105.25. The oxygen-free, high-conductivity copper cell is cooled from the bottom using a low-vibration Gifford-McMahon cryogenic refrigerator.[9] The cylindrical void that is filled with H-D is 6.4 mm in diameter by 3 mm thick; 2-mm-thick CaF windows are glued to either side of the copper cell. CaF was used instead of sapphire because of its lower thermal conductivity but similar IR transmittance at 3.162 μm. A heater and thermometer are attached to the top and bottom of the sample to produce a temperature gradient (~0.5 K maximum) across the sample.

The sample cell is loaded with liquid H-D through a 0.5-mm-diam stainless steel fill tube using a gas source pressure <10 psia. For isotope mixtures, the sample cell is filled with just enough liquid to completely fill it before freezing to eliminate possible preferential condensation of the different isotopes from the gas-phase reservoir because of their different vapor pressures at a fixed temperature. This eliminates

the possibility of a concentration gradient forming because of the different vapor pressures of each isotope instead of from their different triple points. The cell remains connected to an external room-temperature gas source for isomolecular samples since they exhibit a single vapor pressure for each temperature, thus, the frozen sample completely fills the cell for these solid samples. The sample is cooled slowly (hours to days) by reducing the temperature at the top of the cell gradually to a value just below the final freezing temperature of the mixture.

Two flip-in mirrors are mounted before and after the parabolic mirrors. The first provides white-light illumination of the sample and the second sends the transmitted light to an imaging system with a CCD detector. This allows the sample to be viewed as the H-D solidifies. When examined between crossed linear polarizers, the crystal structure of the solid H-D is revealed (see example in Fig. 105.26). A HeNe laser beam can be made coaxial to the IR beam using a flip-in beamsplitter that allows visible alignment of the IR beam path. Using the second flip-in mirror alone with the HeNe beam, the focal spot of the IR beam can be located on the sample's image to provide beam position feedback.

The IR beam is raster scanned across the sample cell to determine if a D_2 concentration gradient is present. The signal from the sample beam is recorded as a function of position at 0.5-mm increments. The signal from the reference beam is recorded periodically throughout the measurement to confirm the stability of the IR laser diode. (Typically, the output was sta-
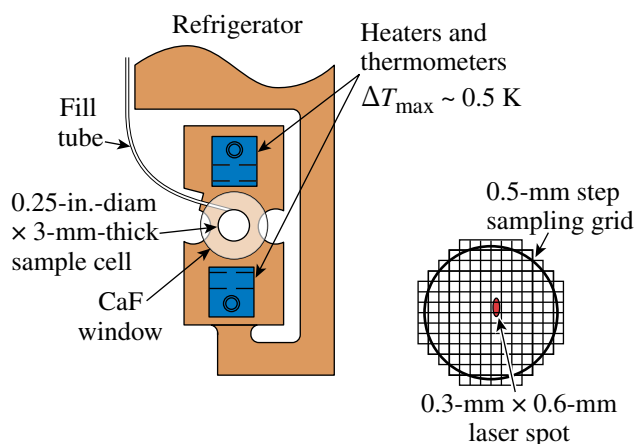

Figure 105.25
The scanning optics configuration and a sketch of the sample cell in which the H-D crystal is formed.
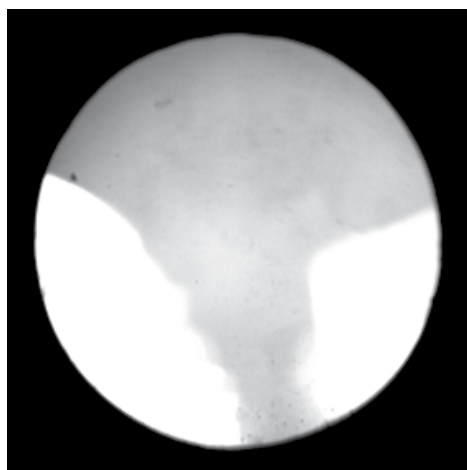
Figure 105.26

An image of a white-light, back-illuminated, solid pure D_2 sample. The crystal structure of the solid is revealed when examined between crossed linear polarizers; three distinct crystallites can be seen. The sample was frozen by reducing the temperature at the top of the sample from 19.2 K to 18.7 K over a 20-h period. The sample began to freeze at a bottom temperature of 18.7 K.

ble to <2% for the duration of the measurement.) The sample is subsequently vaporized at 30 K and the signal from the sample beam is recorded as a function of position for the empty cell. The two measurements are ratioed to create a transmission plot $T(x,z)$, as shown in Fig. 105.27(b). The absorption coefficient $\alpha(x,z)$ is calculated from Beer's Law and includes a correction for the change in refractive index of the sample cell's contents with the solid present and absent (see appendix, p. 33).

Results

The transmission plot of the 25:50:25% H_2:HD:D_2 mixture, along with that of a pure D_2 sample, is shown in Fig. 105.27. (The mean absorption coefficient for each sample is given in Fig. 105.29.) Note that α for the H-D mixture is ~1/20th of that for the pure D_2. This reduction is disproportionate to the reduction in D_2 nearest neighbors—from 12 to 3 in the hexagonal close-packed crystal. In fact, the 3-mm-thick H-D mixture is >96% transmissive even though one in four molecules is D_2. In contrast, a pure D_2 sample is only 40% transmissive. This is attributed to the simultaneous transition absorption requirement of two neighboring D_2 molecules, each absorbing a portion of the incident quantum.[10] Therefore, the interference of non-D_2 molecules between adjacent D_2 molecules greatly reduces the absorption coefficient of the bulk material. Any gradient present in this H-D transmission plot is easily masked by the noise in the data. The sensitivity of the D_2 absorption coefficient to concentration must first be resolved before a change in absorption can be quantified as a concentration gradient.

(a) H-D transmission
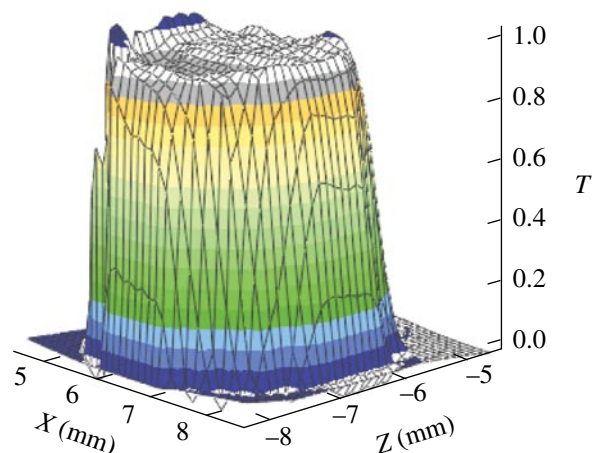
(b) D_2 transmission
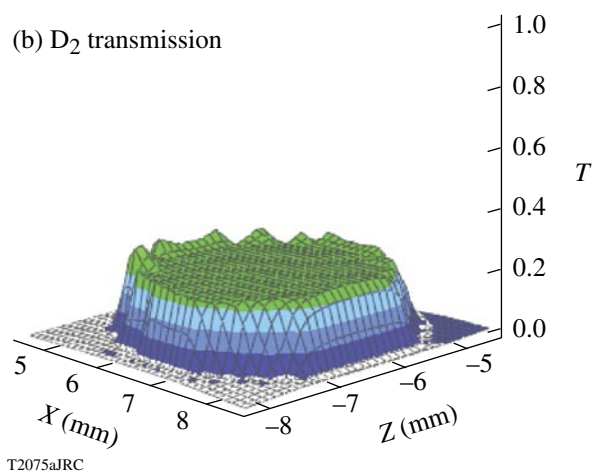
Figure 105.27

Typical transmission plots for (a) 25:50:25% H_2:HD:D_2 and (b) pure D_2. The absorption coefficients are 0.017 and 0.317 mm^{-1}, respectively; a 20× difference for a factor of 4 difference in D_2 concentration that is clearly outside the linear region of Beer's Law.

Beer's Law follows a linear relationship between the absorption coefficient and solute concentration for low concentrations (<10%). At these relatively high concentrations of D_2 in the H-D mixture (25% < D_2 < 100%), however, nonlinear deviations from Beer's Law are expected. The absorption coefficient of the D_2 in the H-D is a function of the D_2 intermolecular distance[11] as follows:

$$\alpha(\omega) \propto \sum_{nn'} (P_n - P_{n'}) \left| \langle n' | \mu | n \rangle \right|^2 \delta(\omega - \omega_{nn'}),$$

where $\omega = 2\pi c/\lambda$ is the angular frequency of the incident radiation, P_n is the probability of occupancy of state n (P_n corresponding to absorption and $P_{n'}$ to spontaneous emission), μ is the dipole moment of the molecule, and $\delta(\omega - \omega_{nn'})$ is the

Dirac delta function centered at the resonant frequency $\omega_{nn'}$. The dipole moment μ is proportional to $Q_{\text{internuclear}} + Q_{\text{eqq}}$, however, where $Q_{\text{internuclear}}$ is related to a van der Waal's interaction and Q_{eqq} is the electric quadrapole–quadrapole interaction which varies as $1/r_e^4$, where r_e is the D₂ intermolecular distance. The intermolecular distance between D₂ molecules in the H-D mixture is inversely proportional to the D₂ concentration. Therefore, by plotting the absorption coefficient of the D₂ in the H-D mixture as a function of the D₂ fraction in the mixture, the slope can be used to quantify a transmission gradient as a concentration gradient.

A variety of H₂-D₂ mixtures were solidified at varying rates and their $\alpha(x,z)$ measured. Three to seven individual samples were frozen and measured for each mixture to obtain adequate statistics. The transmission data is fit to a plane to determine the average transmission and the transmission gradient, as shown in Fig. 105.28. The resulting average absorption coefficient of the D₂ in the H-D mixture (at $\lambda = 3.151$ μm) is plotted as a function of the D₂ molecular fraction f_{D_2} in Fig. 105.29. The function that best fits the data is

$$\alpha\left(f_{D_2}\right) = \exp\left(4.20 \times f_{D_2} - 5.26\right)\text{mm}^{-1}.$$

Conversely, to find the D₂ molecular fraction from the mean absorption coefficient

$$f_{D_2} = \frac{\left[\ln\left(\alpha \times 1\,\text{mm}\right) - 5.26\right]}{4.20}. \tag{1}$$

T2195JRC
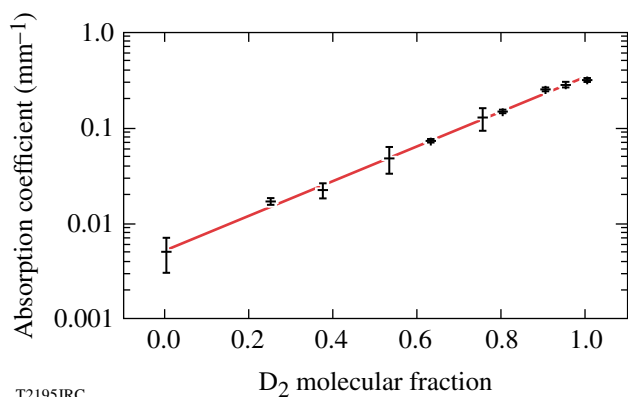
Figure 105.29
The average absorption coefficient of the D₂ in the H-D mixture as a function of the D₂ molecular fraction at an IR diode wavelength of $\lambda = 3.151$ μm. The vertical error bars indicate ±1 standard deviation of the various experimental runs that were averaged for each point. The results from pure H₂ and D₂ samples are included for completeness. The finite absorption coefficient for H₂ indicates the scattering baseline of the experiment.

$$\overline{T} = 0.40$$
$$|\vec{\nabla}T| = 0.019\ \text{mm}^{-1}$$
Goodness of fit = $\sigma/\overline{T} = 8\%$

T2199JRC
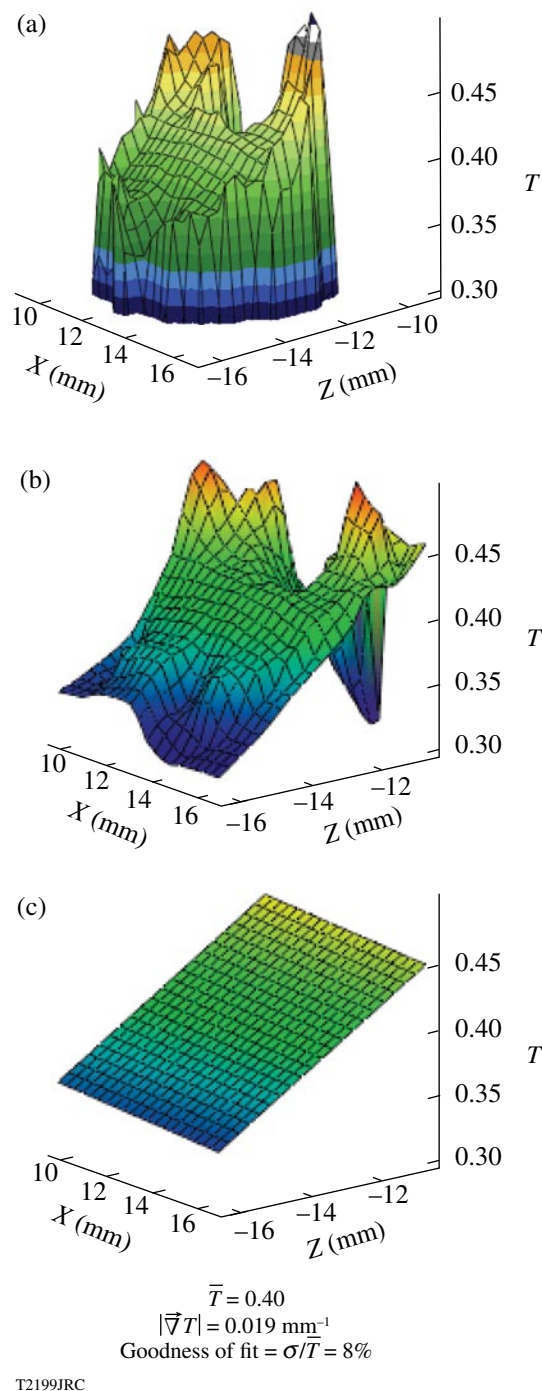
Figure 105.28
The transmission plots are processed from the raw data shown in (a) by first eliminating spurious data points to produce the plot in (b) and then fitting it to a plane, as shown in (c), to subsequently determine the D₂ concentration gradient. The hole at the top of the data is formed during solidification because of the large difference between the liquid and solid densities of hydrogen since the sample cell is filled with just enough liquid to completely fill it before freezing commences.

A plot of the absorption coefficient gradient as a function of freeze time is shown in Fig. 105.30. The samples were generally measured <2 h following solidification. The absorption coefficient gradient appears to be inversely proportional to the cooling time, but there is a large scatter in the data—especially for the shorter cooling times. This may be evidence of molecular diffusion in the bulk solid. Molecular diffusion between adsorbed H-D monolayers on graphite has been observed[5] to be of the order of 5×10^{-6} cm^2/s near the triple point (17 K). This value increases by an order of magnitude at 30 K for adsorbed monolayers, but this temperature obviously cannot be obtained in the unpressurized solid. Molecular diffusion in the bulk may be enhanced for D-T mixtures because of the large amount of energy (~12 keV average) deposited locally from β decay, thus raising the neighboring temperature and disassociating molecular bonds.

T2196JRC
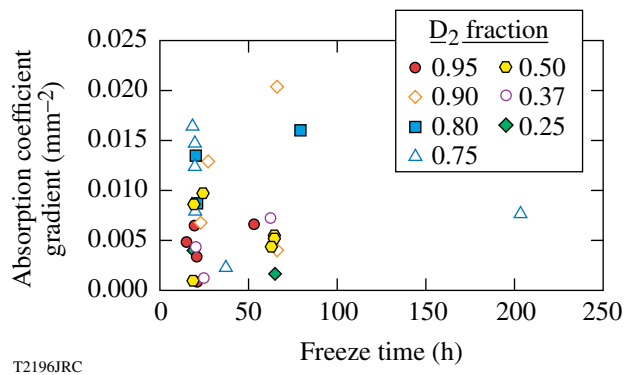
Figure 105.30
The absorption coefficient gradient as a function of freeze time. The vertical groupings indicate that most cooldowns were performed either over ~24 h or over ~72 h. A single long-duration cooldown is shown at the right of the figure. A few anomalous points occur at the top of the figure that may be indicative of IR scattering in the raw transmission data for these points.

It may be argued that scattering sites in the bottom of the sample are producing the apparent concentration gradient. These could originate from the large temperature excursion that the bottom of the sample undergoes during the freezing of the entire sample and the subsequent thermal contraction creating microcracks. This hypothesis is not supported by a plot of the absorption coefficient gradient as a function of initial bottom minus final top temperature (Fig. 105.31). In fact, observable cracks and striations do appear in the sample during the freeze duration but generally anneal out during the course of solidification. In addition, the absorption coefficient gradients for samples of individual isotopes are ~10^{-4} 1/mm^2—several orders of magnitude less than those for the mixtures—indicating that no scattering-induced gradients are present.

The average percentage D_2 concentration gradient $\left(\Delta f_{D_2}/\Delta_z \times 1/f_{D_2}\right)$ is greatest for the lowest concentrations, as shown in Fig. 105.32. Among the samples tested, however, the absolute concentration gradients $\left(\Delta f_{D_2}/\Delta_z\right)$ are of the order of 0.02 to 0.05 mm^{-1}. The large error bars shown for the lowest concentrations indicate the signal-to-noise ratio in the measurement is smallest when the sample is the least absorptive. This is another reason why the data in Fig. 105.29 are most useful

T2201JRC
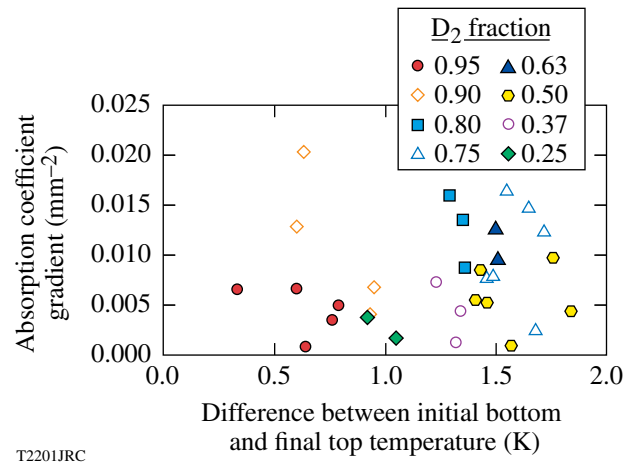
Figure 105.31
A plot of the absorption coefficient gradient as a function of the difference between the initial bottom and the final top temperature. If the gradient observed was due to increased IR scatter in the lower portion of the sample from microcracks, the trend in the data should be diagonal from bottom left to upper right. The data does not reflect this and is more or less randomly distributed.


T2197JR
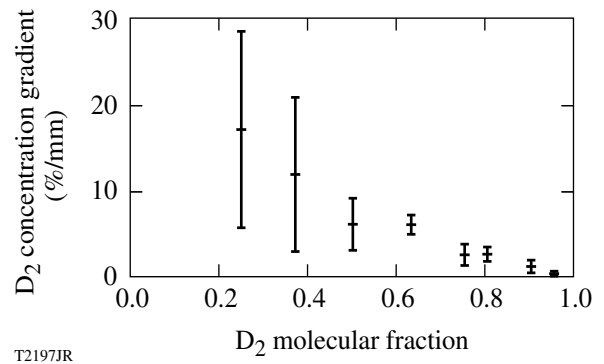
Figure 105.32
The average percentage D_2 concentration gradient in the H-D mixture as a function of the D_2 molecular fraction. The vertical error bars indicate ±1 standard deviation of the various experimental runs that were averaged for each point and are greatest for the lowest concentrations since the signal-to-noise ratio is smallest for the least absorptive samples. The absolute concentration gradients are of the order of 0.02 to 0.05 molecular fraction mm^{-1}.

Table 105.I: Calculated first-freezing temperatures for the 25:50:25% H$_2$:HD:D$_2$ mixture using Eq. (2). Molecular fractions are based on both the pressurization schedule of the gas reservoir when the sample was prepared and on an independent measurement of the sample using cryogenic gas chromatography. The final column is the first-freezing temperature of the remaining 33:67% H$_2$:HD mixture if the D$_2$ completely froze out of the solution first.

Molecule	Triple point (K)	Mass fraction from pressure	Mass fraction from mass spectrometer	Mass fraction with frozen D$_2$
H$_2$	13.96	0.249±0.005	0.26±0.02	1/3
HD	16.60	0.495±0.005	0.50±0.02	2/3
D$_2$	18.73	0.256±0.005	0.24±0.02	0
	First-freezing temperature (K)	16.49	16.42	15.72

Experimentally, the first-freezing temperature for the frozen mixture was 16.53 K and the mixture had completely frozen at ~16 K. This implies that complete fractionation does not occur in the mixture.

for extrapolating the D$_2$ concentration gradient present in a weakly absorbing 25:50:25% mixture of H$_2$, HD, and D$_2$ from more absorptive mixtures.

Another indication that significant fractionation does not occur in a H-D mixture is the thermodynamic properties of the solidification process. Each H-D mixture does not have a specific triple point but exhibits a first-freezing temperature and solidifies over a finite temperature range. First, consider the 25:50:25% mixture of H$_2$, HD, and D$_2$. The temperature at which the mixture begins to freeze (i.e., the first-freezing temperature) θ is given by

$$\theta = \sum_i \left(f_i \times T_{tp,i} \right), \qquad (2)$$

where f_i and $T_{tp,i}$ are the molecular fraction and triple point of the ith component, respectively. Values for this mixture are shown in Table 105.I. Molecular fractions in the table are based on both the pressurization schedule of the gas reservoir when the sample was prepared and on an independent measurement of the sample using cryogenic gas chromatography.[12] Experimentally, the first-freezing temperature for the mixture was 16.53 K and the mixture had completely frozen at ~16.1 K. This implies that complete fractionation does not occur in the mixture since the H$_2$ fraction would not have begun to freeze until 13.96 K. Indeed, if the D$_2$ had initially frozen out of solution, the remaining HD-H$_2$ mixture would not have begun to freeze until 15.72 K, well below the 16.1 K experimentally determined last-freezing temperature.

The first- and last-freezing temperatures were measured for each H-D mixture. As the temperature at the top of the sample was reduced, the highest temperature at the bottom of the

sample at which crystallites began forming was recorded as the first-freezing temperature. Likewise, the highest temperature at the top of the sample at which the sample had completely frozen was recorded as the last-freezing temperature. The data points are shown in Fig. 105.33. This plot is indicative of a classic completely soluble isomorphous system.[13] Such behavior is not unreasonable since the chemical, and therefore crystallographic, nature of each isotope is identical.

T2198JRC
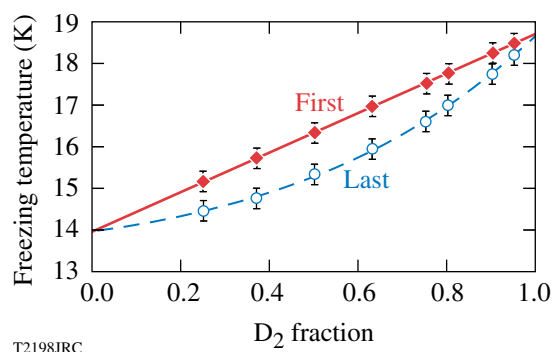
Figure 105.33
The experimentally measured first- and last-freezing temperatures (diamonds and circles, respectively) indicate that the H-D mixtures form a completely soluble isomorphous system. The upper line is from Eq. (2) and uses the known concentration of each mixture and the triple point of each molecule. The lower curve is a third-order least squares polynomial fit to the experimental data. The error bars indicate the ±50 mK uncertainty in the measured temperatures.

Conclusions

The average absorption coefficient of the D$_2$ in a H$_2$-D$_2$ mixture was measured as a function D$_2$ molecular fraction. The absorption coefficient varies exponentially with D$_2$ concentration. This is expected since the relatively large concentrations of D$_2$ in the H-D mixture used in this study deviate from the

low-concentration linear regime over which Beer's Law is valid. There was little separation of the isotopes during the solidification process. The maximum spatial concentration gradients are of the order of 0.02 to 0.05 molecular fraction per millimeter. The average D_2 concentration gradient (percentage) is greatest for the lowest concentrations. The absorption coefficient's gradient was also measured and appears to be inversely proportional to the cooling time, which may be indicative of solid diffusion. Thermodynamically, the mixtures form a completely soluble isomorphous system since the mixture solidifies over a finite temperature range for all concentrations. Possible fractionation during solid-to-vapor-to-solid mass transfer as a result of sublimation and refreezing will be investigated in a future study.

Another observation is that the absorption coefficient for deuterium in the 25:50:25% H_2:HD:D_2 mixture is nearly *twenty times lower* (0.017 mm^{-1} versus 0.317 mm^{-1} for pure D_2). This is attributed to the simultaneous transition absorption requirement of two neighboring D_2 molecules. Therefore, the interference of non-D_2 molecules between adjacent D_2 molecules makes the 3-mm-thick H-D mixture >96% transmissive even though one in four molecules is D_2. Compare this with a 40% transmission for a pure D_2 sample. This will greatly increase the time necessary to layer a D-T–filled capsule using IR–enhanced β-layering versus IR layering with pure D_2 using an IR laser tuned to the 3162 cm^{-1} absorption band of D_2.[14] One solution is to pump the DT molecule at 2888 cm^{-1}, the wave number for the peak absorption for DT.[15] In comparison to 25% D_2, DT makes up 50% of the D-T mixture and, extrapolating the data in Fig. 105.29 to similar behavior with DT concentration, will absorb significantly more IR radiation than the D_2 in the mixture.

Appendix

The Beer–Lambert Law takes on various forms: $A = \alpha' t c$, $I_t/I_0 = e^{-\alpha' t c}$, and $A = \log(I_0/I_t)$, with $\alpha = \alpha' c = 4\pi k/\lambda$, where A is the absorbance, I_0 is the intensity of the incident light, I_t is the intensity after passing through the material, t is the distance that the light travels through the material (i.e., the path length), c is the concentration of absorbing species in the material (mole solute per mole solvent), α' is the molar absorption coefficient, α is the bulk absorption coefficient, λ is the wavelength of the light, and k is the extinction coefficient. In this treatment, since α is a strong nonlinear function of concentration, it will be used instead of the molar absorption coefficient.

The transmission data must be corrected to account for the change in reflectivity of the sample cell upon vaporization of

the solid hydrogen sample. Incorporating Beer's Law above, the transmitted intensity I_t with the solid in the sample cell is given by

$$I_t = I_0 T_1^4 T_2^2 T_3^2 e^{-\alpha t},$$

where I_0 is the incident intensity, α is the absorption coefficient for the solid hydrogen, t is the sample thickness, and the transmittances T are for the interfaces given in Fig. 105.34. After vaporization,

$$I'_t = I_0 T_1^4 T_2^2 T'^2_3;$$

now, let

$$T = \frac{I_t}{I'_t} = T_3^2 \frac{e^{-\alpha t}}{T'^2_3}.$$

Assuming nonabsorbing windows,

$$T_3 = (1 - R_3) \text{ and } T'_3 = (1 - R'_3),$$

where

$$R_3 = \frac{(n_2 - n_3)^2}{(n_2 + n_3)^2} \text{ and } R'_3 = \frac{(n_2 - 1)^2}{(n_2 + 1)^2}$$
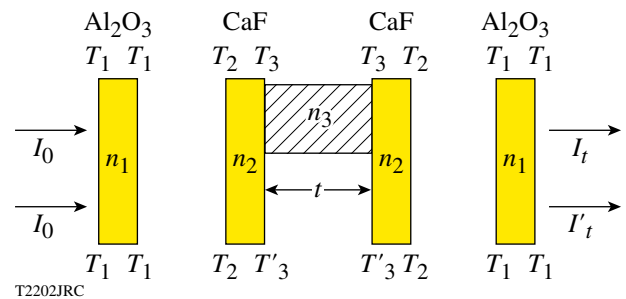
at normal incidence.

Figure 105.34
The attenuation of the sample beam as it passes through the sample cell with and without the solid hydrogen. Both the increase in absorption from the presence of the solid slab and the reduction in reflectivity at the internal boundaries of the cell's windows due to its presence must be accounted for to obtain an accurate absorption coefficient.

The refractive indices n are those shown in Fig. 105.34. Letting

$$\beta = \frac{(1 - R'_3)^2}{(1 - R_3)^2},$$

$$T = \frac{e^{-\alpha t}}{\beta} \text{ and } \alpha = -\frac{\ln(\beta T)}{t}.$$

Therefore, by measuring I_t and I'_t, taking their quotient T, and correcting it using $\beta = 0.964$ at $\lambda = 3.16\ \mu$m for these materials, the absorption coefficient can be measured.

ACKNOWLEDGMENT

REFERENCES

1. P. W. McKenty, T. C. Sangster, M. Alexander, R. Betti, R. S. Craxton, J. A. Delettrez, L. Elasky, R. Epstein, A. Frank, V. Yu. Glebov, V. N. Goncharov, D. R. Harding, S. Jin, J. P. Knauer, R. L. Keck, S. J. Loucks, L. D. Lund, R. L. McCrory, F. J. Marshall, D. D. Meyerhofer, S. P. Regan, P. B. Radha, S. Roberts, W. Seka, S. Skupsky, V. A. Smalyuk, J. M. Soures, K. A. Thorp, M. Wozniak, J. A. Frenje, C. K. Li, R. D. Petrasso, F. H. Séguin, K. A. Fletcher, S. Padalino, C. Freeman, N. Izumi, J. A. Koch, R. A. Lerche, M. J. Moran, T. W. Phillips, G. J. Schmid, and C. Sorce, Phys. Plasmas **11**, 2790 (2004).

2. F. J. Marshall, R. S. Craxton, J. A. Delettrez, D. H. Edgell, L. M. Elasky, R. Epstein, V. Yu. Glebov, V. N. Goncharov, D. R. Harding, R. Janezic, R. L. Keck, J. D. Kilkenny, J. P. Knauer, S. J. Loucks, L. D. Lund, R. L. McCrory, P. W. McKenty, D. D. Meyerhofer, P. B. Radha, S. P. Regan, T. C. Sangster, W. Seka, V. A. Smalyuk, J. M. Soures, C. Stoeckl, S. Skupsky, J. A. Frenje, C. K. Li, R. D. Petrasso, and F. H. Séguin, Phys. Plasmas **12**, 056302 (2005).

3. P.W. McKenty and M.D. Wittman, Bull. Am. Phys. Soc. **50**, 115 (2005).

4. I. Prigogine, R. Bingen, and J. Jeener, Physica (The Hague) **XX**, 383 (1954); *ibid*. 516; *ibid*. 633.

5. M. Bienfait *et al.*, Phys. Rev. B **60**, 11,773 (1999).

6. A. Crane and H. P. Gush, Can. J. Phys. **44**, 373 (1966).

7. J. Van Kranendonk, *Solid Hydrogen: Theory of the Properties of Solid H_2, HD, and D_2* (Plenum Press, New York, 1983), pp. 29–51.

8. L5004-IR Spectrometer System, Laser Components IG, Inc., Hudson, NH, 03051, September 2004, http://www.lasercomponents.com/wwwe/products/index.html (8 February 2006).

9. Displex Low Vibration/Mossbauer Cryostat, DMX-20 Interface, Advanced Research Systems, Inc., Macungie, PA, 18062, 2004, http://www.arscryo.com/dmx20.html (8 February 2006).

10. J. Van Kranendonk, *Solid Hydrogen: Theory of the Properties of Solid H_2, HD, and D_2* (Plenum Press, New York, 1983), pp. 105–129.

11. *ibid*. p. 119.

12. W. T. Shmayda, Laboratory for Laser Energetics, private communication (2005).

13. *Metals Handbook: Metallography, Structures, and Phase Diagrams*, 8th ed. (American Society for Metals, Metals Park, OH, 1973), p. 294.

14. G. W. Collins *et al.*, J. Vac. Sci. Technol. A **14**, 2897 (1996).

15. D. N. Bittner, Shafer Corporation, private communication (2005).

Role of Hydrogen Fractionation in ICF Ignition Target Designs

Introduction

The need of using cryogenic hydrogenic fuels in inertial confinement fusion (ICF) ignition targets has been well established. Efficient implosion of such targets has mandated keeping the adiabat of the main fuel layer at low levels to ensure drive energies are kept at a reasonable minimum. In fact, it has been shown by many authors that the minimum drive energy of an ICF implosion scales roughly as the square of the fuel adiabat.[1–3] The use of cryogenic fuels helps meet this requirement and has therefore become the standard in most ICF ignition designs.

To date, most theoretical ICF ignition target designs have assumed a homogenous layer of deuterium–tritium (DT) fuel kept roughly at or just below the triple point. Such assumptions have lead to several promising ICF target designs[4–7] that have numerically demonstrated ignition and burn under a variety of illumination schemes. Recent work done at the Laboratory for Laser Energetics (LLE), however, has indicated the possibility that, as cryogenic fuel layers are formed inside an ICF capsule, isotopic dissociation of the tritium (T), deuterium (D), and DT can take place, leading to a "fractionation" of the final ice layer.

Fractionation, as illustrated in Fig. 105.35, can lead to isolated areas of the ice layer that are either T rich or D rich. Under such circumstances, the performance and overall viability of previous ignition designs need to be examined.

Motivation

The possibility of isotopic dissociation leading to fractionation within cryogenic hydrogenic fusion fuels was first proposed by Prigogine[8] with initial experimental investigations carried out by Bienfait.[9,10] It is surmised that, because of the different triple point temperatures of the various constituent molecules (T_2, D_2, and DT), as a cryogenic layer is formed, the individual constituents freeze-out separately from the whole. As shown in Fig. 105.35, such a situation could lead to large volumes of the cryogenic layer being totally devoid of DT molecules. The significance of this can be understood when examining the thermonuclear reaction rates for these three molecules as a function of temperature, as shown in Fig. 105.36. The expected operating temperature for inertial confinement ignition target designs, as they approach the ignition threshold, is typically held to be in the 8- to 12-keV range.[11] As can be seen in Fig. 105.36, the reaction rates for both the T + T and

(a) During solidification

(b) Resulting ice layer (if fractionation occurs)

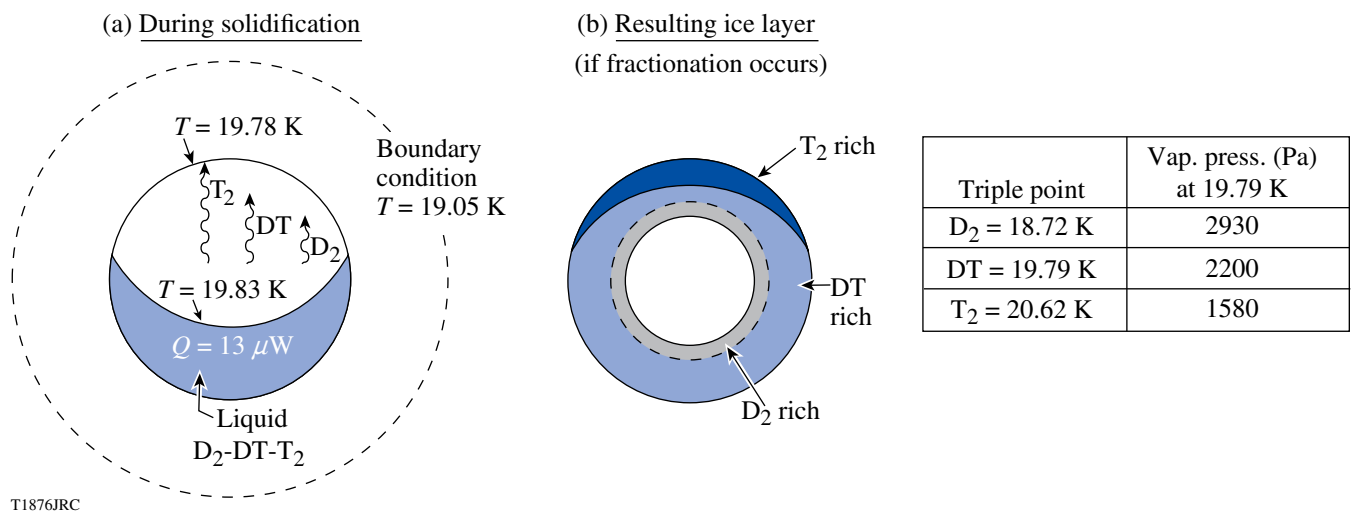| Triple point	Vap. press. (Pa) at 19.79 K
D_2 = 18.72 K	2930
DT = 19.79 K	2200
T_2 = 20.62 K	1580

T1876JRC

Figure 105.35
(a) Fractionation of isotopic hydrogen mixtures can occur because of the variance in the triple point. (b) Such fractionation could lead to isolated fuel layers.

D + D reactions are several orders of magnitude lower than that for the D + T reaction.[12]

Several initial scenarios of fractionation, as illustrated in Fig. 105.35(b), considered complete separation of the constituents into unique and isolated regions of the cryogenic layer. The overall effect of the fractionation on target performance is then dependent on the preponderance and spatial deposition of the separated fusion-fuel molecules. Of particular note is the scenario in which the D_2 molecules are the very last species to solidify. Such a scenario is illustrated in Fig. 105.37(a), where a solid D_2 crust has formed on the inner surface of the ice layer. This is particularly damaging in that when a normal ignition experiment is assembling in preparation for ignition, a central hot spot is required to form at the very center of the target. The majority of the material in this hot spot is made up from the mass from the inner few microns of the ice layer, which, because of the large temperature present at the center due to viscous work, has ablated into the region. As the ablated material is heated, the need for large concentrations of fusing DT molecules and their fusion by-product alpha particles for the initiation of the ignition process is obvious.

The effect of such a scenario on target performance can be quickly examined using the 1-D radiation-hydrodynamic computer code *LILAC*.[13] Several ignition implosion simulations were considered in which the inner surface of cryogenic DT fuel was replaced by solid D_2, as illustrated in Fig. 105.37(a). As shown in Fig. 105.37(b), as this inner layer increases in depth, target performance begins to degrade until eventually the target fails to achieve ignition. This behavior is due to the increasingly DT-depleted fuel that is being ablated into the hot-spot region, failing to produce the necessary alpha particle deposition in the cold, dense fuel surrounding the hot spot.

Another aspect of complete fractionation is the possible formation of a polar cap of pure T_2. Simulations of such scenarios require the implementation of a 2-D radiation-hydrodynamics computer code such as *DRACO*.[14,15] An extreme example of the effect of complete polar separation is given in Fig. 105.38(a).
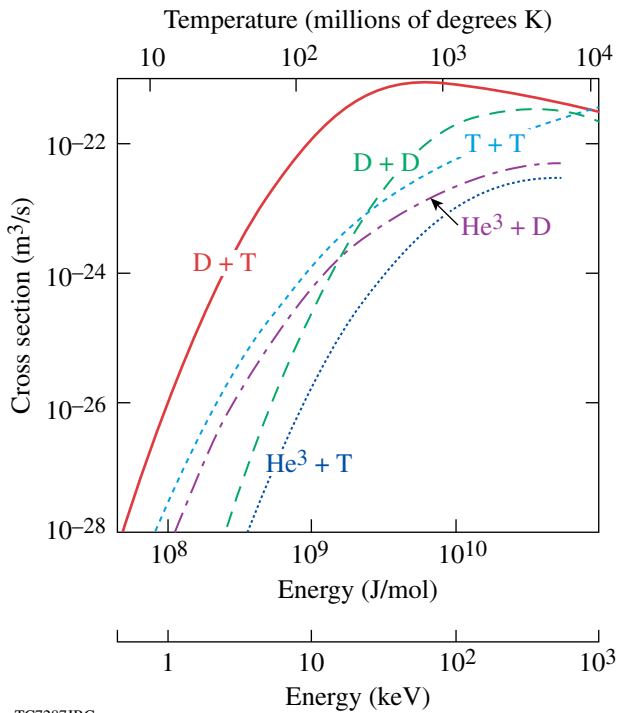
(a)

Figure 105.36
Thermonuclear cross sections for the five most easily activated fusion reactions indicate that DT fusion is the most easily obtained for ICF implosions. (Figure courtesy of the University of California/Lawrence Livermore National Laboratory.[12])
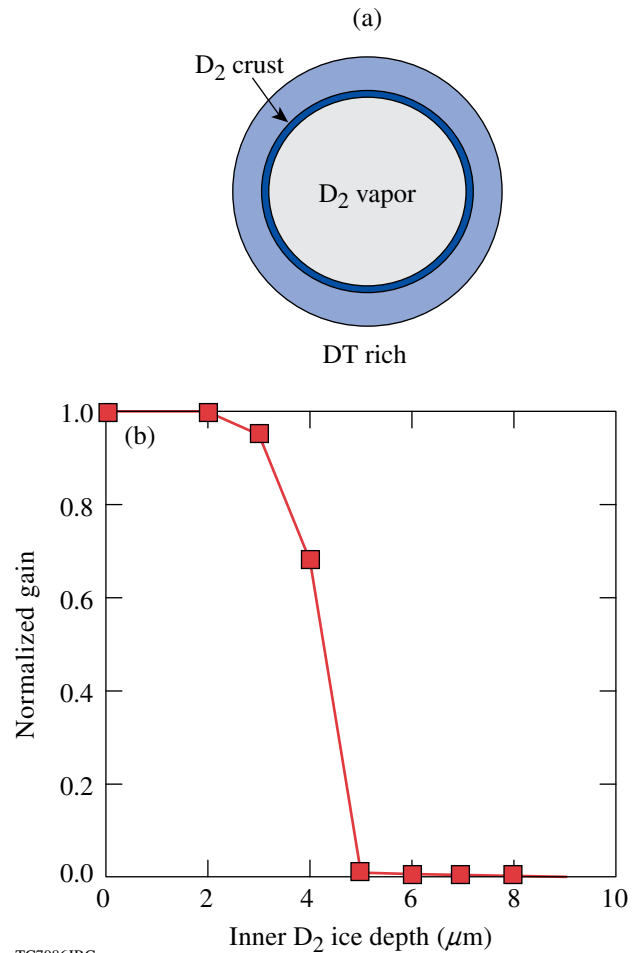
Figure 105.37
(a) Complete inner fractionation denies the ignition hot spot of the necessary tritium, which, (b) in abstenia, can preclude ignition.

Here we consider not only the formation of a northern pole cap of T_2 but, in addition, assume that a southern pole of pure D_2 has also formed. An isodensity plot of this target implosion taken at a time in the experiment after the thermonuclear blast wave has moved through the DT-rich part of the target in the equatorial regions is shown in Fig. 105.38(b). What is apparent in the density plot is that the polar regions of the target have not been able to participate in the burn because of the lack of DT. As such, while the burn wave has severely decompressed the equatorial regions, the polar caps have remained at very high densities because of the compressional nature of the ICF implosion. The overall performance of this design has suffered dramatically with the gain dropping from 45 to about 15.

Results such as these clearly indicate the need to experimentally determine the possibility and overall extent of hydrogenic fractionation in ICF ignition capsules.

Experimental Setup

An experimental test bed to investigate the isotopic fractionation of fusion fuels was designed, built, and implemented at LLE, as illustrated in Fig. 105.39. The system was designed for use with nonradioactive isotopes and, as such, only examines fractionation scenarios involving H_2:HD:D_2 mixtures. We have investigated the possibility of fractionation using a deuterium–hydrogen (H–D) mixture with a similar isotopic ratio to the D–T mixture to be used in future cryogenic experiments
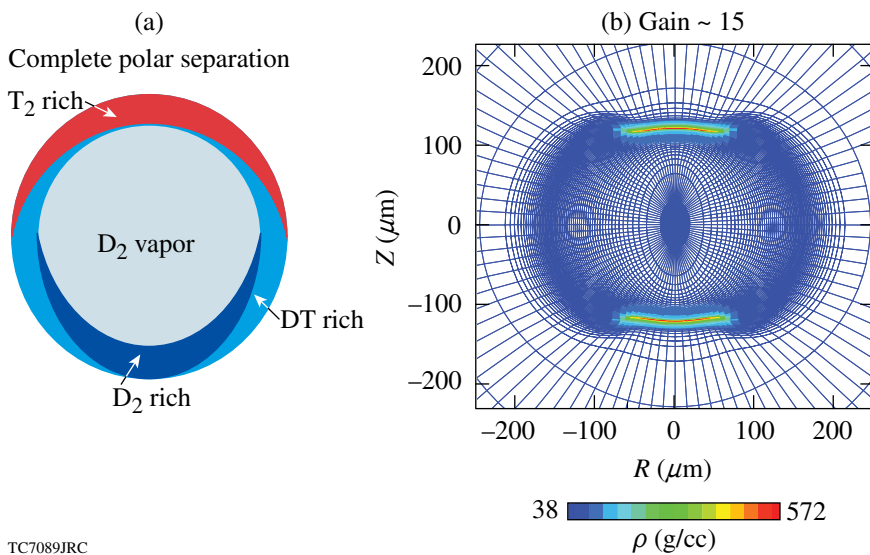

Figure 105.38
(a) A polar cap fractionation scenario exempts the DT-poor poles from the ignited burn, reducing the performance of a high-gain implosion. (b) High-density polar regions are evidence of nonburning fuel.
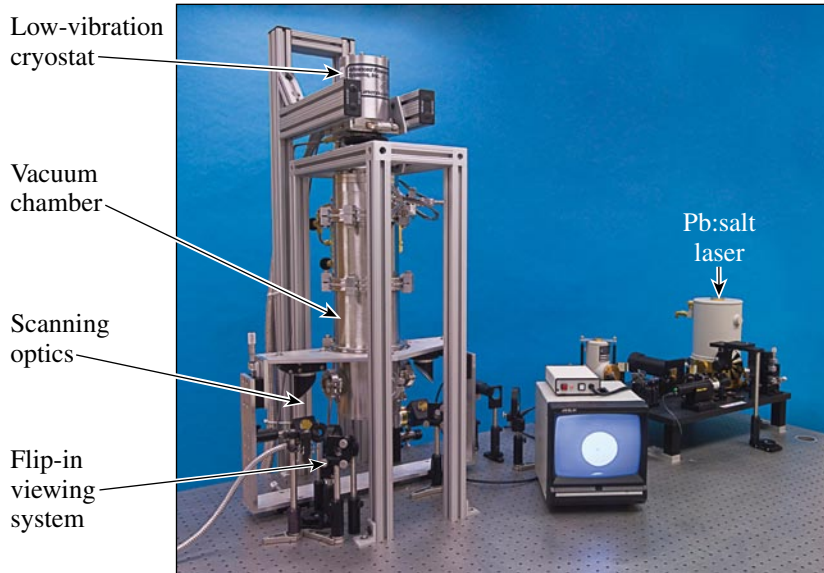

Figure 105.39
A H_2/HD/D_2 fractionation test bed is used to measure the IR absorption coefficient in a cryogenically solidified mixture.

(25% H_2, 50% HD, and 25% D_2) along with a slow-freezing protocol (–10 mK/h over a ~1-K range) that has been demonstrated to produce good-quality targets using the OMEGA Cryogenic Target Handling System. A focused beam from a Pb:salt laser tuned to the 3162 cm^{-1} absorption band of D_2 is raster scanned across a 6-mm-diam, 3-mm-thick sample of the mixture to determine the D_2 concentration as a function of position. This process was performed on samples that were solidified over several hours to several days to look for differences in fractionation due to diffusion of the different molecules to the liquid/solid interface as the sample was cooled.

Several mixtures of various H_2:D_2 ratios were examined in addition to the 25:50:25% H_2:HD:D_2 mixture. By plotting the absorption coefficient of the D_2 in the H–D as a function of the D_2 fraction in the mixture, the slope can be used to quantify a transmission gradient as a concentration gradient. The absorption coefficient for D_2 in a H–D mixture was found to be exponentially dependent on the D_2 molecular fraction in the mixture, as illustrated in Fig. 105.40. From this, a maximum D_2 concentration gradient of 0.02 to 0.05 molecular fraction per millimeter was observed for the samples, as shown in Fig. 105.41. The average D_2 concentration gradient (percentage) is greatest for the 25% molecule fraction of D_2, which is representative of the 25:50:25% H_2:HD:D_2 mixture. The large error bars shown for the lowest concentrations indicate the signal-to-noise ratio in the measurement is smallest when the sample is the least absorptive.

Experimental Results

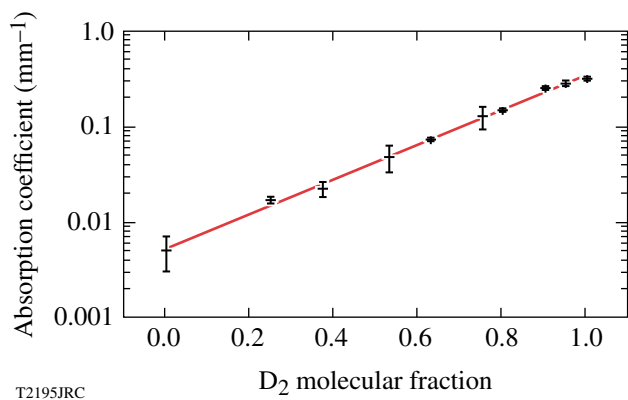A complete and thorough discussion of the experimental results are presented earlier in this issue in **Isotopic Fractionation During Solidification of H_2–HD–D_2 Mixtures** on pp. 29–32. We have included a subset of this discussion to establish the relevant experimental initial conditions needed in the numerical modeling of fractionation.

Initial experiments focused on answering the question of whether or not complete fractionation, the situation where regions of pure, single isotopes freeze-out separately, occurs for these types of isotopes. Of particular interest was the experimentally observed, "first-freezing" (FF) temperature of a given cryogenic sample. The FF temperature is the temperature of the cryostat at which definitive crystal growth is observed. For pure samples or cases of complete fractionation, this would, of course, be the normal triple point of the material as given in Table 105.I on p. 32. Also given in the table are approximations for the FF temperature based on various models for the mass fraction of a given mixture. The FF temperature is calculated from a weighted sum of the product of the assumed isotopic mass fraction f_i and its appropriate triple point temperature $T_{tp,i}$ as given by

$$\sum_i f_i \times T_{tp,i}.$$

From this approximation one can see that the FF temperature for this mixture should lie in the range from 15.72 to 16.49 K. Additionally, the entire mixture should freeze-out into a layer when the FF temperature is reached and held constant.

The experiment was conducted and attention was focused on the mixture as the cryostat temperature approached the first triple point of the mixture constituents (deuterium) at 18.73 K. No appreciable crystal growth was observed. The same was true when the cryostat temperature reached and fell below the triple point of the HD molecule at 16.60 K. This experiment

Figure 105.40
The average absorption coefficient of the D_2 in a H_2–D_2 mixture was measured as a function of the D_2 molecular fraction.
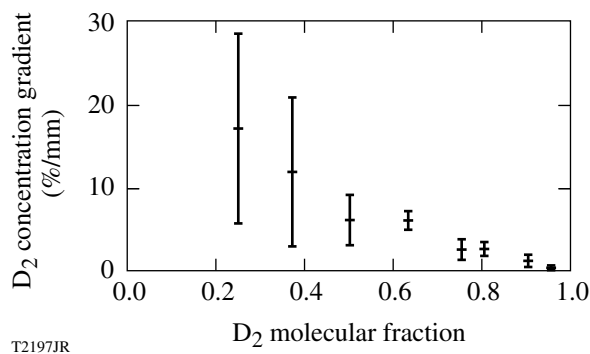

Figure 105.41
The average D_2 concentration gradient (percentage) is greatest for the lowest concentrations.

was repeated several times with the same results and indicates the absence of complete fractionation in cryogenic fusion fuels. As the experiment proceeded, it was only at a temperature of 16.53 K that appreciable crystal growth appeared. However, the entire sample did not freeze-out into a layer as the temperature was held constant. It was only after the cryostat temperature was further lowered to 16.10 K that total solidification of the mixture was observed. While the results from these experiments indicated that complete fractionation of cryogenic fuel layers does not take place, the differential temperatures required to freeze the entire sample did indicate the presence of low levels of fractionation within the mixture.

Additional experiments that examined the spatial dependence of the IR transmission coefficient of a cryogenic sample layered within the low-vibration cryostat were then carried out. As illustrated in Fig. 105.42, the experimental system recorded a spatial variation in the transmission coefficient of the cryogenic sample. Figure 105.42 also shows the singular transmission levels for pure H_2 and D_2 samples. From this image it is clear that fractionation has occurred within the cryogenic fusion-fuel layer. Interpretation of the variance in transmission indicates that fractionation levels in the sample are in excess of 5% from one side of the cell to the other and could in fact be as high as 10% overall.
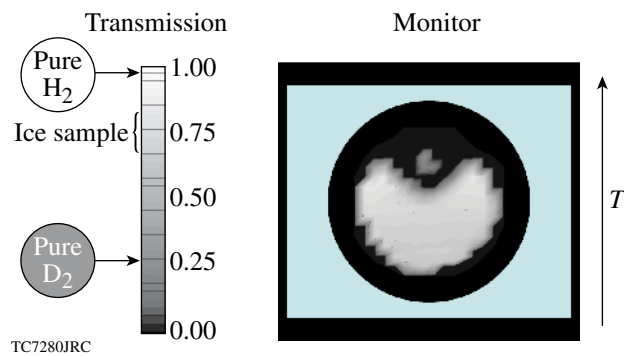

Figure 105.42
The absorption coefficient of the D_2 in the H/D mixture is less than 1/20th of that for pure D_2.

Numerical Results

A numerical fractionation scenario based on the above experimental results was constructed and studied. The particular metric investigated was the effect of the fractionation on target gain. Using the template illustrated in Fig. 105.43, the north polar fractionation within the target was numerically varied up to levels of 100%. As the level of fractionation was increased past ~30%, the increasing lack of DT at the poles

of the target began disrupting the target performance. As can be seen in Fig. 105.44, this process can degrade target performance from a gain of 45 for perfect ice down to less than 10 for the cases with high levels of fractionation. For small levels of fractionation, the ignition and burn phases of the implosion proceed almost completely unaffected by the redistribution of the fusion fuel within the target. It is helpful to remember that in most ICF ignition designs the burnup fraction of fusion fuel is typically only in the 10%–15% range by molecule. As such, the target performance is relatively unaffected by small changes in the distribution of the fusion-fuel molecules. As was discussed earlier, however, as the amount of DT within a specific volume of the target is reduced, the likelihood of that region participating in the ignition burn wave is greatly diminished.

Another indication of how increasing fractionation perturbs target performance can be seen from a comparison of the
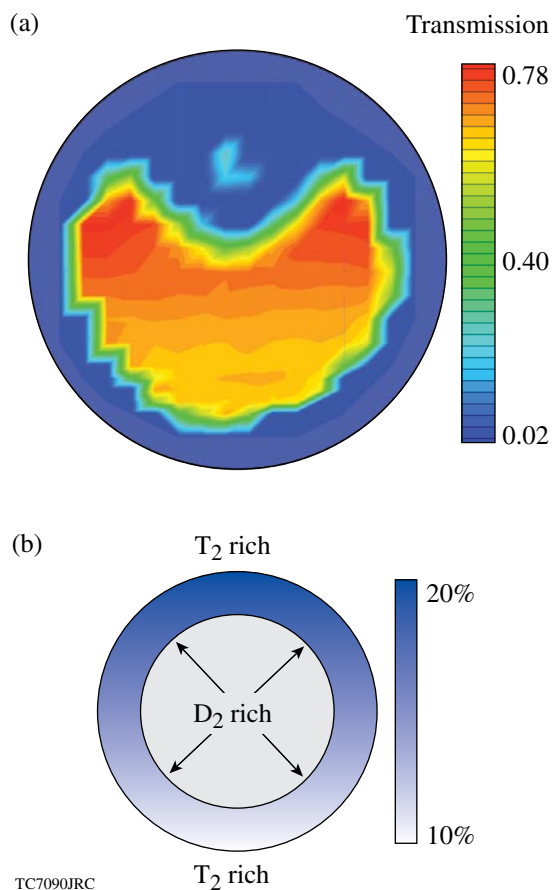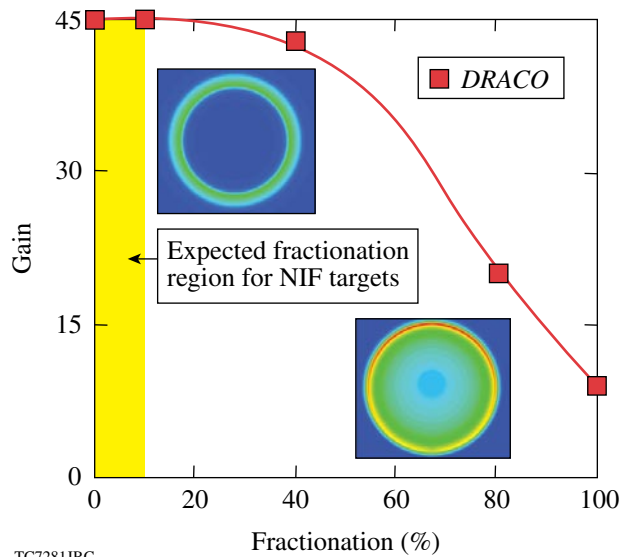

Figure 105.43
(a) Isotopic hydrogen (H_2/HD/D_2) fractionation in a solution has been observed in the laboratory at levels approaching 10%. (b) This information was used to construct a set of initial conditions for numerical studies of fractionation in ICF target designs.

Figure 105.44
Fractionation levels in excess of ~30% are required before ignition target performance is affected. Current estimates place a 10% upper limit on the fractionation—too low to degrade target performance.

isodensity contour plots given as insets in Fig. 105.44. These contours, drawn on the same legend, demonstrate the symmetric decompression of the ice layer in the low fractionation cases. While similar decompression is apparent in the lower hemisphere of the high-fractionation case, the north polar region has remained at high compressed densities because of the region's inability to participate in the DT thermonuclear burn.

While the effects of high levels of fractionation on target performance are disturbing, the good news is that, given the experimental evidence to date, current estimates of the levels of fractionation in NIF ignition target designs are not expected to exceed 10%. As such, fractionation is not viewed as a major threat to the overall performance of ICF ignition design planned for experiments on the NIF, as illustrated as the shaded region of Fig. 105.44.

Conclusion

The need of using cryogenic hydrogenic fuels in ICF ignition target designs has been well established. Efficient implosion of such targets has mandated keeping the adiabat of the main fuel layer at low levels to ensure drive energies are kept at a reasonable minimum. To date, most theoretical ICF ignition target designs have assumed a homogenous layer of DT fuel kept roughly at or just below the triple point. However, recent work done at LLE has indicated the possibility that, as cryogenic fuel layers are formed inside an ICF capsule, isotopic dissociation of the T, D, and DT can take place, leading to a "fractionation"

of the final ice layer. Fractionation studies of fusion-like fuels (H/HD/D) have demonstrated the existence of fractionation in ICF cryogenic fuel layers. However, numerical simulations of ignition target designs, using experimental fractionation scenarios, indicate that small levels of fractionation (~10%) are acceptable for ignition performance on the NIF.

REFERENCES

1. R. Betti, K. Anderson, V. N. Goncharov, R. L. McCrory, D. D. Meyerhofer, S. Skupsky, and R. P. J. Town, Phys. Plasmas **9**, 2277 (2002).

2. M. C. Herrmann, M. Tabak, and J. D. Lindl, Nucl. Fusion **41**, 99 (2001).

3. A. Kemp, J. Meyer-ter-Vehn, and S. Atzeni, Phys. Rev. Lett. **86**, 3336 (2001).

4. T. R. Dittrich *et al.*, Phys. Plasmas **5**, 3708 (1998).

5. P. W. McKenty, V. N. Goncharov, R. P. J. Town, S. Skupsky, R. Betti, and R. L. McCrory, Phys. Plasmas **8**, 2315 (2001).

6. A. J. Schmitt *et al.*, Phys. Plasmas **11**, 2716 (2004).

7. J. L. Perkins and M. Tabak, Bull. Am. Phys. Soc. **49**, 61 (2004).

8. I. Prigogine, R. Bingen, and J. Jeener, Physica (The Hague) **XX**, 383 (1954); *ibid*. 516; *ibid*. 633.

9. M. Bienfait *et al.*, Physica B **234–234**, 159 (1997).

10. M. Bienfait *et al.*, J. Low Temp. Phys. **111**, 555 (1988).

11. J. D. Lindl, Phys. Plasmas **2**, 3933 (1995).

12. P. C. Souers, *Hydrogen Properties for Fusion Energy* (University of California Press, Berkeley, 1986). Figure courtesy of the University of California/Lawrence Livermore National Laboratory and the Department of Energy under whose auspices this work was performed.

13. M. C. Richardson, G. G. Gregory, R. L. Keck, S. A. Letzring, R. S. Marjoribanks, F. J. Marshall, G. Pien, J. S. Wark, B. Yaakobi, P. D. Goldstone, A. Hauer, G. S. Stradling, F. Ameduri, B. L. Henke, and P. Jaanimagi, in *Laser Interaction and Related Plasma Phenomena*, edited by H. Hora and G. H. Miley (Plenum Press, New York, 1986), Vol. 7, pp. 179–211.

14. D. Keller, T. J. B. Collins, J. A. Delettrez, P. W. McKenty, P. B. Radha, B. Whitney, and G. A. Moses, Bull. Am. Phys. Soc. **44**, 37 (1999).

15. P. B. Radha, V. N. Goncharov, T. J. B. Collins, J. A. Delettrez, Y. Elbaz, V. Yu. Glebov, R. L. Keck, D. E. Keller, J. P. Knauer, J. A. Marozas, F. J. Marshall, P. W. McKenty, D. D. Meyerhofer, S. P. Regan, T. C. Sangster, D. Shvarts, S. Skupsky, Y. Srebro, R. P. J. Town, and C. Stoeckl, Phys. Plasmas **12**, 032702 (2005).

Polar-Direct-Drive Simulations and Experiments

Introduction

Polar direct drive (PDD)[1] provides a viable path for direct-drive ignition on the National Ignition Facility (NIF).[2] Ideally, direct-drive ignition experiments require a symmetric arrangement[3–5] of high-powered UV laser beams pointed at the target center with focal spots that fill and overlap the spherical target surface. The NIF will be configured initially for x-ray drive, however, with the beams arranged around the polar axes to illuminate the interior of cylindrical hohlraums via entrance holes located at either end of the cylinder.[6] The PDD concept will enable direct-drive ignition experiments on the NIF while it is in the x-ray-drive configuration. Polar direct drive achieves uniform drive by repointing the beams, designing the on-target spot shapes with customized phase plates,[7,8] employing an optional CH ring that surrounds the equatorial region and acts as a plasma lens, refracting laser energy back toward the target (referred to as the Saturn target, see Ref. 9), and taking advantage of the NIF's flexible pulse-shaping capability.

The PDD concept is currently under experimental investigation on the OMEGA Laser System.[8] The goal of the experiments was to provide an understanding (both experimentally and through simulation) of the laser absorption characteristics resulting from repointing the beams and to test the ability to drive PDD implosions that obtain yields close to energy-equivalent symmetric-drive implosions. The common CH targets provide an adequate test bed for this purpose. (Surrogate cryogenic targets that scale to NIF designs are being planned for future experiments.) As shown in Fig. 105.45(a), a 40-beam subset of the 60-beam OMEGA laser has been chosen to emulate the NIF x-ray-drive configuration. Both the standard PDD and Saturn target designs utilize the OMEGA laser in this 40-beam configuration. Figure 105.45(b) illustrates how the beams are repointed for OMEGA PDD experiments. The Saturn target[9] employs an equatorial CH ring to refract laser energy from the obliquely pointed beams toward the target equator. Radiation from the CH ring also plays a role in driving the equator. The initial simulation and evaluation of these experiments was performed using the hydrodynamics code *SAGE*.[10] Present work uses the hydrodynamics code *DRACO*,[11] an arbitrary Lagrangian Eulerian (ALE) code that includes both radiation transport and fusion particle production and transport as well as a full 3-D laser ray-trace deposition package. *DRACO* can also be configured to run in a sliding-grid Eulerian mode (which is necessary to simulate the Saturn targets to support the shock transit in the space between the CH ring and the target).
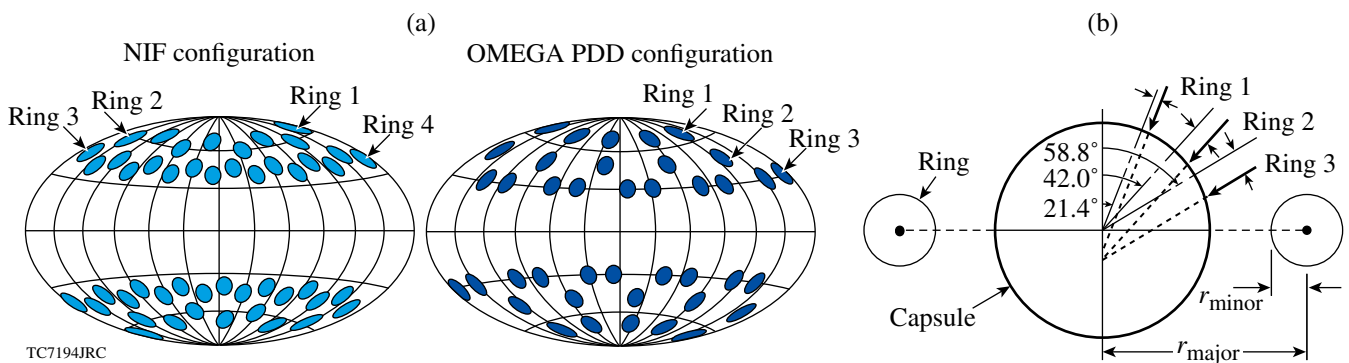
Figure 105.45

(a) Illustration of beam port positions for the NIF and OMEGA indirect-drive configurations. A 40-beam subset of the 60-beam OMEGA Laser System emulates the NIF indirect-drive configuration. (b) The beam pointing schemes described in this paper for the OMEGA PDD program. Rings 1 and 2 (each hemisphere) have five beams each, while Ring 3 (each hemisphere) has ten beams for a total of forty beams. All beams in a ring are offset in the far-field plane perpendicular to the central beam axis (as indicated by the thin arrows) by the amount shown in Table 105.II. The placement of the Saturn ring is also indicated (not to scale).

In **OMEGA Experiments and Simulations** (p. 42), OMEGA PDD experiments and simulations are presented and compared for both types of PDD targets. The *DRACO* simulations of the OMEGA experiments presented here analyze the low-ℓ-mode behavior due to beam overlap and the increased refractive losses due to repointing the beams toward the equator. The angular resolution used in these simulations was 80 zones over a 90° wedge; the low-ℓ-mode structure up to mode $\ell = 22$ is adequately resolved. (Note: there is only significant power in modes up to $\ell = 6$.) The long-wavelength effects of energy balance and beam mispointing as well as the short-wavelength behavior of single-beam nonuniformity are currently under investigation. Good agreement is found by comparing x-ray framing-camera images with *DRACO* simulations. These implosions were all simulated in the sliding-grid Eulerian mode to make a consistent comparison with the Saturn simulations that require Eulerian hydrodynamics.

In **NIF Simulations** (p. 46), substantial gain is predicted with NIF-scale, 2-D *DRACO* implosion simulations. The simulated standard PDD targets consist of cryogenically layered deuterium–tritium (DT) encased with a wetted hydrocarbon (CH) foam[12,13] and a thin CH overcoat layer. The *DRACO* simulations for the NIF also included the effect of the low-ℓ-mode behavior due to beam overlap and repointing and were simulated in the ALE mode. For 1.36 MJ of laser energy, the PDD target gives a gain of 20. In comparison, the gain is 33 if the same target is driven symmetrically with 1.0 MJ of laser energy. The compressed core near stagnation consists of a 40-μm-radius, 10-keV region with a neutron-averaged ρr of 1270 mg/cm^2. The importance of maintaining both shell and shock-front uniformity is stressed.

OMEGA Experiments and Simulations

Experimental confirmation of 2-D *DRACO* hydrodynamic simulations has been obtained by making comparisons with PDD implosions[14] carried out on OMEGA. The implosions were performed with a nominal room-temperature target consisting of 865-μm-diam, 19.7-μm-thick (experimental average) glow-discharge polymer shells filled with D$_2$ gas at a pressure of 15 atm. This type of target has been used extensively on OMEGA.[10,15–17] All capsules were coated with 500 Å of Al to act as a gas retention barrier and are held in place by 17-μm boron fibers glued to the target surface. (Note that the Al layer and boron fibers were not simulated.) The capsule diameters were measured to an accuracy of 1 μm and the shell thickness to 0.2 μm. The Saturn targets reported here consisted of the same capsule supported by three 10-μm-diam alumina "spokes" (which were not simulated), again glued to the target

surface, inside a CH ring of circular cross section with a 1.1-mm major radius and a 150-μm minor radius (shots with a 1.25-mm major radius were also measured but not simulated). The laser drive was a 1-ns flat pulse with ~390 J per beam employing 1-THz, 2-D smoothing by spectral dispersion[18–21] with polarization smoothing.[17] The 40 OMEGA beams were repointed for PDD with a typical accuracy of 15-μm rms using the technique described by Forties and Marshall (Ref. 22). Figure 105.45(b) depicts the beam-pointing scheme used for the experiments and simulations described in this work. Table 105.II details the configurations, giving the lateral offsets from the central beam axis in the far-field plane for three different cases. Figure 105.45(b) also indicates the placement of the Saturn ring.

Table 105.II: PDD offsets, Δr (μm)

	Case	Ring 1	Ring 2	Ring 3
A	Shot 38502 Shot 39281	90	120	120
B	Shot 34669	91	188	196
C	Proposed	74	61	180

As in Refs. 10 and 14, the imploding targets were diagnosed by framed x-ray backlighting. The framing cameras were configured to operate at a magnification of 6 with 10-μm pinholes and an effective resolution of ~11 μm. Each frame's integration time was ~50 ps and the absolute time of a frame was determined by noting the time of backlighter onset (known to be better than 10 ps). Au backlighters were used with a broadband emission ranging from 2.2 to 2.5 keV. Two backlighters were available, one viewing the target from just below the equator ($\theta_{va} = 101°$) and one well above the equator ($\theta_{va} = 63°$). The latter provided a view of the partially imploded plasma even in the presence of a Saturn ring. The delay of the backlighter beams was +0.9 ns relative to the beginning of the laser pulse. All beams used the same 1-ns flattop pulse shape with 100-ps rise and fall times. Peak power occurred from 0.1 ns to 1.0 ns. Backlit radiographs were obtained after the end of the drive pulse (~1.1 ns to 1.7 ns). Stagnation occurs around 1.9 ns.

X-ray radiography was used to measure the magnitude of deviations from spherical symmetry. Early in time, the deviations from sphericity are small and the streaked and framed x-ray imaging shows that the shell trajectory closely matches the predictions of 1-D simulations.[10] Later in time, however, the deviations become larger and increasingly important. The evolution of the shell distortion can be seen in Fig. 105.46(a), where three backlit framed x-ray images taken at times $t = 1.23$, 1.49, and 1.68 ns are shown for OMEGA shot 38502

(19.6-μm CH shell thickness), as viewed from the angle θ_{va} = 101°. This shot utilized the pointing intended for a Saturn target (case A of Table 105.II) but the target was shot without the external CH ring; therefore, strong distortions were expected around the equatorial plane where the target was underdriven. The *DRACO* simulation of this experimental shot was post-processed with the code SPECT3D (Ref. 23) to simulate an x-ray backlighter at the same viewing angle. The *DRACO*/SPECT3D-simulated x-ray radiograph results of shot 38502 are shown in Fig. 105.46(b) at times corresponding to the

experimental images. Both the size and shape of the simulated radiographs are close to those observed.

To provide a quantitative comparison between simulations and experiments, the locations of the x-ray radiograph minima of an OMEGA experiment and the simulated x-ray radiograph from a *DRACO*/SPECT3D simulation can be plotted [as a function of angle (θ') from the vertical image axis]. The x-ray radiograph minima of OMEGA shot 38502 at the viewing angle θ_{va} = 63° as a function of angle (θ') are shown in Fig. 105.47(a) (circles) taken at 1.68 ns, which was extracted from the x-ray radiograph shown in Fig. 105.47(b). The typical error in determining the position of the minimum is ±2 μm, as indicated by the example error bar in Fig. 105.47(a).

The data points extracted from a simulated radiograph are sufficiently smooth that they are well represented by a Legendre polynomial fit. These data are also extracted with
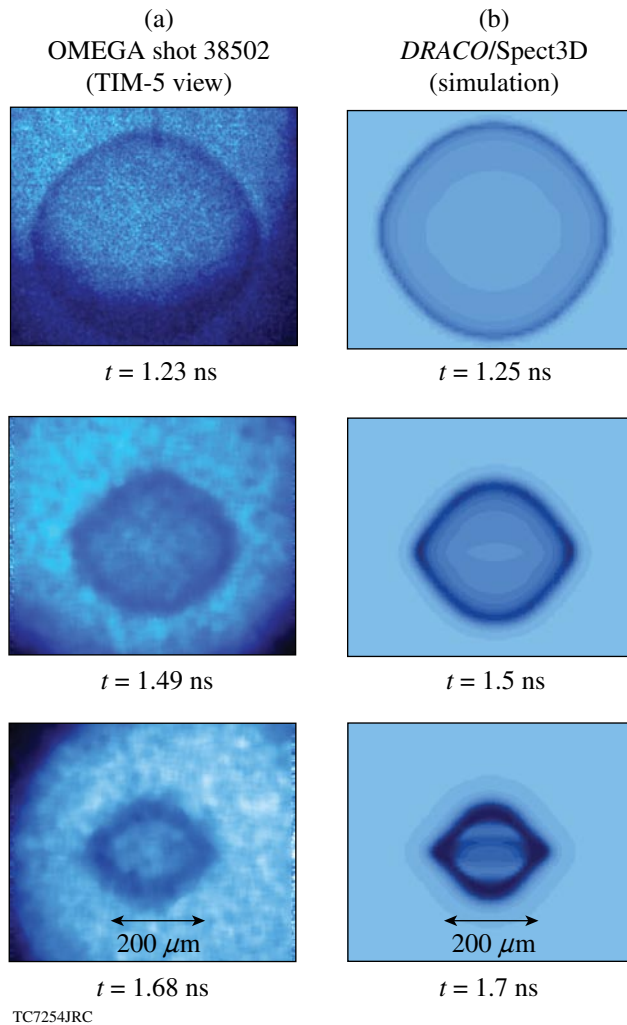

Figure 105.46
(a) Experimental x-ray framing-camera images. The dark rings (minimum x-ray transmission) indicate the evolution of the shell distortion. The times t = 1.2, 1.5, and 1.7 ns are shown for a standard PDD target on OMEGA for shot 38502. (b) Simulated x-ray radiographs at corresponding times produced from *DRACO* simulations that have been post-processed by SPECT3D. Note that the pointing used for this shot is intended for a Saturn target. The radiographs are imaged from TIM-5 at θ_{va} = 101°.

Figure 105.47
(a) The radii of the x-ray transmission minimum as a function of image polar angle (θ') are shown for OMEGA standard-PDD shot 38502 as circles at 1.68 ns relative to a radius of 93.1 μm. A Legendre polynomial fit to the simulated radiograph data is displayed as the black line at 1.7 ns relative to a radius of 94.3 μm. The peak-to-peak deviations are 15 μm for the experimental data and 13 μm for the *DRACO*/SPECT3D simulation. (b) The experimental and (c) simulated radiographs. The radiographs are imaged at θ_{va} = 63°.

an error of ± 2 μm. Since the imploding shells are observed at an angle to the symmetry axis, it is necessary to transform the image's polar angle into the natural coordinates of the Legendre modes, viz.

$$\cos(\theta) = \cos(\theta')\sin(\theta_{va}), \qquad (1)$$

where θ is the polar angle of the spherical coordinate system aligned with the target pole and θ_{va} is the viewing angle used in the experiment. The Legendre decomposition over the first six modes is given by

$$R_{\exp}(\theta') = \sum_{l-1}^{6} A_l \cdot P_l[\cos(\theta)], \qquad (2)$$

where P_l is the Legendre polynomial of order l. This fit approximates the shape of the radiograph to that of a cut through an idealized thin shell. No significant modes above $\ell = 6$ were found, so only the fits up to 6 were included. A Legendre polynomial fit to the transmission minima from the *DRACO*/SPECT3D-simulated x-ray radiograph [Fig. 105.47(c)] is found and plotted in Fig. 105.47(a) (thick line) for the simulation time of 1.7 ns. The peak-to-peak deviations are 15 μm for the experimental data and 13 μm for the *DRACO* simulation.

The framed x-ray radiographs for a Saturn target taken at times $t = 1.21$, 1.46, and 1.65 ns for OMEGA shot 39281 (19.7-μm shell thickness) are shown in Fig. 105.48(a) with the same beam pointings (case A of Table 105.II). *DRACO*/SPECT3D-simulated x-ray radiographs are shown in Fig. 105.48(b) at similar times. Lineouts as a function of θ', similar to those of Fig. 105.47(a), are shown at ~1.65 ns in Fig. 105.49 with the experimental data as circles and the *DRACO*/SPECT3D data as a solid line. The peak-to-peak deviations are 10 μm for the raw data and 9 μm for the *DRACO* simulation. The effect of the external CH ring is readily observed by noting that the equatorial bulge around the equator has been decreased [compare Figs. 105.46 and 105.48 and Figs. 105.47(a) and 105.49] because of increased laser-energy deposition and radiation from the CH ring, which together increase the drive in the equatorial region.[10]

Saturn targets have obtained the best experimental yields to date relative to energy-equivalent, 60-beam symmetrically driven targets. The measured DD neutron yields for both types of PDD targets (standard and Saturn) and, for comparison, the yields obtained from symmetrically irradiated targets (60 beams with an equivalent on-target energy of 15.3 kJ) are

(a) OMEGA shot 39281 (TIM-4 view)

$t = 1.21$ ns $\qquad$ $t = 1.46$ ns $\qquad$ 200 μm $\quad$ $t = 1.65$ ns

(b) *DRACO*/Spect3D (simulation)

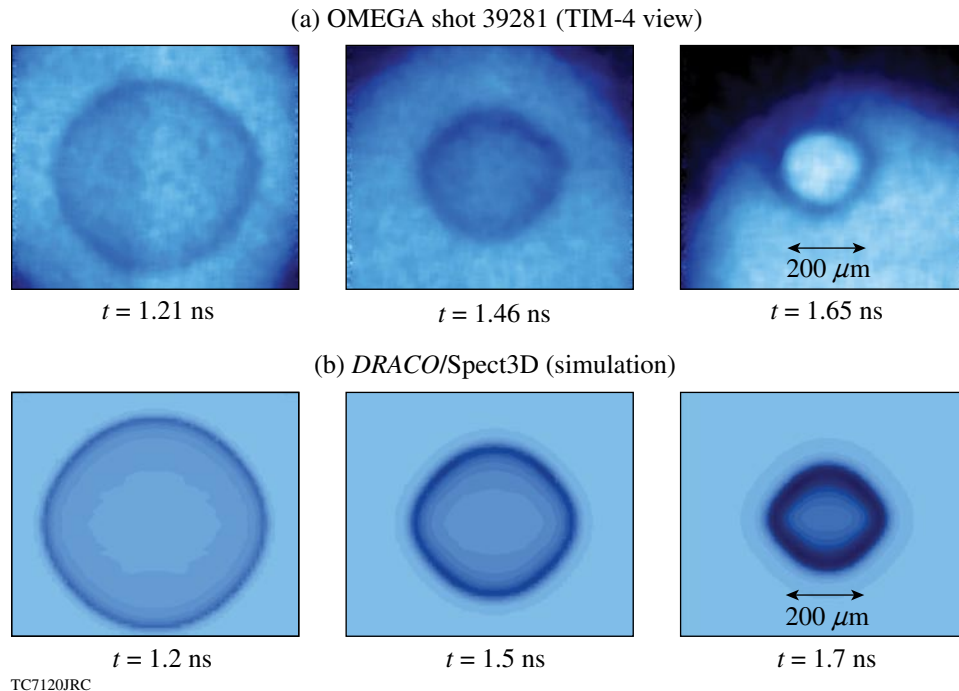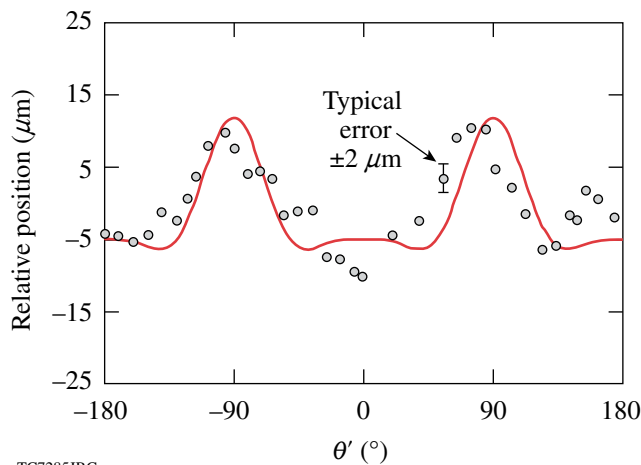$t = 1.2$ ns $\qquad$ $t = 1.5$ ns $\qquad$ 200 μm $\quad$ $t = 1.7$ ns

TC7120JRC

Figure 105.48
(a) Experimental x-ray framing-camera images indicating the evolution of the shell for a Saturn target on OMEGA shot 39281 at times $t = 1.2$, 1.5, and 1.7 ns. (b) Simulated x-ray radiographs using *DRACO* and SPECT3D. The radiographs are imaged at $\theta_{va} = 63°$.

shown in Fig. 105.50. The standard targets obtained ~35% of the symmetric target yields. The spoke-mounted Saturn targets obtained about 75% of the symmetric target yields. The *DRACO*-simulated yield for the energy-equivalent symmetric-drive shot 34644 (19.6-μm shell thickness) was 2.91×10^{11} DD neutrons. This compares to the simulated yields for the standard PDD shot 34669 (19.3-μm shell thickness) and the Saturn shot 38291, 1.28×10^{11} and 1.73×10^{11} DD neutrons, respectively. The normalized yield results for two shots are summarized in Table 105.III. The Saturn target simulation yield increased relative to the standard PDD target but only by 34%, from 44% to 59%, whereas the experimental yield doubled (when comparing the standard PDD to the Saturn target).

Standard PDD targets can benefit from further optimization of pointing, spot shapes, and ring energy balance to produce
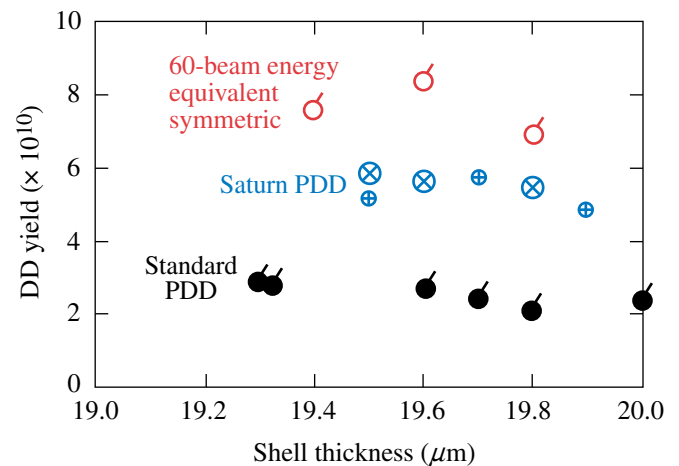
results comparable to the current Saturn target designs. The benefit of finding an optimized standard-PDD design is the ability to fabricate and shoot a cryogenic PDD target. The Saturn design is not practical for cryogenic targets. For the sake of comparison, a warm CH target is used here since current experimental and simulated results exist. The current pointings used for standard PDD (case B in Table 105.II) were chosen on the basis of the existing phase plates on OMEGA (super-Gaussian of order 3.7). An optimization algorithm (separate from *DRACO*) was run that automatically tunes the beam pointing and spot shapes for equal energy beams, given an absorption angular spectrum extracted from a *DRACO* simulation under similar conditions. Different results will be

Figure 105.49

The radius of the x-ray transmission minimum as a function of image polar angle (θ') extracted from the 1.65-ns (right-hand) image of Fig. 105.48(a), shown as circles, relative to a radius of 101.7 μm. A Legendre polynomial fit to the simulated radiograph data extracted from the 1.7-ns (right-hand) image of Fig. 105.48(b) is displayed as the solid line relative to a radius of 106.6 μm. The peak-to-peak deviations are 10 μm for the experimental data and 9 μm for the *DRACO* simulation.

Figure 105.50

The measured DD neutron yields for both types of PDD targets (standard and Saturn) and, for comparison, the yields obtained from symmetrically irradiated targets (60 beams with the same on-target energy of 15.3 kJ). The standard-PDD targets obtained ~35% of the symmetric target yields. The Saturn targets obtained about 75% of the symmetric target yields. All shots employed a 1-ns flattop pulse with 100-ps rise and fall times. All PDD targets used optimal beam pointing ("A" of Table 105.II for Saturn, "B" for standard PDD). The Saturn shots with different major diameters are as indicated on the plot; the small symbols correspond to $r_{major} = 1100$ μm and the large symbols correspond to $r_{major} = 1250$ μm.

Table 105.III: Normalized experimental and simulation yields. The experimental yields are normalized to the energy-equivalent symmetric-drive experiment for shot 34644. The simulation yields are normalized to the simulation of the energy-equivalent symmetric-drive simulation.

	Standard PDD shot 34669	Saturn shot 39281 spoke mount
Experimental yield normalized to symmetric shot 34644	0.35	0.69
Simulation yield normalized to simulation of symmetric shot 34644	0.44	0.59

obtained by making alternate choices of sampled absorption spectra. The nonuniformity during the acceleration phase plays an important role for the long-wavelength distortions characteristic of PDD, especially when the laser energy is absorbed farther away from the critical surface around the equator. For this reason, the angular dependent absorption is taken during the acceleration phase at ~700 ps with the assumption that it is representative of the most influential period. The optimization process first overlaps the beams onto a hard sphere while accounting for the angular dependence of absorption. The spot shapes are changed and also repointed to minimize the nonuniformity of the absorbed energy profile on the surrogate target sphere. The resultant pointing for the different beam rings is 74, 61, and 180 μm. The resulting spot shapes are super-Gaussians of orders 2.58, 2.11, and 2.42, respectively, with 5% intensity contours located at 1.05× the target radius. Optimal PDD designs tend toward lower super-Gaussian orders because the narrower intensity peaks give the rings more independent control, particularly in the troublesome equatorial region; e.g., more energy can be delivered to the equator with minimal influence on the rest of the target. Additionally, the spot shapes are modulated by an order-10 super-Gaussian envelope with a 5% intensity contour at the target radius to maximize the energy delivered to the target (especially by minimizing the over-the-horizon energy near the equator). The energy of the first ring was derated by 15% to prevent overdrive in the polar region; as a consequence, the incident laser energy is only 14.8 kJ. The simulated absolute yield for this proposed configuration is comparable to that of the Saturn design (using 15.6 kJ of laser energy), and the symmetry of the shell is very similar, as shown in Figs. 105.51(a) and 105.51(b). It is expected that the shell symmetry can be improved by further tuning the beam repointing and spot shapes. The yields relative to the simulation of the energy-equivalent symmetric-drive target are 59% and 58%, respectively.

NIF Simulations

Cryogenic, DT-filled, wetted CH-foam targets show great promise for high PDD gains on the NIF.[24] The four rings of beams in the NIF indirect-drive configuration shown in Fig. 105.45(a) are repointed into three rings which are logically grouped by the angle in which the beam centers intersect the initial target radius; they are designated as polar, midlatitude, and equatorial rings. The polar and midlatitude rings are typically not repointed by a significant amount, whereas the equatorial ring is repointed the most, amounting to a transverse shift in the far-field plane of ~850 μm.

A successfully igniting PDD target requires that both shell and shock-front uniformity be maintained at a high level throughout the drive pulse. The equator experiences the highest incident angles, which lead to higher refractive losses and lower hydrodynamic efficiency, 2-D effects such as lateral mass and heat flow become important, and the relative pointing changes as the critical surface moves inward. The shell uniformity can be compromised because of the dynamic nature of the low-ℓ-

Figure 105.51
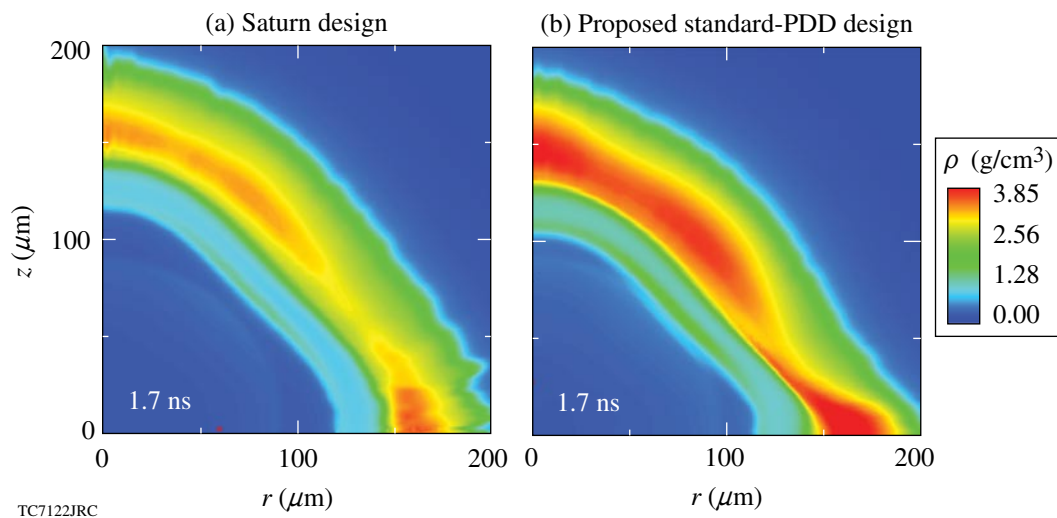(a) The mass density for the OMEGA Saturn configuration near stagnation at 1.7 ns. (b) The mass density for the proposed OMEGA standard PDD configuration at 1.7 ns and the same distance traveled. The yields relative to the simulation of the energy-equivalent symmetric target are 59% and 58%, respectively. The axis of symmetry is along the vertical axis; i.e., the pole is pointing upward.

mode distortions inherent in the PDD setup. Their effect can be controlled, however, through sufficient overall drive uniformity. The uniformity can be optimized through beam pointing, spot shape designs, and time-dependent pulse shaping. The energy deposited near the equator must be increased to compensate for the higher refractive losses (lower energy absorption) and lower hydrodynamic efficiency (due to the laser energy being deposited farther out in the corona). This can be accomplished by using elliptical spot shapes and/or higher power in the equatorial rings.[25] The level of shock-front uniformity determines the symmetry of the shock-heated core and cannot be ignored. An improperly timed shock front can cause a design to fail because of a small and distorted shock-heated hot spot, whereas small adjustments during the foot pulse can make the same target ignite by developing a large and minimally distorted hot spot.

The NIF PDD target presented here is based on a 1.0-MJ, symmetric-drive, cryogenic, DT-filled, wetted CH-foam target with a thin CH overcoat that obtains a gain of 33. The interior DT vapor layer is 1380 μm in radius. The cryogenic DT ice layer is 180 μm thick. The wetted CH-foam layer is 70 μm thick and is modeled by a uniform mass density of 0.392 g/cm^3. A thin CH layer overcoats the target and is 1.2 μm thick. The 1.0-MJ pulse shape used for this target is plotted in Fig. 105.52(a).

For the *DRACO* simulation of the cryogenic, DT-filled, wetted CH-foam target reported here, all the rings have the same primary spot shape: a low super-Gaussian order of 2.2. A secondary elliptical super-Gaussian of the same order is superimposed on the equatorial beams. It has an ellipticity of 5, a relative strength (compared with the primary spot shape) of around 0.45, and a relative shift of 0.15 times the initial target radius. An equation for the composite equatorial spot can be written as

$$I_{eq} = e^{\alpha(x^2 + y^2)^{sg/2}} + 0.45 e^{\alpha\left\{[5(x - 0.15\,r_t)]^2 + y^2\right\}^{sg/2}}, \qquad (3)$$

where $\alpha \equiv \ln(0.05)/r_t^{sg}$, sg $\equiv$ 2.2, and r_t is the initial target radius. The secondary ellipse increases the energy deposition near the equator.

Beam repointing, spot shapes, and the relative pulse strengths of the different beams determine the in-flight shell uniformity. Initial guesses of the spot positions and the spot

shapes are found off-line from *DRACO* using the same optimization technique mentioned in the previous section. Fine-tuning of the beam pointing takes place by running further *DRACO* simulations. The repointings used for the simulations presented here are 23.5°, 44.5°, and 80° for the polar, midlatitude, and equatorial rings, respectively.

An active pulse-shape optimization process internal to *DRACO* is then invoked to determine the relative pulse strengths at each ring by minimizing shell nonuniformity throughout the simulations. The optimized pulse shapes divide roughly into two separate temporal regions: the foot and the main drive. During the foot, the conduction zone is relatively uniform and does not require a large amount of compensation near the equator for a drive similar to the pole. Thus, the relative strengths between the ring pulse shapes are not very dif-
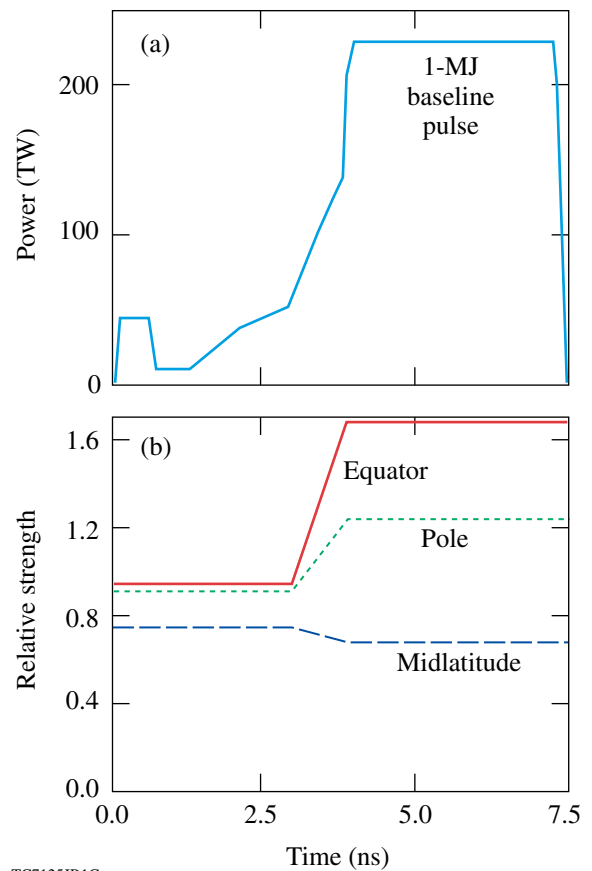

TC7125JR1C

Figure 105.52

(a) Baseline 1.0-MJ pulse designed for a symmetrically driven NIF target. (b) Time-dependent multipliers giving the relative strengths of the three rings of beams (pole, midlatitude, and equator) in a standard PDD configuration. The three PDD pulses (baseline pulse multiplied by the relative strengths) represent 1.36 MJ overall.

ferent. (Fine-tuning for the shock front will still be required.) As the main pulse ablates the shell at a higher rate, however, the conduction zone becomes progressively nonuniform with the greatest standoff distance (separation distance between the energy deposition region and the ablation surface) occurring near the equator, and, consequently, the relative strengths between the ring pulse shapes are different with the most power given to the equatorial ring. The pulse shapes are then smoothed and fine-tuning takes place by adjusting the relative strengths after observing the shell and shock-front distortions during *DRACO* simulations. The main trend of the optimized pulse shapes increases the power in the equatorial beams relative to the other beams during the main drive. The smoothed pulse shapes vary continuously, which makes it difficult to adjust the relative factors between the different pulse shapes for each ring. It is found that using constant relative strengths in the foot that change to new constant factors during the main drive is adequate to tune the pulse shapes. The constant relative strengths in the foot and main drive sections of the pulse are initially chosen as the average value of the optimized pulses in each separate period. The constant relative strengths in the two sections of the pulse are independently adjusted to fine-tune the shell and shock-front uniformity.

Maintaining both the shell and shock-front uniformity is critical to obtaining substantial gains. Correcting only for the shell distortions can have a detrimental side effect of distorting the shock front. If the shock front is distorted, nonuniform shock heating produces a misshaped and small hot spot (defined here as the 10-keV temperature contour, which does not necessarily reflect the uniformity of the shell), leading to a failed target. The shell can have adequate uniformity at stagnation but with a severely distorted and small hot spot. When compared to a simulation that ignites, the 10-keV hot spot is large and conformal to the shell.

The application of this design process is given here for an igniting NIF PDD target with the parameters given in the beginning of this section. The symmetric-drive target and 1.0-MJ baseline pulse in Fig. 105.52(a) are used as a guide for tuning the ring pulse shapes by requiring that the shell trajectory matches that of the symmetric case as close as possible. In addition, the shock-front uniformity must be high enough to produce a large hot spot. The constant multiplication factors of each of the three rings resulting from the optimization algorithm described above are calculated first based on the optimized spot shapes and ring repointings found outside of *DRACO*. Then the constant factors in the main pulse are adjusted to closely match the trajectory of the symmetric-drive

case while also obtaining the best overall low-ℓ-mode shell uniformity. Since only the pulse strengths of the three rings can be adjusted, a limited range of ℓ modes can be controlled (typically $\ell \leq 8$). Once the shell uniformity is tuned, the relative shock strengths are tuned using the foot portion to improve the shock-front uniformity. The shell uniformity is not greatly affected by the typical adjustments needed during the foot to compensate for shock-front distortions. By this point the shock front has roughly the same symmetry as the shell but still needs improvement. It is adequate to compare the shock positions of the pole relative to the equator. The relative shock positions as a function of time with and without shock-front adjustments are plotted in Fig. 105.53. The fine-tuning of the shock-front uniformity aligns the shock front prior to ignition. Without the fine tuning, the misalignment is about 20 μm at 8.0 ns, whereas the tuned shock front achieves almost perfect alignment. The multiplication factors found after the complete tuning process are plotted in Fig. 105.52(b).

TC7125JR2C
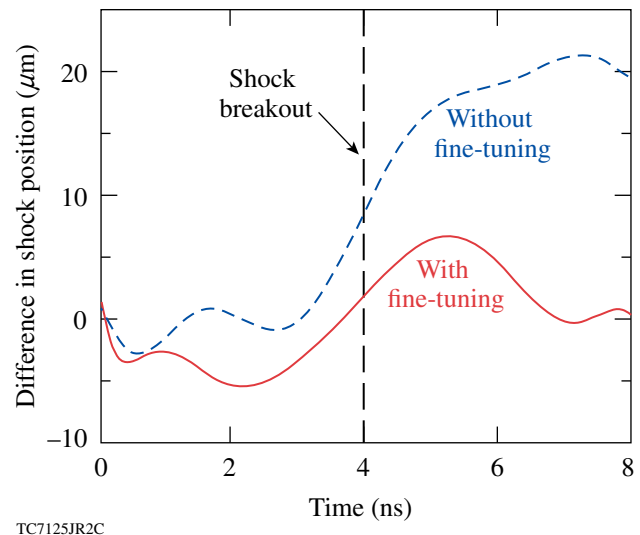
Figure 105.53
Relative shock positions (shock position along the pole minus shock position along the equator) as a function of time with and without fine-tuning of the shock front for the NIF simulations. The dashed line is without fine-tuning. The solid line is after fine-tuning the shock front. The case with fine-tuning ignites.

A *DRACO* simulation in ALE mode was run for the PDD cryogenic, DT-filled, wetted CH-foam target on a 90° wedge. The angular resolution used in the simulations was 60 zones over a 90° wedge; the low-ℓ-mode structure up to mode $\ell = 16$ is adequately resolved. The simulation used the 23.5°, 50°, and 80° pointings for the polar, midlatitude, and equatorial rings. The optimal pulse shapes for the three rings are plotted in Fig. 105.52. Simulated mass density and ion-temperature

profiles near the stagnation of this tuned design, at 8.12 ns, are shown in Fig. 105.54. The 10-keV hot-spot radius is about 40 μm. This simulation produced a gain of 20 using a flux limiter of 0.06 and required 1.36 MJ of laser energy for the PDD configuration compared with the 1.0 MJ required for symmetric drive with a gain of 33. The laser energy is higher because of the required compensation for losses at the equator.
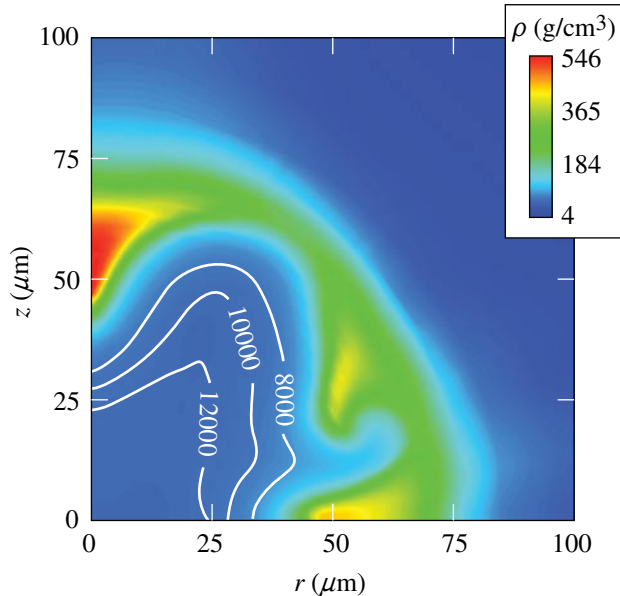
TC7116JRC

Figure 105.54

Mass density ρ and ion temperature contours in electron volts calculated by *DRACO* for a cryogenic, DT-filled, wetted CH-foam PDD target irradiated with 1.36 MJ of laser energy. The temperature contours show the formation of a ~40-μm-radius hot spot. This simulation predicts a gain of 20. The axis of symmetry is along the vertical axis; i.e., the pole is pointing upward.

Conclusions

The *DRACO* simulations of both standard-PDD and Saturn targets agreed well with the experiments during the acceleration phase by observing the characteristics of the shell evolution in the experimental and simulated x-ray radiographs. The simulations also showed the same trend as the experiments in that the Saturn targets produced higher yields than the standard-PDD targets using the existing phase plates on OMEGA (super-Gaussian of the order of 3.7). An optimized standard-PDD design was proposed that used customized phase plates, different pointings and power balance, and was able to produce a yield on par with the current Saturn design but with 5% less incident energy. Further optimization of OMEGA standard-PDD designs is expected and is currently under investigation using the techniques described here and also by employing a shimmed CH ablator on the target.

A 1.36-MJ, cryogenic DT, standard-PDD design for the NIF using the same targets as the 1.0-MJ symmetric-drive design ignited and produced a gain of 20 in a *DRACO* simulation. The PDD design employed customized phase plates, optimized beam repointings, and tuned pulse shapes for the polar, midlatitude, and equatorial rings. Maintaining a high level of shell and shock-front uniformity is found to be critical to obtaining substantial gains. Further simulations are under investigation to test the robustness of this design by including the effects of mispointing, power imbalance, and short-wavelength perturbations.

ACKNOWLEDGMENTS

REFERENCES

1. S. Skupsky, J. A. Marozas, R. S. Craxton, R. Betti, T. J. B. Collins, J. A. Delettrez, V. N. Goncharov, P. W. McKenty, P. B. Radha, T. R. Boehly, J. P. Knauer, F. J. Marshall, D. R. Harding, J. D. Kilkenny, D. D. Meyerhofer, T. C. Sangster, and R. L. McCrory, Phys. Plasmas **11**, 2763 (2004).

2. J. Paisner *et al.*, Laser Focus World **30**, 75 (1994).

3. P. W. McKenty, V. N. Goncharov, R. P. J. Town, S. Skupsky, R. Betti, and R. L. McCrory, Phys. Plasmas **8**, 2315 (2001).

4. E. M. Campbell and W. J. Hogan, Plasma Phys. Control. Fusion **41**, B39 (1999).

5. J. D. Lindl, *Inertial Confinement Fusion: The Quest for Ignition and Energy Gain Using Indirect Drive* (Springer-Verlag, New York, 1998), Chap. 6, pp. 61–82.

6. J. D. Lindl *et al.*, Phys. Plasmas **11**, 339 (2004).

7. T. R. Boehly, R. S. Craxton, T. H. Hinterman, J. H. Kelly, T. J. Kessler, S. A. Kumpan, S. A. Letzring, R. L. McCrory, S. F. B. Morse, W. Seka, S. Skupsky, J. M. Soures, and C. P. Verdon, Rev. Sci. Instrum. **66**, 508 (1995).

8. J. A. Marozas, "Fourier-Transform-Based, Phase-Plate Design Technique: A High-Pass Phase-Plate Design as an Application for OMEGA and the NIF," submitted to the Journal of the Optical Society of America A.

9. R. S. Craxton and D. W. Jacobs-Perkins, Phys. Rev. Lett. **94**, 095002 (2005).

10. R. S. Craxton, F. J. Marshall, M. J. Bonino, R. Epstein, P. W. McKenty, S. Skupsky, J. A. Delettrez, I. V. Igumenshchev, D. W. Jacobs-Perkins, J. P. Knauer, J. A. Marozas, P. B. Radha, and W. Seka, Phys. Plasmas **12**, 056304 (2005).

11. P. B. Radha, V. N. Goncharov, T. J. B. Collins, J. A. Delettrez, Y. Elbaz, V. Yu. Glebov, R. L. Keck, D. E. Keller, J. P. Knauer, J. A. Marozas, F. J. Marshall, P. W. McKenty, D. D. Meyerhofer, S. P. Regan, T. C. Sangster, D. Shvarts, S. Skupsky, Y. Srebro, R. P. J. Town, and C. Stoeckl, Phys. Plasmas **12**, 032702 (2005).

12. R. A. Sacks and D. H. Darling, Nucl. Fusion **27**, 447 (1987).

13. S. Skupsky, R. Betti, T. J. B. Collins, V. N. Goncharov, D. R. Harding, R. L. McCrory, P. W. McKenty, D. D. Meyerhofer, and R. P. J. Town, in *Inertial Fusion Sciences and Applications 2001*, edited by K. Tanaka, D. D. Meyerhofer, and J. Meyer-ter-Vehn (Elsevier, Paris, 2002), pp. 240–245.

14. F. J. Marshall, R. S. Craxton, M. J. Bonino, R. Epstein, V. Yu. Glebov, D. Jacobs-Perkins, J. P. Knauer, J. A. Marozas, P. W. McKenty, S. G. Noyes, P. B. Radha, W. Seka, S. Skupsky, V. A. Smalyuk, J. A. Frenje, C. K. Li, R. D. Petrasso, and F. H. Séguin, "Polar-Direct-Drive Experiments on OMEGA," submitted to Inertial Fusion Science and Applications 2005.

15. F. J. Marshall, J. A. Delettrez, R. Epstein, V. Yu. Glebov, D. R. Harding, P. W. McKenty, D. D. Meyerhofer, P. B. Radha, W. Seka, S. Skupsky, V. A. Smalyuk, J. M. Soures, C. Stoeckl, R. P. Town, B. Yaakobi, C. K. Li, F. H. Séguin, D. G. Hicks, and R. D. Petrasso, Phys. Plasmas **7**, 2108 (2000).

16. F. J. Marshall, J. A. Delettrez, R. Epstein, R. Forties, R. L. Keck, J. H. Kelly, P. W. McKenty, S. P. Regan, and L. J. Waxer, Phys. Plasmas **11**, 251 (2004).

17. T. R. Boehly, V. A. Smalyuk, D. D. Meyerhofer, J. P. Knauer, D. K. Bradley, R. S. Craxton, M. J. Guardalben, S. Skupsky, and T. J. Kessler, J. Appl. Phys. **85**, 3444 (1999).

18. S. Skupsky, R. W. Short, T. Kessler, R. S. Craxton, S. Letzring, and J. M. Soures, J. Appl. Phys. **66**, 3456 (1989).

19. *LLE Review Quarterly Report* **78**, 62, Laboratory for Laser Energetics, University of Rochester, Rochester, NY, LLE Document No. DOE/SF/19460-295 (1999).

20. S. P. Regan, J. A. Marozas, R. S. Craxton, J. H. Kelly, W. R. Donaldson, P. A. Jaanimagi, D. Jacobs-Perkins, R. L. Keck, T. J. Kessler, D. D. Meyerhofer, T. C. Sangster, W. Seka, V. A. Smalyuk, S. Skupsky, and J. D. Zuegel, J. Opt. Soc. Am. B **22**, 998 (2005); S. P. Regan, J. A. Marozas, J. H. Kelly, T. R. Boehly, W. R. Donaldson, P. A. Jaanimagi, R. L. Keck, T. J. Kessler, D. D. Meyerhofer, W. Seka, S. Skupsky, and V. A. Smalyuk, J. Opt. Soc. Am. B **17**, 1483 (2000).

21. J. A. Marozas, J. Opt. Soc. Am. B **19**, 75 (2002).

22. R. A. Forties and F. J. Marshall, Rev. Sci. Instrum. **76**, 073505 (2005).

23. J. J. MacFarlane *et al.*, in *Inertial Fusion Sciences and Applications 2003*, edited by B. A. Hammel, D. D. Meyerhofer, J. Meyer-ter-Vehn, and H. Azechi (American Nuclear Society, La Grange Park, IL, 2004), pp. 457–460; Prism Computational Sciences, Inc., Madison, WI, 53711.

24. S. Skupsky, R. S. Craxton, F. J. Marshall, R. Betti, T. J. B. Collins, R. Epstein, V. N. Goncharov, I. V. Igumenshchev, J. A. Marozas, P. W. McKenty, P. B. Radha, J. D. Kilkenny, D. D. Meyerhofer, T. C. Sangster, and R. L. McCrory, "Polar Direct Drive—Ignition at 1-MJ," submitted to Inertial Fusion Sciences and Applications 2005.

25. S. Skupsky, R. S. Craxton, F. J. Marshall, R. Betti, T. J. B. Collins, R. Epstein, V. N. Goncharov, I. V. Igumenshchev, J. A. Marozas, P. W. McKenty, P. B. Radha, J. D. Kilkenny, D. D. Meyerhofer, T. C. Sangster, and R. L. McCrory, Phys. Plasmas **11**, 276 (2004).

A Magnetorheological-Polishing-Based Approach for Studying Precision Microground Surfaces of Tungsten Carbides

Introduction

Tungsten carbide (WC) hard metals exhibit a unique combination of hardness and toughness, which makes them desirable engineering materials for wear-resistance applications such as cutting and milling tools.[1] The mixing of the hard and brittle WC particles with the more soft and ductile binder produces a composite with optimal mechanical properties.[2,3]

The metallic binder of cemented carbides is usually cobalt; however, when the application exposes the material to an acid environment, a nickel-based binder is favored for its better corrosion resistance. Another approach for improving corrosion resistance is to reduce the amount of binder,[4] namely binderless carbides. This work focuses on Ni-bonded and binderless cemented carbides. All of these materials are nonmagnetic.

The use of tungsten carbide materials in optical systems[5] as either mold masters[6] or mirrors[7] is the motivation behind achieving nanoscale surface roughness from grinding and subsequently polishing. Surface roughness is closely related to the wear mechanism of the material. SEM images of the ground surfaces exposed the similarities between the wear behavior of Ni-bonded and Co-bonded materials, in particular, the formation of a deformed surface layer because of the extrusion of the nickel binder between the WC grains, as described for Co-bonded[3,8] materials. Previous studies by others show that although the tungsten carbide wear mechanism involves brittle fracture, fatigue, and plastic deformation, it is dominated by the extrusion of the soft binder between WC grains.[1,8–10] Redeposited binder and WC debris cover the ground surface, forming a deformed layer[11] that is also known as subsurface damage, which masks the true surface roughness induced by grinding. In a recent study, the deformed layer depth was reported to be near 1.5 μm for ground WC-10 wt% Co composites (20-μm grains) with a 91-μm (approximately 34-μm nominal abrasive size) diamond wheel.[11] Because of the inhomogeneity of the composite carbide grains and the diamond distribution on the grinding wheel, however, the amount of damaged material that needed to be removed during the subsequent polishing stage could not be determined. Therefore, a more deterministic technique is needed to measure the deformed layer depth after grinding.

The goal of this work is a better understanding of the correlation between the response of tungsten carbide hard metals to microgrinding and nanopolishing with the resulting surface microroughness. In recent work done by Randi *et al.*,[12] it was demonstrated that magnetorheological finishing (MRF) can be used to determine subsurface damage depth for optical crystals and glasses. Because both Ni-bonded and the binderless cemented carbides are nonmagnetic, they are excellent candidates for MRF. In this study, we demonstrate that MRF spots can be placed on ground nonmagnetic tungsten carbides and that the spots can be used to evaluate the depth of the damaged layer. We focus on five nonmagnetic WC materials, which include four WC-Ni composites with variations in nickel binder content and one binderless sample, all with different grain sizes.

Experimental Procedures

1. Tungsten Carbide

Five commercial nonmagnetic WC samples were used for this study. The materials are commercially designated as BC12N,[13] K801,[14] M45,[15] M10,[15] and Cerbide.[16] They were selected on the basis of their nickel content and grain size as well as their mechanical properties. The WC grain sizes varied from 0.2 μm to 7 μm, and the nickel binder concentration varied from none (in the binderless carbide) to 12.5 wt%. Hardness measurements were obtained on all materials using a Tukon micro-indenter equipped with a Vickers diamond indenter and a microscope (50× objective), averaging the diagonals of five random indents on the surface with a load of 1 kg and a duration of 15 s. The applied load was enough to produce radial cracks[17] at the corners of the indentations in M10 and Cerbide. These two materials have a low ductility index (DI)[18] $(K_c/H_v)^2$, where K_c is the fracture toughness (kg/mm^2 m$^{0.5}$) and H_v is the Vickers hardness (kg/mm^2). Fracture-toughness values were calculated from the observed cracks using the Evans correlation.[19] The Laugier correlation[20] for WC material (H_v ≥ 10,000 MPa) was applied to calculate the fracture toughness

for the other three materials, which did not exhibit cracking under 1-kg loads. Relevant microstructural, mechanical, and physical properties are listed in Table 105.IV, ranked according to decreasing value of the ductility index.

2. Grinding Experiments

The grinding experiments were performed on the OptiPro SX50 platform,[21] a deterministic computer numerical control (CNC) ultraprecision grinding machine. The SX50 is capable of generating rotationally symmetric spherical and flat surfaces. For all our grinding experiments, a contour-tool grinding configuration for flat surfaces was used (Fig. 105.55) with three different diamond tools, rough, medium, and fine (40-μm, 10- to 20-μm, 2- to 4-μm grit size, respectively). Both the rough and medium tools were made of a bronze matrix while the fine tool matrix was resin. To avoid taking the part off the machine between operations, the tools were trued and dressed in advance using Al_2O_3 dressing sticks that were 320 or 800 grit (29- to 32-μm and 9- to 12-μm grit size, respectively). Table 105.V lists the grinding conditions used where Ω_t is the wheel speed, and Ω_w is the spindle speed.

Each workpiece was glued on a steel base with hot wax and then placed in the grinding machine parallel to the tool axis of rotation. Water–oil emulsion coolant (Opticut solution 5%, 9–10 pH)[22] was delivered to the interface between the workpiece and tool to avoid burn out and thermal damage. The grinding was done with two passes for each tool; i.e., the total material removed depth of cut per tool was 200, 40, and 10 μm (rough, medium, and fine tools, respectively). For example, the

fine grinding was done only after the part had gone through two-pass cycles with the rough and mediums tools. Finally, the workpieces were cleaned using acetone.

3. Investigation of the Deformed Layer

a. Etching of ground surface. After the materials were ground, a small area on the processed surface was etched to remove the deformed nickel binder. The etching solution contained 15-ml deionized water, 15-ml glacial acetic acid, 60-ml hydrochloric acid/32%, and 15-ml nitric acid/65%.[11] Each surface was etched for 3 min, then rinsed with water, and finally cleaned with acetone.

G7099JRC
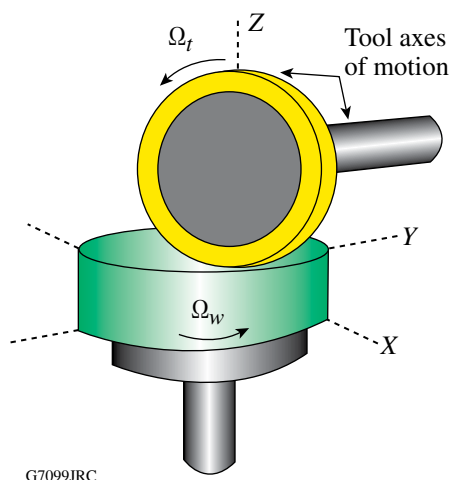
Figure 105.55
Schematics of the contour-grinding configuration adapted from Ref. 30.

Table 105.IV: Material microstructural and mechanical properties.[a]

Material ID	Dimensions (mm) per number of samples	Grain size (μm)	Ni wt%	Hardness Rockwell A	Young's modulus E (GPa)[c]	Vickers hardness H_v (GPa)[e]	Fracture toughness K_c (MPa $\sqrt{m}$)	Ductility index DI $\left(K_c/H_v\right)^2$ (μm)
BC12N[13]	$30 \times 26/2$	1.0	12	87.5–89.0	(614)[d]	12.01±0.13	12.98[g]	1.17
K801[14]	40 Φ/3	7.0	6.3	90.7	618	13.71±0.17	10.15[g]	0.55
M45[15]	30.01 Φ/3	0.6–1.3	12.5[b]	89.5	500	14.78±0.17	8.06[g]	0.30
M10[15]	30.01 Φ/3	0.2–0.6	9.5[b]	92.5	510	18.54±0.2	6.35±0.10[e],[f]	0.12
Cerbide[16]	$56 \times 32/2$	0.4	None	95.5	620	24.72±0.61	5.75±0.04[e],[f]	0.05

[a]Catalog values, unless specified otherwise. [b]Approximate values from EDS measurements. [c]Converted from PSI. [d]Estimated value. [e]Average of five Vickers indentations at 1 kgf. [f]Evans.[19] [g]Calculated values by using Laugier's[20,32,33] correlation $K_c = 2.15 \times 10^6 (E/H_v)^{0.6}$ $(1 + 0.012 E/H_v)^{0.6} H_v^{-1.5}$ for WC-Co composites containing a ductile (i.e., binder) phase, where E is the Young's modulus in units of MPa and H_v is the Vickers hardness in units of MPa for $H_v \geq 10,000$ MPa.

Table 105.V: Contour grinding conditions used on the OptiPro SX50 in a single pass.[a]

Tool grit size (µm)	Depth of cut (µm)	In-feed (Z-axis) (mm/min)	Duration of single pass (s)	Cross feed (X-axis) (mm/min)	Duration of single pass (min)
40[b]	100	0.5	12	1.0	30–40
10–20[b]	20	0.5	2.4	1.0	30–40
2–4[c]	5	0.5	0.6	5.0	6–8

[a]The following parameters remained constant: wheel speed, $\Omega_t = 6800$ rpm and work spindle speed, $\Omega_w = 100$ rpm.
[b]Bronze-bonded, 75 diamond concentration. [c]Resin-bonded, 75 diamond concentration.

b. *Processed surface spotting.* Magnetorheological finishing (MRF)[23,24] is a commercial polishing process for the manufacturing of precision optics. It was used in our experiment to measure the depth of the deformed layer from grinding and the quality of the subsurface subsequently exposed. Specifically, we used a MRF research platform called the spot-taking machine,[25] which polishes spots onto the surface of a nonrotating part by lowering the part surface into contact with a rotating magnetic fluid ribbon under CNC control. The material removal rate is determined from the amount of material removed, i.e., ratio of spot volume, divided by the spotting time. The MRF fluid used in this work consisted of an aqueous mixture of nonmagnetic nanodiamond[26] abrasives, magnetic carbonyl iron, water, and stabilizers. Machine parameters such as the magnetic field strength (~2–3 kG), wheel speed (250 rpm), pump speed (125 rpm), ribbon height (1.6 mm), and depth of the part penetrating into the ribbon (0.3 mm) were kept constant and the spotting time was varied. Spotting was done on unetched regions of rough-ground, medium-ground, and fine-ground surfaces of each material. Multiple spots with time durations of 3, 6, 12, 18, and 40 min were taken on subsets of the generated surfaces as described in **Subsurface Damage Evaluation from the Spotting Experiment** (p. 56).

4. Microscopy of Processed Surfaces

Surfaces were studied using a white-light interferometer, scanning electron microscope (SEM), contact profilometer, and atomic force microscope (AFM). Before analyzing the surfaces, the samples were ultrasonically cleaned in acetone and then rinsed with alcohol; surfaces were dried using a nitrogen gun after ultrasonication and after rinsing.

Metrology was conducted as follows:

• Average microroughness data [peak-to-valley (p–v), and root mean square (rms)] were obtained with a Zygo NewView 5000 noncontacting white-light interferometer[27] over

five 350-µm by 250-µm areas randomly distributed across ground and unetched areas. This instrument has a lateral resolution of ~1 µm and a vertical resolution of ~0.3 nm. Data were similarly obtained inside MRF spots; see details in **Subsurface Damage Evaluation from the Spotting Experiment** (p. 56).

• The morphologies of the processed surfaces after grinding, etching, and MRF were analyzed using a LEO 982 FE SEM equipped with a secondary electron detector, a backscatter detector, and also an energy dispersive x-ray spectroscopy detector (EDS). The preferred imaging configuration was a mix signal of the in-lens and in-chamber secondary electron detectors. The EDS x-ray detector was used to approximate Ni content for WC samples M10 and M45.

• The Taylor Hobson TalySurf 2 PGI stylus profilometer[28] was used to perform 3-D scans of the MRF spots, which were then used to extract the spot physical dimensions, i.e., spot volume, peak removal depth, and spot profile. The stylus tip is a cone with a 60° angle and a 2-µm spherical tip radius of curvature. The instrument has a 12-nm vertical resolution.

• Additional surface scans for selected spots were taken on the Digital Instruments/Veeco Metrology Dimension 3100S-1 AFM[29] over three 10- × 10-µm² areas randomly distributed across areas in spots where the deepest point of fluid penetration (ddp) occurred, as discussed below. This instrument has a vertical noise resolution of less than 0.5 Å.

Experimental Results
1. Surface Roughness and Surface Morphology
   from Grinding
Surface-roughness data for all materials after each grinding stage were taken using the white-light interferometer. Results are reported in Table 105.VI for all surfaces in their as-ground state.

The data given in Table 105.VI show the expected result of smoothing with decreasing diamond abrasive size. The p–v surface roughness varied from ~3280 nm (BC12N) to ~5820 nm (M10) with the coarse tool, from ~550 nm (K801) to ~3850 nm (M10) with the medium tool, and from ~53 nm (M45) to ~86 nm (BC12N) with the fine tool. The smoothest surface after fine grinding was ~7-nm rms (M45).

After the samples were ground with the fine resin tool (2- to 4-μm grit size), a "mirror quality" surface finish was achieved, as shown in Fig. 105.56. Surface roughness measurements were below 100 nm p–v and below 13-nm rms for all materials, as seen in Fig. 105.57. All surfaces had some degree of midspatial frequency artifacts (i.e., cutter marks), however, with a better surface for the circular-shaped parts over the rectangular ones because of the interrupted cut during part rotation. All the grinding tools showed some degree of material accretion from the workpiece.

G7101JRC
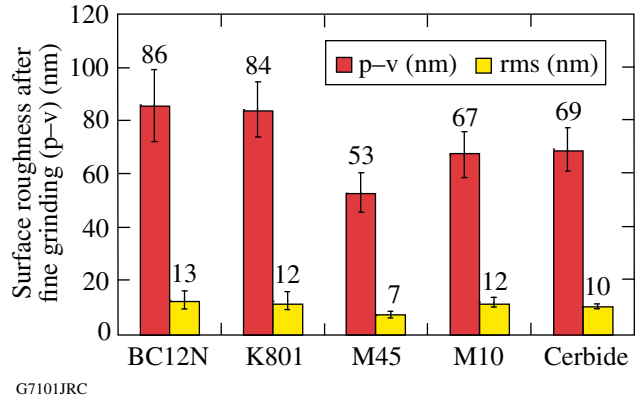
Figure 105.57
Surface roughness of fine-ground surfaces (2- to 4-μm grit size) versus WC material type. The error bars represent the standard deviation of five areal measurements.

G7100JRC
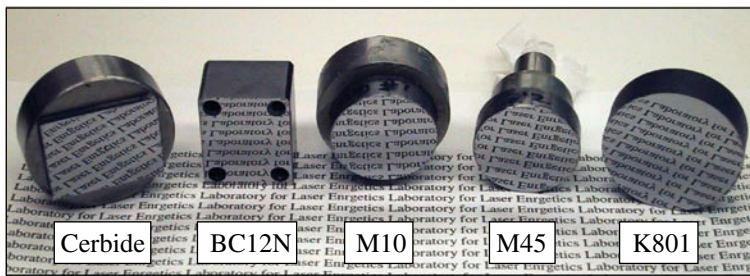
Figure 105.56
Optical image of the "mirror-like" fine-ground WC material after fine grinding (2- to 4-μm grit size). Surface-roughness measurements were below 100-nm p–v and below 13-nm rms.

Table 105.VI: Tungsten carbide surface roughness under contour grinding conditions using rough, medium, and fine tools. Measurements were taken on the white-light interferometer.

	BC12N	K801	M45	M10	Cerbide
	Rough tool (40-μm grit size)				
p–v (nm)	3280±194	3802±289	3915±371	5823±975	3857±326
rms (nm)	154±19	151±30	286±113	695±289	242±67
	Medium tool (10- to 20-μm grit size)				
p–v (nm)	2372±59	552±136	1915±175	3854±265	3322±153
rms (nm)	72±4	27±4	65±11	195±14	142±9
	Fine tool (2- to 4-μm grit size)				
p–v (nm)	86±13	84±10	53±7	67±9	69±8
rms (nm)	13±3	12±3	7±1	12±2	10±1

SEM images illustrated that the topography of the ground surfaces, from rough to fine, were in agreement with the surface-roughness measurements. Figure 105.58 gives the typical morphology of rough-ground surfaces (rough tool, 40-μm grit size). Fragmented WC particles and plastically deformed material (arrows 1 and 2) are observed on the ground surfaces, forming a deformed surface layer, as described by Hegeman *et al.*[11] Material K801, with an average grain size of 7 μm (the coarsest of all materials studied, see Table 105.IV), showed some pullout of individual grains. Figure 105.58(a) shows that the deformed layer is absent in regions of grain pullout[11] (arrow 3). We observed different morphologies of the deformed layer for the different materials. The deformed layer appears smoother for materials with a submicron grain size (0.2 to 0.6 μm) [Fig. 105.58(c) and 105.58(d)]. The plastic deformation of the binderless material is similar to that for the Ni-bonded materials, i.e., fragmented and plastically deformed WC grains (arrows 1 and 2, respectively), suggesting that only small amounts of the binder are present in the deformed surfaces, compared to the bulk material, as observed by Yin *et al.*[5] and Hegeman *et al.*[11] Therefore, the deformed surfaces mostly consist of plastically deformed WC grains.

Figure 105.59 shows SEM images of the fine-ground surfaces that reveal the material microstructure, i.e., the carbide grains and the nickel binder. Fragmented traces of the WC grains are visible inside "pockets" between grains (arrow 1). Traces from single diamond scratches and tool marks[30] can be seen at arrow 2.

All ground surfaces were etched in small regions to remove the nickel binder, exposing the subsurface of the deformed layer. In some areas on the surface the plastically deformed material, as well as WC debris, was removed, leaving small etching pits. The etching procedure also removed bronze and resin tool residue from the surface. Figure 105.60 shows a SEM image of a typical etching pit in a fine-ground surface, which exposed the subsurface of the ground surface. It can be clearly observed that almost all the nickel binder between grains was removed along with fragmented WC particles that were embedded. High-magnification images of the etched pits [Fig. 105.61(a)] showed subsurface damage in the form of cracked grains after rough grinding (40 μm). Figures 105.61(b) and 105.61(c), for both medium and fine tools (10- to 20-μm, and 2- to 4-μm grit size, respectively), reveal no evidence of

(a)

(b)

(c)

(d)

2 μm   2 μm

G7102JR

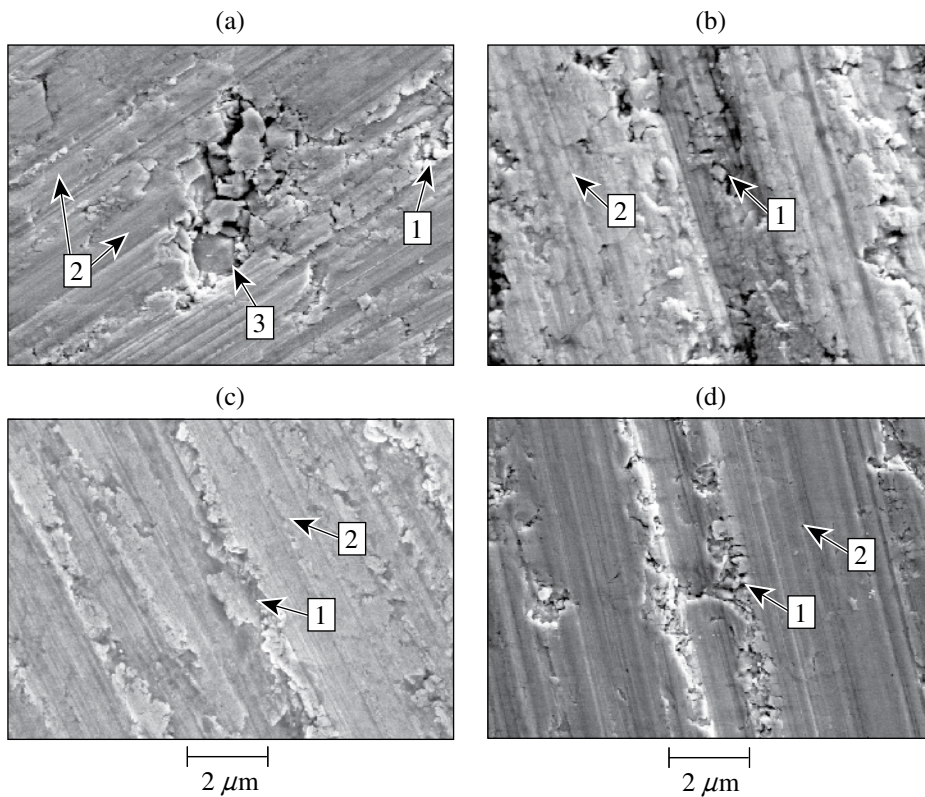Figure 105.58
SEM images of typical rough-ground surfaces (40-μm grit size). Average grain sizes are (see Table 105.IV) (a) K801, 6.3 wt% Ni, 7 μm; (b) M45, 12.5 wt% Ni, 0.6–1.3 μm; (c) M10, 9.5 wt% Ni, 0.2–0.6 μm; and (d) Cerbide, 0.4 μm. Arrows represent (1) fragmented WC, (2) plastically deformed WC, and (3) the pullout of an individual grain.
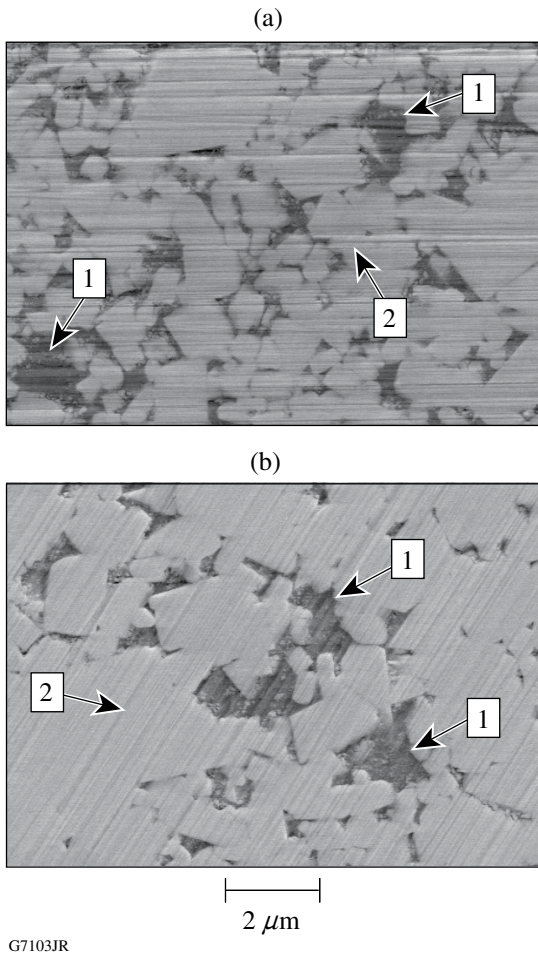
(a)

(b)

2 μm

G7103JR

Figure 105.59
SEM images of fine-ground WC surfaces (2- to 4-μm grit size). (a) BC12N, 12 wt% Ni, 1-μm grain size and (b) K801, 6 wt% Ni, 7-μm grain size (see Table 105.IV). Arrows represent (1) "pockets" between grains and (2) single diamond scratches/tool marks.
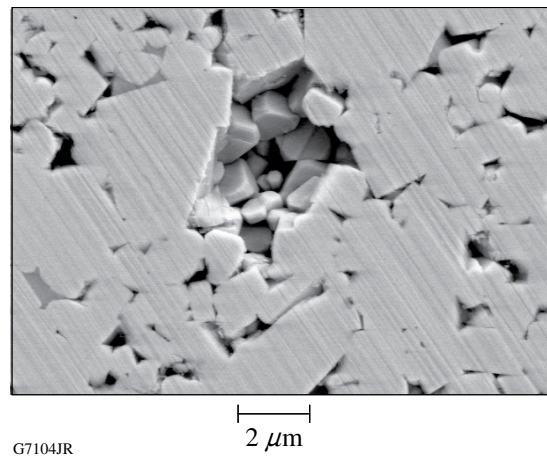

2 μm

G7104JR

Figure 105.60
SEM images of a typical etched pit in a fine-ground (2- to 4-μm grit size) WC surface, K801, 6 wt% Ni, 7-μm grain size (see Table 105.IV).

fractured WC grains, suggesting that the wear mechanism is controlled by plastic flow. The Cerbide ground surface was not affected by the etching, as expected.

2. Subsurface Damage Evaluation from the Spotting Experiment

MRF spots of various durations were taken on all rough-ground surfaces and 6-min spots were taken on both fine- and medium-ground surfaces. Figure 105.62 shows a typical 3-D map of a polished MRF spot indicating the spot leading edge (MRF fluid ribbon entrance/penetration point into the material), spot ddp (deepest point of MRF fluid penetration), and spot trailing edge (point of the fluid leaving the part) using the profilometer. From analyzing the 3-D scans, we were able to extract spot profiles, which were then used to identify the

(a)   (b)   (c)
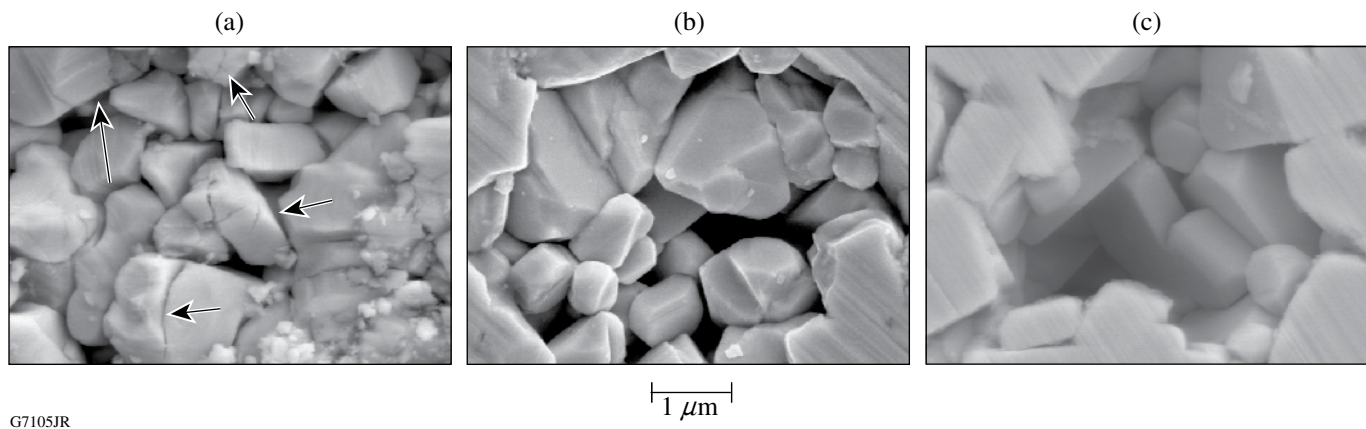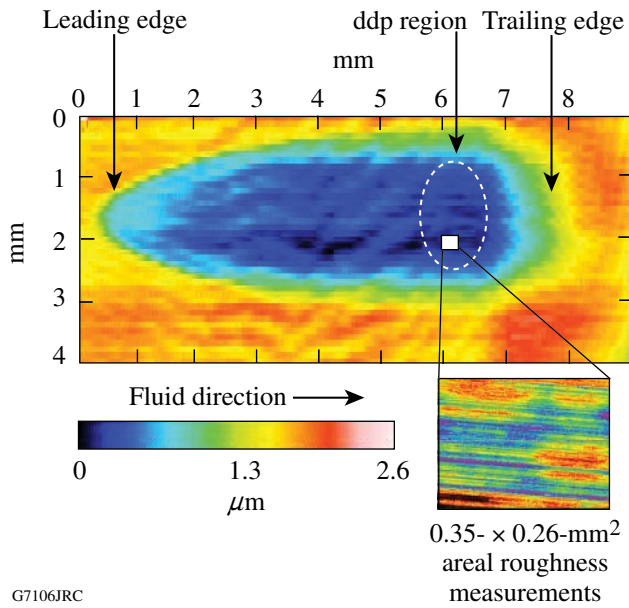

1 μm

G7105JR

Figure 105.61
High-magnification SEM images of etching pits in ground WC composites showing the (a) rough, (b) medium, and (c) fine ground. The arrows in (a) point at cracks in the carbide phase. The materials are (see Table 105.IV) (a) BC12N, 12 wt% Ni, 1-μm grain size and (b) and (c) K801, 6 wt% Ni, 7-μm grain size.
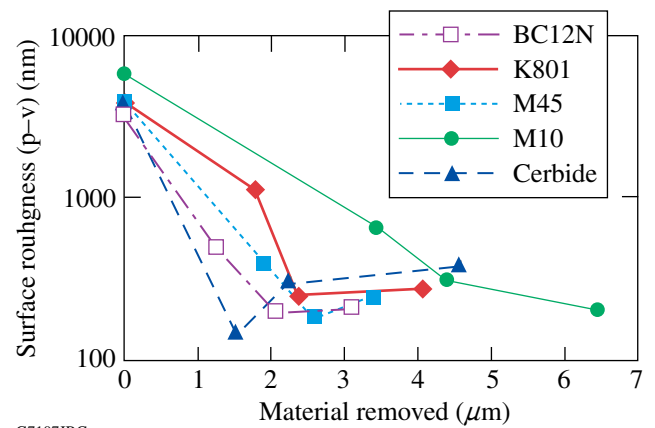
Figure 105.62
3-D image of an MRF spot taken with a Taylor Hobson TalySurf profilometer on WC M10 for 6 min. Arrows indicate the spot leading edge (MRF fluid ribbon entrance/penetration point into the material), spot ddp (deepest point of MRF fluid penetration), spot trailing edge (were the MRF fluid leaves the material), and fluid flow direction. The white rectangle within the ddp region represents one of the five sites over which surface roughness was measured using white-light interferometry.

ddp. The spot volume and maximum depth ddp are listed in Table 105.VII. These spot profiles were not similar to profiles typically observed for other optical glasses and crystals.[25]

After the location of the spot ddp was identified, surface-roughness measurements at five random locations within the ddp region were taken with the white-light interferometer. Results are given in Table 105.VII. To investigate the amount of material needed to be removed by the MRF spot (i.e., the depth of the deformed layer from the grinding cycles), we plotted the evolution of the surface roughness with the maximum amount of material removed (see Fig. 105.63). It was observed that the initial surface roughness is removed for BC12N, K801, M45, and Cerbide when the MRF penetrates past 2.1 to 2.6 μm of the deformed layer thickness. However, surface roughness eventually increased with increasing MRF material removal. A monotonic decrease in surface roughness with increasing material removal was noted for M10. SEM images taken within the ddp region of the optimal spot (i.e., least roughness) confirmed that the deformed layer induced by grinding is completely removed by the MRF process (see Fig. 105.64). It should be emphasized that the clean surfaces shown in Fig. 105.64 are due entirely to the MRF process, without any pre- or post-etching.

Figure 105.63
Evaluation of surface roughness, p–v (nm) semilog, versus MRF spot material removed (μm). The starting condition is the rough-ground surface (p–v roughness in the range of 3.3 to 5.8 μm). After removing 2 to 3 μm of material from the surface, the p–v roughness decreases to 180–310 nm.

Table 105.VII also demonstrates the influence of the initial surface roughness on the surface response inside MRF spots. For initial rough-ground surfaces, surface roughness improved after MRF penetrated 2.1 to 2.6 μm past the deformed layer for BC12N, K801, M45, and Cerbide and 4.4 μm for M10. The p–v surface roughness varied from ~185 nm (M45) to ~303 nm (Cerbide). For initial fine-ground surfaces, the p–v surface roughness varied from ~29 nm (Cerbide) to ~86 nm (BC12N). The smoothest surface for the initial fine-grinding surface conditions was ~3.4-nm rms (Cerbide). We also observed an increase in surface roughness inside MRF spots for materials with a higher ductility index, however, after 1 to 1.8 μm was removed (by the MRF spot).

3. MRF Surface Evolution with Increasing Depth Removed
Further study of the surface after MRF polishing was done for rough-ground K801 with an ~3802-nm initial p–v surface roughness [see Fig. 105.65(a)] where additional MRF spots at varying depths of MRF removal were taken. Figure 105.65 shows that after 1.8 μm of material is removed by the MRF spot, the deformed layer induced is not completely removed [see Fig. 105.65(b)], in agreement with the surface-roughness values. With a longer MRF spotting time, a total of 2.4-μm of material was removed [see Fig. 105.65(c)], an amount sufficient to expose the undisturbed subsurface. However, additional material removal slightly increases the surface roughness. Similar behavior is observed by monitoring the evolution of the rms surface roughness.

Table 105.VII: Summary results of the spotting experiments. Surface-roughness measurements were taken at five random locations within a spot ddp with the white-light interferometer. The maximum spot depth and volume removed were extracted from the profilometer 3-D scans.

Spot time (min)		BC12N	K801	M45	M10	Cerbide
		Initial surface conditions: rough ground				
3	p–v (nm)	505±37	1106±143	399±52	657±216	146±17
	rms (nm)	43±5	46±5	47±5	83±16	25±5
	Depth (μm)	1.3±0.08	1.8±0.01	1.9±0.08	3.4±0.28	1.5±0.03
	Vol. (mm^3)	0.01±0.0	0.01±0.0	0.01±0.0	0.02±0.01	0.01±0.0
6	p–v (nm)	204±10	248±24	185±26	312±20	303±20
	rms (nm)	35±2	39±5	31±11	61±6	55±11
	Depth (μm)	2.1±0.01	2.4±0.03	2.6±0.05	4.4±0.21	2.3±0.12
	Vol. (mm^3)	0.02±0.0	0.02±0.0	0.02±0.0	0.03±0.01	0.03±0.0
12	p–v (nm)	—	287±31	—	—	—
	rms (nm)	—	43±10	—	—	—
	Depth (μm)	—	3.2±0.07	—	—	—
	Vol. (mm^3)	—	0.03±0.0	—	—	—
18	p–v (nm)	212±51	276±60	240±32	205±50	383±56
	rms (nm)	33±5	45±12	40±11	39±10	63±14
	Depth (μm)	3.1±0.08	4.0±0.09	3.4±0.31	6.4±0.06	4.6±0.13
	Vol. (mm^3)	0.02±0.0	0.04±0.0	0.03±0.0	0.06±0.01	0.04±0.0
40	p–v (nm)	—	395±134	—	—	—
	rms (nm)	—	53±9	—	—	—
	Depth (μm)	—	8±0.13	—	—	—
	Vol. (mm^3)	—	0.08±0.0	—	—	—
		Initial surface conditions: medium ground				
6	p–v (nm)	215±5	456±33	107±13	113±21	114±20
	rms (nm)	35±2	27±5	16±1	19±2	20±3
	Depth (μm)	1.8±0.05	1.5±0.03	1±0.04	1.9±0.10	1.5±0.06
	Vol. (mm^3)	0.02±0.0	0.02±0.0	0.01±0.0	0.02 ±0.0	0.02±0.0
		Initial surface conditions: fine ground				
6	p–v (nm)	202±39	185±23	151±26	80±15	29±2
	rms (nm)	27±5	26±4	22±6	9±3	3±0.3
	Depth (μm)	1.9±0.03	2.2±0.05	1.6±0.03	1.7 ±0.02	1±0.06
	Vol. (mm^3)	0.02±0.0	0.02±0.0	0.01±0.0	0.02 ±0.0	0.01±0.0

(a)　(b)　(c)

(d)　(e)

Pores

2 μm

G7108JR
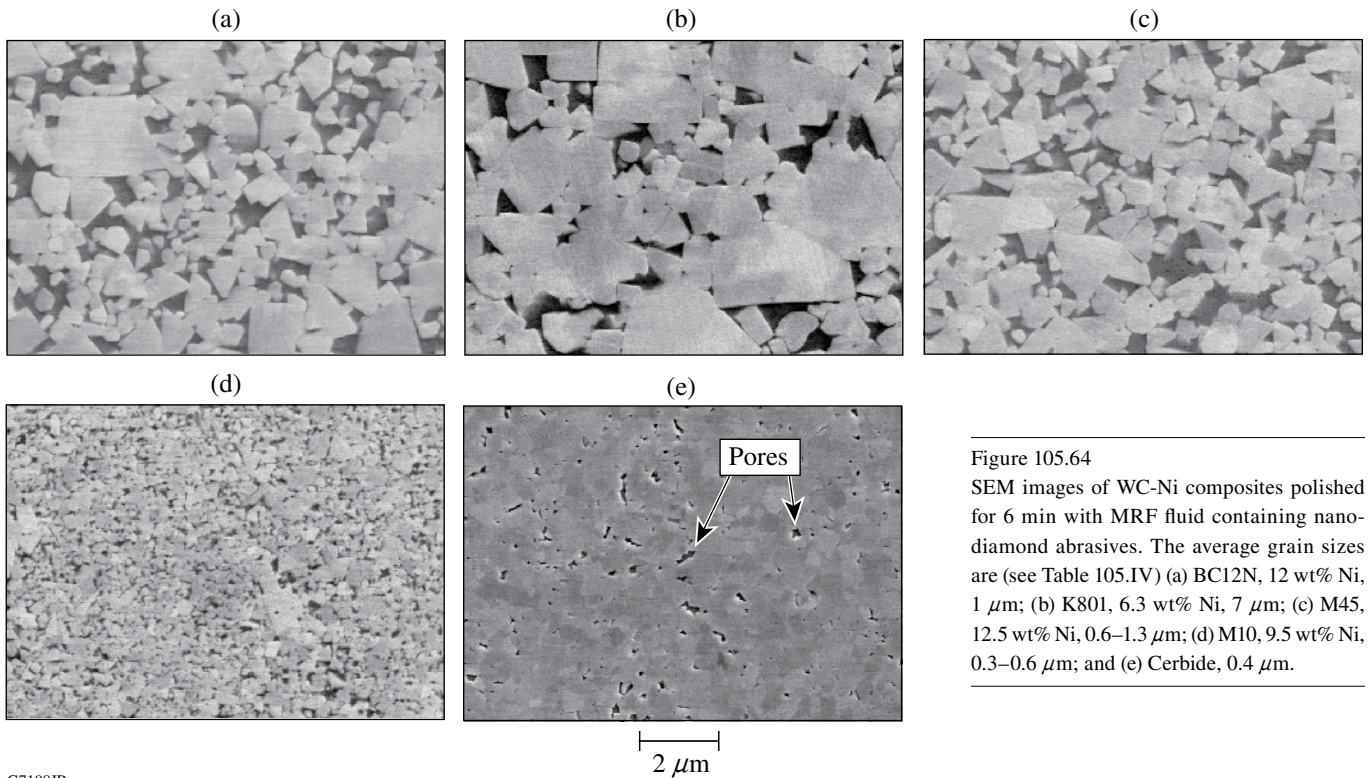
Figure 105.64
SEM images of WC-Ni composites polished for 6 min with MRF fluid containing nano-diamond abrasives. The average grain sizes are (see Table 105.IV) (a) BC12N, 12 wt% Ni, 1 μm; (b) K801, 6.3 wt% Ni, 7 μm; (c) M45, 12.5 wt% Ni, 0.6–1.3 μm; (d) M10, 9.5 wt% Ni, 0.3–0.6 μm; and (e) Cerbide, 0.4 μm.

G7109JRC

Figure 105.65
Surface roughness in the MRF spots, p–v (nm), versus MRF spot material removal in microns for rough-ground K801. Each data point represents a spot time of as rough ground, 3, 6, 12, 18, and 40 min. The SEM images correspond to the (a) initial ground surface and (b) 1.8-, (c) 2.4-, and (d) 8-μm material removed (within the spot ddp region). The error bars represent the standard deviation of five areal measurements.

Discussion

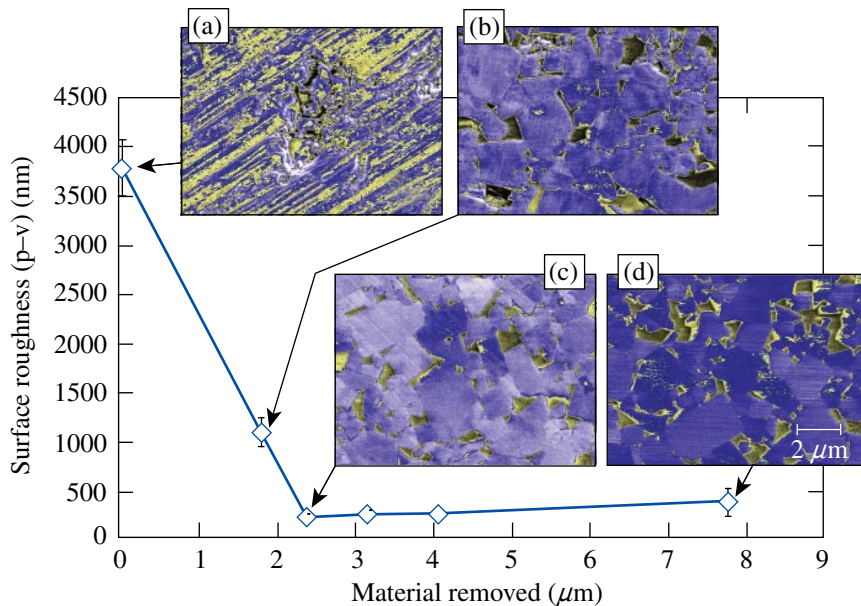The results from the grinding experiments indicate no correlation between grinding-induced surface roughness and the materials' microstructure, i.e., Ni wt% or grain size, for all grinding conditions, as also observed by Yin *et al.*[5] In addition, surface roughness did not correlate well to the materials' hardness. As observed in the case of optical glasses under deterministic microgrinding conditions,[18] surface roughness correlates with the ductility index $(K_c/H_v)^2$ (units of length) for both grinding and MRF processes conditions. Figure 105.66 shows that surface roughness values increased with increasing ductility index value. The true surface roughness is not well characterized as a result of heavily deformed material, fragmented WC, and tool residue over the ground surface.
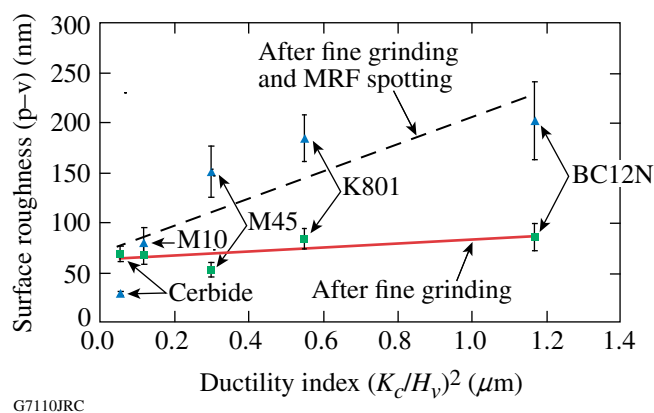

G7110JRC

Figure 105.66
Surface-roughness measurements versus the materials' ductility index $(K_c/H_v)^2$. Data are for surfaces that were fine ground (correlation with ductility index has $R^2 = 0.47$) or fine ground and subsequently MRF spotted (correlation with ductility index has $R^2 = 0.70$).

Etching of the ground surface exposed some of the subsurface damage below the ground surface. SEM high-magnification images in the etching pits exposed cracks in WC grains of rough-ground surfaces, whereas for the medium- and fine-ground surfaces, removal was found to be within the ductile/plastic regime (see Fig. 105.61).

MRF spots are useful for analyzing both the material microstructure as well as for measuring the depth of the deformed surface layer from grinding. By removing an optimal amount of material (proportional to the initial p–v roughness in the rough-ground surfaces), the surface roughness is significantly reduced. However, additional material removal (beyond the optimal amount) resulted in a slight increase in surface roughness for materials with a high ductility index value. These results suggest that to completely remove the deformed surface layer after rough grinding (~40-μm grit size), an amount of material equivalent in depth to the initial p–v surface roughness that needs to be polished/removed. For the materials tested, removing the initial p–v surface roughness values was sufficient to completely eliminate the damaged/deformed surface layer with the exception of WC M10, which showed a monotonic decrease of roughness with the amount of material removed. The increase in surface roughness for the Cerbide can be explained in Fig. 105.64(e), which clearly shows some degree of porosity at the carbide boundaries.

The effect of the initial surface roughness from grinding with rough, medium, or fine tools on the MRF performance is shown in Tables 105.VI and 105.VII. Initial ground surface conditions, either coarse or fine, had a small effect on the resulting surface roughness inside the MRF spot for materials with a high ductility index. The p–v and rms surface roughness improved with a decreasing ductility index for initial fine-grind conditions. However, we found that MRF spot surface roughness was higher than the initial fine-ground surface, e.g., from ~86 nm (BC12N) after fine grinding to ~202 nm (BC12N) following MRF removal in the range of 1 to 2.2 μm.

Further investigation of surface response inside a MRF spot for materials with a high ductility index was done to investigate the eventual slight increase of roughness with the amount of material removed. Figure 105.65 suggests that additional spot time promotes preferential polishing of the nickel binder, which resulted in increasing surface-roughness values. The effect of preferential polishing on surface roughness is also known as grain decoration.[31] A selective AFM scan demonstrates preferential polishing/grain decoration on the resulting surface roughness inside the MRF spot. Figure 105.67(a) shows AFM scans from the ddp in K801 (7-μm average grain size) after an optimal 2.4-μm amounts of material have been recovered (pit depth in the range of 9 to 12 nm), while Fig. 105.67(b) shows the development of preferential grain decoration when an excessive amount (8 μm) has been removed (pit depth in the range of 27 to 61 nm). These features show that MRF spot-derived material removal can be optimized to remove the damaged layer at the surface without acceleration grain decoration. Excessive amounts of MRF removal may lead to grain decoration in a material with a higher ductility index. On the other hand, materials with a lower ductility index like M10 may show a monotonic reduction to surface roughness with the amount of material removed by MRF. This represents true polishing of this material, a desired outcome for the manufacture of mold masters or other optics from WC.
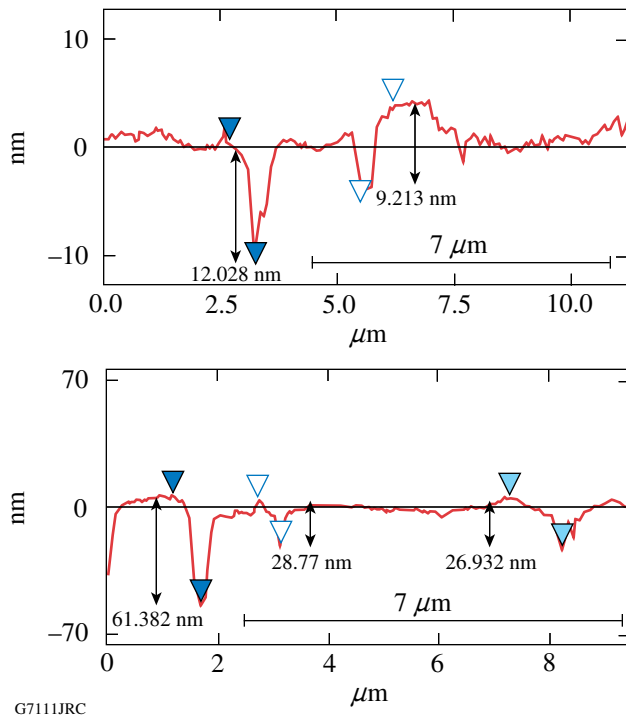
Figure 105.67
AFM surface profiles from the ddp region of a MRF spot taken on K801 (average grain size 7 μm). (a) 2.4 μm and (b) 8 μm were removed. The initial surfaces were rough ground and had a p–v surface roughness of 3.8 μm. The double arrows represent the vertical distance between markers and the scale bar represents the average grain size.

Conclusions

We have studied the response of five nonmagnetic WC composites to deterministic microgrinding. Grinding experiments showed that grinding-induced surface roughness decreased with decreasing diamond abrasive size. Microgrinding with a rough tool (40-μm grit size) involved fracture, leading to a p–v surface roughness in the range of 3.2 to 5.8 μm (150- to 700-nm rms). Microgrinding with medium and fine tools (10- to 20-μm and 2- to 4-μm grit size, respectively) was controlled by plastic flow. The medium tool led to p–v surface roughness values in the range of 0.5 to 3.8 μm (27- to 200-nm rms), whereas the fine tool resulted in surface p–v values in the range of 53 to 86 nm (7- to 13-nm rms). The true grinding-induced surface roughness was concealed by the deformed layer on the ground surface.

We have demonstrated that a MRF spot can be placed on ground surfaces of tungsten carbide and that the spot can be used to evaluate the depth of the surface deformed layer. For the rough and medium tools, the deformed layer is in the range 1.5- to 2.7-μm. The surface roughness of MRF spot at the deepest point of penetration can be used as a guide for estab-lishing the optimal amount of material to be removed by MRF. Optimal MRF removal indeed removes the deformed surface layer caused by grinding. Excessive MRF removal may lead to preferential polishing and removal of the binder phase, also known as grain decoration. By utilizing both surface-roughness measurements and SEM imaging at the spot ddp, we were able to estimate the depth of the deformed layer. Thus, we showed that the depth of the deformed layer can be estimated in two ways. An optical profilometer-based measurement of the p–v surface microroughness of the ground surface provides an upper bound to the deformed layer thickness. This is a desirable estimate given the noncontact nature of this metrology technique. On the other hand, the MRF spot can also be used to reveal the depth of the deformed layer while reducing the surface roughness.

REFERENCES

1. G. S. Upadhyaya, *Cemented Tungsten Carbides: Production, Properties, and Testing*, Materials Science and Process Technology Series (Noyes Publications, Westwood, NJ, 1998).

2. G. Wirmark and G. Dunlop, in *Science of Hard Materials*, edited by R. K. Viswanadham, D. J. Rowcliffe, and J. Gurland (Plenum Press, New York, 1983), pp. 311–338.

3. J. Larsen-Basse, J. Mater. **35**, 35 (1983).

4. S. Imasato *et al.*, Int. J. Refract. Met. Hard Mater. **13**, 305 (1995).

5. L. Yin *et al.*, Int. J. Mach. Tools Manuf. **44**, 533 (2004).

6. W. K. Chen *et al.*, Precis. Eng. **29**, 315 (2005).

7. L. Yin *et al.*, Proc. Inst. Mech. Eng. B, J. Eng. Manuf. **218**, 419 (2004).

8. J. Larsen-Basse and N. Devnani, in *Science of Hard Materials*, edited by E. A. Almond, C. A. Brookes, and R. Warren, Institute of Physics Conference Series, No. 75 (Hilger, Bristol, England, 1986), pp. 883–895.

9. J. Larsen-Basse, in *Science of Hard Materials*, edited by R. K. Viswanadham, D. J. Rowcliffe, and J. Gurland (Plenum Press, New York, 1983), pp. 797–813.

10. W. Precht, R. K. Viswanadham, and J. D. Venables, in *Science of Hard Materials*, edited by R. K. Viswanadham, D. J. Rowcliffe, and J. Gurland (Plenum Press, New York, 1983), pp. 815–828.

11. J. B. J. W. Hegeman, J. Th. M. De Hosson, and G. de With, Wear **248**, 187 (2001).

12. J. A. Randi, J. C. Lambropoulos, and S. D. Jacobs, Appl. Opt. **44**, 2241 (2005).

13. Basic Carbide, Lowber, PA 15660.

14. Kennametal, Inc., Charlotte, NC 28273.

15. Fuji Die Co., Ltd., Ota-ku, Tokyo, Japan.

16. Materials tested were commercially available in January 2005, Cerbide, Inc., Orchard Park, NY 14127.

17. J. Larsen-Basse, in *Tribology—Friction, Lubrication and Wear, Fifty Years On: Proceedings of the Institution of Mechanical Engineers, International Conference* (Mechanical Engineering Publications Ltd., Bury St. Edmunds, Suffolk, 1987), pp. 277–282.

18. J. C. Lambropoulos, T. Fang, P. D. Funkenbusch, S. D. Jacobs, M. J. Cumbo, and D. Golini, Appl. Opt. **35**, 4448 (1996).

19. A. G. Evans, in *Fracture Mechanics Applied to Brittle Materials*, edited by S. W. Freiman (American Society for Testing and Materials, Philadelphia, 1979), Vol. ASTM STP 678, Part 2, pp. 112–135.

20. M. T. Laugier, J. Mater. Sci. Lett. **6**, 768 (1987).

21. OptiPro Systems, Ontario, NY 14519.

22. Opticut GPM 5% in water, pH 9-10, Lighthouse Lubricant Solutions, LLC, Overland Park, KS 66282.

23. S. D. Jacobs, H. M. Pollicove, W. I. Kordonski, and D. Golini, in *International Conference on Precision Engineering*, ICPE '97 (ICPE, Taipei, Taiwan, 1997), pp. 685–690.

24. A. B. Shorey, S. D. Jacobs, W. I. Kordonski, and R. F. Gans, Appl. Opt. **40**, 20 (2001).

25. S. R. Arrasmith, I. A. Kozhinova, L. L. Gregg, A. B. Shorey, H. J. Romanofsky, S. D. Jacobs, D. Golini, W. I. Kordonski, S. J. Hogan, and P. Dumas, in *Optical Manufacturing and Testing III*, edited by H. P. Stahl (SPIE, Bellingham, WA, 1999), Vol. 3782, pp. 92–100.

26. S. D. Jacobs, Finer Points **7**, 47 (1995).

27. Zygo NewView™ 5000 White Light Interferometer, Zygo Corporation, Middlefield, CT 06455.

28. Taylor Hobson TalySurf 2 PGI profilometer, 120-mm traverse unit, 10-mm gauge range, 12-nm vertical resolution, and 0.1-μm accuracy. Stylus specifications: 60° tip angle and 2-μm tip radius, Taylor Hobson, Inc., Rolling Meadows, IL 60008-4231.

29. Digital Instruments/Veeco Metrology Dimension 3100S-1 Atomic Force Microscope, Veeco Instruments, Inc., Woodbury, NY 11797-2902.

30. S. Tong, "Chatter in Contour Deterministic Microgrinding," Ph.D. thesis, University of Rochester, 2004.

31. L. L. Gregg, A. E. Marino, J. C. Hayes, and S. D. Jacobs, in *Optical Manufacturing and Testing V*, edited by H. P. Stahl (SPIE, Bellingham, WA, 2004), Vol. 5180, pp. 47–54.

32. M. T. Laugier, J. Mater. Sci. Lett. **6**, 779 (1987).

33. M. T. Laugier, J. Mater. Sci. Lett. **6**, 897 (1987).

High-Gain, Polarization-Preserving, Yb-Doped Fiber Amplifier for Low-Duty-Cycle Pulse Amplification

Introduction

Erbium-doped fiber amplifiers have become commonplace in telecommunications systems.[1] High-bit-rate pulse trains mean that continuous pumping can be utilized. Additionally, the unknown polarization state of the arriving pulses is ideal for common fiber-optic components and erbium-doped fibers, which typically do not preserve the polarization state of the light passing through them. For other applications, however, such conditions do not apply. Low-duty-cycle pulses leave gain available in the fiber for long durations between pulses, which can lead to parasitic lasing or destructive self-pulsations. The amplification of signals with wavelengths far from the gain peak only enhances this problem since the gain can be substantially lower for such signals. Additionally, the amplification of linear polarizations requires not only a polarization-maintaining (PM) active fiber, but also PM wavelength division multiplexers (WDM's) and other fiber components that can be difficult to fabricate.

Utilizing a double-pass configuration allows for significantly higher gains to be obtained in a single-fiber amplifier than can be achieved in a single pass.[2–5] Additionally, using a Faraday rotator just before the end mirror ensures that the pulse returning from the second pass through the cavity has a polarization state that is orthogonal to that of the input pulse. Consequently, when used in conjunction with a polarizing beam splitter, the output pulse can be separated from the input pulse with high fidelity.[3] Double-pass configurations are ripe for parasitic lasing or destructive self-pulsations in a highly pumped unsaturated amplifier, however, since half a resonator is created intentionally. Special care must be taken to minimize reflections from components, connectors, and splices. Utilizing a timed gate, e.g., an acousto-optic modulator (AOM), at the end of the first pass can ensure stable operation,[3] but this significantly adds to the complexity of the system.

In this work, a double-pass, ytterbium-doped fiber amplifier is presented that overcomes these hurdles to provide high gain for low-duty-cycle pulse repetition rates while preserving the linear polarization state in a single-spatial-mode package that requires no alignment. In **Amplified Spontaneous Emission Considerations** (p. 63) the amplified spontaneous emission (ASE) is modeled in ytterbium-doped fiber amplifiers. In particular, the effects of ASE filtering are studied for use in a double-pass amplifier configuration. The **Experimental Results** (p. 66) are presented on the measurements of a double-pass fiber amplifier built with the various ASE-suppression schemes described in **Amplified Spontaneous Emission Considerations**. Additional discussions regarding the experimental configuration and modeling are given in **Discussion and Conclusions** (p. 68), along with concluding remarks.

Amplified Spontaneous Emission Considerations

The amplified spontaneous emission of fiber amplifiers can be studied via rate-equation modeling.[6] Such a model represents the optical power resolved in wavelength along the length of the fiber and the ytterbium atomic states as a homogeneously broadened inversion. The resultant equations are given by

$$\pm \frac{\partial P^{\pm}}{\partial z} + \frac{1}{v_g}\frac{\partial P^{\pm}}{\partial t} = \Gamma[\sigma_e N_2 - \sigma_a N_1]P^{\pm}$$
$$- \alpha P^{\pm} + 2\sigma_e N_2 \frac{hc}{\lambda^3}\Delta\lambda + S\alpha_{RS}P^{\mp} \quad (1)$$

and

$$\frac{\partial N_2}{\partial t} = \frac{1}{hc}\int \frac{\Gamma}{A}[\sigma_e N_2 - \sigma_a N_1](P^+ + P^-)d\lambda - \frac{N_2}{\tau}, \quad (2)$$

where $P^{\pm}(z, t, \lambda)$ is the forward (+) or backward (–) propagating power as a function of wavelength, time, and axial position along the fiber. N_2 and N_1 are the upper and lower state population densities, respectively, as a function of time and axial position along the fiber and are related by the total ion concentration as $N_t = N_2 + N_1$, which is constant throughout the fiber. Wavelength-dependent parameters in Eqs. (1) and (2) include the geometrical overlap of the fiber mode with the core Γ, modal area A, absorption/emission cross section of the active ion $\sigma_{a/e}$, group velocity v_g, fiber attenuation α, and Rayleigh scattering coefficient α_{RS}. Additional parameters include the upper-state lifetime τ, the fiber-core capture coefficient S, and the optical sampling bandwidth $\Delta\lambda$.

Equation (1) represents the bidirectional power flow through the fiber, including stimulated emission, spontaneous emission, and absorption from the active ions; loss due to the inherent fiber attenuation; and Rayleigh scattering. Since the parameters all have wavelength dependence, only a single equation is mathematically required to represent the behavior of the pump, signal, and ASE.

Equation (2) represents the excited-state population density, which is governed by the absorption and emission of optical power as well as nonradiative decay. One notable omission in Eq. (2) is the wavelength dependence of the excited state governed by the details of the atomic transition manifold. This leads to, for example, excitation due to the absorption of long-wavelength light that can then be used to amplify shorter wavelength light. While this effect is small in the presence of a highly inverted fiber, the impact on the current work is to overestimate the ASE at the gain peak. Since the current goal is to suppress this feature, the model will yield a worse case than is expected experimentally.

For simplicity, the wavelength dependence of A, v_g, α, and α_{RS} are neglected. Since the current work considers core-pumped (as opposed to cladding-pumped) active fibers, Γ can also be well approximated by a constant. The ytterbium cross sections are obtained from the data in Ref. 7. For convenience, these cross sections are fit to a series of Gaussians of the form

$$\sigma_j = \sum_m A_{j,m} \exp\left\{-\left[\left(\lambda - \lambda_{j,m}\right)\middle/w_{j,m}\right]^2\right\}$$

with the coefficients listed in Table 106.I. Other utilized parameters are listed in Table 106.II.

Table 106.I: Gaussian coefficients for ytterbium emission and absorption cross sections.

j	$A_{j,m}$ (10^{-27} m^2)	$\lambda_{j,m}$ (nm)	$w_{j,m}$ (nm)
a	180	950	70
a	360	895	24
a	510	918	22
a	160	971	12
a,e	2325	975	4
e	160	978	12
e	340	1025	20
e	175	1050	60
e	150	1030	90

Table 106.II: Parameters used in simulations.

Parameter	Value
N_t	9.4×10^{24} m^{-3}
Γ	0.85
A	30 μm^2
v_g	c/1.5
α	0.003 m^{-1}
$S\alpha_{RS}$	1.2×10^{-7} m^{-1}
τ	0.84 ms
$\Delta\lambda$	1 nm
λ_{pump}	976 nm
λ_{signal}	1053 nm

Data provided with the ytterbium-doped fiber (Nufern), along with our own measurements on the fiber, determined the values of N_t, Γ, and A. The other values were obtained from Ref. 6. The parameters used are compiled in Table 106.II. A simple finite-difference method is utilized to calculate the power and inversion distributions in the fiber. Initial conditions assume no optical power or inversion within the fiber, and the pump power is included as a boundary condition. A double-pass configuration can also be realized by applying the appropriate boundary conditions.

Unsaturated fiber amplifiers cannot be pumped to arbitrarily high levels because of self-pulsations and oscillation, which limit the length of fiber that can be practically used in a single-pass amplifier. In an unsaturated amplifier this translates to limited available gain. Figure 106.1 shows the forward and reverse amplified spontaneous emission for the case of reverse pumping and very weak signal amplification (no gain depletion) for a 3.5-m length of Yb:fiber with the characteristics in Table 106.II. The small-signal gain, defined as the ratio of output energy to input energy, for a 1053-nm signal and the pump leakage are also shown in this figure. After 140 mW of pump power, the fiber is almost completely inverted, and the remaining pump is lost out of the opposite end of the fiber. The small-signal gain 23 nm off the gain peak is therefore limited to approximately 20 dB.

Since the gain is in fact unsaturated, simply sending the signal back through for a second pass increases the amplification without additional pumping. Such a double-pass configuration, however, also allows the ASE to make a second trip through the gain, which can lead to undesirable oscillation
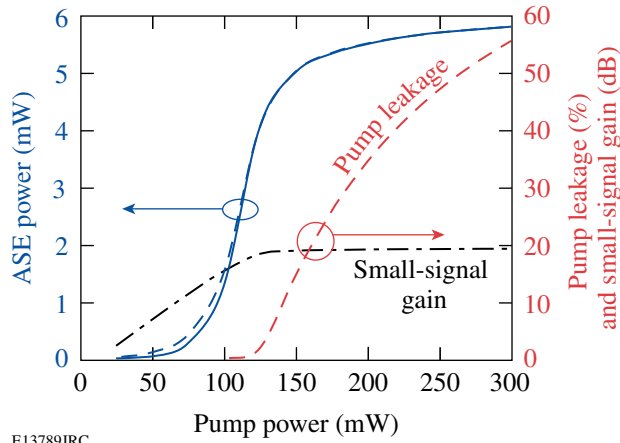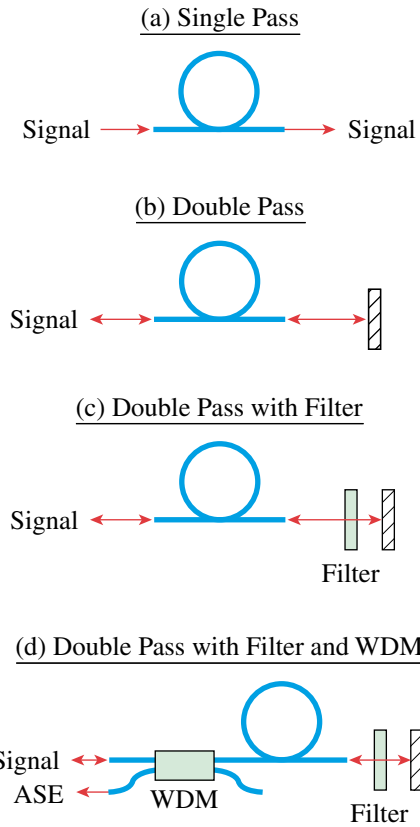
Figure 106.1
Total (spectrally integrated) forward (solid) and reverse (dashed) ASE, 976-nm pump leakage, and 1053-nm small-signal gain as a function of pump power for a 3.5-m-length Yb:fiber.

and self-pulsations. The ASE must therefore be filtered to use a double-pass configuration. Two simple methods of filtration were investigated, as depicted in Fig. 106.2. The first is a bandpass filter, which is inserted between subsequent trips through the active fiber to deny double-pass ASE except in a small bandwidth around the filter peak. The second is a WDM designed to split the ASE peak from the signal, which removes a significant fraction of the ASE power from the signal, provided the signal is not near the gain peak. Four different amplifier configurations are modeled, as shown in Fig. 106.2. The first two are simple single- and double-pass configurations through the fiber. In the third configuration, a bandpass filter is added between subsequent passes through the fiber. The fourth configuration adds a WDM filter to the output of the third configuration.

For these calculations, the filters are assumed to be lossless at the transmission peaks with zero transmission at the nulls. The mirror adds 1 dB of loss to the double-pass amplifiers. Assuming pump and signal wavelengths of 976 and 1053 nm, respectively, the total (spectrally integrated) ASE power out of the different amplifier configurations is shown in Fig. 106.3 as a function of pump power. Because of undepleted gain and pump leakage, the single-pass ASE has a maximum power below 6 mW. In the double-pass configuration, the amplifier becomes saturated by the ASE, which extracts a significant fraction of the gain in the fiber. This linear trend in the ASE growth with pump power leads to an ASE level that is greater than 25 times the single-pass case and means that there will be very limited reduced gain available for the signal. In contrast, the dotted trace shows that the insertion of the bandpass filter
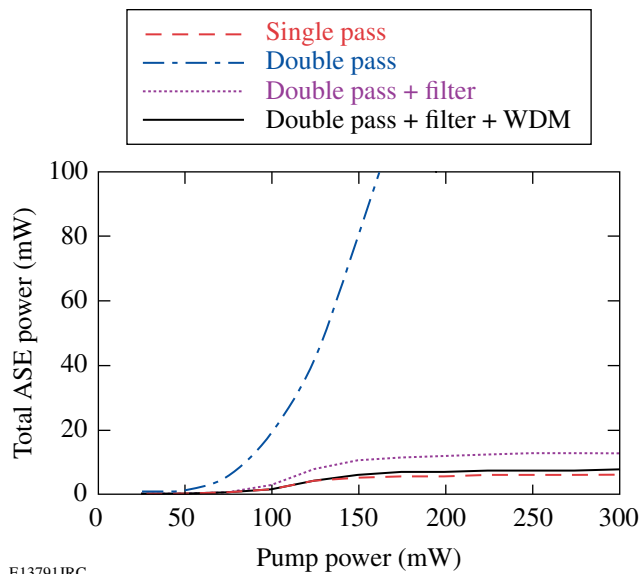

Figure 106.2
Depiction of modeled configurations for (a) single pass, (b) double pass, (c) double pass with an intracavity bandpass filter, and (d) the same as (c) with a WDM filter at the amplifier output.

prohibits the ASE closest to the gain peak from experiencing double-pass gain. The total ASE is therefore limited to small-signal amplification, even with double-pass amplification far off the gain peak, and accumulates no more than twice the power of the single-pass configuration. The insertion of this filter then allows for exponential signal gain from the double-pass amplifier. The addition of the WDM filter (solid curve) reduces the total ASE output power of the double-pass fiber amplifier to only 30% more than the single-pass ASE.

The ASE spectra for the four configurations are shown in Fig. 106.4 at a pump power of 250 mW. The ASE within the bandpass filter is actually stronger than the unfiltered double-pass ASE since the gain is unsaturated. Nonetheless, this lack of gain saturation allows for double-pass gain of the signal in the amplifier. The bandpass filter is therefore critical for operation of this double-pass configuration for the amplification of signals off the gain peak.

E13791JRC

Figure 106.3
Total (spectrally integrated) ASE power at the amplifier output as a function of pump power for the configurations shown in Fig. 106.2 using the fiber from Fig. 106.1.
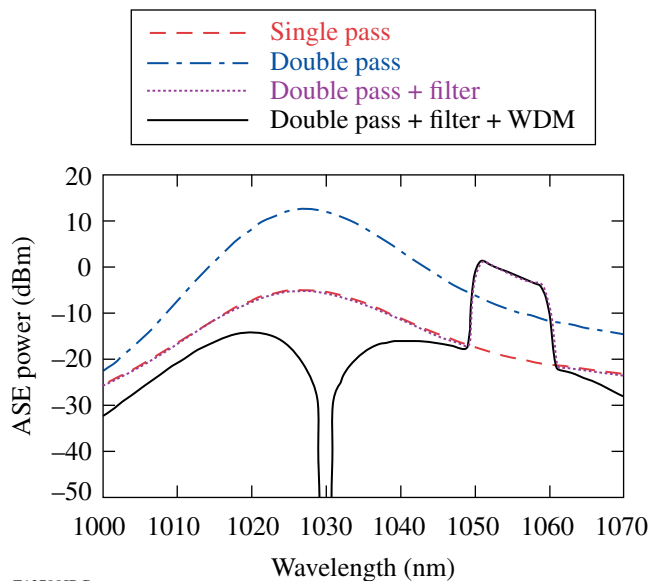

E13790JRC

Figure 106.4
Amplified spontaneous emission spectra at the amplifier output for the configurations shown in Fig. 106.2 using the fiber from Fig. 106.1 with 250 mW of pump power.

Experimental Results

Under the guidance of **Amplified Spontaneous Emission Considerations** (p. 63), a double-pass polarized amplifier was constructed that contained both the bandpass filter and the

WDM and utilized a Faraday mirror with a polarizing beam splitter (PBS) to separate input from output and preserve the linear polarization state. This amplifier configuration is shown in Fig. 106.5 and utilizes both single-mode (SM) and PM fibers. The input signal comes through a PM-pigtailed isolator to prevent any ASE or signal from returning to the seed source. The light then passes through a PM-pigtailed polarizing beam splitter followed by a single-mode, 1030-nm/1053-nm wavelength division multiplexer (WDM) used to reduce ASE. A SM WDM combines the seed light with pump light from a fiber Bragg grating-stabilized pump laser with a second WDM in series for additional isolation of the pump diode from the amplified signal. The combined light is sent into 3.6 m of single-mode, single-clad, ytterbium-doped fiber with an unsaturated absorption coefficient of approximately 70 dB/m at 975 nm. After the first pass of amplification, the signal passes through a Faraday mirror, a factory-aligned, fiber-coupled package containing a Faraday rotator, 10-nm bandpass filter at 1053 nm, and mirror. The reflected light passes back through the Faraday mirror package, the Yb-doped fiber, and the WDM's, one of which acts to filter out the ASE centered at 1030 nm (WDM1). Since the polarization at the PBS is orthogonal to that which entered the PBS because of the Faraday mirror, the light is ejected out a different port and sent through a PM 90/10 splitter to provide polarized signal and sample ports. All fibers were spliced using a Furukawa S183PM fusion splicer, and there are no alignment knobs in the system. The pump was operated continuously and there is no AOM gate so that no temporal alignment is required between the seed pulses and the amplifier.

The seed pulse used in this amplifier was a 2-ns square pulse with 1.56 pJ of energy, resulting in a peak power of 0.78 mW. The seed pulse had an optical wavelength of 1053 nm and a pulse repetition rate of 300 Hz and was linearly polarized with a polarization extinction ratio of 20 dB. Different lengths of Yb-doped fiber were tested in the amplifier to optimize the active fiber length in terms of maximizing gain while maintaining stability as well as operation free from parasitic lasing or self-pulsations. For a given fiber length, a fraction of the fiber remains unpumped and thus lossy to the signal wavelength. If the pumped portion of the fiber has sufficient gain, then the amplifier can Q-switch because of the saturable absorption of the unpumped section of fiber and minute reflections in the system. This can be remedied by making the fiber sufficiently short; however, there is an optimum fiber length for which the fiber provides maximum gain without self-pulsations. For several amplifiers that were constructed, the optimum fiber length
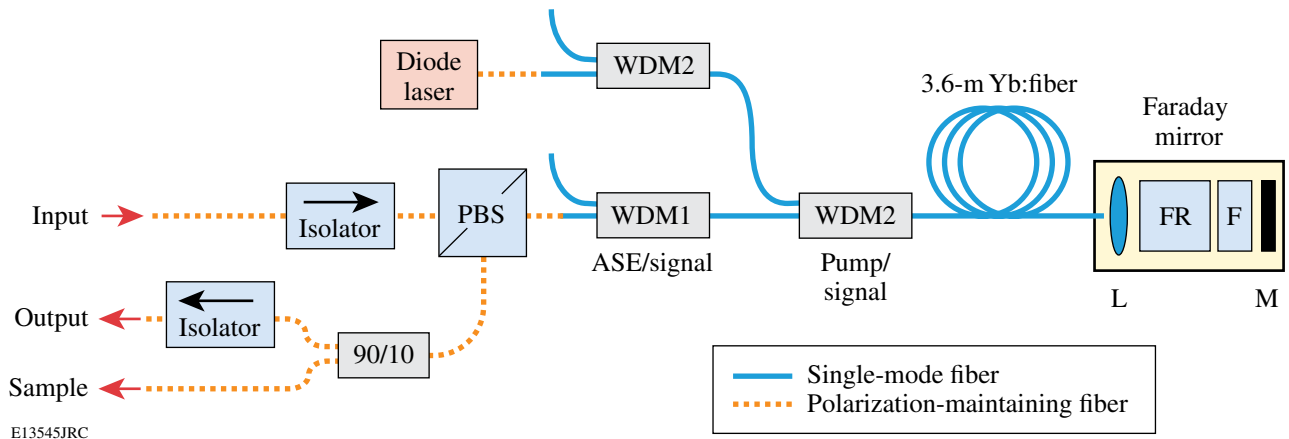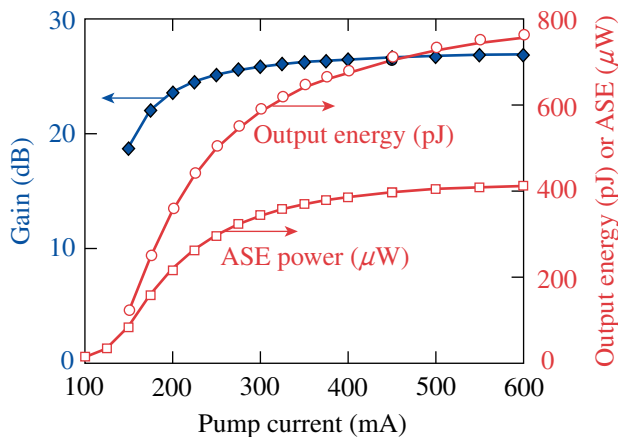
Figure 106.5
Schematic of a high-gain, double-pass amplifier consisting of input and output isolators, a polarizing beam splitter (PBS), an ASE/signal wavelength division multiplexer (WDM1), two pump/signal wavelength division multiplexers (WDM2), 3.6 m of ytterbium-doped fiber, a Faraday mirror, and a 90/10 splitter. The Faraday mirror was a factory-aligned package containing a lens (L), Faraday rotator (FR), bandpass filter (F), and mirror (M). The polarization-maintaining fiber is notated by dotted lines while the single-mode fiber is notated in solid.

was determined to be near 3.5 m, regardless of the variability between components or splice quality. The pump utilized had a threshold of 16 mA and a slope efficiency of 0.68 mW/mA.

Figure 106.6 shows the signal gain, output energy, and total ASE power as a function of pump current. As the pump current is increased beyond 200 mA, the amplifier gain rolls off since the additional pump light is mostly not absorbed in the active fiber, a feature that is also reflected in the ASE curve. It is important to note that because of the low seed energy and repetition rate, the amplifier is unsaturated. Consequently, the

small-signal gain afforded by this amplifier 23 nm off the gain peak is nearly 27 dB.

Self-pulsations were not observed at any pump currents because of the bandpass filter in the Faraday mirror assembly and the 1030-nm/1053-nm WDM that suppresses the stronger gain at shorter wavelengths. Figure 106.7 shows the ASE spectra of the double-pass amplifier for various pump current levels.

Figure 106.7
Amplified spontaneous emission spectra from a dual-pass fiber amplifier for various pumping levels. Also shown are the seed wavelength at 1053 nm and the ASE trace for the amplifier without the 1030-nm/1053-nm WDM, which has been offset for clarity.
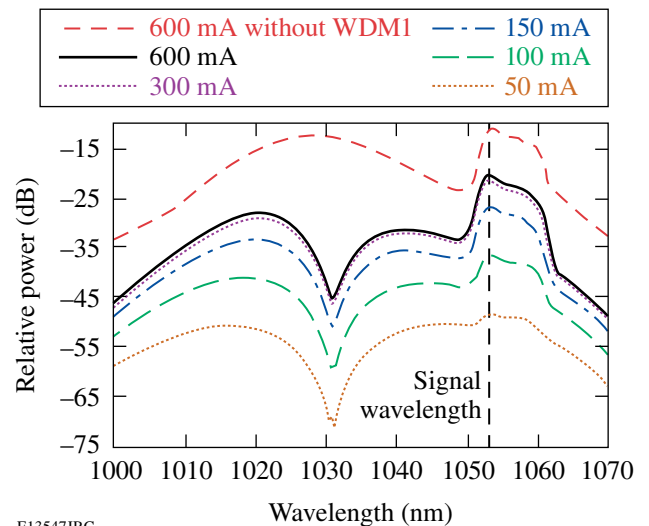

Figure 106.6
Gain, output energy, and ASE power of the experimental amplifier described in Fig. 106.5 as a function of pump current.

The seed wavelength is depicted by the vertical dashed line. The traces clearly show the double-pass gain of the wavelengths in the filter pass band compared to the single-pass gain of those outside the pass band. The top trace in Fig. 106.7, which is offset for clarity, is the ASE spectra for the double-pass amplifier without the 1030-nm/1053-nm WDM. This WDM, combined with the 10-nm bandpass filter, has a significant impact on both the output of the amplifier and the stability against lasing and self-pulsations, as evident in Fig. 106.7, and shows results very similar to the modeling results shown in Fig. 106.4.

It is difficult to define the noise floor of a system with regards to a low-repetition-rate signal. Simply comparing the strength of the signals on an optical spectrum analyzer requires an optical gate such that the spectrum is only integrated for the duration of the pulse. One alternative method compares the peak power of the amplified signal to the ASE power. A more meaningful metric that more accurately represents an optical signal-to-noise figure of merit compares the peak power of the amplified pulse to the ASE power in a limited spectral bandwidth around the seed-pulse wavelength. While the total noise floor is less than –28 dB across the entire operating range, the bandwidth-limited noise floor is better than –48 dB in a 0.1-nm bandwidth around the signal wavelength. Since the amplifier runs unsaturated, the noise floor is essentially constant as a function of pump current.

As mentioned previously, the combination of a Faraday mirror and polarizing beam splitter allows for high-fidelity separation of the input and output signals at the front end of the amplifier while maintaining the linear polarization state of the seed. The polarization extinction of the amplified signal was measured to be 19.9 dB, which is identical to that of the input signal.

Discussion and Conclusions

The pump is a grating-stabilized diode centered at 975.5 nm. The feedback from the fiber Bragg grating (FBG) maintains stable laser operation even in the presence of optical feedback, which can otherwise destabilize a diode laser.[8] However, the amplified seed can be a problem in damaging the diode. Starting with a 2-pJ seed signal of 2-ns duration, the amplified signal becomes ~1 nJ. By some spurious reflection, a second round-trip through the double-pass amplifier is possible, leading to 0.5 μJ. Even in the presence of a pump/signal WDM, the fraction split off from this energetic pulse (~15 dB) leads to a pulse impinging on the face of the pump diode with an energy of 15 nJ and a peak power over 7 W. This can cause catastrophic optical damage on the facet of the laser diode

where the beam size is less than 10^{-7} cm^2. Two components in our system serve to eliminate this problem. The first is the output isolator, which significantly reduces the risk of a high-energy back-reflection into the amplifier. The second is the second pump/signal WDM, which serves as an ~15-dB isolator of the signal pulse into the diode.

The agreement between measurements and simulations is favorable in the prediction of the noise characteristics of the amplifier, as shown in Table 106.III. In particular, using the ratio of small-signal gain over ASE power leads to an amplifier performance metric of 1161 per milliwatt, which agrees exceedingly well with the measurements. Both the signal gain and the ASE power levels were approximately 6 dB too high in the simulations, even when accounting for realistic component loss. There are several reasonable explanations for the discrepancy. First, there is the uncertainty in the loss due to the components and the splices. Second, the addition of the 10-nm filter in the Faraday mirror assembly may cause additional insertion loss due to slight perturbations in the propagation length and/or angle between the mirror and the fiber within the assembly. Finally, some of the parameters used in the simulations were simply taken from previous work.[6,7] In particular, the emission and absorption cross sections can play a large role in determining the output performance of the amplifier. By varying the simulated emission cross section at 1053 nm, it is found that the ASE and gain change by 9.5% and 8.1%, respectively, for a 1% change in the emission cross section alone. Given the variability between measurements of ytterbium absorption and emission cross sections,[7,9] this is likely a strong contributor to the mismatch in absolute values of gain and ASE power.

Table 106.III: Comparison of measured and simulated values for the double-pass fiber amplifier.

Characteristic	Measured Value	Simulation Result
Small-signal gain/ ASE	1175/mW	1161/mW
Total noise floor	–28 dB	–30.6 dB
Noise floor in 0.1-nm bandwidth	–48 dB	–43.5 dB
Small-signal gain	26.6 dB	32.3 dB

The unpumped amplifier has a passive loss of approximately 15 dB. The simulations show an unpumped amplifier loss of 13.9 dB. While some of this loss is due to absorption in the

unpumped Yb-doped fiber, almost 9 dB of this loss is insertion loss of the constituent components. Many of these components are free-space optics that are packaged with fiber pigtails at the vendor. All-fiber components would certainly help to increase the gain of the system as well as the noise figure. The noise figure of the amplifier is given by[10]

$$NF = \frac{2P_{ASE}}{h\nu\Delta\nu_{opt}G}, \qquad (3)$$

where P_{ASE} is the ASE power measured on a bandwidth $\Delta\nu_{opt}$, G is the signal gain, and ν is the optical frequency of the signal. Using measured parameters, the noise figure of the double-pass amplifier in a 0.1-nm bandwidth is 6.6 dB. Considering that the seed is degraded by 2.8 dB because of the insertion loss of the components before the active fiber, this result leads us to conclude that, in spite of operating far from the gain peak in a double-pass configuration, the amplifier is of extremely high quality because of the ASE suppression techniques utilized. Further, our model shows that our double-pass amplifier does not add any penalty to the noise figure, as has been observed in erbium-doped amplifiers used in a simple double-pass configuration.[4]

In conclusion, amplified spontaneous emission suppression techniques were utilized to fabricate a double-pass, ytterbium-doped amplifier with the noise properties of a single-pass amplifier. Simulations based on a rate-equation model were used to analyze the ASE and the impact of the suppression techniques. These techniques were implemented in an align-ment-free, double-pass, ytterbium-doped fiber amplifier with 26-dB gain at a wavelength 23 nm off the gain peak and a −48-dB noise floor while amplifying linearly polarized optical pulses with a low duty cycle.

REFERENCES

1. E. Desurvire, *Erbium-Doped Fiber Amplifiers: Principles and Applications* (Wiley, New York, 1994).

2. S. Hwang *et al.*, IEEE Photonics Technol. Lett. **13**, 1289 (2001).

3. A. Galvanauskas *et al.*, Opt. Lett. **26**, 935 (2001).

4. S. W. Harun, P. Poopalan, and H. Ahmad, IEEE Photonics Technol. Lett. **14**, 296 (2002).

5. L. L. Yi *et al.*, IEEE Photonics Technol. Lett. **16**, 1005 (2004).

6. Y. Wang and H. Po, J. Lightwave Technol. **21**, 2262 (2003).

7. R. Paschotta *et al.*, IEEE J. Quantum Electron. **33**, 1049 (1997).

8. R. W. Tkach and A. R. Chraplyvy, J. Lightwave Technol. **LT-4**, 1655 (1986).

9. N. A. Brilliant *et al.*, J. Opt. Soc. Am. B **19**, 981 (2002).

10. P. C. Becker, N. A. Olsson, and J. R. Simpson, *Erbium-Doped Fiber Amplifiers: Fundamentals and Technology* (Academic Press, San Diego, 1999).

The Development of Methods and Techniques for the Decontamination of Metals and Alloys

Background

Metallic components made of stainless steel, inconel, aluminum, and copper are routinely tritiated through the operation of tritium facilities. A significant disposal cost savings can be realized if the activity of the contaminated metals can be reduced below 0.5 μCi/g. The scope of this project was to determine the effectiveness of tritium removal, measure the residual tritium concentration, and establish the utility of the decontamination techniques in a tritium handling facility environment. To this end, metallic samples have been charged with tritium and stored in a helium environment for the study.

The proposed decontamination techniques were

- linear thermal desorption in an inert environment,

- linear thermal desorption using humidified inert gas,

- linear thermal desorption using inert gas containing different hydrogen peroxide concentrations, and

- radio-frequency–driven plasma decontamination using inert gas as the working medium.

This report describes the decontamination facilities and summarizes the efficacy of dry and humid thermal desorption, hydrogen peroxide decontamination, and radio-frequency–driven plasma decontamination.

Samples

A total of 57 low-carbon-content 316 stainless steel coupons have been contaminated with tritium gas for this study. The samples were not forged or polished, were cut into 2-cm × 5-cm × 0.5-cm-thick rectangles, and cleaned of oils and fingerprints using an acetone wash followed by a de-ionized water rinse. No heat treatment was applied to the samples before their exposure to HT gas at 375 Torr and 300 K for 105 h. The samples were charged with tritium in two batches. Following the dosing, the HT was evacuated and replaced with inert gas. The samples were individually wrapped in paper and then an aluminum wrap and fixed in slots in the container so that the coupons could not touch each other or the container walls. All coupon handling was carried out in an inert gas environment.

Fourteen months later, the container was opened in a helium glovebox operating at a moisture level below the –60°C dew point. Twenty coupons were unwrapped and sealed in a separate container that was backfilled with air for future decontamination tests. The remaining coupons were transferred from the glovebox to the experiment as the need arose in groups of 2 to 4 in a sealed container backfilled with air. None of the coupons was exposed to air for more than 1 week before a desorption run.

Experimental Facilities

1. Linear Thermal Desorption Facility

Linear thermal desorption (LTD) spectroscopy is an established diagnostic in the surface physics community that is used to study the nature of binding sites on surfaces. The target material is heated at a fixed linear rate from room temperature to some maximum value, usually of the order of 1100 K. The gas release rate from the surface is monitored and quantified as a function of the coupon temperature. The outgassing rate typically increases, peaks at one temperature, and then drops. The temperature at which the maximum desorption occurs depends on the linear heating rate and the binding energy for that species. A plot of the peak temperature against the heating rate can be used to extract the desorption energy. The technique has been used to study the release of tritium-labeled species from contaminated surfaces.[1,2]

The LTD facility used in this work is illustrated in Fig. 106.8. A glass furnace outfitted with a heater, thermocouples, and associated support equipment accepts the dosed coupons for the thermal desorption study. Helium purges the furnace during the temperature ramp. The helium carrier is purified to parts per billion levels to preclude contamination of the desorbing species with organic compounds present in the carrier gas.

Effluent collection is an established experimental method for collecting volatile tritiated species.[3] The technique quantifies
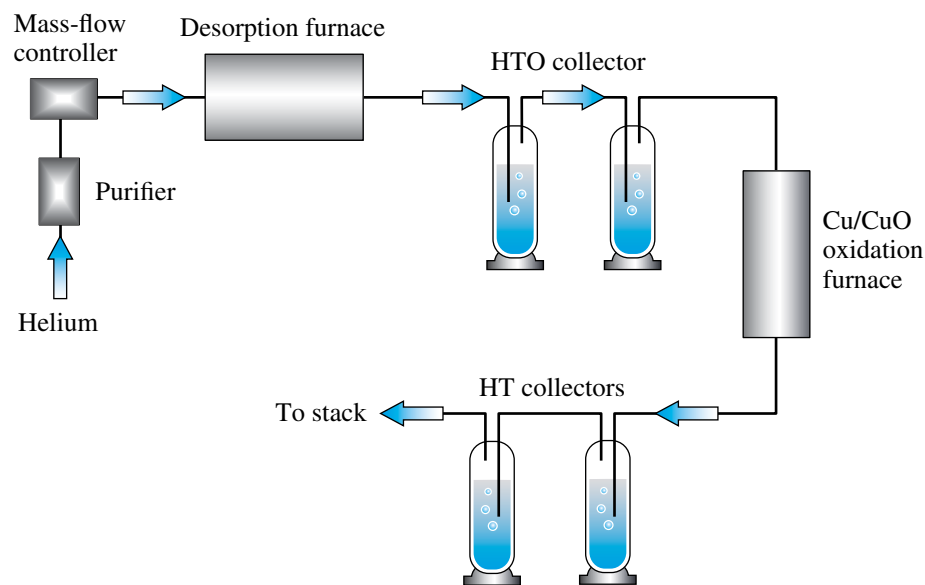
E14411JRC

Figure 106.8
Schematic of the linear thermal desorption facility.

the tritium release, segregates the airborne components into water-soluble and nonwater-soluble species, and permits limited resolution of the organic component released from surfaces.

Tritiated gas released from a dosed coupon is swept from the desorption furnace with the carrier to an array of water bubblers and a Cu/CuO furnace. The first two bubblers collect the water-soluble species and the second set collects the non-soluble species that have been oxidized to water in the Cu/CuO furnace. Bubblers are used in pairs to quantify the trapping efficiency of the upstream bubblers under the given operating conditions. Typically, the primary loss mechanism from each bubbler is the HTO transport in the humidified stream leaving the bubbler. The Cu/CuO furnace operates at 750°C to ensure high oxidation efficiency for volatile organic species, particularly tritiated methane. The entire system is fabricated from glass to minimize tritium retention on walls and catalytic exchange of HT to HTO on hot metal surfaces upstream of the Cu/CuO furnace. Each bubbler is equipped with a septum to permit on-line sampling of the water activity in each bubbler without disrupting the carrier flow. After the first four coupons were decontaminated, the bubbler immediately following the desorption furnace was fitted with an on-line liquid scintillation counter (LSC). The water in the bubbler was replaced with a liquid scintillation cocktail. A cocktail sample was continuously drawn from the bubbler at 1 ml/min, counted in a 0.2-ml detector, and returned to the bubbler. The activity profile was subsequently differentiated to extract the outgassing rate.

In these experiments, each bubbler was filled with 185 ml of liquid and the purge gas residence time in each bubbler was 3.7 min. The Cu/CuO oxidation furnace was periodically re-oxidized by passing air over the copper held at 750°C.

For humidity-stimulated desorption tests and for hydrogen peroxide-induced desorptions, the helium carrier was saturated with either liquid by passing purified helium through a bubbler containing one of the two liquids. The moist stream was blended with a dry helium stream to adjust the liquid content in the carrier entering the desorption furnace. The total helium flow rate was maintained at 50 ml/min for all experiments.

Before and after each LTD spectrum, the resident tritium inventory on the coupon was measured using the surface activity monitor (SAM) illustrated in Fig. 106.9

2. Surface Activity Monitor
Surface activity monitoring is a nondestructive technique based on measuring a decay-beta-induced current emanating from a contaminated surface.[4] The correlation between the emission current and surface activity has been established for metals and some nonmetals.[5–7] Surface activities greater than 2 nCi/cm^2 can be measured by placing the detector on a contaminated surface. The detection limit of the device rests in the ability to build stable amplifiers that can measure down to 1 fA. Decay betas emanating from the subsurface regions of the metal and its attendant oxide layer are attenuated during their progression

into the air. Typically, the device is limited to tritium detection to a depth of the order of 0.1 μm in stainless steel.

In the current work, the surface activity monitor has been modified to measure the total activity of the coupon. In this case, the coupon is inserted into a Faraday cage and the total current released by the coupon is measured. While the minimum detection current is still restricted to 1 fA, the sensitivity of the device to measure the tritium concentration in a coupon will increase with increasing coupon surface area. In the current configuration, the SAM can accommodate a sample 30-cm long × 10-cm wide.

3. Radio-Frequency–Driven Plasma Decontamination Facility

The decontamination facility[8] is illustrated in Fig. 106.9. Coupons were positioned along the long axis of a cylindrical glass vessel and electrically disconnected from the ground. A low-temperature, Tonks–Langmuir, argon plasma was struck between the coupons and the glass wall. The electric potential that developed on each coupon while it was immersed in the plasma was allowed to float at the plasma potential. The working neutral gas pressure was 50 mT. Desorbed species were removed from the vicinity of the coupon by purging the 1.6-liter cylindrical volume with argon at 0.5 Torr-L/s. After each plasma exposure, the coupon was removed and its residual tritium inventory was measured with the SAM. During the longer exposures, the coupon temperature gradually increased from 300 K to 340 K but never exceeded 340 K. Both the floating voltage and the current to ground were monitored in real time during each plasma exposure.
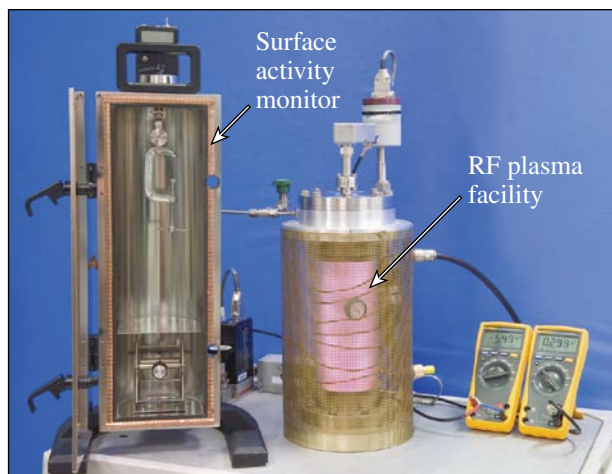

E14412JRC

Figure 106.9
Photograph of the surface activity monitor and the radio-frequency–driven plasma decontamination facility.

Results

1. Data Overview

The decontamination protocols used during this study are summarized in Table 106.IV.

Bubbler 1 and 3 data, the lead bubbler in each set, were collected manually for coupons 1 through 4 by taking a 0.5-ml aliquot according to the sampling rate listed in Table 106.V.

All subsequent B1 data was collected continuously with the in-line liquid scintillation counter described earlier. Periodically, 0.5-ml aliquots of the liquid scintillation cocktail were extracted from bubbler 1 to cross-reference against a calibrated

Table 106.IV: Decontamination protocol used for each coupon.

Coupon number	Desorption furnace ramp rate (°C/min)	Purge stream component	Concentration (ppm)
1	10	Dry	
2	10	Dry	
3	5	Dry	
4	5	Dry	
5	5	Dry	
6	2.5	Dry	
7	2.5	Dry	
8	1.5	Dry	
9	1.5	Dry	
10	1.5	Dry	
11	1.5	Dry	
12	1.5	Dry	
13	1.5	H_2O	3210
14	1.5	H_2O	9630
15	Steps	H_2O	16053
16	Steps	H_2O_2	310
17	Steps	H_2O_2	1550
18	Steps	Dry	
19	RF decontamination		
20	RF decontamination		

Table 106.V: Sampling rate dependence on the furnace ramp rate.

Ramp rate (°C/min)	Sample interval (min)
10	5
5	10
2.5	15
1.5	20

liquid scintillation counter. Figure 106.10 summarizes the evolution of "soluble" activity collected from the first 12 coupons that are listed in Table 106.IV. The evolutions were normalized by the total "soluble" activity collected to permit a comparison of the evolution profiles. These profiles, which are shown in Fig. 106.10, exhibit a dependence on the temperature ramp rate because the coupon temperatures are inferred from the furnace temperature. For example, for a ramp rate of 2°C, the difference between the furnace and coupon temperatures peaks at 20°C. For a 10°C ramp rate, that difference increases to 80°C. In Fig. 106.10, the normalized release profiles were all observed to steepen as the ramp rate decreased from 10° to 1.5°C/min. These curves indicate that most of the activity is released between 200°C and 350°C.
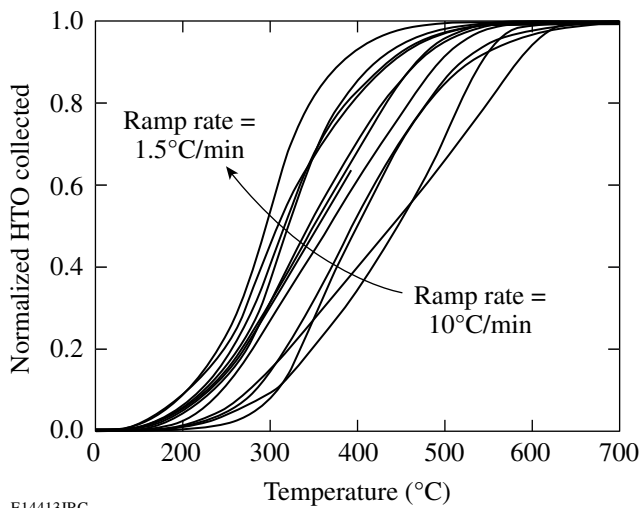

Figure 106.10
Normalized activity of bubbler 1 as a function of furnace temperature.

During these tests, the trapping efficiencies of bubbles 1 and 3 exceed 99.8% except at low bubbler activities where measurement errors are large. If bubblers 2 and 4 have similar collection efficiencies, then less than 4×10^{-6} of the soluble activity entering the first bubbler set will contribute to the activity in the bubbler set following the furnace. Additionally, less than 4×10^{-6} of the activity leaving the furnace escapes the desorption facility. Water soluble and nonsoluble activity released by the coupons is effectively separated by the two bubbler sets at a 50-ml/min helium purge rate. Random sampling of the effluent leaving the fourth bubbler with a portable ionization chamber confirmed that no measurable activity was escaping capture in the desorption facility.

Switching from water to a liquid scintillation cocktail in bubbler 1 to permit on-line monitoring of the activity reduced the trapping efficiency of this bubbler to 95% at high water loadings in the cocktail. Nevertheless, and in part because the second bubbler continued to use water as the capture medium, the total transfer of water-soluble activity to the bubbler set following the furnace only increased by 25-fold, from 4×10^{-6} to 1×10^{-4}. At this overall trapping efficiency and assuming that the water-soluble component is 100 times larger than the insoluble fraction, the water-soluble contribution to the insoluble fraction will represent a 1% overestimate in the nonsoluble activity.

Water vapor is continuously transferred from upstream bubblers toward downstream bubblers. The concomitant rate of activity loss from the upstream bubbler was observed to match the rate of activity accumulation in the second bubbler for both bubbler sets. This indicates that the trapping efficiency of each bubbler was limited by HTO transport from bubbler to bubbler rather than by an inefficient activity transfer from the helium purge stream into the bubbler fluid.

The activity and split between soluble and insoluble components for all decontaminated coupons are presented in Table 106.VI. The coupons are listed in the order in which

Table 106.VI: Summary of the activities and the fraction of soluble and insoluble components collected from each coupon.

Run	HTO (μCi)	HT (μCi)	Total (μCi)	% HTO/total
1	665	176	841	79
2	690	113	803	86
3	1331	92	1424	94
4	902	137	1039	87
5	1080	70	1149	94
6	1018	103	1120	91
7	945	53	998	95
8	1086	34	1120	97
9	854	35	889	96
10	741	6	747	99
11	665	11	676	98
12	1358	26	1384	98
13	1387	37	1424	96
14	931	26	957	97
15	N/A			
16	2228	98	2326	96
17	551	87	638	86
18	895	60	955	94
Average			1088	94

they were desorbed. Equipment failure during the processing of coupon 15 has lead to some questionable results; those values are not presented in the table. Results from detritiating coupon 1 and, to a lesser extent, coupon 2, are skewed toward a higher activity collection in the bubbler set following the furnace because residual activity released from the furnace has contributed to the activity collected in the second bubbler set. Disregarding the coupon-1 data, 94% of the total activity released by the coupons is water-soluble and assumed to be HTO for the present discussion. The mean activity collected from each coupon was 1.1±0.4 mCi.

2. Linear Thermal Desorption in Dry Helium

The evolution of each activity profile from bubbler 1 has been smoothed with a running average that spans six data points, differentiated with respect to time, and normalized by dividing the differentiated curve by the total tritium collected from that coupon. The resulting outgassing curves for four coupons are provided in Fig. 106.11 to compare the sample-to-sample variation in the outgassing rate that can be expected for identical desorption conditions.
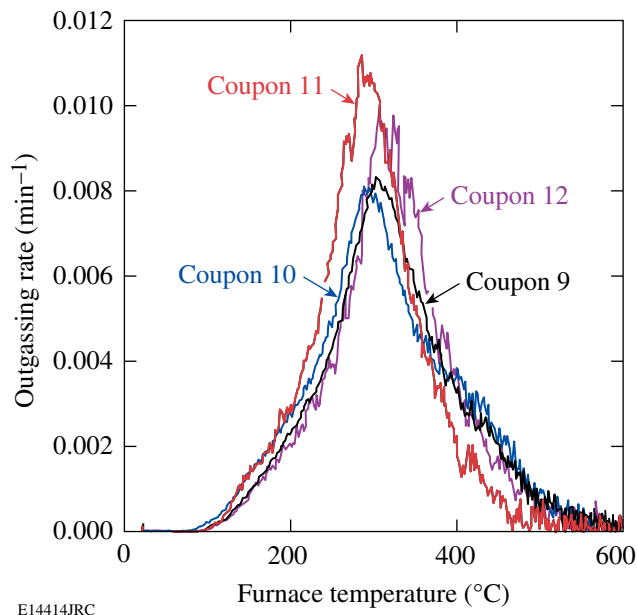

E14414JRC

Figure 106.11
Sample-to-sample variation in the outgassing rate for identical desorption conditions at 1.5°C/min.

The on-line monitoring system collects and records the activity of bubbler 1 every minute. Consequently, the running average used to smooth the data spans a 6-min period. The purge gas residence time in bubbler 1, the mean contact time of the bubbles in the liquid, is 3.7 min at 50 ml/min. The rate

of absorption of HTO into the liquid scintillation cocktail is exponential with a time constant determined by the interfacial area of the bubble (area/volume), overall mass transfer coefficient, and time the bubble spends in the fluid. Given the high trapping efficiency, it is reasonable to assume that the majority of the activity is removed in the first half of the bubbler and that the stirring to equilibrate the activity within the bubbler by the action of bubbles floating to the liquid surface will exceed the gas residence times by at least a factor of 2. Averaging over 6 min should accurately reflect the mean bubbler activity at any given moment in time. The fluctuations in liquid activity seen in Fig. 106.11 are attributed to local variations in the fluid activity arising from the random passage of bubbles close to the LSC sampling point. Similar fluctuations are evident in the activity for the two samples desorbed at 2.5°C/min in dry helium, as shown in Fig. 106.12. The run-to-run variation in the outgassing measurement is less than 20% in both examples.

E14415JRC
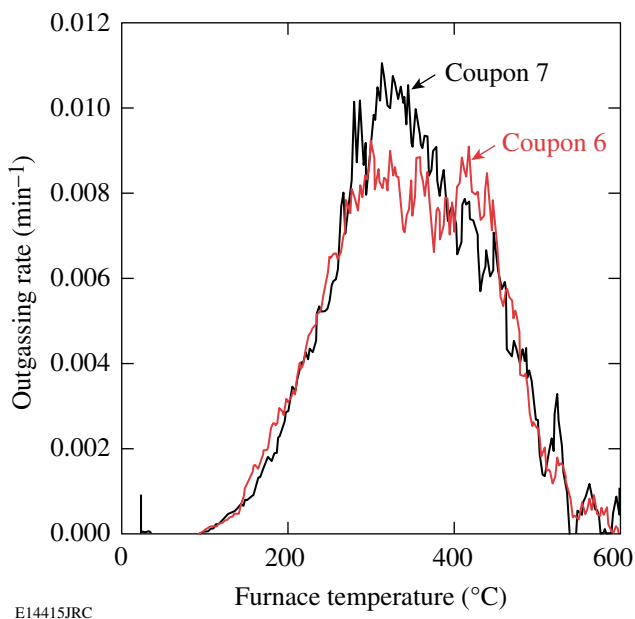
Figure 106.12
Sample-to-sample variation in the outgassing rate for identical desorption conditions at 2.5°C/min.

The normalized outgassing rate dependence on the temperature ramp rate of the desorption furnace is provided in Fig. 106.13. Three features are evident.

The profiles become progressively more skewed as the ramp rate increases. This suggests that the desorbing species did not have time to equilibrate with the surface during desorption at the higher ramp rates. The skewed evolution profiles may be more representative of the release of the actual species bound to

E14416JRC

Figure 106.13
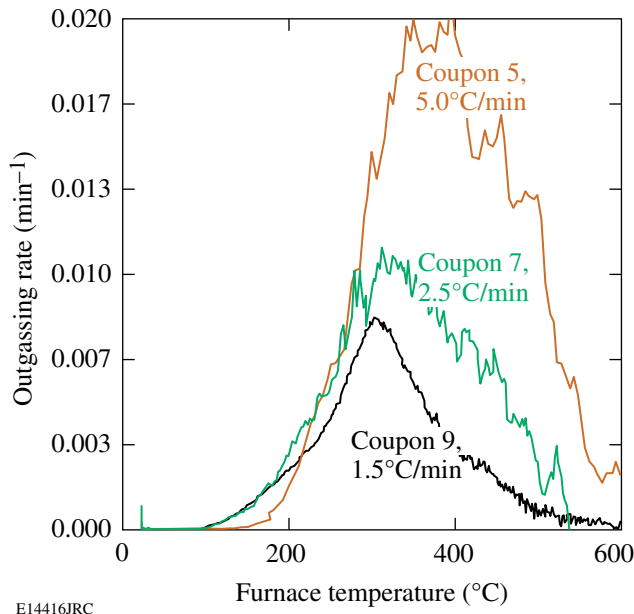The outgassing rate dependence on the temperature ramp rate of the desorption furnace for coupons 5, 7, and 9.

E14417JRC

Figure 106.14
The outgassing rate dependence on the temperature of the desorption furnace in a dry helium purge. Coupon 18 contained 0.96 mCi.

E14418JRC

Figure 106.15
The outgassing rate dependence on the temperature of the desorption furnace in a wet helium purge. Coupon 15 contained 0.69 mCi. The helium purge rate was 50 ml/min, with a water content of 16050 ppm.

the surface. That is, either different species or the same species with different surface-binding energies are being released at the higher ramp rates without thermally accommodating with the surface before release. In contrast, the symmetric profile evident in the 1.5°C/min ramp rate case suggests that surface-bound species can migrate on the surface to lower energy states before release to the gas phase.

The shift in the desorption peaks as one proceeds to higher ramp rates is an artifact of the experimental setup, as discussed earlier.

Finally, the normalized outgassing rate increase with increasing ramp rate is a consequence of limited activity on the surface. As discussed in **Data Overview** (p. 72), the total activity released from each coupon was of the order of 1.1 mCi. As a result, increasing the ramp rate requires a commensurate increase in the outgassing rate if the total quantity of material released is to remain constant.

3. Thermal Desorption in a Helium Stream Bearing H_2O
    The normalized outgassing rate from coupons soaked at fixed temperatures while exposed to a helium purge containing 0- and 16050-ppm water is provided in Figs. 106.14 and 106.15, respectively.

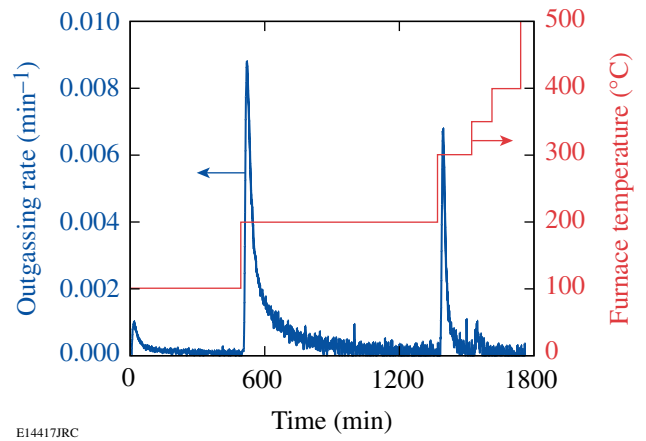These figures indicate that the preponderance of the activity is released between 100°C and 300°C. Furthermore, a comparison of the two figures suggests that the presence of water in the helium purge stream stimulates tritium release at all temperatures. That removal rate appears to be limited by diffusion from the subsurface to the surface. At all temperatures, once the near-surface tritium has been depleted, the activity outgassing rate reduces to zero. Increasing the coupon temperature from 200°C to 300°C increases the tritium diffusion rate to the surface, as expected. Increasing the coupon temperature beyond 300°C does not noticeably increase activity release in the dry helium purge case, but it does stimulate the release of more tightly bound residual

activity when water vapor is present in the purge stream. Increasing the coupon temperature to 500°C results in negligible additional activity release in both cases. The residual activity following each bakeout is negligible in both cases based on SAM measurements.

4. Thermal Desorption in a Helium Stream Bearing H_2O_2

The normalized outgassing rate from coupons soaked at fixed temperatures while exposed to a helium purge containing 310- and 1550-ppm hydrogen peroxide is provided in Figs. 106.16 and 106.17, respectively.

In both cases, at coupon temperatures below 150°C, the outgassing rate is rate controlled by tritium diffusion from the subsurface to the solid/gas interface as for the dry and humid

helium purge runs. Above 150°C, however, activity removal decreases with the logarithm of time, suggesting the rate-limiting step is peroxide transport to the reaction zone. Furthermore, the reaction rate increases with increased hydrogen peroxide concentrations. Negligible activity is removed beyond a coupon temperature of 250°C.

To illustrate these observations more clearly, the two outgassing curves have been overlaid on the semilogarithmic curve provided in Fig. 106.18. The diffusion-limited outgassing regime below 150°C is evident for both coupons. In the 1550-ppm case, however, activity is removed approximately threefold more aggressively than in the 310-ppm case. Above 150°C, the reaction rate depends on the logarithm of time, doubling for a fivefold increase in hydrogen peroxide concentration.

E14419JRC

Figure 106.16
The outgassing rate dependence on the temperature of the desorption furnace in a helium purge containing 310-ppm hydrogen peroxide. Coupon 16 contained 2.33 mCi.

E14420JRC

Figure 106.17
The outgassing rate dependence on the temperature of the desorption furnace in a helium purge containing 1550-ppm hydrogen peroxide. Coupon 17 contained 0.64 mCi.
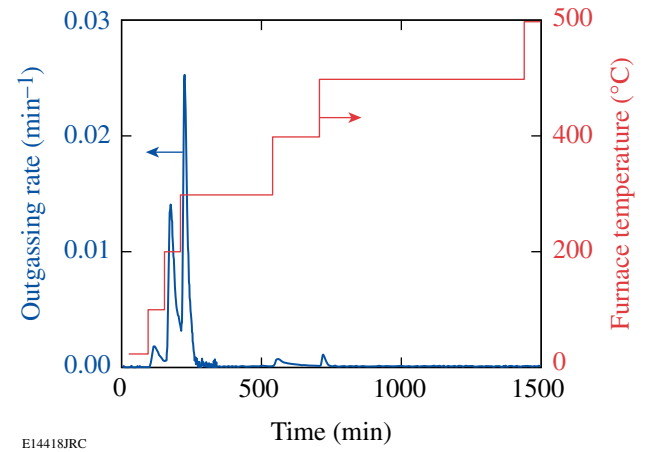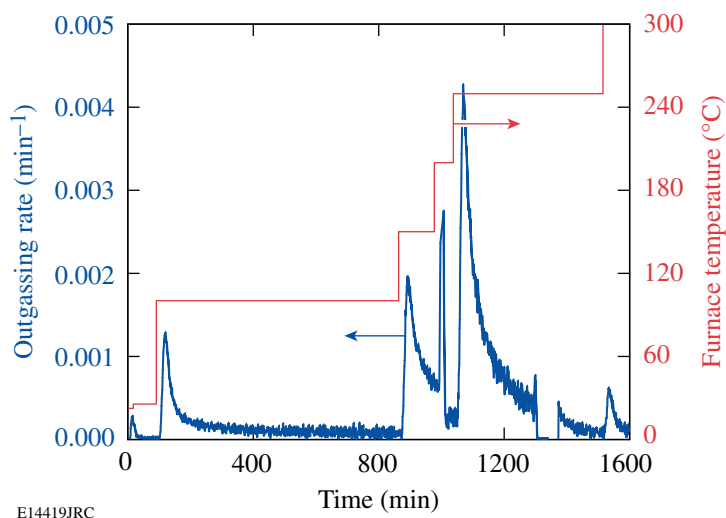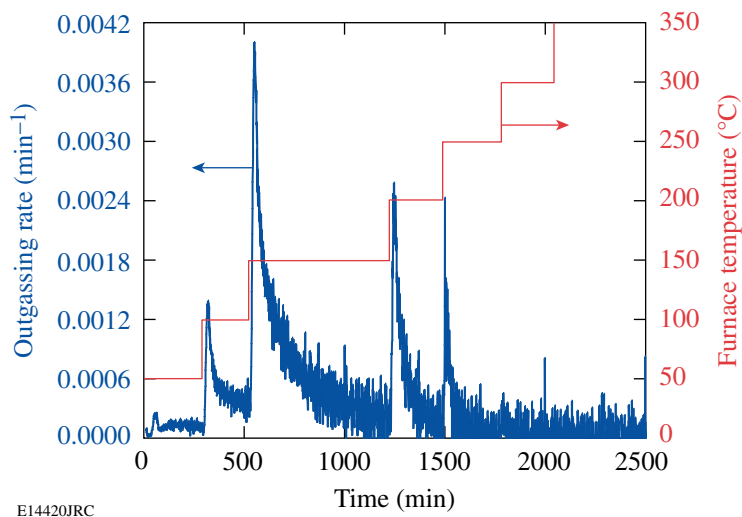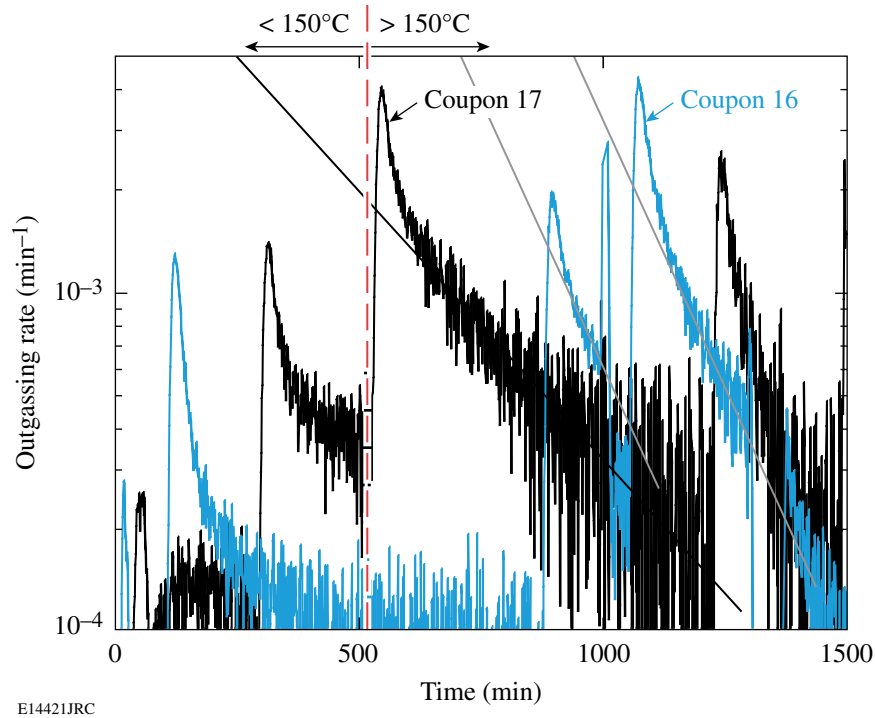
Figure 106.18
The outgassing rate dependence on both coupon temperature and hydrogen peroxide concentration.

5. Correlation Between SAM and LSC Measurements

A continuous beta flux emanates from a tritiated metallic surface. This flux is uniquely related to the near-surface tritium concentration

$$I_{sat} = \frac{A}{2W} \int_0^{E_T} eE\Phi(E)dE, \tag{1}$$

where A is the emitting area, W is the mean energy invested in forming ion pairs (33.7 eV/ion pair in air at 1 bar), e and E are the electronic charge and the energy of the decay electron, respectively, and $\Phi(E)$ is the energy distribution of the flux emanating from the surface. The factor of 2 accounts for the half of the decay electrons that are emitted in the direction of the metal bulk and cannot contribute to ion-pair formation in the air.

In the limit where the tritium resides on the surface or in the proximity of the surface, i.e., the attenuation of the decay electron energy before the electrons reach the air interface can be neglected, Eq. (1) simplifies to

$$I_{sat} = \frac{eE_m}{2W} \lambda n_s,$$

where n_s is the number of tritium atoms on the surface decaying at the rate λ to emit an electron stream of mean energy E_m (5.7 keV). Introducing the numeric values,

$$I_{sat} = \frac{1.602 \times 10^{-19} \times 5700}{2 \times 33.7} \lambda n_s \tag{2}$$

$$= 0.0135\, \lambda n_s, \tag{3}$$

where λn_s is the activity on the surface in becquerels and I_{sat} is measured in femtoamperes (fA), or

$$I_{sat} = 0.5007\, \lambda n_s, \tag{4}$$

where λn_s is expressed in nanocuries and I_{sat} is in femtoamperes.

This current is collected on the anode in the SAM, boosted in one of two ranges by an onboard transimpedance amplifier, and displayed as a voltage. The transfer function for the two ranges is

$$V(\text{mV}) = 0.196 \times I(\text{pA}) \tag{5}$$

on scale 1 and

$$V(mV) = 0.212 \times I(fA) \qquad (6)$$

on scale 2. Both ranges have been calibrated against a NIST-traceable standard for this work.

Substituting for the current in Eqs. (4) and (5) and Eqs. (4) and (6) yields

$$\lambda n_s = 10.2 \times V(mV) \qquad (7)$$

microcuries on scale 1 and

$$\lambda n_s = 9.43 \times V(mV) \qquad (8)$$

nanocuries on scale 2.

The activity of each coupon was measured before and after treatment in the SAM, and the surface activity was estimated using either Eq. (7) or (8). Table 106.VII compares SAM measurements with the total activity collected by the bubblers.

Table 106.VII: Comparison of the SAM measurements with the total activity collected for each coupon.

Run	Total (μCi)	SAM (μCi)	% SAM/total
1	841	632	75
2	803	588	73
3	1424	N/A	
4	1039	698	67
5	1149	764	66
6	1120	813	73
7	998	662	66
8	1120	842	75
9	889	682	77
10	747	511	68
11	676	499	74
12	1384	835	60
13	1424	740	52
14	957	513	54
15	N/A	527	
16	2326	1113	48
17	638	434	68
18	955	654	68

This data is displayed in Fig. 106.19 with its estimated error. The error in the SAM data is taken to be of the order of 2% of the value. The error in the LSC data is expected to reach up to 10% of the value. The primary source of error in the LSC data is a sampling error. The liquid activity was sampled by extracting 0.5±0.05-ml aliquots for counting. Systematic errors are assumed to be negligible compared to the sampling error since both measurement techniques rely on differing principles and both measurement schemes have been independently calibrated. If the origin is included in the linear regression analysis, the SAM registers 70% of the LSC value with a correlation of 0.93 and a 10% offset in slope. If the origin is not included, the SAM registers 70% of the LSC value with a 20% offset in slope and a 0.84 correlation coefficient. In either case, approximately 70% of the total activity collected from the coupon is visible to the SAM.

E14422JRC
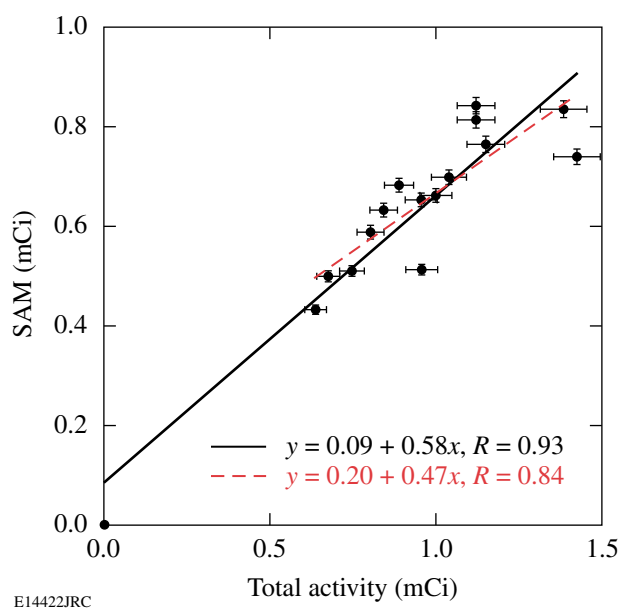
Figure 106.19
Surface activity correlation between SAM measurements and LSC data for each coupon.

The range of 5.7-keV electrons decreases from 400 nm in water to 50 nm in stainless steel. More energetic 18.6-keV electrons will reach 5000 nm in water and 600 nm in stainless steel. If we idealize the stainless surface as a metal covered with 100 monolayers of water and each layer is approximately 0.3 nm thick, then the water layer on the surface will be of the order of 30 nm thick. All decay electrons originating from the water layer will contribute to the surface activity measurement. Additionally, electrons originating from the water–metal interface will reach the air–water interface with some attenuation while electrons originating at a depth of

50 nm with energies below 5.7 keV will not contribute to the SAM measurement. The SAM to LSC ratio in Fig. 106.19 suggests that approximately 70% of the tritium desorbed from the coupon resides in areas shallower than 50 nm in the stainless steel.

For exposures of the order of an hour and at room temperature, most of the tritium will reside in the water layers on the metal or close to the water–metal interface in the stainless steel.[9] The amount of tritium sorbed on a room-temperature stainless steel coupon is directly proportional to the exposure time[10] until, in effect, each resident water molecule bound to the surface is labeled with a triton; that is, the mean surface activity reaches 48 μCi/cm^2. Under these exposure conditions, about 10% of the tritium penetrated approximately 100 nm into the metal. More recent experiments indicate that tritium can diffuse up to 400 μm into the metal[11] and that the tritium concentration in the metal drops off with the error function of the square root of the diffusivity time product when the exposure temperature is above 370 K, in accordance with the classical equations for hydrogen diffusivity in metals. Below 370 K, classical diffusion based on lattice diffusivity does not appear to apply. Presumably, grain-boundary and triple-point diffusion contribute more significantly to the total hydrogen transport into the metal.

SAM measurements are linearly related to the surface/ near-surface activity, as discussed previously. Earlier studies referenced in this article indicate that sample-to-sample variations are small for samples exposed under identical conditions. The variability between the SAM and LSC measurement data observed in the current sample set is attributed to coupon handling following exposure. As discussed, 70% of the tritium resides in the top 50 nm of the surface. Up to 10% of the activity in this layer could be removed with a single coupon handling. The action of wrapping and unwrapping the coupons can easily represent a variation of 20% in the surface-activity measurement. The deviation between the linear regression provided in Fig. 106.19 and each SAM measurement listed in Table 106.VII has been expressed in a percentage of the expected SAM measurement and plotted against the total coupon activity in Fig. 106.20. The measurements fluctuate about the linear regression value for each measurement with the range +16%/–21%, as expected.

6. Radio-Frequency–Driven Plasma Decontamination
The effectiveness of using a plasma discharge to decontaminate tritiated metal is illustrated in Figs. 106.21 and 106.22. In these tests, each coupon was removed from storage under
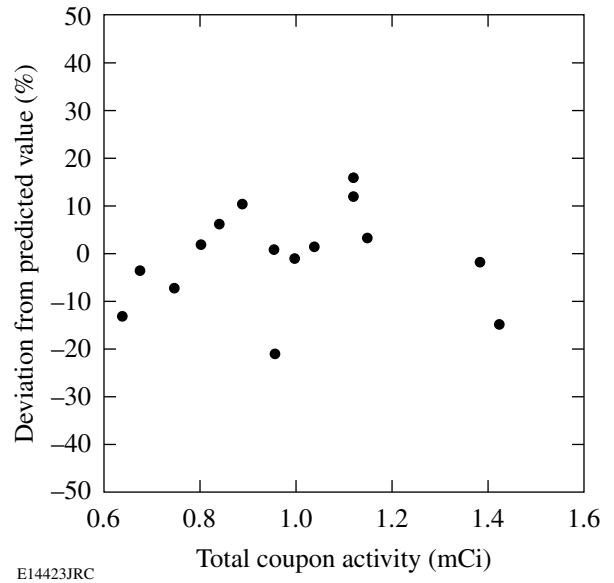
Figure 106.20
Deviation of individual SAM measurements from the expected SAM measurement for a range of coupon activities.

helium gas, its surface activity measured using the SAM, and then transferred to the decontamination chamber shown in Fig. 106.9. During the measurement and transfer, the coupon was exposed to air for approximately 5 min. The decontamination chamber was evacuated, an argon purge through the chamber initiated, and the discharge struck. The time during which the coupon was exposed to a plasma increased from

Figure 106.21
Residual surface activity following exposure to RF-driven plasma.

E14425JR

Figure 106.22
Residual surface activity following 2-min exposures to RF-driven plasma.

7 min in the first exposure to 18.7 h in the last. The original surface activity and the activities immediately following each exposure are plotted as a function of cumulative exposure in Fig. 106.21.
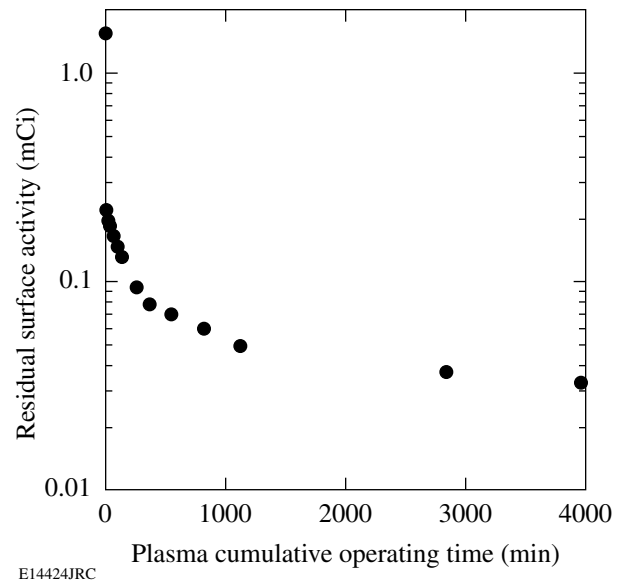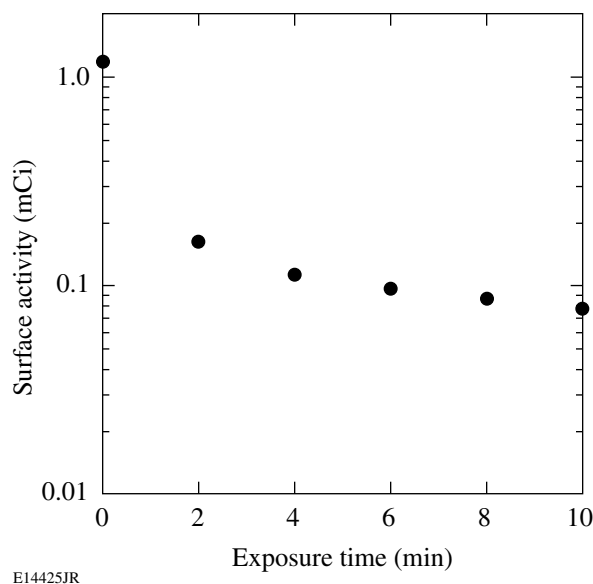
This figure illustrates that 86% of the surface activity is removed in the first 7 min of plasma exposures. After almost 4000 min of additional exposure, 2% of the original activity remains in the coupon.

Figure 106.22 illustrates the rate of activity removal for sequential 2-min plasma exposures of a second coupon under the same discharge conditions used for the previous sample. This figure indicates that 86% of the initial surface activity is actually removed within the first 2 min of exposure.

An argon discharge in a 10-cm-diam cylinder with a neutral pressure of 50 mTorr will support an electron temperature approaching 30,000 K and a sheath potential of 1.2 eV. Argon-neutral atoms and ions will bombard a coupon immersed in this plasma with an average energy of 1.2 eV. During the tests illustrated in Figs. 106.21 and 106.22, the ion current drawn by the coupon was of the order of 1 mA. Equivalently, particles struck the coupon surface at the rate $1 \times 10^{-3}/1.6 \times 10^{-19} \approx 6 \times 10^{15}$ particles/s.

The hard sphere radius of water is 0.145 nm. Each monolayer of water on the coupon surface will contain 1.5×10^{15} particles/cm$^2 \times 27$ cm^2 (the coupon surface area) $\approx 4 \times 10^{16}$ particles.

If we assume the coupon is covered with approximately 30 monolayers (ML) of water,[†] then the number of water molecules desorbed from the surface during a 2-min discharge per incoming argon atom will be

$$\frac{30 \text{ ML} \times 4 \times 10^{16} \text{\#}/\text{ML}}{2 \text{ min} \times 60 \text{ s}/\text{min} \times 6 \times 10^{15} \text{ ions}/\text{s}}.$$

This relationship suggests that 1.7 water molecules are released per argon ion.

Typically, the first layer of water bonds to the metal surface via the lone pair electrons with an energy of the order of 0.4 to 0.7 eV. That is, those electrons not involved in the hydrogen bonding are shared with the metal surface so that the water molecule is oriented with the oxygen facing the surface and the two hydrogen atoms pointed away from the surface. All additional water layers are held to the surface via hydrogen bonds to the first layer molecules with energies of the order of 0.2 to 0.3 eV per bond. The O-H dissociation energy is 5.18 eV. Argon ions from the plasma drop through the sheath, increase their energy from roughly 0.03 eV to 1.2 eV, and deposit that energy on the coupon surface. On average, this energy can break up to four water-to-surface bonds, a fraction of which would be released from the surface. Water desorption is preferred to water dissociation.

The estimated release of 1.7 water molecules per incoming argon ion is consistent with the observations provided in Figs. 106.21 and 106.22. Both figures show that the tritium removal efficiency drops rapidly following the first 2 min. The removal rate is no longer argon ion flux limited but tritium atom supply limited. Tritium must first diffuse to the metal surface before it can be removed from the coupon. This suggests that heating the coupon would accelerate tritium removal during this phase of the decontamination. The discharge is a highly efficient method for removing tritiated water from a metal surface.

Summary and Conclusions

The efficacy of removing tritium from stainless steel surfaces using the following four different approaches has been studied:

• thermal desorption in a dry purge
• thermal desorption in a wet purge

[†]Stainless steel exposed to ambient air with a relative humidity in the vicinity of 40% to 50% will contain up to 100 monolayers of water. The time for the water content on a surface to equilibrate with the water vapor pressure in the air is of the order of a few seconds.

- thermal desorption in a purge containing hydrogen peroxide
- radio-frequency–driven argon plasma irradiation.

Thermal desorption experiments indicate that the averaged activity desorbed from each coupon was 1.09 mCi. A standard deviation of 0.4 mCi in these measurements is attributed to coupon handling during the wrapping and unwrapping of individual coupons.

The activity of each coupon was measured using a surface activity monitor. The SAM measured 70% of the actual tritium desorbed from the coupons. This suggests that 30% of the tritium resides deeper than 600 nm in the metal matrix before decontamination. Such penetration depths are consistent with the 105-h exposure durations used to prepare the coupons. More than 80% of the tritium desorbed from the coupons was released as a water soluble.

It appears that some tritium diffuses from depths below 50 nm, i.e., from the metal bulk during the decontamination process, most likely as atoms, recombines with hydroxyls at the surface or isotopically exchanges with molecular water still resident on the surface, and then desorbs.

Desorption in a dry helium purge is tantamount to boiling molecular water from the coupon surface. A minimum metal temperature of 600°C is required to remove the bulk of the tritium. SAM measurements following the high-temperature desorptions do not indicate the presence of tritium. Based on Eq. (8), the mean-surface/near-surface activity to a depth of 200 nm into the metal must be less than

$$\frac{9.43\,\mathrm{nCi/mV} \times 0.25\,\mathrm{mV}}{27\,\mathrm{cm}^2 \times 200\,\mathrm{nm} \times 9\,\mathrm{g/cc}} = 485\,\mathrm{nCi/g} = 0.5\,\mu\mathrm{Ci/g},$$

where 0.25 mV is the minimum detectable voltage that can be measured with certainty. This value represents the SAM's detection limit for these coupons.

Desorption in a wet helium purge also approximates boiling molecular water from the coupon surface. Nevertheless, the presence of water promotes some activity release. The higher normalized outgassing rates observed in the presence of water vapor are most likely attributable to isotopic exchange at the metal surface. Negligible tritium release is observed above 500°C. As in the dry helium purge case, the rate-limiting step in activity removal appears to be tritium diffusion from the water layers or the metal bulk.

At 100°C and for low hydrogen peroxide concentrations, activity removal from the coupon surface follows the same rate-limiting mechanism observed under dry and moist purge conditions, i.e., tritium diffusion through the metal oxide layers. Increasing the hydrogen peroxide concentration fivefold to 1550 ppm without changing the coupon temperature shifts the rate-limiting mechanism from diffusion through the metal oxide to hydrogen peroxide arrival at the metal surface. Negligible activity remains in a coupon following a decontamination using a 1550-ppm hydrogen peroxide-doped helium purge over a coupon heated to 250°C.

Radio-frequency–driven plasma decontamination removes the layers of molecular water extremely rapidly. Subsequently, diffusion from the metal bulk limits the rate of activity removal. It appears that the overall time needed to decontaminate metal with this approach can be realized with an initial exposure to the plasma at room temperature followed by additional plasma exposures at elevated metal temperatures.

This study has shown that water or water-soluble components represent the majority of the activity released from metal exposed to tritium gas for 105 h. Earlier studies have shown similar results for short exposure durations. Additionally, most of the tritium that has diffused into the bulk returns to the surface, recombines with hydroxyl radicals, and is released as water. Some of the re-emergent tritium combines with hydrogen and is released as HT.

ACKNOWLEDGMENT

REFERENCES

1. Y. Belot, H. Camus, S. Raviart, A. B. Antoniazzi, and W. T. Shmayda, Fusion Technol. **28**, 1138 (1995).

2. A. B. Antoniazzi and W. T. Shmayda, Fusion Technol. **26**, 673 (1994).

3. W. T. Shmayda, A. B. Antoniazzi, and R. A. Surette, Ontario Hydro Research Division, Toronto, Canada, Report No. 92-51-K (1992).

4. W. T. Shmayda, N. P. Kherani, and D. Stodilka, in *Fusion Technology 1996*, edited by C. Varandas and F. Serra (Elsevier, Amsterdam, 1997), pp. 1245–1248.

5. N. P. Kherani and W. T. Shmayda, Fusion Technol. **28**, 893 (1995).

6. W. T. Shmayda and N. P. Kherani, U.K. Patent No. 2,301,222 (11 August 1999).

7. C. R. Shmayda, W. T. Shmayda, and N. P. Kherani, Fusion Sci. Technol. **41**, 500 (2002).

8. A. B. Antoniazzi and W. T. Shmayda, in *Fusion Technology 1992*, edited by C. Ferro, M. Gasparotto, and H. Knoepfel (Elsevier Science Publishers B.V., Amsterdam, 1993), pp. 1680–1684.

9. N. P. Kherani, D. Stodilka, and W. T. Shmayda, Ontario Hydro Technologies, Toronto, Canada, Report No. A-IT-96-52-CON (1996).

10. N. M. Masaki, T. Hirabayashi, and M. Saeki, Fusion Technol. **15**, 1337 (1989).

11. A. N. Perevezentsev *et al.*, Fusion Sci. Technol. **48**, 208 (2005).

Basic Principles of Direct-Drive Ignition Target Design

Introduction

Inertial confinement fusion (ICF) is an approach to fusion that relies on the inertia of the fuel mass to provide confinement. The confined fuel must reach a high temperature and density to produce enough $D + T \longrightarrow \alpha(3.5\ \text{MeV}) + n(14.1\ \text{MeV})$ reactions so that the total energy released is much larger than the driver energy required to compress the fuel. The capsule in an ICF implosion, which is a spherical cryogenic deuterium–tritium (DT) shell filled with DT vapor, is irradiated directly by laser beams (direct-drive approach) or by x rays emitted by a high-Z enclosure (hohlraum) surrounding the target (indirect drive).[1] Only a small portion of the fuel is heated to ignition conditions in a typical ignition target. This part of the fuel forms a hot spot that initiates a burn wave that ignites the remaining fuel. In the direct-drive approach, the following stages of an implosion can be identified: At the beginning of the laser pulse, the outer portion of the pellet heats up and expands outward, creating a plasma atmosphere around the pellet. Then a critical electron density $n_{\text{cr}} = \pi m c^2 / e^2 \lambda_L^2$ is established outside the cold portion of the shell, where m is the electron mass, c is the speed of light, e is the electron charge, and λ_L is the laser wavelength. The laser energy is absorbed in a narrow region near the critical surface via the inverse bremsstrahlung, and the absorbed energy is transported, mainly by electrons, toward the colder portion of the shell. The cold material, heated by the thermal conduction, expands outward. Such an expansion creates an ablation pressure that, similar to the rocket effect, compresses the pellet. At the beginning of implosion, the ablation pressure launches a shock wave that propagates ahead of the thermal ablation front and increases the fuel entropy. Then, as the first shock breaks out at the rear surface of the shell, the transmitted shock is formed. It converges through the vapor to the capsule center. After reflection from the center, the shock moves outward and interacts with the incoming shell. At this point, the velocity of the inner portion of the shell starts to decrease, reversing its sign at stagnation. This is a crucial point of the implosion since no more "pdV" compression work can be done to the hot spot after the stagnation, and the only remaining heating source is the energy deposition of α particles produced by fusion reactions inside the hot spot (α heating).

At the deceleration phase of the implosion, the kinetic energy of the shell is transferred into the internal energy of the hot spot. To ignite the fuel, the energy gain due to the pdV work of the imploding shell and α heating must be larger than the energy losses due to thermal conduction and radiation. This requirement sets a minimum value for the implosion velocity v_{imp} of the shell.

The following sections review the basic concept of ICF ignition, present the simplest direct-drive ignition target design, and discuss stability issues.

Basic Concepts

To burn a substantial fraction of the fuel mass, the fuel density at stagnation must be very large. This can be easily shown if we assume that the main fuel at the peak compression is assembled as a uniform-density sphere with a radius R_f and density ρ_m.[1,2] The reaction rate is given by $\mathrm{d}n/\mathrm{d}t = n_D n_T \langle \sigma v \rangle$, where $\langle \sigma v \rangle$ is the average reactivity, n_D and n_T are the density of deuterium and tritium, respectively, and n is the number density of the reacted fuel. Assuming a 50/50 DT mixture, $n_D = n_T = n_0/2 - n$, where n_0 is the initial density. To calculate the total number of reactions, we integrate $N = \int_0^{t_d} V(t)(\mathrm{d}n/\mathrm{d}t)dt$ over the burn duration time t_d, where $V(t)$ is the volume of the burning fuel. The burn time is determined by the fuel disassembly rate. Since there is no external force to keep the fuel together after the stagnation, the outer region of the fuel expands, launching a rarefaction wave toward the center. The rarefaction wave propagates at the local sound speed c_s and it takes approximately $t_d = R_f/c_s$ for the whole sphere to decompress and cool down, quenching the fusion reactions. During the decompression, only the high-density portion of the fuel inside the radius $R(t) = R_f - c_s t$ is burning. Since the total number of reactions is proportional to the time integral of the burning fuel volume, we can define an effective confinement time t_c as $\int_0^{t_d} V(t)dt = V_0 t_c$, where $V_0 = 4\pi R_f^3/3$. The integration gives $t_c = t_d/4$. If the number of fused atoms is small, $n \ll n_0$, then the total number of reactions becomes $N = n_0^2 \langle \sigma v \rangle V_0 t_c/4$. The ratio $f = N/N_0$ is commonly referred to as a burn fraction, where $N_0 = n_0 V_0/2$

is the initial number of DT pairs. Substituting N into f gives $f = n_0 R_f \langle \sigma v \rangle / 8 c_s = \rho_m R_f / (8 c_s m_{DT} / \langle \sigma v \rangle)$, where m_{DT} is the DT ion mass. The combination $8 c_s m_{DT} / \langle \sigma v \rangle$ has a minimum value of 6 g/cm^2 at the ignition conditions; to have an efficient burn, the fuel must reach $\rho_m R_f > 1$ g/cm^2 at peak compression (more accurate calculations show that $f = 0.3$ at $\rho_m R_f = 3$ g/cm^2). Using such an estimate, we can determine the maximum density of the assembled fuel and convergence ratio of the shell at ignition. Assuming that a fraction f_H of the laser energy E_L goes into the shell kinetic energy $M v_{imp}^2 / 2$, the shell mass M can be expressed as $M = 2 f_H E_L / v_{imp}^2$. The fraction f_H is a product of the hydrodynamic efficiency (defined as a ratio of the shell kinetic energy to the absorbed laser energy, typically ~10% for a direct-drive implosion) and the laser absorption fraction of ~0.6. This yields $f_H \sim 0.06$. The fuel mass at stagnation can be rewritten as $M = 4\pi (\rho_m R_f)^3 / 3\rho^2$. Equating the two expressions for the mass, we obtain the fuel density at the peak compression

$$\rho_m = v_{imp} \sqrt{\frac{2\pi (\rho_m R_f)^3}{3 f_H E_L}}. \tag{1}$$

The value of $\rho_m R_f \simeq 2$ g/cm^2 is fixed by the fuel burnup fraction. The implosion velocity cannot be much less than 3×10^7 cm/s to have a temperature increase inside the hot spot during the shell deceleration (energy gain exceeds the energy losses at such a velocity). Using these values gives $\rho_m (\text{g/cm}^3) \simeq 160 / \sqrt{E_L (\text{MJ})}$, where the laser energy is measured in megajoules. For an $E_L = 1$ MJ facility, $\rho_m = 160$ g/cm$^3 \simeq 630 \rho_{DT}$, where $\rho_{DT} = 0.25$ g/cm^3 is the density of cryogenic uncompressed DT mixture at $T = 18$ K. To find the shell convergence ratio $C_r = R_0 / R_f$ required to achieve such a high density, we write the mass conservation equation $4\pi \rho_{DT} R_0^3 (1 - f_A) / A_0 = 4\pi \rho_m R_f^3 / 3$, where $A_0 = R_0 / \Delta_0$ is the initial aspect ratio, R_0 and Δ_0 are the inner radius and thickness of the undriven shell, and f_A is the fraction of the shell mass ablated during the implosion. For a typical direct-drive ignition design, $f_A \simeq 0.8$. This leads to

$$C_r \simeq \left(\frac{5}{3} A_0 \frac{\rho_m}{\rho_{DT}} \right)^{1/3}. \tag{2}$$

Taking $A_0 = 4$ and $\rho_m / \rho_{DT} = 630$ gives $C_r = 16$.

So far, we considered only conditions for the high-ρR fuel assembly. To initiate the burn wave inside the main fuel, as mentioned earlier, the hot spot must first reach ignition con-

ditions. Since the reaction rate is proportional to p^2 ($dn/dt \sim n^2 \langle \sigma v \rangle$ and $\langle \sigma v \rangle \sim T^2$ for $T > 6$ keV, this gives $dn/dt \sim p^2$), high pressure must be achieved inside the hot spot. We can estimate the pressure evolution inside the hot spot during the deceleration phase by considering an adiabatic compression of a gas by a spherical piston. The adiabatic condition relates the pressure and density as $p \sim \rho^{5/3}$. Then the mass conservation yields $\rho R^3 = \rho_d R_d^3$ or $\rho \sim R^{-3}$, where ρ_d and R_d are the mass density and radius at the beginning of deceleration. This gives

$$p = p_d \left(\frac{R_d}{R} \right)^5. \tag{3}$$

Strictly speaking, the hot-spot compression cannot be considered as adiabatic during the deceleration phase because of thermal conduction effects. A detailed calculation including thermal conduction losses,[3] however, shows that an R^{-5} law is valid in a more general case (not including α deposition). This can be easily explained if we consider pressure as an internal energy density. The thermal conduction deposits part of the hot-spot energy into heating the inner layer of the surrounding cold shell. The heated layer then ablates and the ablated mass returns the lost energy back into the hot spot. With the help of Eq. (3), we can calculate the shell trajectory during the deceleration using Newton's law;

$$M \frac{d^2 R}{dt^2} = 4\pi p R^2. \tag{4}$$

Integrating the latter equation gives

$$v^2 = v_{imp}^2 + \frac{4\pi p_d R_d^3}{M} (1 - C_{rd}^2), \tag{5}$$

where $C_{rd} = R_d / R$. At stagnation, $v = 0$ and Eq. (5) yields the total convergence ratio

$$C_{rd} \sim \sqrt{1 + \frac{E_k}{E_i}}, \tag{6}$$

where $E_k = M v_{imp}^2 / 2$ and

$$E_i = \frac{4\pi}{3} \frac{p_d}{(\gamma - 1)} R_d^3 = 2\pi p_d R_d^3$$

is the shell kinetic energy and the total internal energy of the gas at the beginning of the deceleration phase, respectively, and γ is the ratio of specific heats [we used $\gamma = 5/3$ in Eq. (6)]. The relation (6) is satisfied only approximately since it does not take into account the pressure increase due to α deposition. Such an effect is important, however, only near stagnation. Using the limit $E_k \gg E_i$, the maximum pressure takes the form

$$p_m = \frac{1}{p_d^{3/2}}\left(\frac{E_k}{3V_d}\right)^{5/2}, \qquad (7)$$

where $V_d = 4\pi R_d^3/3$. Equation (7) shows that to achieve the hot-spot ignition (high pressure) we must minimize, for a given kinetic energy, the gas pressure and radius R_d at the beginning of shell deceleration (when the reflected shock starts interacting with the shell). The next section will explain how such a minimization is achieved in a direct-drive ignition target.

Direct-Drive Ignition Target Design

High density and convergence ratio requirements put a limitation on the maximum entropy increase in the shell during an implosion. Let us assume that the pressure increases from its initial value p_0 inside the shell to the ablation pressure p_a at the maximum laser intensity. The density ρ is at its maximum when the shell entropy increase is zero ($\Delta s = 0$) during the compression (adiabatic implosion); $\rho/\rho_0 = \left(p_a/p_0\right)^{1/\gamma} e^{-\Delta s/c_p}$, where c_p is the specific heat at constant pressure and ρ_0 is the initial density. It is not feasible, however, to drive a perfectly adiabatic implosion. Shock waves, radiation preheat, hot-electron preheat, and others increase the entropy during the shell compression. We can minimize the hydrodynamic part in the entropy change, nevertheless, by accurately timing all hydrodynamic waves launched into the target during the laser drive. The shell entropy is commonly characterized by the adiabat $\alpha = p/p_F$, which is defined as the ratio of the shell pressure p to the Fermi-degenerate pressure (mainly because of electrons) p_F calculated at the shell density. The Fermi pressure of an electron gas has the form $p_F = \mu\rho^{5/3}$, where $\mu = (3\pi^2)^{2/3}\hbar^2 Z^{5/3}/5m_i^{5/3}m$, m and m_i are electron and ion masses, respectively, $\hbar$ is the Planck constant, and Z is the ion charge. For fully ionized DT, $\mu = 2.15\left[\text{Mbar}/\left(\text{g}/\text{cm}^3\right)^{5/3}\right]$. Since the shell entropy during an implosion is a crucial parameter, the target design in ICF is characterized by the adiabat value. For example, an "$\alpha = 3$ design" means that the pressure inside the shell during the implosion in such a design is three times larger than the Fermi-degenerate pressure of the fully ionized DT.

Next we consider the simplest direct-drive target design, which consists of a spherical DT-ice shell filled with DT gas. The main fuel in the shell is kept at cryogenic temperatures (~18 K) to maximize the fuel mass and minimize the shell entropy. The initial shell thickness is Δ_0 and the inner shell radius is $R_0 \gg \Delta_0$. The target is driven by a laser pulse that consists of three distinct regions: a low-intensity foot, a transition region, and the main drive [see Fig. 106.23(a)]. The main parameters of the laser pulse are the foot length t_0, end of the rise time t_r, end of the pulse t_{end}, foot power P_0, and maximum power P_{max}. During the foot, a shock wave (SW1) launched at the beginning of the pulse propagates through the shell. The adiabat of the post-shock material depends on the shock strength, which, in turn, is a function of the laser intensity. Thus, the foot power P_0 is chosen to set the post-shock material on a desired adiabat α. Analytical models[1,4] predict that the drive pressure and the laser intensity I are related as $p(\text{Mbar}) = 40\left(I_{15}/\lambda_L\right)^{2/3}$, where I_{15} is measured in 10^{15} W/cm^2 and λ_L is the laser wavelength measured in
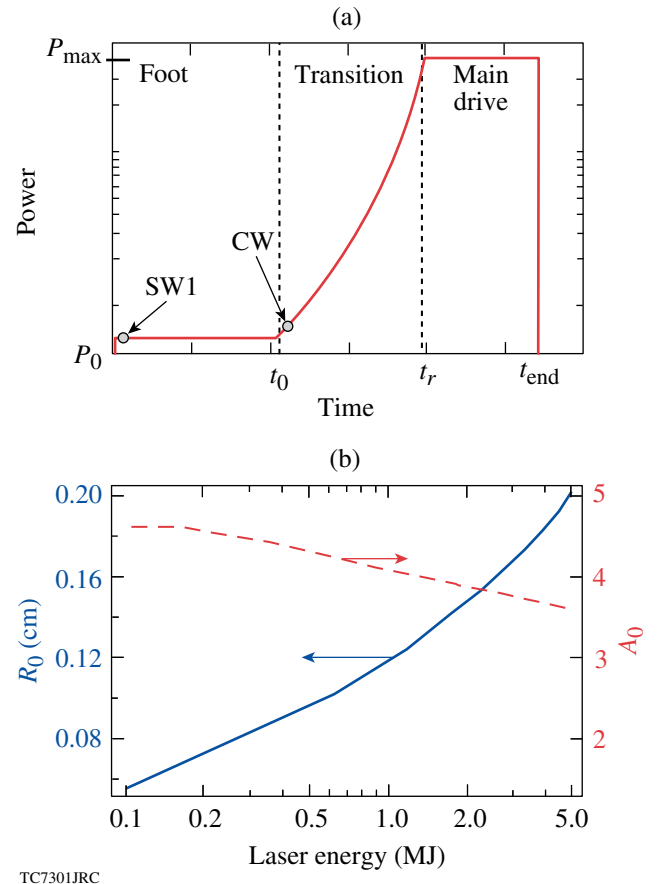

Figure 106.23
(a) Laser drive pulse for a direct-drive target. (b) The dimensions of direct-drive ignition targets versus laser energy ($v_{\text{imp}} = 4.5 \times 10^7$ cm/s).

microns. Substituting $p = \alpha\mu\rho_1^{5/3}$ into the latter equation shows that the laser intensity scales with α in a DT shell driven by a $\lambda_L = 0.351$ μm laser as $I_{12} = 4\alpha^{3/2}$, where the intensity is measured in TW/cm^2 and the post-shock density is $\rho_1 \simeq 4\rho_{DT} = 1$ g/cm^3 in the strong-shock limit. The 3/2 power law does not take into account an intensity dependence in the laser absorption. When the latter is included (with the help of numerical simulations), the required laser intensity becomes $I_{12} = 7\alpha^{5/4}$. Using this result, we obtain a relation between the foot power and the shell adiabat; $p_0(TW) = 90\,R_0^2\left(1 + 1/A_0\right)^2\alpha^{5/4}$. Next, as the laser intensity increases during the transition time, a compression wave (CW) is launched into the shell. To prevent an adiabat increase, such a wave should not turn into a strong shock inside the shell. This determines the intensity slope in the transition region. To maintain an adiabatic compression during the rise time, one can use Kidder's solution[5] for the drive pressure. This gives the power history during the transition time

$$P = \frac{\hat{P}}{\left[1 - \left(t/T_c\right)^2\right]^\omega}, \tag{8}$$

where T_c and $\hat{P}$ are normalization coefficients determined from matching P with P_0 at $t = t_0$ and $P = P_{max}$ at $t = t_r$. Numerical simulations show that moderate variations in ω ($2 < \omega < 7$) do not significantly affect the shell adiabat. Since there are limitations on the maximum power imposed by both instabilities because of the laser–plasma interaction and damage threshold issues, the laser power cannot follow Eq. (8) at all times. Thus, we assume that the laser power becomes flat after time t_r when P reaches the peak power P_{max} [see Fig. 106.23(a)].

Next, we consider what determines the values of t_0 and t_r. The CW, as any linear sound wave in hydrodynamics, travels with the local sound speed and eventually catches up with the SW1. After coalescence, both the shock strength and the adiabat of the post-shock material increase. Minimizing the shell adiabat, we must prevent the CW and SW1 coalescence inside the shell. This sets the minimum value of t_0. Conversely, if t_0 is too large, the SW1 and CW will be well separated in time. As the SW1 breaks out at the shell's rear surface, the surface starts to expand, launching a rarefaction wave (RW) toward the ablation front. The RW establishes some velocity, pressure, and density gradients in its tail. Since the CW and RW travel in opposite directions, they meet inside the shell. At this instant, the CW starts to propagate along the hydrodynamic gradients established by the RW. It is well known in hydrodynamics that a sound wave traveling along a decreasing density turns into a shock sooner than a sound wave traveling through a uniform or increasing density. As the CW turns into a shock,

the latter will excessively increase the shell entropy, reducing the shell convergence ratio. The foot duration t_0 can be related to the shell adiabat α and the initial shell thickness Δ_0. Using Hugoniot jump conditions across the shock, one can easily obtain the shock velocity; neglecting spherical convergence effects, $U_s(p_1 \gg p_0) = \sqrt{(\gamma + 1)p_1/2\rho_0}$, where p_0 and p_1 are the initial and post-shock pressure, respectively. The SW1 transit time through the shell becomes $t_{sh} = \Delta_0/U_s$. The CW travels through the shock-compressed shell with a thickness $\Delta_c = \Delta_0\rho_0/\rho_1$, where ρ_0 and ρ_1 are the initial and post-shock density, respectively. The CW propagation time is $t_{cw} = \Delta_c/c_1$, where $c_1 = \sqrt{\gamma p_1/\rho_1}$. Thus, the foot length takes the form $t_0 = t_{sh} - t_{cw}$. Using expressions for the shock velocity and the adiabat yields the following equations for t_0 and t_{sh}:

$$t_0(ns) = 0.016\frac{\Delta_0(\mu m)}{\sqrt{\alpha}}$$

and $\tag{9}$

$$t_{sh}(ns) = 0.03\frac{\Delta_0(\mu m)}{\sqrt{\alpha}},$$

where $\gamma = 5/3$. Similar to t_0, the rise time t_r is also determined by avoiding an additional strong-shock formation. The transition region cannot be too short; the CW otherwise turns into a shock. The time t_r also cannot be too large. This is due to the formation of a second shock wave (SW2) inside the shell. It is easy to show that an adjustment wave (AW) is formed as the leading edge of the RW breaks out at the ablation front. Each fluid element inside the RW is accelerated according to $dv/dt = -\partial_x p/\rho$. At the head of the RW, ρ is equal to the shell density compressed by the SW1 and CW. When the leading edge reaches the ablation front, the density suddenly drops, creating a large gradient in the acceleration of fluid elements. This forms a local excess in the pressure that starts to propagate in the form of a compression (adjustment) wave along a decreasing density profile of the RW tail. As mentioned earlier, the AW traveling along a decreasing density turns into a shock inside the shell.[6] Thus the SW2 is formed even for a constant-intensity laser pulse.

The formation of the AW can also be shown by comparing the following density profiles: In the first case, the profile is created by a rarefaction wave traveling across a uniform-density foil. For the second profile, we take a solution of the motion equation for an accelerated foil. The solution for a rarefaction wave profile can be found using a self-similar analysis.[7] Calculated at the breakout time of the leading edge, the density becomes

$$\rho = \rho_{a1}\left(\frac{\bar{x} + d_1}{d_1}\right)^3, \tag{10}$$

where $\bar{x}$ is the position in the frame of reference moving with the ablation front ($\bar{x} = 0$ at the ablation front), $\gamma = 5/3$, and d_1 is defined as $\rho(-d_1) = 0$. Conversely, during the shell acceleration, the density profile can be found by solving Newton's equation

$$\rho g = \frac{\partial p}{\partial x}. \tag{11}$$

Assuming that the entropy is uniform across the entire shell, the pressure is related to the density as $p = \mu\alpha\rho^{5/3}$, and the solution of Eq. (11) takes the form

$$p = p_a\left(1 + \frac{\bar{x}}{d_2}\right)^{5/2}, \tag{12}$$

where $d_2 = 5\mu^{3/5}\alpha^{3/5}p_a^{2/5}/2g$. Then, the adiabatic relation $\rho = (p/\mu\alpha)^{3/5}$ gives

$$\rho = \rho_{a2}\left(\frac{\bar{x} + d_2}{d_2}\right)^{3/2}. \tag{13}$$

The comparison of Eqs. (10) and (13), keeping the same mass for the two profiles, gives the relation between the shell thicknesses

$$d_2 = \frac{5}{8}\left(\frac{p_{a1}}{p_{a2}}\right)^{3/5} d_1. \tag{14}$$

Since $p_{a1} \leq p_{a2}$ (the shell is accelerated during the main pulse where the intensity reaches the maximum value), we conclude that the shell during the acceleration should be more compact than that produced by a rarefaction wave; $d_2 < d_1$. This is possible only if a compression wave is launched into the shell at the beginning of the acceleration.

Even though the SW2 cannot be avoided, its strength and effect on target performance can be minimized by appropriately choosing t_r. An intensity rise prior to the leading edge of the RW breakout at the ablation front helps to steepen the density profile, reducing the AW strength. If t_r is too large and the SW2 formation occurs during the drive-pressure rise, the SW2 will be too strong, raising the pressure in the vapor. Thus, t_r must be between the SW1 breakout at the rear surface and the leading edge of the RW breakout at the ablation front (in other

words, the laser must reach the peak power while the leading edge of RW is inside the shell). This concludes the pulse-shape specification for a simple direct-drive ignition design.

Next, we determine the optimum target radius R_0 and shell thickness Δ_0 for a given laser energy. The following effects must be considered: After the SW1 breaks out at the back of the shell, a transmitted shock is formed in the vapor. This shock reaches the center, reflects, and eventually interacts with the incoming shell. During the reflected-shock propagation through the shell, the shell decelerates (deceleration phase of an implosion). If R_0 is too large, the laser is turned off well before the beginning of the deceleration phase. The shell then coasts inward between the end of the drive pulse and beginning of deceleration. Both the front and back surfaces of the shell expand, in the frame of reference moving with the main fuel, during the coasting phase, reducing the shell density. To maximize the density, the duration of the coasting phase must be minimized. This sets an upper limit on R_0. In the opposite case, when R_0 is too small, the reflected shock interacts with the shell while the laser pulse is still on. The pressure inside the shell in this case increases above the drive-pressure value and the shell acceleration therefore goes to zero, preventing an effective transfer of the laser absorbed energy into the kinetic energy of the shell. Thus, the end of the pulse in an optimized design should occur after the main shock reflection from the target center, but before the beginning of the deceleration phase.

Accounting for the optimization arguments listed earlier, we plot the shell radius and initial aspect ratio $A_0 = R_0/\Delta_0$ versus the incident laser energy in Fig. 106.23(b), keeping the maximum laser intensity at $I_{max} = 10^{15}$ W/cm^2 and the implosion velocity at $v_{imp} = 4.5 \times 10^7$ cm/s. Calculations show that the target dimensions do not have a strong dependence on the shell adiabat. The shell radius is fitted well with a 1/3-power law $R_0 = 0.06\left[E_L(\text{MJ})/0.1\right]^{1/3}$. The shell thickness, on the other hand, has a stronger energy dependence; $\Delta_0 = 0.012\left[E_L(\text{MJ})/0.1\right]^{1/2.6}$. A deviation from the $E_L^{1/3}$ scaling in Δ_0 (which is expected from a simple $E_L \sim D^3$ argument, where D is a scale length of the problem) is due to a scale-length dependence in the laser absorption (the smaller the target, the steeper the density scale length, and, therefore, the smaller absorption fraction). This results in an increased initial aspect ratio for the lower laser energies, as shown in Fig. 106.23(b).

Using the obtained target dimensions and laser pulse shapes, the gain curves and the maximum shell ρR can be calculated with a one-dimensional hydrocode. These are shown in Fig. 106.24. Figure 106.24(a) indicates that the designs with the
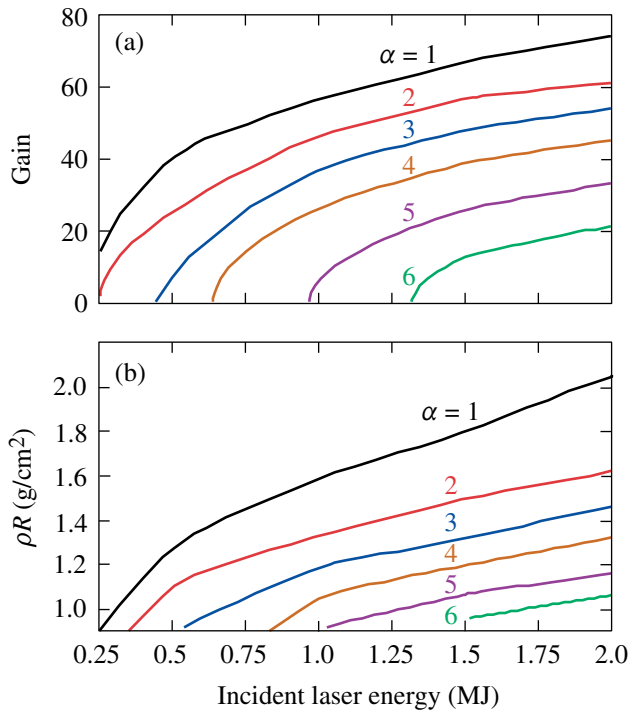
Figure 106.24
(a) Gain curves and (b) maximum ρR for ignition direct-drive targets.

shell adiabat up to $\alpha = 6$ are expected to ignite on the National Ignition Facility with the incident laser energy $E_L = 1.5$ MJ.

Stability

Hydrodynamic instabilities put severe constraints on target designs because they limit the maximum convergence ratio and temperature of the hot spot.[1,8] The dominant hydrodynamic instability in an ICF implosion is the Rayleigh–Taylor (RT) instability. The RT instability inevitably occurs in systems where the heavier fluid is accelerated by the lighter fluid.[9] Such conditions arise during the shell compression in ICF implosions where the heavier shell material is accelerated by the lighter blowoff plasma. The RT instability growth amplifies the shell distortions seeded by initial surface roughness and laser non-uniformities (laser "imprint"). If allowed to grow to substantial amplitudes, the shell nonuniformities reduce the shell ρR and the neutron yield. Fortunately for ICF implosions, the thermal conduction that drives the ablation process creates several stabilizing effects that reduce both the nonuniformity seeding and the RT growth rates.[10,11] Seeding due to the laser nonuni-formity is determined by how quickly the plasma atmosphere is created around the imploding shell. The laser irradiation is absorbed at some distance from the cold shell. The larger this distance (the conduction zone), the larger the smoothing effect

of the thermal conductivity within the conduction zone and the smaller the laser imprint. The RT modes are also stabilized by the thermal conductivity that drives the mass ablation of the shell material. The ablation process is characterized by the ablation velocity V_a, which is defined as the ratio of the mass ablation rate to the shell density $V_a = \dot{m}/\rho_{\mathrm{sh}}$. The larger the value of the ablation velocity, the larger the ablative stabiliza-tion. Taking thermal smoothing and ablative stabilization into account, one can make a general statement that the higher the initial intensity of the drive laser pulse (larger P_0), the smaller the nonuniformities and the more stable the implosion. Indeed, the higher intensity tends to create the conduction zone in a shorter time, reducing the laser imprint. In addition, the ini-tial shock launched by the higher-intensity pulse is stronger, resulting in higher shell adiabat. This reduces the shell density, increasing the ablation velocity. Furthermore, a lower density leads to an increase in the shell thickness and a reduction in the perturbation feedthrough from the ablation front to the shell's rear surface (which becomes unstable during the deceleration phase of the implosion). There is a price to pay, however, for the greater stability. As the stronger shock propagates through the shell, it places the shell material on a higher adiabat. This leads to a reduction in target gain and shell ρR, as shown in Fig. 106.24. A common practice in designing direct-drive tar-gets is to find the delicate balance between a reduction in the target performance due to an increase in the adiabat and the increase in shell stability.

In optimizing the target design, one can take into consid-eration that the RT modes are surface modes peaked at the ablation surface of the shell. To reduce the instability growth, it is therefore sufficient to raise the adiabat only at the outer region of the shell, which ablates during the implosion. If the inner portion of the shell is kept on a lower adiabat, the shell and vapor compressibility will not be reduced during the final stage of implosion and the neutron yields will be unaffected by this selective adiabat increase (adiabat shaping). The shell adiabat is shaped by launching a shock, whose strength decreases as it propagates through the shell.[12] This places an adiabat gradient directed toward the ablation front. A time variation in the shock strength is imposed by replacing the foot with an intensity picket in front of the main-drive pulse. The picket launches a strong shock that propagates through the shell. As the laser intensity drops at the end of the picket, the shocked material starts to expand and a rarefaction wave is launched toward the shock. After the rarefaction and the shock coalesce, the shock strength decays, reducing the adiabat of the shock-compressed material. Implementing the adiabat shaping to the direct-drive ignition target designs shows a significant improvement in shell

stability without compromising the target gain. This is illustrated in Fig. 106.25, where two target designs with (a) a foot and (b) an intensity picket in front of the main drive are shown at the end of the acceleration phase. The isodensity contours are obtained using the two-dimensional hydrocode *ORCHID*.[13] An improvement in the shell stability increases our confidence in the success of the direct-drive ignition campaign on NIF.
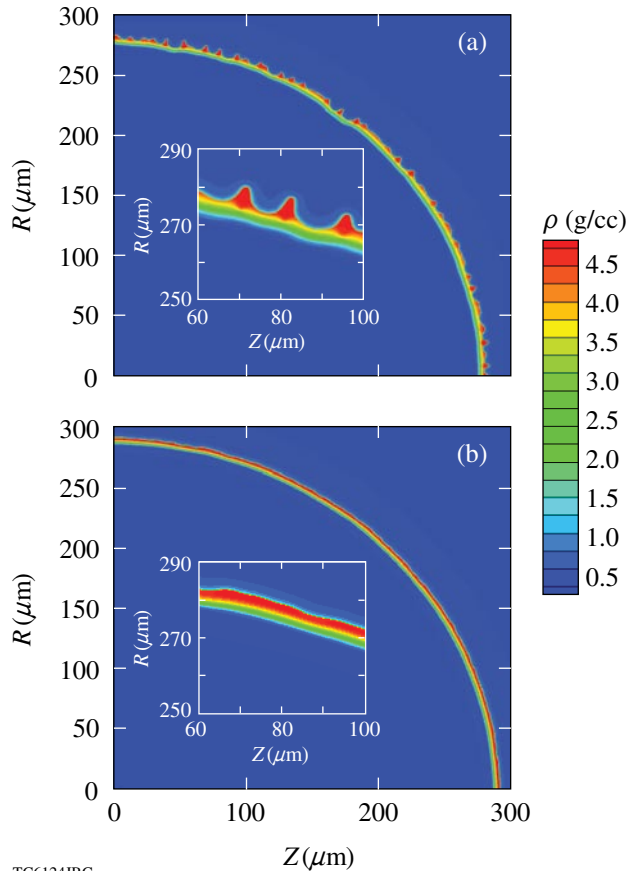
Figure 106.25
Isodensity contours of the (a) standard and (b) picket OMEGA $\alpha = 3$ target designs.

REFERENCES

1. J. D. Lindl, *Inertial Confinement Fusion: The Quest for Ignition and Energy Gain Using Indirect Drive* (Springer-Verlag, New York, 1998).

2. M. D. Rosen, Phys. Plasmas **6**, 1690 (1999).

3. R. Betti, K. Anderson, V. N. Goncharov, R. L. McCrory, D. D. Meyerhofer, S. Skupsky, and R. P. J. Town, Phys. Plasmas **9**, 2277 (2002).

4. W. M. Manheimer, D. G. Colombant, and J. H. Gardner, Phys. Fluids **25**, 1644 (1982).

5. R. E. Kidder, Nucl. Fusion **14**, 53 (1974).

6. R. Betti, V. Lobatchev, and R. L. McCrory, Phys. Rev. Lett. **81**, 5560 (1998).

7. L. D. Landau and E. M. Lifshitz, *Fluid Mechanics*, 2nd ed., Course of Theoretical Physics, Vol. 6 (Butterworth-Heinemann, Newton, MA, 1987).

8. S. Atzeni and J. Meyer-ter-Vehn, *The Physics of Inertial Fusion: Beam Plasma Interaction, Hydrodynamics, Hot Dense Matter*, International Series of Monographs on Physics (Clarendon Press, Oxford, 2004).

9. S. Chandrasekhar, in *Hydrodynamic and Hydromagnetic Stability*, International Series of Monographs on Physics (Clarendon Press, Oxford, 1961).

10. J. Sanz, Phys. Rev. Lett. **73**, 2700 (1994).

11. V. N. Goncharov, R. Betti, R. L. McCrory, P. Sorotokin, and C. P. Verdon, Phys. Plasmas **3**, 1402 (1996).

12. V. N. Goncharov, J. P. Knauer, P. W. McKenty, P. B. Radha, T. C. Sangster, S. Skupsky, R. Betti, R. L. McCrory, and D. D. Meyerhofer, Phys. Plasmas **10**, 1906 (2003).

13. R. L. McCrory and C. P. Verdon, in *Computer Applications in Plasma Science and Engineering*, edited by A. T. Drobot (Springer-Verlag, New York, 1991).

Tests of the Hydrodynamic Equivalence of Direct-Drive Implosions with Different D_2 and ^{3}He Mixtures

Introduction

Ignition and high gain in inertial confinement fusion (ICF)[1–3] requires an understanding of how the choice of materials affects implosion dynamics. ICF ignition targets are typically spherical capsules with an outer shell made of plastic or beryllium, a cryogenic layer of deuterium–tritium (DT) ice, and gaseous DT at the center. The direct-drive approach to ICF[4] implodes the target by direct illumination using multiple laser beams. Laser ablation of the capsule's outer surface drives the remaining payload inward, compressing and heating it to a state where nuclear fusion can occur.

Surrogate materials or configurations provide a convenient test bed to study different aspects of ignition designs.[5,6] These surrogates are chosen to best mimic the implosion characteristics of the original design. For example, although ignition designs use an equal mole DT mixture, pure D_2 is commonly used as a surrogate. The different mass densities, however, can cause a difference in implosion dynamics (in particular through the Atwood number, which differs by a factor of 2 at the fuel–shell interface during the deceleration phase[7]).

To explore the effects of fill composition on the implosion dynamics of surrogate fuels, a series of experiments using different ratios of D_2 and ^{3}He was performed. Evaluation of surrogate materials is best done when the materials are chosen to be as nearly hydrodynamically equivalent as possible. D and ^{3}He have a special property in which they have the same value of $(1 + Z)/A$, allowing mixtures of D_2 and ^{3}He to be chosen such that the mass density and the total particle density upon full ionization are identical. This results in the same Atwood number (affecting hydrodynamic instabilities[2,7]) and the same equation of state (EOS).

An additional advantage of these surrogate targets is that products from the D-D nuclear reaction can be measured for all mixtures, whereas measuring the D-D products from a DT implosion has proven difficult for ignition-relevant implosions because of the large background of D-T neutrons. A final advantage of D_2 and ^{3}He mixtures is their emission of D-^{3}He protons

that have been extensively used to diagnose ICF implosions on OMEGA.[8–10] **Experimental Setup** (p. 90) is a description of the setup and diagnostics used in the experiments. **Expected Scaling** (p. 92) describes the yield scaling expected of hydrodynamically equivalent implosions. **Experimental Observations** (p. 93) describes the results observed in the experiments as well as comparisons to the expected scaling and 1-D radiation-hydrodynamic simulations. The **Discussion** (p. 97) details possible explanations, and a **Summary** is given on p. 99.

Experimental Setup

Direct-drive implosions were conducted on OMEGA,[11] with 60 beams of frequency-tripled (351-nm) UV light in a 1-ns square pulse and a total energy of 23 kJ. SG4 phase plates[12] and 2-D, 1-THz bandwidth smoothing by spectral dispersion of the laser beam were used;[13] the beam-to-beam energy imbalance was typically between 2% and 4% rms. The spherical targets were CH-shell capsules with diameters between 860 μm and 880 μm; a wall thickness of 15, 20, 24, or 27 μm; and a flash coating of about 0.1-μm aluminum.

The gaseous fill of the capsules was composed of mixtures of D_2 and ^{3}He such that the atomic composition varied from pure D to nearly pure ^{3}He. Two classes of fill pressure were used, low (equivalent to 3-atm D_2) and high (equivalent to 15-atm D_2), with predicted convergence ratios of 37 and 14, respectively. The mixtures within each class are considered hydrodynamically equivalent in that they have the same mass density (and therefore the same Atwood number during the deceleration phase) and, upon full ionization (above a few electron volts), the same total particle density and EOS (ideal monatomic).

Capsule fills are hydrodynamically equivalent if the fill pressures of D_2 (X atm) and ^{3}He (W atm) are chosen to obey

$$X = \frac{3}{4}W = X_0, \tag{1}$$

where X_0 is the hydrodynamically equivalent pure-D_2 fill pressure, which is equal to either 3 atm or 15 atm in this article. The deuterium ion fraction by atom f_D scales with X and X_0 as
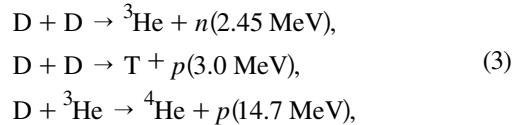
$$f_D = \frac{3X}{X + 2X_0}. \qquad (2)$$

Since there are only two components to the fill gas, $f_{^3He} = 1 - f_D$.

Two standard gas mixtures were used to fill targets of all types: pure D_2 ($f_D = 1.0$) and a D_2-^{3}He mixture with a 1:1 atomic ratio ($f_D = 0.5$). A series of shots with different mixtures of D_2 and ^{3}He was undertaken for the 20- and 24-μm-thick, high-pressure capsules. In addition to the premixed $f_D = 1.0$ and 0.5 compositions, compositions with $f_D = 0.07$, 0.27, and 0.78 were used.[14]

The error in the fill composition for the "standard" ($f_D = 0.5$) D_2-^{3}He mixture is about 1% of f_D, since it comes premixed. Fill composition errors for the other composition ratios, which must be mixed to order, are also small—less than 3% (Ref. 15) of f_D. This error estimate includes uncertainties in the original fill pressure as well as uncertainties in the leak rates of D_2 and ^{3}He through the storage cell and through the target shell as it is handled before shot time. The total fill pressure is known to better than 10% and is independent of the fill composition.[15]

The following primary nuclear reactions occur in implosions of targets filled with mixtures of D_2 and ^{3}He:

$$D + D \rightarrow {}^3He + n(2.45~\text{MeV}),$$
$$D + D \rightarrow T + p(3.0~\text{MeV}), \qquad (3)$$
$$D + {}^3He \rightarrow {}^4He + p(14.7~\text{MeV}),$$

where the number in parentheses is the mean birth energy of the second product. Figure 106.26 shows the temperature depen-
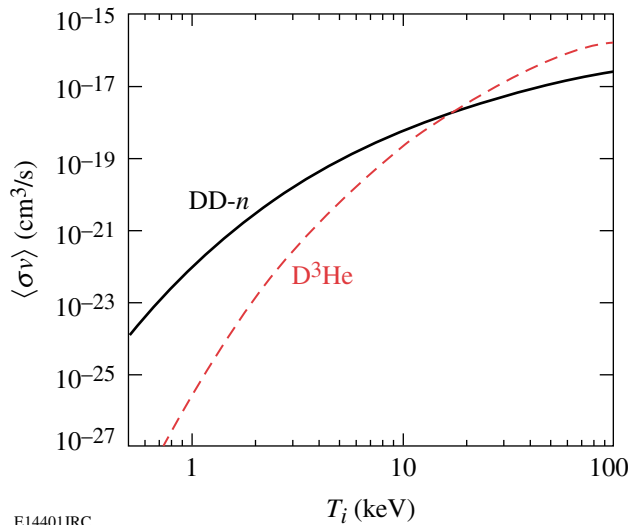
E14401JRC

Figure 106.26
DD-n and D^{3}He thermal reactivities as a function of ion temperature.

dence of the thermal reactivities of the D-^{3}He reaction and the n branch of the D-D reaction, as determined by Bosch and Hale.[16] The branching probability of the n and p branches of the D-D reaction are nearly equal over the temperatures of interest.

The principle diagnostics for this work were neutron time-of-flight (nTOF) scintillators[17] to measure the neutron branch of the D-D reaction and multiple wedged-range-filter (WRF) proton spectrometers[8] to measure the protons from the D-^{3}He reaction. The nTOF detectors measure neutron yield and DD burn-averaged ion temperature determined from the Doppler broadening of the neutron signal.

The WRF spectrometers measure the D^{3}He proton spectrum with high resolution (~100 keV). Transient magnetic fields[18] in the implosion corona can redistribute the initially isotropic proton flux emitted by the capsule by 20% rms (typical).[8] The average of the multiple (2 to 7) spectrometers is used to obtain an estimate of the total yield. The mean downshift of the D^{3}He protons from their birth energy of 14.7 MeV is used to infer the areal density (ρR) of the imploded capsule averaged over the D^{3}He proton production.[8]

An alternative measurement of the burn-averaged ion temperature is given by the "ratio method."[19] The ratio of primary yields can be used to infer the ion temperature using the thermal reactivities (Fig. 106.26) and the fuel composition. The ratio of DD-n to D^{3}He reactivities changes by more than three decades from 1 keV to 10 keV, giving a determination of temperature that is not highly sensitive to the exact yields. Differences in burn duration or burn volume of the two constituent reactions result in only minor corrections to the inferred temperature (for example, see the very similar burn histories for DD-n and D^{3}He compression in Fig. 106.27). This correction is small mainly because both reactions are dominated by the high-temperature region near the center.

Temporal diagnostics of the nuclear products include the neutron temporal diagnostic (NTD)[20] for measuring the DD-n burn history and the proton temporal diagnostic (PTD) for measuring the D^{3}He burn history.[21,9] The D^{3}He burn history typically exhibits two periods of proton emission:[22] The first is the "shock burn," which occurs after the first convergence of the shock, near the end of the coasting phase, and before the capsule has fully compressed. About 300 ps later is the "compression burn" (see Fig. 106.27), which occurs during the deceleration and stagnation phases. Spectral measurements of the emitted D^{3}He protons from such capsules can often be decomposed into such "shock" and "compression" components because of the different areal densities they pass through while escaping the capsule (~10 mg/cm^2
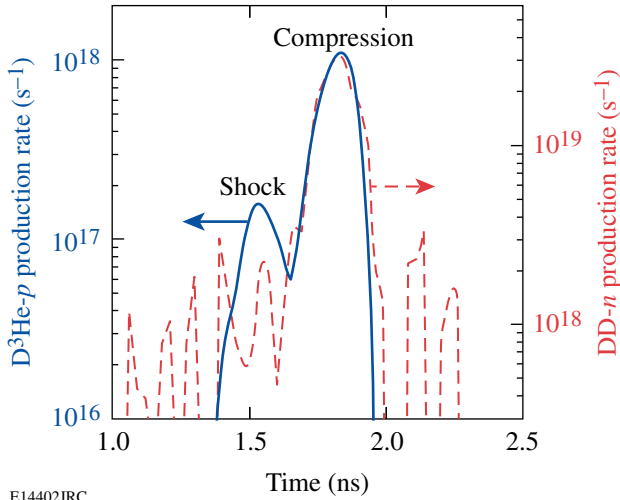
E14402JRC

Figure 106.27

Measured D-^{3}He proton (solid) and DD-n (dashed) nuclear production histories of a 24-μm-thick CH shell filled with 6 atm of D_2 and 12 atm of ^{3}He (shot 38525). Distinct shock and compression components are seen in the D-^{3}He production history, whereas there is no evidence of neutrons at shock time in the DD-n production history. The noise level in the burn histories is about 10^{18}/s for DD-n and less than 10^{16}/s for D^{3}He.

at shock and ~60 mg/cm^2 during compression). Because of the much weaker temperature dependence of the DD-n reactivity, the contribution of the high-temperature, low-density shock burn phase to the total yield is much lower than for D^{3}He (typically 0.5% to 1% rather than 5% to 20%).

One-dimensional radiation-hydrodynamic simulations of these implosions were done using the code $LILAC^{23}$ with a flux limiter of 0.06. Composition scaling simulations were run by changing the initial fill composition while using the same target and laser conditions. To obtain yields of both reactions using compositions of $f_D = 0.0$ and 1.0, the results of those simulations were post-processed as having a trace of the minority species.

Expected Scaling

The nuclear yield is the spatial and temporal integral of the product of reactant densities times the temperature-dependent thermal reactivity of the nuclear reaction under consideration;

$$Y_n = \int \frac{1}{2} n_D^2(\vec{r},t) \langle \sigma v \rangle_{DD-n} d^3\vec{r} dt,$$

$$Y_p = \int n_D(\vec{r},t) n_{^3He}(\vec{r},t) \langle \sigma v \rangle_{D^3He} d^3\vec{r} dt,$$

(4)

where Y_n and Y_p are the D-D neutron and D-^{3}He proton yields, n_D and $n_{^3He}$ are the number densities of D and ^{3}He, and $\langle \sigma v \rangle$

is the local thermal reactivity averaged over a Maxwellian ion velocity distribution with temperature T_i. The particle densities and ion temperature will, in general, be functions of position and time. The factor of 0.5 in the DD-n yield accounts for the double-counting of identical reactants.

For the hydrodynamically equivalent mixtures of D_2 and ^{3}He considered here and using the relation $n_i = \rho/Am_p = \rho/(3-f_D)m_p$, the yields can be re-expressed in terms of f_D;

$$Y_n = \frac{f_D^2}{(3-f_D)^2} \int \frac{\rho^2(\vec{r},t)}{2m_p^2} \langle \sigma v \rangle_{DD-n} d^3\vec{r} dt,$$

(5)

$$Y_p = \frac{f_D(1-f_D)}{(3-f_D)^2} \int \frac{\rho^2(\vec{r},t)}{m_p^2} \langle \sigma v \rangle_{D^3He} d^3\vec{r} dt,$$

where m_p is the proton mass and ρ is the mass density. The factor $(3-f_D)^2$ is equal to A^2 and adjusts for the slightly different ion number densities of D_2 and ^{3}He plasmas at equal mass density. The advantage of this form is that the dependence on the fill composition that determines the difference between hydrodynamically equivalent targets is taken out of the integral.

Figure 106.28 shows the predicted scaling of the D-D neutron and D-^{3}He proton yields as a function of fill composition for hydrodynamically equivalent fuels. Although the character of the composition scaling is very different for the different nuclear
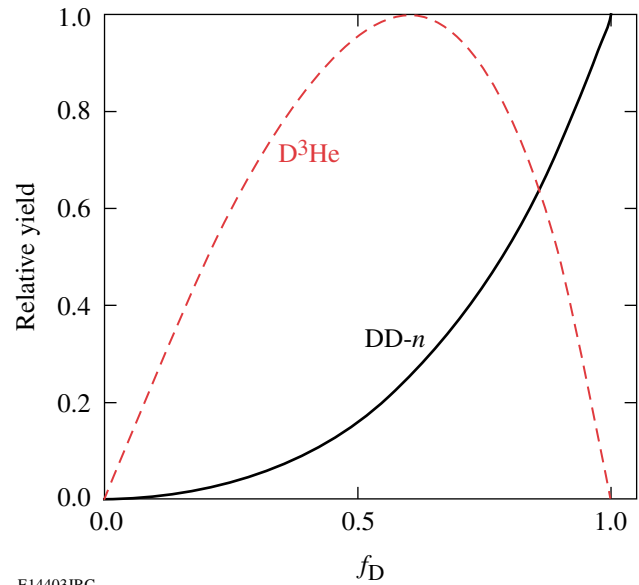

E14403JRC

Figure 106.28

Yield dependence of the DD-n and D^{3}He reactions on the D fraction by atom (f_D).

reactions, both curves are independent of the implosion dynamics, so the composition contribution to the yield can be factored out.

All subsequent yields in this article will be scaled according to Eq. (6) unless otherwise noted;

$$\tilde{Y}_n = Y_n \frac{(3 - f_D)^2}{f_D^2},$$

$$\tilde{Y}_p = Y_p \frac{(3 - f_D)^2}{f_D(1 - f_D)},$$

(6)

where $\tilde{Y}_n$ and $\tilde{Y}_p$ denote the scaled DD-n and D^{3}He yields, respectively.

Experimental Observations

The hydrodynamic equivalence of D$_2$ and ^{3}He mixtures is most clearly demonstrated by measurements of implosion timing. The time of peak neutron emission (DD-n bang time) as well as the duration of the neutron emission (characterized by the full width at half maximum as measured by the NTD) are independent of f_D. In addition, the time of peak proton emission during the compression phase (D^{3}He compression bang time) and the duration of proton emission (characterized by the FWHM of the compression peak as measured by PTD) are also independent of f_D. Figure 106.29 plots the bang time and burn duration of both nuclear products as a function of f_D for both 20- and 24-μm-thick CH shells. Bang times and burn durations of the two nuclear products are also in good agreement with each other, an example of which can be seen fully in Fig. 106.27.

The measured yield of these hydrodynamically equivalent implosions deviates from the anticipated scaling shown in Fig. 106.28. The deviation of the scaled DD-n and D^{3}He compression yields ($\tilde{Y}_n$ and $\tilde{Y}_{p-c}$) for 20- and 24-μm CH shells with high-pressure fills is shown in Fig. 106.30. The yields have been scaled to the fill composition according to Eq. (6) and, in addition, have been normalized to the yield at $f_D = 0.5$ to emphasize the composition scaling for different measurements. Yields from targets with D-rich and ^{3}He-rich fuels are typically twice as high as yields from targets with $f_D = 0.5$. This trend is seen for both DD-n and D^{3}He yields and for both 20- and 24-μm shells.[24]

This observed deviation is not seen in 1-D simulations (dashed line in Fig. 106.30), which instead more nearly follows the hydrodynamically equivalent scaling with only minor deviations. Table 106.VIII shows the absolute yields of the normalization points at $f_D = 0.5$ as observed experimentally
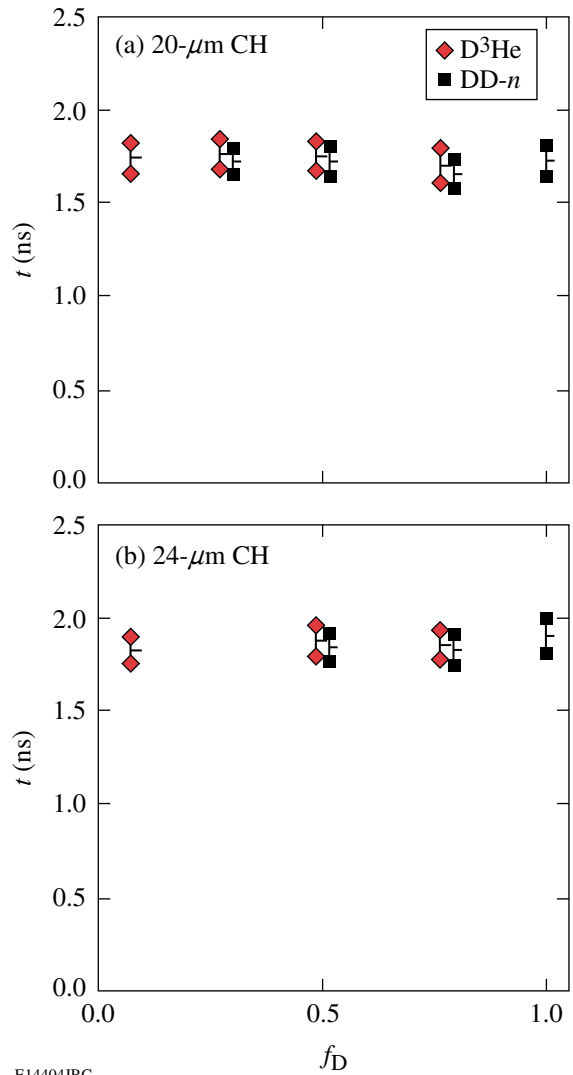
Figure 106.29

Nuclear bang time and burn duration as a function of fill composition for implosions with (a) 20 μm and (b) 24 μm of CH. Open diamonds and solid squares are the times of the half maximum of the peak emission of the D-^{3}He protons and DD-neutrons, respectively.

and as calculated by *LILAC* as well as the absolute DD-n yield at $f_D = 1.0$. The DD-n experimental yield over calculated yield (YOC) is 21% for $f_D = 0.5$ and 42% or 48% for $f_D = 1.0$.

A comparison of the YOC for DD-n and D^{3}He on shots with $f_D = 0.5$ illustrates the utility of simultaneous measurement of two nuclear reactions. As shown in Table 106.VIII, the D^{3}He compression YOC is about 35% compared to the DD-n YOC of 21%. The difference in the YOC's for the two nuclear reactions is due to their probing the deviation between the simulated and actual implosion in different ways as a result of their different temperature sensitivies.

Table 106.VIII: Absolute (unscaled) compression yields of DD-n for $f_D = 1.0$ and 0.5 shots and D^{3}He for $f_D = 0.5$ shots as observed experimentally and as calculated by *LILAC*. The experimental yield over calculated yield (YOC) is also shown.

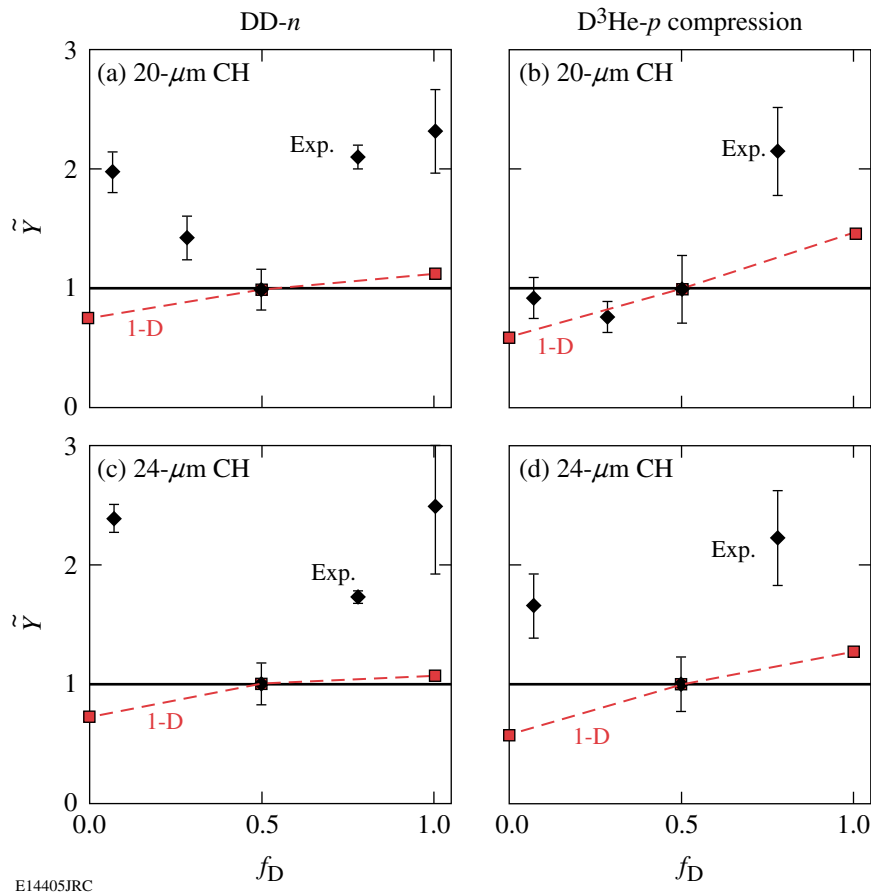| Shell	Type	$f_D = 1.0$	$f_D = 0.5$	
		Y_n ($\times 10^{10}$)	Y_n ($\times 10^{10}$)	Y_{p-c} ($\times 10^8$)
20-μm CH	Observed	18.7	1.29	6.28
20-μm CH	Calculated	44.6	6.29	18.4
20-μm CH	YOC	42.0%	20.5%	34.1%
24-μm CH	Observed	9.0	0.58	1.46
24-μm CH	Calculated	18.7	2.80	4.22
24-μm CH	YOC	48.1%	20.7%	34.6%

E14405JRC

Figure 106.30

Scaled DD-n and D^{3}He compression yields for high-pressure ($X_0 = 15$ atm) fills of shells with 20 and 24 μm of CH. (a) $\tilde{Y}_n$, 20 μm; (b) $\tilde{Y}_{p-c}$, 20 μm; (c) $\tilde{Y}_n$, 24 μm; (d) $\tilde{Y}_{p-c}$, 24 μm. All yields have been scaled to fill composition according to Eq. (6) and normalized to the yields at $f_D = 0.5$. True hydrodynamically equivalent implosions would scale to the same yield (solid line). 1-D simulations with *LILAC* (open squares, dashed line) deviate slightly from hydrodynamic equivalence but not nearly as much as experimental measurements (solid diamonds). The diamonds are the average yield and standard deviation from similar capsules. The 20-μm plots show data reduced from a total of 42 shots, and the 24-μm plots show data reduced from a total of 24 shots.

The "factor of 2" deviation of the yield scaling seen in these 20- and 24-μm CH shell, high-pressure composition campaigns has also been seen over a diverse set of target configurations. Targets with 15-, 20-, 24-, and 27-μm-thick CH shells and with both high and low fill pressures were filled with the two standard compositions; f_D = 1.0 and 0.5. Implosions of targets with both composition types emit DD-neutrons, and therefore a comparison of $\tilde{Y}_n$ for like implosions with different compositions was done. Figure 106.31 shows the ratio of scaled yields $\tilde{Y}_n(f_D = 1.0)/\tilde{Y}_n(f_D = 0.5)$ for these implosions. The points at 15 atm and at 20 and 24 μm are the same as the points at f_D = 1.0 in Figs. 106.30(a) and 106.30(c). Data reduced from 118 shots predominantly gives a ratio greater than two where a ratio of 1 is anticipated for all capsule types.

The observed ion temperatures are not sufficient to explain the observed yield deviation. The mean ion temperature was measured using two methods: nTOF Doppler broadening and the yield ratio method. The nTOF does not show a trend in the ion temperature, whereas the ion temperature from the ratio method suggests increasing temperatures for higher D content fuels (see Fig. 106.32). Post-processing of 1-D *LILAC* simulations gives burn-averaged temperatures that are not strongly dependent on fill composition. Areal density measurements
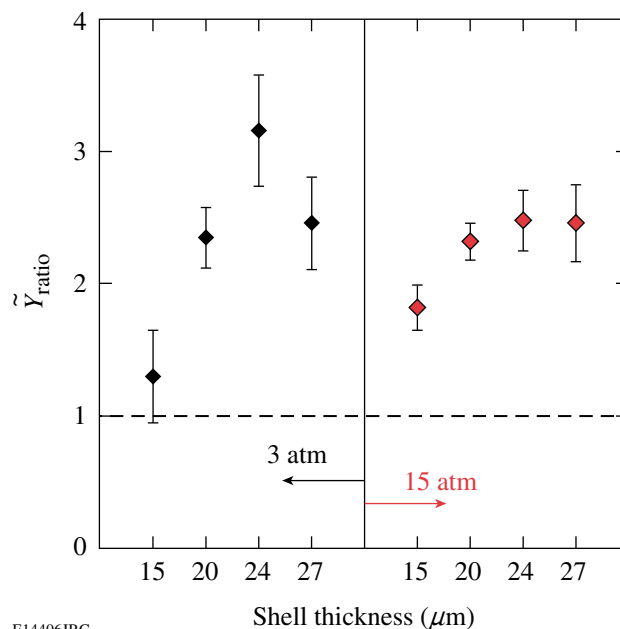
E14406JRC

Figure 106.31
The ratio of measured $\tilde{Y}_n$ for f_D = 1.0 shots over $\tilde{Y}_n$ for f_D = 0.5 shots. The ratio anticipated by the scaling in Fig. 106.28 is 1 (horizontal dashed line) for all target parameters. The points are the ratio of scaled average yields, and the errors are the quadrature sum of the standard deviations of the mean of the two fill compositions. The plot shows data reduced from 118 shots.
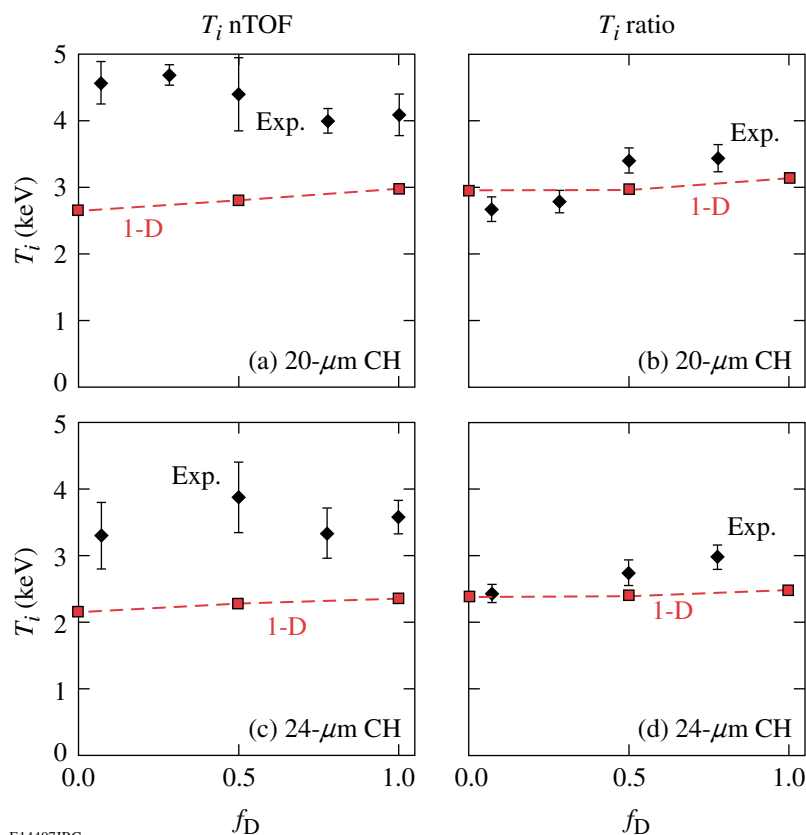
E14407JRC

Figure 106.32
Ion temperature as a function of fill composition, as determined by the nTOF for high-pressure fills of (a) 20-μm and (c) 24-μm shells and using the ratio method for (b) 20 μm and (d) 24 μm. The diamonds are the average and standard deviation of experimental observations. The squares and dashed lines are 1-D *LILAC*.

using the downshift of primary D³He protons (D-³He fuels) or secondary D³He protons (pure D_2 fuel) show a lower value at compression time for $f_D = 0.5$ (for 24-μm shells, Fig. 106.33), suggesting slightly less compression for those shots.

A similar deviation from the anticipated scaling is also seen for the D³He shock yield $\left(\tilde{Y}_{p-s}\right)$, which is emitted about 300 ps earlier than the compression yield and is produced under very different conditions before the start of the deceleration phase and the onset of turbulent mixing[22] at temperatures twice as high as

that at compression time and at mass densities less than 10% of those at compression time. Figure 106.34 shows the scaled D³He shock yield and the shock-yield-averaged ρR for implosions with 24-μm CH shells. The results at shock time are reminiscent of the results at compression time with a lower scaled yield and ρR for the $f_D = 0.5$ shots than for D-rich or ³He-rich mixtures.

A summary of results from figures in this section is listed in Table 106.IX for different mixtures of high-pressure fills in shells with 20 and 24 μm of CH.
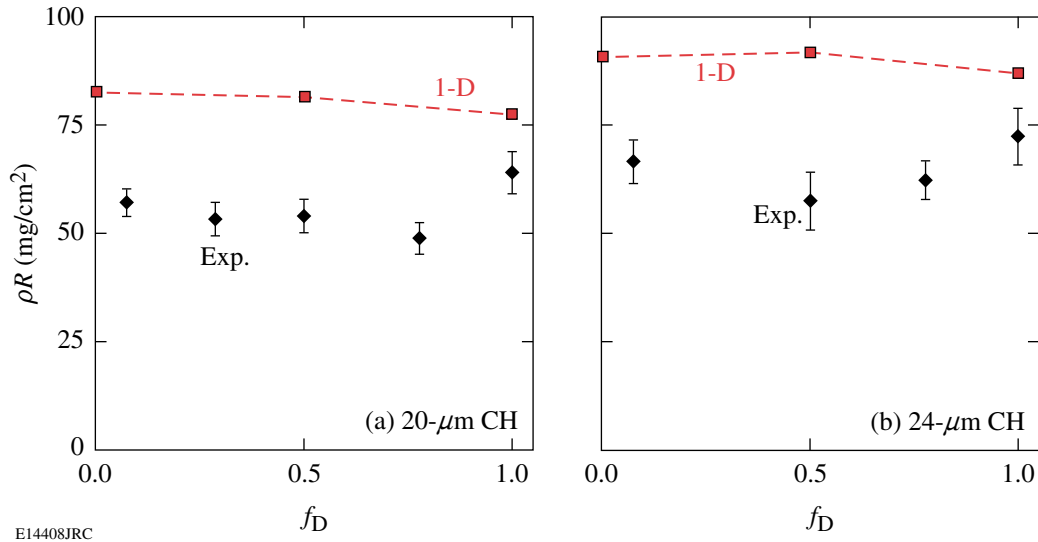

E14408JRC

Figure 106.33
Inferred compression burn averaged ρR as a function of fill composition for high-pressure fills of (a) 20-μm-thick and (b) 24-μm-thick shells. The diamonds are the average and standard deviation of experimental observations. The squares and dotted lines are 1-D *LILAC*. For each plot, the higher ρR corresponds to more compression since all targets started with the same shell thickness.
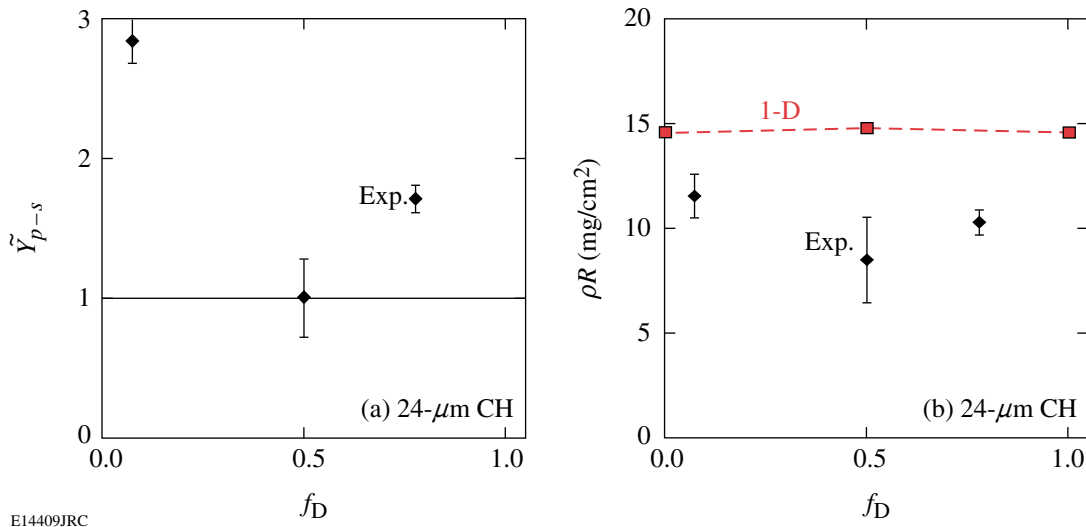

E14409JRC

Figure 106.34
D³He shock results for 24-μm CH capsules. (a) Scaled shock yield and (b) shock-yield-averaged ρR as a function of fill composition. The solid line is hydrodynamically equivalent scaling. The squares and dotted line are 1-D *LILAC*. Diamonds are the average and standard error of experimental observations.

Table 106.IX: D fraction by atom, number of shots averaged, DD-n, D^{3}He compression and shock yields (scaled by fill composition and normalized to $f_D = 0.5$), ion temperature, areal density, and DD bang time for high-pressure fills for two different shell thicknesses.

Shell	f_D	Number of shots	$\lvert \tilde{Y}_n \rvert$	$\lvert \tilde{Y}_{p-c} \rvert$	$\lvert \tilde{Y}_{p-s} \rvert$	T_i nTOF (keV)	T_i ratio (keV)	ρR (mg/cm^2)	t_{bang} (ns)
CH[20]	1.00	22	2.32	–	–	4.1	–	64	1.73
CH[20]	0.78	5	2.10	2.15	0.77	4.0	3.4	49	1.65
CH[20]	0.50	8	1.00	1.00	1.00	4.4	3.4	54	1.72
CH[20]	0.28	4	1.43	0.77	0.85	4.7	2.8	53	1.73
CH[20]	0.07	3	1.98	0.93	1.23	4.6	2.7	57	–
CH[24]	1.00	10	2.48	–	–	3.6	–	72	1.91
CH[24]	0.78	2	1.73	2.22	1.71	3.3	3.0	62	1.83
CH[24]	0.50	9	1.00	1.00	1.00	3.9	2.7	58	1.87
CH[24]	0.07	3	2.38	1.65	2.84	3.3	2.4	64	–

Discussion

A closer look at the possibility of a measurement error is certainly warranted when observations deviate so far from the scaling derived from simple principles as well as from computer simulations. The individual measurement error on a given shot is about 10% for both DD-n and D^{3}He yields; however, the shot-to-shot yield variation for nominally identical shots is closer to 20% rms. Averaging the results from many like shots reduces the standard deviation of the mean considerably, in most cases below 10%. Systematic yield uncertainties in the diagnostics are unlikely to cause the yield scaling. The yield measurements for the two nuclear reactions use different diagnostics, using different principles, yet measured the same deviation.

The deviation in the yield scaling from Eq. (4) must then be explained through the differences in composition, temperature, density, burn volume, or burn duration of the target during the implosion. According to temporal measurements of nuclear burn histories, the implosion timing does not depend on the fill composition. Uncertainty in the composition is at most a couple of percent, which is not enough to affect the yields by a factor of 2. In addition, composition errors affect the DD-n and D^{3}He yield scaling in different ways (Fig. 106.28), yet the same deviation is seen for both.

The observed trend of the ratio-inferred ion temperature could be part of the story because of the strong dependence of the thermal reactivities of both reactions at the temperatures of interest. The DD-n and D^{3}He reactivities scale approximately as T_i^4 and T_i^7 near $T_i = 3$ keV. A linear fit through the observed ratio-inferred T_i in Fig. 106.32(d) was used to adjust

the hydrodynamically equivalent $\tilde{Y}_n$ scaling. The solid curve in Fig. 106.35(a) plots this T_i ratio yield scaling against the observed yields from Fig. 106.30(c). This corrected scaling looks better for D-rich fuels but deviates further than the uncorrected hydrodynamically equivalent scaling from the observed yields for ^{3}He-rich fuels. Since there was no clear trend in the nTOF-derived temperatures, a similar yield scaling fit was not done using the nTOF temperatures.

The two remaining factors of fuel density and burn volume are related to the compression of the capsule, which can be inferred by measurements of ρR. A simple model of the implosion that assumes that the shell temperature and shell aspect ratio at bang time does not depend on fill composition determines that the yield scales approximately as $(\rho R)^3$. The open circles in Fig. 106.35(b) plot this ρR yield scaling against the observed yields from Fig. 106.30(c). Higher ρR's were observed for high and low D concentrations compared to the 50/50 mixture. The shape predicted from the $(\rho R)^3$ scaling is in qualitative agreement with the measurements, though it does not show quite as strong a scaling.

Although additional measurements suggest that some combination of ion temperature and density might be sufficient to explain the observed yield deviation, these factors must come from some physical mechanism, a number of which will be explored below.

The deviation from the assumed hydrodynamic equivalence is unlikely to be explained by 2-D or 3-D hydrodynamic effects, including hydrodynamic instabilities and turbulent mixing that
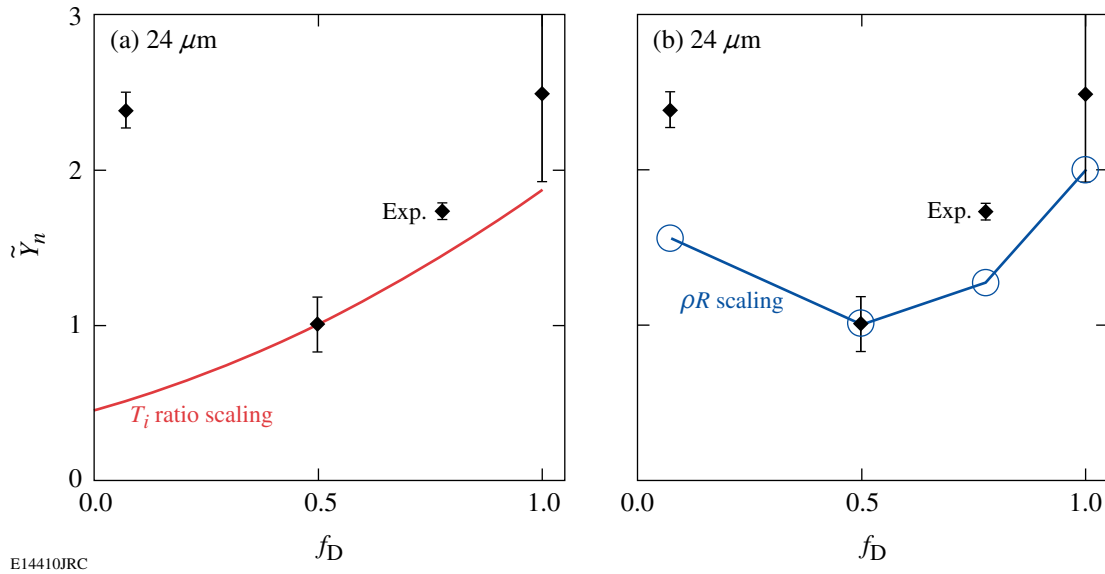
E14410JRC

Figure 106.35
Measured (solid diamonds) DD-n yields as a function of f_D for 24-μm shells with high pressure from Fig. 106.30(c). In these plots, the hydrodynamically equivalent scaling has been adjusted to take into account the effects of measured ion temperature and areal density on the yield. (a) The solid line is a T_i-corrected scaling curve, based on a linear fit to the experimental T_i ratios in Fig. 106.32(d). (b) The open circles and connecting line include a ρR correction based on the measured ρR values shown in Fig. 106.33(b).

would reduce the burn volume and truncate the burn duration. A similar trend was experimentally observed over a wide range of physical situations in which 2-D hydrodynamic effects would likely have behaved very differently. Implosions with thicker shells are considered to be more hydrodynamically stable,[25] yet the same yield trend is seen for 20- and 24-μm shells with a high fill pressure. Implosions with a low fill pressure are considered less hydrodynamically stable, yet the yield trend is the same as for the high fill pressure (Fig. 106.31). A similar trend is also seen for D^{3}He shock burn measurements, despite the fact that it has been shown that there is no atomic-level mixing in the burn region at shock time.[22] Thus, pure hydrodynamics cannot explain the observed differences.

A wealth of data seems to exclude pure hydrodynamic differences between these mixtures as the mechanism for the observed variation in their yields (as it should be since they were chosen to be hydrodynamically equivalent). The deviation from hydrodynamic equivalence is likely to be due to the microscopic details of the mixture. It may have something to do with the variation in the average Z in the fuel, which varies from 1 (pure D$_2$) to nearly 2 (^{3}He rich), the difference in ion masses or a subtlety in the statistical treatment of mixtures.

Bremsstrahlung radiation scales as $\sim \rho^2 T_e^{1/2} Z^3 / A^2$, which for these mixtures differs by a factor of 3.6 from pure D$_2$ (low)

to pure ^{3}He, assuming the same density and temperature. A factor of 3 difference in the radiated power may then trigger differences in the absorption in the CH and initiate changes in the implosion dynamics. However, the yield discrepancy trend is about the same for cases with significantly different radiative properties, such as for low-pressure and high-pressure fills as well as at both shock and compression time. The difference in density in these scenarios radically affects the efficiency of bremsstrahlung radiation. In addition, the yield deviation is not monotonic with the D fraction, so bremsstrahlung radiation seems unlikely as the sole mechanism.

Thermal conduction in these dynamic implosions can be difficult to calculate because of nonequilibrium conditions and other nonlocal effects. To get a sense of the scaling, however, consider the Spitzer–Harm electron thermal conduction[26]

$$q_{SH} = -K \nabla T,$$

$$K \propto \delta(Z) \frac{T_e^{5/2}}{Z m_e^{1/2} \ln \Lambda},$$

$$\delta(Z) = \frac{Z + 0.24}{Z + 0.42}. \qquad (7)$$

Ignoring the Coulomb logarithm variation, pure D_2 has a 32% higher classical conductivity than pure ^{3}He and is 17% higher than the standard D_2-^{3}He mixture (using "average" ions). Ion thermal conduction has a similar form, but with a much stronger Z dependence.[27] Ion conduction is relatively small when the ion and electron temperatures are equal but can become important when the ion temperature is higher, such as for shock heating. But for both types of thermal conduction, the trend is again monotonic with a D fraction.

Shock heating initially puts most energy into heating the ions, with more energy going to heavier ions.[28] Equal-density mixtures of D_2 and ^{3}He will absorb the same total amount of energy from a shock front, but mixtures with a higher concentration of ^{3}He will have a higher initial ion temperature due to the higher average ion mass (and corresponding lower ion density). A slight difference in this initial state of the gas might, after compression, be enough to change the dynamics and the resulting nuclear yields. The compression condition will be quite a bit different for the different implosion types (high and low pressure, thin and thick shells), yet the same deviation is seen in many cases. It is also difficult to explain the nonmonotonic trend with this picture.

It is possible that there is stratification of the ion species during the deceleration phase. The scaled performance of the "pure" fuels seems to be greatest, so perhaps the mixture of different species is important. During the deceleration phase, the ^{3}He concentration might be slightly enhanced near the center. The hot center will then have a lower nuclear yield due to scarcer D ions. In this picture, though, the ^{3}He-rich fuels should also have a reduced yield, so the nonmonotonic trend is again a problem.

The plausibility of stratification can be considered using simple arguments. Because of the high density during the compression phase, any concentration enhancement will have to come through a difference in diffusion of the D and ^{3}He ions. With plasma parameters typical of the fill early in the compression burn (4 keV, 3 g/cc), it is found that the time it takes even one particle to diffuse across the capsule is very much longer than the implosion time.

Kinetic effects could play an important role in the observed yield scaling. A non-Maxwellian velocity distribution could significantly alter nuclear production, particularly at the time of shock collapse, where the distribution is far from Maxwellian. It has also been suggested that yield degradation could result from the loss of ions in the tail of the distribution, which normally dominate the nuclear production. The longer mean free paths of the ions in the tail may allow them to escape the fuel region if the $\rho R < 10$ mg/cm^2 (Ref. 29). It is not sufficient, though, that kinetic effects only change the nuclear production; a kinetic effect must change the nuclear production nonmonotonically with the D fraction and by a factor of 2 between pure and mixed D and ^{3}He.

Many processes used to explain the observed yield scaling have been considered here but no single mechanism is sufficient to explain the trend.

Summary

In summary, experimental observations of the scaling of nuclear yields from implosions with hydrodynamically equivalent mixtures of D_2 and ^{3}He deviate from the scaling determined using a simple consideration of composition ratios as well as from a scaling based on 1-D radiation-hydrodynamic simulations. This deviation is particularly puzzling since the trend is not monotonic with the D fraction; the scaled D^{3}He yield is lower than the scaled yields on both the D_2-rich and ^{3}He-rich sides.

The same scaling deviation is observed in diverse physical situations, including implosions of targets with initial fill pressures of 3 and 15 atm and target shell thicknesses of 15, 20, 24, and 27 μm of CH. A similar yield scaling deviation is observed for both DD-n and D^{3}He yields despite the drastically different dependence of their yields on composition and temperature. Overall, a similar scaling deviation is seen for both the shock and compression components of the D^{3}He yield, corresponding to times separated by several hundred picoseconds and reflecting very different plasma conditions.

It has been shown that measurements of the burn-averaged ion temperature, using two different methods, are insufficient to explain the entire yield scaling deviation. Errors in the initial fill composition of the D_2 and ^{3}He mixtures and differences in the implosion timing have also been excluded. Measurements of the burn-averaged areal density ρR suggest that D_2 and ^{3}He mixtures with a f_D near 0.5 might experience less compression, resulting in a lower yield.

A number of possible mechanisms that may cause the scaling are considered, but no dominant mechanism has been identified. Differences in the radiative and transport properties of different D_2 and ^{3}He mixtures are included in 1-D simulations, but apparently do not have as great an effect on the yield as what was observed. Hydrodynamic instabilities in 2-D and

3-D appear to be ruled out. The initial gas state set by the converging shock, ion species stratification, and kinetic effects were also considered.

This study raises some concern as to the near equivalence of D_2 as a DT fuel surrogate for studying implosion dynamics. Even when the mass density of the D_2 and ^{3}He mixtures is the same, we see discrepancies in the yield although it is not clear what mechanism causes the discrepancy and whether it is due to a difference in the average Z, ion masses, or transport properties of mixed materials. To explore such issues, further scrutiny of the ion conductivity and its effects on implosion dynamics is underway, which may be an important factor because of its strong Z dependence.

An investigation of the yield scaling at constant Z could be accomplished by using different fuel mixtures, including mixtures of D and T, and an extension of this study with mixtures of D_2, ^{3}He, and either H_2 or ^{4}He. Experiments are being actively planned that would vary the D and T mixture with the intention of simultaneously measuring the absolute yield of both DT and DD,[30] the results of which will have direct relevance for ignition target fills and will take us a step closer to understanding the present conundrum.

REFERENCES

1. J. Nuckolls *et al.*, Nature **239**, 139 (1972).

2. J. D. Lindl, *Inertial Confinement Fusion: The Quest for Ignition and Energy Gain Using Indirect Drive* (Springer-Verlag, New York, 1998).

3. S. Atzeni and J. Meyer-ter-Vehn, *The Physics of Inertial Fusion: Beam Plasma Interaction, Hydrodynamics, Hot Dense Matter*, International Series of Monographs on Physics (Clarendon Press, Oxford, 2004).

4. S. E. Bodner, D. G. Colombant, J. H. Gardner, R. H. Lehmberg, S. P. Obenschain, L. Phillips, A. J. Schmitt, J. D. Sethian, R. L. McCrory, W. Seka, C. P. Verdon, J. P. Knauer, B. B. Afeyan, and H. T. Powell, Phys. Plasmas **5**, 1901 (1998).

5. F. J. Marshall, J. A. Delettrez, V. Yu. Glebov, R. P. J. Town, B. Yaakobi, R. L. Kremens, and M. Cable, Phys. Plasmas **7**, 1006 (2000).

6. R. L. McCrory, R. E. Bahr, R. Betti, T. R. Boehly, T. J. B. Collins, R. S. Craxton, J. A. Delettrez, W. R. Donaldson, R. Epstein, J. Frenje, V. Yu. Glebov, V. N. Goncharov, O. Gotchev, R. Q. Gram, D. R. Harding, D. G. Hicks, P. A. Jaanimagi, R. L. Keck, J. Kelly, J. P. Knauer, C. K. Li, S. J. Loucks, L. D. Lund, F. J. Marshall, P. W. McKenty, D. D. Meyerhofer, S. F. B. Morse, R. D. Petrasso, P. B. Radha, S. P. Regan, S. Roberts, F. Séguin, W. Seka, S. Skupsky, V. Smalyuk, C. Sorce, J. M. Soures, C. Stoeckl, R. P. J. Town, M. D. Wittman, B. Yaakobi, and J. D. Zuegel, Nucl. Fusion **41**, 1413 (2001).

7. S. P. Regan, J. A. Delettrez, V. Yu. Glebov, V. N. Goncharov, J. P. Knauer, J. A. Marozas, F. J. Marshall, R. L. McCrory, P. W. McKenty, D. D. Meyerhofer, P. B. Radha, T. C. Sangster, S. Skupsky, V. A. Smalyuk, C. Stoeckl, J. R. Rygg, J. A. Frenje, C. K. Li, R. D. Petrasso, and F. H. Séguin, Bull. Am. Phys. Soc. **50**, 113 (2005).

8. F. H. Séguin, J. A. Frenje, C. K. Li, D. G. Hicks, S. Kurebayashi, J. R. Rygg, B.-E. Schwartz, R. D. Petrasso, S. Roberts, J. M. Soures, D. D. Meyerhofer, T. C. Sangster, J. P. Knauer, C. Sorce, V. Yu. Glebov, C. Stoeckl, T. W. Phillips, R. J. Leeper, K. Fletcher, and S. Padalino, Rev. Sci. Instrum. **74**, 975 (2003).

9. J. A. Frenje, C. K. Li, F. H. Séguin, J. Deciantis, S. Kurebayashi, J. R. Rygg, R. D. Petrasso, J. Delettrez, V. Yu. Glebov, C. Stoeckl, F. J. Marshall, D. D. Meyerhofer, T. C. Sangster, V. A. Smalyuk, and J. M. Soures, Phys. Plasmas **11**, 2798 (2003).

10. F. H. Séguin, J. L. DeCiantis, J. A. Frenje, S. Kurebayashi, C. K. Li, J. R. Rygg, C. Chen, V. Berube, B. E. Schwartz, R. D. Petrasso, V. A. Smalyuk, F. J. Marshall, J. P. Knauer, J. A. Delettrez, P. W. McKenty, D. D. Meyerhofer, S. Roberts, T. C. Sangster, K. Mikaelian, and H. S. Park, Rev. Sci. Instrum. **75**, 3520 (2004).

11. T. R. Boehly, D. L. Brown, R. S. Craxton, R. L. Keck, J. P. Knauer, J. H. Kelly, T. J. Kessler, S. A. Kumpan, S. J. Loucks, S. A. Letzring, F. J. Marshall, R. L. McCrory, S. F. B. Morse, W. Seka, J. M. Soures, and C. P. Verdon, Opt. Commun. **133**, 495 (1997).

12. F. J. Marshall, J. A. Delettrez, R. Epstein, R. Forties, R. L. Keck, J. H. Kelly, P. W. McKenty, S. P. Regan, and L. J. Waxer, Phys. Plasmas **11**, 251 (2004).

13. S. Skupsky and R. S. Craxton, Phys. Plasmas **6**, 2157 (1999).

14. The $f_D = 0.78$ shots plotted on the 20-μm-CH figures actually had 19-μm-thick shells.

15. M. J. Bonino, Laboratory for Laser Energetics, private communication (2006).

16. H.-S. Bosch and G. M. Hale, Nucl. Fusion **32**, 611 (1992).

17. R. A. Lerche and T. J. Murphy, Rev. Sci. Instrum. **63**, 4880 (1992).

18. Tangential electric fields have not been excluded as the cause for the anisotropic proton emission, but for these implosions there is no radial E field when the protons are emitted.

19. C. K. Li, D. G. Hicks, F. H. Séguin, J. A. Frenje, R. D. Petrasso, J. M. Soures, P. B. Radha, V. Yu. Glebov, C. Stoeckl, D. R. Harding, J. P. Knauer, R. L. Kremens, F. J. Marshall, D. D. Meyerhofer, S. Skupsky, S. Roberts, C. Sorce, T. C. Sangster, T. W. Phillips, M. D. Cable, and R. J. Leeper, Phys. Plasmas **7**, 2578 (2000).

20. R. A. Lerche, D. W. Phillion, and G. L. Tietbohl, Rev. Sci. Instrum. **66**, 933 (1995).

21. C. Stoeckl, V. Yu. Glebov, S. Roberts, T. C. Sangster, R. A. Lerche, R. L. Griffith, and C. Sorce, Rev. Sci. Instrum. **74**, 1713 (2003).

22. R. D. Petrasso, J. A. Frenje, C. K. Li, F. H. Séguin, J. R. Rygg, B. E. Schwartz, S. Kurebayashi, P. B. Radha, C. Stoeckl, J. M. Soures, J. Delettrez, V. Yu. Glebov, D. D. Meyerhofer, and T. C. Sangster, Phys. Rev. Lett. **90**, 095002 (2003).

23. J. Delettrez, R. Epstein, M. C. Richardson, P. A. Jaanimagi, and B. L. Henke, Phys. Rev. A **36**, 3926 (1987).

24. Except for the D^{3}He yield from ^{3}He-rich, 20-μm-thick target implosions.

25. S. P. Regan, J. A. Delettrez, V. N. Goncharov, F. J. Marshall, J. M. Soures, V. A. Smalyuk, P. B. Radha, B. Yaakobi, R. Epstein, V. Yu. Glebov, P. A. Jaanimagi, D. D. Meyerhofer, T. C. Sangster, W. Seka, S. Skupsky, C. Stoeckl, D. A. Haynes, Jr., J. A. Frenje, C. K. Li, R. D. Petrasso, and F. H. Séguin, Phys. Rev. Lett. **92**, 185002 (2004).

26. L. Spitzer, Jr. and R. Härm, Phys. Rev. **89**, 977 (1953).

27. S. I. Braginskii, in *Reviews of Plasma Physics*, edited by Acad. M. A. Leontovich (Consultants Bureau, New York, 1965), Vol. 1, p. 205.

28. Ya. B. Zel'dovich and Yu. P. Raizer, *Physics of Shock Waves and High-Temperature Hydrodynamic Phenomena*, edited by W. D. Hayes and R. F. Probstein (Dover Publications, Mineola, NY, 2002).

29. D. B. Henderson, Phys. Rev. Lett. **33**, 1142 (1974).

30. Only recent technological advances have made the detection of DD neutrons in the background of DT neutrons feasible. See V. Yu. Glebov, D. D. Meyerhofer, T. C. Sangster, C. Stoeckl, S. Roberts, C. A. Barrera, J. R. Celeste, L. S. Dauffy, C. J. Cerjan, D. C. Eder, R. L. Griffith, S. W. Haan, B. A. Hammel, S. P. Hatchett, N. Izumi, J. R. Kimbrough, J. A. Koch, O. L. Landen, R. A. Lerche, B. J. MacGowan, M. J. Moran, E. W. Ng, T. W. Phillips, P. M. Song, R. Tommassini, B. K. F. Young, S. E. Caldwell, G. P. Grim, S. C. Evans, L. Disdier, M. Houry, I. Lantuejoul, G. A. Chandler, G. W. Cooper, R. J. Lepeer, R. E. Olson, C. L. Ruiz, M. A. Sweeney, S. P. Padalino, C. Horsfield, and B. A. Davis, "Development of Nuclear Diagnostics for the National Ignition Facility," to be presented at the 16th Topical Conference on High-Temperature Diagnostics, Williamsburg, VA, 7–11 May 2006.

Deterministically Polarized Fluorescence from Uniaxially Aligned Single-Dye Molecules

Introduction

In single-photon sources (SPS's) based on single-emitter fluorescence, a laser beam is focused into an area containing a low concentration of single emitters so that only one emitter becomes excited. The single emitter produces a single photon at a time.[1–4] There are various known methods for the production of single photons at definite time intervals, which are based on a single atom,[5,6] a single trapped ion,[7] a single molecule,[8–10] a single color center in diamond,[11] or the Coulomb-blockade effect in a micropin junction with quantum well as the active layer.[12–14] Tremendous progress has been made in the realization of SPS's based on excitonic emission from single heterostructured semiconductor quantum dots excited by pulsed laser light (see Refs. 1 and 3). In heterostructured quantum-dot SPS's,[15–28] microcavities have been used for spontaneous emission enhancement in the form of a whispering-gallery-mode resonator (turnstile device), 1-D photonic band gap, 3-D pillar microcavity, and 2-D photonic crystals. A weakness of heterostructured quantum-dot SPS's is that they operate *only at liquid-helium temperatures*. In addition, they are not readily tunable. To date, three approaches have been suggested for *room-temperature* SPS's: single molecules,[8–10,29–37] colloidal semiconductor quantum dots (nanocrystals),[38,39] and color centers in diamond.[11,40–43] The color-center source suffers from the challenge that it is not easy to couple out the photons and that the spectral bandwidth of the light is typically quite large (~120 nm).

Both single molecules and colloidal semiconductor nanocrystals dissolved in a proper solvent can be embedded in photonic crystals to circumvent the deficiencies that plague the other systems. Colloidal semiconductor nanocrystals dissolved in PMMA were placed inside a 2-D photonic crystal cavity.[44] The nanocrystal emission at room temperature mapped out the cavity resonances and was enhanced relative to the bulk emission. A planar cavity was recently used to control the single-dye molecule fluorescence spectra and decay rate.[45] The primary problems with using fluorescent dyes and colloidal semiconductor nanocrystals in cavities are the emitters bleaching and blinking, nontunability of the source, and nondeterministic polarization of photons.

Our solution is based on a new material concept using single-emitter excitation in specially prepared *liquid crystal hosts*, which can exist both as monomers (fluid media) and oligomers or polymers. The advantages of using liquid crystal hosts are that they may be self-assembled in structures with photonic band-gap properties, and, at the same time, such a host can protect the emitters from bleaching. This source is a *room-temperature* alternative to cryogenic SPS's based on semiconductor heterostructures. In addition, the liquid crystal host provides both polarization purity and tunability of the source. Recent advances in liquid crystal technology, especially in the fabrication of electric-field/temperature-controlled 1-D, 2-D, and 3-D photonic crystal structures and the infiltration of photonic crystals with liquid crystals, can be used in SPS preparation with properties that other SPS methods failed to provide.

Recently we reported a first demonstration of dye-fluorescence antibunching in liquid crystal hosts[35–37] that is evidence of the single-photon nature of the source. One-dimensional (Fig. 106.36) and two-dimensional (Fig. 106.37) photonic crystal structures were prepared.[35–37,46] One-dimensional photonic band-gap structures in cholesteric liquid crystals possess an additional advantage over conventional 1-D photonic crystals. Because the refractive index *n* varies gradually rather than abruptly in cholesterics, there are no losses into the waveguide modes, which, in the case of conventional 1-D photonic crystals, arise from total internal reflection at the border between two consecutive layers with a different *n*. These waveguide losses can reach ~20%.

In addition, we observed a significant diminishing of dye bleaching by special preparation of liquid crystals; dye molecules did not bleach for periods of more than one hour under cw excitation.[35–37] (The first impressive experiments on avoiding dye bleaching in the hosts have been reported in Refs. 9 and 30. In Ref. 9, single terrylene-dye molecules in a *p*-terphenyl molecular crystal host did not bleach during several hours of pulsed, several-megahertz, pulse-repetition-rate excitation).

This article highlights another advantage of liquid-crystal hosts—*deterministically polarized* fluorescence from single-
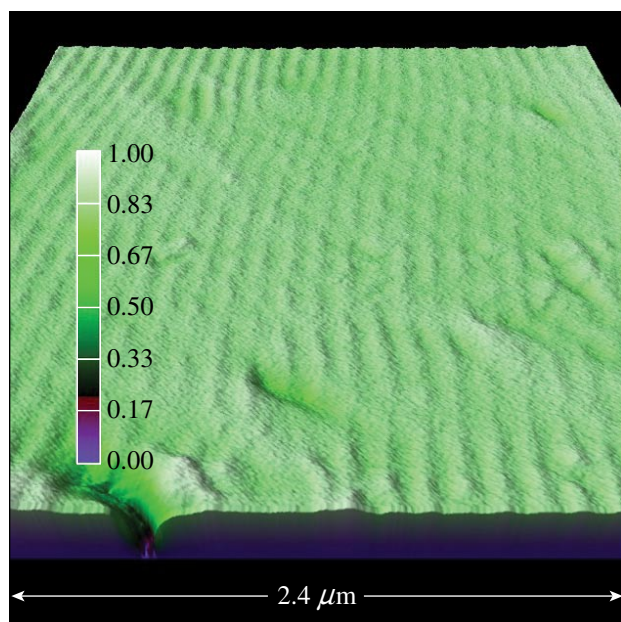
Figure 106.36
Perspective view of the AFM topographical image of a 1-D photonic band gap, planar-aligned, glassy, cholesteric liquid crystal.
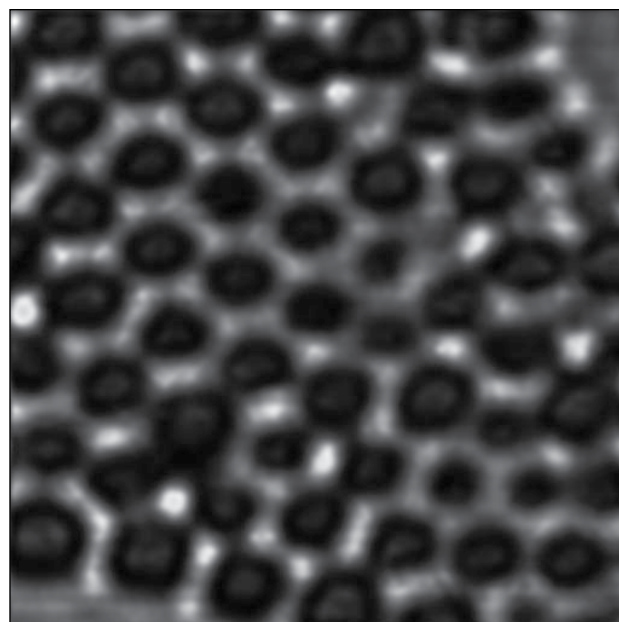
Figure 106.37
Near-field optical image of a 2-D photonic crystal self-assembly of a glassy cholesteric liquid crystal (5-μm × 5-μm scan).

dye molecules.[47–49] Single molecules of DiIC$_{18}$(3) dye were embedded in a planar-aligned, glassy, *nematic* liquid crystal host and were aligned by liquid crystal molecules.

Experimental Setup

Single-molecule fluorescence microscopy was carried out on a Witec alpha-SNOM device in confocal transmission mode. Figure 106.38 shows the schematic of this experiment. The dye-doped liquid crystal sample was placed in the focal plane of a 1.4 numerical aperture, oil-immersion microscope objective. The sample was attached to a piezoelectric, XYZ translation stage. Light emitted by the sample was collected by a confocal setup using a 1.25 numerical aperture, oil-immersion objective with an aperture in the form of an optical

fiber. The cw, spatially filtered (through a single-mode fiber), 532-nm, diode-pumped, Nd:YAG laser output excited single molecules. In focus, the intensities used were of the order of several kW/cm^2.

For polarized fluorescence measurements, we used a 50/50 polarizing beam splitter cube (as opposed to our antibunching correlation measurements,[35–37] in which a nonpolarizing beam splitter was used) with the confocal microscope apertures in the form of a 100-μm-core optical fiber placed in each arm of the beam splitter's output (Fig. 106.38). Residual transmitted excitation light was removed by two consecutive dielectric interference filters, yielding a combined rejection of better than 6 orders of magnitude at 532 nm.
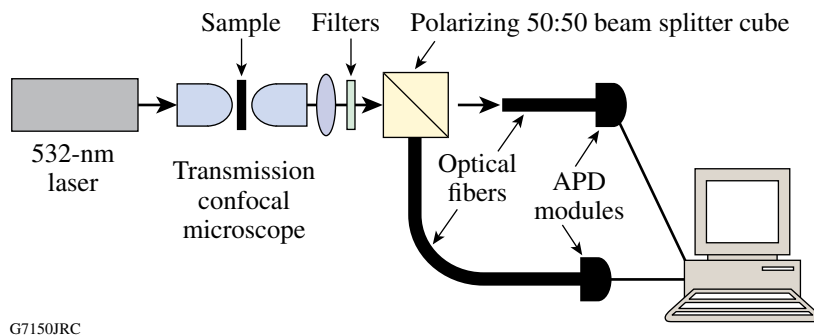
Figure 106.38
Experimental setup.

Photons in the two arms were detected by identical cooled avalanche photodiode modules (APD) in single-photon–counting Geiger mode (Perkin Elmer SPCM AQR-14).

Experimental Results: Deterministically Polarized Single-Molecule Fluorescence

For these experiments, we used $DiIC_{18}(3)$ dye (Fig. 106.39) in planar-aligned, glassy, nematic liquid crystal hosts[50] with a concentration of ~10^{-8} M. The nematic liquid crystal state of this material, which exists at elevated temperatures, is preserved at room temperature by slowly cooling the liquid crystal to the glassy state with frozen nematic order. We prepared ~100-nm-thick films of this glassy, nematic liquid crystal that was doped with dye molecules that were aligned deterministically through photoalignment using Staralign LPP coating and linearly polarized UV light. This new alignment technique prevents material contamination by particulates. We succeeded in the preparation of such an alignment over areas exceeding 10 mm × 10 mm (Refs. 47–49).

Figure 106.40 shows images of single-molecule fluorescence for polarization components (a) perpendicular and (b) parallel to the alignment direction under 532-nm cw excitation. These two components in the sample plane have been separated with a polarizing beam splitter cube (Fig. 106.38). Figure 106.40 clearly shows that for this sample, the polarization direction of the fluorescence of single molecules is predominantly in the direction perpendicular to the alignment of liquid crystal molecules. It is important that the background levels of Figs. 106.40(a) and 106.40(b) are the same (~10 counts/pixel or ~640 counts/s). The single-molecule fluorescence signal at maximum exceeds this background by up to 15 times.

The polarization anisotropy is defined here as $\rho = (I_{par} - I_{perp})/(I_{par} + I_{perp})$, where I_{par} and I_{perp} are fluorescence intensities for polarization components parallel and perpendicular to the alignment direction.[51] Processing the images in Fig. 106.40 shows that from a total of 38 molecules, 31 molecules have a negative ρ value (Fig. 106.41). The same
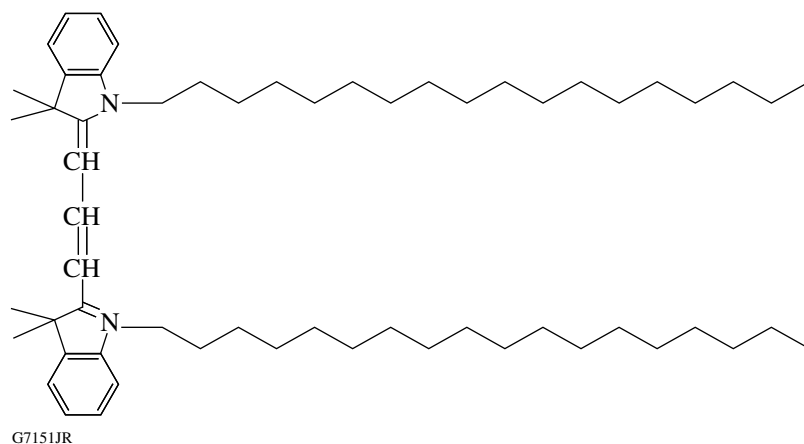

G7151JR

Figure 106.39
Molecular structure of $DiIC_{18}(3)$ dye.
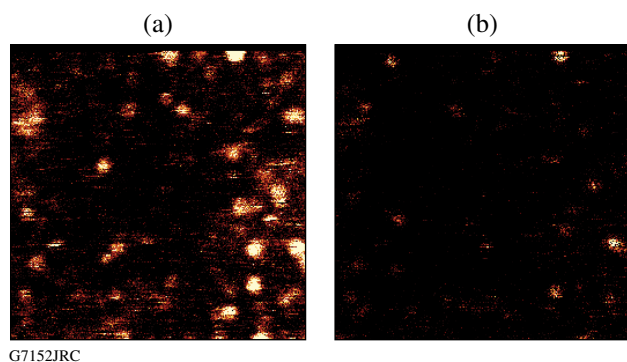
(a)　　　　(b)

G7152JRC

Figure 106.40
Confocal fluorescence microscopy images of $DiIC_{18}(3)$ single-molecule fluorescence in a planar-aligned, glassy, nematic liquid crystal host (10-μm × 10-μm scan): (a) polarization perpendicular to the alignment direction and (b) parallel polarization.
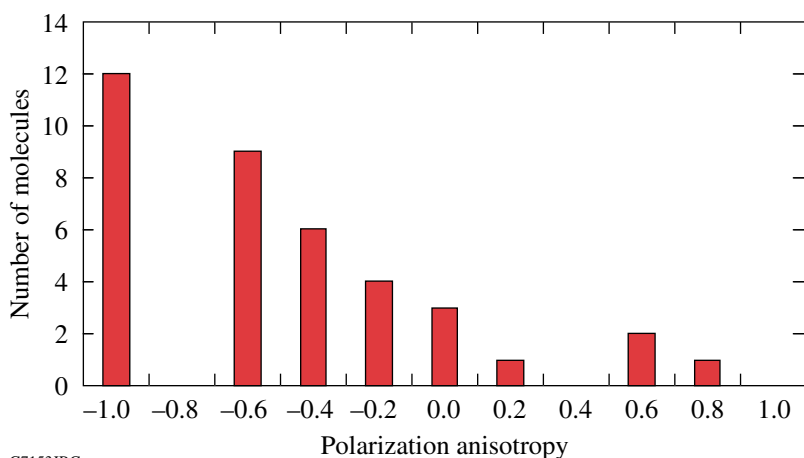
Figure 106.41
A histogram of the polarization anisotropy of 38 molecules of $DiIC_{18}(3)$ dye in a planar-aligned, glassy, nematic liquid crystal host.

sign of the polarization anisotropy was obtained in spectrofluorimeter measurements for a sample with a high (~0.5%) by weight concentration of the same dye in a planar-aligned, glassy, nematic liquid crystal layer that is ~4.1-μm thick [Fig. 106.42(a)]. Figure 106.42(b) shows *circular* polarized fluorescence from a planar-aligned, glassy, *chiral*-nematic (cholesteric) liquid crystal layer that is ~4.1-μm thick and has a 0.5% by weight concentration of $DiIC_{18}(3)$ dye.

This predominance of "perpendicular" polarization in Figs. 106.40, 106.41, and 106.42(a) can be explained by the $DiIC_{18}(3)$'s molecular structure (Fig. 106.39). The two alkyl chains likely orient themselves parallel to the rod-like liquid crystal molecules, but the emitting/absorbing dipoles that are nearly parallel to the bridge (perpendicular to alkyl chains) will be directed perpendicular to the liquid crystal alignment. $DiIC_{18}(3)$ molecules orient in the same manner in cell mem-

branes.[52,53] It should be noted that in Ref. 54, single terrylene dye molecules were uniaxially oriented in rubbed polyethylene; however, this paper did not provide the results on deterministically polarized fluorescence of single molecules.

Note that the images in Fig. 106.40 were taken by raster scanning the sample relative to the stationary, focused laser beam. The scan direction was from left to right, line by line, from top to bottom. The size of the bright features is defined by the point-spread function of the focused laser beam. These images not only contain information about the spatial position of the fluorescent molecules, but also about the changes of their fluorescence in time. Dark horizontal stripes and bright semicircles instead of circles represent the blinking and bleaching of the molecules in time. Blinking and bleaching are a common single-molecule phenomenon and convincing evidence of the single-photon nature of the source. The explanation of the nature of the long-
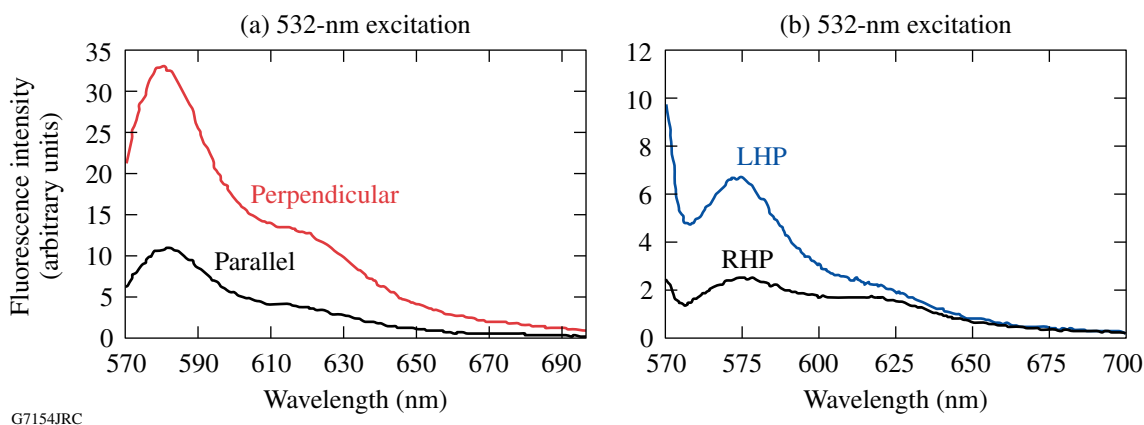
Figure 106.42
Spectrofluorimeter measurements of a polarized fluorescence of $DiIC_{18}(3)$ dye doped in planar-aligned, glassy, liquid crystal hosts under excitation with a nonpolarized, 532-nm light. (a) Fluorescence spectra in a nematic host for different linear polarizations. (b) Fluorescence spectra in a cholesteric host for circular polarization of different handedness.

time blinking from milliseconds to several seconds remains a subject of debate in the literature (see, e.g., Ref. 55).

The maximum count rate of single-molecule images was approximately 10 kcounts/s (~160 counts/pixel with ~4 s per line scan, 256 pixels per line) with a fluorescence molecule lifetime of approximately several nanoseconds. Note that the detector dark counts were fewer than 100 counts/s.

Seven molecules in Figs. 106.40 and 106.41 have either positive or zero anisotropy. These molecules can be either a small amount of impurities in the Staralign photoalignment agent, which have not been bleached even after the UV irradiation of Staralign-coated slips, or impurities of the glassy oligomer host.[56] Figure 106.43(a) shows single-molecule fluorescence images of the Staralign photoalignment agent before UV irradiation. The single-molecule fluorescence microscopy method is very sensitive to material impurities. We sometimes observed single-molecule fluorescence from the impurities in glassy LC oligomers [Fig. 106.43(b)] even when a chromatographic analysis did not detect them. For this reason, the Polyimide and Nylon 6/6 thin films usually used for buffing alignment were not utilized in our experiments because of the finding that they possess a higher fluorescence count rate than single molecules of fluorescence dyes.

(a)   (b)

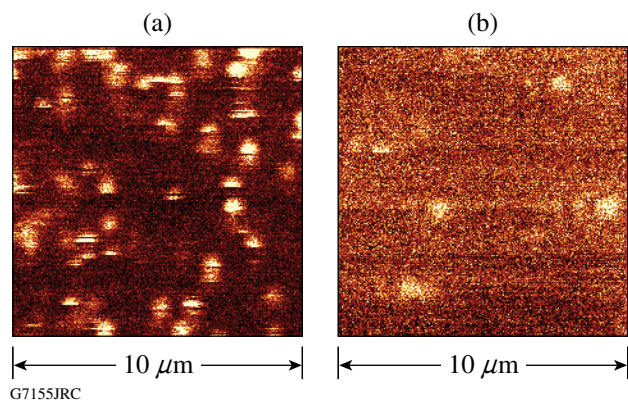|← 10 μm →| |← 10 μm →|

G7155JRC

Figure 106.43
Parasitic fluorescence from single-molecule impurities in the Staralign photoalignment agent without (a) UV treatment and (b) undoped oligomer material.

Conclusions

This article shows the advantages of using liquid crystals as the hosts for single-photon sources; deterministically polarized fluorescence from single emitters embedded in liquid crystal hosts was demonstrated for the first time at room temperature. Single-dye molecules were deterministically aligned by liquid crystal molecules in one direction and produced deterministically linearly polarized single photons.

Circularly polarized single photons with deterministic handedness [see, e.g., Fig. 160.42(b) for a high dye concentration] can be produced efficiently using 1-D photonic band gaps in cholesteric liquid crystals matching the dye-fluorescence band. We hope to increase SPS efficiency in cholesteric liquid crystal, 1-D photonic-band-gap structures from the current 4% to at least 40% (see Ref. 35) to narrow the fluorescence bandwidth (to ~1 to 10 nm) and decrease the fluorescent lifetime from a few nanoseconds to the hundreds of picoseconds necessary for high-speed communications. One-dimensional photonic bandgap structures in cholesteric liquid crystals, 2-D/3-D photonic crystals in holographic polymer-dispersed liquid crystals,[57] a 3-D photonic crystal structure of a liquid crystal blue phase,[58] and photonic crystals/microstructured fibers infiltrated with liquid crystals[59,60] may be prepared for this purpose. By using various fluorescence emitters [dye molecules, colloidal semiconductor nanocrystals (dots and rods), carbon nanotubes, and rare-earth ions], it will be possible to extend the working region of the source from the visible to communication wavelengths (1.3 and 1.55 μm).

REFERENCES

1. Y. Yamamoto *et al.*, Prog. Informatics, No. 1, 5 (2005).

2. B. Lounis and M. Orrit, Rep. Prog. Phys. **68**, 1129 (2005).

3. P. Kumar *et al.*, Quantum Information Processing **3**, 215 (2004).

4. P. Grangier, B. Sanders, and J. Vučković, eds., New J. Phys. **6** (2004).

5. A. Kuhn, M. Hennrich, and G. Rempe, Phys. Rev. Lett. **89**, 067901 (2002).

6. J. McKeever *et al.*, Science **303**, 1992 (2004).

7. Ch. Schwedes *et al.*, Phys. Rev. A **69**, 053412 (2004).

8. C. Brunel *et al.*, Phys. Rev. Lett. **83**, 2722 (1999).

9. B. Lounis and W. E. Moerner, Nature **407**, 491 (2000).

10. F. Treussart *et al.*, Phys. Rev. Lett. **89**, 093601 (2002).

11. A. Beveratos *et al.*, Eur. Phys. J. D **18**, 191 (2002).

12. A. Imamoglu and Y. Yamamoto, Phys. Rev. Lett. **72**, 210 (1994).

13. J. Kim *et al.*, Nature **397**, 500 (1999).

14. E. Moreau *et al.*, Appl. Phys. Lett. **79**, 2865 (2001).

15. P. Michler *et al.*, Science **290**, 2282 (2000).

16. C. Santori *et al.*, Phys. Rev. Lett. **86**, 1502 (2001).

17. J. Vućković *et al.*, Appl. Phys. Lett. **82**, 3596 (2003).

18. C. Santori, D. Fattal, and J. Vućković, Nature **419**, 594 (2002).

19. W.-H. Chang *et al.*, Phys. Rev. Lett. **96**, 117401 (2006).

20. V. Zwiller *et al.*, Appl. Phys. Lett. **78**, 2476 (2001).

21. Z. Yuan *et al.*, Science **295**, 102 (2001).

22. G. S. Solomon, M. Pelton, and Y. Yamamoto, Phys. Rev. Lett. **86**, 3903 (2001).

23. B. Gayral *et al.*, Appl. Phys. Lett. **72**, 1421 (1998).

24. D. Englund *et al.*, Phys. Rev. Lett. **95**, 013904 (2005).

25. A. Daraei *et al.*, Appl. Phys. Lett. **88**, 051113 (2006).

26. D. C. Unitt *et al.*, Phys. Rev. B **72**, 033318 (2005).

27. C. Santori *et al.*, New J. Phys. **6**, 89 (2004).

28. M. Benyoucef *et al.*, New J. Phys. **6**, 91 (2004).

29. W. P. Ambrose *et al.*, Chem. Phys. Lett. **269**, 365 (1997).

30. L. Fleury *et al.*, Phys. Rev. Lett. **84**, 1148 (2000).

31. F. Treussart *et al.*, Opt. Lett. **26**, 1504 (2001).

32. P. Kumar *et al.*, J. Am. Chem. Soc. **126**, 3376 (2004).

33. C. W. Hollars, S. M. Lane, and T. Huser, Chem. Phys. Lett. **370**, 393 (2003).

34. D. A. Bussian *et al.*, Chem. Phys. Lett. **388**, 181 (2004).

35. S. G. Lukishova, A. W. Schmid, A. J. McNamara, R. W. Boyd, and C. R. Stroud, Jr., IEEE J. Sel. Top. Quantum Electron. **9**, 1512 (2003).

36. S. G. Lukishova, A. W. Schmid, C. M. Supranowitz, N. Lippa, A. J. McNamara, R. W. Boyd, and C. R. Stroud, Jr., J. Mod. Opt. **51**, 1535 (2004).

37. *LLE Review Quarterly Report* **94**, 97, Laboratory for Laser Energetics, University of Rochester, Rochester, NY, LLE Document No. DOE/ SF/19460/485, NTIS Order No. PB2006-106666 (2003). Copies may be obtained from the National Technical Information Service, Springfield, VA 22161.

38. B. Lounis *et al.*, Chem. Phys. Lett. **329**, 399 (2000).

39. G. Messin, Opt. Lett. **26**, 1891 (2001).

40. A. Beveratos *et al.* Phys. Rev. Lett. **89**, 187901 (2002).

41. C. Kurtsiefer *et al.*, Phys. Rev. Lett. **85**, 290 (2000).

42. R. Brouri *et al.*, Opt. Lett. **25**, 1294 (2000).

43. A. Beveratos *et al.*, Phys. Rev. A **64**, 061802(R) (2001).

44. I. Fushman, D. Englund, and J. Vućković, Appl. Phys. Lett. **87**, 241102 (2005).

45. M. Steiner *et al.*, ChemPhysChem **6**, 2190 (2005).

46. S. G. Lukishova and A. W. Schmid, "Near-Field Optical Microscopy of Cholesteric Oligomeric Liquid Crystal Layers," to be published in Molecular Crystals and Liquid Crystals.

47. S. G. Lukishova, A. W. Schmid, R. Knox, P. Freivald, R. W. Boyd, and C. R. Stroud, Jr., presented at Quantum Optics II, Cozumel, Mexico, 6–9 December 2004. For presentation see http://speckle.inaoep.mx/ QOII/ppts/Lukishova.pdf.

48. S. G. Lukishova, A. W. Schmid, R. Knox, P. Freivald, R. W. Boyd, C. R. Stroud, Jr., and K. L. Marshall, in *Conference on Lasers and Electro-Optics/Quantum Electronics and Laser Science and Photonic Applications, Systems and Technologies 2005* (Optical Society of America, Washington, DC, 2005), Paper QTuE6.

49. S. G. Lukishova, A. W. Schmid, R. Knox, P. Freivald, R. W. Boyd, C. R. Stroud, Jr., and K. L. Marshall, presented at IQEC/CLEO 2005, Tokyo, Japan, 11–15 July 2005 (Paper JWH1-2).

50. H. M. P. Chen, D. Katsis, and S. H. Chen, Chem. Mater. **15**, 2534 (2003).

51. I. Chung, K. T. Shimizu, and M. G. Bawendi, Proc. Natl. Acad. Sci. USA **100**, 405 (2003).

52. B. C. Stevens and T. Ha, J. Chem. Phys. **120**, 3030 (2004).

53. D. Axelrod, Biophys. J. **26**, 557 (1979).

54. J. Y. Butter *et al.*, ChemPhysChem **7**, 261 (2006).

55. F. Vargas *et al.*, J. Chem. Phys. **117**, 866 (2002).

56. S. G. Lukishova, A. W. Schmid, R. P. Knox, P. Freivald, A. McNamara, R. W. Boyd, C. R. Stroud, Jr., and K. L. Marshall, "Single-Photon Source for Quantum Information Based on Single Dye Molecule Fluorescence in Liquid Crystal Host," to be published in Molecular Crystals and Liquid Crystals.

57. M. J. Escuti, J. Qi, and G. P. Crawford, Opt. Lett. **28**, 522 (2003).

58. W. Cao *et al.*, Nature Materials **1**, 111 (2002).

59. E. Yablonovitch, Nature **401**, 539 (1999).

60. T. Larsen *et al.*, Opt. Express **11**, 2589 (2003).

Fiber-Coupled Single-Photon Detectors Based on NbN Superconducting Nanostructures for Practical Quantum Cryptography and Photon-Correlation Studies

Practical quantum cryptography (QC) systems require ultrafast and high-quantum-efficiency (QE) single-photon detectors (SPD's)[1] with precise timing characteristics[2] and sufficiently low dark counts. For fiber-optic QC systems, SPD's working at the standard near-infrared (NIR) telecommunication wavelengths, namely 1.3 μm and/or 1.55 μm, with counting rates well above 10 MHz are required. In this wavelength range, the most popular InGaAs avalanche photodiodes have limited applicability because of their very large dark counts and significant afterpulsing.

We have already reported on our development of novel superconducting SPD's (SSPD's) based on nanostructured NbN superconducting meanders maintained at temperatures far below the NbN critical temperature T_c.[3–5] The physics of the SSPD operation principle have been explained within a phenomenological, hot-spot formation photoresponse model.[6,7]

The purpose of this article is to present the design and performance of a system of two integrated single-photon detectors based on two fiber-coupled SSPD's. Our two-channel system is designed for implementation in the telecommunication wavelength QC as well as for antibunching-type correlation studies of NIR photons emitted by quantum dots. Contrary to previous designs of fiber-coupled superconducting photon detectors, which required either room-temperature[8] or cryogenic[9] fiber positioning and adjustment, we developed a permanent optical-fiber coupling, which allows multiple thermal cycling of our detectors, robust performance, and room-temperature–like operation.

Figure 106.44 presents schematics of a complete cryogenic construction of our detectors. The insert is placed and sealed inside a standard liquid helium transport dewar. Two NbN SSPD's are glued on the bottom flange insert, as shown in Fig. 106.44(a), with the photon input and electrical output provided via a single- or multimode fiber and a semirigid coaxial cable, respectively. The SSPD nanostructures under study were fabricated according to a technological procedure described in detail in Ref. 10. We used 10-μm × 10-μm^2 NbN superconducting meander-type structures with 4-nm-thick,

120-nm-wide stripes and a 0.6 filling factor (stripe width to stripe width plus separation ratio). The implemented devices were characterized by the critical current density of 2 to 6 MA/cm^2 at 4.2 K and $T_c \approx 10$ K.
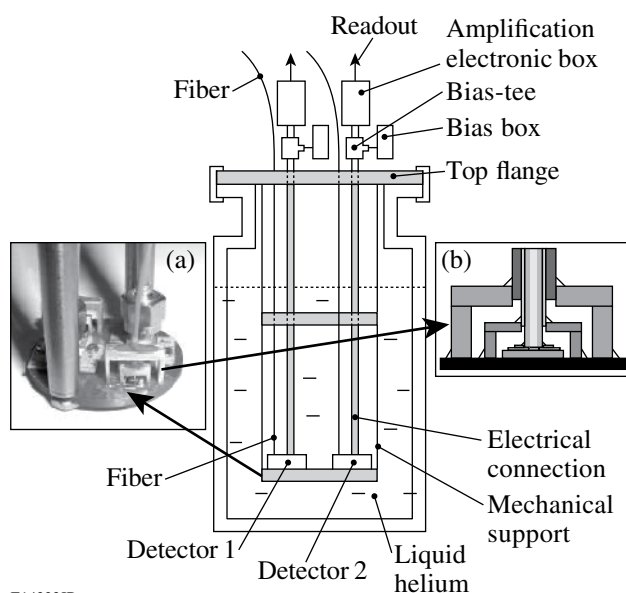
Figure 106.44
Schematic of the two-channel, single-photon detector operating in a helium transport dewar. (a) Cryogenic end plate with two detectors pigtailed to fibers and the electrical output SMA connectors and cryogenic semirigid cables. (b) Cross section of the fiber detector's mechanical holding structure with a fiber positioning photoresist ring.

For accurate coupling between the SSPD and the fiber, we used a specially designed micromechanical photoresist ring placed directly over the SSPD. The 30-μm-thick coupling rings were fabricated using a photolithography process and positioned over the NbN meander with an accuracy of ≤1 μm using the meander's original alignment marks.[11] A cross section of the photoresist ring and the fiber attachment mechanical support (two bridge-like aluminum holders) is presented in Fig. 106.44(b). Outside the dewar, as indicated in Fig. 106.44, each electrical channel was connected through a broadband

(0.08 to 26 GHz) bias-tee to a constant-voltage biasing circuit and a two-stage amplifier with 62-dB total gain and 0.05- to 4-GHz bandwidth. Optical fibers were equipped with standard FC-type connectors. The transport dewar, filled with 60 liters of helium, allowed for over 2 months of uninterrupted operation of our detectors.

We have so far fabricated a total of ten detectors (five integrated pairs) of which eight were coupled with single-mode fibers and two with multimode fibers. The basic qualification of the detector performance was the measurement of the system QE (SQE)[3,12,13] using highly attenuated, 40-ps-wide, 1540-nm-wavelength, 1-MHz repetition rate pulses from a semiconductor laser. The photon flux was precisely calibrated at the room-temperature fiber input (FC connector) and was the measure of the number of photons per optical pulse incident on the SSPD.

The detection probabilities (DP's) of several of our devices versus the number of photons per pulse delivered by the fiber to the NbN structure are presented in Fig. 106.45. The measurements were performed for the bias current $I_b = 0.95\ I_C$, where I_C is the SSPD critical current at 4.2 K. The behavior observed

in Fig. 106.45 is in very good agreement with our previous observations.[3-6] At low-incident photon fluxes, our experimental data show the linear DP dependence, demonstrating the single-photon detection mechanism.[6] At high-light power levels, we observe DP saturation at the 100% level as virtually all laser pulses are counted. We define the SQE of our detectors by taking the DP value at the photon flux level corresponding to an average of one photon per pulse.

The SQE values for our best, average, and worst detectors are collected in Table 106.X with the device QE (DQE) values measured for the 1550-nm wavelength immediately after the SSPD fabrication. Taking the SQE/DQE ratio for each device, we have estimated and listed (see Table 106.X) the coupling factor K between the SSPD structure and the fiber. Simple calculations show (see Ref. 11) that the maximum $K \geq 0.9$ can be achieved when the fiber detectors' vertical separation is <20 μm. However, K decreases rapidly with increasing horizontal misalignment and, for deviations ≥ 8 μm K, drops below 0.1. Table 106.X demonstrates that only device #11 exhibits a relatively large $K = 0.333$ factor while the "average" K is only 0.03, suggesting significant misalignment in the horizontal plane. Since the photoresist ring anchoring the fiber was positioned with 1-μm precision, we suspect that the observed low K values have their origin in an uncontrolled fiber tilting, resulting in an angled front surface of the fiber pigtailed to the detector. Thicker photoresist rings with tighter control of the inner circle diameter should significantly improve K.

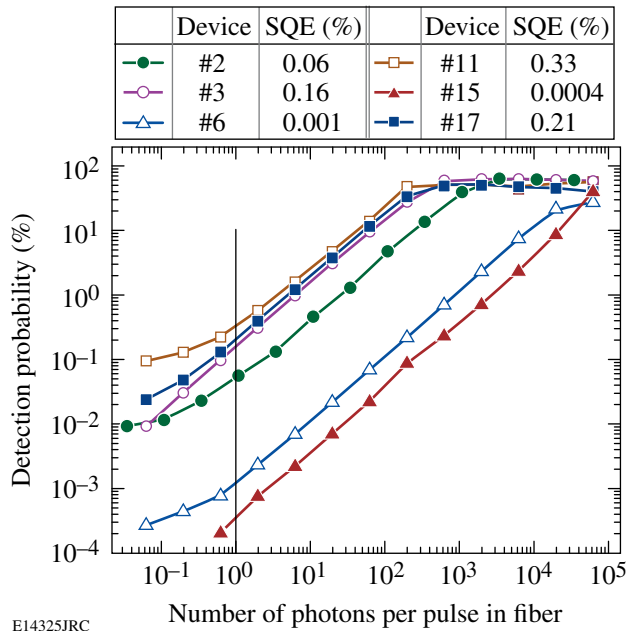|	Device	SQE (%)		Device	SQE (%)
●	#2	0.06	□	#11	0.33
○	#3	0.16	▲	#15	0.0004
△	#6	0.001	■	#17	0.21

E14325JRC

Figure 106.45
Photoresponse detection probability dependencies of the tested fiber-coupled NbN SSPD's on an average number of photons of the 1540-nm wavelength per pulse illuminating the detectors. For comparison purposes, the SQE value of the multimode fiber device #3 has been adjusted by taking into account the actual number of photons reaching the SSPD area. The thin vertical line indicates the 1 photon/pulse flux and corresponds to the SQE definition.

Table 106.X: Device and system QE values for single-mode, 12-μm core diameter, fiber-coupled NbN SSPD detectors.

Detector #	DQE (%)	SQE (%)	Coupling factor K
11	1.0	0.33	0.333
2	2.1	0.06	0.029
17	6.4	0.21	0.033
6	2.0	0.001	0.0005
15	2.1	0.0004	0.0002

The reason for very low K values in devices #6 and #15 are apparently microcracks of the fiber core, which are likely to happen during the very first cooling cycle of the detector. The latter seems to be supported by the fact that in all our devices K remained unchanged after the initial one or two thermal cycles (300 K to 4.2 K and back) and the fatal detector failures were typically observed during/after the first cooldown. Postmortem mechanical inspection showed the fiber cracks in the damaged detectors.

The performance of detectors equipped with multimode (50-μm core diameter) fibers was not as good as expected (see, e.g., device #3 in Fig. 106.45) and the corresponding SQE and K values were rather low. The photon beam profile in the core of a multimode fiber has a Gaussian distribution; thus, even in case of optimum alignment, only ~10% of the power from the fiber reaches our 100 μm^2 SSPD. It is clear that larger area (e.g., 10×20 μm^2 or even 20×20 μm^2) SSPD's and fibers with reduced core diameters are needed to make the multimode fiber devices practical.

The dark count measurements performed on our detectors with the fiber room-temperature input blocked and biased at $I_b = 0.95$ I_C resulted in 2 (device #6) to 90 (device #11) counts per second, clearly depending on the detector's K factor. The observed dark counts are significantly higher than that measured in our earlier free-space NbN detectors.[3] The apparent reason is the 300-K thermal background radiation picked by the fiber's room-temperature end.

The SSPD's used to fabricate our fiber-coupled detectors were large-area meanders to maximize K. As recently documented,[14,15] such structures exhibit large kinetic inductance, which limits their photoresponse temporal characteristics. In our time-domain measurements, we used 5-GHz-bandwidth, single-shot and 50-GHz-bandwidth, sampling oscilloscopes for capturing transient waveforms and for jitter studies, respectively. Figure 106.46 shows a photoresponse signal (dotted line) of one of our detectors. The measured transient is characterized
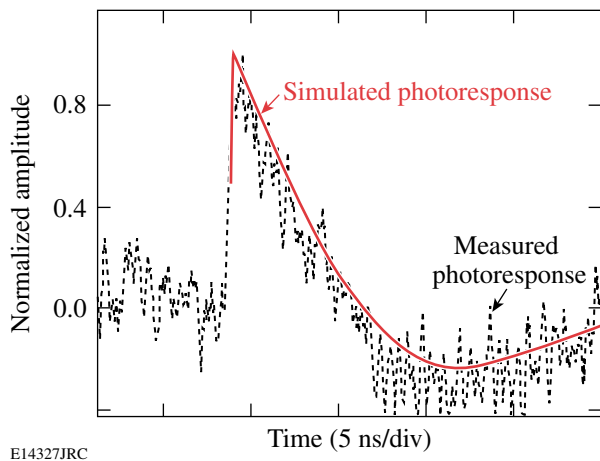
by a 250-ps rise time, 5-ns fall time, and a full width at half maximum (FWHM) equal to about 2.5 ns. We compared the measured pulse shape with numerical simulations (solid line) based on a model developed in Ref. 15 and confirmed that the kinetic inductance was responsible for a nanosecond-wide photoresponse of large-area SSPD's.

The experimental jitter profile (not shown) had a Gaussian shape and exhibited a FWHM of 35 to 37 ps for detectors with single-mode fibers. We note that the jitter measured in the fiber-coupled detectors is two times longer than the 18-ps value reported earlier for free-space–coupled SSPD's.[3] The large kinetic inductance of the SSPD's may contribute to the jitter increase, although we believe that the excess jitter is due to such extrinsic elements as the laser-diode jitter and relatively long (>1 m) fiber and electrical cables.

Finally, we used our integrated, two-detector system in cross-correlation–type experiments. A train of 500-fs-wide (stretched by the fiber) pulses from a Ti:sapphire laser with a 940-nm wavelength and an 82-MHz repetition rate was split by a 50/50 beam splitter and directed simultaneously to the two detectors. Next, the signal from each detector was sent to a discriminator and fed to a start/stop-type correlator. The detector with a low SQE of 0.005% worked as a start device, while our best (#11) detector provided the stop signal. The resulting experimental second-order correlation function is shown in Fig. 106.47. The correlation signal is very clean and exhibits a FWHM of 390 ps, which can be regarded as the

E14327JRC

Figure 106.46
Time-resolved photoresponse of a fiber-coupled, 100-μm^2 area SSPD (dotted line) and the simulated signal (solid line) based on the calculated 420-nH value of the SSPD kinetic inductance and the 0.05- to 4-GHz bandwidth amplifier.
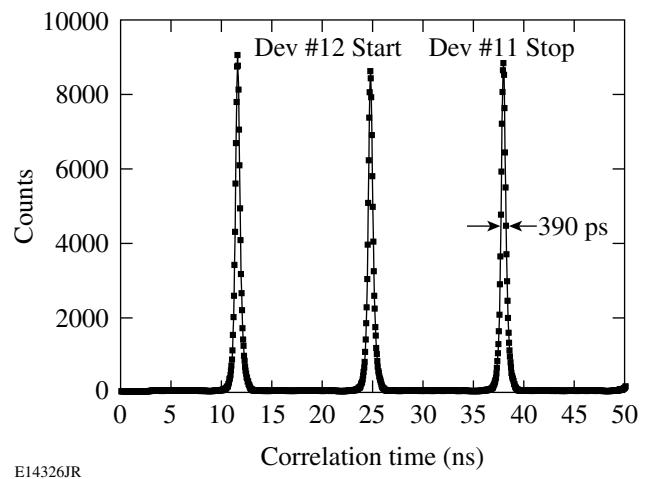

E14326JR

Figure 106.47
Experimental cross-correlation function of a pair of fiber-coupled detectors measured for 500-fs-wide incident optical pulses. The measured correlation FWHM is 390 ps.

figure of merit of the complete detection system (amplifiers, discriminator, correlator, cables, terminators, and detectors) since the incident optical pulses are negligibly short. We note that, despite a relatively long (few nanosecond in duration) response times of our detectors, the correlation pulses are sub-nanosecond. The latter, we believe, is due to the very low jitter and the short (250-ps) photoresponse rise time of the SSPD's and demonstrates the ability of our fiber-coupled detectors to successfully perform antibunching-type correlations observed in photons emitted by true single-photon sources such as single quantum dots.[16]

In conclusion, we have fabricated and tested fiber-based, single-photon detectors with a SQE of 0.3% at the 1550-nm telecommunication wavelength and fiber-coupling factor of up to 33%. The integrated two-detector arrangements can be placed inside a standard helium dewar and, from the operator's point of view, can be regarded as a room-temperature system. Our detectors are intended as practical devices for fiber-based QC systems since, despite their relatively low SQE, they are characterized by a counting rate above 200 MHz, jitter below 40 ps, and dark-count rates below 100 Hz. We have also demonstrated that the system cross-correlation time of two detectors counting femtosecond optical pulses is as low as 390 ps, making our fiber-coupled SSPD's very attractive for time-resolved, antibunching-type studies of single-photon sources. Our current research focuses on an improvement of the SQE and we expect to reach the 3% to 5% level because of the increase in DQE of our SSPD's and the achievement of reproducible K values of 30% or more. Very-large-area meander structures and devices coupled to quarter-wave resonators will be also implemented, especially in detectors with multimode fibers.

ACKNOWLEDGMENT

REFERENCES

1. J. C. Livas *et al.*, in *Free-Space Laser Communication Technologies VII*, edited by G. S. Mecherle (SPIE, Bellingham, WA, 1995), Vol. 2381, pp. 38–47.

2. C. Kurtsiefer *et al.*, in *Quantum Optics in Computing and Communications*, edited by S. Liu, G. Guo, H.-K. Lo, and N. Imoto (SPIE, Bellingham, WA, 2002), Vol. 4917, pp. 25–31.

3. A. Verevkin, A. Pearlman, W. Słysz, J. Zhang, M. Currie, A. Korneev, G. Chulkova, O. Okunev, P. Kouminov, K. Smirnov, B. Voronov, G. N. Gol'tsman, and R. Sobolewski, J. Mod. Opt. **51**, 1447 (2004).

4. A. Korneev, P. Kouminov, V. Matvienko, G. Chulkova, K. Smirnov, B. Voronov, G. N. Gol'tsman, M. Currie, W. Lo, K. Wilsher, J. Zhang, W. Słysz, A. Pearlman, A. Verevkin, and R. Sobolewski, Appl. Phys. Lett. **84**, 5338 (2004).

5. G. N. Gol'tsman, K. Smirnov, P. Kouminov, B. Voronov, N. Kaurova, V. Drakinsky, J. Zhang, A. Verevkin, and R. Sobolewski, IEEE Trans. Appl. Supercond. **13**, 192 (2003).

6. G. N. Gol'tsman, O. Okunev, G. Chulkova, A. Lipatov, A. Semenov, K. Smirnov, B. Voronov, A. Dzardanov, C. Williams, and R. Sobolewski, Appl. Phys. Lett. **79**, 705 (2001).

7. A. D. Semenov, G. N. Gol'tsman, and A. A. Korneev, Physica C **351**, 349 (2001).

8. A. J. Miller *et al.*, Appl. Phys. Lett. **83**, 791 (2003).

9. J. Zhang, N. Boiadjieva, G. Chulkova, H. Deslandes, G. N. Gol'tsman, A. Korneev, P. Kouminov, M. Leibowitz, W. Lo, R. Malinsky, O. Okunev, A. Pearlman, W. Słysz, K. Smirnov, C. Tsao, A. Verevkin, B. Voronov, K. Wilsher, and R. Sobolewski, Electron. Lett. **39**, 1086 (2003).

10. G. N. Gol'tsman, A. Korneev, I. Rubtsova, I. Milostnaya, G. Chulkova, O. Minaeva, K. Smirnov, B. Voronov, W. Słysz, A. Pearlman, A. Verevkin, and R. Sobolewski, Phys. Stat. Sol. C **2**, 1480 (2005).

11. P. Grabiec, W. Słysz, M. Węgrzecki, J. Bar, W. Milczarek, G. N. Gol'tsman, A. Verevkin, and R. Sobolewski, Poland Patent No. P-367391 (patent pending, 2004).

12. A. Verevkin, J. Zhang, R. Sobolewski, A. Lipatov, O. Okunev, G. Chulkova, A. Korneev, K. Smirnov, G. N. Gol'tsman, and A. Semenov, Appl. Phys. Lett. **80**, 4687 (2002).

13. W. Słysz, M. Węgrzecki, J. Bar, P. Grabiec, M. Górska, C. Latta, V. Zwiller, A. Pearlman, A. Cross, A. Korneev, P. Kouminov, K. Smirnov, B. Voronov, G. Gol'tsman, A. Verevkin, M. Currie, and R. Sobolewski, in *Infrared Photoelectronics*, edited by A. Rogalski, E. L. Dereniak, and F. F. Sizov (SPIE, Bellingham, WA, 2005), Vol. 5957, pp. 310–319.

14. R. H. Hadfield *et al.*, Appl. Phys. Lett. **87**, 203505 (2005).

15. A. J. Kerman *et al.*, Appl. Phys. Lett. **88**, 111116 (2006).

16. V. Zwiller *et al.*, Appl. Phys. Lett. **78**, 2476 (2001).

Transition Metal Dithiolene Near-IR Dyes and Their Applications in Liquid Crystal Devices

Introduction

The development of an ideal series of dyes for liquid crystal (LC) device applications represents a formidable synthesis challenge for chemists. To be considered useful for applications in LC devices, the class of dyes under consideration must have (1) a high solubility in the host matrix; (2) good long-term chemical, thermal, and optical stability; (3) low impact on the LC order parameter; (4) a large molar absorptivity; (5) low electrical conductivity; (6) large dichroic ratio; and (7) a λ_{max} located in the region of interest that can be tuned to some extent by relatively simple modifications in molecular structure. Dyes that possess all or nearly all of these properties are, for the most part, readily available for visible-region applications because of the large market for information display applications, which has provided incentive for the synthesis of a large number of highly suitable compounds. In comparison, the total range of dyes that are suitable for applications in the near-IR region is limited to around ten chemical classes. The majority of these dyes were designed for laser applications such as Q-switching and are either ionic or highly polar in nature and, thus, only soluble in polar solvents (e.g., acetone and methanol). Their solubility in LC hosts is very poor (around 0.01 to 0.05 wt%), which limits their potential absorption efficiency in an LC device to an optical density (OD) of <0.1 for a 25-μm material path length. Table 106.XI compares the physicochemical properties, solubility, and absorption characteristics of the currently known classes of near-IR absorbing dyes. Only five dye classes are soluble in nonpolar solvents and thus could be expected to show reasonable solubility in an LC

Table 106.XI: The properties of near-IR dyes evaluated as potential guest–host dopants for LC devices.

Dye class	Species	λ_{max} range (nm)	Solvents	Solubility in LC hosts (wt%)
Cyanine	Organic cationic	735 to 1100	Polar (acetone, methanol)	0.01 to 0.05 (Q-switch 5)
Azulenium	Organic cationic	728	Polar (acetone, methanol)	—
Pyrilium/ thiapyrilium	Organic cationic	748 to 879	Polar (acetone, methanol)	—
Iminium	Organic cationic	725 to 1090	Polar (acetone, methanol)	—
Squarilium/ croconium	Organic cationic	700 to 845	Polar (acetone, methanol)	—
Transition metal dithiolenes	Organometallic (zerovalent or anionic)	600 to 1600	Nonpolar (hexane, toluene)	10
Quinones/ anthraquinones	Organic zerovalent	748 to 810	Nonpolar (hexane, toluene)	2 to 3
Phthalocyanines	Organometallic zerovalent	630 to 830	Nonpolar (hexane, toluene)	—
Azo	Organic or organometallic zerovalent	700 to 900	Nonpolar (hexane, toluene)	2 to 3
Indoanilines	Organic zerovalent	660 to 800	Nonpolar (hexane, toluene)	—

host. Transition metal dithiolenes stand out as the most promising and interesting candidate of this group. They are highly soluble in nonpolar solvents (including LC hosts), their wavelength range spans from 600 nm in the visible to 1600 nm in the near IR (the latter wavelength is of special importance in military and telecommunications applications), and they possess excellent thermal and photochemical stability.

Interest in transition metal dithiolenes and their properties has been steadily increasing in recent years. They have been investigated as passive infrared absorbers for thermal imaging, photography, lithography, and electrophotography;[1] Q-switching–saturable absorbers for lasers,[2] optical limiters, and, in all-optical switching,[3,4] "unimolecular metals" exhibiting metal-like conductivity down to 0.6 K;[5] a "redox switch" for the binding and release of simple aliphatic olefins;[6] and as guest–host dyes for LC electro-optic devices for near-IR applications.[7,8] Earlier work by Muller–Westerhoff[9] and Ohta[10] established that these materials can possess numerous different stable LC phases depending on the structure of the terminal functional groups. This attribute was shown to be important for applications in LC guest–host systems since the presence of LC mesomorphism allows higher dye concentrations to be added to the LC host without substantially reducing its order parameter.[7,8]

In this article we present an overview of the physical and optical properties of transition metal dithiolene complexes that make them of special interest for near-IR applications in LC devices and discuss in detail our past and present research efforts in the design, synthesis, and characterization of both nonchiral and enantiomerically enriched forms of these interesting series of materials. The latter compounds are of special interest for device applications because of their low melting points (below room temperature in many cases) and ability to induce chirality in a nematic LC host when added as a dye dopant. As such, they could provide two separate modes of tunability when introduced into a liquid crystal material: (1) an electronic absorption mode that is tunable by alteration of the molecular structure through synthesis and (2) a selective reflection mode that is tunable by composition (concentration of the chiral dye in the host), electric field, and temperature. Some specific application examples for transition

metal dithiolenes as near-IR dyes in LC electro-optical devices are also given. We conclude by presenting our most recent results that demonstrate the capability of computational chemistry to predict, prior to synthesis, both the near-IR electronic absorbance spectra and the helical twisting power (HTP) of transition metal dithiolenes as a function of molecular structure.

Properties of Transition Metal Dithiolenes

Transition metal dithiolene complexes[11,12] in which the central metal is in a zerovalent state (oxidation number = 0) exhibit strong absorption bands in the 600- to 1600-nm region of the spectrum and are highly soluble in nonpolar organic solvents (e.g., toluene and hexane) as well as LC materials. The central metal can be any transition metal capable of forming square planar complexes, but complexes based on nickel, palladium, and platinum are the most common. Figure 106.48 shows the generic molecular structure of the transition metal dithiolene core.

The strong near-IR absorption maximum observed in transition metal dithiolenes is a function of both extensive electron delocalization about the dithiolene ring system and the interaction of this delocalized system with available d-orbitals on the central metal (Fig. 106.49).[13] This interaction can be described using the linear combination of the atomic orbitals–molecular orbital (LCAO–MO) theory in which the atomic orbitals of the individual atoms are combined to form a series of lower-energy "bonding" and higher-energy "antibonding" molecular orbitals. The absorption of photons of sufficient energy results in the promotion of electrons from occupied (bonding) molecular orbitals to unoccupied (antibonding) molecular orbitals. The lowest-energy transition, and thus the one that occurs at the longest wavelength, is the transition between the highest occupied molecular orbital (HOMO) and the lowest unoccupied molecular orbital (LUMO) and is referred to as the "band gap." This HOMO–LUMO transition is the one responsible for the strong near-IR absorption in the transition metal ditholenes.[11,13] A secondary electronic transition of weaker energy also occurs in the visible region between 500 and 600 nm in these materials. A change in the oxidation state of the metal eliminates the near-IR absorption, greatly strengthens absorption in the visible region, and renders the complexes soluble only in polar solvents. Substi-

where X = H   and R = C_nH_{2n+1}
       Ph OC_nH_{2n+1}
       PhR $N(CH_3)_2$
   SR

M = Ni, Pd, Pt
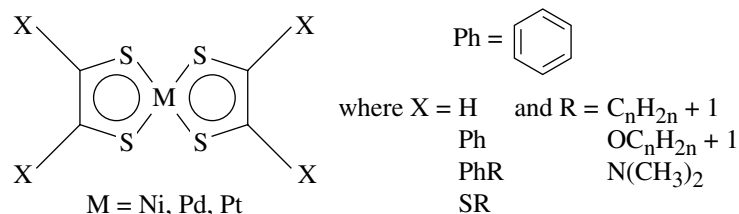
G4947aJR

Figure 106.48
The general molecular structure of transition metal dithiolenes. The physical properties of the complex are determined by the nature of the terminal functional groups, designated as X.

tution of the central metal with a different zerovalent transition metal also produces changes in the near-IR $\lambda_{\max}$. Platinum and palladium complexes show a 20- to 30-nm hypsochromic (blue) shift and bathochromic (red) shift, respectively, as compared to nickel complexes with the same ligand structure.
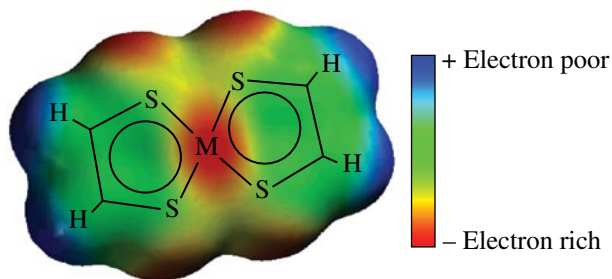
G4948aJRC

Figure 106.49
Ground-state charge distribution map of the nickel dithiolene core. The sulfur and nickel atoms are the most electron-rich areas in the molecule.

The nature of the functional groups attached to the metal dithiolene core has a large effect on both the position of the electronic absorption maximum and the solubility of the dye in the host matrix. Conventional wisdom teaches that the best way to shift the electronic absorption maximum to longer wavelengths is to maximize the extent of electron delocalization by utilizing aromatic ring structures with an extensive π-delocalization capability (phenyl, naphthyl, and anthracenyl) either as functional groups or incorporated within the central core of

the molecule. Although effective, this approach has the dual disadvantage of increasing the melting point of the complex while decreasing its solubility. Counterintuitively, we found that thioether groups bonded directly to the dithiolene core not only shift the near-IR absorption of the complex to longer wavelengths but also *enhance* their solubility in LC hosts. As a direct result of this finding, we focused our attention on preparing new transition metal dithiolene complexes based on thioether terminal groups. Because platinum dithiolene complexes absorb at shorter wavelengths and palladium complexes have proven to be very difficult to synthesize and isolate in a form pure enough for device applications, we continued to use nickel as the central metal of choice for these new materials.

Absorbance Dichroism

Transition metal dithiolenes are excellent candidates for near-IR guest–host devices because of their high molar absorptivity (>30,000), remarkable thermal and photochemical stability, and high solubility in LC hosts as compared to other near-IR dyes. Figure 106.50 (top) shows the field-induced dichroism of a mixture of 1% of the nematic liquid crystalline metal complex "BisBuSDNi" in the nematic LC K-15 measured in a 24-μm-thick, antiparallel-rubbed cell with (1) no field applied and (2) a 10-V, 100-KHz square wave applied to switch the cell into the homeotropic orientation. The drop in absorbance indicates positive dichroism; the contrast ratio at 860 nm is 5:1. An OD of 2.4 is easily achievable in the off state, and OD's of 3.5 have been measured in similar cells at higher dye concentrations.[7]
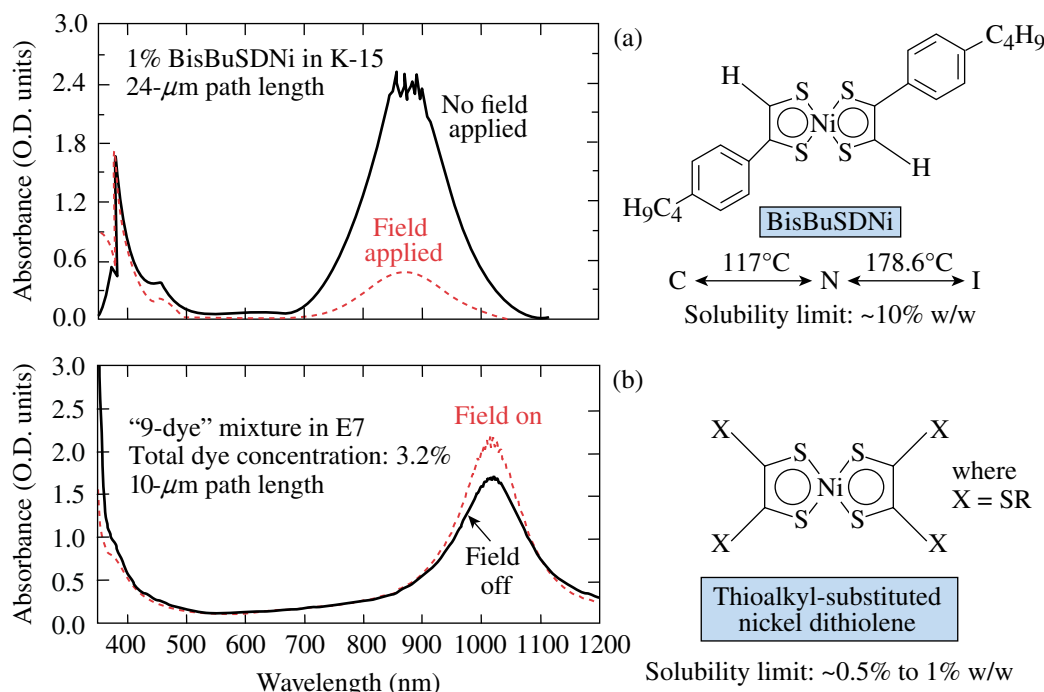

G5972aJRC

Figure 106.50
(a) Change in absorbance with applied voltage for a 1% concentration of "BisBuSDNi" in a 24-μm-thick, antiparallel-rubbed cell. An OD of 3.5 at 860 nm is achievable at higher dye concentrations. (b) Field-induced dichroic behavior of a mixture of nine thioalkyl-substituted nickel dithiolene dyes in Merck E7. Increasing the number of terminal substituents from two to four and altering their structure changes the sign of the dichroism from positive to negative.

Changes in molecular structure can cause substantial changes in both the position of the dye λ_{max} and the nature of the field-induced dichroism. Figure 106.50 (bottom) shows the field-induced behavior of a mixture of nine thioalkyl-substituted nickel dithiolene dyes in Merck E7. The total dye concentration was 3.2%, and the cell path length was 10 μm. This new series of dyes shows a small degree of *negative* dichroism, whereas the materials synthesized previously showed only *positive* dichroism.

Solubility in an LC Host

Solubility testing of thioalkyl-substituted nickel dithiolene dyes in the LC host E7 (Merck) was conducted at selected concentrations between 0.3 wt% to 1 wt% along with several phenyl-substituted nickel dithiolenes as reference compounds. Each dye was dissolved into 2 ml of the host by heating the host/dye mixture to 100°C with stirring for several hours. Upon cooling, each sample was filtered through a 0.45-μm Teflon membrane filter to remove any insoluble material. All samples were checked daily, both visually and by microscopic inspection at 100× magnification, for evidence of dye precipitation. For samples that showed precipitation, new mixtures were prepared at lower concentrations until a stable dye concentration was achieved.

Computational chemistry methods were employed in a parallel and complementary effort to aid in predicting the appropriate functional group combinations that would yield materials with the desired solubility and spectroscopic parameters.[14] Because limitations in the computational methods precluded solubility calculations in either anisotropic solvents or solvent systems composed of mixtures of compounds, Merck CB-15,

an isotropic chiral cyanobiphenyl compound, was used to establish *qualitative* solubility trends.

The solubility of a given solute in a solvent can be approximated by calculating its solvation energy and comparing this value with the bonding, or "reorganization," energy. The solvation energy ΔG_{solv} is defined as[15]

$$\Delta G_{solv} = \Delta G_{elec} + \Delta G_{cov} + \Delta G_{disp}$$

$$+ \Delta G_{vib} + \Delta G_{lib} + \Delta G_{other}, \qquad (1)$$

where ΔG_{solv} is the solvation energy, ΔG_{elec} is the electrostatic solute–solvent interaction, ΔG_{cov} is the energy to form a solute-shaped cavity, ΔG_{disp} is the London and van der Waals interactions, ΔG_{vib} is the change in vibrational energy due to damping, ΔG_{lib} is the conversion of rotations and translations to librations, and ΔG_{other} is the solvent enthalpic and entropic structure (PV term, etc.). The value ΔG_{solv} can be used as a qualitative indicator of general solubility of the dye solutes in the same host with a larger positive value generally indicating a greater solubility in the solvent host matrix. Table 106.XII gives a compilation of melting points, near-IR absorbance, and solubility (calculated versus experimental results) for a series of substituted nickel dithiolene complexes with substituted phenyl and alkylthio terminal groups. General trends that can be drawn from the data in Table 106.XII are, that as the terminal groups are changed from substituted phenyl to alkylthio, (1) the melting points of the complexes drop drastically, (2) the near-IR λ_{max} of the complexes are shifted substantially to longer wavelengths,

Table 106.XII: Comparison of melting points, near-IR absorbance maxima, and solubility data (both calculated and experimental) for a series of phenyl-substituted and alkylthio-substituted nickel dithiolene dyes in Merck CB-15 and E7 hosts. A larger *positive* value for ΔG_{solv} indicates higher solubility.
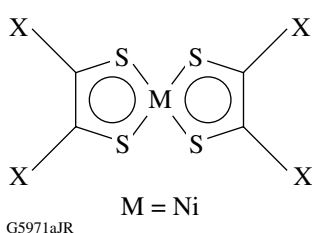
Terminal (X) group	Melting point (°C)	λ_{max} in E7 (nm)	CB-15		Merck E7
			Solubility limit (wt%)	ΔG_{solv}	Solubility limit (wt%)
$-SC_8H_{17}$	73	1020	1.0	–7.6725	0.50
$-SC_7H_{15}$	81.5	1020	0.5 to 1.0	–7.7164	0.50
$-SC_4H_9$	101	1020	0.5 to 1.0	–7.7190	0.50
$-PhC_4H_9$	228 to 230	910	0.3 to 0.5	–14.4373	0.50
$-PhN(CH_3)_2$	280 to 283	1056	0.3 to 0.5	–17.4080	0.05
$-PhOC_9H_{19}$	184 to 189	970	0.1 to 0.3	–21.6724	0.30
$-PhOC_4H_9$	246 to 248	970	0.1 to 0.3	–21.6950	0.30

M = Ni

G5971aJR

and (3) the solubility of the complexes in both CB-15 and E7 (both calculated and experimental) increases.

Materials Synthesis

The synthesis of nickel dithiolene dyes and their precursor ligands was conducted using modifications of literature methods and have been reported elsewhere. Three basic methods have been employed, depending on the degree of substitution desired in the complex and its overall symmetry. Mesogenic nickel dithiolenes were synthesized by a

modification[7] of an earlier three-step procedure reported by Mueller–Westerhoff *et al.*,[9,11] as shown in Fig. 106.51. Although relatively simple, this method has some disadvantages in that the products are difficult to separate from the tarry by-products formed from phosphorous pentasulfide and, as a result, the yield of purified product is very low (5% to 15%). A second method that is useful for the preparation of alkylthio-substituted nickel dithiolenes is based on literature methods reported by Wainwright and Underhill,[16] N. Svenstrup *et al.*,[17] and A. Charlton *et al.*,[18] as shown in Fig. 106.52. The method
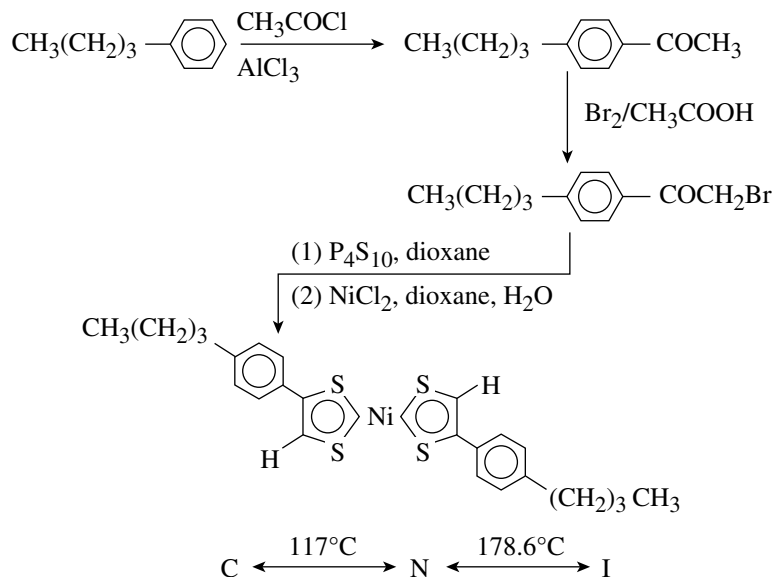

Figure 106.51
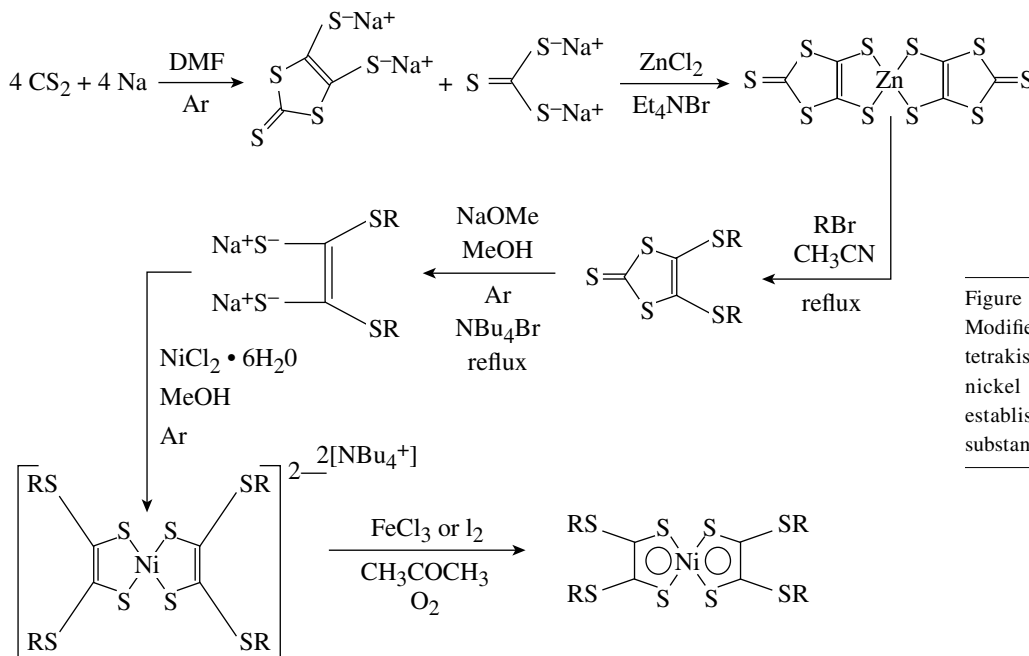The synthesis method for rod-like nickel dithiolene compounds possessing a liquid crystal phase.

Figure 106.52
Modified synthesis scheme for preparation of tetrakis (alkylthio) bis(ethylene-1,2-dithiolene) nickel (0) complexes. Modifications to the established literature procedures resulted in substantially improved yields of product.

is applicable to both chiral and nonchiral terminal groups. For nonchiral terminal groups, yields of the complexes ranged from 27% to 68%, while yields of complexes with bulkier, enantiomerically enriched terminal groups were substantially lower (5%–10%). A third method allows the insertion of a flexible alkyl spacer ranging from 2 to 9 carbons between the thio group attached to the dithiolene core and an enantiomerically enriched chiral terminal group based on nonracemic carboxylic acids or alcohols, as shown in Fig. 106.53. The large, flexible, and bulky terminal groups make them somewhat difficult to isolate and purify. Currently, the overall yields for these materials are quite low, ranging from a few percent up to around 15% for materials with shorter alkyl spacer groups.

Enantiomerically Enriched Nickel Dithiolene Complexes

Table 106.XIII gives the generic structure and physical properties, respectively, of these nickel dithiolene complexes with enantiomerically enriched terminal groups. The most remarkable feature of this series of chiral materials is how rapidly and dramatically their melting points decrease as the length and breadth of the terminal groups increase. With the exception of the S-(+)-2-methylbutylthioether derivative, all of the other materials are liquids at room temperature.

Another interesting attribute of these new chiral metal dithiolenes is that they are capable of inducing a chiral nematic phase when added to a nematic LC host. Figure 106.54 shows
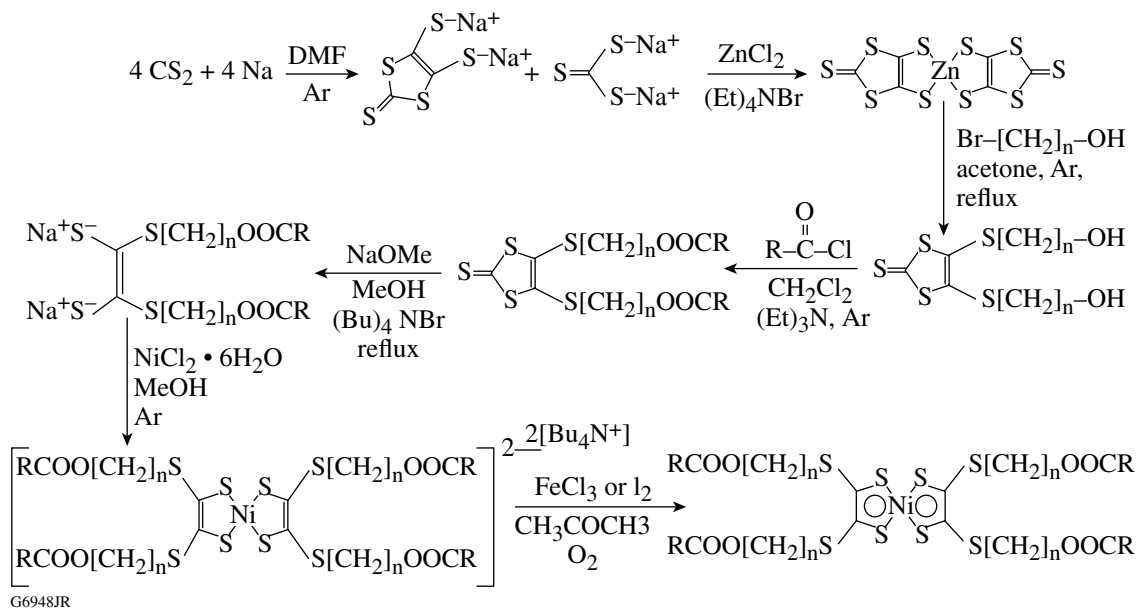
(a)

(b)
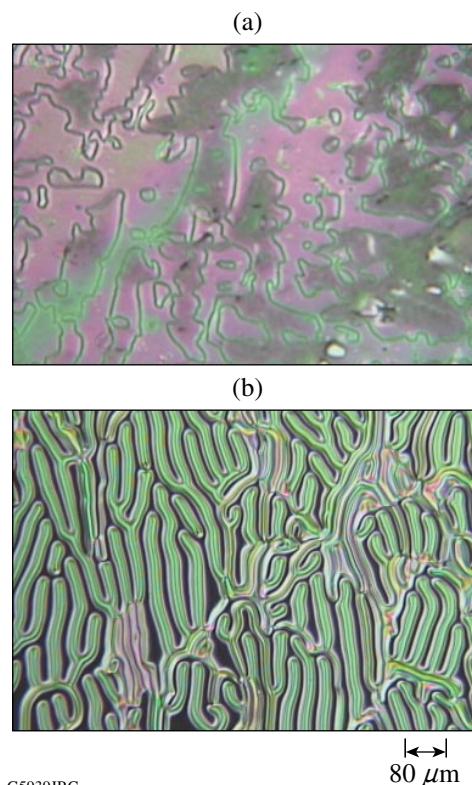
80 μm

G5939JRC

Figure 106.54

Chirality transfer to an LC host by doping with a chiral nickel dithiolene complex. (a) Pure Merck E7 and (b) Merck E7 containing 0.5% of the S-(+)-2 methylbutyltioether-substituted nickel dithiolene.

G6948JR

Figure 106.53

Synthesis scheme for chiral transition metal dithiolenes incorporating a flexible spacer between the terminal groups and the dithiolene core.

photomicrographs under crossed polarizers of a sample of Merck E7 before and after doping with 0.5% of the S-(+)-2 methylbutylthioether-substituted nickel dithiolene. The fingerprint texture generated in the doped sample (helical pitch, length = 80 μm) is clear evidence that the chirality of the metal complex has been transferred to the LC host.

Device Applications

Transition metal dithiolenes have many possible commercial, military, and scientific applications in LC electro-optical devices for the near-IR region. Their high solubility in LC hosts, capability of exhibiting mesomorphism, excellent thermal and photochemical stability, dichroic capability, and broad wavelength range have

Table 106.XIII: Physical properties of the new chiral nickel dithiolene complexes.
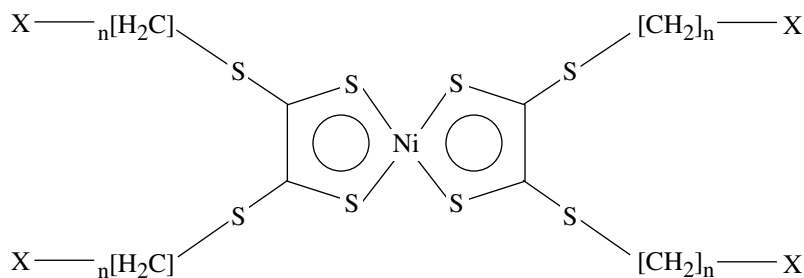
X group	Spacer (n)	MP (°C)	λ_{max} (nm) (a) E7 (b) Toluene	Helical pitch length (E7, μm)
	0	108.5	1020[a]	80
	0	−43	1020[a]	30
	3	−45	1009[b]	
	6	−50	1009[b]	
	9	−49	1009[b]	
	3	<25	1008[b]	
	6	−46	1008[b]	
	9	−46	1008[b]	
	3	−52	1005[b]	
	6	−45	1005[b]	
	9	−46	1010[b]	
	3	<25	1011[b]	
	6	−52	1011[b]	
	9	<25	1011[b]	

G5973JR

made them of interest for use in LC devices for near-IR optical modulation, switching, nonlinear optics, and sensor protection.[14] In addition to these applications, nonchiral nickel dithiolenes have been extensively investigated as a component of the liquid crystal point diffraction interferometer (LCPDI), a phase-shifting, common-beam-path interferometer that uses an LC electro-optic device as the modulation element.[19,20] Because both the object and reference beams follow the same path, the LCPDI is relatively insensitive to the mechanical vibrations, temperature fluctuations, and air turbulence that plague conventional phase-shifting inter-ferometers. The LC host used in the LCPDI must be doped with a dye to compensate for differences in the cross sectional area of the sample and reference beams to ensure good fringe contrast (Fig. 106.55). Ideally, the dye should have as low a dichroism as possible to maintain constant interference fringe contrast with applied voltage. The LCPDI is being investigated as a beamline diagnostic for the 60-beam, 40-TW, 1054-nm OMEGA Laser System used in the Department of Energy's inertial confinement fusion research at the Laboratory for Laser Energetics. The large physical size and the need for vibration isolation make conventional near-IR phase-shifting interferometers impractical for these characterization activities since each of the 60 beams would have to be propagated a long distance across free space to reach the interferometer table. To date, transition metal dithiolenes are the only class of near-IR dyes that have the necessary combination of physical properties suitable for a near-IR LCPDI device.

The addition of chirality to the dithiolene core now opens new application possibilities. Since these new materials are non-
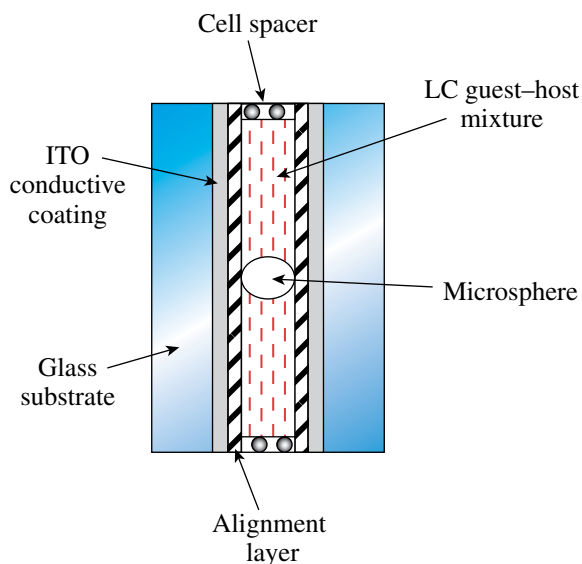
Figure 106.55
A schematic representation of the liquid crystal point diffraction interfere-ometer (LCPDI) device.

centrosymmetric, they may exhibit interesting nonlinear optical properties, either on their own in the liquid state or as a dopant in a suitable host. The demonstrated induction of chirality in nematic phases by doping with a chiral nickel dithiolene suggests the pos-sibility of devices for sensor protection in the near IR that have two modes of tunability: one mode through the absorbance of the nickel dithiolene dye (tunable by synthesis) and a second tunable mode employing selective reflection wavelength shifting induced by electric field or temperature changes (see i.e., Fig. 106.56).
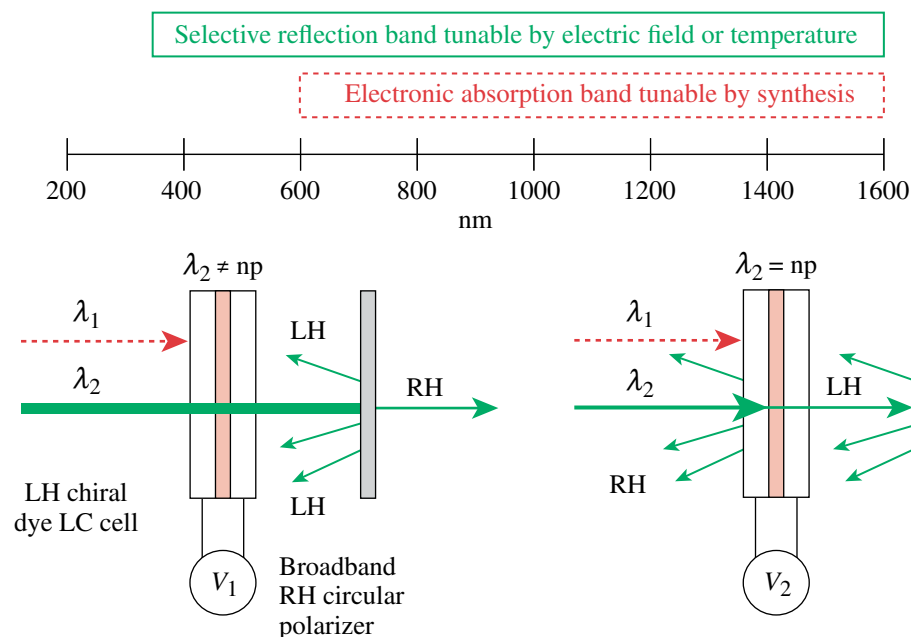
Figure 106.56
Device concept for sensor protection in the near IR based on chiral nickel dithiolene dyes. The device has two modes of tunability: one mode through the absorbance of the nickel dithiolene dye (tunable by synthesis) and a second tunable mode employing selective reflection wavelength shifting induced by electric field or temperature changes. Selective reflection occurs when the incident wavelength λ equals the product of the average refractive index of the LC material and its pitch length P.

Computational Chemistry Modeling of Nickel Dithiolene Systems

Advances in the science of computational chemistry over the past 20 years, the widespread availability and increasing ease of use of computational chemistry software, and an exponential reduction in the cost and size of extremely powerful computer hardware now make some degree of computational predictive capability for physical properties (e.g., solubility, electronic and vibrational spectra, reactivity, molecular configuration, and chirality) within the reach of nearly every laboratory that is involved in new materials research and development. Previously and out of necessity, researchers would have to follow an empirical approach of synthesizing, isolating, characterizing, and purifying hundreds of different compounds to establish structure–property relationships that could be used to further direct the design and development effort toward the desired goal. Of these hundreds of compounds synthesized, only a handful would have the necessary combination of physical characteristics to be deemed worthy of further study and development. Such a process is not only time consuming, labor intensive (weeks to months to completely synthesize and characterize each compound), and costly, but can also be highly frustrating for organic chemists engaged in the synthesis of new materials—especially for those with limited resources. Modern hardware and user-friendly software now make it possible to model new compounds and their physical properties with remarkable accuracy within a few hours or days, which only a few years ago would have taken from weeks to months of work to achieve the same results.

Nowhere has there been more evidence of the predictive capability of computational chemistry than in the pharmaceutical industry, where computational molecular design techniques have been used to great advantage for a number of years in the rapid development of new drugs with enhanced biological activity and specificity at lower cost. More recently, computational chemical methods have been applied to the molecular engineering and design of liquid crystal materials for use both in the multibillion dollar information display industry and the optoelectronic, photonics, military, and life sciences sectors. In all of these examples, the vast majority of the target materials systems consist of *organic molecules* composed mainly of carbon, hydrogen, and nitrogen in combination with a few other elements (e.g., sulfur, fluorine, and phosphorous). The state of the art in computational chemistry modeling in these materials is well developed, and computational algorithms and procedures are well defined in a large body of existing literature. The application of computational chemistry techniques to transition metal organometallics and particularly the transition

metal dithiolenes, represents a substantial challenge mainly for several reasons that include (1) the lack of previous research activity in the area from which to draw direction from, (2) the extremely small number of parameter files (basis sets) that can adequately account for the unique nature of the coordinate-covalent bonds that are formed in these materials, (3) the intensive computational resources required to accomplish the calculations, and (4) the scarcity of computational chemistry software capable of modeling organometallic systems. In what follows, we describe the computational modeling methodology that we have developed and applied to nickel dithiolene systems to predict, prior to synthesis, properties that include (a) the near-IR electronic absorbance spectra and (b) the helical twisting power (HTP) of the nickel dithiolene complex in a host medium for enantiomerically enriched materials. This effort is believed to be the first time that such calculations of this nature have been attempted in nickel dithiolene systems or in any other transition metal organometallic complex.

1. Modeling of Electronic Transitions States and Near-IR Absorbance Spectra

The process of modeling electronic absorbance spectra is composed of three key steps.

• *The free energy of the molecular structure with respect to its conformation is minimized.*

Molecular mechanics calculations employing Newtonian mechanics and empirical force fields are used to generate a particular molecular conformation that represents an energy-minimized state with respect to bond angles, electrostatic repulsions, and steric factors. This energy-minimized structure represents an approximate equilibrium conformation that must be further refined using quantum mechanical methods.

• *The electron distribution in the molecule is determined, and the available electronic energy levels and excited states are calculated.*

Either semiempirical or *ab initio* quantum mechanical methods can be used for this task. Semiempirical methods use some approximations and are employed when a certain degree of computational accuracy can be sacrificed in exchange for reduced computational resources and run time. *Ab initio* methods provide a much more detailed and accurate description of the quantum mechanical aspects of a molecular structure but do so at a cost of increased computational resource requirements and time. The substantially improved accuracy of *ab initio* calculations made them the preferred method for modeling the

exceedingly complex electronic distribution and excited-state transitions found in nickel dithiolenes.

Ab initio calculations are based on a detailed description of the quantum mechanical aspects of a molecular structure using the Schrödinger equation, defined as

$$H_{op}\Psi = E\Psi, \qquad (2)$$

where H_{op} is defined as the Hamiltonian operator, Ψ as the wave function of the system, and E as the energy of the system. The Hamiltonian of the system represents its kinetic and potential energy. In a three-dimensional system, the Hamiltonian operator is defined as

$$H_{op}\Psi = \frac{-h^2}{2m}\left(\frac{\partial^2\Psi}{\partial x^2} + \frac{\partial^2\Psi}{\partial y^2} + \frac{\partial^2\Psi}{\partial z^2}\right) + U\Psi, \qquad (3)$$

where h is Planck's constant divided by 2π and m is the mass of an electron. The terms x, y, and z are the Cartesian coordinates of an electron with respect to the nucleus, while U refers to the potential energy of the system.[21]

A wave function is a mathematical expression that describes the wave nature of an electron after certain restrictions are placed on it by basis sets, which give specific information on the electronic structure and orbitals of the atoms as well as describing the path and behavior of electrons. The wave function expression is a group of Gaussian-type orbital equations for which the generic equation is

$$\Psi = Nx^l y^m z^n e^{-\alpha r^2}, \qquad (4)$$

where x, y, and z are the Cartesian coordinates; l, m, and n are positive integer values that describe the angular momentum of the orbital, r is the distance to the center of the atom, N is the normalization constant, and α represents the orbital exponent of the Gaussian function.

Because the Schrödinger equation cannot be solved directly for a many-electron system, various approximation methods can be used to make it solvable. The Hartree–Fock method uses three approximations to estimate the many-electron wave function; these include (1) the *Born–Oppenheimer approximation* (assumes that all nuclei are motionless with respect to the electron), (2) the *linear combination of atomic orbitals (LCAO) approximation* (assumes that electron orbitals may be expressed as one-electron basis functions centered on each atom), and

(3) the *Hartree–Fock approximation* (which assumes that the sum of all single-electron calculations of a molecule is the same as the multi-electron calculation of the molecule). Because of inaccuracies associated with the Hartree–Fock approximation, the entire Hartree–Fock computational method becomes less accurate with increasing molecular size.[22]

Unlike the Hartree–Fock method, which uses an exact Hamiltonian with approximate wave functions written in terms of a product of one-electron functions, the density function theory (DFT) method replaces the many-electron wave function with electronic density as the basic quantity.[23] The DFT method is widely employed in the field of computational chemistry and is considered to be a good method to use with transition metal complexes.

- *Calculation of the allowable ground-state to excited-state transitions that are responsible for the electronic absorbance spectrum.*

The expected excited-state electronic transitions are determined by including the configuration interaction (CI) model in the *ab initio* quantum mechanical calculations. The CI model is derived from Hartree–Fock calculations that are expanded to incorporate electronic excitation and changing shell levels.

Because there was no single software package capable of handling all of the computational tasks, a total of four separate software packages running on two different computing platforms were required. Molecular mechanics computations were conducted using Spartan 4 (Wavefunction, Inc.) on a 2-Ghz, dual-processor Intel XEON server. *Ab inito* and electronic spectra calculations were conducted using the open-source computational package GAMESS (General Atomic and Molecular Electronic Structure System) from Iowa State University on a SGI Altix Server using sixteen 2.5-GHz Itanium 2 processors. Input-to-output file format conversions from Spartan to GAMESS were accomplished using Open Babel (www.source-forge.net), while the final spectral output from GAMESS was processed, displayed, and plotted using the WebMO graphical user interface (http://webmo.net/index.html).

Specifying the appropriate conditions to conduct the *ab inito* calculations using GAMESS proved to be extremely challenging. Parameter options and appropriate basis sets for the calculations must be selected and specified properly to achieve valid results. For relatively small organic molecules there is existing literature to guide the selection of appropriate options and parameter sets, but in the case of nickel dithiolenes
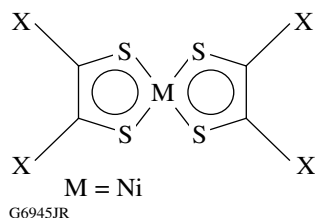
there is no pre-existing body of literature from which to draw guidance. The proper calculation conditions were determined through a combination of (1) an extensive study of the general literature on *ab initio* molecular modeling theory, (2) review of the handful of existing references on *ab initio* modeling in unrelated transition metals and their complexes, and (3) testing the selected modeling parameters and conditions by means of an iterative trial and error process. The calculation options that were ultimately selected and used in testing the model and its application to new nickel dithiolene systems are

- *SCFTYP (self-consistent field wave function):* Specifies the basic calculation type that is used. For our work, the restricted Hartree–Fock[24] (RHF) and density functional theory[25] (DFT) options were used. The RHF method was ultimately chosen for the final calculations because (1) it was found to be more accurate than the DFT method in initial test trials, and (2) since the CI calculations required to calculate the absorbance spectra are based on the RHF calculations, they cannot be run concurrently with the DFT option.

- *CITYP (configuration interaction model type):* Includes and specifies CI models in the *ab initio* calculations for electronic spectra calculations.

- *BASIS and GBASIS:* Specifies the type of basis set used for the calculation and what type of basis set function to choose, respectively. The minimal basis sets (GBASIS = STO) and split-valence basis sets (GBASIS = N31) were chosen initially because they were one of the few basis sets that were capable of producing accurate calculations for the electronic structure of nickel dithiolenes. The minimal basis set used was STO-3G (Refs. 26 and 27) with three Gaussian functions. Split-valence basis sets used were 6-31G with six Gaussian functions, and 6-31G(d) (Ref. 28) with both six Gaussian functions and functions that included *d*-orbital calculations. The split-valence basis sets proved to be more accurate because they correctly predicted that valence electrons do most of the bonding. The 6-31G(d) basis set specifies the inclusion of *d*-orbitals in the calculations, thus increasing their accuracy.

- *SCF and DIRSCF:* Specifies whether the self-consistent field wave function will be calculated directly or indirectly.[29] Hartree–Fock calculations make use of a large number of two-electron repulsion integrals that are stored and retrieved from hard disk storage. The direct SCF calculation re-evaluates the integrals directly without storing to disk during each Hartree–Fock iteration, which dramatically speeds up processing time.

- *CIS and NSTATE:* Specifies the method for determining the electronic structure[30] and how many different peaks in the electronic spectrum should be selected for the calculations, respectively. The optimal value for NSTATE was 10, as lower values would generate inaccurate results while higher values would significantly increase calculation times without any significant gain in accuracy.

- *DAMP:* Aids in allowing the system to converge to an energy minimum state during SCF calculations.[31,32] *Ab initio* calculations were found to fail consistently in nickel dithiolene systems unless this option was added.

The accuracy of the computational method was tested by modeling a series of nickel dithiolenes reported previously in the literature by Mueller–Westerhoff *et al.*,[13] calculating the expected near-IR absorbance spectrum and comparing the resultant values to the literature data in several different solvents (Table 106.XIV). A Pearson correlation *r* (a measure of the fit of a least squares linear regression through the data set) between the calculated and experimental near-IR absorbance data was determined for the compounds in Table 106.XIV. The correlation coefficient R^2 describes the proportion of the points that can be accounted for by the linear regression. For the near-IR absorbance data in Table 106.XIV, a correlation coefficient

Table 106.XIV: Calculated and experimental near-IR peak absorbance data for a series of nickel dithiolene compounds previously prepared and reported in the literature.

M = Ni
G6945JR

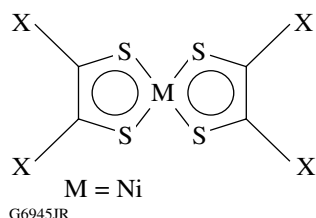| Terminal group	Experimental solvent	Experimental wavelength (nm)	Calculated wavelength (nm)
X = H	Hexane	720	720.91
X = CH$_3$	CHCl$_3$	774	843.08
X = CF$_3$	Pentane	715	775.05
X = S-C$_4$H$_9$	CHCl$_3$	1104	1012.31
X = C$_6$H$_5$	CHCl$_3$	866	845.19
X = 2-napthyl	CHCl$_3$	905	993.08
X$_1$,X$_4$ = H X$_2$,X$_3$ = C$_6$,H$_5$	CH$_2$Cl$_2$	805	857.78

of 0.910117443 was obtained, which represents an excellent correlation between calculated and experimental results for a majority of the compounds modeled, considering that the theoretical model assumes that the molecule is not solvated (i.e., in a vacuum). The excellent correlation is strong evidence of the predictive capability of the computational method and validates its use in predicting electronic transition states in nickel dithiolene systems that have yet to be synthesized.

Table 106.XV shows the results obtained when the new computational method was applied to a series of yet-to-be synthesized nickel dithiolene systems with ligands of varying structure. The goal of this exercise was to be able to establish structure–property relationships that could be used in the design of new materials with an advantageous combination of physical and optical properties (high host solubility, large absorbance oscillator strength, and control of the peak absorbance maximum) through ligand selection. One nickel dithiolene complex with C_6 alkyl terminal groups that has been previously prepared is also included in the table as a reference. One significant trend that can be observed on examination of the table is that the near-IR peak wavelength is red-shifted when

sulfur-containing groups are bonded directly to the dithiolene core, whereas for phenyl groups the near-IR maximum is blue-shifted. This observed trend is somewhat counterintuitive as it is normally accepted that the addition of aromatic groups in conjugation with another aromatic structure generally shifts the absorbance maximum of the molecule to *longer* wavelengths than do alkoxy or thioakyl groups because of resonance stabilization (the energy gap between electron levels is reduced, thus allowing electronic-state transitions to occur at a lower energy and longer wavelengths). Clearly, the *d*-orbitals on the sulfur-containing terminal groups are providing a greater degree of resonance stabilization in this case than the phenyl groups. The nature of this stabilization is not yet understood and will be investigated in the future.

A serious limitation of the current modeling method is that GAMESS appears to be unable to produce accurate electronic spectral data for nitrogen-containing compounds. Computational failures were routinely encountered in every attempt to model nitrogen-containing nickel dithiolene structures. The same results were obtained in attempts to model even very simple, classical nitrogen-containing organic compounds. The source of the problem at this point is still unresolved, but it appears to be a basic functional issue with GAMESS itself and not with our specific computational methodology or parameter files. An investigation of this issue is ongoing.

2. Modeling of Chirality and HTP

In an effort to gain a better understanding of the relationship between absolute molecular configuration and optical rotation direction, there has been increasing interest in representing chirality in a more quantitative, mathematical manner. It is somewhat surprising that the computational prediction strategy so successfully exploited by the pharmaceutical industry has only been applied very recently to the prediction of "chiroptical" properties of LC systems for advanced optical and photonics applications. The earliest reported activity in this area was by Lisetski *et al.*,[33–35] who used atomic coordinates determined either experimentally by x-ray diffraction or computationally from molecular models to calculate the HTP for a series of cholesteryl esters.

More recently, chirality has been determined computationally using two different approaches that are innately different in their level of development, ease of use, and efficiency. The first of these methods, explored in 1995 by Zabrodsky *et al.*,[32,36] attempts to find the absolute distance between the corresponding atoms of the two configurations of a chiral molecule if they were to be superimposed over one another. One disadvantage

Table 106.XV: Predicted electronic spectral maxima for a series of candidate nickel dithiolene compounds that have yet to be synthesized. The first entry in the table is a compound that has been synthesized and included for reference.

M = Ni

G6945JR

Terminal groups	Experimental wavelength (nm)	Predicted wavelength (nm)
X = C_6H_5	866	845.19
X = S-H		1053
X = S-Ph		972
X_1, X_4 = S-H X_2, X_3 = S-Ph		1004
X_1, X_4 = H X_2, X_3 = S-Ph		1038
X_1, X_4 = H X_2, X_3 = S-H		1055

of this method is that it is extremely computationally intensive because of the large number of iterations required to arrive at solutions that are meaningful.

In 1995 Osipov *et al.*,[37] building on the work of Listeski *et al.*,[33–35] proposed a second, simpler method based on the calculation of a "figure of merit" for chirality that they termed the chirality index (G_0). Recently, Solymosi *et al.*[38] improved upon the chirality index by introducing a scaling factor that allows comparison between molecules with different numbers of atoms. This scaled chirality index (G_{0S}) is used to find the contributions of individual atoms and atom groups to the overall (global) chirality of the molecule. This scaled chirality index is useful even in its abstract form; any asymmetry, if it exists, will be revealed by the nonzero value of G_{0S}. A symmetrical molecule returns a chirality index value of zero in nearly every case. Promising correlations between G_{0S} and important applications properties such as circular dichroism (CD) and the HTP of a chiral dopant in a liquid crystal host also have been shown by Neal *et al.*,[39] and Osipov and Kuball.[40]

The scaled chirality index can be used to compare molecules of different sizes and is constructed to be maximized for a molecule with a strong steric stress and to vanish for any molecule that contains the point symmetry element S_n (a rotation-reflection axis), which would preclude chiral behavior. The chirality index is also capable of predicting the sign of the optical activity.

The numerical expression for the scaled chirality index is

$$
G_{0S} = \frac{4!}{N^4}\frac{1}{3}\left\{ \sum_{\substack{\text{all permutations of} \\ i,j,k,l = 1}}^{N} w_i w_j w_k w_l \right.
$$

$$
\left. \times \frac{\left[(\mathbf{r}_{ij} \times \mathbf{r}_{kl}) \times \mathbf{r}_{il}\right](\mathbf{r}_{ij} \times \mathbf{r}_{jk})(\mathbf{r}_{jk} \times \mathbf{r}_{kl})}{\left(r_{ij}r_{jk}r_{kl}\right)^n r_{il}^m} \right\}, \quad (5)
$$

where $\mathbf{r}_{ij}$ values are the atomic radii of the atoms contained in the chiral group upon which the chirality calculations are conducted and w_i, w_j, w_k, and w_l are values that represent the weighting factors of the individual atoms i thru l. We used this numerical expression to develop a multiplatform, multithreaded computational program to efficiently compute the chirality index for molecules of up to 250 atoms within minutes on most high-performance computer systems. Initial computations were performed on a SGI Origin 2000 server (sixteen 400-MHz

processors) running SGI IRIX 6.5, which would typically complete a chirality index calculation for a molecule with 200 atoms in approximately 4 h. The same code recompiled to run on a SGI Altix server (sixteen 2.5-GHz Itanium 2 processors) running Red Hat Enterprise Linux Release 3 computed the chirality index for the same compound with 200 atoms in approximately 5 min.

Finally, using the scaled chirality index, it is possible to determine the contributions of each atom to G_{0S} using

$$
G_{0SA} = G_{0S} - \frac{4!}{N^4}\frac{1}{3}
$$

$$
\times \left\{ \sum_{\substack{\text{all permutations of} \\ i,j,k,l = 1 \cdots \hat{A} \cdots N}} w_i w_j w_k w_l \right.
$$

$$
\left. \times \frac{\left[(\mathbf{r}_{ij} \times \mathbf{r}_{kl}) \times \mathbf{r}_{il}\right](\mathbf{r}_{ij} \times \mathbf{r}_{jk})(\mathbf{r}_{jk} \times \mathbf{r}_{kl})}{\left(r_{ij}r_{jk}r_{kl}\right)^n r_{il}^m} \right\}, \quad (6)
$$

where A is a specific atom in a molecule. Knowledge of the individual atom contributions can help to identify which molecular substructures or terminal groups have the greatest influence on the overall chirality of the molecule.

The HTP of a chiral material is essentially a measure of its ability to rotate incident linearly polarized light as a function of its concentration (if it is dissolved in a LC host material) or as a function of path length (if it is pure LC material). The HTP ($\beta_{\mathbf{M}}$) is defined mathematically as

$$
\beta_{\mathbf{M}} = \left(pc_W r\right)^{-1}, \quad (7)
$$

where p is the pitch length of the chiral medium[39] (the distance needed for polarized light to rotate 360° through the medium), c_W is the weight concentration, and r is the enantiomeric purity of the chiral material. As Eq. (7) shows, a material with a large HTP will be more effective at rotating plane-polarized light at much lower concentrations (or shorter path lengths) than a material with a small HTP. Materials with a large HTP are also more desirable because they can be used in much lower concentrations to achieve an equivalent optical effect, which not only reduces materials and device costs (chiral materials are usually the most expensive component of an LC mixture), but also avoids potential solubility and miscibility problems that occur when higher concentrations of chiral dopants with a small HTP are used.

Recent work by Neal et al.[39] shows a good correlation between HTP and G_{0S}. The correlation between G_{0S} and HTP has also been validated by the research of Osipov and Kuball,[40] which lays the foundation for the relationship between CD and HTP. Circular dichroism is observed when an optically active material absorbs left- and right-hand circular polarized light differently as a function of wavelength. The correlation between G_{0S} and HTP was shown to be applicable only to rigid molecular systems.[39]

For flexible molecules, the scaled chirality index only accounts for one of many possible conformational isomers ("conformer") of a molecule. Thus, in molecules with a high degree of rotational freedom, a new method has been developed to account for a large number of conformers. This method defines a complex chirality parameter χ_0 based on the Connoly[41] surface of a chiral molecule. This parameter, which can be computed very rapidly, has been used most effectively in conjunction with a Monte Carlo simulation.[42] In the simulation, a molecule is moved stepwise into millions of different conformations and the parameter is calculated for each conformer. Through this computationally intensive method, the prediction of HTP has been extended to flexible molecules in a limited number of cases.[43]

In the bulk of the previous literature on scaled chirality index calculations, the weight factor (w_i) is set to 1.0 to create a uniform density distribution. When using this method, it has been shown through the analysis of individual atom contributions that the main contributors to G_{0S} are (1) atoms located at points of steric stress and (2) atoms located a large distance from the molecular core (these are most frequently hydrogen atoms). Only one other weighting method has ever been applied. Solymosi et al.[44] set the weight of each atom equal to its van der Waals volume in their study of ferroelectric LC systems. This weighting method took into account the effect of excluded volume and was appropriate for use in the prediction of spontaneous polarization.

Our approach substituted the atomic mass into the calculation as the weight (w_i = atomic mass), as first suggested by Solymosi et al.[38] To our knowledge, we were the first to use atomic mass as the weighting factor for the chirality index.[41] We hypothesized that the application of atomic mass would negate the effects of distance from the molecular core and enhance the effects of steric stress. Because the atoms at the greatest distance from the core are usually hydrogen and those at points of steric stress are carbon and/or other heavier elements, appropriate weighting was expected to enhance the

accuracy of the chirality index and lead to a greater predictive power for important properties like HTP.

Briefly stated, the calculation of the scaled chirality index involves a series of five steps: (1) The desired molecular structure is created and energy minimized using conventional molecular mechanics computational software. (2) All possible groups of four neighboring atoms within the molecule are selected and used to form the corners of a tetrahedral symmetry element. (3) The edge lengths of each tetrahedron are calculated and put into the chirality index equation to compute the chirality for a given tetrahedral element. (4) Summing all tetrahedral element contributions to the chirality gives the overall chirality index (no contributions from symmetric tetrahedra). (5) A scaling factor is applied to compensate for the variation in the number of tetrahedral symmetry elements as a function of molecular size. In our case, the *actual mass of each atom in every tetrahedral element* is taken into account, yielding the *weighted, scaled chiral index G_{0SW}*.

The effectiveness of the new weighted, scaled chirality index calculation was tested by calculating the HTP for six well-known rigid and flexible chiral molecular systems (binaphthol derivatives, helicenes, chiral steroid esters, phenylpropanoic acid derivatives, and mono- and bis-aminoanthraquinones with chiral substituents)[41] and comparing the calculated data to experimental HTP data from the literature.[45–52] A Pearson correlation of the calculated HTP data to the experimental HTP data was determined for each molecular system and as a global correlation for all systems. The Pearson correlation r is a measure of the fit of a least squares linear regression through the data set. Likewise, the correlation coefficient R^2 describes the proportion of the points that can be accounted for by the linear regression. For rigid molecular systems, the overall correlation was very strong for both the unweighted and weighted chirality indices, as shown by the linear regression fit for the plots of the chiral indices versus the experimental HTP data in Fig. 106.57.[41] Although these molecules are all relatively rigid, the most flexible molecules within the systems appear to have the poorest correlation to experimental HTP data. A close examination of individual atom contributions reveals the benefits that the weighting system was expected to provide: the hydrogen atoms are not large contributors and the effects of steric stress are pronounced. The use of atomic mass predicts HTP more accurately when the experimental HTP is higher than 100 μm^{-1}. In the case of the flexible systems, although the overall correlations were not as strong (as was expected to be the case from previous work by Neal et al.),[39] the use of atomic mass to weight the chirality index did enhance the
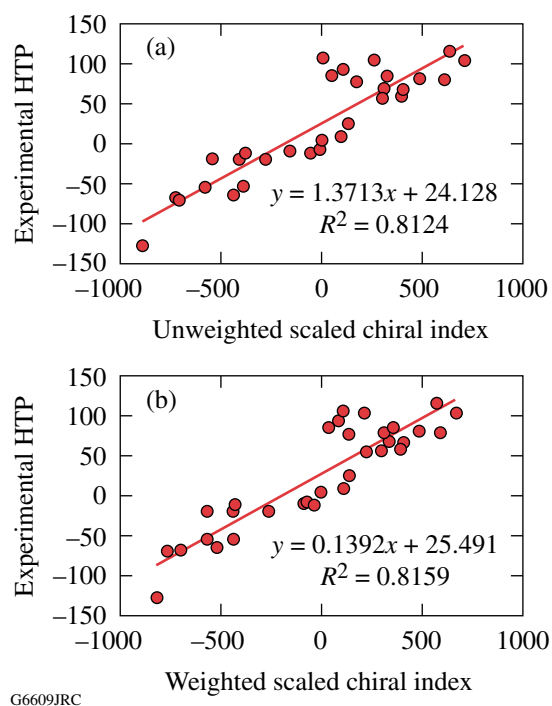
G6609JRC

Figure 106.57
The weighted (a) and unweighted (b) scaled chiral indices of all 32 rigid molecules plotted against the experimental helical twisting power data. A linear regression is used to determine the strength of the correlation. The R^2 value of the weighted index (0.82) is slightly stronger than that of the unweighted index (0.81).

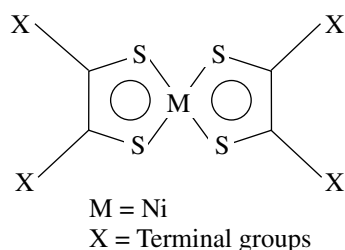quality of the correlation between calculated and experimental results significantly.[41]

With the effectiveness of the new chirality index method now established, we applied it to the calculation of weighted and scaled chirality indices for the enantiomerically enriched nickel dithiolenes described previously in **Enantiomerically Enriched Nickel Dithiolene Complexes** (p. 117) and shown in Table 106.XIII. This chirality index data was then used to calculate the theoretical HTP for each chiral metal complex.[41] The results of these calculations, along with available experimental HTP data, are shown in Table 106.XVI. Each X group can contain 1 to 3 chiral centers for a total of 4 to 12 chiral centers in each molecule. The rigid correlation was used both for the first two compounds where there was no spacer group ($n = 0$) and for all compounds with $n \leq 6$, while the flexible correlation was used for compounds with $n > 6$. For the materials with spacer groups, their low melting points made their purification very difficult and, as a result, sufficient quantities of high-purity materials were not available for experimental determination of the HTP.

Comparison of the calculated HTP values for the compounds in Table 106.XVI that contain a spacer group predicts that for materials with the same terminal X group, the HTP is expected to decrease with increasing spacer length. When the flexible spacer length is nine, the calculated HTP values are all generally the same. There is also good agreement between the calculated and experimental values for HTP in the two compounds with no spacer group, which, to a very limited extent, verifies the predictive capability of the approach. A full assessment of the predictive capabilities of the weighted, scaled chirality index requires isolation and purification, in sufficient quantities, of the remaining chiral nickel dithiolenes in Table 106.XVI for experimental HTP studies. This effort is currently in progress.

Because G_{0S} can fluctuate dramatically on the basis of the lowest energy state of the energy-minimized conformer,

Table 106.XVI: The chiral X groups and helical twisting power data for a series of nickel dithiolene IR dyes.

M = Ni
X = Terminal groups

G6945JR

Terminal group	Experimental solvent	Experimental wavelength (nm)	Calculated wavelength (nm)
X = H	Hexane	720	720.91
X = CH$_3$	CHCl$_3$	774	843.08
X = CF$_3$	Pentane	715	775.05
X = S-C$_4$H$_9$	CHCl$_3$	1104	1012.31
X = C$_6$H$_5$	CHCl$_3$	866	845.19
X = 2-napthyl	CHCl$_3$	905	993.08
X$_1$, X$_4$ = H X$_2$, X$_3$ = C$_6$, H$_5$	CH$_2$Cl$_2$	805	857.78

extreme care must be taken when attempting to use the chirality index as a global predictor for HTP. The high dependence of G_{0S} on the minimum conformer energy state also accounts for the poor correlation of the scaled chirality index for flexible molecules. In this case, the computed energy-minimized conformer structure may not completely represent the actual conformer structure (or structures) that would be most likely to occur in nature. A better method for the prediction of HTP would take into account the many possible conformational geometries of a given molecule when computing the chirality through the use of Monte Carlo simulations.

Another limitation of the scaled chirality index method in its present form is that it is capable of accounting for factors such as temperature or dopant/host interactions only in nematic LC hosts. An improved chirality index that can incorporate both of these factors for other LC hosts would allow for a more accurate correlation, including global correlations between different molecular systems.[53] If the weighted, scaled chirality index method can be combined with a Monte Carlo simulation of geometric conformers (currently limited by processor speed), this enhanced chirality index could significantly increase the efficiency of chiral materials development. The latter point is the focus of our current and ongoing investigations.

Summary

Transition metal dithiolenes offer exciting new research opportunities in both materials chemistry and device applications. These new dyes are highly soluble in LC hosts, possess excellent thermal and photochemical stability, have structure-dependent dichroism, and can show LC mesomorphism on their own with the proper terminal functional groups. These properties, combined with their broad wavelength range, are all valuable attributes for near-IR LC device applications. The addition of enantiomerically enriched terminal groups to the dithiolene core results in a novel family of near-IR dyes that have low melting points (in many cases well below room temperature) and can induce both chirality and optical absorption when added to a nematic LC material. This new class of "liquid chiral dyes" is expected to give rise to a host of application possibilities in areas such as nonlinear optics and sensor protection.

The application of computational chemistry techniques to transition metal dithiolenes as described in this work represents a substantial technical achievement, given the lack of previous research activity in modeling transition metal organic complexes in general. The computational modeling methodology that we have developed was successfully applied to nickel dithiolene systems in the prediction of both the near-IR electronic absorbance spectra and (for enantiomerically enriched materials) the helical twisting power in a host medium. These calculations represent what we believe to be the first of this type attempted for nickel dithiolene systems, or, for that matter, in any other transition metal organometallic complex. With these new computational techniques now in hand, the concept of designing and predicting, prior to synthesis, which structural elements will provide the most promising new transition metal dithiolene complexes for optical and photonics applications now becomes a very realistic objective.

REFERENCES

1. H. Suzuki and G. Hayashi, U.S. Patent No. 4,763,966 (15 July 1985).

2. K. Drexhage and U. Mueller-Westerhoff, U.S. Patent No. 3,743,964 (3 July 1973).

3. J.-F. Bai *et al.*, J. Mater. Chem. **9**, 2419 (1999).

4. C. S. Winter *et al.*, Mol. Cryst. Liq. Cryst. **235**, 181 (1993).

5. H. Tanaka *et al.*, Science **291**, 285 (2001).

6. K. Wang and E. I. Stiefel, Science **291**, 106 (2001).

7. K. L. Marshall and S. D. Jacobs, Mol. Cryst. Liq. Cryst. **159**, 181 (1988).

8. K. L. Marshall, M. J. Guardalben, S. M. Corsello, M. S. Moore, I. A. Lippa, and R. P. Brecker, presented at the 16th Interdisciplinary Laser Science Conference (ILS-XVI), Providence, RI, 22–26 October 2000.

9. U. T. Mueller-Westerhoff *et al.*, Mol. Cryst. Liq. Cryst. Lett. **56**, 249 (1980).

10. K. Ohta *et al.*, Mol. Cryst. Liq. Cryst. **147**, 15 (1987).

11. U. T. Mueller-Westerhoff, B. Vance, and D. I. Yoon, Tetrahedron **47**, 909 (1991).

12. P. Espinet *et al.*, Coord. Chem. Rev. **117**, 215 (1992).

13. U. T. Mueller-Westerhoff and B. Vance, in *Comprehensive Coordination Chemistry: The Synthesis, Reactions, Properties, and Applications of Coordination Compounds*, 1st ed., edited by Sir G. Wilkinson, R. D. Gillard, and J. A. McCleverty (Pergamon Press, Oxford, England, 1987), Vol. 2, pp. 595–631.

14. K. L. Marshall, B. Schudel, and I. A. Lippa, in *Liquid Crystals VII*, edited by I.-C. Khoo (SPIE, Bellingham, WA, 2003), Vol. 5213, pp. 201–212.

15. M. Colvin, Lawrence Livermore National Laboratory, Continuum Models of Solvation, 2000, http://gutenberg.llnl.gov/~colvin/solvation/solv.html (10 January 2000).

16. C. E. A. Wainwright and A. E. Underhill, Mol. Cryst. Liq. Cryst. **234**, 193 (1993).

17. N. Svenstrup *et al.*, Synthesis **8**, 809 (1994).

18. A. Charlton *et al.*, J. Mater. Chem. **4**, 1861 (1994).

19. K. L. Marshall, B. Klehn, B. Watson, and D. W. Griffin, in *Advanced Characterization Techniques for Optics, Semiconductors, and Nanotechnologies*, edited by A. Duparré and B. Singh (SPIE, Bellingham, WA, 2003), Vol. 5188, pp. 48–60.

20. *LLE Review Quarterly Report* **81**, 37, Laboratory for Laser Energetics, University of Rochester, Rochester, NY, LLE Document No. DOE/SF/19460-335 (1999).

21. K. B. Wiberg, *Physical Organic Chemistry* (Wiley, New York, 1964).

22. W. J. Hehre, *A Guide to Molecular Mechanics and Quantum Chemical Calculations* (Wavefunction, Irvine, CA, 2003).

23. W. J. Hehre, *Ab Initio Molecular Orbital Theory* (Wiley, New York, 1986).

24. C. C. J. Roothaan, Rev. Mod. Phys. **23**, 69 (1951).

25. P. M. W. Gill, Aust. J. Chem. **54**, 661 (2001).

26. W. J. Hehre *et al.*, J. Chem. Phys. **52**, 2769 (1973).

27. M. S. Gordon *et al.*, J. Am. Chem. Soc. **100**, 2670 (1978).

28. M. M. Francl *et al.*, J. Chem. Phys. **77**, 3654 (1982).

29. M. Häser and R. Ahlrichs, J. Comput. Chem. **10**, 104 (2004).

30. R. M. Shroll and W. D. Edwards, Int. J. Quantum Chem. **63**, 1037 (1997).

31. E. R. Davidson, J. Comput. Phys. **17**, 87 (1975).

32. H. Zabrodsky and D. Avnir, J. Am. Chem. Soc. **117**, 462 (1995).

33. L. N. Lisetskii, Ukr. Fiz. Zh. **27**, 1321 (1982).

34. G. S. Chilaya and L. N. Lisetski, Mol. Cryst. Liq. Cryst. **140**, 243 (1986).

35. L. A. Batrachenko and L. N. Lisetskii, Zh. Strukt. Khim. **32**, 146 (1991).

36. H. Zabrodsky, S. Peleg, and D. Avnir, J. Am. Chem. Soc. **114**, 7843 (1992).

37. M. A. Osipov, B. T. Pickup, and D. A. Dunmur, Mol. Phys. **84**, 1193 (1995).

38. M. Solymosi *et al.*, J. Chem. Phys. **116**, 9875 (2002).

39. M. P. Neal *et al.*, J. Chem. Phys. **119**, 3567 (2003).

40. M. A. Osipov and H.-G. Kuball, Eur. Phys. J. E **5**, 589 (2001).

41. A. G. Noto and K. L. Marshall, in *Liquid Crystals IX*, edited by I.-C. Khoo (SPIE, Bellingham, WA, 2005), Vol. 5936, pp. 157–163.

42. D. J. Earl and M. R. Wilson, J. Chem. Phys. **120**, 9679 (2004).

43. D. J. Earl, Phys. Rev. E **71**, 021706 (2005).

44. M. Solymosi *et al.*, Ferroelectrics **227**, 169 (2002).

45. N. Ferrarini *et al.*, Liq. Cryst. **24**, 219 (1998).

46. D. J. Earl and M. R. Wilson, J. Chem. Phys. **119**, 10,280 (2003).

47. H.-G. Kuball *et al.*, Mol. Cryst. Liq. Cryst. **352**, 195 (2000).

48. M. J. Cook and M. R. Wilson, J. Chem. Phys. **112**, 1560 (2000).

49. F. Brandenburger *et al.*, Liq. Cryst. **28**, 1035 (2001).

50. Y. Aoki *et al.*, Mol. Cryst. Liq. Cryst. **346**, 35 (2000).

51. Y. Aoki *et al.*, Bull. Chem. Soc. Jpn. **71**, 2219 (2001).

52. H.-G. Kuball *et al.*, J. Mater. Chem. **5**, 2167 (1995).

53. H. Kamberaj *et al.*, Mol. Phys. **102**, 431 (2004).

High-Contrast Plasma-Electrode Pockels Cell (PEPC)

Introduction

Many high-energy laser systems under development for inertial confinement fusion (ICF) use a multipass amplifier architecture.[1,2] A large-aperture optical switch, which is capable of withstanding high fluence, is often utilized in these systems to control the number of passes that a laser pulse makes through the amplifier cavity. Conventional Pockels cells that use ring electrodes cannot be scaled to the large apertures required for ICF lasers. Therefore, the plasma-electrode Pockels cell (PEPC) technology, which uses high-conductivity plasmas as electrodes, was developed at Lawrence Livermore National Laboratory (LLNL) for use in ICF laser systems.[3–6]

Most existing multipass high-energy laser systems use frequency conversion to direct second- or third-harmonic light onto the target. This is not the case, however, for the high-energy petawatt-class laser system that is being constructed on OMEGA EP at the Laboratory for Laser Energetics.[1] In this short-pulse system, the light is not frequency converted before being sent to the target. Any light reflected by the target can therefore experience gain as it propagates back up the system. Because the amplifiers are unsaturated, a retroreflected pulse can experience high gain, posing a significant threat of system damage. Isolation of the amplifier cavity from back-reflected light is, therefore, required on this system.

In addition to the more typical role of holding the pulse in the cavity for four passes, the OMEGA EP PEPC will be used to provide isolation from target retroreflections. This concept is illustrated in Fig. 107.1. Figure 107.1(a) shows a block diagram of a portion of the OMEGA EP Laser System; Fig. 107.1(b) is a timing diagram showing the state of the PEPC switch. The pulse from the laser sources area is injected into the beamline at the transport spatial filter (TSF) at time T and enters the
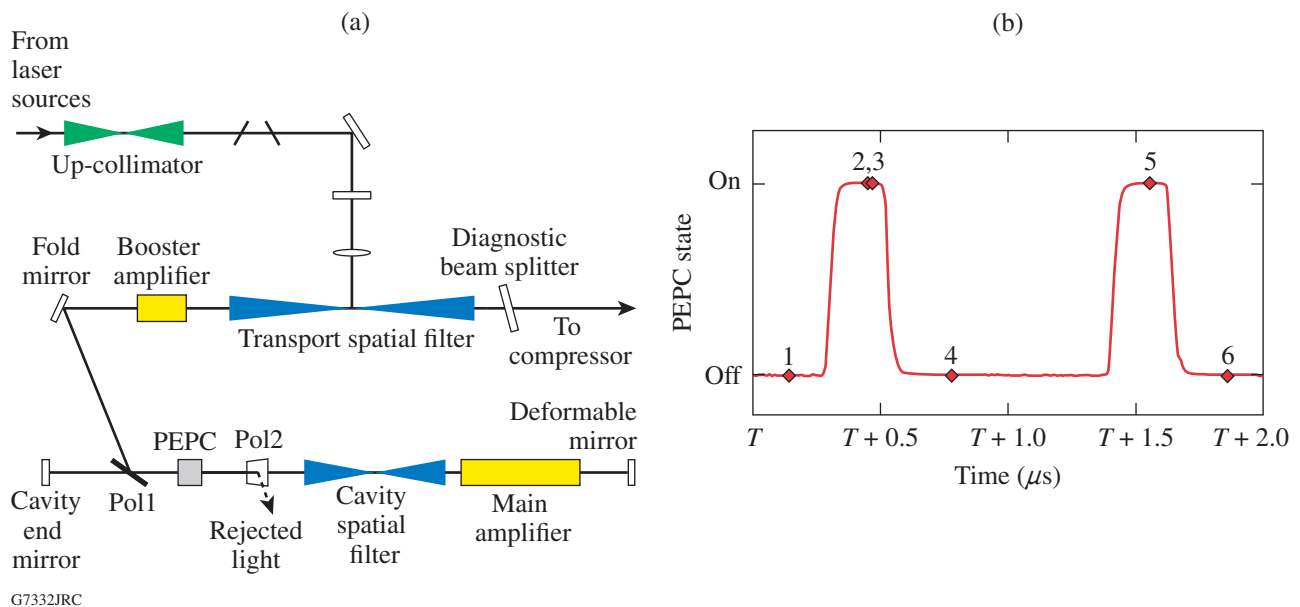
Figure 107.1
(a) Diagram of the OMEGA EP Laser System showing the PEPC in relation to key beamline components. (b) Timing diagram showing the state of the PEPC as a function of time. Times during which the laser pulse passes through the PEPC are highlighted.

amplifier cavity by reflecting from the cavity polarizer. The pulse makes Pass 1 through the PEPC while the PEPC is in its unenergized state. The pulse is amplified by two passes through the main amplifier chain before returning for Pass 2 through the PEPC, which will then be switched to its active state. This allows the laser pulse to remain in the amplifier cavity for two more passes. At Pass 4, the PEPC is again unenergized to couple the pulse out of the amplifier cavity, from which it is transported to the target chamber. Approximately 700 ns later, the retroreflected pulse couples back into the amplifier cavity for Pass 5 through the PEPC. The PEPC must be energized at this time to switch the retroreflected pulse out of the cavity to a beam dump via a polarizer labeled Pol 2 in Fig. 107.1(a). Any residual light that is not switched out of the cavity will be reamplified; therefore, the PEPC must be in the unenergized state upon its return at Pass 6 to ensure that the light is not trapped in the cavity and further amplified.

This new role of providing isolation places greater demands on the switching contrast ratio (the ratio of maximum transmission to minimum transmission of the PEPC between two ideal polarizers). To control the amplified passes through the cavity (Passes 1 through 4), the PEPC is required to provide a contrast of >100:1 averaged over the clear aperture, or >50:1 locally. To provide sufficient isolation on the OMEGA EP system for Passes 5 and 6, however, the PEPC is required to switch with a contrast ratio exceeding 500:1 locally, i.e., at all points in the clear aperture.

This requirement exceeds the performance reported on existing PEPC cells, which are typically limited to approximately 100:1 locally, primarily due to stress-induced birefringence in the vacuum-loaded windows.[5,7] This article describes a redesigned PEPC that achieves a significantly higher contrast. It addresses the development of a window geometry that exhibits low stress-induced birefringence required to increase contrast and presents observations of a PEPC switching contrast ratio that reliably exceeds the 500:1 requirement.

High-Contrast PEPC Design

The prototype PEPC cell, seen in operation in Fig. 107.2, was built to evaluate design concepts for increasing the switching contrast. A cross-sectional sketch of the system (Fig. 107.3) highlights the main features of the PEPC cell. The design was based on the LLNL PEPC in use by the National Ignition Facility (NIF) and was repackaged for use in a single-beam configuration.[7] The main structural components, the two halves of the cell body, are made of aluminum and are anodized to provide a dielectric barrier from the plasma. Sandwiched between the cell
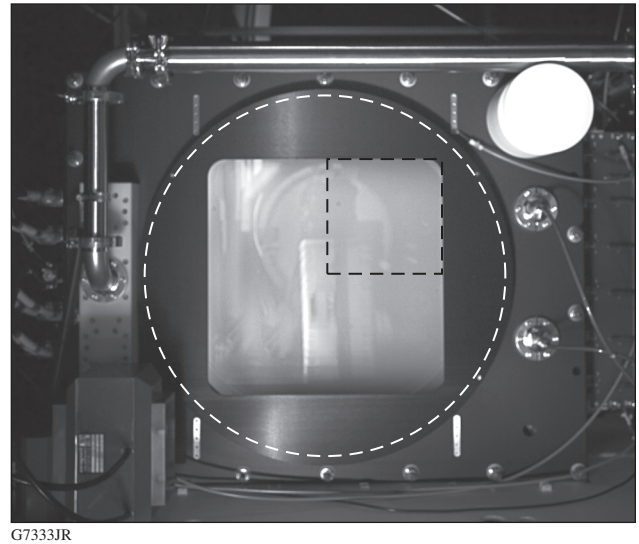

G7333JR

Figure 107.2
Photograph of the prototype PEPC during plasma ignition. The outline of the windows is indicated by the white dashed circle, and the region analyzed by the stress birefringence model is indicated by the black dashed square.

body halves is a glass midplane, with the electro-optic crystal potted in the center using an aerospace silicone epoxy. The electro-optic crystal is a $40 \times 40 \times 1$-cm plate of Z-cut KDP grown via the rapid-growth method at LLNL.[8] Fused-silica windows, which will be discussed in more detail in **Reduction of Window Stress Birefringence** (p. 131), are mounted on the cell body. These windows are circular, as indicated by the white dashed line in Fig. 107.2.

The plasma electrodes are formed in two chambers between the glass midplane and the windows. The cell is evacuated using a turbomolecular pump and back-filled with helium to 80 mT. Graphite electrodes are mounted on either end of the plasma cavity. The anodes are segmented into six button-type electrodes and the cathodes are planar magnetrons. A simmer discharge is initiated by breaking down the gas between the cathode and a nearby starter anode rod. A low-density discharge is maintained across the plasma channel for 450 ms. Near the end of the simmer discharge, a 10-μs, 4-kV pulse is applied, which increases the plasma density to >10^{12} cm^{-3} to create high-conductivity electrodes.[9] When the plasma is in this high-conductivity state, a 250-ns, 18-kV switch pulse applied between the plasmas produces the electric field necessary to impart a half-wave retardance on the 1053-nm incident beam. The electrode size produces a plasma channel that is 8 cm wider than the vertical extent of the clear aperture, thereby mitigating the effects of plasma pinching.[10,11]
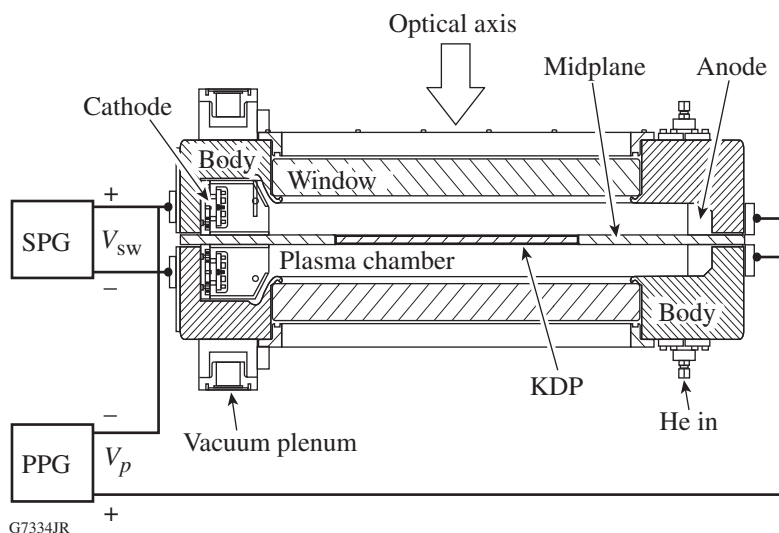
Figure 107.3
Cross-sectional view of the PEPC cell showing the key elements of the PEPC system. SPG denotes the switch pulse generator, and PPG indicates two plasma pulse generators.

Reduction of Window Stress Birefringence

The primary contrast limitation in the NIF PEPC cell design is the stress-induced birefringence in the square windows that form the air-vacuum barrier for the plasma. To achieve the contrast level required for OMEGA EP, it was necessary to understand the root cause of this birefringence. A finite-element analysis (FEA) code (ANSYS) was used to model the stress fields induced in both square windows, such as those used in the LLNL PEPC cells, and the proposed circular windows.

FEA models of the windows were generated using 20-node quadrilateral elements with a resolution in X and Y (the plane parallel with the faces of the window) equal to 10 mm and a resolution in Z equal to 1 mm. Only one quadrant of the window was modeled because of symmetry. To better simulate edge effects, a finer mesh was used near the edges of the window. Each window was assumed to be simply supported on the perimeter of the vacuum face with a uniform pressure applied to the opposite surface. The von Mises stresses were obtained from the model at every point on the sampling mesh. Because it was found that the resulting birefringence asymptotically approached a solution with decreasing step size in Z, these stresses were linearly interpolated in Z to improve the resolution through the thickness of the window.

The Wertheim stress optic law was applied to the FEA results to predict the net birefringence.[12] By modeling the birefringent window between two ideally crossed polarizers, the passive contrast could be predicted at every point. The numerical limit for the passive contrast ratio, limited by the numerical accuracy of the FEA code, was found to be approximately 5000:1. Figure 107.4 shows model predictions for both

a square $430 \times 430 \times 35$-mm fused-silica window used in the LLNL PEPC cells and a 600-mm-diam, 40-mm-thick circular fused-silica window that was used for the LLE PEPC. In Figs. 107.4(a) and 107.4(c), 3-D maps of the magnitudes of the von Mises stresses in one quadrant of the clear aperture are shown, i.e., the region plotted in Fig. 107.4 corresponds to the black dashed square indicated in Fig. 107.2. The corresponding 2-D map of the passive contrast ratio in that same region of the square window is depicted in Fig. 107.4(b). In the case of the circular window, the calculated contrast ratio was beyond the numerical limit, and therefore no corresponding contrast ratio map is shown for this case.

The results show clearly the difference in performance between the square-window geometry and the new circular-window geometry. The model of the square window predicted a concentration of stress near the corner of the clear aperture and a resultant degradation of the contrast ratio in the corners of the clear aperture that has been reported elsewhere.[5,7] In contrast, the calculation for the circular window reveals that the model predicted no measurable degradation of the contrast ratio for this window.

This result cannot be attributed to lower stress in the circular window because the stress in the circular window was nearly 40% higher than in the square window. However, the stress in the circular window possesses a high degree of odd symmetry, with compressive stress on the air side effectively canceling the birefringence arising from the tensile stress on the vacuum side of the window. Therefore, the net birefringence experienced by the laser pulse after propagation through the entire circular window is negligible. The stresses in the square

(a)

0.6   1.7   2.8   3.9   5.0

$\times 10^6$ N/m^2

(b)   Contrast ratio

>5000
3000
1000
500
300
<100

(c)

0.8   2.3   3.8   5.3   6.8
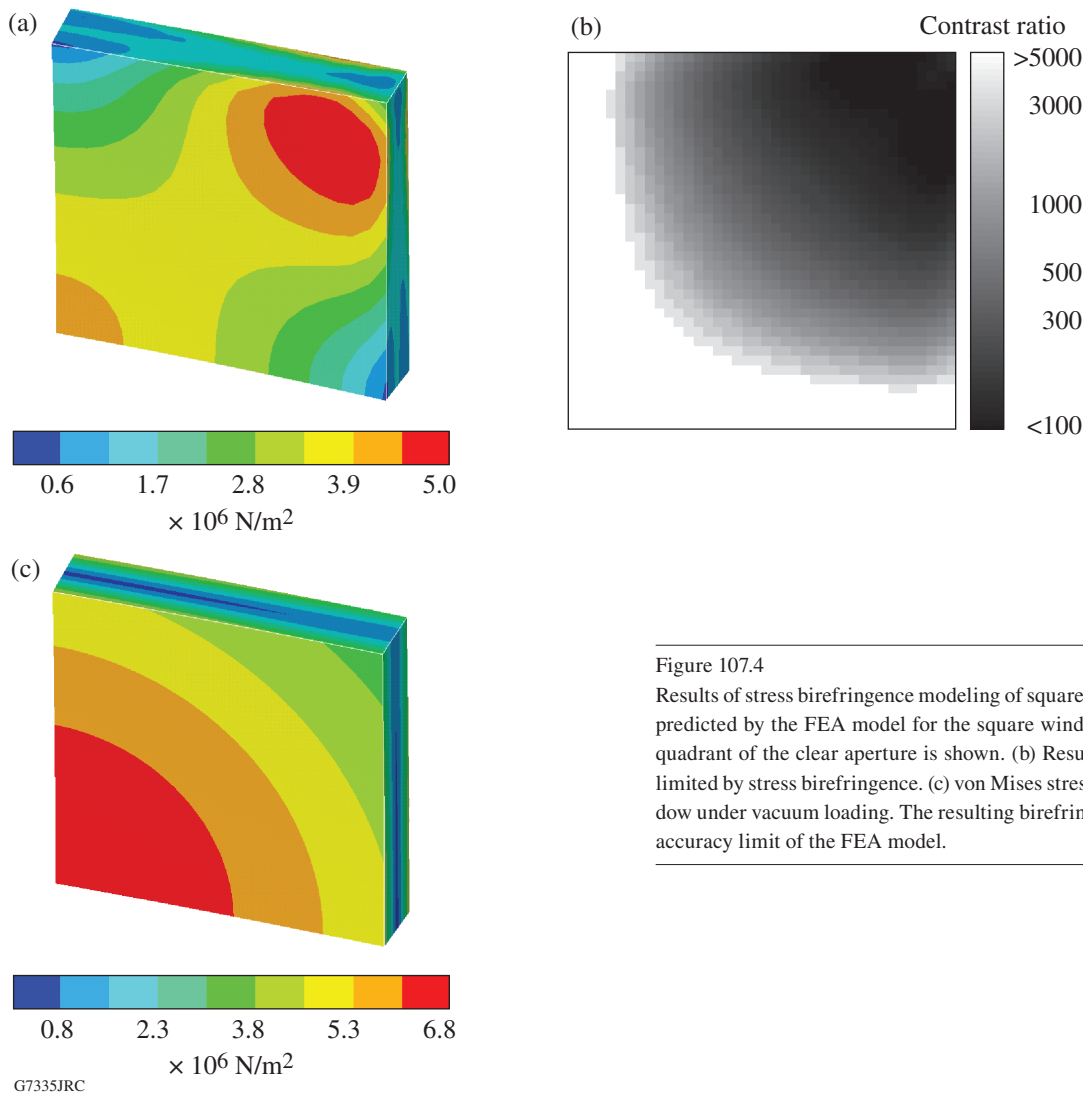
$\times 10^6$ N/m^2

G7335JRC

Figure 107.4

Results of stress birefringence modeling of square windows. (a) von Mises stresses predicted by the FEA model for the square window under vacuum loading. One quadrant of the clear aperture is shown. (b) Resulting predicted contrast ratio as limited by stress birefringence. (c) von Mises stresses predicted for a circular window under vacuum loading. The resulting birefringence was within the numerical accuracy limit of the FEA model.

window lack this degree of symmetry near the corners, where a significant retardation results. By the same logic, the result would not be expected to be significantly affected by the slightly higher thickness of the circular window, as was verified numerically.

Experimental Apparatus and Results

In this section, the characterization of the PEPC performance, the experimental testing apparatus, and a time-resolved polarimeter using a full-aperture beam is described, and the performance measured on the system is presented.

1. Full-Aperture Time-Resolved Polarimeter

The switching contrast of the PEPC was measured using the polarimeter system sketched in Fig. 107.5. A Q-switched Nd:YLF laser provided laser pulses that were sufficiently short (<30 ns) to adequately sample the 200-ns switch pulses. The Gaussian beam was made uniform by a refractive top-hat generator, then expanded to approximately a diameter of 20 mm. A photodiode monitored the laser pulse energy and a prepolarizer fine-tuned the incident polarization to be aligned to the KDP crystal. A reflective beam expander featuring a pair of parabolic mirrors expanded the beam to a diameter of 60 cm and directed it toward the PEPC aperture.

The PEPC was mounted on a structure that allowed adjustment to the tip and tilt angles. This allowed a conoscopic alignment technique to be used to align the PEPC crystal axis to the illuminating beam.[13] The structure also allowed horizontal translation of the entire PEPC cell and enabled measurement of the obscured region.
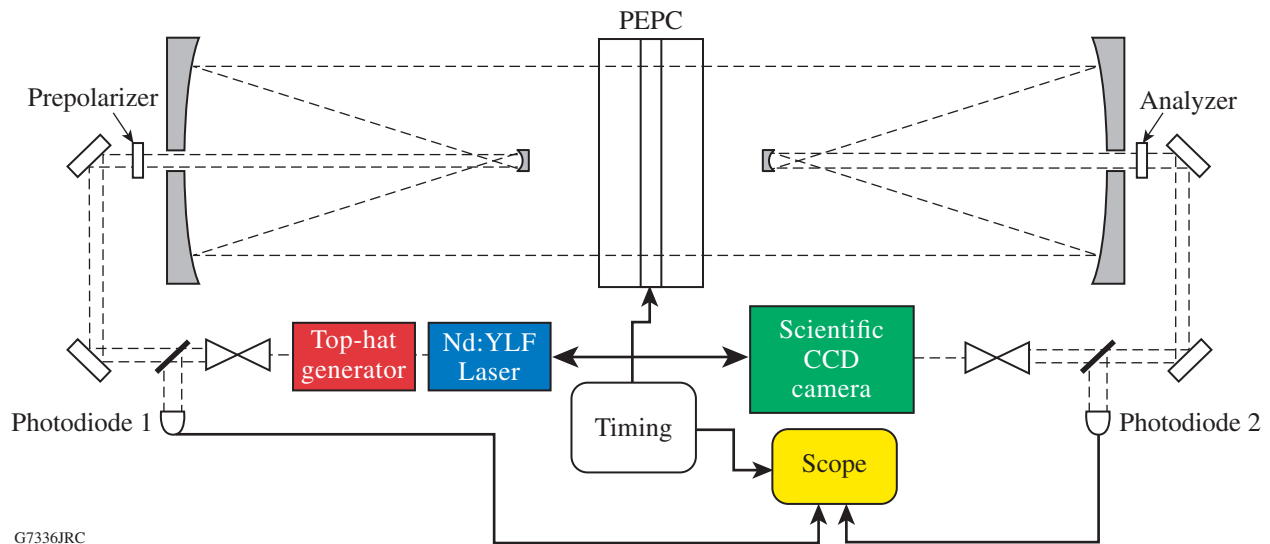
Figure 107.5
Diagram of the full-aperture polarimeter system used to test the PEPC performance.

The transmitted beam was down-collimated using an identical reflective beam expander and then passed through an analyzing polarizer. A beam sampler reflected a portion of the beam to a second photodiode. An image of the PEPC aperture was formed from the remaining beam onto a cooled 16-bit scientific CCD camera.

The laser was synchronously pulsed with the PEPC switch pulse using timing signals generated by a pulse generator. The timing system was also used to trigger an oscilloscope to capture waveform data from the photodiodes. The photodiode signals were used to measure the spatially averaged contrast over the full aperture, and the image data from the CCD camera were used to measure the contrast locally.

The contrast-ratio measurement proceeded by measuring the transmitted pulse energy with the system in a high-transmission state (or bright state) and repeating this measurement with the system in a low-transmission (dark) state. The ratio of the measurements (with background subtracted from the camera data) formed the switching contrast. To increase the dynamic range of the measurement, calibrated neutral-density filters were inserted for the bright measurements to avoid saturating the sensors while using an illumination level that would provide a measurable signal for the dark measurements. Locally, the contrast-ratio measurement is limited by the Polarcor polarizers to >10,000:1, with the minima occurring in two opposing corners of the clear aperture. Averaged over the full aperture,

contrast ratios exceeding 30,000:1 can be reliably measured. Figure 107.6 shows a local contrast map produced with no PEPC cell in the system and illustrates the measurement limit of the system. The obscuration in the center of the contrast map is due to the mounts for the two secondary mirrors.

2. Passive Contrast Results

Passive contrast measurements were conducted to assess performance limits imposed by birefringence in the PEPC windows and imperfections in the KDP crystal. They were first performed with the cell at atmospheric pressure to assess any inherent birefringence caused by dislocations in the KDP crystal or by mounting-induced stress in the fused-silica windows. The resulting contrast map is shown in Fig. 107.7(a). The minimum contrast ratio in this unloaded condition was approximately 2500:1, corresponding to a region of the window that was slightly stressed due to the window mounting. The full-aperture contrast ratio, measured using the photodiodes, was 19,800:1±1800:1, the error range being one standard deviation. Thus, the combined effects of window-mounting stress and KDP crystal imperfections were sufficiently low to achieve a local minimum contrast ratio well in excess of 1000:1.

The vacuum-loaded condition was then tested by evacuating the cell to below 100 mT and measuring the passive contrast in the same manner. The result of this measurement is shown in the contrast map in Fig. 107.7(b). In the vacuum-loaded condition, the minimum contrast ratio dropped only to ~2000:1 and
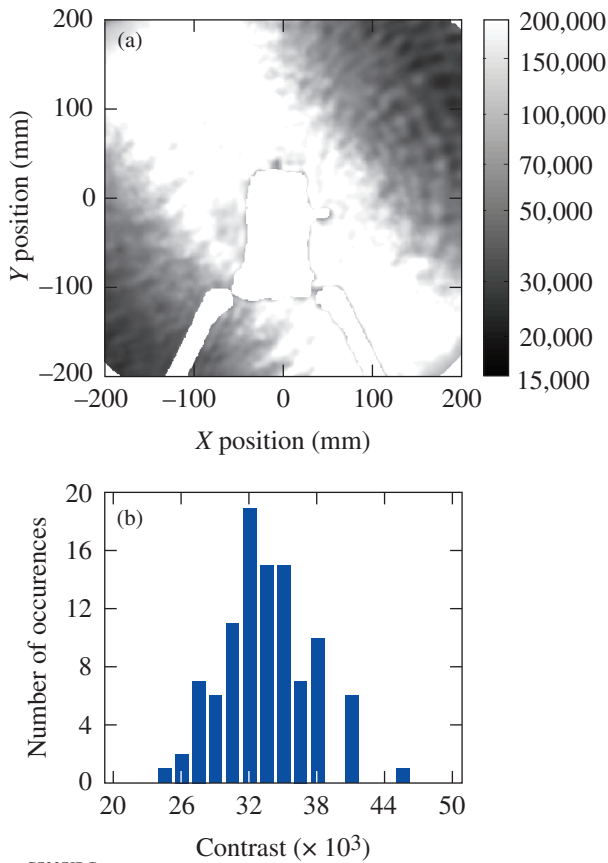
G7337JRC

Figure 107.6
Baseline passive contrast-ratio measurements performed without the PEPC cell introduced into the polarimeter, indicating the maximum measurable contrast ratio. (a) Local contrast map obtained from image data. (b) Histogram of full-aperture contrast measurements obtained from photodiode data.
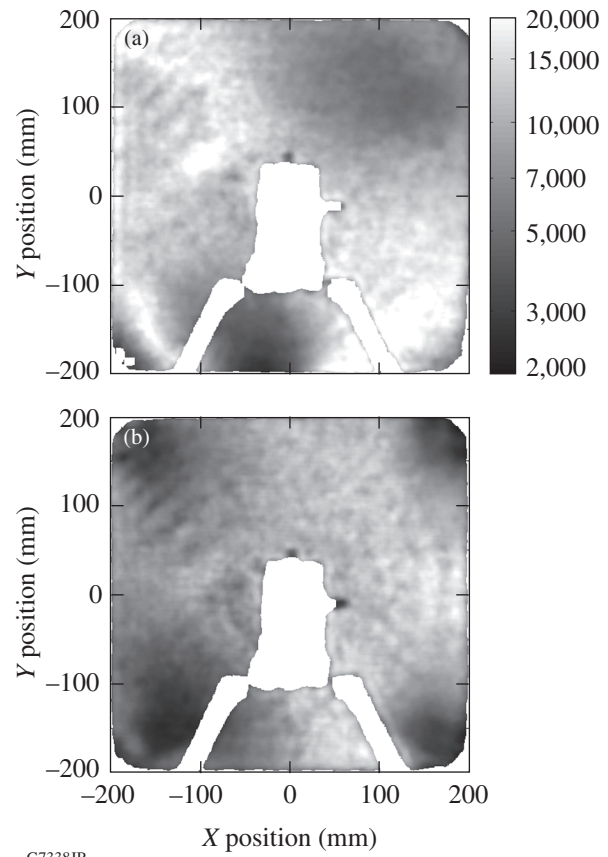

G7338JR

Figure 107.7
Passive contrast-ratio measurements performed with the PEPC cell in the polarimeter: (a) PEPC cell at atmosphere and (b) PEPC cell pumped down to <100 mT.

the full-aperture contrast was 20,400:1±1800:1. Some stress birefringence is evident, leading to a somewhat suppressed contrast ratio near the corners. The birefringence is low enough, however, to allow switching contrast well in excess of our contrast ratio requirement of >500:1.

It should be noted that in addition to using circular windows, certain other conditions are necessary to achieve this result. One requirement is that the window must be fully supported on compliant O rings. O rings are used to provide a vacuum seal around the windows and rest inside dovetail O-ring glands in the aluminum cell body. If the cross-section diameter of the O-ring material is too small, such that the O ring fully compresses into the gland under the vacuum load, the window comes into direct contact with the aluminum cell body and local stresses are formed that severely degrade the contrast ratio. This problem was alleviated by using an O ring with a sufficient diameter to

overfill the O-ring gland under vacuum loading, resulting in the window floating on top of the O ring.

3. Active Contrast Results

To assess the active-switching performance for isolating the target retroreflection at Pass 5, the prepolarizer and analyzer were aligned to each other and the laser pulse synchronized to arrive during the middle of the PEPC switch pulse [i.e., Pass 5 in Fig. 107.1(b)]. Bright-state images were obtained by setting the switch voltage to 0 V, and dark-state images were obtained with the switch voltage set to the half-wave voltage.

Figure 107.8 shows contrast results measured using this method. The surface map was generated by averaging 20 measurements acquired with the cell in three different horizontal positions. A mosaic of the three local contrast-ratio measurements was formed to minimize the obscuration from the sec-
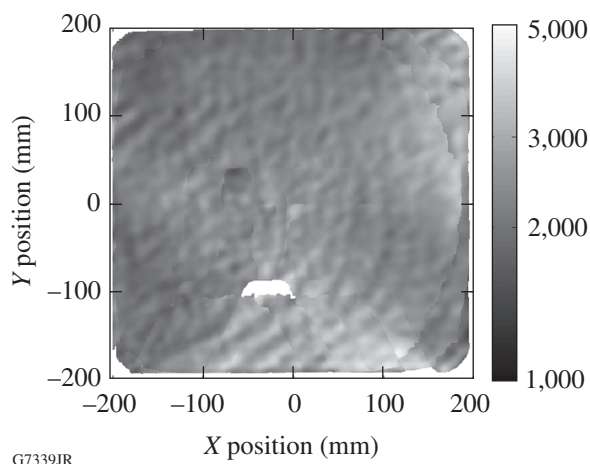
134

G7339JR

Figure 107.8
Map of the Pass-5 active contrast ratio measured over the clear aperture of the PEPC cell. The map was generated by overlapping three sequences of measurements with the PEPC cell in different positions laterally, thus minimizing the obscuration due to the secondary mirror mount.

ondary mirror mounts. The minimum contrast was 1390:1 in the averaged measurement, with the minimum occurring at the upper left-hand corner of the plot (corresponding to the top of the cathode side of the cell). Measuring the minimum contrast in each individual shot, the result was $\langle C_{\min} \rangle$ = 1130:1±170:1. Both means of evaluating the results indicate that the 500:1 minimum contrast specification was comfortably exceeded. Over the full aperture, the contrast was 2280:1±150:1 as measured with the photodiodes.

The switching contrast corresponding to Pass 6 was also measured by setting the analyzer to the crossed position with respect to the prepolarizer for the dark-state measurements. The laser pulse timing was delayed relative to the Pass-5 measurements by 300 ns, which is the propagation time of the laser pulse from the PEPC to the deformable mirror and back into the OMEGA EP beamline. This delay places the laser pulse after the falling edge of the switch pulse, as required [see Pass 6 in Fig. 107.1(b)]. Bright-state measurements were acquired by aligning the analyzer to the prepolarizer and turning the PEPC off. The local minimum for the Pass-6 switching contrast ratio was 1010:1 based on an average of 20 measurements. The single-shot minimum contrast ratio was $\langle C_{\min} \rangle$ = 1210:1±720:1. The shot-to-shot variability was higher in this experiment due to variations in the overshoot at the end of the switch pulse shape. All measured shots, however, did meet the required 500:1 specification.

4. Reliability

Having demonstrated high-contrast switching performance from the PEPC, the reliability of the system was investigated. Poor contrast during a high-energy shot presents a significant risk to system safety, and thus the PEPC must meet its contrast specification reliably.

The primary cause of intermittent failures was observed to be plasma pinching, which causes a narrow region of poor switching contrast at the top or bottom of the aperture. The frequency of this occurrence was found to be strongly dependent on the operating pressure of the cell. Figure 107.9 shows the probability of a low-contrast fringe, derived from measurements of a series of 100 PEPC shots taken at various operating pressures. The probability of a low-contrast fringe decreases exponentially with pressure, becoming negligible beyond ~70 mT. Using a gated-image intensifier, the plasma discharge during the switch pulse was observed over the range of operating pressures shown in Fig. 107.9. At low pressures (below ~40 mT), the discharge was observed to occur only along a narrow strip in the clear aperture. With increasing cell pressure, the plasma spread, eventually filling the clear aperture; on the basis of this, 80 mT was selected as the standard operating pressure.

The reliability of the cell was tested by operating the PEPC for a full day and measuring the contrast throughout the day. Figure 107.10(a) shows the results of an all-day test simulating the use conditions in OMEGA EP in which the PEPC cell
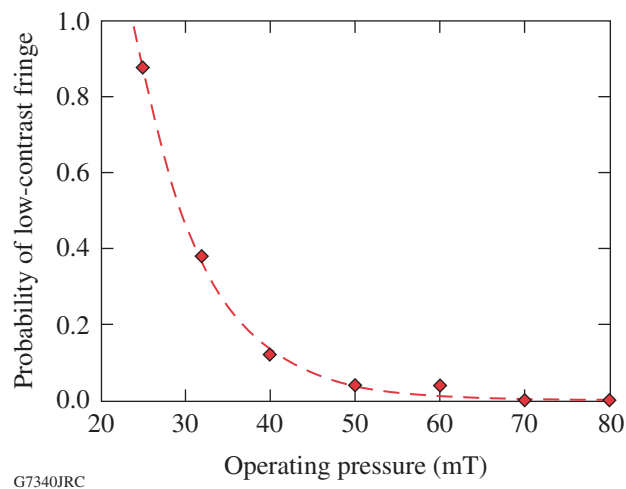

G7340JRC

Figure 107.9
Measured probability of a low-contrast fringe occurring due to locally poor plasma conductivity, as a function of operating pressure.
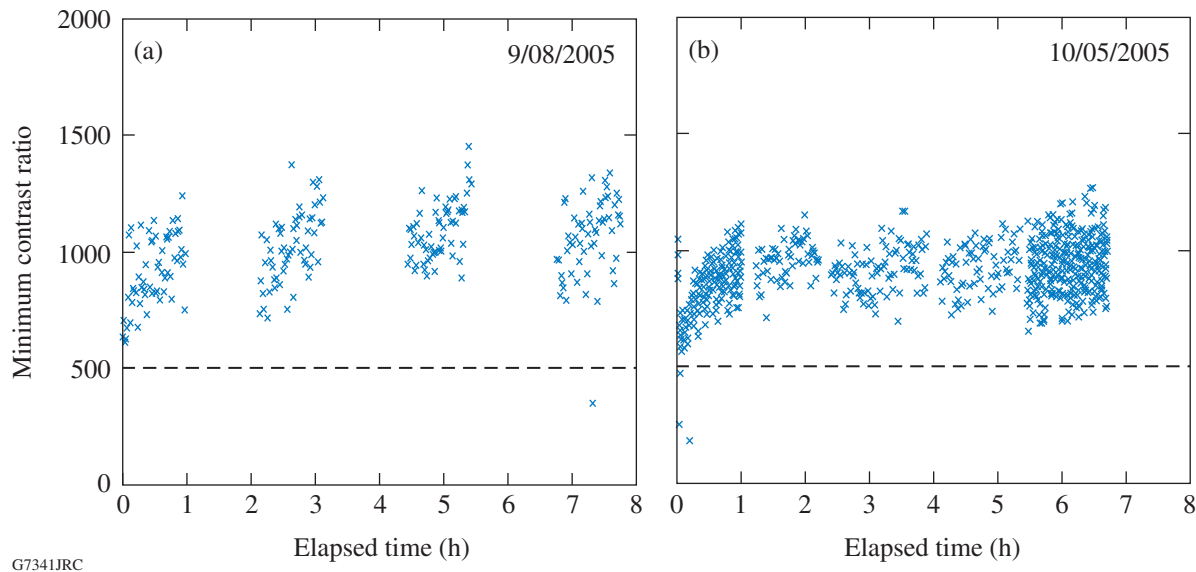
Figure 107.10
Plots of minimum local contrast ratio for individual shots during extended testing over >6 h. (a) 1-h on/off use conditions simulated and (b) PEPC run nearly continuously.

may be operated at a 1/10-Hz pulse rate for 1-h-long intervals every 2 h. In this test, the contrast was measured once per minute, although the PEPC was fired every 10 s. Of the 240 measurements that were taken during that time, one shot had a low-contrast region along the bottom edge of the clear aperture because of plasma nonuniformity. The test was repeated for continuous operation over a full day, with the results shown in Fig. 107.10(b). Images were acquired every 10 s for the first and last hours, and at 1-min intervals in between. After a 20-min warm-up period, poor shots were not observed in this test—out of over 900 measurements.

Discussion

The OMEGA EP PEPC system prototype has demonstrated that high-switching contrasts exceeding 500:1 throughout the clear aperture are obtainable using PEPC technology. The key has been the reduction of stress birefringence using circular windows. When high packing densities are required, i.e., for laser systems with a large number of closely spaced beamlines, circular windows are not feasible. This is an effective solution for systems like OMEGA EP, however, with a small number of beamlines separated by a few meters.

Work is now under way on high-contrast PEPC's for the OMEGA EP beamlines, which are currently in the integration stage. This high-contrast PEPC technology will be deployed shortly into the OMEGA EP beamlines and will provide switching and retroreflection protection for future experimental campaigns using the laser system.

REFERENCES

1. L. J. Waxer, D. N. Maywar, J. H. Kelly, T. J. Kessler, B. E. Kruschwitz, S. J. Loucks, R. L. McCrory, D. D. Meyerhofer, S. F. B. Morse, C. Stoeckl, and J. D. Zuegel, Opt. Photonics News **16**, 30 (2005).

2. G. H. Miller, E. I. Moses, and C. R. Wuest, Opt. Eng. **43**, 2841 (2004).

3. J. Goldhar and M. A. Henesian, Opt. Lett. **9**, 73 (1984).

4. M. A. Henesian and J. Goldhar, Opt. Lett. **9**, 516 (1984).

5. M. A. Rhodes *et al.*, Appl. Opt. **34**, 5312 (1995).

6. R. Bailly-Salins, C. Sudres, and J.-P. Marret, in *Third International Conference on Solid State Lasers for Application to Inertial Confinement Fusion*, edited by H. Lowdermilk (SPIE, Bellingham, WA, 1999), Vol. 3492, pp. 148–155.

7. M. A. Rhodes, S. Fochs, and P. Biltoft, Fusion Technol. **32**, 1113 (1998).

8. N. P. Zaitseva *et al.*, J. Cryst. Growth **180**, 255 (1997).

9. C. D. Boley and M. A. Rhodes, IEEE Trans. Plasma Sci. **27**, 713 (1999).

10. C. D. Boley and M. A. Rhodes, in *Solid State Lasers for Application to Inertial Confinement Fusion: Second Annual International Conference*, edited by M. L. Andre (SPIE, Bellingham, WA, 1997), Vol. 3047, pp. 672–679.

11. S. N. Fochs, M. A. Rhodes, and C. D. Boley, in *Solid State Lasers for Application to Inertial Confinement Fusion: Second Annual International Conference*, edited by M. L. Andre (SPIE, Bellingham, WA, 1997), Vol. 3047, pp. 680–691.

12. M. G. Wertheim, Comptes. Rendus Acad. Sci. Fr. **32**, 289 (1851).

13. M. J. Guardalben, Engineering and Laboratory Notes, Opt. Photonics News (Supplement), **8** (1997).

Absolute Calibration of Kodak Biomax-MS Film Response to X Rays in the 1.5- to 8-keV Energy Range

Introduction

X-ray film is in common use for recording the absolute x-ray fluence in high-temperature plasma experiments. The typical energy range is 1 to 10 keV, where imaging of plasma x-ray emission and spectroscopy of ionic species are often performed. Film finds use in laser-generated plasma x-ray diagnostics and in a number of related plasma-fusion-energy research fields such as in *x*-pinch, *z*-pinch, and magnetic-fusion-energy research. While directly exposed x-ray film cannot be used to time resolve the intensity of x rays, it can often be used where other means of image recording cannot.

An example of such a calibrated x-ray film is Kodak direct-exposure film (DEF).[1] DEF film was absolutely calibrated[2] in the 1- to 10-keV energy range. The results were fitted to a semi-empirical mathematical model of the film as described by Henke *et al.*[3] and extended to DEF film,[2] which has two emulsion layers (one on each side). Kodak has ceased production of DEF film, and absolute calibration of a suitable replacement is needed for the eventual time when the supplies of existing DEF are exhausted. The absolute calibration of a Kodak replacement film, Biomax-MS (BMS), now in production, is the subject of this work. The measurements were taken in the x-ray laboratory at the Laboratory for Laser Energetics. Also, comparative measurements of BMS to DEF film sensitivity were taken on the OMEGA laser facility[4] and are compared to the results of Chandler *et al.*[5]

Experimental Technique

Film calibration was accomplished with an e-beam–generated x-ray source, a crystal/multilayer monochromator, a film pack, and an absolutely calibrated x-ray photon detector. The apparatus is shown schematically in Fig. 107.11. X rays are produced in a vacuum system with the e-beam striking the desired target. The beam passes outside the vacuum system through a thin Be window (8.5 μm thick) after which the remaining path of the beam is through He gas at just over 1 atm. This minimizes beam absorption. A monochromatic beam of x rays is produced by placing a crystal or multilayer diffractor in the path of the beam with the angle of incidence equal to

the Bragg angle θ_B for the wavelength desired and the detector (film or photon counter) set to the angle $2\theta_B$. The line energies produced by this method and the corresponding monochromators and angles used to produce the monochromatic beam are given in Table 107.I.

The x-ray source intensity is measured with a liquid-nitrogen–cooled, lithium-drifted silicon Si(Li) detector[6] read out with a pulse-height analyzer. An aperture of precisely measured dimensions (4.99±0.01 by 0.47±0.01 mm, 2.35±0.06 mm^2) is placed over the entrance window of the photon detector, allowing the photon flux density to be calculated from the count rate. Since the beam is truly monochromatic, all counts above the
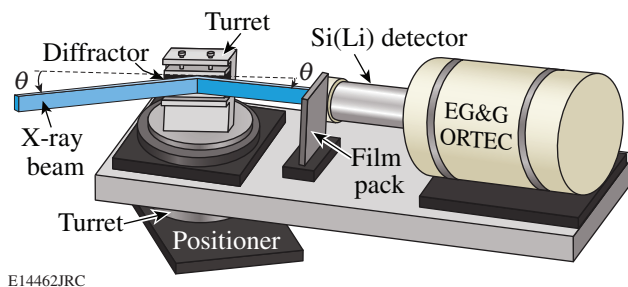
E14462JRC

Figure 107.11
Schematic of the experimental arrangement used to calibrate Biomax-MS (BMS) film.

Table 107.I: Atomic line, line energy, monochromators, Bragg plane spacing (2*d*), and Bragg angles used for these measurements.

Line	Energy (keV)	Monochromator	2*d* (Å)	θ_{Bragg} (°)
Al Kα	1.49	WB$_4$C	26.300	18.44
Ag Lα	2.98	WB$_4$C	26.300	9.10
Ti Kα	4.51	LiF(200)	4.027	43.06
Fe Kα	6.40	LiF(200)	4.027	28.76
Cu Kα	8.04	LiF(200)	4.027	22.49

noise threshold are included. Background is negligible. During film exposures, the beam intensity is measured before and at the end of the exposure. The fluence on film is determined from the average count rate and the fluence error determined from the pre- and post-exposure beam-intensity variation. Exposure times varied from as little as 2 min to as long as 3.7 h for the highest energy and density.

Film was developed by the standard method recommended by Kodak,[7] common to both DEF and BMS. The test exposures were digitized with a calibrated PerkinElmer microdensitometer (PDS) using a 0.25-numerical-aperture (NA) lens and a $50 \times 50\text{-}\mu\text{m}$ digitizing aperture.

Absolute Measurements

A typical exposure on film is shown in Fig. 107.12(a). The exposed region of the film was limited to an image of the x-ray beam's exit aperture (nominally 1×7 mm). Figure 107.12(b) shows a lineout across the PDS digitized region. The photon detector measurements were taken in the central 0.5×5-mm region, and the average density was inferred from a similar-sized region of the digitized density values. The horizontal gradient of the film density is due solely to the aperture, while no vertical gradient was seen in the exposures. The results of the exposures are shown in Figs. 107.13(a)–107.13(e). The DEF and BMS densities are plotted as a function of the incident fluence for the five x-ray energies used in this work [no DEF exposure was taken using Al $K\alpha$ (1.49 keV)]. The expected DEF density values determined from the Henke model[2] are shown with dashed lines. In general, the measured DEF density values agree well with those calculated from the model, although the
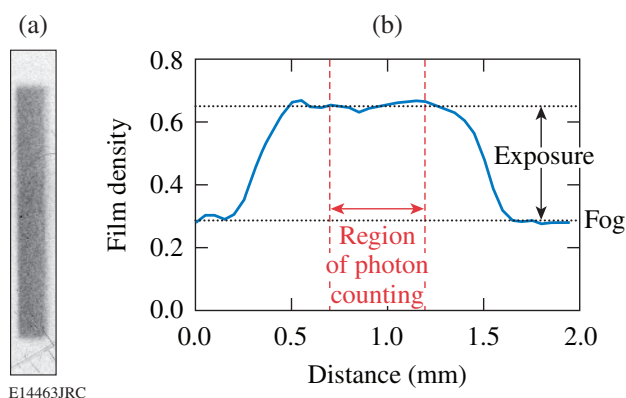
measurements are systematically lower. This is likely due to the age of the film, which has an average fog level of ~0.5, considerably higher than that of fresh film (~0.25). This can lower the film's sensitivity.

The Henke model values are used as a basis to determine the relative sensitivity of BMS film to DEF film. At Al $K\alpha$ (1.49 keV) and Ag $L\alpha$ (2.98 keV) the sensitivities are comparable. The sensitivity of BMS drops farther compared to DEF at higher energies and is considerably lower (~2× less sensitive) at the highest energy measured [Cu $K\alpha$ (8.04 keV)]. This is a consequence of the choice of emulsion (two thin emulsion layers, one on each side of the film[8]) and is expected. The BMS measured densities versus photon fluence and energy are used to determine the best-fit parameters of a mathematical model of the film response, given in a companion article in this issue (**Response Model for Kodak Biomax-MS Film to X Rays**, p. 142).[8] The results of this model fitting are shown with solid lines in Figs. 107.13(a)–107.13(e).

Comparative Measurements

Simultaneous measurements over the energy range from ~2 keV to 8 keV were obtained by placing DEF and BMS film at the image planes of two images of a four-image Kirkpatrick–Baez (KB) microscope system,[9] which uses a transmission grating for wavelength (equivalently energy) dispersion.[10] The image magnification was 20 and the wavelength dispersion was 0.586 Å/mm. Figures 107.14(a) and 107.14(b) show images obtained with DEF and BMS film on an experiment performed with the 60-beam OMEGA Laser System.[4] The laser target was a 15-atm-D_2-filled, 27-μm-thick-plastic-shell target imploded with 23 kJ of 351-nm laser light using a 1-ns square pulse shape. The grating-dispersed emission from the intense core region is indicated with arrows on the DEF-recorded image [Fig. 107.14(a)]. The exposure levels obtained with BMS film on the same target experiment [Fig. 107.14(b)] are significantly lower. The sensitivity of the two films is compared by using the known grating dispersion of this system to determine the film density as a function of energy, and by the assumption that the two imaging systems are identical. Figure 107.14(c) shows the DEF and BMS film-density energy spectra obtained from the images shown in Figs. 107.14(a) and 107.14(b). The density obtained with BMS film is seen to be significantly less than that obtained with DEF film above ~3 keV.

(a)   (b)

E14463JRC

Figure 107.12
Typical exposure on (a) BMS film and (b) lineout through digitized density values. The exposure is determined by subtracting the fog level from the observed density.
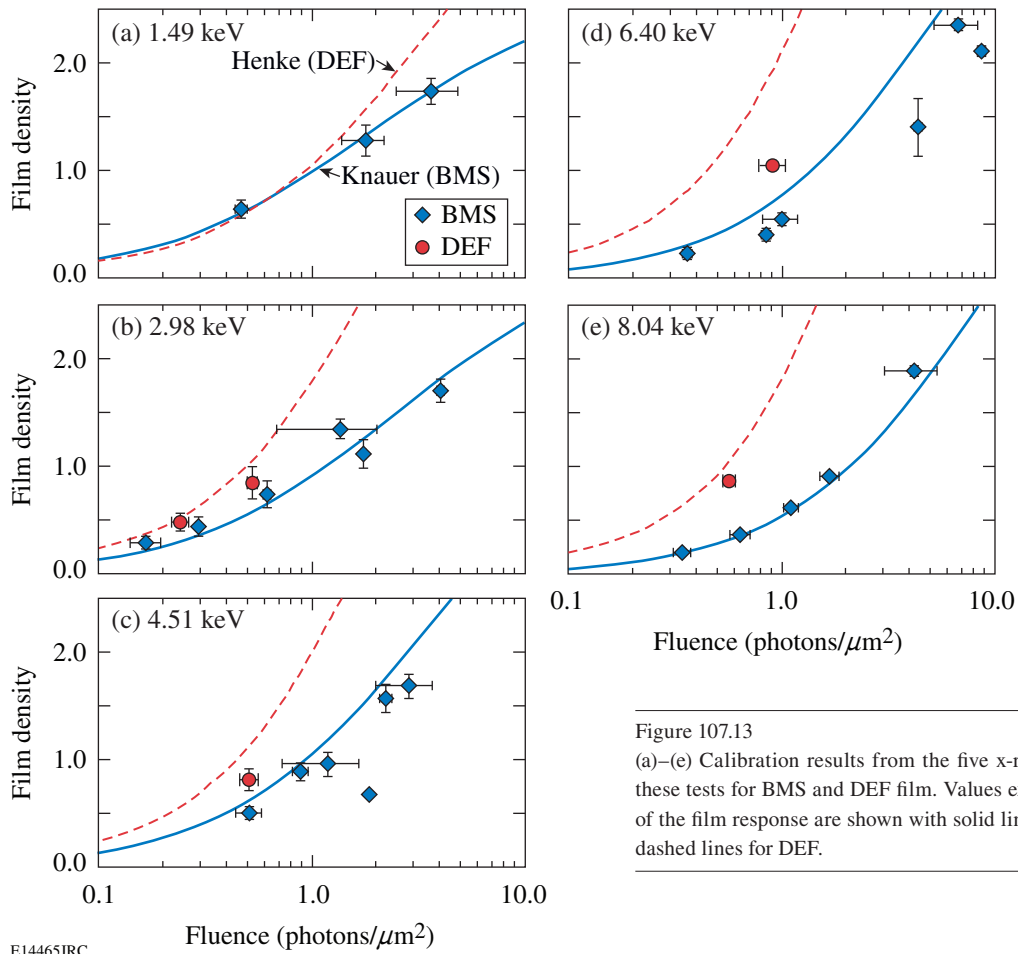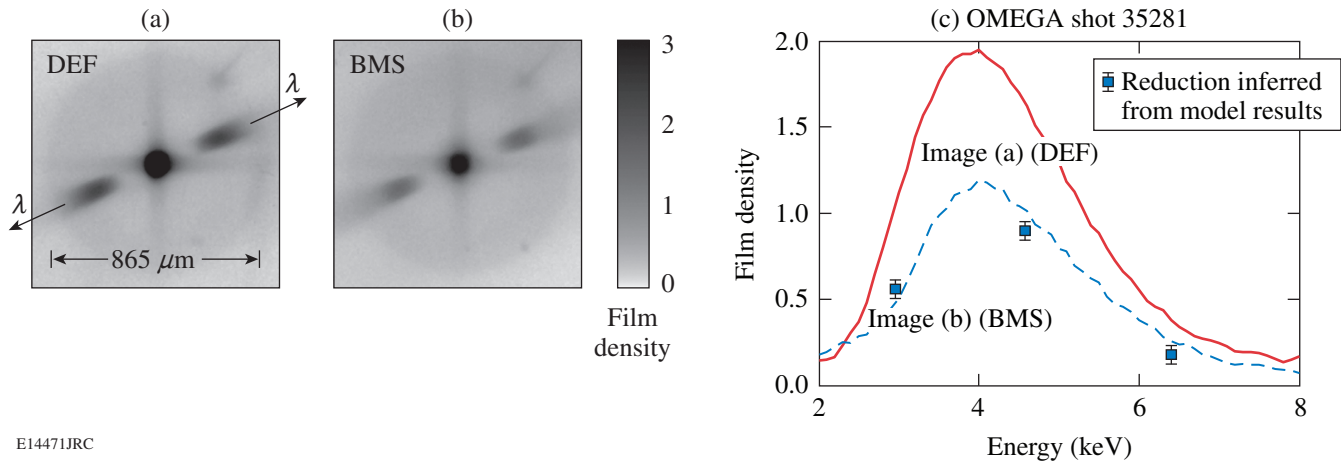
Comparison of these results with the absolute measurements presented earlier is accomplished with the two mathematical models. The Henke et al.[2] model of DEF response [dashed lines in Figs. 107.13(a)–107.13(e)] is used to determine the

E14465JRC

Figure 107.13
(a)–(e) Calibration results from the five x-ray energies used for these tests for BMS and DEF film. Values expected from models of the film response are shown with solid lines for BMS film and dashed lines for DEF.

E14471JRC

Figure 107.14
Comparison of DEF and BMS film response determined by two images taken with a grating-dispersed KB microscope on a single OMEGA target shot. (a) DEF-recorded image; (b) BMS-recorded image; (c) film-density/energy spectra from DEF and BMS determined from (a) and (b).

corresponding fluence, and the Knauer *et al.*[8] model is used to calculate the values expected for BMS film. The values determined for 2.98, 4.51, and 6.40 keV are shown as data points in Fig. 107.14(c). The error bars represent uncertainty in the film-density values of ±0.05. The inferred density values are in close agreement with the BMS-measured film-density spectrum at all three energies. The BMS density is less than the DEF density by approximately a factor of 2 above 3 keV. Chandler *et al.*[5] have made similar comparative measurements of DEF and BMS film using a spectrometer and x rays from an *x*-pinch source. They find an asymptotic BMS to DEF density ratio of ~0.55 at the high-energy limit of their measurements (3 to 6 keV). This is in good agreement with both the absolute measurements and comparative measurements presented in this work.

ACKNOWLEDGMENT

REFERENCES

1. Kodak DEF film was manufactured by the Eastman Kodak Company, Rochester, NY 14650.

2. B. L. Henke *et al.*, J. Opt. Soc. Am. B **3**, 1540 (1986).

3. B. L. Henke *et al.*, J. Opt. Soc. Am. B **1**, 818 (1984).

4. T. R. Boehly, D. L. Brown, R. S. Craxton, R. L. Keck, J. P. Knauer, J. H. Kelly, T. J. Kessler, S. A. Kumpan, S. J. Loucks, S. A. Letzring, F. J. Marshall, R. L. McCrory, S. F. B. Morse, W. Seka, J. M. Soures, and C. P. Verdon, Opt. Commun. **133**, 495 (1997).

5. K. M. Chandler, S. A. Pikuz, T. A. Shelkovenko, M. D. Mitchell, D. A. Hammer, and J. P. Knauer, Rev. Sci. Instrum. **76**, 113111 (2005).

6. An ORTEC Poptop Si(Li) detector was used for these calibrations: Model #1019P, S/N 303-T7076 with bias set to 1000 V negative as per manufacturer's calibration instructions.

7. DEF and BMS film was developed in an auto film processor using gentle agitation as follows: 5 min in Kodak GBX developer, 30 s in stop bath, and 6 min in fixer. A post rinse in photoflo and water followed.

8. J. P. Knauer, F. J. Marshall, B. Yaakobi, D. Anderson, B. A. Schmitt, K. M. Chandler, S. A. Pikuz, T. A. Shelkovenko, M. D. Mitchell, and D. A. Hammer, presented at the 16th Annual Conference on High-Temperature Plasma Diagnostics, Williamsburg, VA, 7–11 May 2006 (Paper WP41); also this LLE Review.

9. F. J. Marshall and Q. Su, Rev. Sci. Instrum. **66**, 725 (1995).

10. F. J. Marshall, J. A. Delettrez, R. Epstein, and B. Yaakobi, Phys. Rev. E **49**, 4381 (1994).

Response Model for Kodak Biomax-MS Film to X Rays

Introduction

X-ray–sensitive film is used for a variety of imaging and spectroscopic diagnostics for high-temperature plasmas. New film becomes available as older films are phased out of production. Biomax-MS is a "T-grain" class of film that is proposed as a replacement for Kodak direct-exposure film (DEF). A model of its response to x rays is presented. Data from dimensional measurements of the film, x-ray transmission measurements, scanning electron microscope (SEM) micrograph images, and x-ray calibration are used to develop this sensitivity model of Biomax-MS film as a function of x-ray energy and angle of incidence. Relative response data provide a check of the applicability of this model to determine the x-ray flux from spectrum data. This detailed film characterization starts with simple mathematical models and extends them to T-grain–type film.

Kodak Biomax-MS film is manufactured as a double-emulsion film made with a T-grain silver halide. A schematic showing the physical layout of this film is shown in Fig. 107.15. An emulsion is coated onto both the top and bottom of a thick polyester base; the layers are assumed to be symmetric, i.e., the top emulsion layer is identical to the bottom emulsion layer. T-grain–type silver-halide grains have a large surface area but are very thin. They are best described as plates, not spheres. These plates are modeled as layers of grains suspended in a gelatin matrix. There is a protective coating of gelatin over the silver-halide gelatin structure. The bulk film parameters are the thickness of the polyester base, t_b; thickness of the emulsion layer, T; thickness of the overcoat, t_0; and volume fraction of silver-halide grains within the gelatin grain emulsion layer, V_f. Figure 107.16 shows an SEM picture of the structure of the Biomax-MS film. This is an image of a cleaved edge of the film showing the layers of thin silver-halide grains surrounded by gelatin.

Description of Model

X rays are incident on the film from the top at an angle of θ relative to the film surface, transmitted through the gelatin and base, and absorbed in the silver-halide grains in the top and
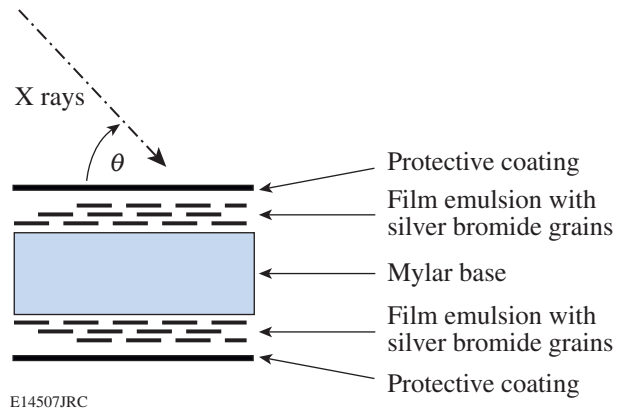

Figure 107.15
Schematic of the Biomax-MS film structure. An emulsion of grains of silver halide suspended in a gelatin is coated onto the top and bottom of a polyester base of thickness t_b.
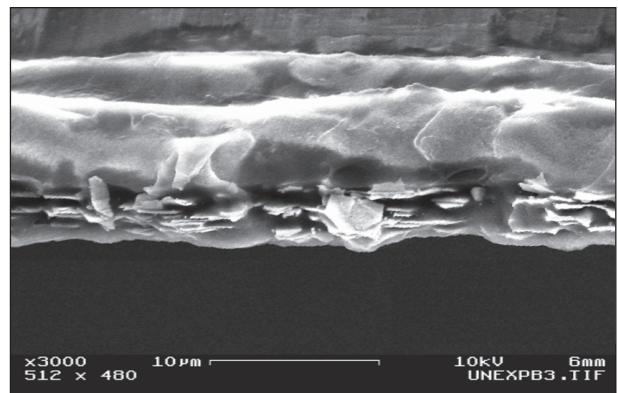

Figure 107.16
An SEM image of the edge of a cleaved edge of Biomax-MS film. The thin, layered structure of the emulsion is clearly visible within the gelatin medium.

bottom emulsion layers. The absorption of one x-ray photon is assumed to be sufficient to render that grain, and only that grain, developable. Once developed, the silver-halide grain becomes a silver structure that is opaque to light, allowing a measurement of the film's optical density. It is assumed here that the individual grain layers are independent and the total film transmission is equal to the product of each individual layer's transmission—the Nutting[1] model for optical density measurement. It has been shown to work to values of optical density near the film saturation. The silver-halide grains are modeled as being all silver bromide (AgBr) and the gelatin is modeled as $C_8H_{16}N_2O_5$. These are the same assumptions used to model the response of DEF film.[2]

The reader is referred to Henke *et al.*[2–4] and Brown *et al.*[5] for a detailed description of how film x-ray response is modeled. Only a brief discussion of the model and the differences required to model a T-grain film is presented in this article. Film response is defined as the relation of the recorded optical density (OD) to the incident x-ray flux (I). Reference 2 modeled the film response as $\alpha(E)\text{OD} = f[\beta(E)I]$ with the dependence of the response to the x-ray energy contained in the $\alpha(E)$ and $\beta(E)$ terms. The x-ray response model of a Biomax-MS double emulsion film is

$$\alpha\text{OD} = a \cdot \ln\left[\frac{1 + b\sin(\theta)\beta I}{1 + b\tau_e\sin(\theta)\beta I} \frac{1 + b\tau_b\tau_e\sin(\theta)\beta I}{1 + b\tau_e\tau_b\tau_e\sin(\theta)\beta I}\right] \quad (1)$$

with

$$\alpha = \left[\mu'/\sin(\theta)\right], \quad (2a)$$

$$\beta = e^{-\left[\mu_0 t_0/\sin(\theta)\right]}\left\{1 - e^{-\left[\mu_1 d/\sin(\theta)\right]}\right\}, \quad (2b)$$

$$\tau_e = e^{-\left[\mu' T/\sin(\theta)\right]}, \quad (2c)$$

$$\tau_b = e^{-\left[\mu_b t_b/\sin(\theta)\right]}, \quad (2d)$$

and

$$\mu' = \mu_0 - \frac{1}{d}\ln\left\{1 - V_f\left[1 - e^{-(\mu_1 - \mu_0)d}\right]\right\}. \quad (2e)$$

Variables in Eqs. (1) and (2) with their units are defined in Table 107.II.

Table 107.II: List of variables used in modeling x-ray response of Biomax-MS film.

	Parameter	Units
θ	Angle of incidence	
μ_1	X-ray mass absorption of grain (AgBr)	μm^{-1}
μ_b	X-ray mass absorption of base (Mylar)	μm^{-1}
μ_0	X-ray mass absorption of gelatin matrix	μm^{-1}
d	Silver-halide grain thickness	μm
t_b	Base thickness	μm
T	Emulsion thickness	μm
V_f	Volume of fraction of grains	
t_0	Protective layer thickness	μm
a	Optical density constant	μm^{-1}
b	Flux constant	μm^2

Equations (1) and (2a)–(2e) form a heuristic model for the physical response of Biomax-MS film to x rays. Transmission of x rays through the emulsion layer (τ_e) and film base (τ_b) is given by Eqs. (2c) and (2d). Equation (2e) is the linear x-ray absorption coefficient (μ') for the emulsion layer. The emulsion layer is modeled as a heterogeneous mixture of AgBr and gelatin. The transmission of x rays through the protective top coat and subsequent absorption in a ArBr grain (β) are given by Eq. (2b). Reference 3 describes a methodology to determine the OD from the number of exposed grains (M) that uses the reciprocal of the exposed grain scale length, $(1/M) \times (dM/dx)$. This reciprocal scale length is given by Eq. (2a). The film response in OD calculated by using Eq. (1) has two terms in the argument of the logarithm. These terms come from the "thin-emulsion model"[2,3] applied to the top and bottom emulsion layers, respectively.

The primary difference in this model compared to the Henke model for DEF film is the added $\sin(\theta)$ term in Eq. (2b) for the absorption of a photon in a silver-halide grain and $\sin(\theta)$ terms multiplying the x-ray flux in both the numerator and denominator of Eq. (1). These terms reflect the fact that the grains are thin plates rather than spherical: a is related to the maximum optical depth OD_s of the film and has the same dimensions as $\alpha(\text{cm}^{-1})$, and b is related to the developed silver structure area with dimensions of μm^2. Tabulated x-ray, mass absorptions,[6] and bulk mass densities are used to compute the linear x-ray absorption coefficients [μ_{linear} (cm^{-1}) = $\mu_{\text{tabulated}}$ (cm^2/g) $\times \rho_{\text{bulk}}$ (g/cm^3)]. In this model, $\rho_{\text{polyester}} = 1.4$ g/cm^3, $\rho_{\text{gelatin}} = 1.4$ g/cm^3, and $\rho_{\text{AgBr}} = 6.47$ g/cm^3.

Determination of Model Parameters

A digital micrometer was used to measure the total thickness of the polyester base, undeveloped film, and the developed film. The micrometer faces were flat and not spherical to minimize the compression of a soft layer by the force of measurement. The polyester base was measured to be 179±1 μm, the thickness of the undeveloped film was 188±1 μm, and the thickness of the developed fully exposed film was 187±1 μm. There is little difference between the thickness of the undeveloped film and the exposed developed film, indicating that there is only a small change in grain volume when silver halide is changed to silver. The thicknesses of the two emulsion layers and their overcoats are 9±2 μm. The emulsion layer thickness T is calculated from the total emulsion thickness once the overcoat thickness t_0 is determined.

The SEM image shown in Fig. 107.16 was used to determine the silver-halide grain thickness. This image was rotated so that the grains were horizontal, and lineouts of the spatial profile across the grain images were used. Silver-halide grain thickness is defined to be the full width at half maximum of the spatial profile for each grain.

X-ray transmission data for Mn Kα, Mn Kβ, Cu Kα, and Cu Kβ were acquired to determine the volume fraction of silver-halide grains in the emulsion layer. First, the digital micrometer data were checked by calculating the polyester base thickness needed to match the measured x-ray transmission. The base thickness calculated from these data is 180±5 μm. This is in good agreement with the micrometer measurement. X-ray transmission through the emulsion layer can be shown to be proportional to the product of the volume fraction times the emulsion thickness $V_f \times T$, 1.3±0.4 μm. V_f is then calculated once T is known.

The remaining parameters a, b, and t_0 are determined by fitting the model for optical density to the x-ray exposure data and minimizing χ^2. The absorption of higher-energy x rays (Ti Kα, Fe Kα, and Cu Kα) is low in the overcoat and, thus, insensitive to t_0. The model formula was used to determine the constants a and b from the measured sensitivity by doing a nonlinear minimization of the calculated χ^2 of the high-energy x-ray data. A nonlinear minimum χ^2 fit for the low energy (Al Kα and Ag Lα) was then used to determine t_0 since the low-energy x rays are more affected by the overcoat. The developing process used and the densitometer measurement of the film are described in a companion paper by Marshall *et al.*[7] Biomax-MS film parameters determined by the above methodology are listed in Table 107.III along with the corresponding values for DEF from Ref. 2.

This model was used to calculate the x-ray flux in photons/μm^2 to give an exposure in optical density of 0.5, 1.0, and 2.0 for Biomax-MS film as a function of x-ray energy from 1.0 to 10.0 keV. The Henke model was used to calculate the same information for DEF film. In general, the Biomax-MS film is less sensitive, i.e., requires more photons/μm^2 for the same optical density than DEF film. Biomax-MS sensitivity is

Table 107.III: List of values, errors, and method of determination for Biomax-MS film parameters. DEF values for comparison are taken from Ref. 2.

	Biomax-MS	DEF
Micrometer data		
Base thickness (t_b)	179±1 μm	185 μm
Emulsion thickness (T)	4±1 μm	13 μm
SEM data		
Grain thickness (d)	0.12±0.03 μm	1.6 μm
X-ray transmission data		
Volume fraction of grains (V_f)	0.34±0.08	0.4
Calibration data		
Protective layer thickness (t_0)	0.4±0.1 μm	1 μm
Optical density constant (a)	0.58±0.01 μm^{-1}	0.68 μm^{-1}
Flux constant (b)	12.4±0.3 μm^2	1.69 μm^2

equal to or somewhat greater than that of DEF only for x-ray energies <2 keV and for optical densities <2.0. This confirms measurements previously reported by Chandler *et al.*[8] on the comparison of Biomax-MS to DEF sensitivity.

Marshall *et al.*[7] reported in a companion paper on the comparison of the response of Biomax-MS to that of DEF for spectrally dispersed data recorded with a transmission grating in a KB microscope. These data were converted to x-ray intensity versus energy with the model described in this article and the Henke model for DEF. The results are plotted in Fig. 107.17, where the maximum optical density recorded on DEF was ~1.8 and the maximum for Biomax-MS ~1.0. The calculated x-ray flux from the DEF exposure agrees very well with the x-ray flux calculated from the Biomax-MS exposure. The incident angle of the x rays onto the film for these data was ~90°.

Relative sensitivity data were also recorded for x rays in a Rowland circle crystal spectrometer. A flat crystal was used to record the x-ray spectrum from an OMEGA shot from 2 to 6 keV. The x rays were recorded with an incident angle of ~50°. Again, the models for DEF and Biomax-MS were used to convert the film optical density to x-ray flux. The results shown in Fig. 107.18 indicate that calculated x-ray fluxes agree to 20% for the DEF and Biomax-MS data.

Conclusions

The x-ray flux calculated from DEF using the model of Henke *et al.*[2] and from Biomax-MS using this model are generally in agreement. The emulsion layer is thinner for Biomax-MS than it is for DEF; therefore, the absorption of higher-energy x rays is less in the Biomax-MS film than in the DEF film. This is reflected in the significantly reduced sensitivity for Biomax-MS when compared to DEF at x-ray energies >4 keV. The grain geometries are also very different: the DEF grains are typically spherical, while the Biomax-MS grains are flat plates with a large surface area and small thickness.
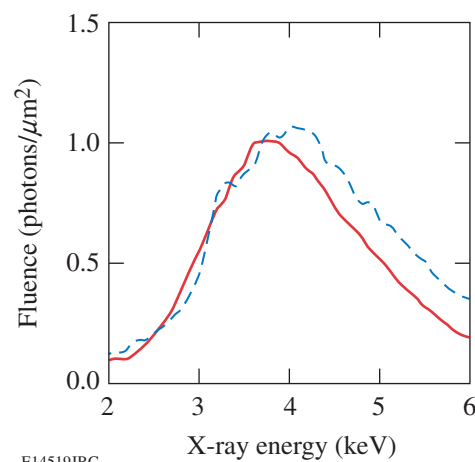
Figure 107.17
Comparison of the x-ray fluence calculated from KB microscope–dispersed spectra. The calculated DEF x-ray fluence is plotted as a solid line, and the calculated Biomax-MS x-ray fluence is plotted as a dashed line.
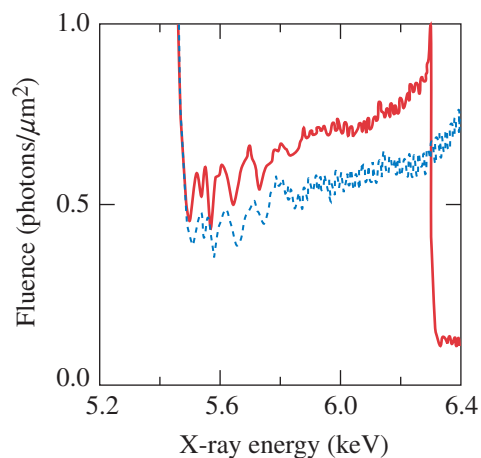
Figure 107.18
X-ray fluence calculated for a Rowland circle spectrometer for both DEF and Biomax-MS films. The solid curve is the x-ray fluence versus energy calculated from DEF film, and the dashed curve is calculated from the Biomax-MS film.

REFERENCES

1. J. C. Dainty and R. Shaw, *Image Science: Principles, Analysis and Evaluation of Photographic-Type Imaging Processes* (Academic Press, London, 1974), p. 39.

2. B. L. Henke *et al.*, J. Opt. Soc. Am. B **3**, 1540 (1986).

3. B. L. Henke *et al.*, J. Opt. Soc. Am. B **1**, 818 (1984).

4. B. L. Henke *et al.*, J. Opt. Soc. Am. B **1**, 828 (1984).

5. D. B. Brown, J. W. Criss, and L. S. Birks, J. Appl. Phys. **47**, 3722 (1976).

6. B. L. Henke, E. M. Gullikson, and J. C. Davis, At. Data Nucl. Data Tables **54**, 181 (1993).

7. F. J. Marshall, J. P. Knauer, D. Anderson, and B. A. Schmitt, presented at the 16th Annual Conference on High-Temperature Plasma Diagnostics, Williamsburg, VA, 7–11 May 2006 (Paper WP40).

8. K. M. Chandler, S. A. Pikuz, T. A. Shelkovenko, M. D. Mitchell, D. A. Hammer, and J. P. Knauer, Rev. Sci. Instrum. **76**, 113111 (2005).

High-Yield Bang Time Detector for the OMEGA Laser

Introduction

The time interval from the beginning of the laser pulse to the peak of neutron emission (bang time) is an important parameter in inertial confinement fusion (ICF)[1] experiments. The neutron bang time is very sensitive to energy absorption and the subsequent hydrodynamic response of the target and can be directly compared with numerical simulation. Several detectors[2–4] that have been developed to measure the neutron bang time in ICF experiments include a fast (<25-ps) streak-camera–based neutron temporal diagnostic (NTD).[5] An NTD is currently installed on the OMEGA laser[6] at LLE. The NTD streak camera, located at about 3 m from the target, is saturated by neutron yields above 3×10^{13}. OMEGA has produced yields of 10^{14} (Ref. 7), and fast-ignition experiments currently planned[8] at the OMEGA Laser Facility are expected to produce neutron yields above 10^{14}. A new high-yield neutron bang time (HYNBT) detector has been developed at LLE to measure the bang time in these very high yield experiments. The HYNBT has also been developed as a prototype neutron bang time detector for high neutron yields at the National Ignition Facility (NIF). The present work is a continuation of the NIF prototype development published earlier.[9]

HYNBT Design and Setup

The HYNBT detector design, shown in Fig. 107.19, consists of three chemical-vapor-deposition (CVD) diamond detectors of different sizes and sensitivities placed in a lead-shielded housing. The HYNBT uses commercially purchased[10] "optical-quality" polycrystalline DIAFILM CVD wafers. The HYNBT wafers are disks with the following dimensions: 10-mm diameter, 0.5 mm thick (Ch1); 5-mm diameter, 0.25 mm thick (Ch2); and 2-mm diameter, 0.5 mm thick (Ch3). On each side of the CVD wafer 10 nm of Cr and 50 nm of Au were deposited to provide electrical contact. Each CVD wafer was assembled in an individual aluminum housing with an SMA connector. Figure 107.20 shows the Ch3 housing before and after assembly. Each detector was pre-tested, and the three channels were assembled in a stainless steel cylinder. Figure 107.21 shows the HYNBT before and after assembly. The thin-walled
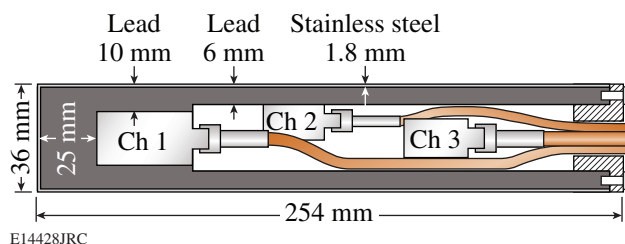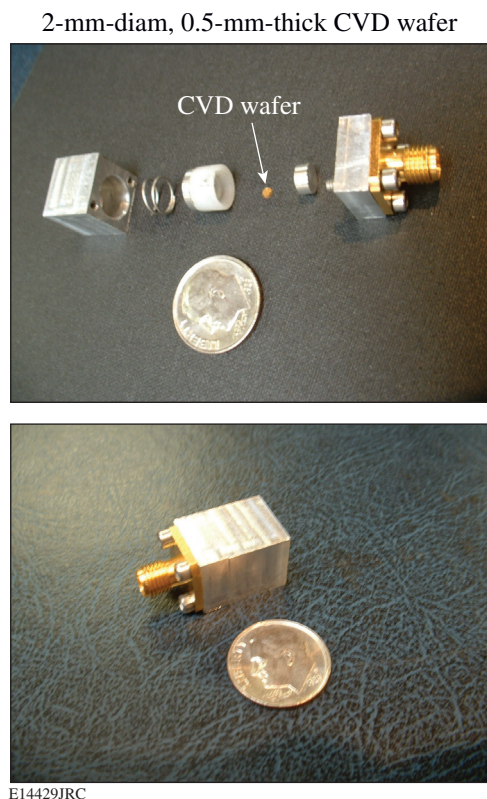

Figure 107.19
Design of the HYNBT detector.

2-mm-diam, 0.5-mm-thick CVD wafer

Figure 107.20
The HYNBT Ch3 housing before and after assembly.

train is recorded on the fourth channel, using a fast photodiode to provide a time reference to the laser. The fiducial analysis and fitting procedure are described in Ref. 4.

HYNBT Performance

The HYNBT was tested on OMEGA with both DT and D_2 implosions. Figure 107.22 shows typical oscilloscope traces of the three HYNBT channels for a shot yielding 4.4×10^{12} DT neutrons. The measured signals were fit by a convolution of a Gaussian and an exponential decay, as described in Ref. 4. The parameter of the exponential decay represents the collection time of the carriers in the CVD diamond wafer. At a constant bias voltage, the decay parameter depends on the thickness and diameter of the CVD wafer. The optimum decay parameter for
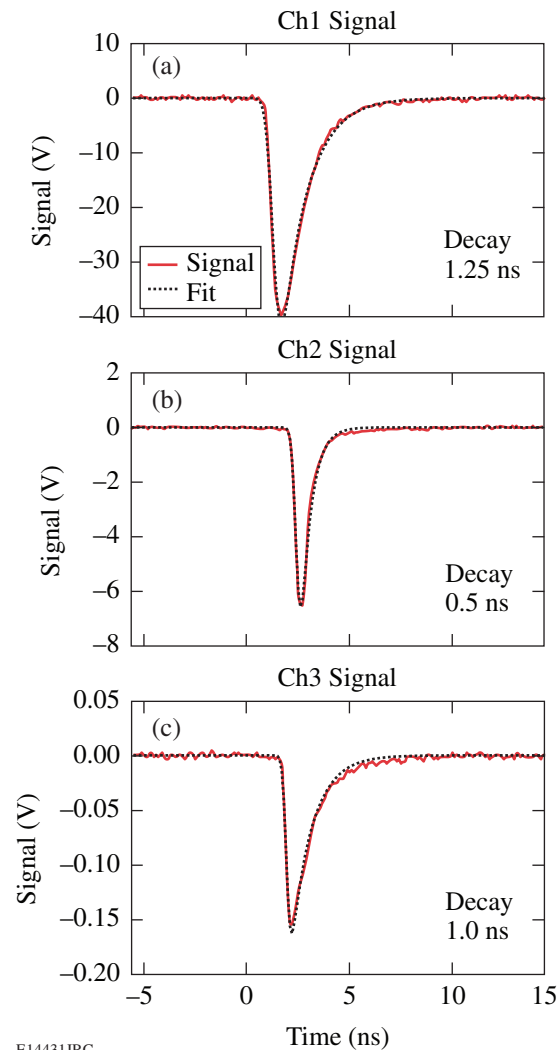

Figure 107.21
The HYNBT before and after final assembly.

stainless steel cylinder acts as a Faraday cage decreasing the electromagnetic pulse (EMP) noise. Lead shielding inside the steel cylinder protects the CVD diamond detectors from hard x rays. This shielding is not necessary for current experiments on OMEGA and was installed in anticipation of hard x rays produced by the interaction of the short laser pulse with the gold cone or shell in fast-ignition experiments.[8] RG-142 coaxial cables are used because of their double-braid shielding design and low sensitivity to neutrons.[11] The 3-m-long, RG-142 cables are connected to 22-m-long, LMR-400 cables. Inside the OMEGA Target Bay, the cables are routed radially with respect to the target chamber center to minimize the interaction of neutrons with the cables. The bandwidth of the LMR-400 cables is higher than that of the RG-142 cables, but they are much more sensitive to neutrons.[11] This two-cable solution is a compromise between bandwidth and neutron-induced background signals. The HYNBT is deployed in the same re-entrant tube as LLE's NBT,[4] 50 cm from the target chamber center. All of the HYNBT channels were biased at 750 V using a bias-tee (Picosecond Pulse Labs, model 5531). The signals from the HYNBT CVD diamond detectors were recorded on three channels of a 3-GHz, 10-GS/s, Tektronix TDS-694 oscilloscope. The OMEGA optical fiducial pulse

Figure 107.22
The HYNBT signal for shot 42120 with a DT neutron yield of 4.4×10^{12}.

each HYNBT channel was determined from the fit of a large number of the shots for each channel (low noise, not saturated) and was fixed for the timing analysis of all shots. The Gaussian fit parameters are free parameters for every shot to account for different yields, bang times, ion temperatures, and trigger shifts. The neutron pulse's arrival time is defined to be the center of the Gaussian portion of the fit. Figure 107.23 shows the signal amplitude of three HYNBT channels as a function of DT neutron yield. The straight lines are linear fits to the data for each channel. The first HYNBT channel saturates above a 100-V signal, and the second channel saturates above 80 V. At a yield of 1×10^{15}, the third channel will have a signal of ~20 V and will not be saturated. The three HYNBT channels can measure the neutron bang time in DT implosions over the yield range from 1×10^{10} to 1×10^{15}.

The timing accuracy of the HYNBT was studied by measuring the time differences among channels. Figure 107.24(a) shows the time difference between two HYNBT channels recorded on multiple shots over two shot days in May 2005. The DT yields varied from 8.4×10^{12} to 3.5×10^{13}. The rms of the time difference between these two channels is 13 ps. The HYNBT was tested five times during 2005. Figure 107.24(b) shows the time difference between the HYNBT channels appropriate for the neutron yield range during the tests. In November 2005, Ch2 of the HYNBT was used to test a gamma bang time (GBT) detector based on an optical light pipe concept;[12] the time difference between the HYNBT and the GBT had an rms of 15 ps. In all cases the internal time resolution of the HYNBT was better than 20 ps.
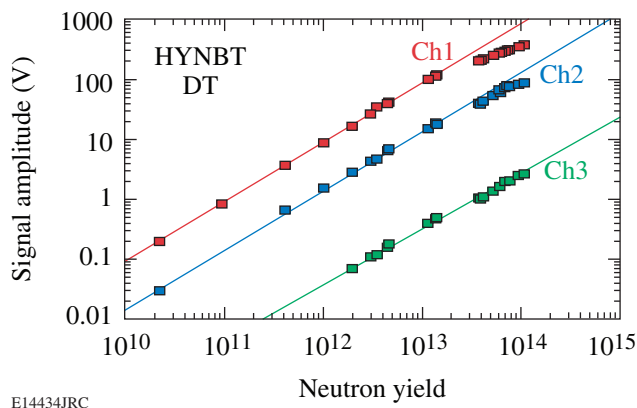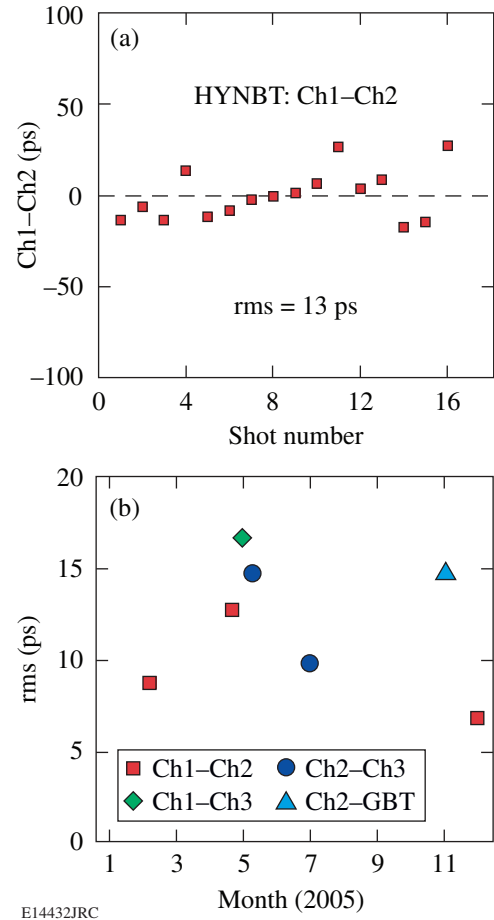

Figure 107.24
(a) Time difference between HYNBT Ch1 and Ch2 in May 2005; (b) rms of time differences between the HYNBT channels in 2005.

E14434JRC

Figure 107.23
Signal amplitudes of the HYNBT channels.

The timing calibration of the HYNBT bang time relative to the OMEGA laser pulse was established by cross-calibration against the NTD.[5] Figure 107.25 shows the cross-calibration of the HYNBT channels and the NTD performed in December 2005, with DT yields varying from 3.0×10^{12} to 1.4×10^{13}. A good correlation between the NTD and the HYNBT is observed with an rms difference of 40 ps. This is larger than the 28-ps rms expected for the difference between two independent measurements, each with a time precision of 20 ps. The discrepancy is explained by direct neutron hits on the NTD, charged-coupled-device (CCD) camera that reduces its temporal resolution.

Although the HYNBT was designed to measure DT neutron bang time, it can also measure bang time in high-yield D_2 shots on OMEGA. Since CVD diamond detectors are less sensitive to D_2 than to DT neutrons, only the first HYNBT channel
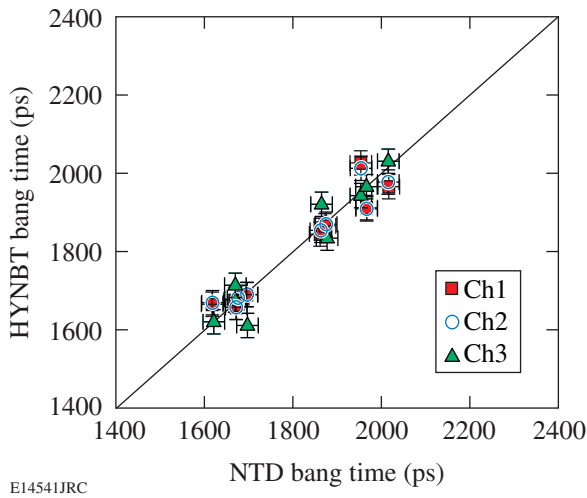
E14541JRC

Figure 107.25
Timing cross-calibration between the HYNBT and the NTD for DT implosions. A line of equal bang times for both instruments is shown for comparison.

is sufficiently sensitive for D_2 implosions on OMEGA. Figure 107.26 shows oscilloscope traces of the first HYNBT channel for shots yielding 1.1×10^{10} and 9.3×10^{10}. At a D_2 yield of 1×10^{10} the signal amplitude is only 10 mV and is affected by EMP and digital noise since the minimum scale setting of the TDS-694 oscilloscope is 10 mV/div. Figure 107.27 shows the first-channel signal amplitude as a function of D_2 yield, and Fig. 107.28 shows the cross-calibration against the NTD. To minimize the influence of noise on the cross-calibration timing, only shots with yields above 3×10^{10} were included. With ~50-ps rms, the D_2 cross-calibration is not as accurate as the DT cross-calibration because most of the signal amplitudes in Fig. 107.28 were below 100 mV.

EMP mitigation techniques used with the HYNBT design reduced the EMP noise to a level about 10× smaller than that measured with LLE's NBT.[4] Figure 107.29 shows the EMP noise levels in the least-sensitive Ch3 for different shot conditions. Figure 107.29(a) shows less-than-2-mV noise levels for the standard direct-drive shot. Figure 107.29(b) shows the EMP noise level for a direct-drive shot with backlighting. Backlighting produced additional EMP noise, and for these shot types, the noise level is below 4 mV. The indirect-drive shot with a scale-5/8 hohlraum is shown in Fig. 107.29(c) with the EMP noise below 4 mV. For all shots on OMEGA the EMP noise level in the HYNBT is below 4 mV.

Due to the lead shielding, the HYNBT is insensitive to hard-x-ray signals in direct-drive and most typical indirect-
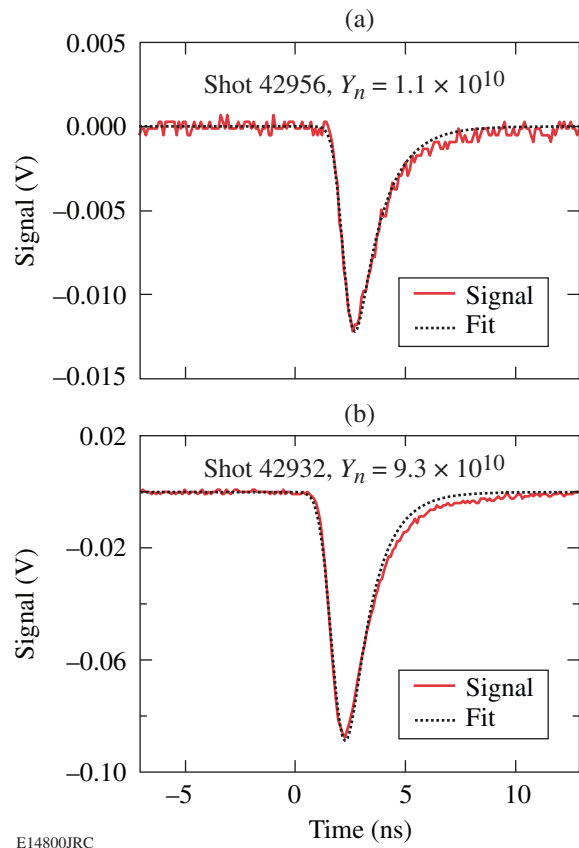

E14800JRC

Figure 107.26
The oscilloscope traces of the first HYNBT channel for D_2 shots: (a) shot 42956 with a yield of 1.1×10^{10}; (b) shot 42932 with a yield of 9.3×10^{10}.
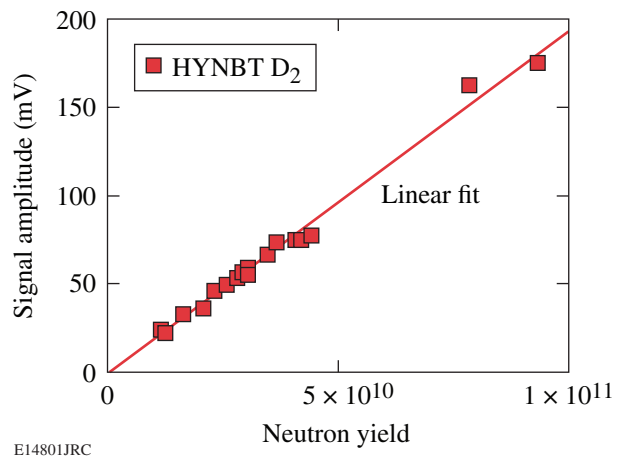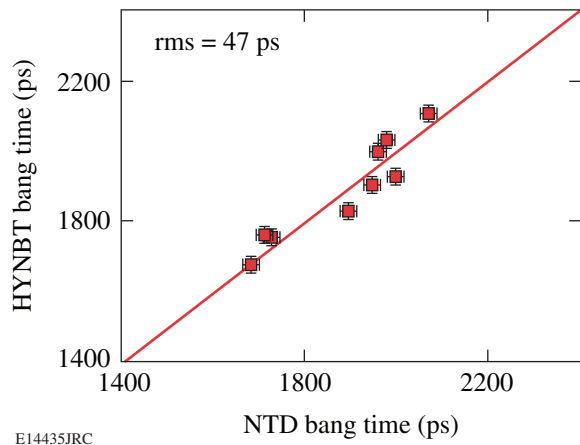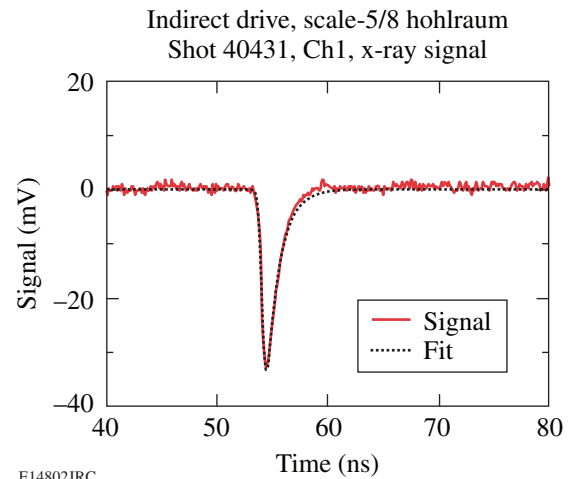

E14801JRC

Figure 107.27
The HYNBT first-channel signal amplitude as a function of D_2 yield.

Figure 107.28
Timing cross-calibration between the HYNBT first channel and the NTD for D_2 implosions. A line of equal bang time for both instruments is shown for comparison.
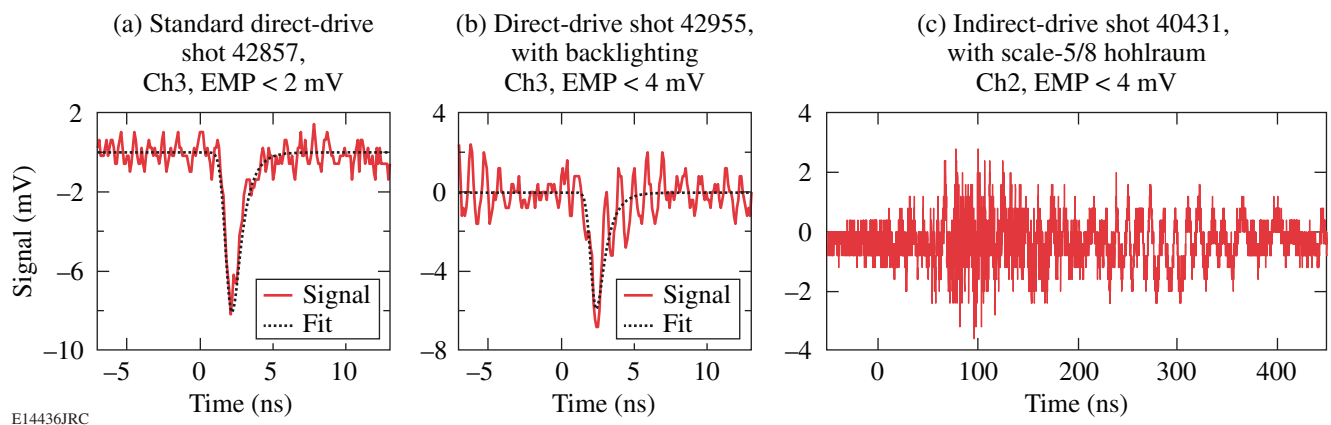

Figure 107.30
X-ray signal from the scale-5/8-hohlraum, indirect-drive shot 40433 on the HYNBT first channel.

drive shots. Only the most sensitive HYNBT channel was able to record a 30-mV x-ray signal from a scale-5/8 hohlraum, indirect-drive shot that produces ~100× more hard x rays than direct-drive shots (shown in Fig. 107.30). This relatively low signal is temporally separated from the neutron signal and will not compromise the HYNBT bang time.

HYNBT on the NIF

The HYNBT was also developed as a prototype neutron bang time detector for the NIF. This is a continuation of earlier work[9] on a NIF bang time prototype. Since publication of this earlier work, the design requirements have changed: Instead of

a low-to-moderate-yield, general-purpose diagnostic, the NIF NBT detector is now required for moderate-to-high yields in the pre-ignition and early-ignition campaigns. At these yields, the original scintillator and photomultiplier channel described in Ref. 9 cannot be used. The NIF NBT is virtually identical to the OMEGA HYNBT with three or four CVD diamond channels. This design will make the NIF NBT more compact, simpler, and less expensive than an NBT employing a photomultiplier. It will be located about 40 to 60 cm from the target in a diagnostic insertion manipulator, together with other NIF diagnostics. In contrast to the OMEGA HYNBT, the shielding on the front of the NIF NBT (facing the target) will be remov-

Figure 107.29
EMP noise in HYNBT Ch3 for different shots conditions: (a) standard direct-drive shot 42857; (b) direct-drive shot 42955 with backlighting; and (c) indirect-drive shot 40431 with a scale-5/8 hohlraum.

able so that x rays can be used for temporal calibration.[9] The calibration will use x-ray emission from a gold target irradiated by a short laser pulse. The distance from the target, x-ray shielding, and cable length of the HYNBT on OMEGA are comparable to those required on the NIF. The sensitivity of the NIF NBT channels will be comparable to the corresponding HYNBT channels. The dynamic range of the NIF NBT can be increased by increasing the sensitivity of the first channel, decreasing the sensitivity of the third channel, and adding an even less sensitive fourth channel. The first-channel CVD wafer can be changed from a 10-mm-diam, 0.5-mm-thick CVD wafer to a 10-mm-diam, 1-mm-thick CVD wafer. This will increase the sensitivity by a factor of 2, which corresponds to yields of 2.5×10^{10} in D_2 and 5×10^9 in DT implosions. If NIF NBT operation will be required at lower yields, the detector can be moved closer to the target. The fourth, least-sensitive channel can be made from a smaller and thinner CVD wafer, from a neutron-hardened CVD wafer, or from a CVD wafer with impurities. All of these factors decrease the sensitivity of the CVD diamonds and shorten the temporal response. The maximum operational yield of the NIF NBT will not be determined by CVD diamond saturation but by neutron-induced signals in the coaxial cables.[11] The study of neutron-induced signals in the coaxial cables will continue on OMEGA. With an optimal cable, the upper-yield range of the NIF NBT is expected to be about 10^{17}.

Summary

A simple, low-cost, high-yield neutron bang time (HYNBT) detector has been developed and implemented on OMEGA. The HYNBT consists of three chemical-vapor-deposition (CVD) diamond detectors of different sizes and sensitivities placed in a lead-shielded housing. The HYNBT is located in a re-entrant tube 50 cm from the center of the target chamber. The HYNBT has been temporally cross-calibrated against the streak-camera–based neutron temporal diagnostic (NTD) for both D_2 and DT implosions. The HYNBT has an internal time resolution better than 20 ps. The three HYNBT channels can measure the neutron bang time in DT implosions over a yield range of 1×10^{10} to 1×10^{15} and above 5×10^{10} for D_2 implosions. The HYNBT can be implemented on the National Ignition Facility.

REFERENCES

1. J. D. Lindl, *Inertial Confinement Fusion: The Quest for Ignition and Energy Gain Using Indirect Drive* (Springer-Verlag, New York, 1998).

2. R. A. Lerche *et al.*, Rev. Sci. Instrum. **59**, 1697 (1988).

3. N. Miyanaga *et al.*, Rev. Sci. Instrum. **61**, 3592 (1990).

4. C. Stoeckl, V. Yu. Glebov, J. D. Zuegel, D. D. Meyerhofer, and R. A. Lerche, Rev. Sci. Instrum. **73**, 3796 (2002).

5. R. A. Lerche, D. W. Phillion, and G. L. Tietbohl, Rev. Sci. Instrum. **66**, 933 (1995).

6. T. R. Boehly, D. L. Brown, R. S. Craxton, R. L. Keck, J. P. Knauer, J. H. Kelly, T. J. Kessler, S. A. Kumpan, S. J. Loucks, S. A. Letzring, F. J. Marshall, R. L. McCrory, S. F. B. Morse, W. Seka, J. M. Soures, and C. P. Verdon, Opt. Commun. **133**, 495 (1997).

7. J. M. Soures, R. L. McCrory, C. P. Verdon, A. Babushkin, R. E. Bahr, T. R. Boehly, R. Boni, D. K. Bradley, D. L. Brown, R. S. Craxton, J. A. Delettrez, W. R. Donaldson, R. Epstein, P. A. Jaanimagi, S. D. Jacobs, K. Kearney, R. L. Keck, J. H. Kelly, T. J. Kessler, R. L. Kremens, J. P. Knauer, S. A. Kumpan, S. A. Letzring, D. J. Lonobile, S. J. Loucks, L. D. Lund, F. J. Marshall, P. W. McKenty, D. D. Meyerhofer, S. F. B. Morse, A. Okishev, S. Papernov, G. Pien, W. Seka, R. Short, M. J. Shoup III, M. Skeldon, S. Skupsky, A. W. Schmid, D. J. Smith, S. Swales, M. Wittman, and B. Yaakobi, Phys. Plasmas **3**, 2108 (1996).

8. C. Stoeckl, J. A. Delettrez, J. H. Kelly, T. J. Kessler, B. E. Kruschwitz, S. J. Loucks, R. L. McCrory, D. D. Meyerhofer, D. N. Maywar, S. F. B. Morse, J. Myatt, A. L. Rigatti, L. J. Waxer, J. D. Zuegel, and R. B. Stephens, Fusion Sci. Technol. **49**, 367 (2006).

9. V. Yu. Glebov, C. Stoeckl, T. C. Sangster, S. Roberts, R. A. Lerche, and G. J. Schmid, IEEE Trans. Plasma Sci. **33**, 70 (2005).

10. Harris International, New York, NY 10036.

11. V. Yu. Glebov, R. A. Lerche, C. Stoeckl, G. J. Schmid, T. C. Sangster, J. A. Koch, T. W. Phillips, C. Mileham, and S. Roberts, presented at ICOPS 2005, International Conference on Plasma Sciences, Monterey, CA, 20–23 June 2005 (Paper 10281).

12. M. Moran, G. Mant, V. Glebov, C. Sangster, and J. Mack, presented at the 16th Annual Conference on High-Temperature Plasma Diagnostics, Williamsburg, VA, 7–11 May 2006 (Paper TP22).

Operation of Target Diagnostics in a Petawatt Environment

Introduction

Sensitive electronic detectors are difficult to operate in petawatt laser–target interaction experiments. The laser–plasma interaction at relativistic intensities ($>10^{18}$ W/cm^2) in the focus of a high-energy, short-pulse laser system creates copious amounts of relativistic electrons ($E > 1$ MeV), hard x rays, and charged particles. Conversion efficiencies of up to 50% into MeV electrons[1] and 5% into MeV protons[2] have been reported. The energetic particles hit detectors inside the target chamber, creating a background signal and potentially damaging sensitive electronic structures. The MeV x rays easily escape the target chamber and impact diagnostic instrumentation inside the target area. Since the Compton-scattering cross section is significant at these energies, sidescattered and backscattered photons contribute to the background signal. X-ray fluorescence from high-Z material in the target area adds to this background. An electromagnetic pulse (EMP) is created when charged particles and x rays interact with structures inside the target chamber. This pulse will strongly affect and potentially damage any electronic device in or near the target chamber. EMP can also add background to electrical signals from detectors close to the target. It is conducted outside the target chamber through any cable or nonconducting window.[3] Due to those problems, many diagnostics used in petawatt laser experiments rely on passive detectors such as x-ray film, nuclear activation,[4] imaging plate,[5] radio-chromic film,[6] and CR39 track detectors.[7] In many cases, electronic detectors provide higher sensitivity, higher dynamic range, better temporal resolution, and faster feedback after each laser shot. Strategies are being developed to mitigate the impact of EMP on electronic detectors inside and outside the target chamber and to shield them against background radiation. In this article, detector-development efforts for experimental campaigns at the petawatt facility[8,9] of the Rutherford Appleton Laboratory (RAL) are presented showing successful approaches to improve the signal-to-background ratio on electronic detectors and to harden them against EMP. A variety of detectors, such as single-photon-counting, x-ray, charge-coupled-device (CCD) cameras, diamond x-ray detectors, and scintillator–photomultiplier neutron detectors, will be discussed. A new high-energy (1 kJ at 1 ps, 2.6 kJ at 10 ps) petawatt laser (OMEGA EP)[10,11] is currently under construction at the Laboratory for Laser Energetics. Strategies to minimize the impact of EMP on diagnostics inside the target chamber of OMEGA EP will be presented.

Experimental Setup

The Rutherford Appleton Laboratory's Vulcan petawatt laser delivers a 0.5-ps pulse of up to ~500 J in a 60-cm-diam beam, which is focused by an f/3 off-axis parabola into a <10-μm-diam focal spot. Due to losses in the compressor and wavefront aberrations, less than 50% of the laser energy is contained within the central portion of the focal spot, leading to an estimated maximum intensity on target of about 4×10^{20} W/cm^2. As seen in Fig. 107.31, the petawatt target chamber is well shielded by 10 cm of lead on top and on three sides. The access corridor to the target chamber entry doors, which are unshielded, is backed by a 10-cm lead, 60-cm-concrete curtain shield. The diagnostics under discussion were set up at different locations in the target area, on the target chamber, and in the target chamber (see Fig. 107.31). The single-photon-counting, x-ray, CCD camera was mounted 3.8 m from target chamber center (TCC) on a 1-m-long vacuum tube outside the target chamber wall. A chemical-vapor-deposition (CVD) diamond hard-x-ray (>50-keV) detector was mounted either inside or outside the target chamber at ~1 m from the TCC. Diamond photoconductive devices (PCD's) for soft x rays (<2 keV) were used either inside the target chamber at ~50 cm from TCC or at the target chamber wall at 2.8 m. A scintillator–photomultiplier neutron detector was placed at 6.5 m from TCC behind a second 20-cm-lead curtain shield. This curtain shield is set up to protect a large-area neutron scintillator array.[12]

Single-Photon-Counting CCD

In a single-photon-counting x-ray CCD spectrometer, the photon flux is attenuated so that every CCD pixel is hit by, at most, one photon. At moderate x-ray energies (<50 keV) a significant fraction of photons deposit all of their energy in one pixel; therefore, the histogram of the pixel values is proportional to the incident photon spectrum. This type of spectrometer has the benefit of requiring no alignment but can be affected by a
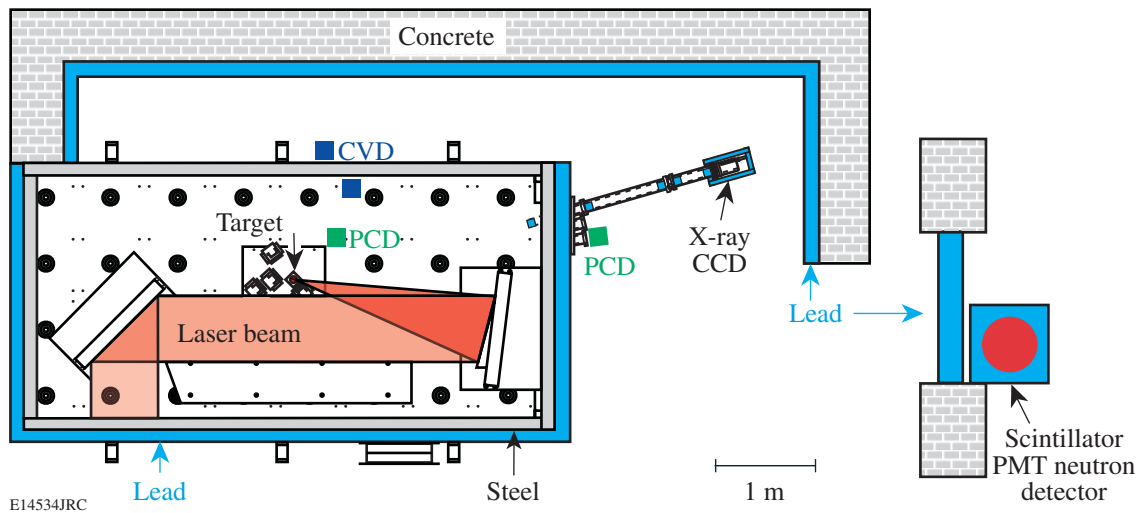
E14534JRC

Figure 107.31
Overview of the target area at the RAL petawatt facility showing the shielding setup and layout of the x-ray CCD, CVD diamond, diamond PCD, and scintillator–photomultiplier detectors.

poor signal-to-background ratio. Detailed shielding strategies for single-photon-counting x-ray CCD spectrometers can be found in the literature.[13] The most important finding reported was the importance of shielding not only the direct line of sight, but against Compton-scattered and fluorescence x rays from the side and back of the camera (see Fig. 107.31).

Diamond Hard-X-Ray Detector

CVD diamond detectors[14] are an attractive choice as hard-x-ray or neutron detectors in high-energy, ultrafast laser–plasma experiments. CVD diamonds are radiation hard, thus able to cope with the large fluxes of x rays and particles. They are fast and have a large dynamic range, which makes them able to discriminate fast particles (x rays and electrons) from slower particles, such as protons and neutrons. The detector used in these experiments was made by DeBeer's Industrial Diamond Division by microwave-assisted plasma deposition as described in Ref. 11. The diamond wafer was cylindrical, 10 mm in diameter, and 1 mm thick, with 8-mm-diam Cr-Au (10/500 nm, respectively) contacts on both sides. The CVD detector was run at a 1000-V bias through a high-voltage, high-speed bias-tee,[15] and the signals were recorded on a 1-GHz digital sampling scope.[16] Figure 107.32 shows signals recorded from a CVD detector placed either inside the target chamber or outside the target chamber. The distance to TCC was ~1 m in both cases (see Fig. 107.31). To bring the signal to the outside of the chamber, an extra ~1-m RG58 cable was connected to a BNC vacuum feedthrough. The cable run outside the target chamber into the oscilloscope was identical. The laser was set

to ~1-ps pulse length at best focus. For the experiment with the detector inside the target chamber, a 360-μm CH/CD/CH foil was irradiated using 390 J of laser energy and a 140-μm CD foil was irradiated with 330 J laser energy with the detector outside the target chamber. The signal inside the target chamber is severely compromised by EMP noise pickup almost as high as the x-ray peak. The only noise seen in the signal outside the target chamber is the digitizing noise of the scope. Because of a lower scope sensitivity setting, the digitizing noise is higher
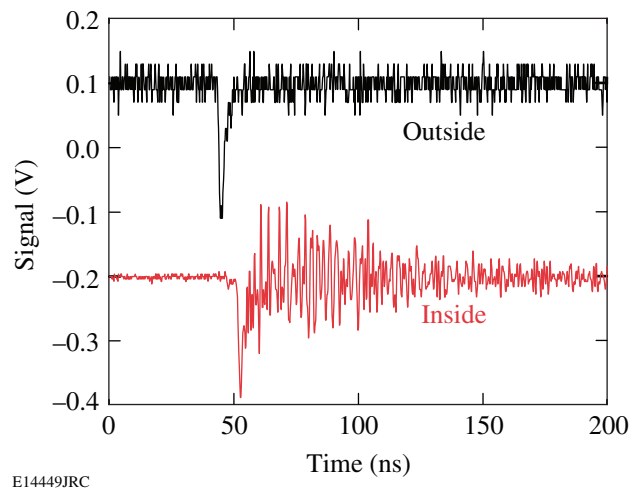

E14449JRC

Figure 107.32
Signals from the CVD diamond hard-x-ray detector recorded at 1 m from the target inside and outside the target chamber.

on the outside. The timing difference in the x-ray peak is due to the different cable lengths to the oscilloscope. The fact that the x-ray signal experiences little change by moving the detector outside the target chamber, where the x rays are attenuated by an additional 1 cm of steel, shows that the x rays recorded by the CVD detectors are significantly above 100 keV.

Diamond Soft-X-Ray Detector

Diamond photoconductive devices (PCD's)[17] are frequently used as soft-x-ray detectors (<2 keV) because they are sensitive ($\sim 6 \times 10^{-4}$ A/W) and very fast (<200 ps) and have a flat x-ray response and a high dynamic range. Because of the high band gap of 5.5 eV, they are not sensitive to laser light. A six-channel PCD array was used in these experiments, each detector consisting of a 0.5-mm- or 1-mm-thick, 1×3-mm-area diamond mounted in a modified SMA connector[18] [see Figs. 107.33(a) and 107.33(b)]. The detectors were biased through a custom-made six-channel bias-tee to 1000 V. Different-thickness CH and Al filters were used to modify the spectral response of the individual detectors. The detectors were fitted with a lead shield that limited the solid angle to an area close to the target [see Fig. 107.33(c)]. The PCD array was used either inside the target chamber at ~50 cm from TCC or on the target chamber wall at ~2.8 m (see Fig. 107.31). Figure 107.34 shows data from one channel on two shots recorded with the PCD array inside the target chamber, illustrating the benefit of the high dynamic

range of the diamond PCD. Both targets were CH/CD/CH foils of 360-μm thickness irradiated with a 1-ps pulse at nominally best focus. The only apparent difference was the laser energy of 340 J in Fig. 107.34(a) and 500 J in Fig. 107.34(b). The first signal at 65 ns can be attributed to x rays from the target and changes by only a factor of 6 between the two shots. A second signal is seen around 100 ns attributed to protons coming from the target. This proton signal is not visible at all in Fig. 107.34(a) but completely saturated the detector in Fig. 107.34(b). The number of shots in this experimental campaign was very limited; therefore it was not possible to reproduce the second shot in Fig. 107.34(b) and use additional attenuation to prevent clipping on both signals. These large variations in the signals pose a significant danger to the recording system as shown in Fig. 107.35. In this case, the PCD array was mounted on the target chamber wall, which limited the x-ray signal to ~2 V in this shot, but the influx of protons was so intense that the PCD shorted completely and dumped all the charge present in the cable through the bias-tee into the input amplifier of the scope. In this case, the cable between the bias-tee and the detector was very short; consequently the energy flowing into the amplifier was limited so the scope recovered from this event. A longer cable or a less-resilient amplifier would have caused permanent damage to the oscilloscope. Because of the lower signal amplitudes, the PCD array is more susceptible to EMP pickup at the target chamber wall. Figure 107.36 shows signals from
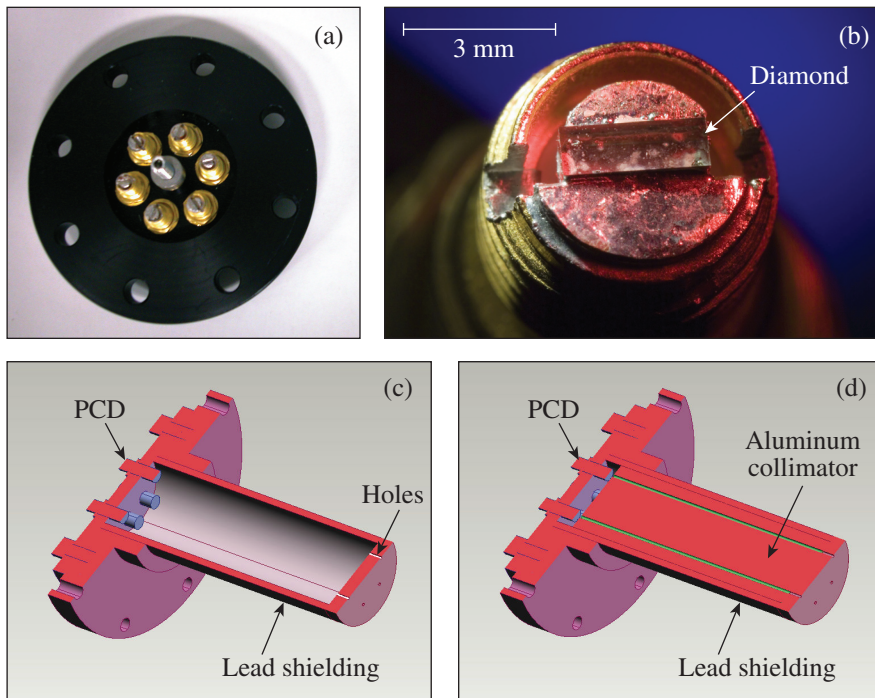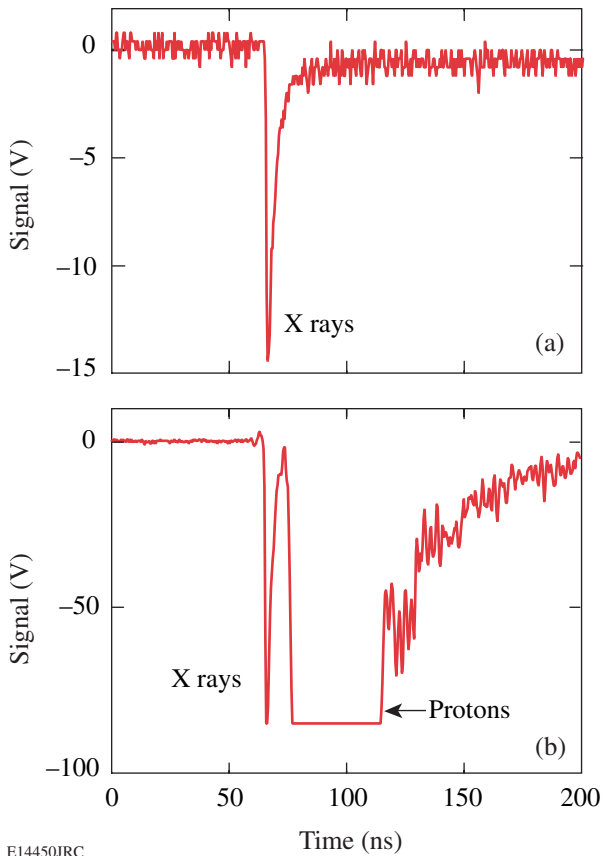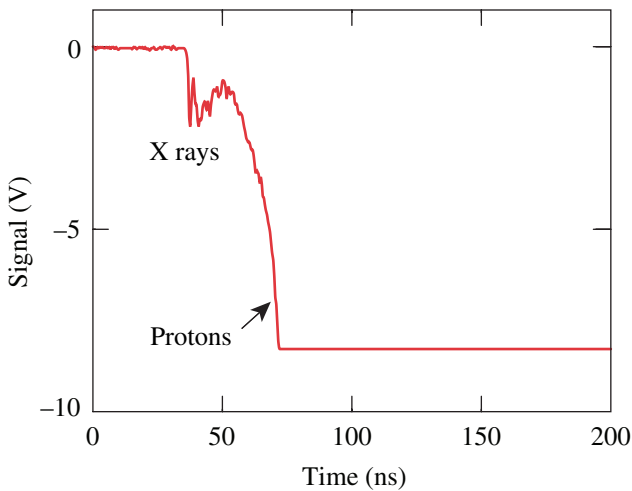

Figure 107.33

(a) Setup of the six-channel diamond PCD detector. (b) A $1 \times 1 \times 3$-mm^3 diamond is mounted in a modified SMA connector. (c) A lead collimator limits the solid angle to an area close to the target. (d) An additional aluminum collimator is inserted into the lead collimator for EMP shielding.

E14460JRC

one channel of the PCD array where the noise from the EMP is significant, (a) without and (b) with additional EMP shielding. The additional EMP shielding consisted of an Al cylinder with six holes for the x rays to reach the PCD array that fits inside the lead collimator [see Fig. 107.33(d)]. This shielding reduced the EMP signals, as seen in the traces between 50 to 100 ns, by roughly a factor of 2 from ~200 to ~100 mV. Since the primary x-ray peak at 50 ns is only ~200 mV, the shielding is not sufficient in this case, but this concept can be further optimized by lengthening the collimator and reducing the hole diameter, thus minimizing further the EMP energy that can couple into the detector.

Scintillator–Photomultiplier Detector

Scintillator–photomultiplier (PMT) detectors have been used extensively for neutron detection in inertial confinement fusion experiments.[19] Since the cross section for a neutron interacting with matter is quite small and the number of neutrons produced in ultrafast laser–plasma interaction experiments is not very

Figure 107.34
Data from one channel of the diamond PCD array mounted inside the target chamber from two shots on 360-μm-thick CH/CD/CH targets irradiated with a 1-ps pulse at best focus with (a) 340 J and (b) 500 J of laser energy.

Figure 107.35
Trace from one channel of the PCD array mounted on the target chamber wall, showing that the device shorts out at high proton fluxes.
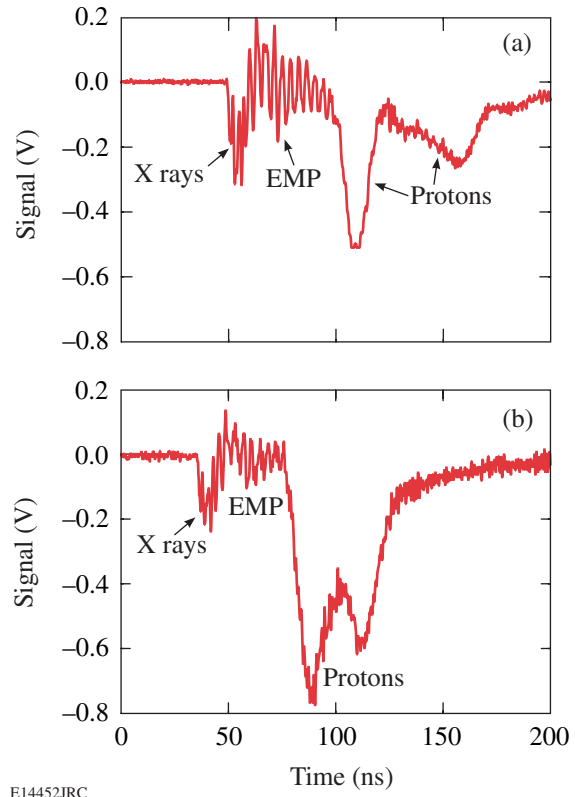
Figure 107.36
Signals from one PCD showing the EMP pickup of an (a) unshielded detector compared to (b) a detector with an additional Al collimator for EMP shielding.

large (~10^8 neutrons have been reported[20]), a large detector volume is required to obtain a measurable neutron signal. The detector used in these experiments has an 18-cm-diam, 10-cm-thick PILOT U[21] scintillator coupled to an XP2020 PMT.[22] A very thick, 5-cm lead shield placed around the scintillator and 25 cm toward the target is required to avoid saturation of the PMT from hard x rays because of its very high gain (of the order of 10^7), even though the interaction cross section of MeV x rays with the scintillator is quite low. Figure 107.37 shows a scintillator signal recorded from a neutron-producing 200-μm-thick CD target irradiated with 558 J of laser energy at 1 ps and best focus compared to a 25-μm Au foil irradiated by 500 J. Even with the very thick shielding, a significant signal from high-energy x rays is detected in both cases, whereas only the CD target data show a second structure ~100 ns later that can be attributed to neutrons of <20-MeV energy. A peak from 2.45-MeV D_2 neutrons was not detected in these experiments; it would appear at ~340 ns in Fig. 107.37. Adding more lead does not significantly increase the signal-to-background ratio because the x-ray attenuation at the minimum of the lead x-ray attenuation cross section (2 to 5 MeV) is comparable to the neutron attenuation length at several-MeV neutron energy.

EMP Mitigation on OMEGA EP

OMEGA EP, a new high-energy petawatt laser system currently under construction at LLE,[10,11] will provide two short-pulse (~1- to 100-ps), 1053-nm beams with a maximum energy

Figure 107.37
Neutrons were seen from CD targets using the scintillator–photomultiplier detector. Results from a non-neutron-producing Au target are shown for comparison.

E14454JRC

of 2.6 kJ at 10 ps, limited only by the current damage threshold of the compression gratings. These short-pulse beams can be combined collinearly and coaxially for fast-ignitor channeling experiments in the OMEGA target chamber or sent to a new OMEGA EP target chamber. Both target chambers are 1.6-m-radius Al spheres of ~7.5-cm thickness. Two additional long-pulse beams can provide up to ~6.5 kJ of 351-nm UV light with up to a 10-ns pulse length into the OMEGA EP target chamber. The two short-pulse beams can also be used as long-pulse UV beams in the OMEGA EP target chamber. The short-pulse beams are focused with an $f/2$ parabola to a <10-μm-radius spot containing 80% of the energy. The intensity in the focal spot is predicted to be in excess of 3×10^{20} W/cm^2. A single OMEGA EP beam will have up to 5× higher energy available compared to the Vulcan petawatt laser. Since both target chambers are of comparable volume, extensive efforts will be required to minimize background and mitigate EMP effects. EMP effects will be most severe for diagnostics, which are inserted into the target chamber using the OMEGA 10-in. manipulators (TIM's). For prompt electronic detectors inside the target chamber (e.g., the diamond PCD's discussed earlier), a grounding scheme is proposed that minimizes the potential for EMP pickup[23] (see Fig. 107.38). The sensor is housed inside a Faraday enclosure, which will be inserted through the TIM into the target chamber. The Faraday enclosure is grounded to the target chamber. The sensor package is electrically isolated inside the Faraday enclosure, and the coaxial signal cable is routed through an electrically conducting conduit into the recording device sitting inside a shielded and grounded diagnostic rack. Special care will be taken to minimize any apertures where electromagnetic energy could couple into the Faraday enclosure and the sensor package. Any currents induced by EMP inside the target chamber will flow through the Faraday enclosure into the target chamber and back to the target. Currents outside the target chamber will flow through the conduit, so the influence on the measurement through the coaxial cable will be minimized. Sensors that do not produce a prompt electrical signal at shot time (like CCD's or streak cameras) will use a different EMP shielding approach. The Faraday enclosure in these detectors will also serve as a pressure vessel to maintain atmospheric pressure around the readout and control electronics. Fiber optics will be used to transmit command information and data. A single dc voltage fed into the enclosure and converted into the required voltages inside the pressure vessels using shielded and filtered dc–dc converters will power these systems. Using a relatively high voltage of 28 V will limit any effects of EMP noise pickup on the feed lines even if it exceeds several volts for many milliseconds.
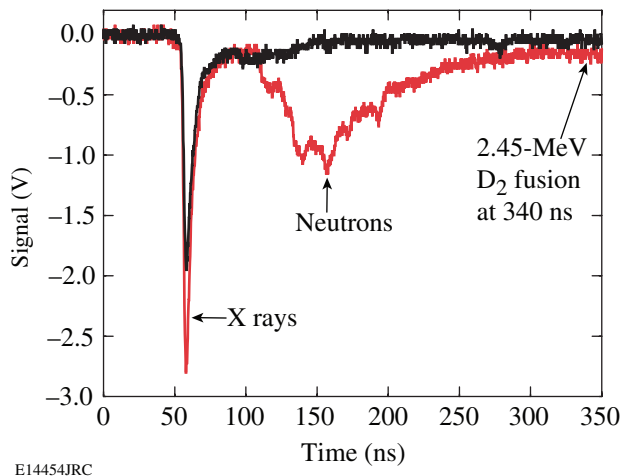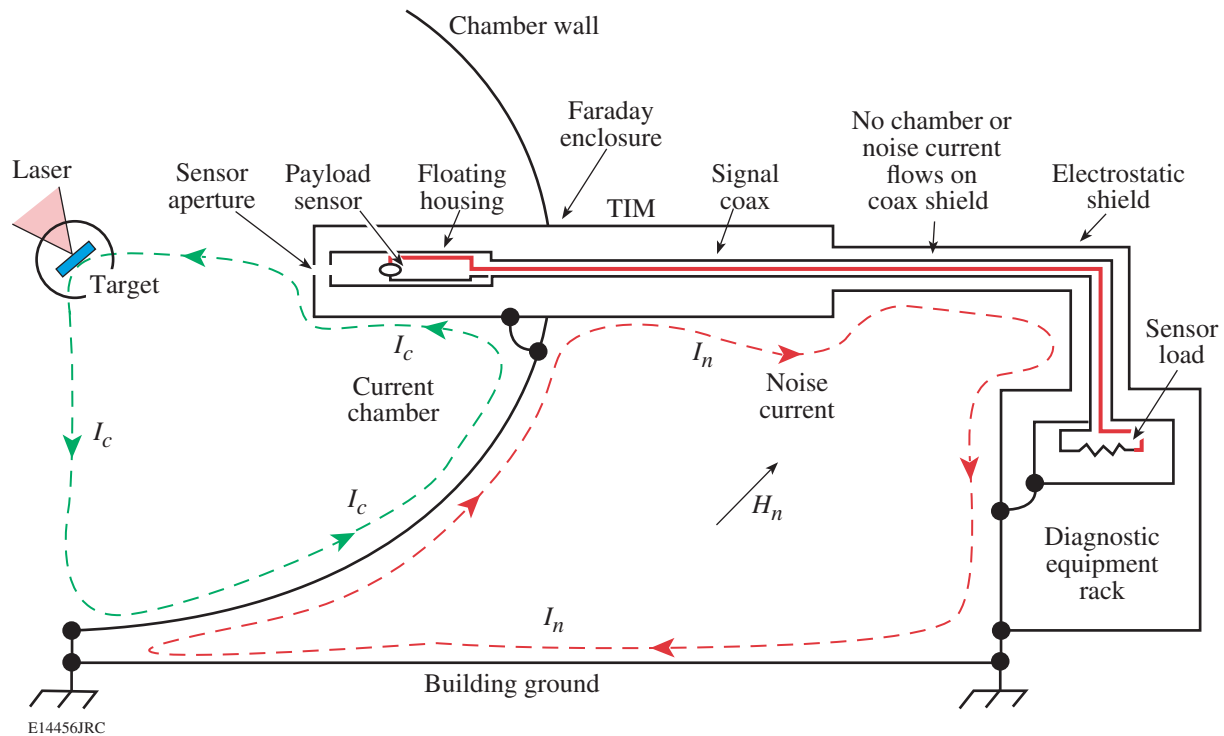
Chamber wall

Faraday
enclosure

No chamber or
noise current
flows on
coax shield

Laser

Sensor
aperture

Payload
sensor

Floating
housing

Signal
coax

Electrostatic
shield

TIM

Target

Sensor
load

I_c

Current
chamber

I_n

Noise
current

I_c

I_c

I_c

H_n

Diagnostic
equipment
rack

I_n

I_n

Building ground

E14456JRC

Figure 107.38
Proposed grounding and shielding for the TIM diagnostic-insertion setup on OMEGA EP.

Discussion

To minimize x-ray background in high-energy petawatt laser-interaction experiments, it is necessary to shield not only the direct line of sight, but also the full solid angle around the detector, because Compton-scattered and fluorescence photons can enter the detector from all sides. The high variability of the x rays or particles emitted from the target poses a significant risk to sensitive recording equipment, especially if a detector is run with a high bias voltage, like diamond PCD's, CVD diamond detectors, and certain photodiodes. EMP pickup is of special concern inside the target chamber, where EMP can easily overwhelm weak signals from detectors as seen with the PCD detectors on Vulcan. If possible it is much better to mount the detector outside the target chamber in a much lower EMP environment. These lessons learned from the RAL peta-watt experiments will be applied in the experiments on the upcoming OMEGA EP high-energy petawatt facility, where optimized grounding strategies and detector configurations are being implemented.

REFERENCES

1. K. Yasuike *et al.*, Rev. Sci. Instrum. **72**, 1236 (2001).

2. S. P. Hatchett *et al.*, Phys. Plasmas **7**, 2076 (2000).

3. J. L. Bourgade, V. Allouche, J. Baggio, C. Bayer, F. Bonneau, C. Chollet, S. Darbon, L. Disdier, D. Gontier, M. Houry, H. P. Jacquet, J.-P. Jadaud, J. L. Leray, I. Masclet-Gobin, J. P. Negre, J. Raimbourg, B. Villette, I. Bertron, J. M. Chevalier, J. M. Favier, J. Gazave, J. C. Gomme, F. Malaise, J. P. Seaux, V. Yu. Glebov, P. Jaanimagi, C. Stoeckl, T. C. Sangster, G. Pien, R. A. Lerche, and E. Hodgson, Rev. Sci. Instrum. **75**, 4204 (2004).

4. M. A. Stoyer, T. C. Sangster, E. A. Henry, M. D. Cable, T. E. Cowan, S. P. Hatchett, M. H. Key, M. J. Moran, D. M. Pennington, M. D. Perry, T. W. Phillips, M. S. Singh, R. A. Snavely, M. Tabak, and S. C. Wilks, Rev. Sci. Instrum. **72**, 767 (2001).

5. Y. Okano *et al.*, J. Appl. Phys. **95**, 2278 (2004).

6. R. A. Snavely, M. H. Key, S. P. Hatchett, T. E. Cowan, M. Roth, T. W. Phillips, M. A. Stoyer, E. A. Henry, T. C. Sangster, M. S. Singh, S. C. Wilks, A. MacKinnon, A. Offenberger, D. M. Pennington, K. Yasuike, A. B. Langdon, B. F. Lasinski, J. Johnson, M. D. Perry, and E. M. Campbell, Phys. Rev. Lett. **85**, 2945 (2000).

7. K. L. Lancaster, S. Karsch, H. Habara, F. N. Beg, E. L. Clark, R. Freeman, M. H. Key, J. A. King, R. Kodama, K. Krushelnick, K. W. D. Ledingham, P. McKenna, C. D. Murphy, P. A. Norreys, R. Stephens, C. Stoeckl, Y. Toyama, M. S. Wei, and M. Zepf, Phys. Plasmas **11**, 3404 (2004).

8. C. B. Edwards *et al.*, in *25th International Congress on High-Speed Photography and Photonics*, edited by C. Cavailler, G. P. Haddleton, and M. Hugenschmidt (SPIE, Bellingham, WA, 2003), Vol. 4948, pp. 444–451.

9. C. N. Danson *et al.*, in *Inertial Fusion Sciences and Applications 2001*, edited by K. A. Tanaka, D. D. Meyerhofer, and J. Meyer-ter-Vehn (Elsevier, Paris, 2002), pp. 479–483.

10. L. J. Waxer, D. N. Maywar, J. H. Kelly, T. J. Kessler, B. E. Kruschwitz, S. J. Loucks, R. L. McCrory, D. D. Meyerhofer, S. F. B. Morse, C. Stoeckl, and J. D. Zuegel, Opt. Photonics News **16**, 30 (2005).

11. C. Stoeckl, J. A. Delettrez, J. H. Kelly, T. J. Kessler, B. E. Kruschwitz, S. J. Loucks, R. L. McCrory, D. D. Meyerhofer, D. N. Maywar, S. F. B. Morse, J. Myatt, A. L. Rigatti, L. J. Waxer, J. D. Zuegel, and R. B. Stephens, Fusion Sci. Technol. **49**, 367 (2006).

12. J. L. Collier *et al.*, *Central Laser Facility Annual Report 2002/2003*, 168, Rutherford Appleton Laboratory, Chilton, Didcot, Oxon, England, RAL Report No. RAP-TR-2003-018 (2003).

13. C. Stoeckl, W. Theobald, T. C. Sangster, M. H. Key, P. Patel, B. B. Zhang, R. Clarke, S. Karsch, and P. Norreys, Rev. Sci. Instrum. **75**, 3705 (2004).

14. G. J. Schmid, R. L. Griffith, N. Izumi, J. A. Koch, R. A. Lerche, M. J. Moran, T. W. Phillips, R. E. Turner, V. Yu. Glebov, T. C. Sangster, and C. Stoeckl, Rev. Sci. Instrum. **74**, 1828 (2003).

15. Picosecond Pulse Labs, Boulder, CO 80301.

16. Oscilloscope Model No. TDS684, Tektronix, Inc., Beaverton, OR 97077.

17. D. R. Kania *et al.*, Rev. Sci. Instrum. **61**, 2765 (1990).

18. Alameda Applied Sciences Corporation, San Leandro, CA 94577.

19. M. D. Cable and M. B. Nelson, Rev. Sci. Instrum. **59**, 1738 (1988).

20. P. A. Norreys *et al.*, Plasma Phys. Control. Fusion **40**, 175 (1998).

21. Nuclear Enterprises Ltd., United Kingdom.

22. Koninklijke Philips Electronics N.V., The Netherlands.

23. M. E. Morris *et al.*, Lawrence Livermore National Laboratory, Livermore, CA, UCRL-TM-212140, NIF-0111782 (April 2005).

Gain Apodization in Highly Doped, Distributed-Feedback (DFB) Fiber Lasers

Introduction

Fiber lasers have been the subject of much research over the past ten years. They can provide high reliability, fiber compatibility, high output power, good beam quality, narrow bandwidth, low phase noise, and low relative intensity noise (RIN).[1–4] These characteristics make them promising alternatives to solid-state and semiconductor lasers. Distributed-feedback (DFB) fiber lasers can be designed with a grating structure to provide high output power (up to 60 mW), single frequency,[5] single polarization,[6] and high optical signal-to-noise ratio (OSNR).[6] DFB fiber lasers have been widely used in sensing,[7] communication systems,[8–11] and high-precision spectroscopy,[12] all of which require single-mode, single-frequency lasers.

To obtain higher-power DFB fiber lasers, doping levels have been increased to allow more pump light to be absorbed with the doping densities of commercial Yb-doped fibers approaching 1×10^{25}/cm³ (e.g., INO, Nufern). With the commercial availability of 500-mW pump lasers, the absorption transition easily becomes saturated. As the majority of the pump light is absorbed or converted into lasing photons, however, the remainder of the fiber is essentially unpumped. The transition length between the pumped and unpumped regions is given by the small-signal absorption, which is of the order of a millimeter or less. This gain apodization effect with pumped and unpumped sections of the DFB laser has so far been neglected.

In this article, the effects of gain apodization in DFB fiber lasers are investigated. In particular, the impact on threshold behavior is explored along with its effect on output power and mode discrimination. In the following sections (1) the conventional model based on coupled-wave equations is reviewed and applied to our case of fiber lasers; (2) the physics of gain apodization in DFB lasers is explored and compared to conventional configurations; (3) the impact of gain apodization on phase-shifted DFB fiber lasers is investigated; (4) lasing thresholds and the output power ratio from both ends of the fiber lasers are analyzed; and, finally, (5) techniques for using gain apodization as an optimization tool are discussed.

Coupled-Wave Matrix Model

Although DFB lasers are widely used for single-mode operation, in general their mode spectrum is more complicated. In a uniform index-coupled DFB fiber laser without phase shift or end mirrors, DFB lasers can operate in one of two degenerate longitudinal modes symmetrically located along the Bragg frequency of the grating. Nominally, only a single mode runs because of fabrication imperfections that cause slight asymmetry.

Coupled-mode theory[13,14] can be used to analyze the threshold behavior in simple DFB lasers. Figure 107.39 is a schematic of the coupling between forward and backward waves in waveguides induced by periodic modulation of the refractive index n. For a uniform fiber grating with uniform gain, the coupled-wave equations can be written as[15]

$$dE_A \big/ dz = \kappa \exp\big[i(2 \, \Delta\beta z - \phi)\big]E_B + gE_A,$$
$$dE_B \big/ dz = \kappa \exp\big[-i(2 \, \Delta\beta z - \phi)\big]E_A - gE_B, \tag{1}$$

where E_A and E_B are the complex amplitudes of the forward and backward propagating waves, $\Delta\beta = \beta - m\pi/\Lambda$ is the propagation constant difference between the wave in the z direction and the mth Bragg frequency of the grating ($m = 1$ for first-order gratings), ϕ is the wave phase at the position $z = 0$, κ is the coupling coefficient between the forward and
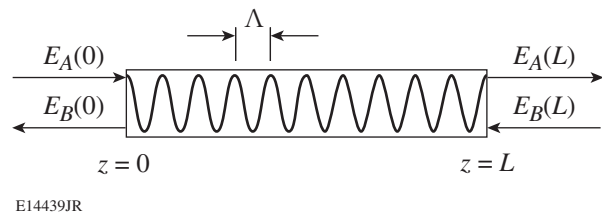

E14439JR

Figure 107.39
Schematic of coupled waves in periodic active waveguides.

backward waves in the grating, and g is the gain coefficient of the active medium collocated with the grating. In the absence of reflections from either side of the structures, Eq. (1) can be solved analytically.

To model a more complicated structure, e.g., where the gain is not constant along z, a matrix method[15,16] can be used to concatenate the solutions to Eq. (1). In this formalism, a non-uniform periodic structure is broken into segments of uniform period structures each with the solution

$$\begin{bmatrix} E_A(z_{j+1}) \\ E_B(z_{j+1}) \end{bmatrix} = \begin{pmatrix} F_{11}^j & F_{12}^j \\ F_{21}^j & F_{22}^j \end{pmatrix} \begin{bmatrix} E_A(z_j) \\ E_B(z_j) \end{bmatrix}, \quad (2)$$

where the matrix elements are the solutions to Eq. (1) given by

$$F_{11}^j = \left[\cosh(\gamma_j L_j) + i\,\Delta\beta_j'\, L_j \sinh(\gamma_j L_j)/(\gamma_j L_j) \right]$$
$$\times \exp(i\beta_B^j L_j),$$

$$F_{12}^j = -\kappa_j L_j \sinh(\gamma_j L_j) \exp\left[-i(\beta_B^j L_j + \phi_j) \right]/(\gamma_j L_j),$$

$$F_{21}^j = -\kappa_j L_j \sinh(\gamma_j L_j) \exp\left[i(\beta_B^j L_j + \phi_j) \right]/(\gamma_j L_j), \quad (3)$$

$$F_{22}^j = \left[\cosh(\gamma_j L_j) - i\,\Delta\beta_j'\, L_j \sinh(\gamma_j L_j)/(\gamma_j L_j) \right]$$
$$\times \exp\left[-i(\beta_B^j L_j) \right],$$

and where $\Delta\beta_j' = \Delta\beta_j + ig_j$, $\gamma_j^2 = \kappa_j^2 - (\Delta\beta_j')^2$, and $\beta_B^j = \pi/\Lambda_j$. With this formalism the active gratings can be split into N sections where the total matrix will be $F_t = F_N F_{N-1} \ldots F_2 F_1$. For a nonuniform DFB fiber laser, the coupling coefficient κ and gain coefficient g can change with the position z. For DFB fiber lasers without a phase shift, the phase terms in Eq. (3) can be written as $\phi^k = \phi^{k-1} + 2\beta_B^k L^{k-1}$, where $k = 1,2,\ldots N$. For phase-shifted DFB fiber lasers, the phase terms in Eq. (3) can be written as $\phi^k = \phi^{k-1} + 2\beta_B^k L^{k-1} + \Delta\phi^k$, $k = 1,2,\ldots N$. Adding the boundary conditions $E_A(0) = E_B(L) = 0$, the gain threshold condition can be obtained from the relation $F_{t11} = 0$ (Ref. 15). Nominally, this relation will produce a mode spectrum with different modes appearing at different frequencies $\Delta\beta$.

For high-power operation, it is desirable not only to have a low threshold but also to have most of the light coming out of only one side of the cavity. By using the total matrix F_t, the output power ratio from both ends of the fiber can be written as

$$\frac{P_1}{P_2} = \left| \frac{E_B(0)}{E_A(L)} \right|^2 = \left| F_{21}^2 \right|, \quad (4)$$

where P_1/P_2 presents the ratio of the power coupling out at $z = 0$, as compared to $z = L$.

Gain-Apodization Physics

To understand the physics introduced by gain apodization, the formalism in the previous section is applied to three cases. In all cases, the grating strength κ and period Λ are kept constant and no phase shift will be included. The peak reflectivity of the grating is determined by $R = \tanh^2(\kappa L)$, and, so that the desired generality is not lost, typical values for κ and L are chosen. In the following sections, the coupling coefficient of the fiber grating is $\kappa = 1$ cm^{-1} and the grating lengths are 3 cm in most cases. Since the length under which the gain will drop from its maximum value to zero is less than 1 mm, the gain apodization along the z axis will be approximated by a step function. The gain-apodized DFB fiber laser is schematically shown in Fig. 107.40(a), where the L_1 section is highly doped with the uniform gain coefficient g and L_2 has no gain. This case will be compared to two other cases: The first, a DFB fiber laser of length L_1 and uniform gain but no unpumped section, is shown in Fig. 107.40(b). The second case, shown in

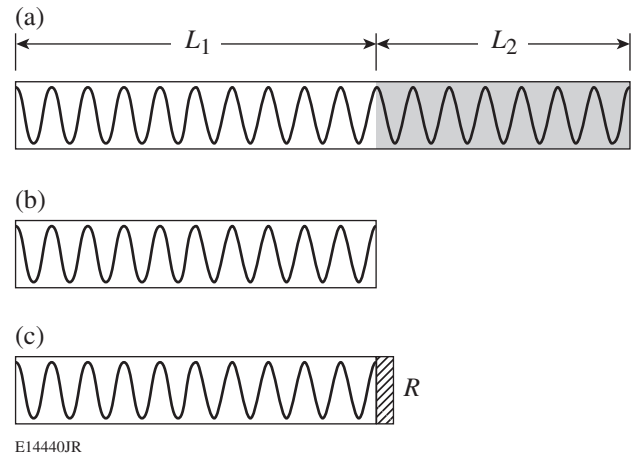

(a)

L_1 L_2

(b)

(c)

R

E14440JR

Figure 107.40
Schematic of the (a) gain-apodized DFB fiber laser, (b) uniform DFB fiber laser, and (c) uniform DFB fiber laser with end reflector $R_2 = \tanh^2(\kappa L_2)$. The shaded regions indicate sections with no gain.

Fig. 107.40(c), is the same laser as shown in Fig. 107.40(b) but with a reflector at the end of the cavity where the grating would be in the apodized case. The reflectivity value is chosen to be the peak reflectivity of the unpumped fiber grating of the case shown in Fig. 107.40(a), namely, $R_2 = \tanh^2(\kappa L_2)$. This value was chosen to directly compare to the apodized case shown in Fig. 107.40(a).

The gain thresholds for these cases where $L_1 = 2.5$ cm and $L_2 = 0.5$ cm are shown in Fig. 107.41. The horizontal axis is the normalized frequency $\Delta \beta L$ (where $L = L_1 + L_2$), while the vertical axis is the normalized gain threshold $g_{th}L_1$. The gain is normalized with L_1 since the value of gL_1 relates to the pump power. The mode spectra of the three different lasers are nearly identical since the lasing cavities are of nearly equal length. When compared to the short DFB laser, the gain-apodized DFB lasers show a nearly 30% reduction in lasing threshold due to its passive grating section. The DFB with the reflector similarly shows a reduction in the lasing threshold for its first-order mode. However, the threshold reduction applies significantly to all modes since the reflector is spectrally uniform. For the gain-apodized DFB laser, whose passive section has spectral dependence, the additional reflector also aids in modal discrimination with higher-order modes.
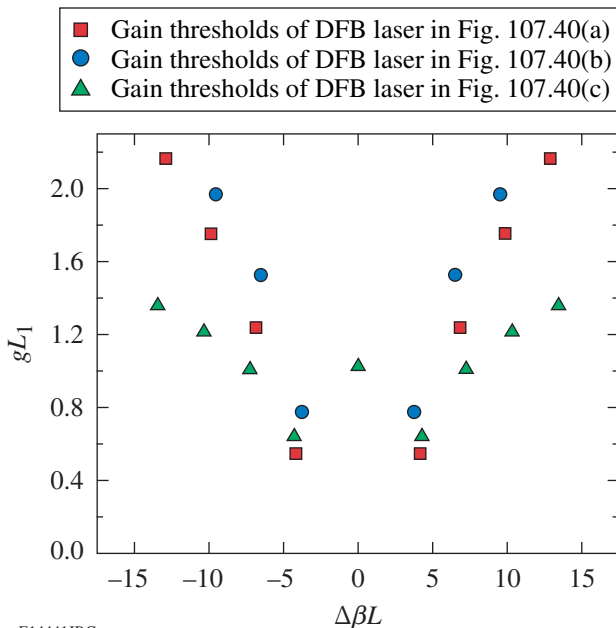
It is also important to note that although the passive grating system introduces system asymmetry, the zeroth-order mode cannot reach the lasing threshold since the phase of the transition between the two sections is maintained. Nevertheless, Fig. 107.41 demonstrates the advantage of using gain apodization for reduced lasing threshold without the penalty of decreased spectral purity.

Figure 107.42 shows the gain threshold for DFB lasers plotted with the Bragg grating reflection spectrum to understand the interplay of active versus grating length. The grating reflection spectrum can be formulated as[17]

$$R_g(\delta) = \left| r_g(\delta) \right|^2 = \left| \frac{i\kappa \sin(qL)}{q\cos(qL) - i\delta\sin(qL)} \right|^2, \qquad (5)$$
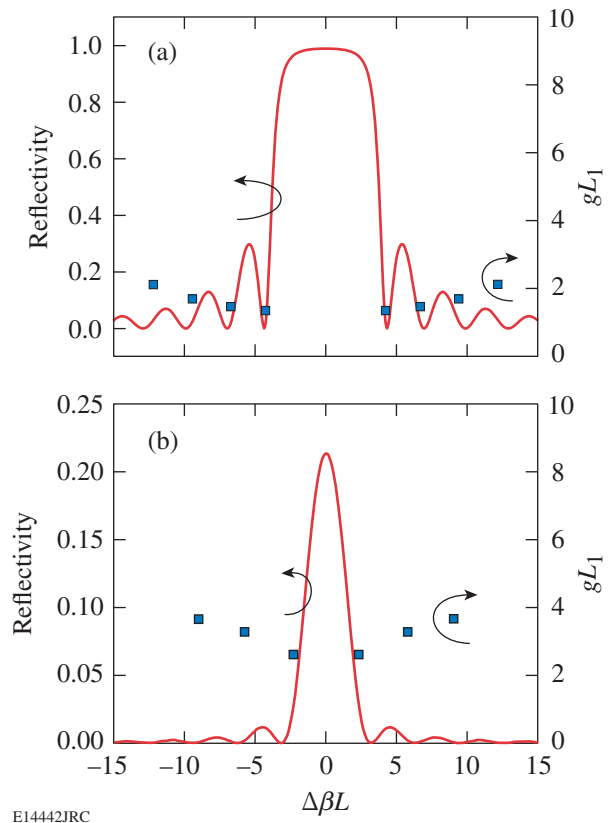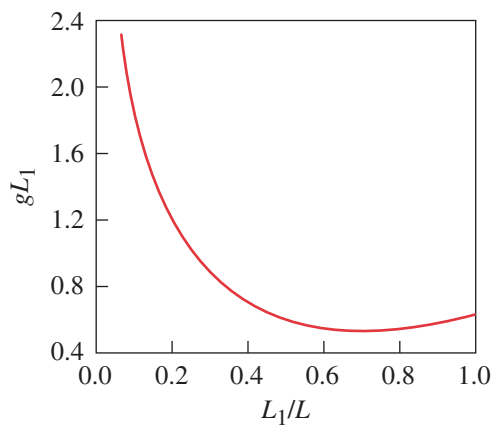
E14442JRC

Figure 107.42
(a) The modal frequencies of a gain-apodized DFB fiber laser with $L_1 = 0.5$ cm, $L_2 = 2.5$ cm, and a reflection spectrum of a 3-cm fiber Bragg grating. (b) The modal frequencies of a 0.5-cm uniform-gain DFB fiber laser and a reflection spectrum of a 0.5-cm fiber Bragg grating.

- ■ Gain thresholds of DFB laser in Fig. 107.40(a)
- ● Gain thresholds of DFB laser in Fig. 107.40(b)
- ▲ Gain thresholds of DFB laser in Fig. 107.40(c)

E14441JRC

Figure 107.41
Gain thresholds of the DFB fiber laser configurations shown in Fig. 107.40.

where $\delta(\omega) = (\bar{n}/c)(\omega - \omega_B) \equiv \beta(\omega) - \beta_B$, κ is the coupling coefficient of the grating, L is the grating length, and $q = \pm\sqrt{\delta^2 - \kappa^2}$.

To exaggerate the physics, the active portion of the gain-apodized DFB fiber laser is chosen to be $L_1 = 0.5$ cm with the passive portion longer, $L_2 = 2.5$ cm. The mode spectrum of this laser and the corresponding reflectivity of a 3-cm fiber Bragg grating (FBG) are shown in Fig. 107.42(a). For comparison, Fig. 107.42(b) shows the mode spectrum of a conventional 0.5-cm-long DFB laser with the reflectivity spectrum of a 0.5-cm FBG. It is clear from these figures that the mode spectrum of the gain-apodized laser is determined by the entire grating rather than only by the active portion.

Figure 107.43 shows the lowest modal gain threshold versus gain length L_1 for the gain-apodized DFB laser. From this figure, it is clear that the minimum threshold for L_1/L is close to 0.7; the gain threshold is 17.9% less compared to the uniform DFB fiber laser ($L_1/L = 1$). For gain lengths L_1/L less than unity, the longitudinal distribution of light extends into the unpumped region, creating an effectively higher reflectivity. Since no gain is extracted from this region, the effective grating strength is increased, thus creating a lower gain threshold. For values of L_1/L that are too small (less than 0.7 in this case), the grating-length product becomes too small to produce sufficient reflection, effectively increasing the laser threshold via reduced feedback. Figure 107.43 demonstrates that gain apodization can decrease the laser threshold if properly tailored.

Impact on Phase-Shifted DFB Lasers

It is convenient to avoid mode degeneracy by introducing a phase shift in the middle of the grating. As is well known, the π-phase shift will enable a narrowband filter in the grating-forbidden band, thereby allowing the zeroth-order mode to have a low lasing threshold.[18] Considering the influence of this geometry, it is instructive to understand the role of gain apodization on phase-shifted DFB fiber lasers.

Figures 107.44(a) and 107.44(b) show the lowest-mode gain threshold and the mode discrimination of the uniform-gain, phase-shifted DFB fiber lasers. As before, the total cavity length L is 3 cm and the coupling coefficient is 1 cm^{-1}. The results show that the apodization with the lowest gain threshold also has nearly the largest mode discrimination. Slightly different to the optimum L_1/L of 0.7 for a normal DFB laser in Fig. 107.43, the optimum gain-apodization profile will be where
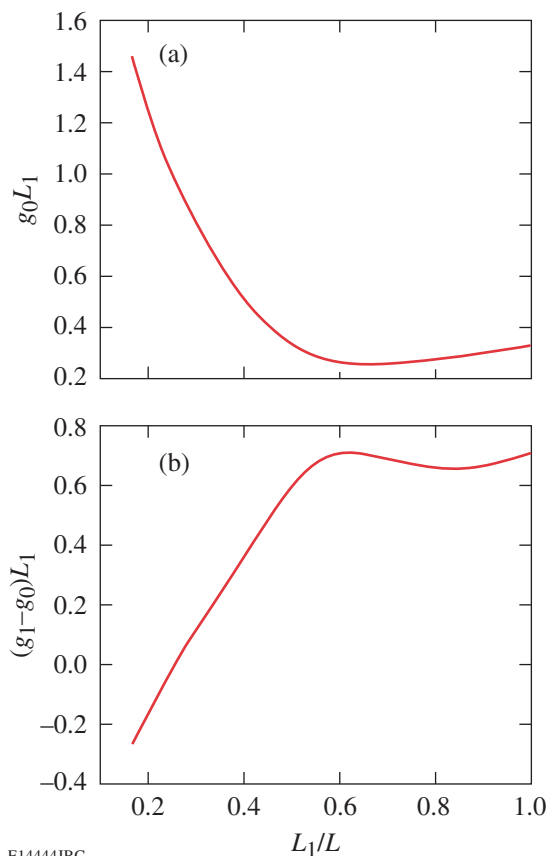

E14444JRC

Figure 107.44
(a) The lowest-mode gain threshold versus L_1/L. (b) The mode-1 and mode-0 gain threshold difference versus L_1/L.

E14443JRC

Figure 107.43
The gain thresholds of the lowest-order mode as a function of gain-apodization profile.

L_1/L is close to 0.6. From Fig. 107.44(a), the gain threshold can be reduced 21.2%, compared to the normal phase-shifted DFB fiber laser with nearly the same modal discrimination, as shown in Fig. 107.44(b).

Since the gain apodization has introduced system asymmetry, the output power ratio from both ends of the laser will also be modified. To investigate these characteristics, the output power ratio of Eq. (4) is plotted against the apodized gain length L_1/L in Fig. 107.45. The power ratio from both ends of the fiber changes monotonically with the apodization gain length L_1/L. Higher output power from the pumped end of the cavity can be obtained at the optimum pumped length L_1/L for the minimum threshold shown in Fig. 107.44(a); the power ratio can be increased by 12.4%. This asymmetry, combined with the 21.2% threshold reduction, can lead to a substantial increase in output power solely because of gain apodization.

Discussion and Conclusions

It was shown in the previous section that gain apodization can have a beneficial impact on phase-shifted DFB lasers. It has been previously shown that DFB laser performance can be improved by changing the location of the phase shift and varying κ along the laser axis.[19,20] To obtain the highest single-frequency output from DFB fiber lasers, the gain-apodization length, phase-shift location, and coupling coefficient profile must all be optimized. While this presents a challenging numerical problem, genetic algorithms have proven useful in optimizing laser and amplifier designs.[21–23]
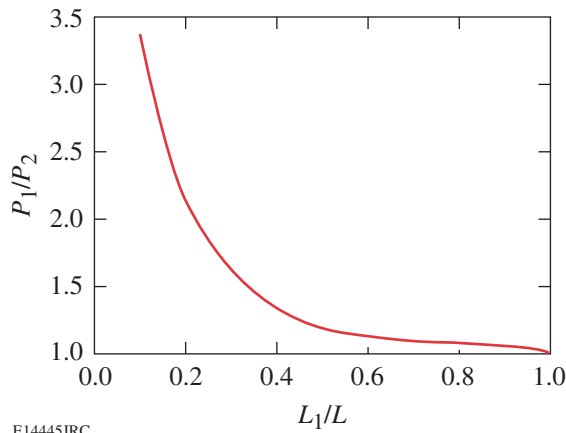
While the lasing threshold itself will determine the gain-apodization profile for a given DFB laser, this effect can be intentionally introduced. Two separate sections of photosensitive fiber, only one of which is doped with active ions to provide gain, can be spliced together before a grating is written into the fiber. In this way, the independent control of the gain profile, grating strength, and phase-shift location can be used to optimize of DFB laser performance.

In conclusion, the effects of gain apodization in highly doped DFB fiber lasers were investigated. In particular, apodization of the longitudinal gain profile resulted in a lower lasing threshold than a laser with uniform gain without the penalty of modal discrimination. For the case studied, the lasing threshold was reduced by almost 18% for a conventional DFB laser and over 21% for a DFB laser with a π-phase shift. Furthermore, the longitudinal asymmetry introduced by gain apodization yielded a significantly higher ratio of output power from opposite ends of the laser. Methods of engineering and optimizing such a gain-apodized DFB fiber laser were also discussed.

REFERENCES

1. G. A. Cranch, M. A. Englund, and C. K. Kirkendall, IEEE J. Quantum Electron. **39**, 1579 (2003).

2. K. H. Ylä-Jarkko, IEEE Photonics Technol. Lett. **15**, 191 (2003).

3. L. Qiu *et al.*, IEEE Photonics Technol. Lett. **16**, 2592 (2004).

4. S. Foster, IEEE J. Quantum Electron. **40**, 1283 (2004).

5. Ch. Spiegelberg *et al.*, in *Optical Fiber Communications Conference, 2003*, OSA Trends in Optics and Photonics (TOPS), Vol. 86 (Optical Society of America, Washington, DC, 2003).

6. M. Ibsen *et al.*, in *Lasers and Electro-Optics, 1999 (CLEO '99)* (Optical Society of America, Washington, DC, 1999), Paper CWE4, pp. 245–246.

7. J. T. Kringlebotn, W. H. Loh, and R. I. Laming, Opt. Lett. **21**, 1869 (1996).

8. R. Gross, R. Olshansky, and M. Schmidt, IEEE Photonics Technol. Lett. **2**, 66 (1990).

9. U. Gliese, E. L. Christensen, and K. E. Stubkjaer, J. Lightwave Technol. **9**, 779 (1991).

E14445JRC

Figure 107.45
The output power ratio from the fiber ends versus L_1/L.

10. J. Hübner, P. Varming, and M. Kristensen, Electron. Lett. **33**, 139 (1997).

11. F. Liu *et al.*, Electron. Lett. **36**, 620 (2000).

12. R. Böhm *et al.*, Opt. Lett. **18**, 1955 (1993).

13. H. Kogelnik and C. V. Shank, J. Appl. Phys. **43**, 2327 (1972).

14. W. Streifer, D. R. Scifres, and R. D. Burnham, IEEE J. Quantum Electron. **QE-13**, 134 (1977).

15. M. Yamada and K. Sakuda, Appl. Opt. **26**, 3474 (1987).

16. S. Radic, N. George, and G. P. Agrawal, IEEE J. Quantum Electron. **31**, 1326 (1995).

17. G. P. Agrawal, *Lightwave Technology: Components and Devices* (Wiley, Hoboken, NJ, 2004).

18. G. P. Agrawal, J. E. Geusic, and P. J. Anthony, Appl. Phys. Lett. **53**, 178 (1988).

19. K. Yelen, L. M. B. Hickey, and M. N. Zervas, IEEE J. Quantum Electron. **40**, 711 (2004).

20. K. Yelen, M. N. Zervas, and L. M. B. Hickey, J. Lightwave Technol. **23**, 32 (2005).

21. C. Cheng, Z. Xu, and C. Sui, Opt. Commun. **227**, 371 (2003).

22. M. Gao *et al.*, Opt. Express **12**, 5603 (2004).

23. C. Cheng and S. He, Microw. Opt. Technol. Lett. **22**, 343 (1999).

Cryogenic DT and D$_2$ Targets for Inertial Confinement Fusion

Introduction

Laboratory-based ignition via inertial confinement fusion (ICF)[1] will be achieved by imploding a spherical capsule containing a frozen layer of deuterium and tritium (DT) fuel on the MJ-class National Ignition Facility (NIF)[2] currently under construction at Lawrence Livermore National Laboratory (see Fig. 108.1). Virtually all ICF ignition target designs are based on a spherical low-Z ablator containing a solid, cryogenic DT-fuel shell surrounding a low-density DT vapor at, or slightly below, the triple point. There are two fundamental target designs for ignition: capsules directly illuminated by the laser (direct drive[3]) and capsules driven by a uniform x-ray radiation field created by illuminating the inside surface of a high-Z cylindrical hohlraum (indirect drive[4]). Figure 108.2 illustrates the drive concept and capsule design for both direct- and x-ray-drive ignition targets. X-ray-drive ignition capsules[5] are based on a thick, copper-doped Be ablator surrounding a relatively thin DT-ice layer; capsules for direct-drive ignition[3] consist of a very thin plastic shell surrounding a relatively thick DT-ice layer. When these capsules are illuminated by either the laser or the x-ray field inside a hohlraum, the ablator material is rapidly heated and driven away from the capsule. The resulting shock compresses the DT-fuel shell, raising the pressure in the central gas region (or core) to several Mbar. Once the laser irradiation ceases, the fuel shell begins to decelerate, further compressing and heating the core as the shell's kinetic energy is converted to thermal energy via PdV work. To initiate a thermonuclear burn, the temperature and areal density of the core must reach approximately 10 keV and 300 to 400 mg/cm^2, respectively.[4] Under these conditions, the rate of energy deposited in the fuel by the 3.5-MeV ^{4}He nuclei from the DT–fusion reaction is greater than the energy lost by electron conduction or x-ray emission, and a thermonuclear burn wave propagates through the dense fuel shell in a few tens of picoseconds. This is much shorter that the fuel-disassembly time of a few hundred picoseconds.

1.8 MJ

Under construction at LLNL
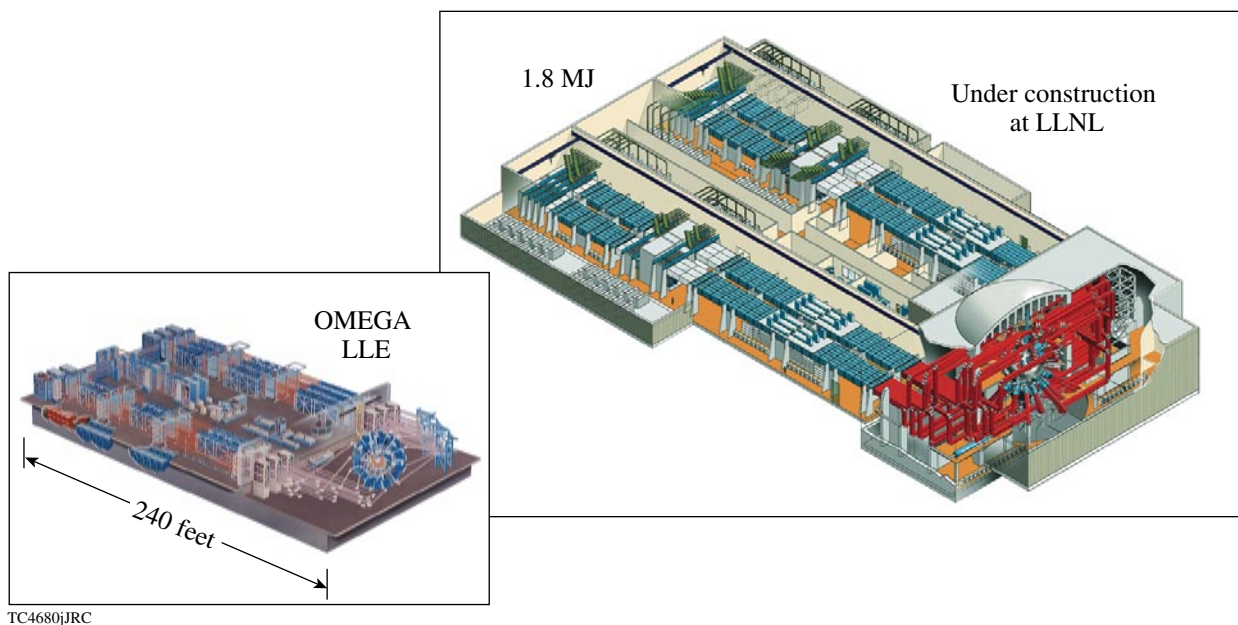
OMEGA LLE

240 feet

TC4680jRC

Figure 108.1
The National Ignition Facility (NIF) is under construction at Lawrence Livermore National Laboratory and will begin ignition experiments with cryogenic DT targets in 2010. LLE's OMEGA laser is being used to develop the scientific and technical basis for ignition on the NIF. OMEGA performs 40 to 50 cryogenic D$_2$ and DT implosions annually in support of the ignition mission.
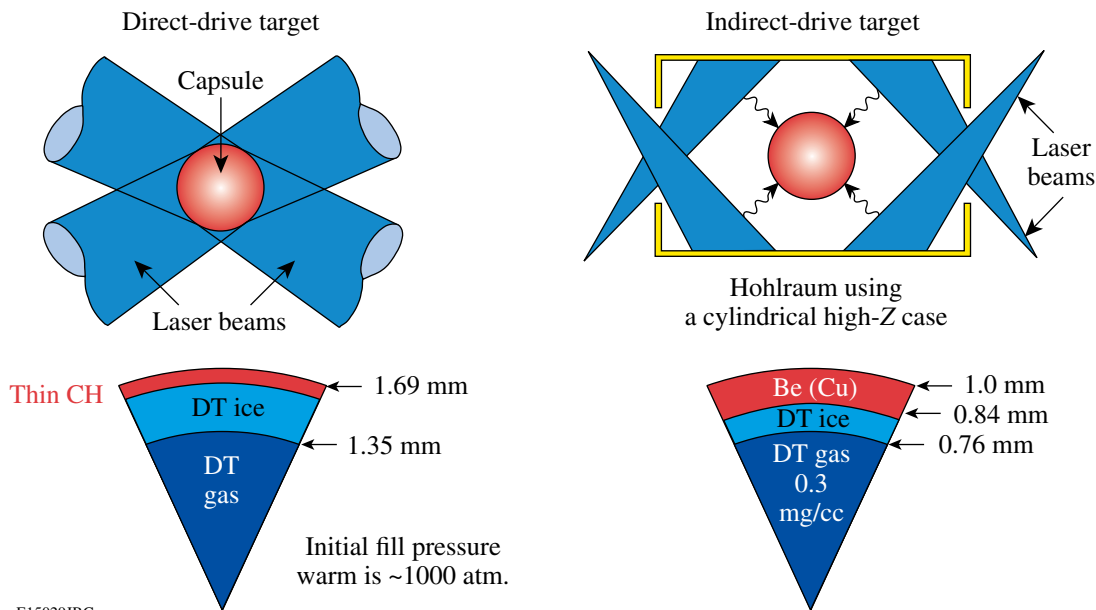
Figure 108.2
The basic ignition-target designs are shown along with the fundamental concepts for direct and indirect (or x-ray) drive.

For nearly two decades, LLE has been developing the scientific and engineering basis to create and characterize cryogenic DT capsules and to study the implosion performance under scaled-ignition conditions. Cryogenic fuel shells are the preferred configuration for ICF because the fuel can be compressed isentropically, minimizing the laser energy required to achieve ignition conditions.[6] Since beginning cryogenic target implosions on the 60-beam, 30-kJ UV OMEGA laser[7] (see Fig. 108.1), 118 cryogenic D_2 (Refs. 8–11) and 15 cryogenic DT capsules have been imploded. While the compressed-fuel densities and core temperatures of these cryogenic DT implosions will never meet the criteria for ignition, measured fuel areal densities (the product of the fuel density and the radial extent of the fuel) have been inferred in excess of 100 mg/cm². This is an important step toward the demonstration of energy gain via ICF and ultimately the realization of inertial fusion energy.[12]

The uniformity of the inner surface of the DT-ice layer is one of the critical factors that determine target performance.[3,4] As the high-density fuel shell decelerates and compresses, inner-surface perturbations grow due to the Rayleigh–Taylor instability.[13] These perturbations include ablation-front features that feed through the fuel shell[14] and native inner-ice-surface roughness from the layering process described in **Cryogenic D_2 and DT Target Fabrication and Characterization** (p. 170). The ablation-front perturbations are generated primarily by laser nonuniformities and the feedout of inner-ice-surface perturbations carried by the reflected shock. These ablation-front perturbations

can be controlled by conditioning the laser pulse[15] or by careful design of the hohlraum used to create a homogenous radiation field around the capsule for indirect drive.[16] If the initial amplitude of the inner-surface perturbations is too large, the hot core is disrupted and the conditions for ignition and burn do not occur. This leads to an ignition requirement that the inner-surface ice roughness be less than 1-μm rms in all modes.[3,4]

The OMEGA laser is the only facility in the world routinely imploding cryogenic D_2 and DT targets. The target-handling concepts on OMEGA are based on work that began nearly 30 years ago. The next section will review some of the historical accomplishments that had a direct impact on the design of the OMEGA system. One of the fundamental breakthroughs for ignition was the realization of β-layering in 1986. The next section will also describe the β-layering process. Later sections will (1) discuss the development of optical and x-ray-characterization techniques to assess the quality of the DT layers produced by β-layering; (2) describe the systems used to implode these targets on the OMEGA and NIF lasers; and (3) present the results of the first cryogenic DT implosions on OMEGA.

Historical Perspective
Following the concept declassification, J. H. Nuckolls *et al*. first discussed the concept of laser fusion in 1972.[1] Powerful lasers would be used to implode a shell or sphere of solid DT reaching breakeven at relatively modest laser energies (at least by today's standards). While the physical assumptions in this

and other early work turned out to be overly optimistic with respect to the required laser energy, the basic target design—a shell of solid DT—has remained unchanged. After this seminal publication appeared, work began on the development of target concepts for creating thin cryogenic-DT layers (both solid and liquid). The early work (throughout much of the 1970s and 1980s) focused on thin glass shells filled with high-pressure DT gas. Typical scales were 100-μm-diam shells with up to 100 atm of DT gas. When cooled using thermal conduction, the DT layers were typically less than 10 μm thick.

In 1977, Henderson and Johnson at KMS Fusion[17] reported the first irradiation of a cryogenic DT capsule with a laser. The target was a 60-μm-diam, thin-walled glass shell filled with 10 atm of DT (60:40). The capsule was cooled via point-contact conduction and was exposed to ambient chamber infrared (IR) radiation (the point-contact cooling overwhelmed the IR heating from the chamber). These capsules were illuminated with a laser power of approximately 0.2 TW and produced a neutron yield between 10^6 and 10^7, an order of magnitude higher than the same capsules illuminated at room temperature. This demonstrated the advantage of using the high-density cryogenic-fuel layer for ICF. At about the same time, Miller[18] described a new method for producing cryogenic-fuel layers based on what came to be known as the fast-refreeze technique. This technique produced layers with a considerably more uniform thickness than point conduction. The fast-refreeze technique relies on a static heat-exchange gas (He) for rapid cooling of the capsule. Once frozen, the ice in the capsule is melted using a laser beam. The vapor then condenses uniformly on the inside of the glass shell and refreezes before gravity can induce the liquid to flow. This technique quickly became the standard for cryogenic target development well into the 1980s.

In 1978, Musinski *et al.*[19] adapted the fast-refreeze technique for the targets being imploded at KMS Fusion. To eliminate the He exchange gas prior to laser illumination and to minimize the exposure of the cold capsule to ambient IR radiation in the target chamber, they introduced the principle of a cryogenic retractable shroud. Here, the exchange gas is limited to a small volume around the capsule inside the shroud. Their calculations suggested that the exposure time had to be less than 10 ms once the shroud was removed or the thin DT-ice layer would melt due to ambient chamber IR radiation. Thus, within only a few years, three of the key concepts underpinning the success of the OMEGA Cryogenic Target Handling System had been developed: (1) redistribution of the ice using external radiation, (2) thermal control of the capsule isotherm via a cold exchange gas, and (3) a fast retractable shroud to minimize the

target exposure to ambient chamber radiation. These concepts were employed on the 24-beam OMEGA laser[20] in 1987 and 1988 to implode over 100 cryogenic-DT-filled, fast-refreeze glass capsules leading to compressed DT densities of 100 to 200 times liquid density.[21]

By the late 1980s, it was realized that the fast-refreeze technique could not be used to create thick, uniform DT-fuel layers. Thicker DT layers were required for the advanced targets being designed for the proposed upgrade of the OMEGA laser to 60 beams and 30-kJ UV. Fundamentally, the thin glass shell exploding pusher targets originally envisioned for ignition and gain did not work. The demonstration of β-layering in 1988 by Hoffer and Foreman[22] revolutionized the development of targets for ICF and fusion ignition. The "β-heating" concept to produce highly uniform DT-ice layers inside capsules had been suggested by Martin as early as 1985 (Ref. 23) and published formally in 1988 (Ref. 24). The concept is deceptively simple. The radioactive decay of the tritium produces an electron with an average energy of about 6 keV. At 6 keV, the electron range in solid DT is only 1 to 2 μm, so the energy is deposited locally and, consequently, the bulk of the ice is heated uniformly. With a spherically symmetric isotherm on the capsule surface, the radial temperature gradient induced by the β-heating causes DT to sublimate from the slightly thicker and, consequently, slightly warmer regions inside the capsule and deposit on the slightly cooler, thinner regions (see Fig. 108.3). If the capsule surface is kept just below the triple point, the ice will ultimately relax to a uniform radial thickness.
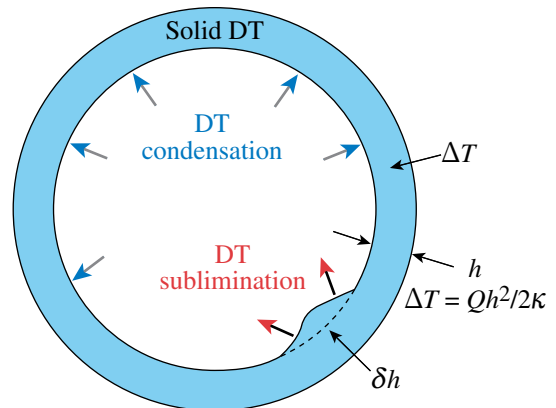
E15072JRC

Figure 108.3
Schematic showing the basic concept behind β-layering in a cryogenic DT shell. If the outside of the shell is maintained at a temperature slightly below the DT triple point, a temperature gradient develops across the ice due to the radioactive decay of the tritium; the emitted electron (average energy of 6 keV) deposits energy, locally heating the bulk of the ice. Consequently, radially thicker (warmer) regions sublimate inside the shell and condense on radially thinner (cooler) locations, eventually relaxing to a uniformly thick shell.

In 1996, Collins *et al.*[25] showed that IR radiation could be used to excite the vibration–rotation band in solid D_2 (or HD), leading to a redistribution or smoothing similar to that induced by β-layering in DT. The process is virtually identical to β-layering as the IR heats the bulk of the ice. With symmetric IR illumination and adequate power, the layer uniformity in D_2 should be as good as in DT.[26] In this way, cryogenic D_2 capsules can be used as ignition surrogates without the radiological impacts associated with DT (e.g., tritium contamination, neutron activation, neutron-induced radiation effects in diagnostics, etc.). Indeed, as mentioned in the **Introduction** (p. 167), the initial ignition-scaled cryogenic capsule implosions on OMEGA were based on D_2 fuel; DT was introduced only recently following extensive operational experience and a thorough systems readiness review.

Cryogenic D₂ and DT Target Fabrication and Characterization

Physically mounting a capsule to be imploded by a multi-beam laser system presents a great challenge for both direct- and x-ray-drive illumination. Mounting the capsule can have a profound effect on the resulting layer quality due to the thermal perturbations caused by the structures around the capsule. Target performance requires a high degree of irradiation uniformity (i.e., the capsule surface cannot be shadowed) and minimal mass perturbations on the surface of the capsule (some mechanical structure must physically attach to the capsule).

To meet these criteria for a direct-drive capsule, LLE implemented a concept based on spider silks[27] [see Fig. 108.4(a)]. Here the capsule is mounted at the center of a "C"-style frame using four strands of spider silk (the silk diameter is typically less than 1 μm). The strands are either glued directly to the surface of the capsule or the entire assembly is overcoated with a thin layer (typically 0.2 μm) of parylene to bond the silks to the capsule. The diameter of the cryogenic targets imploded on the OMEGA laser is set by scaling the ignition target design for the NIF to the energy available;[3] this leads to a capsule diameter of 860 μm for implosions on the OMEGA laser.

For OMEGA, these thin CH shells are permeation filled with an equimolar mixture of DT to 1000 atm. At pressure, the shell and gas are slowly cooled to a few degrees below the DT triple point (19.8 K), while the pressure differential across the shell is maintained below 1 atm to avoid buckling. This is the most critical step in the filling process. Once the DT gas solidifies, the capsule is transferred to a moving cryostat;[8,9] this cryostat is used to maintain the appropriate thermal environment around the capsule until it is imploded. Inside the moving cryostat, the capsule is kept at the center of a gold-coated copper layering
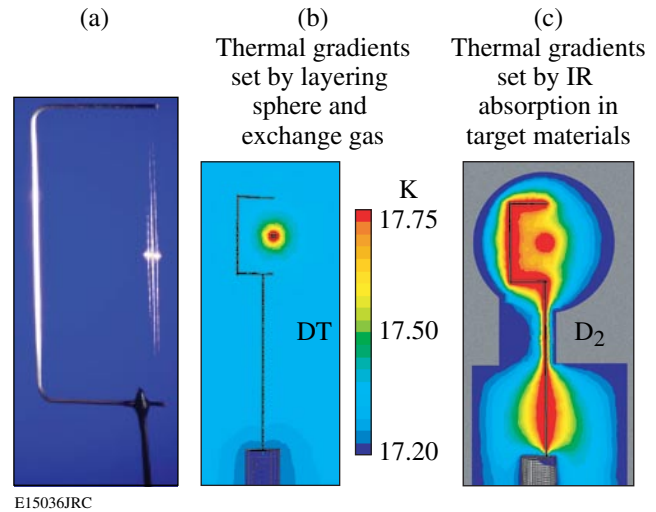

| (a) | (b) Thermal gradients set by layering sphere and exchange gas | (c) Thermal gradients set by IR absorption in target materials |

Figure 108.4

(a) To create a cryogenic target, an 860-μm-diam CH shell is initially mounted to a beryllium "C"-style frame using four strands of spider silk. (b) Thermal modeling shows that isotherm at the surface of a cryogenic DT-filled capsule is highly uniform. (c) However, the IR radiation used to layer D_2 ice also heats the beryllium "C"-mount and the spider silks, causing a significant distortion in the isotherm at the surface of the capsule. This can lead to a significant asymmetry in the ice thickness for cryogenic D_2 targets.

sphere with two orthogonal viewing ports for alignment and ice-surface characterization (discussed below). A thermal model of this system [see Figs. 108.4(b) and 108.4(c)] shows that the isotherm at the surface of a DT capsule is spherical and that none of the target-support structures or layering-sphere asymmetries (e.g., sapphire windows for viewing the target) influence the isotherm [Fig. 108.4(b)]. By controlling the pressure of the exchange gas and the temperature of the copper layering sphere, a spherical isotherm at the DT triple point can be maintained at the ice surface inside the capsule and β-layering produces high-quality layers within a matter of hours.

With IR illumination, the thermal model indicates that there can be significant geometrical distortions in the capsule surface isotherm [Fig. 108.4(c)]. These distortions are caused by IR radiation absorbed on the target support structures (the Be C-mount and the silk).[26] For example, the D_2 ice facing the Be C-mount is typically thinner since the Be frame is warmer than the He exchange gas. This modeling suggested three changes that significantly improved the D_2-ice-layer quality: (1) the pressure of the exchange gas was increased to further homogenize the thermal perturbations, (2) the target structures were plated with gold to reduce the IR absorption, and (3) a diffuser was added to the IR heating port to more uniformly distribute the radiation in the layering sphere (which acts as an integrating sphere for
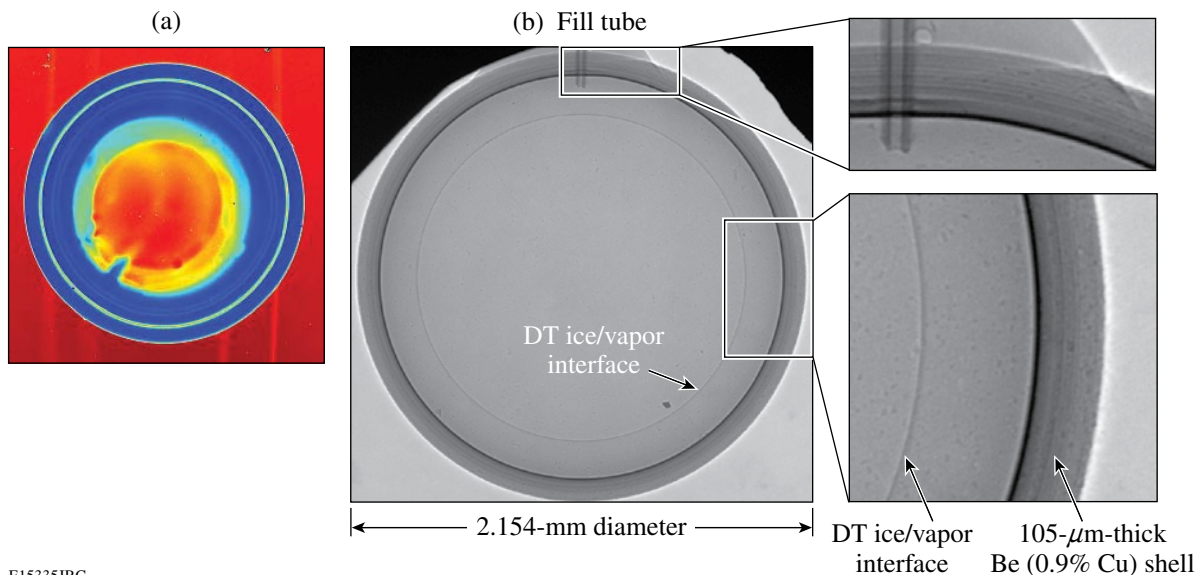
the IR). With these improvements, the average ice-layer quality in D_2 capsules improved by a factor of 2.

For x-ray drive on the NIF, Be capsules are mounted at the center of a cylindrical high-Z hohlraum using a "tenting" scheme.[5] The thermal environment around the capsule is established by the hohlraum geometry. Azimuthally symmetric heaters are placed along the hohlraum axis to produce a more spherically symmetric isotherm at the capsule surface.[28] The Be shells are filled in generally less than 30 min using a narrow fill tube connected to a DT reservoir. Simulations suggest that the fill-tube perturbation will not significantly affect implosion performance.[29] The β-layering process inside the hohlraum has been rigorously tested in the laboratory and will be incorporated into the Load, Layer, and Characterization System (LLCS) under development for the NIF Cryogenic Target System (NCTS). Once a uniform layer is achieved, the temperature of the ice is cooled further to reduce the DT vapor density in the central void region. At 1.5 K below the triple point, the vapor density is 0.3 mg/cc; this is the x-ray-drive-ignition requirement. Cooling the capsule below the triple point is not a requirement for the baseline direct-drive-ignition design.

Apart from the need to monitor the ice layers during formation, simulation codes require inner-ice-surface characterization information to properly predict target performance; therefore, it is important to image the liquid/ice-layer surface with high resolution. For transparent ablators (e.g., CH or CD shells), the location of the inner ice surface is measured using optical shadowgraphy.[30] The capsule is backlit using an optical plane wave (typically a pulsed source with a duration of less than 1 ms to minimize any motional blurring; the energy absorbed by the capsule is negligible). The light is totally internally reflected off the inner surface of the ice, creating a bright ring in the image plane that represents the location of the inner surface relative to the center of the capsule. This bright ring can be seen in Fig. 108.5(a)—a shadowgraph of the first DT capsule to achieve an inner-ice-surface smoothness of 1-μm rms. The resolution of the shadowgraph is less than 0.1 μm. The ring represents an azimuthal measure of the radial variation of the ice along a slice through the center of the capsule normal to the optical viewing axis. This ring is "unwrapped" azimuthally around the center of the capsule to form a line in radius-azimuth space. A power spectrum of the ice roughness as a function of the mode number is generated by fitting the Fourier amplitudes of the radial variation as a function of the azimuth.[31]

For opaque ablators (e.g., Be or low-density foams), x-ray phase-contrast imaging is used to determine the location of the inner ice surface.[32] Phase-contrast imaging relies on spatial gradients in the real part of the refractive index to produce image contrast. These gradients occur at the Be/ice and ice/vapor (the

(a) (b) Fill tube

DT ice/vapor interface

←——— 2.154-mm diameter ———→

DT ice/vapor interface   105-μm-thick Be (0.9% Cu) shell

E15335JRC

Figure 108.5

(a) A typical optical shadowgraph of a cryogenic DT layer. The bright band is a measure of the radial variation of the inner ice surface for a slice through the center of the target. (b) A typical x-ray phase-contrast image of a beryllium shell containing a DT-ice layer. The phase-contrast image provides structural detail within the shell and the ice. The inner band represents a measure of the radial variation of the inner ice surface along a slice through the center of the capsule.

central void region) interfaces of a layered target, causing local curvature in the transmitted wave that leads to interference and a modulation in the x-ray intensity. Even for a virtually transparent medium (e.g., the region around the interface of the ice and DT vapor), phase gradients modulate the intensity of an x-ray wave and can be used to determine the precise location of the ice surface along a slice through the capsule normal to the x-ray-propagation axis. Figure 108.5(b) shows an example of an x-ray phase-contrast image. The capsule is a 105-μm-thick Be shell containing an ~180-μm-thick DT-ice layer. The ice/vapor interface is unwrapped in radius-azimuth space, and a power spectrum as a function of the mode number is generated as described above.

Because of the inherent symmetry of the direct-drive layering sphere, it is possible to rotate a direct-drive capsule with respect to the viewing axes in the characterization station. By rotating the capsule, any number of independent shadowgraphs can be obtained and used to create a 3-D representation of the inner ice surface. Such a representation (based on 48 independent shadowgraphs) is shown in Fig. 108.6 for two different DT-ice layers. Since the viewing axes are not orthogonal to the rotation axis, the poles of the capsules cannot be characterized. The contours represent surface deviations in microns relative to a perfect sphere at the average ice-surface radius. The peak-to-valley surface variation for both capsules is ~2 μm out of a total ice thickness of ~95 μm. Full $Y_{\ell m}$ Legendre amplitudes can be fit to this surface for modes up to 12 (the limiting factor is the missing data at the poles), and the procedure described by Hatchett and Pollaine[33] is used to estimate the 2-D equivalent of the Legendre modes for $\ell > 12$. The ignition specification is typically quoted as a power spectrum for modes from 1 to 1000, although in practice the resolution of the measurement limits meaningful power to modes less than 100 or so.[34] For direct drive, this specification is 1.0-μm rms in all modes and ≤0.25-μm rms in modes greater than 10. Both of the targets shown in Fig. 108.6 meet the inner-ice-surface smoothness requirement for direct-drive ignition on the NIF. Figure 108.7 compares the power-spectrum decomposition of the ice-surface roughness for six targets imploded consecutively on the OMEGA laser and the ignition specification (heavy solid line). For the best capsule, the measured power spectrum is 0.72-μm rms in all modes and 0.24-μm rms above mode 10, comfortably exceeding the ignition requirement.

Layering and characterization of a DT-fuel layer in a hohlraum for x-ray-drive ignition present significant challenges. For capsules in a hohlraum, the presence of the fill tube can create a thermal asymmetry leading to a low-mode variation in the ice thickness around the fill tube (generally thicker ice since the fill
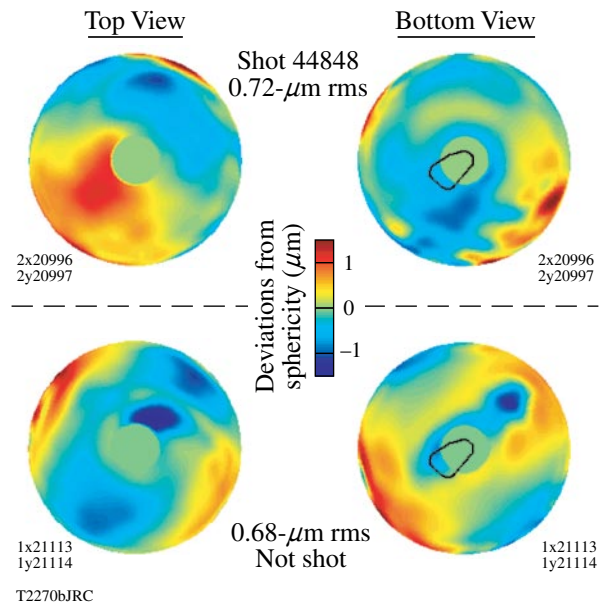

Figure 108.6
A 3-D representation of the inner ice surface can be created by fitting to a large number of independent shadowgraphs. Top and bottom views are shown for two different capsules that meet the direct-drive-ignition requirement for the inner ice smoothness. The contour mapping represents deviations of the inner ice surface from a sphere at the average radius. Because the viewing axes are not orthogonal to the rotation axis, there is no data at the poles.
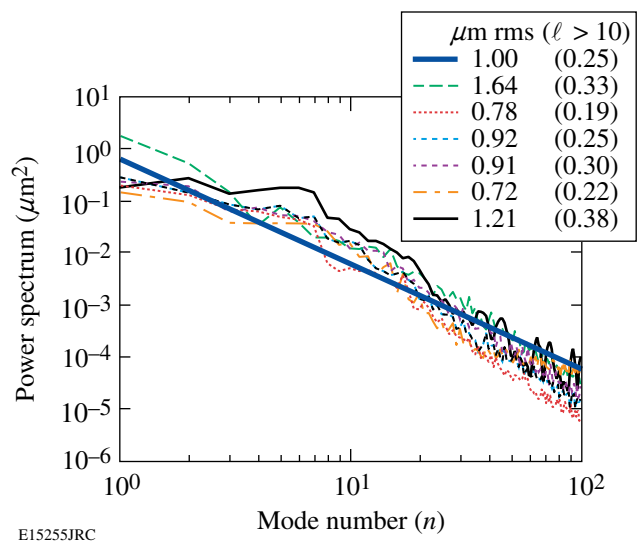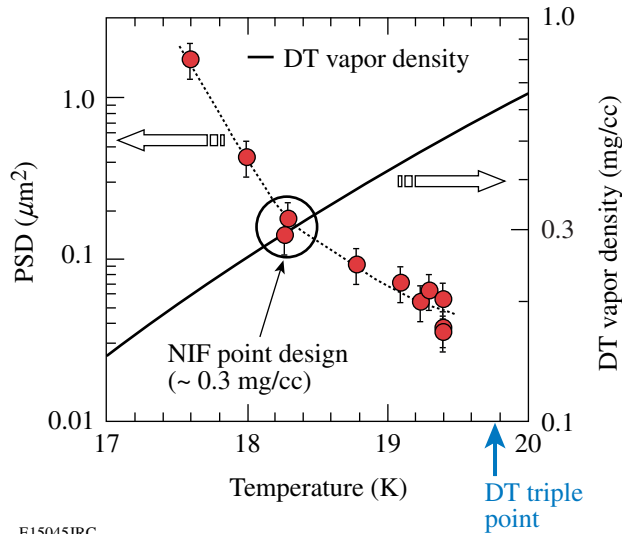

Figure 108.7
The power per mode for six DT cryogenic targets as a function of mode number. These targets were shot consecutively over a period of several weeks on OMEGA. The direct-drive-ignition specification for the inner ice smoothness is shown as the heavy solid line.

tube is colder). Furthermore, as the ice as cooled below the triple point, mid- and high-mode roughness begins to appear as the ice contracts and the β-layering process begins to shut down. However, by cooling very slowly from the triple point to 18.3 K (the ignition requirement), the ice roughness remains at the ignition specification for modes 10 and above. The behavior of the ice roughness in modes 10 to 128 as a function of ice temperature is shown in Fig. 108.8.


E15045JRC

Figure 108.8
The power-spectral density for a prototype x-ray-drive cryogenic DT target as a function of the ice temperature. The power spectral distribution (PSD) is summed for modes 10 to 128. The ice-temperature requirement for x-ray-drive ignition is 18.3 K. This target meets the ignition requirement over this mode range at the required ice temperature.

Imploding Cryogenic Targets on OMEGA and the NIF

The original Cryogenic Target Handling System (CTHS) on the 24-beam OMEGA laser[20] incorporated the concepts discussed in **Historical Perspective** (p. 168). These concepts included an opposed-port shroud-retraction scheme using a linear induction motor and He gas cooling to support the fast-refreeze layering process. A shearing interferometer was implemented for layer characterization (thickness and uniformity). The thermally passive shroud and the actively cooled target stalk are shown in Fig. 108.9. The inset picture in Fig. 108.9 shows the "horseshoe" target assembly with a 300-μm-diam glass shell mounted using several strands of spider silk (rather than using glue to bond the silk to the capsule, the capsule and silk were overcoated with 0.2 μm of parylene following assembly). During the late 1980s, this system imploded over 100 glass-shell targets with 5-μm-thick DT layers, achieving 200 times liquid density in the DT.[21]
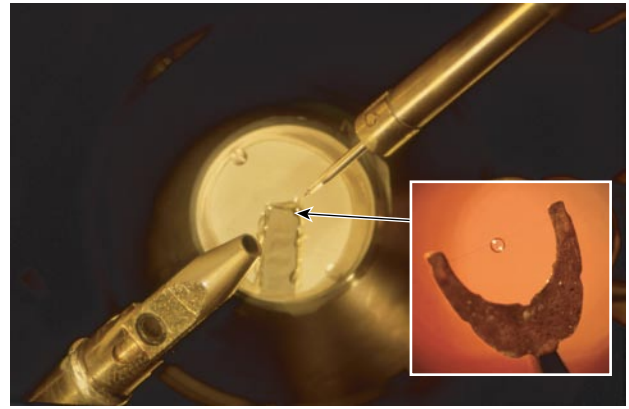
E15336JRC

Figure 108.9
The shroud and target inserter from the 24-beam OMEGA Cryogenic Target Handling System are shown. The thermally passive removable shroud is the structure at the lower left. The inset shows a picture of the "horseshoe"-style mount for the capsule. Strands of spider silk are used to mount the capsule between the tips of the mount.

By the early 1990s, target designs were being developed for ignition that required considerably thicker DT layers with very high layer uniformity.[35] The fast-refreeze technique and thin glass shells were no longer adequate. New concepts were developed by General Atomics and LLE to support scaled-ignition target implosions on the new 60-beam OMEGA laser (completed in 1996). The new requirements for the CTHS included (1) a separate high-pressure-permeation fuel-filling system that was both D$_2$ and DT capable, (2) variable ice-layer thickness up to 100 μm in mm-diameter-scale, thin-walled CH capsules, (3) the capability to fill up to 12 targets per week, (4) IR-enhanced layering for D$_2$ and β-layering for DT fuel, (5) an independent layer-characterization station based on optical shadowgraphy, (6) a moving cryostat to deliver the target from the tritium facility to the target chamber, (7) target-alignment accuracy relative to the target chamber center (TCC) of 5 μm, (8) an opposed-port shroud-retraction scheme with a target exposure time of less than 100 ms before laser irradiation, and (9) a vertical shroud pull.

The operation of the CTHS on OMEGA has been well documented.[8–11] Since 2001, 118 cryogenic D$_2$ and 15 cryogenic DT capsules have been imploded. The key to the success of the OMEGA CTHS is the moving-cryostat concept. A photograph of the moving cryostat is shown in Fig. 108.10 with and without the thermally passive upper shroud. The moving cryostat includes a local He-gas cryogenic cooler on the thermally controlled lower shroud, a four-axis position controller (X, Y, Z, and θ) for the target stalk, a rigid docking interface to the target chamber, He exchange-gas regulation, and a thermally passive upper shroud with sapphire windows aligned to the OMEGA Target

Viewing System. With the moving-cryostat concept, critical target functions are performed away from the target chamber (i.e., permeation filling, layering, and characterization). Consequently, there is little or no impact on the utilization of the laser system when imploding cryogenic targets. An overview of the target handling process is shown in Fig. 108.11. The targets are permeation filled in a separate cryostat over a period of approximately four days and then transferred to the moving cryostat. The moving cryostat is then mated to the Characterization Station (still within the tritium facility). Once the appropriate layer is achieved (this typically requires 1 to 2 days for D_2 and less than 1 day for DT), the moving cryostat is taken to the bay beneath the OMEGA target chamber (a distance of about 200 ft). The moving cryostat is aligned with the lower pylon and then raised 22 ft through a vacuum interface to the center of the target chamber. Target alignment is performed using an automated centering routine to predetermined coordinates that account for static alignment offsets due to the sapphire windows. At shot time, a linear induction motor (LIM) removes the upper shroud using a precise acceleration/deceleration trajectory. The trajectory minimizes mechanical coupling between the LIM motion and the target. The target is exposed to the ambient chamber radiation for 90 ms prior to laser irradiation.

The conceptual basis for the NIF Cryogenic Target System (NCTS)[28,36] is significantly different from the OMEGA CTHS. The Load, Layer, and Characterization System (LLCS) is being developed to operate just outside the NIF target chamber but mechanically integrated with the target inserter and target chamber. Using the LLCS, DT will be loaded at about 50 psi into a 1-cc reservoir at the target base. This reservoir is connected to the Be capsule via a narrow (of the order of 10-μm OD) fill tube. The entire assembly is cooled to within a few degrees of the DT triple point (19.8 K). The reservoir is then heated to between 50 and 70 K, causing the DT to condense inside the Be shell. X-ray phase-contrast imaging will be used to monitor the DT meniscus (and consequently the amount of fuel in the shell) during the fill. Once the required amount of fuel is in the shell, the layering and characterization process proceeds as described in **Cryogenic D_2 and DT Target Fabrication and Characterization** (p. 170). Following the final characterization, the target is moved to the center of the NIF target chamber and aligned with the 192 laser beams. The target is protected from condensation and room-temperature IR radiation from the chamber by a clam-shell shroud (see Fig. 108.12). Several seconds before the shot, the shroud is opened. Heaters on the hohlraum compensate for the sudden IR illumination and maintain a constant hohlraum temperature. Any target vibration induced by the shroud opening damps during the 1 to 2 s prior to laser illumination.

Cryogenic DT Target Performance

All of the DT (and a few of the recent D_2) capsules imploded to date on OMEGA have been driven with a laser pulse designed to keep the fuel on an adiabat α of approximately 1 to 3, where α is the ratio of the internal pressure to the Fermi-degenerate pressure.[3]
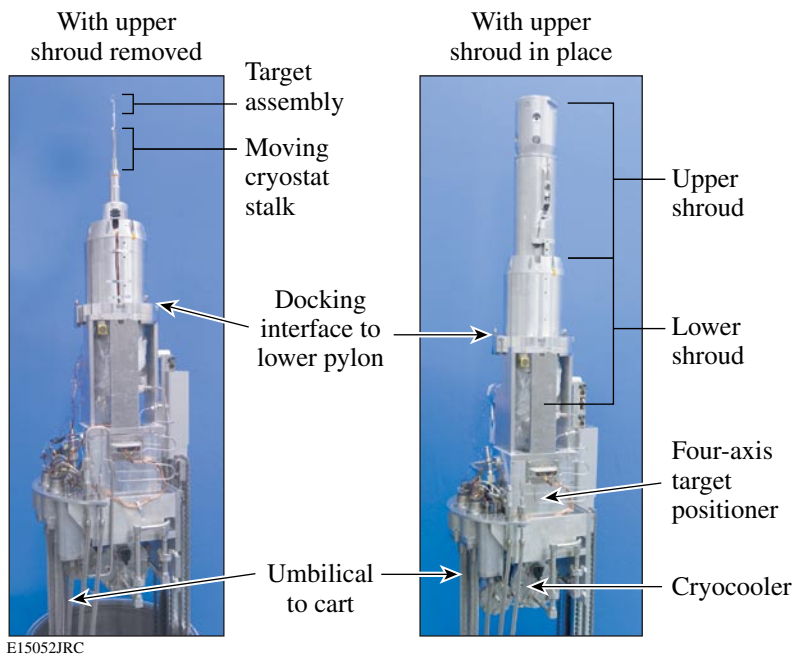

Figure 108.10
The 60-beam OMEGA moving cryostat with (right) and without (left) the upper shroud. The moving cryostat is the heart of the OMEGA Cryogenic Target Handling System. The upper shroud is removed to expose the capsule at shot time. The capsule exposure time is approximately 90 ms.
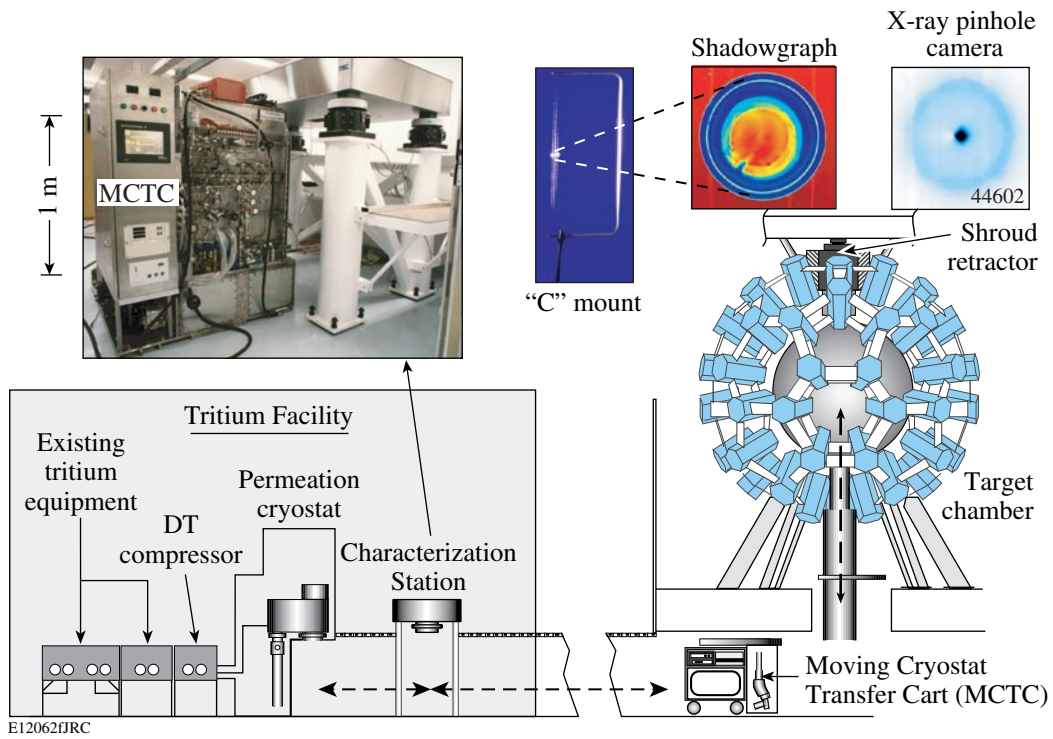
E15052JRC

E12062fJRC

Figure 108.11
Target-handling operations are conducted away from the target chamber to increase the utilization of the laser facility. This includes the filling, layering, and characterization steps that are done within the LLE tritium facility. Once a target is ready to implode, the Moving Cryostat Transfer Cart (MCTC) is positioned below the chamber and the moving cryostat with the target is raised 22 ft to dock with the support structures on the target chamber. The entire shot sequence can be repeated approximately every 2 h.
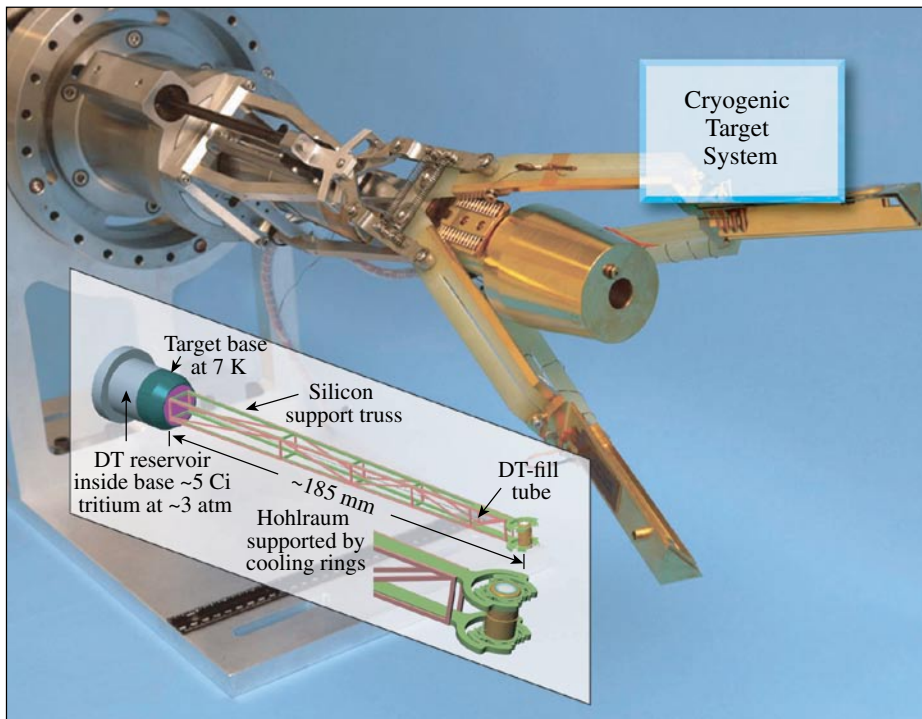
E15055JRC

Figure 108.12
An x-ray-drive target on the NIF will be protected from the ambient chamber radiation using a clam-shell-style retractor. The clam-shell retractor can be opened slowly to avoid inducing excessive vibration because the target can withstand several seconds of chamber exposure before significant temperature perturbations develop on the capsule surface. The hohlraum/reservoir schematic shown in the inset fits on the end of the cold head in the middle of the figure.

These drive pulses scale to ignition, and consequently the areal densities during the fusion burn are expected (based on a 1-D radiation hydrocode simulation[36]) to be in excess of 200 mg/cm^2 (this corresponds to ~300× liquid density for the DT) and to approach 250 mg/cm^2 at peak density. The areal density monotonically increases during the fusion burn, and the neutron- or burn-averaged areal density $\langle\rho R\rangle_n$ will be less than the peak areal density ρR_{peak}. The fusion burn truncates prior to peak density (or compression) due to the thermal quenching caused by mixing of colder fuel with the hot spot.[37] Charged-particle diagnostics[38] are used to infer $\langle\rho R\rangle_n$ from D$_2$ implosions, while x-ray diagnostics[39] are used to infer ρR_{peak} from both D$_2$ and DT implosions.

The energy loss of secondary protons in the compressed D$_2$-fuel shell shows that the neutron-averaged areal density for $\alpha \sim 2$ implosions is as high as 100 to 110 mg/cm^2. A secondary proton spectrum from shot 45009 is shown in Fig. 108.13. The figure shows both the measured spectrum (solid circles with statistical error bars) and the birth spectrum (shaded region) in the core. The average energy loss in the dense-fuel shell is several MeV, corresponding to an areal density of 110 mg/cm^2. The low-energy tail suggests considerable low-mode instability growth late in time. These late-time protons probe regions of significantly higher fuel areal density but not necessarily regions representative of the overall shell areal density. For example, the
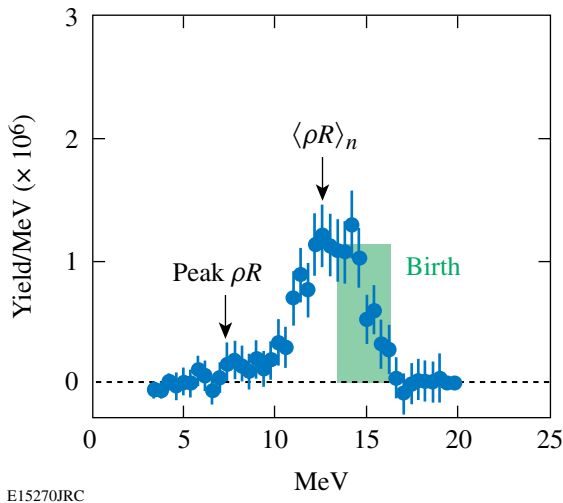
end point of this spectrum (at about 7 MeV) would correspond to an areal density of approximately 250 mg/cm^2 (based on a total dE/dx of over 5 MeV). For higher-yielding implosions, the areal-density evolution during the burn $\rho R(t)$ can be fit based on the technique described by Frenje and Smalyuk.[40]

The ρR_{peak} can be inferred based on the opacity of the shell by using the core self-emission to effectively backlight the shell. Figure 108.14 shows the measured x-ray spectrum from the core of shot 44948. This shot used a drive pulse to put the fuel shell on an adiabat close to 1. Since the x rays are generated by bremsstrahlung in the hot core, the spectrum is expected to be exponential with the slope related to the electron temperature near peak compression. If the fuel shell is sufficiently dense, x-ray absorption (free-free scattering) occurs and the spectrum deviates from the expected exponential behavior, and this deviation can be used to infer the density of the compressed fuel.[41] The x-ray spectrum in Fig. 108.14 indicates significant absorption between 1 and 2 keV. The opacity of the fuel shell is proportional to $\rho^2 RT^{-1/4}$, where ρ is the mass density of the compressed fuel, ρR is its areal density, and T is the electron temperature (inferred from the slope of the spectrum). The 1-D radiation hydrodynamic code $LILAC$[42] has been used to estimate the mass density ρ and minimum temperature of the compressed fuel by adjusting the temperature of the cold fuel and the thermal conductivity of the

E15270JRC

Figure 108.13
A measured secondary proton spectrum (solid circles) from a cryogenic D$_2$ implosion ($\alpha \sim 2$) is compared with the expected birth spectrum (shaded box). The protons lose energy as they pass through the dense fuel layer surrounding the hot core. The energy loss is proportional to the areal density of the dense fuel layer. For this implosion, the energy loss implies an areal density in excess of 100 mg/cm^2; the low-energy tail suggests the peak areal density is well above 100 mg/cm^2.
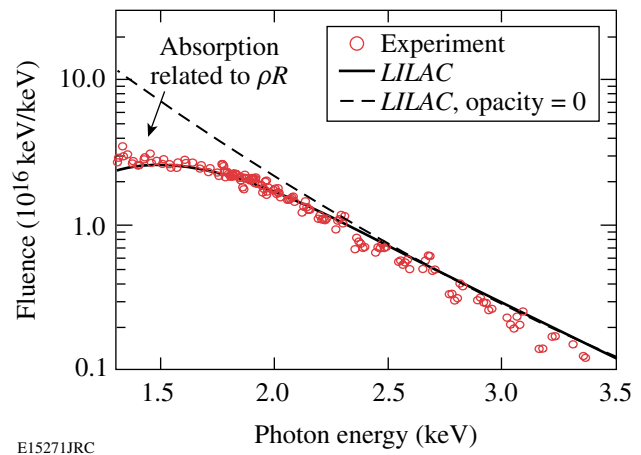

E15271JRC

Figure 108.14
Significant absorption is seen in the continuum x-ray spectrum emitted from the core of a cryogenic D$_2$ implosion ($\alpha \sim 1$) at x-ray energies below 2 keV. The emitted spectrum is expected to be exponential, and the deviation at low x-ray energies is consistent with a significant fuel areal density. The compressibility of the fuel shell in the 1-D radiation hydrocode $LILAC$ can be modified to fit the emitted spectrum to estimate the fuel density. The dashed line shows the expected exponential behavior of the x-ray emission if the opacity is artificially removed in the simulation.

hot core to match the emitted spectrum in both absolute fluence and shape (these adjustments mimic multidimensional mode growth and the consequent reduction in shell compression). The *LILAC* simulation that best agrees with the data is shown as the solid curve. The fuel density in the simulation suggests that ρR_{peak} may be as high as 190 ± 20 mg/cm^2. Two-dimensional simulations are underway to confirm this 1-D fuel-density estimate. The dashed curve in Fig. 108.14 is the predicted x-ray spectrum based on zero opacity. The curve is not purely exponential below 2 keV. If the opacity is calculated based on a purely exponential source spectrum and the density is taken from the *LILAC* simulation, the inferred ρR_{peak} would still be 180 mg/cm^2. Note that, if confirmed by further simulations, this estimate of the density represents a lower limit on the inferred peak areal density—if the density is less than predicted by the simulation, the measured opacity suggests that ρR_{peak} must be larger than the 180- to 190-mg/cm^2 estimate.

Summary

The cryogenic DT targets being imploded on OMEGA are energy-scaled versions of the baseline direct-drive-ignition design for the National Ignition Facility. This is the culmination of nearly three decades of research and development. Most of the components for the x-ray-drive ignition targets are at or near specification.

The β-layering process for producing a smooth inner ice surface in the direct-drive cryogenic DT targets imploded on OMEGA is well understood. The most important aspect of this process is controlling the symmetry of the isotherm on the outer surface of the capsule. This can now be done routinely, and over half of the cryogenic DT capsules imploded on OMEGA met the ignition requirement for the smoothness of the inner ice surface (<1-μm rms in all modes) at shot time. Optical shadowgraphy and phase-contrast imaging are used to characterize the inner ice surface for transparent (e.g., CH or CD shell) and opaque (e.g., Be and foam shells) ablators, respectively. The resolution of these techniques is adequate to characterize the ice smoothness to well below the ignition requirements for both direct and x-ray drives.

The Cryogenic Target Handling System on the OMEGA laser has deep roots in past work. Many of the fundamental concepts employed today were developed nearly three decades ago to perform the first cryogenic DT implosions using DT-filled, thin-glass-shell targets and two-beam irradiation. While these early target designs ultimately did not scale to ignition, the success of the current OMEGA program and the anticipated success of the future NIF ignition experiments owe much to these early pioneers.

REFERENCES

1. J. Nuckolls *et al.*, Nature **239**, 139 (1972).

2. W. J. Hogan, E. I. Moses, B. E. Warner, M. S. Sorem, and J. M. Soures, Nucl. Fusion **41**, 567 (2001).

3. P. W. McKenty, V. N. Goncharov, R. P. J. Town, S. Skupsky, R. Betti, and R. L. McCrory, Phys. Plasmas **8**, 2315 (2001).

4. J. D. Lindl, *Inertial Confinement Fusion: The Quest for Ignition and Energy Gain Using Indirect Drive* (Springer-Verlag, New York, 1998); J. D. Lindl *et al.*, Phys. Plasmas **11**, 339 (2004).

5. S. W. Haan *et al.*, Fusion Sci. Technol. **49**, 553 (2006); S. W. Haan *et al.*, Phys. Plasmas **12**, 056316 (2005); S. W. Haan *et al.*, Nucl. Fusion **44**, S171 (2004).

6. S. Atzeni and J. Meyer-ter-Vehn, *The Physics of Inertial Fusion: Beam Plasma Interaction, Hydrodynamics, Hot Dense Matter*, International Series of Monographs on Physics (Clarendon Press, Oxford, 2004).

7. T. R. Boehly, D. L. Brown, R. S. Craxton, R. L. Keck, J. P. Knauer, J. H. Kelly, T. J. Kessler, S. A. Kumpan, S. J. Loucks, S. A. Letzring, F. J. Marshall, R. L. McCrory, S. F. B. Morse, W. Seka, J. M. Soures, and C. P. Verdon, Opt. Commun. **133**, 495 (1997).

8. C. Stoeckl, C. Chiritescu, J. A. Delettrez, R. Epstein, V. Yu. Glebov, D. R. Harding, R. L. Keck, S. J. Loucks, L. D. Lund, R. L. McCrory, P. W. McKenty, F. J. Marshall, D. D. Meyerhofer, S. F. B. Morse, S. P. Regan, P. B. Radha, S. Roberts, T. C. Sangster, W. Seka, S. Skupsky, V. A. Smalyuk, C. Sorce, J. M. Soures, R. P. J. Town, J. A. Frenje, C. K. Li, R. D. Petrasso, F. H. Séguin, K. Fletcher, S. Padalino, C. Freeman, N. Izumi, R. Lerche, and T. W. Phillips, Phys. Plasmas **9**, 2195 (2002).

9. T. C. Sangster, J. A. Delettrez, R. Epstein, V. Yu. Glebov, V. N. Goncharov, D. R. Harding, J. P. Knauer, R. L. Keck, J. D. Kilkenny, S. J. Loucks, L. D. Lund, R. L. McCrory, P. W. McKenty, F. J. Marshall, D. D. Meyerhofer, S. F. B. Morse, S. P. Regan, P. B. Radha, S. Roberts, W. Seka, S. Skupsky, V. A. Smalyuk, C. Sorce, J. M. Soures, C. Stoeckl, K. Thorp, J. A. Frenje, C. K. Li, R. D. Petrasso, F. H. Séguin, K. A. Fletcher, S. Padalino, C. Freeman, N. Izumi, J. A. Koch, R. A. Lerche, M. J. Moran, T. W. Phillips, and G. J. Schmid, Phys. Plasmas **10**, 1937 (2003).

10. P. W. McKenty, T. C. Sangster, M. Alexander, R. Betti, R. S. Craxton, J. A. Delettrez, L. Elasky, R. Epstein, A. Frank, V. Yu. Glebov, V. N. Goncharov, D. R. Harding, S. Jin, J. P. Knauer, R. L. Keck, S. J. Loucks, L. D. Lund, R. L. McCrory, F. J. Marshall, D. D. Meyerhofer, S. P. Regan, P. B. Radha, S. Roberts, W. Seka, S. Skupsky, V. A. Smalyuk, J. M. Soures, K. A. Thorp, M. Wozniak, J. A. Frenje, C. K. Li, R. D. Petrasso, F. H. Séguin, K. A. Fletcher, S. Padalino, C. Freeman, N. Izumi, J. A. Koch, R. A. Lerche, M. J. Moran, T. W. Phillips, G. J. Schmid, and C. Sorce, Phys. Plasmas **11**, 2790 (2004).

11. F. J. Marshall, R. S. Craxton, J. A. Delettrez, D. H. Edgell, L. M. Elasky, R. Epstein, V. Yu. Glebov, V. N. Goncharov, D. R. Harding, R. Janezic, R. L. Keck, J. D. Kilkenny, J. P. Knauer, S. J. Loucks, L. D. Lund, R. L. McCrory, P. W. McKenty, D. D. Meyerhofer, P. B. Radha, S. P. Regan, T. C. Sangster, W. Seka, V. A. Smalyuk, J. M. Soures, C. Stoeckl, S. Skupsky, J. A. Frenje, C. K. Li, R. D. Petrasso, and F. H. Séguin, Phys. Plasmas **12**, 056302 (2005).

12. J. D. Sethian *et al.*, Nucl. Fusion **43**, 1693 (2003); J. D. Lindl, B. A. Hammel, B. G. Logan, D. D. Meyerhofer, S. A. Payne, and J. D. Sethian, Plasma Phys. Control. Fusion **45**, A217 (2003); R. L. McCrory, S. P. Regan, S. J. Loucks, D. D. Meyerhofer, S. Skupsky, R. Betti, T. R. Boehly, R. S. Craxton, T. J. B. Collins, J. A. Delettrez, D. Edgell, R. Epstein, K. A. Fletcher, C. Freeman, J. A. Frenje, V. Yu. Glebov, V. N. Goncharov, D. R. Harding, I. V. Igumenshchev, R. L. Keck, J. D. Kilkenny, J. P. Knauer, C. K. Li, J. Marciante, J. A. Marozas, F. J. Marshall, A. V. Maximov, P. W. McKenty, D. D. Meyerhofer, J. Myatt, S. Padalino, R. D. Petrasso, P. B. Radha, T. C. Sangster, F. H. Séguin, W. Seka, V. A. Smalyuk, J. M. Soures, C. Stoeckl, B. Yaakobi, and J. D. Zuegel, Nucl. Fusion **45**, S283 (2005).

13. V. A. Smalyuk, V. N. Goncharov, J. A. Delettrez, F. J. Marshall, D. D. Meyerhofer, S. P. Regan, and B. Yaakobi, Phys. Rev. Lett. **87**, 155002 (2001).

14. R. Betti, V. Lobatchev, and R. L. McCrory, Phys. Rev. Lett. **81**, 5560 (1998).

15. S. P. Regan, J. A. Marozas, R. S. Craxton, J. H. Kelly, W. R. Donaldson, P. A. Jaanimagi, D. Jacobs-Perkins, R. L. Keck, T. J. Kessler, D. D. Meyerhofer, T. C. Sangster, W. Seka, V. A. Smalyuk, S. Skupsky, and J. D. Zuegel, J. Opt. Soc. Am. B **22**, 998 (2005).

16. S. H. Glenzer *et al.*, Phys. Plasmas **7**, 2585 (2000).

17. T. M. Henderson and R. R. Johnson, Appl. Phys. Lett. **31**, 18 (1977).

18. J. R. Miller, in *Advances in Cryogenic Engineering*, edited by K. D. Timmerhaus (Plenum Press, New York, 1978), Vol. 23, pp. 669–675.

19. D. L. Musinski *et al.*, Appl. Phys. Lett. **34**, 300 (1979).

20. F. J. Marshall, S. A. Letzring, C. P. Verdon, S. Skupsky, R. L. Keck, J. P. Knauer, R. L. Kremens, D. K. Bradley, T. Kessler, J. Delettrez, H. Kim, J. M. Soures, and R. L. McCrory, Phys. Rev. A **40**, 2547 (1989).

21. R. L. McCrory, J. M. Soures, C. P. Verdon, F. J. Marshall, S. A. Letzring, S. Skupsky, T. J. Kessler, R. L. Kremens, J. P. Knauer, H. Kim, J. Delettrez, R. L. Keck, and D. K. Bradley, Nature **335**, 225 (1988).

22. J. K. Hoffer and L. R. Foreman, Phys. Rev. Lett. **60**, 1310 (1988).

23. A. J. Martin, R. J. Simms, and D. L. Musinski, *KMS Annual Technical Report*, 99, KMS Fusion, Inc., Ann Arbor, MI, KMSF Report No. 1348 (1985) (unpublished).

24. A. J. Martin, R. J. Simms, and R. B. Jacobs, J. Vac. Sci. Technol. A **6**, 1885 (1988).

25. G. W. Collins *et al.*, J. Vac. Sci. Technol. A **14**, 2897 (1996).

26. D. R. Harding, D. D. Meyerhofer, S. J. Loucks, L. D. Lund, R. Janezic, L. M. Elasky, T. H. Hinterman, D. H. Edgell, W. Seka, M. D. Wittman, R. Q. Gram, D. Jacobs-Perkins, R. Early, T. Duffy, and M. J. Bonino, Phys. Plasmas **13**, 056316 (2006).

27. M. J. Bonino, "Material Properties of Spider Silk," M.S. Thesis, University of Rochester, 2003.

28. J. D. Moody *et al.*, J. Phys. IV France **133**, 863 (2006).

29. J. Edwards *et al.*, Phys. Plasmas **12**, 056318 (2005).

30. J. A. Koch *et al.*, Fusion Technol. **38**, 123 (2000).

31. D. H. Edgell, W. Seka, R. S. Craxton, L. M. Elasky, D. R. Harding, R. L. Keck, and M. D. Wittman, Fusion Sci. Technol. **49**, 616 (2006).

32. D. S. Montgomery, A. Nobile, and P. J. Walsh, Rev. Sci. Instrum. **75**, 3986 (2004); B. J. Kozioziemski *et al.*, J. Appl. Phys. **97**, 063103 (2005).

33. S. Pollaine and S. Hatchett, Nucl. Fusion **44**, 117 (2004).

34. D. H. Edgell, W. Seka, R. S. Craxton, L. M. Elasky, D. R. Harding, R. L. Keck, L. D. Lund, and M. D. Wittman, J. Phys. IV France **133**, 903 (2006); D. S. Montgomery *et al.*, J. Phys. IV France **133**, 869 (2006).

35. *LLE Review Quarterly Report* **23**, 125, Laboratory for Laser Energetics, University of Rochester, Rochester, NY, LLE Document No. DOE/SP40200-03 (1985).

36. T. P. Bernat *et al.*, Phys. IV France **133**, 857 (2006).

37. P. B. Radha, J. Delettrez, R. Epstein, V. Yu. Glebov, R. Keck, R. L. McCrory, P. McKenty, D. D. Meyerhofer, F. Marshall, S. P. Regan, S. Roberts, T. C. Sangster, W. Seka, S. Skupsky, V. Smalyuk, C. Sorce, C. Stoeckl, J. Soures, R. P. J. Town, B. Yaakobi, J. Frenje, C. K. Li, R. Petrasso, F. Séguin, K. Fletcher, S. Padalino, C. Freeman, N. Izumi, R. Lerche, and T. W. Phillips, Phys. Plasmas **9**, 2208 (2002).

38. F. H. Séguin, J. A. Frenje, C. K. Li, D. G. Hicks, S. Kurebayashi, J. R. Rygg, B.-E. Schwartz, R. D. Petrasso, S. Roberts, J. M. Soures, D. D. Meyerhofer, T. C. Sangster, J. P. Knauer, C. Sorce, V. Yu. Glebov, C. Stoeckl, T. W. Phillips, R. J. Leeper, K. Fletcher, and S. Padalino, Rev. Sci. Instrum. **74**, 975 (2003).

39. B. Yaakobi, R. Epstein, and F. J. Marshall, Phys. Rev. A **44**, 8429 (1991).

40. V. A. Smalyuk, P. B. Radha, J. A. Delettrez, V. Yu. Glebov, V. N. Goncharov, D. D. Meyerhofer, S. P. Regan, S. Roberts, T. C. Sangster, J. M. Soures, C. Stoeckl, J. A. Frenje, C. K. Li, R. D. Petrasso, and F. H. Séguin, Phys. Rev. Lett. **90**, 135002 (2003); J. A. Frenje, C. K. Li, F. H. Séguin, J. Deciantis, S. Kurebayashi, J. R. Rygg, R. D. Petrasso, J. Delettrez, V. Yu. Glebov, C. Stoeckl, F. J. Marshall, D. D. Meyerhofer, T. C. Sangster, V. A. Smalyuk, and J. M. Soures, Phys. Plasmas **11**, 2798 (2003).

41. F. J. Marshall, J. A. Delettrez, R. Epstein, and B. Yaakobi, Phys. Rev. E **49**, 4381 (1994).

42. M. C. Richardson, P. W. McKenty, F. J. Marshall, C. P. Verdon, J. M. Soures, R. L. McCrory, O. Barnouin, R. S. Craxton, J. Delettrez, R. L. Hutchison, P. A. Jaanimagi, R. Keck, T. Kessler, H. Kim, S. A. Letzring, D. M. Roback, W. Seka, S. Skupsky, B. Yaakobi, S. M. Lane, and S. Prussin, in *Laser Interaction and Related Plasma Phenomena*, edited by H. Hora and G. H. Miley (Plenum Publishing, New York, 1986), Vol. 7, pp. 421–448.

Structural Dynamics of Cryogenic Target Assemblies

Introduction

The laser direct-drive approach to inertial confinement fusion (ICF) utilizes an array of high-power laser beams to uniformly compress a target capsule filled with hydrogen isotopes in a spherically symmetric implosion. Higher fuel densities, and therefore higher yields, may be achieved from targets that are filled with fuel under high pressure and cooled to form an ice layer on the inner surface of the capsule.[1] Cryogenic target assemblies for the OMEGA Laser System currently consist of a 900-μm-diam $\times$ 4- to 6-μm-wall glow discharge polymer (GDP) capsule[2] filled with a 100-μm layer of deuterium and tritium (DT) or deuterium (D_2) ice around a gaseous core. The capsule is suspended on four strands of spider silk from a beryllium frame[3] as shown in Fig. 108.15. During a typical implosion, laser illumination of the target rapidly heats and ablates the outer capsule material. Conservation of momentum drives

the remaining capsule material and fuel toward the center of the target sphere where the initially gaseous fuel forms a "hot spot" that ignites fusion reactions, which propagate radially outward through the main fuel layer.[4]

During an implosion, hydrodynamic instabilities in the ablation front can reduce the energy yield by distorting the hot spot or dispersing the main fuel layer. These instabilities, like Rayleigh–Taylor instability in classical fluids, initiate at small irregularities or perturbations in the ablation front. Asymmetries such as uneven laser illumination of the target or the presence of features on the outside surface of the capsule are potential triggers of instability during the acceleration phase of an implosion. While beam smoothing and power balancing can ensure highly uniform illumination at target chamber center (TCC),[5,6] target displacements of 5 μm or more[7] from TCC can unbalance the illumination enough to initiate hydrodynamic instability. Consequently, stringent requirements are imposed on the position of ICF targets at the time of implosion. Target-positioning systems must address both static and dynamic (oscillatory) displacements. While static displacements due to position control resolution, window offsets, and events such as removal of thermal shielding (shroud) immediately before firing the laser are a significant concern, they will be addressed in a future article.

In addition to meeting stringent position stability requirements, the mechanical supports for target capsules must also satisfy thermal and mass symmetry requirements. The mechanical supports must have a low thermal conductivity to minimize thermal gradients that perturb the ice layer within the capsule. Furthermore, the supports must not contribute a significant mass asymmetry to the capsule. Consequently, cryogenic target capsules for the OMEGA Laser System are suspended on four strands of spider silk that have a high modulus of elasticity (6.4 GPa), low density (1200 Kg/m^3), and is available in small diameters (0.9 μm), all of which minimize thermal and mass asymmetries. Furthermore, spider silk remains flexible at cryogenic temperatures.

The displacement amplitude of a capsule assembly is a function of the applied excitation force and the dynamic
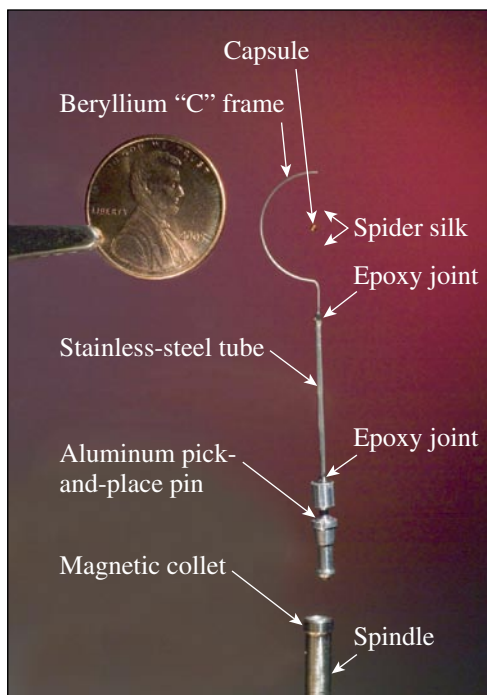

G7559JRC

Figure 108.15
OMEGA Cryogenic Target Assembly.

response characteristics of the target assembly and surrounding structure. Numerous mechanical systems in and around the target chamber may generate periodic or transient forces that excite target vibration. Potential excitation sources include the cryogenic cooling system (helium compressor and cold head), vacuum pumps, solenoids, and forces applied by shroud retraction immediately before firing the laser. Continuously running systems such as induction motors typically excite vibration at discrete frequencies, whereas events that generate transient forces (impulses) such as opening and closing valves usually excite vibration over a broad frequency range. Either reducing excitation forces or isolating the target from the excitation is a very effective means for controlling target vibration, but doing so is not always practical. In such cases, the structural dynamics of the system become important.

The response of multidegree-of-freedom systems, such as the target assembly, to a given forcing function (F) is governed by a set of second-order differential equations so long as the stiffness remains constant; $M\ddot{X} + C\dot{X} + KX = F$. This set of equations relating the masses (M) of the degrees of freedom to the damping (C) and stiffness (K) linking the degrees of freedom constitutes an eigenvalue problem. Under the assumption of a harmonic response, the equations may be solved for eigenvalues that represent the natural frequencies of the system and associated eigenvectors that represent the relative displacement amplitudes of each degree of freedom or mode shape. To avoid high vibration amplitudes due to resonance, the natural frequencies must not coincide with those of forces that are strongly coupled with the associated mode shape. In situations where it is not possible to detune the natural frequencies from excitation sources, such as in the presence of broadband excitation, the vibration amplitude is then limited only by the system damping.

Finite element and experimental modal analyses are used to identify natural frequencies and characterize the associated mode shapes of cryogenic target assemblies for OMEGA. This information is used to interpret *in-situ* vibration data collected at TCC and to investigate the effect of proposed design changes on vibration.

Experimental Modal Analysis

Modal testing is a procedure for directly measuring the natural frequencies and mode shapes of a structure. For reasons of convenience, the target assembly was tested in air at room temperature and atmospheric pressure. A test article, identified as Cryo-ME-21, was constructed using a capsule with mass that is equivalent to a typical production capsule filled with

hydrogen. It is important to note that the dynamic response characteristics under cryogenic conditions are likely to differ from those measured under the test conditions due to changes in the effective stiffness (strain) of the spider silk supporting the capsule and to the reduced damping under vacuum. Differential thermal expansion between the spider silk and beryllium frame and temperature dependence of the elastic moduli are expected to shift the natural frequencies of the target assembly. Material properties of the spider silk are not known at temperatures in the vicinity of the hydrogen's triple point.[8] The impact of cooling on a target's natural frequencies has not been studied in depth, but high-speed video of a few targets suggests that cooling the target increases the silk's natural frequencies by 0% to 7%.

A commercially available shaker system consisting of an electrodynamic actuator and a flexure table was used to excite vibration of the target assembly. The flexure table is intended to limit motion of the target base to translation in one direction. The target assembly was mounted on the shaker table with the beryllium C frame oriented at a 45° angle to the primary motion of the shaker so that both in-plane and out-of-plane modes of vibration could be excited simultaneously, as shown in Fig. 108.16. A random noise signal, capable of exciting vibration over the frequency range of interest up to 2 kHz, was used to drive the shaker at an amplitude of 25 μm, which is consistent with the excitation measured at TCC. Motion of the shaker (excitation) was measured using a piezoelectric accelerometer mounted at the base of the spindle, which connects the target assembly to the stalk (3 cm below the bottom of the pin shown in Fig. 108.15).
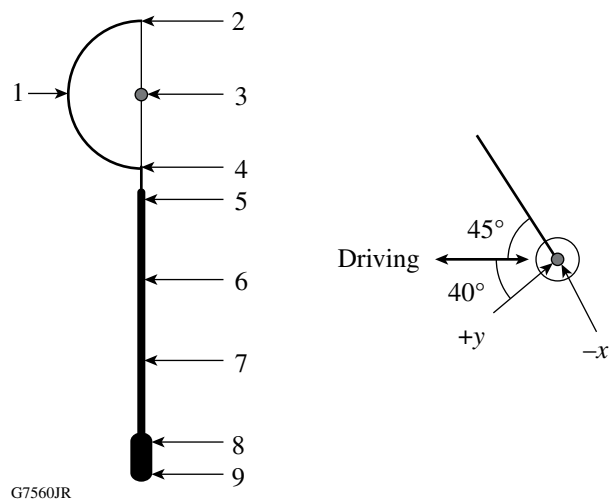

G7560JR

Figure 108.16
Measurement locations on target assembly.

The response of the target assembly to the applied base excitation was measured at the nine points shown in Fig. 108.16. A laser vibrometer was used to measure velocity of each point in two orthogonal directions corresponding approximately to in-plane (x) and out-of-plane (y) of the beryllium C frame. Use of an optical measurement method, as opposed to mounting accelerometers on the target assembly, is necessary to avoid adding mass that would change the natural frequencies of the target assembly.

Data from the test were processed using a multichannel dynamic signal analyzer to compute H1 frequency response function (FRF) estimates[9] that represent the amplitude and phase of the response as functions of frequency. In the FRF calculation, the amplitude at a given frequency is normalized by dividing the response (velocity) of each point on the structure by the excitation (acceleration) at a common reference location on the shaker table. To prevent errors in the fast Fourier transformation (FFT), which forms the basis for this calculation, a weighting window was applied. Discontinuities between the beginning and end values of nonperiodic signals were suppressed by a Hanning window, which reduces the signal amplitude at the beginning and end of the sampling interval. The FRF amplitudes were scaled to resolve the excitation force into the target x and y directions, which were oriented at approximately 45° angles to the excitation. Transmissibility functions were calculated for each measurement point by differentiating the FRF's to produce nondimensional amplitude ratios. Figure 108.17 shows composite transmissibility functions that were created by averaging the transmissibility amplitudes in each direction.
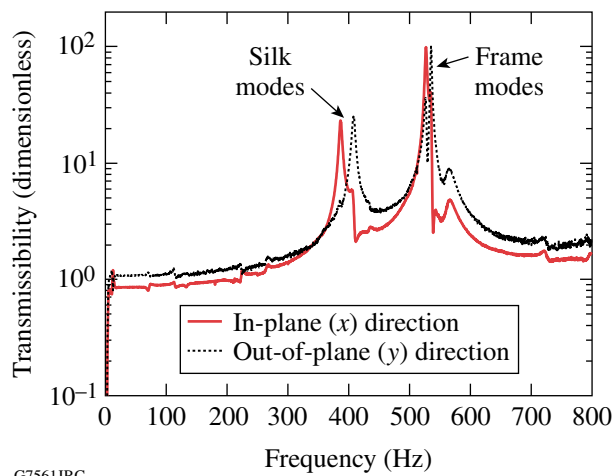

Figure 108.17
Target assembly transmissibility.

The transmissibility functions from the target assembly were analyzed using Polymax[10] curve-fitting functions to extract natural frequencies, modal damping values, and associated mode shapes. Graphically, the peaks in the transmissibility function indicate natural frequencies, and the relative amplitudes correspond to the mode shapes. Highly damped modes have lower and broader peaks in the transmissibility function. Curve fitting the transmissibility data identified the four stable modes listed in Table 108.I, where damping is expressed both as a percentage of critical and as an exponential decay time constant. At these natural frequencies, the coherence of all the measurements is greater than or equal to 95%. The other peaks in the spectrum (most notable at 570 Hz) are artifacts of secondary axis motion by the shaker.

Table 108.I: Experimental modal analysis results.

Mode	Frequency (Hz)	Damping	Description
1	386	0.6% (0.07 s)	In-plane silk translation
2	408	0.6% (0.07 s)	Out-of-plane silk translation
3	526	0.5% (0.06 s)	In-plane frame bending
4	535	0.1% (0.30 s)	Out-of-plane frame bending

Figure 108.18 shows the mode shapes associated with the four natural frequencies. The relative amplitude and direction of vibration at each measurement location are indicated by arrows. Mode 1 (386 Hz) and mode 2 (408 Hz) are dominated by translation of the capsule in and out of the plane of the C frame under silk tension. In tests on 16 mass-equivalent targets, the natural frequency of the silk mode in the y direction is consistently greater than in the x direction (with an average separation of 24 Hz). In mode 3 (526 Hz) and mode 4 (535 Hz) the mode shapes are dominated by bending of the C frame in plane (x) and out of plane (y) with the capsule moving out of phase with the frame.

Analytical Modal Analysis

A finite-element model of the target assembly was created to predict its dynamic response characteristics. To validate the model, boundary conditions, damping, and room-temperature material properties were used to predict the natural frequencies and mode shapes measured experimentally. Once validated, uses for the model include studies of the sensitivity to variation in uncertain parameters (such as spider silk properties), evaluation of proposed design changes, and prediction of the response
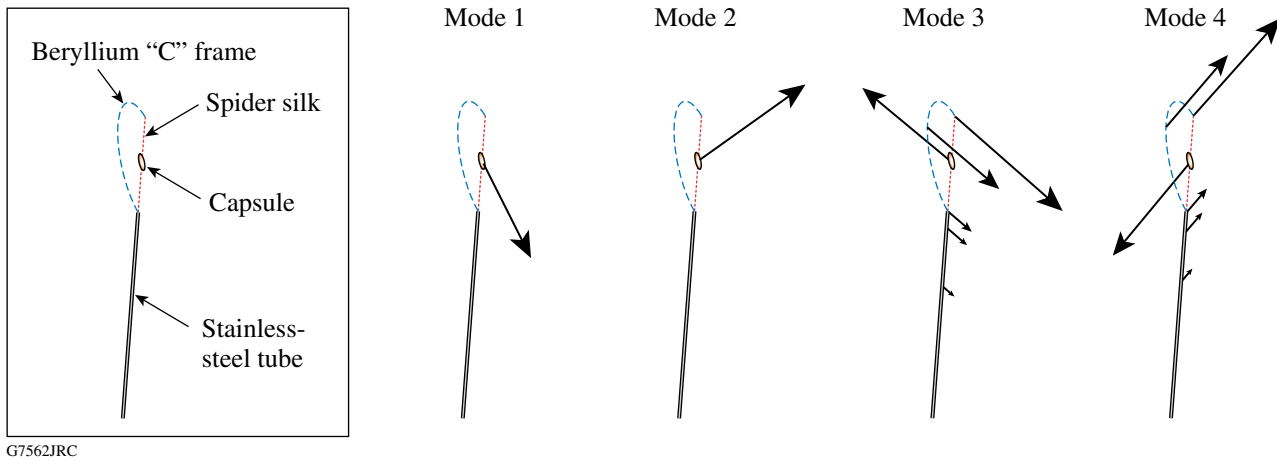
G7561JRC

G7562JRC

Figure 108.18
Experimental mode shapes.

characteristics under cryogenic conditions (if material properties such as Young's modulus, density, and coefficient of thermal expansion are determined or adequately approximated).

Construction of a Finite-Element Model

The target assembly consists of six relatively simple components (capsule, spider silk, beryllium C frame, stainless-steel tubing, the pin, and adhesives). Material properties for the components are listed in Table 108.II. Damping ratios from the experimental modal analysis results were applied to the model. In general, the system is assumed to respond in a linear manner or approximate a linear response for limited displacements. Specific modeling assumptions and methods for the components are described in the following sections.

Table 108.II: Material properties.

Material	Young's modulus (GPa)	Poisson's ratio	Density (kg/m^3)
Spider silk[6]	6.4	0.24	1200
Stainless steel[11]	193	0.29	7800
Aluminum[11]	70	0.33	2700
Beryllium[11]	300	0.10	1850
Epoxy[11]	5.0	0.35	1550

1. Target Capsule

The target capsule was modeled as a rigid body using a point mass element. Before assembling the target used for the experimental modal analysis (Cryo-ME-21), the capsule mass, outside diameter, and wall thickness were measured to be 56 μg, 878 μm, and 25 μm, respectively. It should be noted that

the test article has the same outside diameter and a greater wall thickness than production targets to make its mass equivalent to a DT-filled production capsule. The capsule geometry and mass were used to calculate the rotational moment of inertia about an axis through its center of mass. The rotational inertia of the adhesive attaching the capsule to the four strands of spider silk was assumed to be negligible. While the mass of the test article is the same as that of a filled production target, the rotational inertia will differ because the density of GDP is over 3.5 times that of DT ice. While the rotational inertia of the mass-equivalent capsule is 14% greater than a typical production capsule filled with DT ice, the modes of interest, which consist primarily of translation, are not significantly affected.

The capsule was connected to four spider silks via a series of eight stiff, zero-mass beam elements. Each beam ran from the point mass to contact points on the outer surface of the capsule as measured under a microscope. The separation between the silk contact points in the horizontal (xy) plane may vary by up to 10 μm due to ambiguity in the assembly process. Figure 108.19 shows a magnified view of the target-point mass and how it is assembled to the spider silk in the finite-element model.

2. Spider Silk Modeling

The spider silk strands were modeled using link elements that act in tension only. During the assembly process, tension is applied to each strand of silk by stretching to a nominal strain of 5.6%. With the strain below the yield point, the modulus of elasticity was assumed to be constant. The four silk strands supporting the capsule were collected from a single "drop line," which has been shown to have consistent properties over its entire length.[8] Specimens from the same drop line were
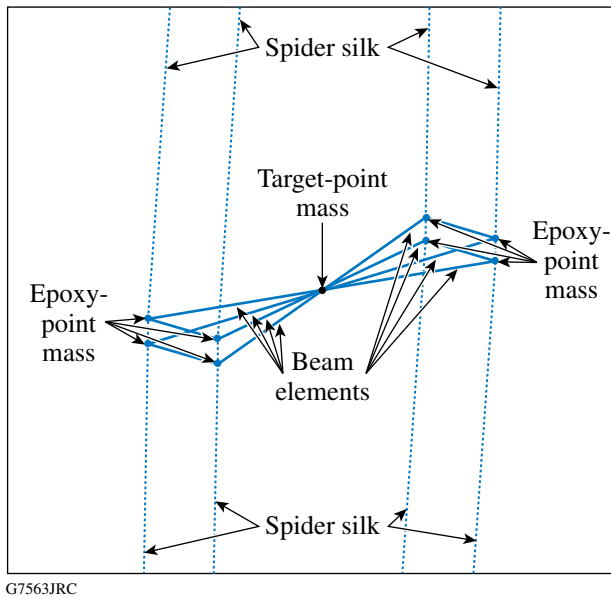
G7563JRC

Figure 108.19
The target-point-mass assembly in the finite-element model.

G7565JRC

Figure 108.21
Silk beryllium connection elements.

analyzed under a scanning electron microscope to determine the number of fibers and their cross-sectional area. Another specimen from the same drop line was tested to determine its modulus of elasticity.

The silk was attached to the target, as shown in Fig. 108.19. Small, stiff, zero-mass beams were used to create the attachment point between the silk and the beryllium C frame. The beams ran from the center of the beryllium wire to the theoretical tangential contact points between the outside diameter of the wire and the silk. Figure 108.20 shows how the model was created. Figure 108.21 is a geometric representation of element size and configuration.

G7564JRC

Figure 108.20
Silk beryllium connection mass.

3. C Frame and Support Tube

Beam elements were used to model the wire frame that supports the spider silk and the tube that connects the frame to the pin. The beryllium-wire C frame was assumed to have a round cross section with a constant diameter determined by measuring the test article. The stainless-steel support tube was assumed to have a circular cross section with constant diameter and wall thickness based on nominal values from the manufacturer.

4. Support Pin and Collet

The support pin at the bottom of the target assembly was modeled using a six-degrees-of-freedom beam element. The magnetic collet joint that attaches the target assembly to the spindle was assumed to be very stiff and was modeled by constraining the pin to the spindle (excitation source) in all six degrees of freedom. If the assumption of an ideal collet joint is not valid, the predicted natural frequencies of the first bending mode will be higher than the measured values. Excitation from the shaker was simulated by applying a harmonic acceleration to the collet in the x and y directions.

5. Epoxy Joints

Epoxy joints connecting the beryllium C frame to the stainless-steel tube and the stainless-steel tube to the pick-and-place pin were modeled using six single-degree-of-freedom spring elements. The springs were created between two coincident nodes. Half of the mass of the epoxy joint was applied to each of the coincident nodes. Figure 108.22 shows a cross section of a representative pin joint. The C-frame joint was not analyzed due to hazards associated with machining beryllium. During assembly, the tube is pushed against one side of the hole in the pin as shown in Fig. 108.22.
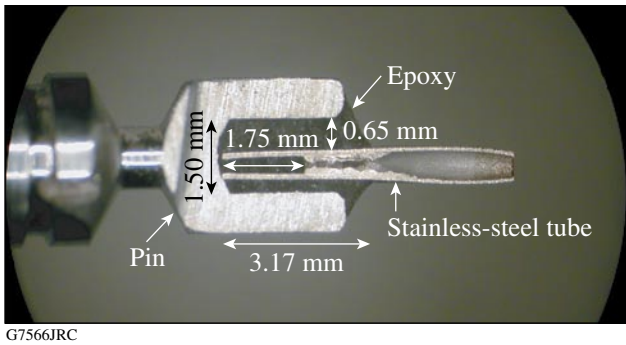
G7566JRC

Figure 108.22
Cross section of pin and stainless steel tube.

Likewise, the beryllium wire is pushed against the side of the tube in the positive x direction as shown in Fig. 108.23. Detailed finite-element models of the epoxy joints were used to assess their stiffness in each direction. Forces and bending moments were applied individually in each direction, and solutions were obtained for the resulting displacements. The effective stiffness of the joint was calculated and applied to the corresponding spring elements in the target model; however, the mass and stiffness of epoxy in the joints may vary from target to target.
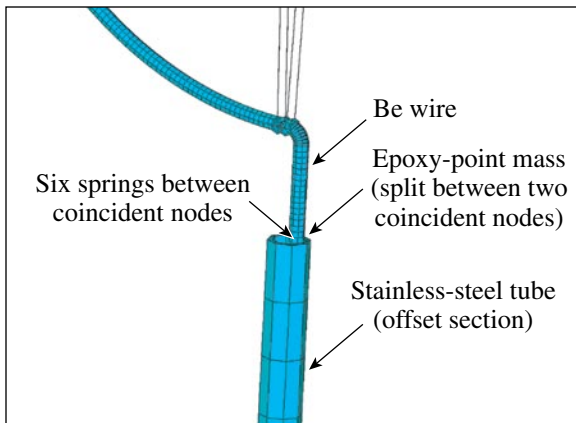
G7567JRC

Figure 108.23
Beryllium wire connection to stainless-steel tube.

Analysis Results

The model was used to calculate the dynamic response characteristics of the target assembly at room temperature. Natural frequencies and associated mode shapes of the target assembly were calculated through modal analysis of the model. Damping values from the experimental modal analysis results, which represent both structural and aerodynamic affects, were applied to the model. A harmonic analysis based on supposition of the response to a sine sweep was used to calculate the frequency response function shown in Fig. 108.24.
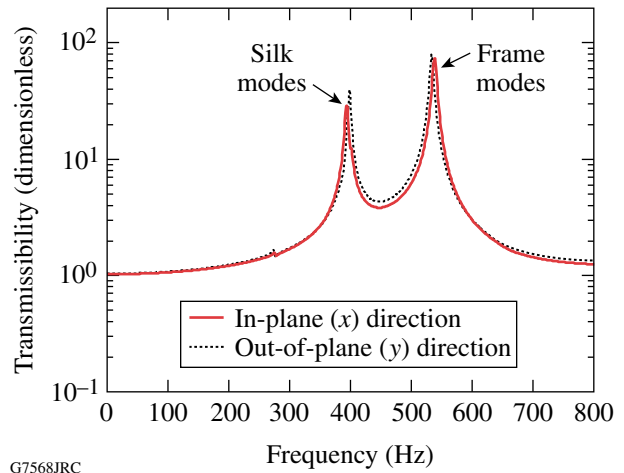
G7568JRC

Figure 108.24
Transmissibility functions.

Correlation of Analytical and Experimental Results

The model was validated by comparing the predicted frequencies and mode shapes with the experimental values. Table 108.III shows the correlation between the measured natural frequencies and the corresponding predicted values. Prediction of frequencies within 3% of the experimental values suggests that the model is valid for assessments of potential design changes and sensitivity studies.

Table 108.III: Natural frequency correlation.

Mode description	Experimental frequency (Hz)	Analytical frequency (Hz)	Difference
In-plane (x) silk translation	386	393	1.9%
Out-of-plane (y) silk translation	408	400	−1.9%
In-plane (x) frame bending	526	538	2.3%
Out-of-plane (y) frame bending	535	535	0.0%

The mode shapes associated with the largest peaks in the FRF's are similar to the experimental results presented in Fig. 108.18. At 278 Hz, the model predicts a mode dominated by the capsule spinning about the z axis with an orbital component that produces translation when the geometric center of the silk/capsule contact points is offset from the capsule's center of mass. The laser vibrometer used in the experiment measures only translation and is therefore not well suited to detect the first mode. While a small peak in the experimental FRF (268 Hz) corresponds closely with the predicted frequency of the first rotational mode, the peak

is attributed to a mode of the shaker. Modal assurance criteria (MAC)[12] are used to compare the predicted and experimental mode shapes dominated by translation of the measurement points. A scalar MAC value is calculated for each pair of analytical and experimental mode shapes to determine their consistency. Fundamentally, the MAC values are based on "R^2" correlation coefficients used in linear regression. A MAC value close to 100% indicates a high degree of correlation, and a value close to zero indicates uncorrelated modes. The MAC matrix shown in Table 108.IV indicates that the predicted mode shapes correlate closely with the experimental modes shapes at corresponding frequencies (diagonal terms in the matrix).

Table 108.IV: Modal assurance criteria.

		Experimental			
	Frequency (Hz)	386	408	526	535
Analytical	393	93	16	16	12
	400	6	84	11	18
	538	26	0	84	17
	535	0	26	16	82

The separation between the *x*- and *y*-direction silk modes near 400 Hz is affected by a variety of parameters including the silk attachment offset from the capsule center of mass, the distance between adjacent points, and uneven silk tension. However, the cumulative effect of improved model fidelity in these areas separates the silk modes by only 7 Hz and does not explain the measured 22-Hz separation. Furthermore, the fact that the out-of-plane silk mode consistently has a higher natural frequency (24±6 Hz on average for mass-equivalent targets) suggests that a systematic source of asymmetry remains unmodeled. However, none of the experimental data collected to date suggests a correlation between the gain (amplitude) and frequency separation of the silk modes.

The model predicts a natural frequency of the in-plane, frame-bending mode, which is higher than the out-of-plane mode. While the experimental results presented here contradict the model's prediction, data from eight similar mass-equivalent targets support the prediction. On average the in-plane mode has a natural frequency that is higher by 0.6±5.9 Hz. This variability is consistent with sensitivity studies performed on the quantity and distribution of adhesive and assembly tolerances in the epoxy joints.

Applications

Information gained from the study of target dynamics is being used to understand and reduce capsule vibration at TCC. During simulated shots (without firing the laser), the vibration of mass-equivalent target capsules has been measured with high-speed video (HSV) cameras. Analysis of the data from two cameras with roughly orthogonal views yields three-dimensional capsule displacements at frequencies up to 1 kHz. The broadband vibration amplitude varies from 5 to 100 μm at the time when the laser would fire (less than 100 ms after retraction of a thermal shroud that maintains the capsule at 20 K). Auto-power spectra functions calculated from the HSV data indicate that capsule displacement is typically dominated by vibration at a few discrete frequencies, as shown in the spectrum from a representative target in Fig. 108.25. The HSV measurements and modal test were performed on different targets. The *x*- and *y*-direction, silk-mode natural frequencies of the target from which the HSV data were collected were 254 and 275 Hz, respectively, and the frame-mode natural frequencies were 592 and 589 Hz, respectively. Two peaks in the HSV auto-power spectrum (270 and 291 Hz) correspond very closely with the silk-mode natural frequencies. A 10-Hz decrease in the frequencies of these two peaks during the first few seconds after shroud removal suggests that the governing stiffness decreases quickly (probably due to warming of the spider silk). Based on observation of similar sets of corresponding peaks from other targets (at different frequencies), these peaks in the HSV auto-power spectra are attributed to the silk modes. However, the frame modes, which do not typically appear in the HSV data, are either not excited or are more heavily damped. Consequently, efforts to control target vibration at TCC need to focus on the silk modes and the peaks around 50 Hz, which are not attributable to the target assembly. The modes around 50 Hz are not discussed in this work.
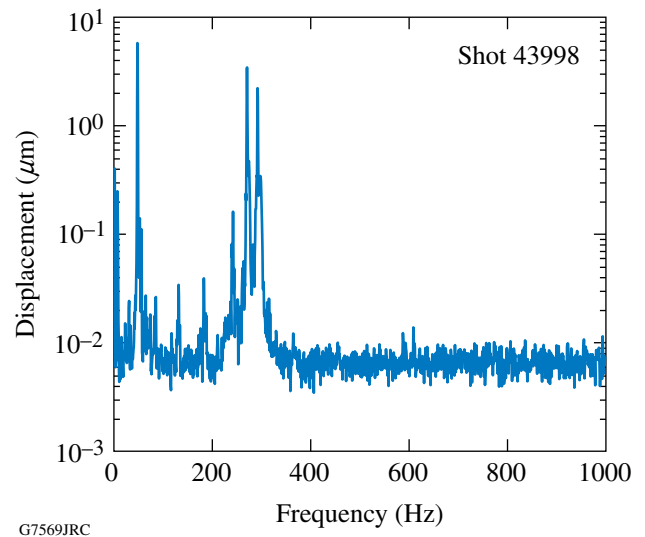

G7569JRC

Figure 108.25
High-speed video spectrum.

Frequency response functions of production targets are measured at one location (the capsule) for quality-assurance purposes before filling the capsule with fuel. The silk-translation natural frequencies of the 66 targets produced from May through September 2006 ranged from 650 Hz to over 1200 Hz. Note that the empty capsule has considerably less mass and therefore higher silk-translation natural frequencies than the mass-equivalent target. The silk-translation modes of empty production targets are also more heavily damped when tested on the shaker due to the reduced mass and increased velocity. The frame-mode natural frequencies of production targets are typically very close to those of mass-equivalent targets. Figure 108.26 shows an FRF from a representative production (target ID Cryo-2062-669) target with an empty capsule.

The finite-element model was used to predict the dynamic response characteristics of the production target (Cryo-2062-669) once the empty capsule was filled with either 33 μg of D_2 or 42 μg of DT fuel. The model, which does not account for thermal effects, predicts silk natural frequencies of 410 and 450 Hz when filled with D_2 and 380 and 415 Hz when filled with DT. The impact of cooling on target natural frequencies has not been studied in depth, but high-speed video of a few targets suggests that cooling the target increases the silk natural frequencies by 0% to 7%. Once cooled, the target is expected to have natural frequencies of 455 and 495 Hz if filled with D_2 and frequencies of 420 and 455 Hz if filled with DT.

G7570JRC

Figure 108.26
Experimental FRF of an empty production target capsule.

Variability in the spider silk dimensions and material properties is an unfortunate consequence of working with a naturally occurring material. Sensitivity of the target assembly dynamics to variations in the spider silk properties was investigated with the finite-element model. For an unfilled target, Fig. 108.27 shows the predicted variation in natural frequency of the first translational silk mode as a function of strain, silk modulus, silk diameter, and capsule mass. For an initial strain of 5.6% (the nominal value in the current production process),
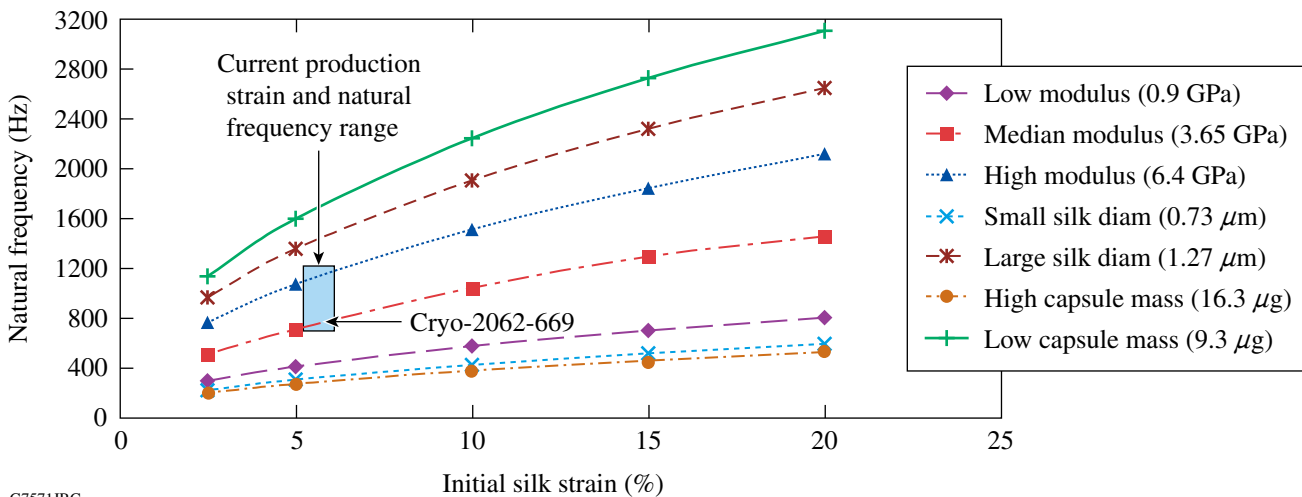

G7571JRC

Figure 108.27
Silk mode sensitivity to strain, modulus, diameter, and capsule mass.

the natural frequency of the first silk translation mode can vary by approximately 670 Hz due to a three-standard-deviation variation in the elastic modulus.[8] Variation in the diameter of the silk (three standard deviations) increases the range to 1050 Hz. Variations in capsule wall thickness from 3.6 μm to 6.3 μm affect the silk translation natural frequencies by changing the mass (9.5 to 16.5 μg) and increasing the range of natural frequencies to 1330 Hz.

The predicted mean and standard deviations of silk-mode natural frequency based on the sensitivity analysis (920±220 Hz) are greater than the values (865±160 Hz) obtained from measuring the natural frequencies of the 66 targets produced from May through September. However, the experimental bandwidth of the shaker was limited to 1200 Hz, and applying this constraint to the FEA data (under the assumption of a Gaussian distribution) reduces the range to 910±201 Hz. Future target-frequency-response tests will have a 2-kHz bandwidth that encompasses the three-standard-deviation range of silk-mode frequencies. The discrepancy between the predicted and measured frequency ranges indicates that the effective modulus of the tested targets is lower and more consistent than published values. Seasonal effects on silk properties may broaden the experimental uncertainty bounds; these will be studied in the future.

Filling the targets with D_2 or DT fuel changes the predicted (three-standard-deviation) range of silk-mode natural frequencies (assuming 5.6% initial strain) to 150 to 750 Hz, and 130 to 670 Hz, respectively. The variation in silk-mode natural frequencies could be reduced by adjusting the silk strain during target fabrication to compensate for variations in silk properties. However, the elastic modulus measurement process employed in this study would not be practical for routine use in target fabrication. For the purpose of tuning the silk-mode natural frequencies, a more expedient and less accurate measurement would suffice.

Overlap between the frequency ranges for the frame and silk translation modes presents the possibility of coupling between the modes. As a silk mode and a frame mode approach the same frequency, the associated mode shapes shown in Fig. 108.18 become increasingly similar. The effect of coupling was investigated as a potential cause for high vibration of some production targets. Interaction between the modes is measured in terms of the target capsule's transmissibility value (gain) at the natural frequencies. The FRF's in Fig. 108.28 illustrate the effect of increasing the silk-mode natural frequency. In addition to increasing the gain of both silk and frame modes, coupling

also shifts the frame-mode frequencies higher by roughly 75 Hz. Figure 108.29 shows the gain of the frame and silk modes plotted as functions of the silk-mode natural frequency. When the silk-mode natural frequency coincides with that of the frame modes (526 Hz and 538 Hz), coupling increases the frame-mode gain by a factor of 4 and the silk-mode gain by a factor of 2 with respect to the measured silk-mode natural frequency (400 Hz).
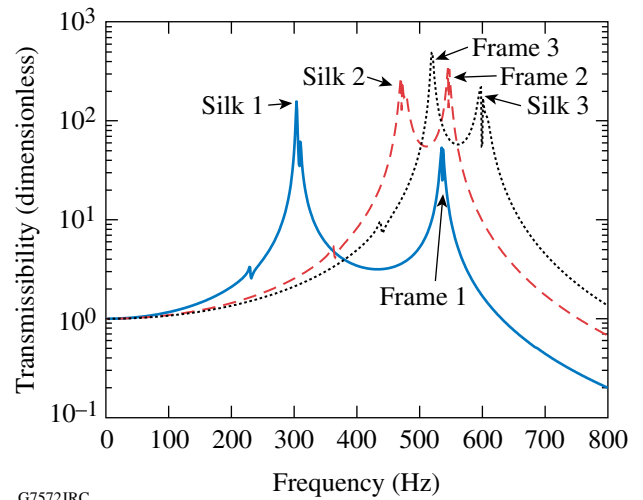
G7572JRC

Figure 108.28
FRF's showing coupling effect.
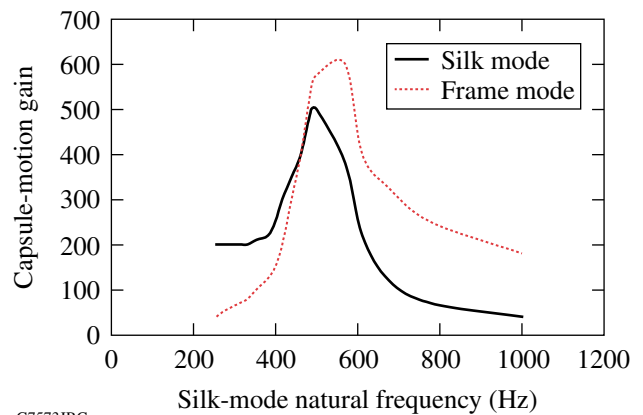
G7573JRC

Figure 108.29
Silk- and frame-mode coupling.

To prevent coupling, acceptance criteria will be established for an empty target's natural frequencies. The single-degree-of-freedom model shown on p. 180 provides simple and accurate (based on correlation with the finite-element model) predictions of the silk-mode natural frequencies of a fully fueled target (f_{full}) based on the measured natural frequency when

empty (f_{empty}). Targets with fully fueled silk natural frequencies between 85% and 125% of the frame natural frequencies will be rejected.

$$f_{full} = f_{empty} \times \sqrt{\frac{\text{capsule mass}}{\text{capsule mass + fuel mass}}}. \qquad (1)$$

Analysis of the HSV data reveals several clues regarding the excitation. First, excitation of silk translation modes in targets with silk natural frequencies ranging from 270 to 570 Hz indicates the presence of a broadband excitation source such as an impulse or random noise. Second, the absence of vibration at the frame-mode natural frequencies implies weak coupling between the excitation source and frame modes or high damping of the frame modes. Potential excitation sources including shroud separation forces and target clearance to the thermal shroud during retraction are currently being investigated.

Conclusion

The analytical model predicts natural frequencies of translation modes within 3% of those obtained experimentally. Correlation of target capsule vibration at TCC with the target dynamic response characteristics obtained from this study indicates that the silk modes are a primary cause of capsule displacement during shots. While increasing the silk-mode natural frequencies would typically reduce the displacement amplitude, coupling between the silk and frame modes is believed to counteract the benefits until the silk-mode frequencies are significantly greater than those of the frame modes. Increasing the silk natural frequencies would probably introduce significant mass asymmetry. Therefore, the authors are designing a new cryostat that will not excite the silk modes and are exploring stiffer capsule-support concepts.

ACKNOWLEDGMENT

REFERENCES

1. T. C. Sangster, J. A. Delettrez, R. Epstein, V. Yu. Glebov, V. N. Goncharov, D. R. Harding, J. P. Knauer, R. L. Keck, J. D. Kilkenny, S. J. Loucks, L. D. Lund, R. L. McCrory, P. W. McKenty, F. J. Marshall, D. D. Meyerhofer, S. F. B. Morse, S. P. Regan, P. B. Radha, S. Roberts, W. Seka, S. Skupsky, V. A. Smalyuk, C. Sorce, J. M. Soures, C. Stoeckl, K. Thorp, J. A. Frenje, C. K. Li, R. D. Petrasso, F. H. Séguin, K. A. Fletcher, S. Padalino, C. Freeman, N. Izumi, J. A. Koch, R. A. Lerche, M. J. Moran, T. W. Phillips, and G. J. Schmid, Phys. Plasmas **10**, 1937 (2003).

2. A. Nikroo *et al.*, General Atomics, San Diego, CA, GA–A23881 (2002).

3. D. T. Goodin *et al.*, in *Proceedings of the 17th IEEE/NPSS Symposium on Fusion Engineering* (IEEE, New York, 1997), Vol. 1, pp. 309–312.

4. J. D. Lindl, Phys. Plasmas **2**, 3933 (1995).

5. P. W. McKenty, V. N. Goncharov, R. P. J. Town, S. Skupsky, R. Betti, and R. L. McCrory, Phys. Plasmas **8**, 2315 (2001).

6. D. D. Meyerhofer, J. A. Delettrez, R. Epstein, V. Yu. Glebov, V. N. Goncharov, R. L. Keck, R. L. McCrory, P. W. McKenty, F. J. Marshall, P. B. Radha, S. P. Regan, S. Roberts, W. Seka, S. Skupsky, V. A. Smalyuk, C. Sorce, C. Stoeckl, J. M. Soures, R. P. J. Town, B. Yaakobi, J. D. Zuegel, J. Frenje, C. K. Li, R. D. Petrasso, D. G. Hicks, F. H. Séguin, K. Fletcher, S. Padalino, C. Freeman, N. Izumi, R. Lerche, T. W. Phillips, and T. C. Sangster, Phys. Plasmas **8**, 2251 (2001).

7. R. S. Craxton, ed. *OMEGA Upgrade Preliminary Design*, Laboratory for Laser Energetics, University of Rochester, Rochester, NY, LLE Document No. DOE/DP 40200-101 (1989).

8. M. J. Bonino, "Material Properties of Spider Silk," M.S. Thesis, University of Rochester, 2003.

9. J. S. Bendat and A. G. Piersol, *Engineering Applications of Correlation and Spectral Analysis* (Wiley, New York, 1980).

10. LMS International, Leuven, Belgium.

11. A material properties database, MatWeb is a division of Automation Creations, Inc., Blacksburg, VA 24060, December 2006, http://www.matweb.com (11 December 2006).

12. R. J. Allemang and D. L. Brown, in *Proceedings of the International Modal Analysis Conference & Exhibit* (Society for Experimental Mechanics, Schenectady, NY, 1982), pp. 110–116.

Measuring *E* and *B* Fields in Laser-Produced Plasmas with Monoenergetic Proton Radiography

The generation of electromagnetic fields (*E/B*) by interactions of laser light with matter is a process of fundamental interest in high-energy-density (HED) physics.[1] The primary mechanism behind field formation is the loss of energetic electrons from the heated region, resulting in the breakdown of neutrality. Many processes can then contribute to field generation and evolution, but their relative importance depends on interaction parameters.[1–5] For long-pulse, low-intensity laser light, the dominant source for *B*-field generation is noncollinear electron density and temperature gradients ($\nabla n_e \times \nabla T_e$); the dominant source for *E* fields is $\nabla P/n_e$, a consequence of nonuniform laser irradiation.[1–5] For circular laser spots, the *B* fields have a toroidal configuration with scale length comparable to the spot size. In a regime with low *Z* and high temperature, where resistivity is low, *B*-field growth is usually linear in time and is balanced primarily by convective losses (i.e., the *B* field is "frozen in").[1–3,5] Under these circumstances, *B*-field evolution can be described by the Faraday equation combined with a simplified version of the generalized Ohm's law:

$$\frac{\partial \mathbf{B}}{\partial t} \approx \nabla \times (\mathbf{v} \times \mathbf{B}) - \frac{1}{en_e} \nabla n_e \times \nabla T_e, \qquad (1)$$

where **v** is the plasma fluid velocity.

In addition to their importance to fundamental HED physics, these fields have important implications for several current problems. In inertial confinement fusion (ICF), magnetic fields (~MG) are generated inside a hohlraum by long-pulse (~1-ns) laser illumination.[6–8] Such fields can reduce heat flow since cross-field thermal conductivity is modified by a factor of $\left(1 + \omega_{ce}^2 \tau^2\right)^{-1}$, where ω_{ce} is the electron gyro frequency and τ is the collision time. The result is altered distributions of electron temperature and density, enhancing laser–plasma instabilities, and implosion asymmetries.[6–8] The experiments described here are the first to directly measure fields generated by the types of laser beams used in direct- and indirect-drive ICF.

Previous work focused largely on short-pulse, high-intensity lasers,[9–11] and field measurements were based on Faraday rotation,[10] probes,[4] or high-order laser harmonics.[11] It has also been proposed that proton radiography could provide a method for measuring fields through the deflections they induce in proton trajectories; recent work by Mackinnon *et al.*[12] demonstrated that high-resolution images containing deflection information could be obtained, although no direct connections were made between images and fields. In their experiment, backlighter protons were generated by irradiating a solid tungsten target with a high-intensity petawatt laser beam (300-fs duration with an intensity of 1×10^{19} W/cm^2); the result was a large proton flux and a continuous energy spectrum up to ~50 MeV. These protons were passed through a mesh and used to image a plasma generated by a single laser beam (300 ps) on a 120-μm Cu wire. More recently, work by Romagnani *et al.*[13] utilized side-on proton radiography to study the *E* field generated by a high-intensity (~10^{18} W/cm^2), short-pulse (~1.5-ps) laser driving an Au foil; the probing proton flux had a continuous energy spectrum and was generated from a 10-μm Au foil irradiated by an ~300-fs-long, 2×10^{19} W/cm^2 laser pulse.

A novel imaging technology has been developed that combines a monoenergetic proton backlighter with a matched detection system.[14,15] Protons are generated as nuclear fusion products from the reaction D + ^{3}He $\longrightarrow \alpha$ + *p* in exploding-pusher implosions of D^{3}He-filled, glass-shell capsules;[16] the proton birth energy is E_p = 14.7 MeV with a small amount of thermal broadening. For the experiments described here, backlighter implosions were driven by 20 OMEGA laser beams; a typical measured proton spectrum is shown in Fig. 108.30, indicating a proton yield of ~3×10^8. The spatial size of the proton source was measured with a proton-emission imaging system,[17] which determined that the source was nearly spherical and had approximately a Gaussian radial emission profile with a full width at half maximum (FWHM) of ~45 μm. The timing of the proton production was measured by a proton temporal diagnostic (PTD);[18] protons were produced during an interval of ~150 ps, and the time of onset of the burn was adjustable. The protons were detected by a CR-39 track detector configured for imaging.[15] This approach has distinct advantages over radiography with broadband proton sources (such as intense-laser–induced sources); it allows us to optimize

a special detector design and to make precise connections between particle deflections and field magnitudes.
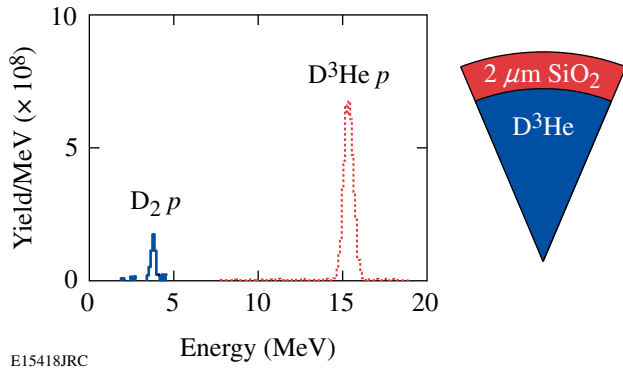

Figure 108.30

Measured energy spectra of monoenergetic D^{3}He and D$_2$ protons generated in an implosion of a thin-glass shell filled with D^{3}He gas (OMEGA shot 42767). The data described in this article correspond to the D^{3}He protons; use of the 3-MeV D$_2$ protons will be explored in future work.

Our experimental setup, illustrated schematically in Fig. 108.31, was designed for quantitative imaging of fields generated by the interaction of a laser with a plastic (CH) foil. In each experiment, 14.7-MeV backlighter protons were passed through meshes with 150-μm periods (to form discrete, 75-μm beamlets with ~2000 protons each) and used to simultaneously image two separate laser–plasma interactions: one imaged face on and the other imaged from the side. The laser–plasma interactions on each CH foil were induced by a single laser *interaction* beam with a 0.351-μm wavelength, incident 23° from the
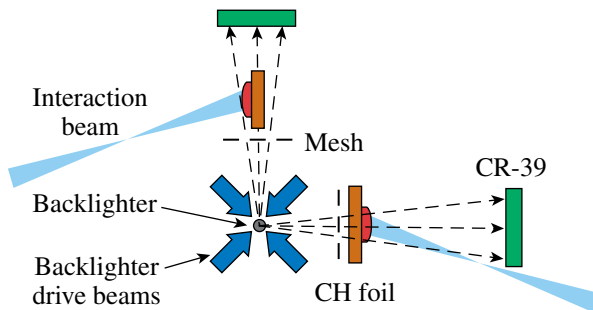

Figure 108.31

Schematic illustration of our experimental setup and the physical relationship among the proton backlighter (imploded D^{3}He-filled capsule), mesh, CH foils, CR-39 imaging detectors, and OMEGA laser beams, as used for simultaneous radiography of two separate laser–foil interactions (face-on and side-on). The distances of components from the backlighter were 0.8 cm for mesh, 1 cm for foil, and 36 cm for the detector.

normal direction. The laser had a square pulse either 1 ns or 0.6 ns long, with an energy of 500 J or 250 J. The diameter of the laser beam on the foil (containing 95% of the energy deposition) was determined by the phase plate,[19] which was either SG2 (500 μm) or SG4 (800 μm); the resulting laser intensity was of the order of 10^{14} W/cm^2. X-ray emission indicates that the plasmas have n_e ~ 10^{20} to 10^{22}/cm^3 and T_e ~ 1 keV.

The interaction of the laser with the CH foil was modeled with the 2-D *LASNEX* hydrocode.[20] The magnetic-field package[21] in *LASNEX* includes the full Braginskii cross-field transport model and spontaneously generates fields in the presence of nonparallel temperature and density gradients. The proton transport through these fields and plasmas was modeled with the *LSP* hybrid PIC (particle-in-cell) code.[22] Because only a single energy (14.7 MeV) was used, directly comparing simulations and experimental data provides unambiguous quantitative information about fields. Simulations[8] indicate that face-on radiography is largely sensitive only to the *B* field,[23] while side-on radiography is primarily sensitive only to the *E* field. This allows *E* and *B* fields to be measured separately.

Figure 108.32(a) shows face-on images acquired from three different shots. Laser timing was adjusted so the 14.7-MeV protons arrived at the foil at 0.0, 0.33, and 0.64 ns, respectively, after the laser interaction beam was turned on. The laser beam had an SG4 phase plate (800-μm diameter), with a 1-ns pulse and 500 J of energy. The measured images are very similar to the *LASNEX* + *LSP* simulations shown in Fig. 108.32(b), in terms of both the time dependence of the apparent diameter of the plasma bubble and the amount of distortion of the mesh pattern inside the plasma bubble region due to the magnetic lens effect. Significant distortions occurred near the border of the bubble, where the proton beamlets were deflected by a strong *B* field and piled up to form a sharp circular ring; smaller distortion at the center indicates a smaller, but measurable *B* field there. These features are largely reproduced by simulations illustrated in Fig. 108.33, showing that toroidal *B* fields are concentrated on a hemispherical shell surrounding the ablative plasma bubble; they have maximum amplitude near the edge but fall to zero at the center. The *B* fields can be estimated from the data by using the linear displacement ξ of the beamlets in an image from where they would be without the distortion, together with the geometry of the imaging system and the scale length ($L_B \equiv B/\nabla B$) in the direction perpendicular to the image $\left(B \propto E_p^{0.5} L_B^{-1}\right)$. L_B was estimated to be $L_B \sim L_\parallel \equiv n_e/\nabla n_e$, which is about the radius of the plasma bubble. This estimated L_B is within a factor of 2 of what one would infer from the simulations near the edge of the bubble. The inferred peak *B* values of about 0.5 MG agree
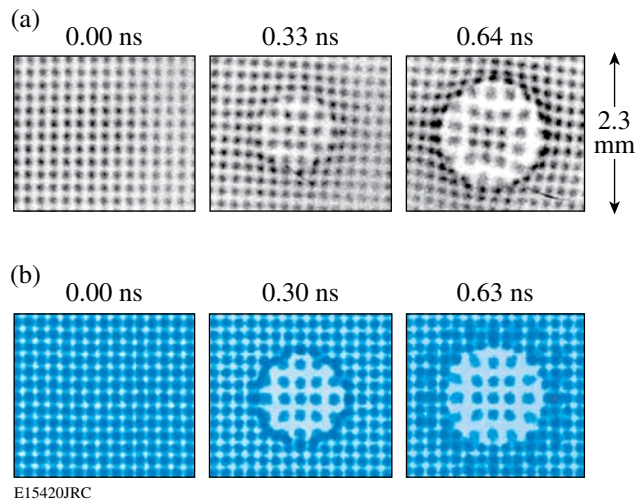
(a)

Figure 108.32

(a) Measured face-on, 14.7-MeV proton images showing the effects of the magnetic field generated by laser–plasma interactions. Each image is labeled by the time interval between the arrival at the foil of the interaction beam and the arrival of the imaging protons. The interaction beam had a 1-ns pulse length. The labeled dimensions of the image are scaled to the location of the foil. Note that the apparent 188-μm separation of beamlets in the unperturbed sections of the images corresponds to the separation at the mesh (150 μm) magnified by the ratio (source-to-foil distance)/(source-to-mesh distance). (b) Images simulated by *LASNEX + LSP* for the conditions that produced the experimental images shown in (a).
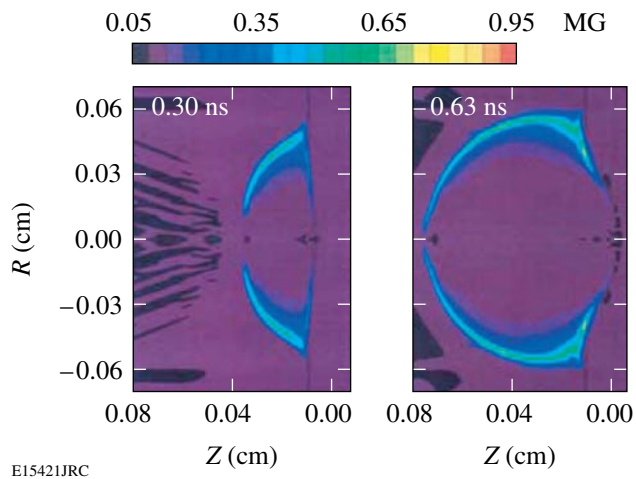
Figure 108.33

Time evolution of *B*-field strength on a cross section of the plasma bubble, simulated by *LASNEX* for the experimental conditions of Fig. 108.32. In each case, the horizontal coordinate *z* is the distance from the foil (assuming the laser is incident from the left), and the vertical coordinate *R* is the distance from the central axis of the plasma bubble. The largest field occurs near the surface of the plasma bubble, and the largest line integral parallel to the *z* direction occurs near the bubble edge.

well with simulations. In contrast to previous experiments and simulations, where the plasmas were usually generated by a short-pulse laser (~1 to 100 ps), we used long pulses that result in time evolution on a scale longer than our 150-ps sampling time; this allows us to clearly measure the time evolution of the field structure as shown in Fig. 108.32.

We can be more quantitative about data-simulation comparisons. The displacements ξ of individual beamlet positions in the images represents not lateral displacements at the foil but angular deflections from interactions with fields near the foil that result in lateral displacement at the detector. Angles of deflection can be inferred directly from displacements ξ by using the experiment dimensions, but quantitative comparisons between measured and simulated images are most easily made in terms of image dimensions and values of ξ. In Fig. 108.32, for example, we can look at the apparent diameter of the plasma bubbles (where beamlet "pileup" occurs). At ~0.3 ns it is about 1.5 mm for both simulation and data, although the value for the real image is harder to measure exactly because the pileup position is not as well defined. At ~0.6 ns, both data and simulation show diameters of about 1.6 mm. Next we can look at the displacements ξ in the centers of the images, which are proportional to the magnetic field in the centers of the bubbles. At ~0.3 ns, ξ is about 40 μm for both data and simulation, showing good agreement at that time. At 0.64 ns, the agreement is not so good since ξ is about 50 μm for the simulation but approximately zero for the data. Finally, we look outside the bubbles and see that the data show a slight mesh distortion that is not apparent in the simulations; this could suggest that the simulations underestimated the plasma resistivity, or that the interaction laser had more energy in its wings than assumed in the simulations. The simulations have done a good job of modeling the overall behavior of the plasma bubble, indicating that basic physics issues were properly addressed, but some differences merit further investigation.

Images acquired with different distributed phase plates used to condition the laser focal spots are contrasted in Fig. 108.34: SG4 for the first row (800 μm) and SG2 for the second row (500 μm). In all cases the laser pulses had similar energy and pulse shape (~250 J, 0.6 ns square), so the laser intensity for the second row was ~2.6 times higher. This resulted in deflection of the central beamlets by nearly a factor of 10 more in the central region for SG2 than for SG4 at ~0.4 ns, but not at ~0.7 ns. This is consistent with our *LASNEX* simulations, which show that a significant *B* field is generated in the central region at earlier times, but moves to the edge of the plasma because of plasma expansion.
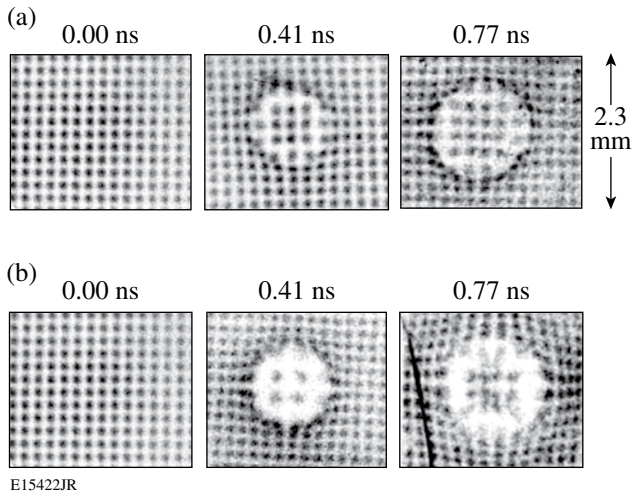
Figure 108.34

14.7-MeV-proton radiographs recorded for experiments with a similar interaction laser pulse (~0.6 ns square, ~250 J) but different phase plates: (a) SG4 and (b) SG2. The smaller diameter of the SG2 beam resulted in an intensity ~2.6 times higher than SG4, causing greatly increased image distortion.

The images shown in Fig. 108.35 show a consequence of using no phase plate for the interaction beam. Both images were recorded around 0.3 ns and utilized similar interaction beam diameters, pulse shapes, and laser energy. Compared to the image recorded with phase plate (a), the image recorded without (b) shows a more-chaotic pattern, implying a B field with medium-scale structure (at ~20% to 30% of the bubble size). This observation is consistent with theoretical expectations. An unconditioned OMEGA laser beam has nonuniformities at scales of ~40 μm. This can lead to medium-scale, random
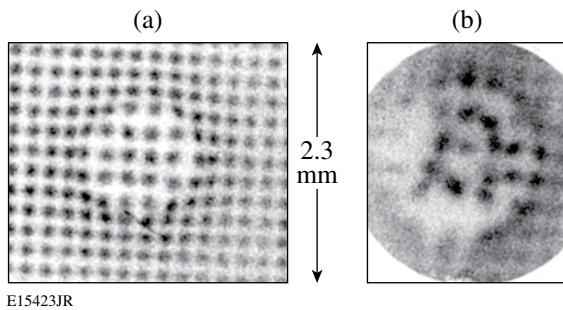

Figure 108.35

Effects of phase plates on the B-field structure are demonstrated by 14.7-MeV proton radiographs made by using interaction beams (a) with and (b) without phase plates under conditions otherwise similar. [Image (b) is from an earlier experiment in which the field of view was smaller and the outer (gray) part of the imaged area was covered by a 70-μm mylar washer.] Chaotic structure is clearly seen in image (b).

plasma structures, in particular those associated with very localized regions of strong $\nabla n_e \times \nabla T_e$, including the resonance absorptions at local oblique incidence, filaments, laser hot spots, and instabilities.[1–5] When phase plates are used, they convert the medium-scale laser nonuniformities to a smaller scale of ~2 μm (the speckle size). Short-wavelength plasma structures are more easily smoothed by thermal transport than medium-wavelength structures, so plasmas are more uniform when phase plates are deployed.

Side-on measured (a) and simulated (b) images are shown in Fig. 108.36 for the same shot that generated the center image shown in Fig. 108.34(b). The displacements of the beamlets away from the foil represent the effect of the electric field generated by $\nabla P/n_e$. The size of the apparent beamlet displacement ($\xi \approx 60$ μm) is used to estimate the E-field strength $\left(E \propto \xi E_p L_\perp^{-1} \right)$; by assuming that the field operates over a scale length $L_\perp$ comparable to the radius of the plasma bubble, $E \approx 1.5 \times 10^8$ V/m was deduced. The magnitude of the beamlet displacement in the experiment is very similar to what is seen in the simulation.
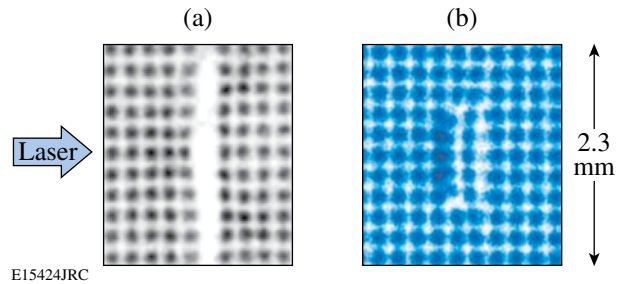

Figure 108.36

(a) Data and (b) simulation for the side-on images. The distortion in the center column of (a) resulted from the E field. The large separation between the two center columns of beamlets in (a) is due to attenuation by the CH foil, which is 50 μm thick but 3 mm long in the direction parallel to the proton trajectories. This effect is not seen in (b) because proton–foil interactions were not modeled in the *LSP* simulation. The magnitude of the beamlet displacement in the experiment is very similar to what is seen in the simulation.

In summary, we studied electromagnetic fields generated by the interaction with plasmas of long-pulse, low-intensity laser beams that are particularly relevant to inertial confinement fusion experiments. The field strengths have been measured using novel monoenergetic proton radiography methods. High-resolution, time-gated radiography images of a plastic foil driven by a 10^{14}-W/cm^2 laser implied B fields of ~0.5 MG and E fields of ~1.5×10^8 V/m. The experiments also demonstrated the smoothing effects of laser phase plates by showing that they substantially reduce medium-scale chaotic field structure.

Overall, there was good agreement between experiment and *LASNEX + LSP* simulations, as demonstrated here for the first time, although there exist intriguing differences that merit further investigation. In addition, experiments and simulations, soon to be conducted, will carefully study late times in the evolution of the field structure and probe structures for which the 2-D symmetry implicit in the *LASNEX + LSP* simulations will be broken.

ACKNOWLEDGMENT

REFERENCES

1. S. Eliezer, *The Interaction of High-Power Lasers with Plasmas* (Institute of Physics Publishing, Bristol, England, 2002).

2. L. Spitzer, *Physics of Fully Ionized Gases*, 2nd rev. ed., Interscience Tracts on Physics and Astronomy (Interscience, New York, 1962).

3. S. I. Braginskii, in *Reviews of Plasma Physics*, edited by Acad. M. A. Leontovich (Consultants Bureau, New York, 1965), Vol. 1, p. 205.

4. J. A. Stamper *et al.*, Phys. Rev. Lett. **26**, 1012 (1971); D. G. Colombant and N. K. Winsor, Phys. Rev. Lett. **38**, 697 (1977).

5. M. G. Haines, Phys. Rev. Lett. **78**, 254 (1997).

6. S. H. Glenzer *et al.*, Phys. Rev. Lett. **87**, 045002 (2001).

7. P. Amendt *et al.*, Bull. Am. Phys. Soc. **49**, 26 (2004).

8. R. P. J. Town *et al.*, Bull. Am. Phys. Soc. **50**, 123 (2005).

9. M. A. Yates *et al.*, Phys. Rev. Lett. **49**, 1702 (1982).

10. M. Borghesi *et al.*, Phys. Rev. Lett. **81**, 112 (1998).

11. U. Wagner *et al.*, Phys. Rev. E **70**, 026401 (2004).

12. A. J. Mackinnon, P. K. Patel, R. P. Town, M. J. Edwards, T. Phillips, S. C. Lerner, D. W. Price, D. Hicks, M. H. Key, S. Hatchett, S. C. Wilks, M. Borghesi, L. Romagnani, S. Kar, T. Toncian, G. Pretzler, O. Willi, M. Koenig, E. Martinolli, S. Lepape, A. Benuzzi-Mounaix, P. Audebert, J. C. Gauthier, J. King, R. Snavely, R. R. Freeman, and T. Boehly, Rev. Sci. Instrum. **75**, 3531 (2004).

13. L. Romagnani *et al.*, Phys. Rev. Lett. **95**, 195001 (2005).

14. C. K. Li, F. H. Séguin, J. A. Frenje, J. R. Rygg, R. D. Petrasso, R. P. J. Town, P. A. Amendt, S. P. Hatchett, O. L. Landen, A. J. Mackinnon, P. K. Patel, V. Smalyuk, J. P. Knauer, T. C. Sangster, and C. Stoeckl, Rev. Sci. Instrum. **77**, 10E725 (2006).

15. F. H. Séguin, J. A. Frenje, C. K. Li, D. G. Hicks, S. Kurebayashi, J. R. Rygg, B.-E. Schwartz, R. D. Petrasso, S. Roberts, J. M. Soures, D. D. Meyerhofer, T. C. Sangster, J. P. Knauer, C. Sorce, V. Yu. Glebov, C. Stoeckl, T. W. Phillips, R. J. Leeper, K. Fletcher, and S. Padalino, Rev. Sci. Instrum. **74**, 975 (2003).

16. C. K. Li, D. G. Hicks, F. H. Séguin, J. A. Frenje, R. D. Petrasso, J. M. Soures, P. B. Radha, V. Yu. Glebov, C. Stoeckl, D. R. Harding, J. P. Knauer, R. L. Kremens, F. J. Marshall, D. D. Meyerhofer, S. Skupsky, S. Roberts, C. Sorce, T. C. Sangster, T. W. Phillips, M. D. Cable, and R. J. Leeper, Phys. Plasmas **7**, 2578 (2000).

17. F. H. Séguin, J. L. DeCiantis, J. A. Frenje, S. Kurebayashi, C. K. Li, J. R. Rygg, C. Chen, V. Berube, B. E. Schwartz, R. D. Petrasso, V. A. Smalyuk, F. J. Marshall, J. P. Knauer, J. A. Delettrez, P. W. McKenty, D. D. Meyerhofer, S. Roberts, T. C. Sangster, K. Mikaelian, and H. S. Park, Rev. Sci. Instrum. **75**, 3520 (2004).

18. J. A. Frenje, C. K. Li, F. H. Séguin, J. Deciantis, S. Kurebayashi, J. R. Rygg, R. D. Petrasso, J. Delettrez, V. Yu. Glebov, C. Stoeckl, F. J. Marshall, D. D. Meyerhofer, T. C. Sangster, V. A. Smalyuk, and J. M. Soures, Phys. Plasmas **11**, 2798 (2004).

19. Y. Lin, T. J. Kessler, and G. N. Lawrence, Opt. Lett. **20**, 764 (1995).

20. G. B. Zimmerman and W. L. Kruer, Comments Plasma Phys. Control. Fusion **2**, 51 (1975).

21. P. D. Nielsen and G. B. Zimmerman, Lawrence Livermore National Laboratory, Livermore, CA, UCRL-53123 (1981).

22. D. R. Welch *et al.*, Nucl. Instrum. Methods Phys. Res. A **464**, 134 (2001).

23. In addition, *E* fields can be eliminated as a cause of deflections in face-on images by utilizing, in part, the monoenergetic character of the protons to show that, on the picosecond timescale, electrons would short out the *E* fields that would be required to create the circular patterns.

Evaluation of Cleaning Methods for Multilayer Diffraction Gratings

Introduction

Multilayer dielectric (MLD) diffraction gratings are essential components for the OMEGA EP short-pulse, high-energy laser system, so they must have both high optical-diffraction efficiency and high laser-damage threshold. The cleanliness of optical surfaces intended to be deployed in high-peak-power laser systems is of paramount importance, and the fabrication of these MLD gratings involves processes that utilize a wide variety of both organic materials (photoresists, photoresist solvents, and photoresist developers) and inorganic materials (metals and oxides of various cationic elements) that may remain behind either on the surfaces or in the grooves of the MLD structure after processing. Because a substantial number of these materials can have significant optical absorbance, the incomplete removal of these residues puts the MLD gratings at an increased risk of experiencing catastrophic laser-induced damage. Although there exists a certain amount of anecdotal and empirical evidence as to the effectiveness of certain wet-chemical cleaning processes, which appear to be effective in removing trace residues from grating manufacturing, there does not exist to date a truly systematic study that strives to relate the chemical composition of contaminants introduced during the fabrication process of "structured" optical components (such as MLD gratings) with laser-induced damage. To this end, we have investigated the effectiveness of a number of wet-chemical cleaning processes currently used by the semiconductor industry for cleaning LLE-fabricated MLD gratings. The goal of this investigation was to identify a process or processes that were sufficiently aggressive in the removal of residual processing contaminants but not so aggressive as to produce physical/chemical damage to the MLD grating structure that would reduce its high diffraction efficiency.

The following chemical processes were evaluated for MLD cleaning:

Piranha Process: Piranha solution is a mixture of a strong acid (sulphuric acid, H_2SO_4) and a strong oxidizing agent (hydrogen peroxide, H_2O_2), which produces an extremely energetic solution. This composition is one of the most commonly used cleaning processes for the removal of organics (i.e., residual resist) from a surface and is usually used at a high temperature.[1,2] Although Piranha solution is highly effective in removing organic contamination, it does not remove all inorganic contaminants. Piranha solution must be prepared immediately before use, has a very limited shelf life, and cannot be stored in normal closed containers due to an explosive pressure buildup caused by the gradual loss of hydrogen peroxide gas.

Piranha + SC-1 Process: The cleaning method that is commonly used to remove inorganic contamination after Piranha clean (described above) is SC-1 (Standard Clean 1) coupled with megasonics (high-frequency ultrasonic energy).[1,3] The SC-1 solution of ammonia hydroxide, hydrogen peroxide, and DI water is also cable of removing additional organic contaminants. The megasonics aid in removing the inorganic contamination. The cavitation force generated by the megasonic frequency lifts off the contamination and also keeps these particles from re-adhering to the surface.

Hydrozone Process: Hydrozone+,[4] developed as a replacement for Piranha clean, uses ozone gas dissolved in DI water. An aqueous solution at elevated temperatures is sprayed across a surface while dry ozone gas is admitted into the cleaning chamber. The ozone diffuses through the thin boundary layer of water, in which the water hydrolyzes the organic bonds, making them susceptible to attack by O_3. The elevated water temperature maximizes the reaction rate. The reaction by-products (CO_2 and H_2O) and resist fragments are carried away in the boundary layer of water.

EKC-265[5] and Rezi-28[6] Process: These two semi-aqueous organic mixtures have been formulated as ready-to-use solutions. They contain chemistries that are effective in removing residual photoresist and post-etch and ash residues. These residue removers are formulated to be used at lower operating temperatures than standard Piranha cleans.

Nanostrip Process: Nanostrip[7] is a ready-to-use stabilized formulation of sulphuric acid (H_2SO_4) and hydrogen peroxide

(H_2O_2) compounds. This formulation was designed to remove photoresist and other organic materials at ambient temperatures and can be stored at room temperature indefinitely in closed containers without the risk of an explosive pressure buildup.

Experimental Setup

Table 108.V lists the various cleaning-process parameters evaluated for this study. Each of the processes in Table 108.V was evaluated using 100-mm-diam MLD gratings fabricated at LLE.

The grating-fabrication-process steps include (1) photoresist coated using a positive-tone resist; (2) exposure of the photoresist at 365 nm using a holographic process; (3) photoresist development; (4) reactive ion-beam etching (RIBE) of the grating pattern; (5) O_2 ion-etch clean utilizing LLE-standard-process parameters; and (6) a final wet-cleaning step. Each grating was evaluated for diffraction efficiency and laser-damage threshold both before and after the final cleaning step. All cleaned gratings were further evaluated by scanning electron microscopy (SEM), with time-of-flight secondary ion-mass spectrometry (ToF-SIMS) analysis performed on a select group of four samples.

Results

1. Diffraction Efficiency

Each cleaned MLD grating was tested for diffraction efficiency and laser-damage threshold. Pre- and post-clean diffraction efficiencies were measured across the grating using *s*-polarized light at 1054 nm with an incident beam angle of 61°

(diffracted beam angle of 72°). Since there is a large variation in pre-clean diffraction efficiency, the cleaning process should increase the efficiency to our specification, but it should not decrease it to a level below our specification. Figure 108.37 shows the pre- and post-clean diffraction efficiencies for the various chemistries used. As can be observed, all of the cleaning processes meet our specification of >97% except the Piranha + SC-1. Based on SEM evidence shown later, we believe that the base SC-1 chemistry had a negative effect on the grating. The ECK-265 and Piranha-cleaned samples had the highest post-clean diffraction efficiency.
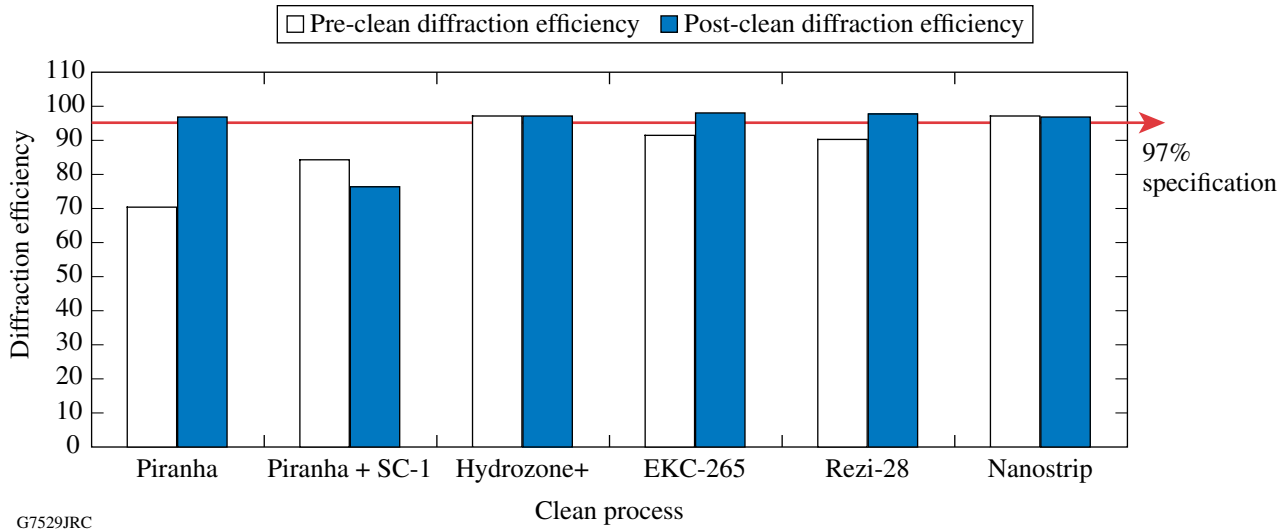
2. Laser-Damage Threshold

Laser-damage testing was conducted using 10-ps-pulsed, *s*-polarized light at 1053 nm with an incident beam angle of 61° (diffracted beam of 72°). The LLE specification for the damage threshold of our MLD gratings is 2.7 J/cm^2 at 10-ps pulse length. Figure 108.38 shows the damage-threshold values that were measured for the different cleaning processes.

The damage-threshold results indicate that only the Piranha, Nanostrip, and EKC-265 cleaning processes are capable of producing clean gratings that achieve the LLE specification.

The Nanostrip process was evaluated at different immersion times to see how this affected the laser-damage threshold. The laser-damage threshold was found to decrease with increased immersion time. This decrease in damage threshold could be due to re-deposition of organics on the surface since this work was performed in a static (un-agitated) lab-scale bath. Similarly,

Table 108.V: Process chemistries and conditions.

Process	Chemistry	Time	Temperature	Methods
Piranha	$H_2SO_4 + H_2O_2$ (various ratios)	30 min 60 min 4 h 8 h	– 60°C 90°C 110°C	Overflow bath, lab-scale beakers
Piranha + SC-1	{$H_2SO_4 + H_2O_2$ (4:1)} + {$NH_4OH + H_2O_2 + DI$ (1:1:10)}	30-min Piranha + 10-min SC-1	90°C Piranha + 70°C SC-1	Overflow bath with 3-MHz megasonics
Hydrozone + (Semitool)	$Di + O_3 + NH_4OH$	10 min 25 min	90°C –	Single plate spray
EKC-265 (EKC Tech)	Semi-aqueous organic mixture	30 min	70°C	Overflow bath with 3-MHz megasonics
Rezi-28 (J. T. Baker)	80% aqueous base	10 min	40°C	Overflow bath
Nanostrip (Cyantek)	Stabilized formulation of $H_2SO_4 + H_2O_2$	4 h 8 h 24 h	60°C – –	Lab-scale beakers

Figure 108.37
Pre- and post-clean diffraction efficiency.
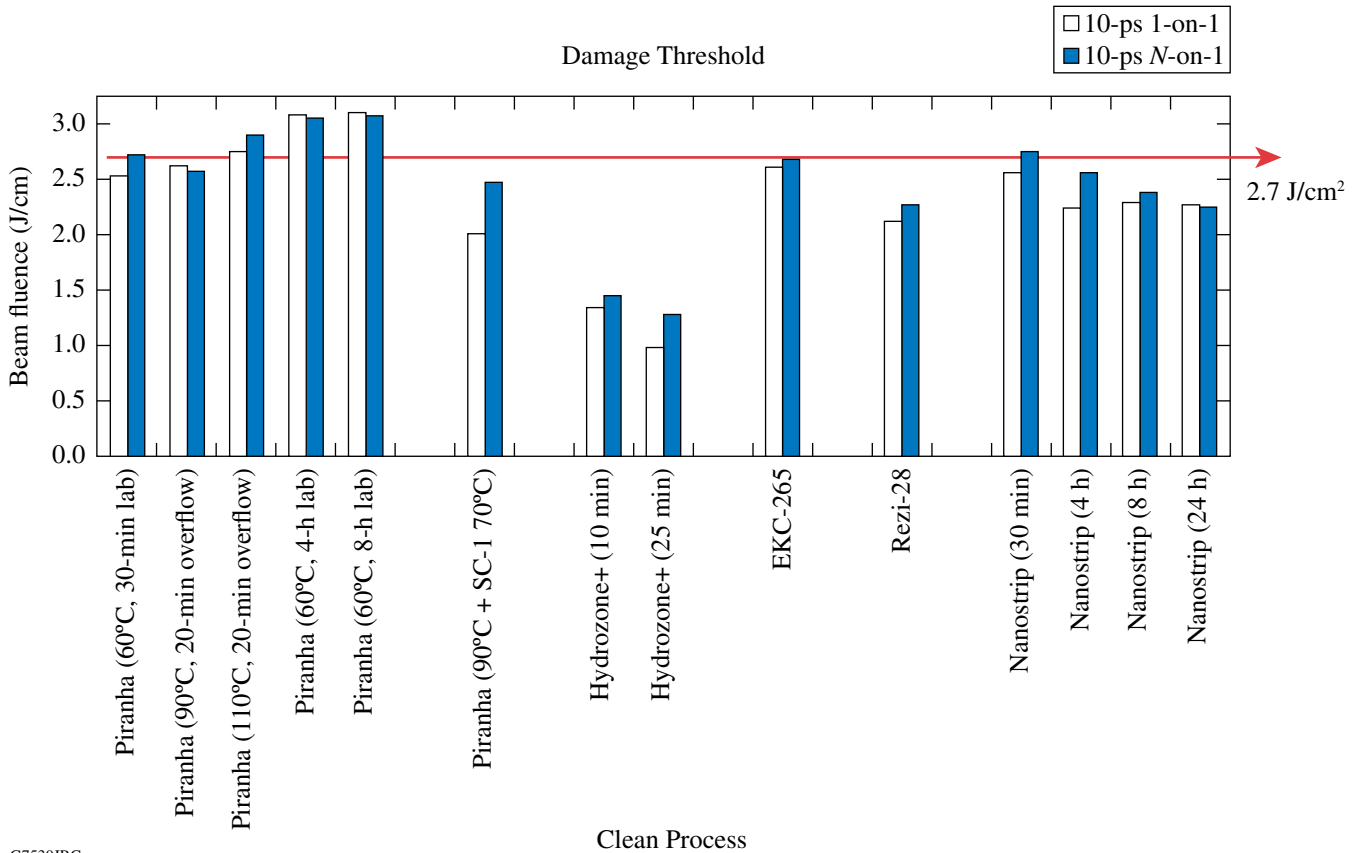
Figure 108.38
Post-clean damage threshold.

the Piranha process was evaluated at different times and temperatures. For this cleaning process, the laser-damage threshold increased as the temperature increased from 90°C and 110°C when processed in a recirculating overflow bath. Increasing the immersion time (in a static lab-scale bath) at the lower 60°C temperature also resulted in an increase in the laser-damage threshold. Additional Designs of Experiment studies are being run to fully understand reaction-rate issues of Piranha clean.

3. SEM Analysis

Scanning electron microscopy (SEM) images were collected and analyzed for each of the MLD gratings that were cleaned in this study. The SEM images of the EKC-265–cleaned and Piranha-cleaned gratings indicate there was no visual residual contamination within the grating trenches. The SEM images, along with the associated diffraction efficiency and laser-damage threshold data for these gratings, are shown in Fig. 108.39.

The SEM images along with the associated diffraction efficiency and laser-damage threshold data for the Hydrozone+, Rezi-28, and Piranha + SC-1–cleaned gratings are shown in Fig. 108.40. The Hydrozone+, Rezi-28, and Piranha + SC-1–cleaned gratings had lower laser-damage threshold values than the EKC-275– and Piranha-cleaned gratings. The Piranha + SC-1 cleaning process damaged the diffraction grating. We believe the SC-1 portion of this cleaning process, which uses a concentrated basic ammonium hydroxide solution, attacked the top amorphous SiO_2 grating layer, which caused it to decompose. Additional work is required to fully understand the failure mechanism. The Rezi-28 clean was not effective in removing the bulk photoresist from the gratings, while the Hydrozone+ clean left visual contamination within the grating trenches.

ToF-SIMS Analysis

Time-of-flight secondary ion mass spectrometry (ToF-SIMS) was performed on four different LLE diffraction-grating samples. The four samples analyzed were (1) photoresist-coated MLD (pre-clean process), (2) MLD-etched and O_2 ion-etch clean (pre-clean process), (3) Piranha-cleaned MLD, and (4) Hydrozone+-cleaned MLD.

The ToF-SIMS analysis was performed at Surface Science Western, University of Western Ontario (London, Ontario, Canada). The instrument used was an ION-TOF (GmbH), ToF-SIMS IV. A 25-keV, pulsed Bi_3^+ cluster, primary ion beam with a target current of 0.6 pA and a beam diameter of ~1.5 μm was rastered over a 500×500-μm^2 area on each sample. The mass range used was 10 to 1000 amu. Due to the insulating nature of the samples, a pulsed-electron flood gun was employed to neutralize charging. The analysis is sensitive to the outer one to three monolayers of the sample surface under static conditions (total primary ion dose $<10^{13}$ ions/cm^2). This technique is
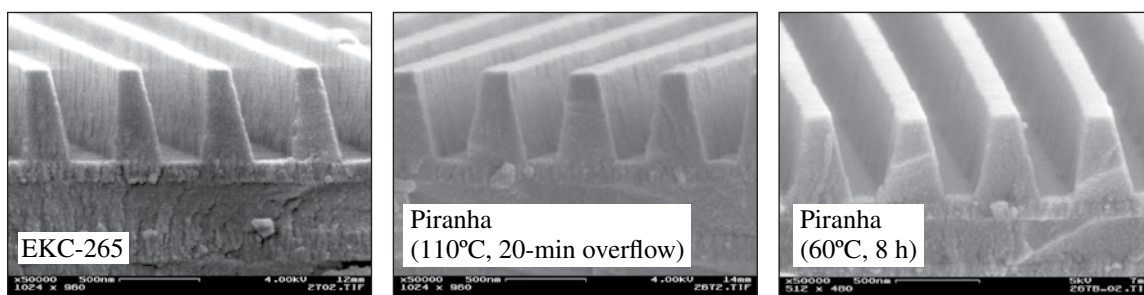
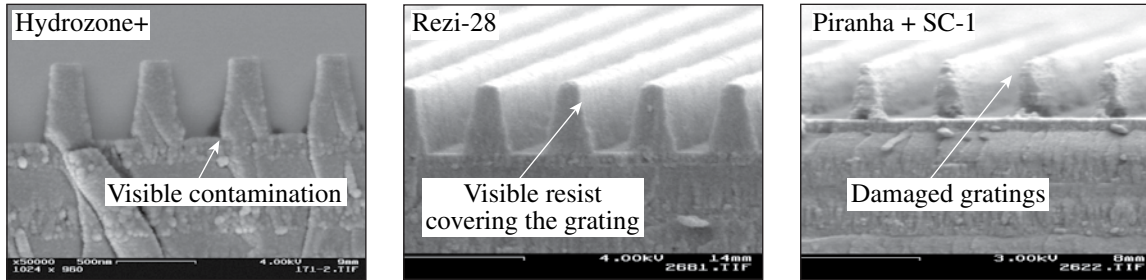| Process	Pre-clean diffraction efficiency	Post-clean diffraction efficiency	10-ps 1-on-1 (J/cm^2)	10-ps N-on-1 (J/cm^2)
EKC-265	91.5	98.1	2.61	2.68
Piranha (110°C, 20-min overflow)	70.5	96.9	2.75	2.9
Piranha (60°C, 8 h)	Not measured	Not measured	3.1	3.07

G7436JR

Figure 108.39
EKC-265 and Piranha SEM analysis with associated efficiency and damage threshold.

not absolutely quantitative; however, using peak area ratios and related normalization methods for similar substrates, meaningful and sensitive relative comparisons can be made.[8]

In order to have a numerical comparison between the samples, selected positive- and negative-ion species were chosen.

Corresponding peaks were extracted and normalized to 100% (total peak areas). The normalized species are summarized in Figs. 108.41–108.43. Figure 108.41 lists species that are related to the photoresist (residual organics). This graph indicates that resist-related species remained on the surface after cleaning. The Piranha-cleaned sample had the lowest levels of resist-

Process	Pre-clean diffraction efficiency	Post-clean diffraction efficiency	10-ps 1-on-1 (J/cm^2)	10-ps N-on-1 (J/cm^2)
Hydrozone+ (10 min)	97.1	97.2	1.34	1.45
Rezi-28	90.2	97.8	2.12	2.27
Piranha 110°C + SC-1	84.2	76.4	2.01	2.47

G7435JR

Figure 108.40
Hydrozone+, Rezi-28, and Piranha + SC-1 SEM images.
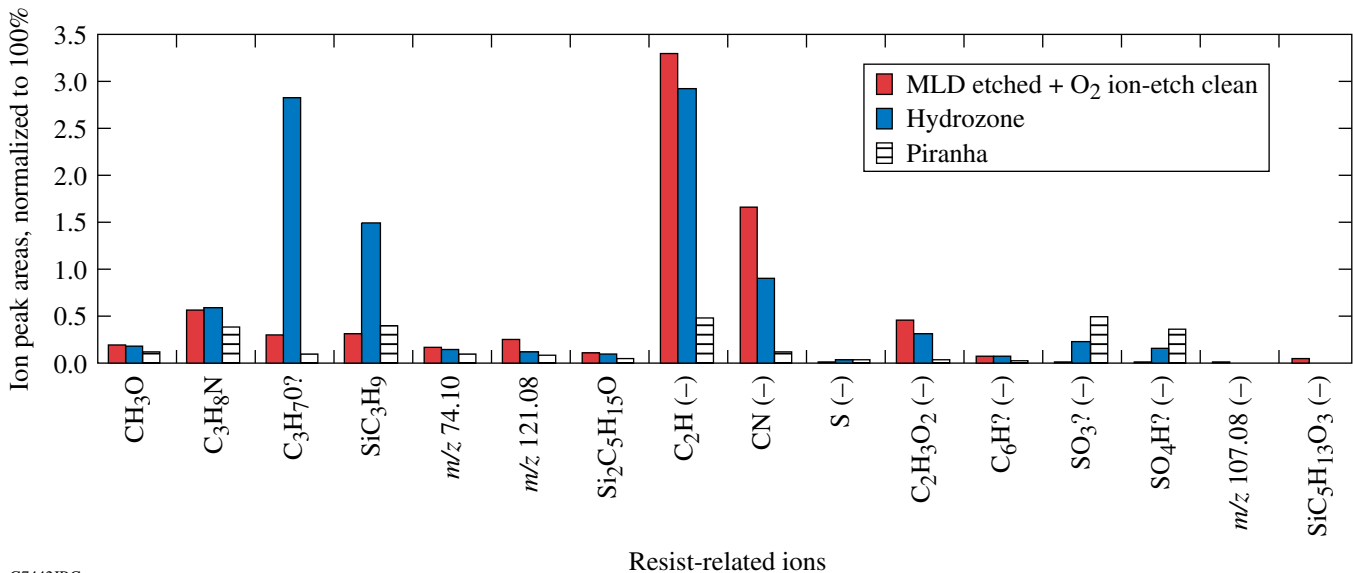
G7442JRC

Figure 108.41
Resist-related species. Note: Not all mass-to-charge (*m/z*) ions are able to be fully characterized. The resist sample is not shown since the level of resist-related ions approaches 100%.

related species remaining after cleaning, but there are still residual resist species that need to be removed.

The species predominantly associated with the SiO_2 grating are indicated in Fig. 108.42. Samples that have high Si-related ion peaks indicate that the surface is relatively clean since the top grating surface is SiO_2. The lack of Si-related ion peaks indicates that there were other contaminants on the surface. As shown, the Piranha and Hydrozone+ clean samples had a high signal for Si and Si_xO_y species, indicating that there is less contamination. The MLD O_2 ion-etch clean sample does not show any signal for Si or Si_xO_y species. This indicates that there was a layer of other contamination on the SiO_2 surface. The species associated with the MLD O_2 ion-etch clean sample are mainly metals, which

could be originating from contamination within the etch and ash chambers (shown in Fig. 108.43). Most of these metals, however, were removed during the cleaning process.

Time-of-flight secondary ion mass spectrometry (ToF-SIMS), "shallow"-depth-profile (few tens of nanometers into the surface) scans were taken to understand the contamination of the Piranha sample. To acquire positive and negative shallow-depth profiles, a second 3-keV Cs^+ sputter ion beam was used, with a raster area of 500×500 μm^2 and a target current of 12 nAS. The Bi_3^+ analysis area is centered within the sputter crater, with a raster size of 200×200 μm^2. Using a raster size smaller than the sputter-crater size allows one to avoid edge effects during the depth profiling. By alternating the Bi_3^+ analysis and the Cs^+ sputter beams and
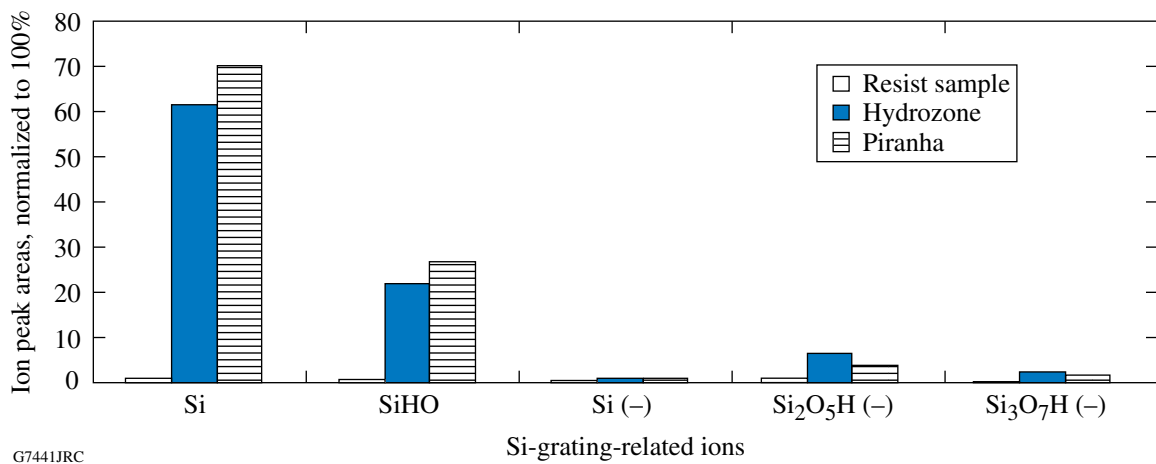

G7441JRC

Figure 108.42
Si-related species. MLD etched + O_2 ion-etch sample does not have a Si-related signal due to other contamination covering the surface.
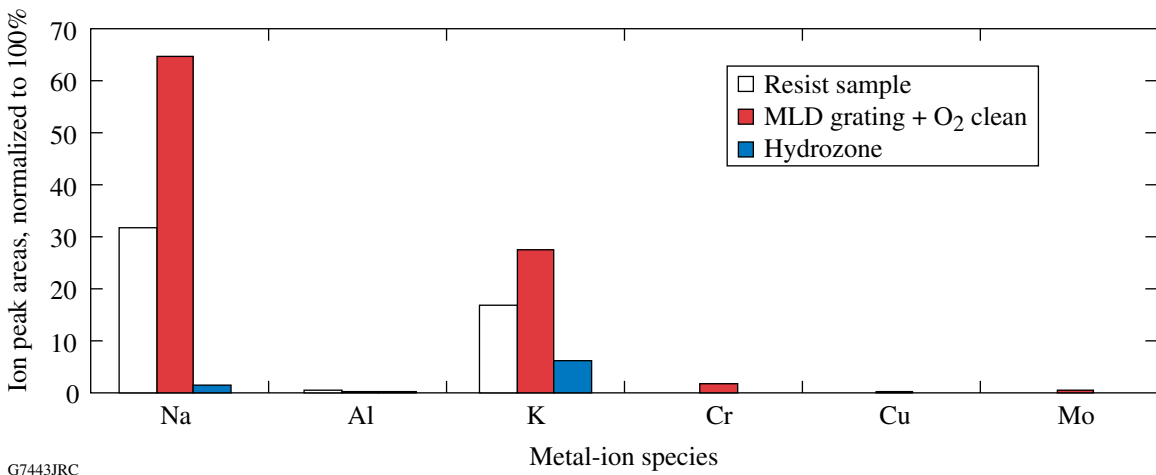

G7443JRC

Figure 108.43
Metal-related species. Piranha-clean (not shown) process removes most metals.

inserting an electron-flood-gun pulse between for charge neutralization, a depth profile into the surface is acquired.[9]

Figure 108.44 plots the raw intensity of the positive ions detected versus the sputter time for the Piranha-cleaned sample. This sample yields various ions with Si^+ being the dominant one. Directly at the grating surface there was an abundance of Si^+ (silicon ion), $SiOH^+$ (silicon hydroxide ion), K^+ (potassium ion), O^+ (oxygen ion), Na^+ (sodium ion), Cr^+ (chromium ion), Fe^+ (iron ion), and Al^+ (aluminum ion). As the analysis probed deeper into the SiO_2 surface, additional major ions detected were Si^+, K^+, $SiOH^+$, O^+, Na^+, Fe^+, and Al^+. The Si^+ and $SiOH^+$ ions were from the SiO_2 grating, as one would expect. The oxygen originated from the etch process and was being "implanted" into the SiO_2 grating surface during the reactive ion-beam etch (RIBE). The metals Cr^+, Fe^+, and Al^+ originated from the etch chamber and became implanted into the SiO_2 grating surface. The potassium and sodium ions were surmised to come from multiple contamination sources. Some of the possible sources of this contamination could have been the rinse water, developer, materials used during cleaning (beakers), and general handling. Additional tests need to be done to better understand this contamination.

The concentration of negative-ion species detected versus sputter time is plotted in Fig. 108.45. The major ions detected were O^- (oxygen ion), SiO_2^- (silicon oxide), F^- (fluorine ion), Si^- (silicon ion), SO_3^- (sulfate ion), Cl^- (chlorine ion), CN^- (cyanide ion), C_2H^- (carbon ion), and C^- (carbon ion). The oxygen, fluorine, chorine, and carbon ions were implanted from the etch process and chamber. The silicon-related ions originated from the silicon oxide grating, while the sulfate ion originated from the sulfuric acid–cleaning process.

Conclusions

Using 100-mm-diam MLD gratings fabricated at LLE, we evaluated different cleaning methods designed to optimize both optical diffraction efficiency and laser-damage threshold of these gratings for the OMEGA EP Laser System. Pre- and post-clean diffraction efficiency and laser-damage threshold were measured for each of the samples. Scanning electron microscopy (SEM) images were collected and analyzed to understand if any visual surface contamination existed after cleaning. Additionally, a baseline time-of-flight secondary ion-mass spectrometry (ToF-SIMS) and shallow-depth profile analysis was performed to understand the type of contamination remaining after the different process steps.

The diffraction efficiency, laser-damage threshold, and SEM images all show that the Piranha clean merits further exploration. The MLD gratings cleaned by the Piranha processes had the highest diffraction efficiency and laser-damage-threshold
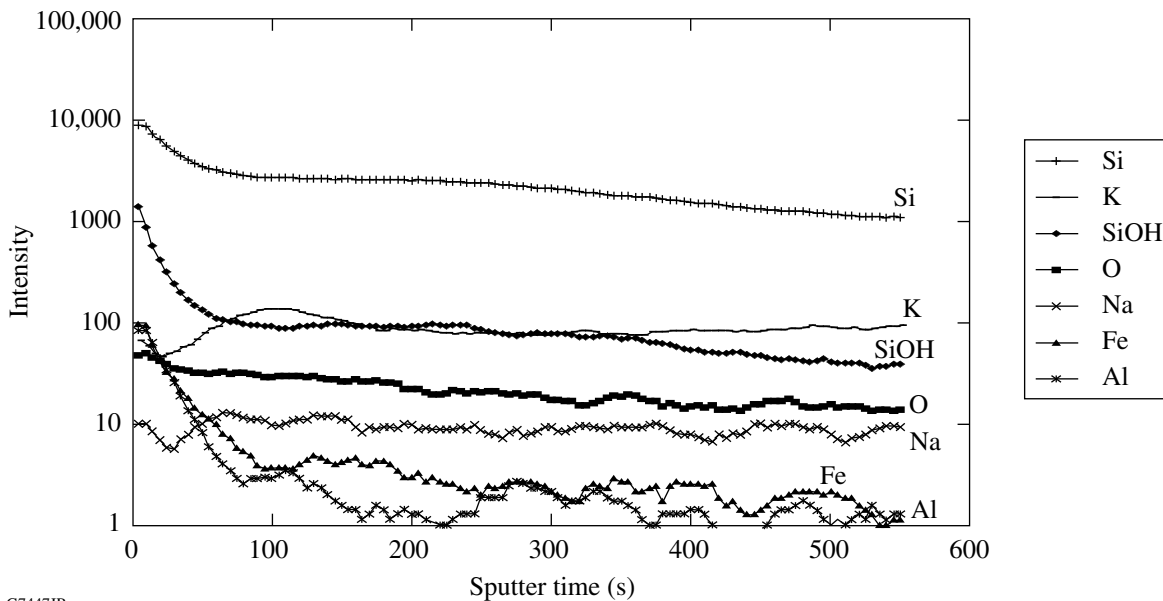
Figure 108.44
Piranha-clean positive-ion depth profile.
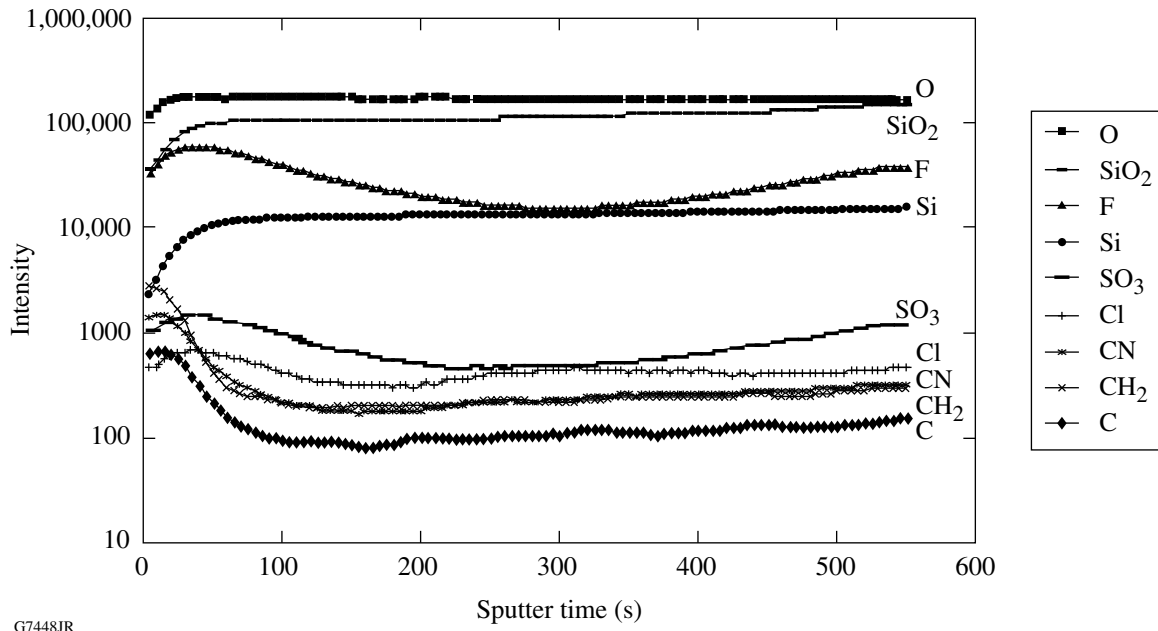
G7447JR

G7448JR

Figure 108.45
Piranha-clean negative-ion depth profile.

values. The SEM images also validated these results by showing no visual contamination after cleaning.

ToF-SIMS analysis was performed on four types of samples from the LLE grating project to acquire a baseline for surface residual contamination. The encouraging results show that the cleaning process can remove a large portion of the photoresist (organic) contamination even without optimization of cleaning-process variables. It was further found that there is a monolayer of contamination (mostly metal ions) after etch and O_2 ion-etch clean processing. The shallow-depth profile analysis provides an understanding of the contaminants implanted in the grating surface, which in turn allows identification of the source of most of the ions detected. Understanding the sources and depth of "implantation" of these ions will assist LLE in developing an optimized grating-cleaning process. Further Design of Experiment studies will be evaluated to understand the interaction of the variables within the cleaning process. LLE will continue to use SEM and ToF-SIMS analysis to characterize the surface after each cleaning test.

ACKNOWLEDGMENT

REFERENCES

1. W. Kern, *Handbook of Semiconductor Wafer Cleaning Technology: Science, Technology, and Applications*, Materials Science and Process Technology Series (Noyes Publications, Park Ridge, NJ, 1993), pp. 3–56.

2. S. Clark, Bold Technologies, Inc., West Jordan, UT 84088, http://www.bold-tech.com/technical/piranha_etch.html (2000).

3. R. S. Ridley, Sr. et al., in *1998 IEEE/SEMI Advanced Semiconductor Manufacturing Conference* (IEEE, Boston, 1998), pp. 235–242.

4. Semitool, Kalispell, MT 59901.

5. EKC265 product sheet, EKC Technology, Inc., Hayward, CA 94545, November 2006, http://www2.dupont.com (6 November 2006).

6. Rezi-28 product sheet, Mallinckrodt Baker, Inc., Phillipsburg, NJ 08865, November 2006, http://www.mallbaker.com (11 November 2006).

7. NANO-STRIP™ product sheet, Cyantek Corporation, Fremont, CA 94539-5652, http://www.cyantek.com (2006).

8. Dr. James Francis, ToF-SIMS Results, Surface Science Western, email reports and private communication (6 April 2006).

9. Dr. James Francis, ToF-SIMS Report, Surface Science Western, email reports and private communication (9 August 2006).

Design and Analysis of Binary Beam Shapers Using Error Diffusion

Introduction

Controlling the amplitude and phase of light is crucial in many technological applications, such as imaging, lithography, astronomy, and laser physics. In high-power laser systems, there is a need for precise beam shaping. Square beams with super-Gaussian profiles are used to optimize the fill factor of amplifiers. The spatially dependent gain of amplifiers can be, to a large extent, precompensated, i.e., the spatial intensity of the beam to be amplified is shaped before amplification so that regions of higher gain in the amplifier correspond to regions of lower intensities in the input beam. To avoid damage or small-scale self-focusing, local intensity variations should be minimized and intensities kept below damaging intensities; therefore, there is a need for accurate beam-shaping systems with fine controls. While spatial light modulator (SLM) technology[1] is well developed, it is not a perfect fit for these applications, since the damage threshold of most SLM's is lower than the required operating fluences for some applications. Because of saturation in laser amplifiers and nonlinear effects such as those encountered in optical parametric chirped-pulse amplification,[2] precompensation may need to be performed at locations in the system where the fluence is already significant (for example, after a first stage of amplification). Beam shaping has been demonstrated using the modal discrimination of a laser cavity or regenerative amplifier cavity (for example, using intracavity phase masks[3,4]), but no elaborate beam-shaping function has been performed beyond the realization of flat-top beams. Additionally, some degree of complexity is added by the realization of a laser cavity combining amplification and shaping, compared to an architecture where these functions are performed by independent elements that can be optimized separately. A large variety of techniques have been demonstrated to generate a spatially varying transmission, such as photographic plates,[5] mirrors with variable reflectivity,[6] elements with spatially varying birefringence,[7] and elements with spatially varying transmission based on total internal reflection.[8] It is unclear, however, if any of these techniques has the required versatility and reliability.

Historically, the solution for shaping high-energy laser beams has been to propagate the beam in a glass substrate with metal patterns on the input surface, where regions coated with metal block the light while clear regions have a 100% transmission. Super-Gaussian beams can, for example, be generated by serrated tooth apodizers,[9] i.e., apodizers with a high-frequency periodic structure where the duty cycle varies as a function of the distance to the center of the plate, which provides a smooth apodization function after Fourier filtering. These apodizers are appropriate for edge-only shaping, i.e., realizing a smooth transition from the high transmission at the center of the beam to the absence of transmission on the edges. However, they cannot generate more-complex shaping functions. Smooth shaping functions can be generated using a vacuum-deposited layer of a metal such as aluminum.[10] More control can be obtained via binary pixelated arrays of metal pixels, as used on the National Ignition Facility[11] to precompensate for the spatial gain variation of large glass amplifiers.[12]

Figure 108.46 displays two examples of target transmission. In Fig. 108.46(a), the target transmission is a 40th-order super-Gaussian that is used in high-power lasers to optimize the fill factor in large-scale slab amplifiers, while decreasing the detrimental effects of diffraction that would occur with a sharp-edge square beam. The corresponding lineout is plotted in Fig. 108.46(c). In Fig. 108.46(b), the target transmission corresponds to the precompensation of the spatially dependent gain of 58 passes in 40-cm-diam Nd:glass disks, as required for OMEGA EP.[13] The corresponding lineout, plotted in Fig. 108.46(d), demonstrates the required nonsymmetric shape due to the uneven distribution of the orientations of the disks. While the apodizing function of Fig. 108.46(a) can be synthesized with serrated tooth apodizers, this approach does not work for the more-complex function of Fig. 108.46(b). Such precompensation is mandatory for large-scale laser systems.[10]

Gray-scale rendering with black or white features is crucial in printing applications, where it is usually referred to as digital half-toning or spatial dithering.[14] Among many other algorithms,[14] the error diffusion algorithm has been identified as particularly efficient at providing gray-scale images with visually pleasing results.[15] Because of the analogy between image
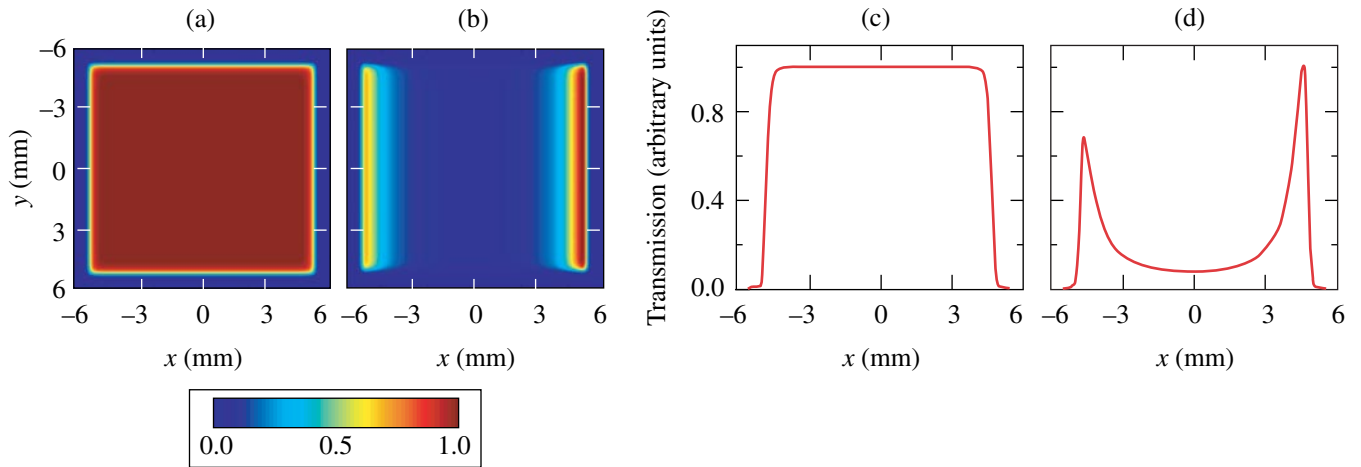
Figure 108.46

(a) Example of 40th-order super-Gaussian intensity; (b) example of intensity distribution required to precompensate for the spatial gain variation in OMEGA EP; (c) lineout of the intensity of (a) at the center of the beam along the x direction; (d) lineout of the intensity of (b) at the center of the beam along the x direction.

rendering and transmission shaping, it is of interest to study the performance of error diffusion when designing binary masks leading to continuous beam-shaping functions. The purpose of this article is to provide insight into the potential and limitations of this technique. The principle of error diffusion and its application to the design of pixelated binary masks are presented first. The performance of the obtained masks in terms of beam shaping is then studied in the context of high-power laser systems. Finally, the influence of feature size on the shaping performance is studied analytically and via simulations.
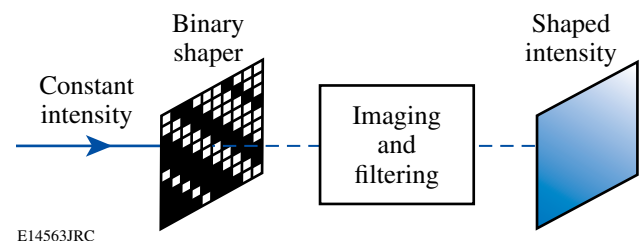
Error Diffusion Principle

1. Shaping of a Coherent Light Source

It is assumed that a coherent source with constant intensity $I_0 = |E_0|^2$ is incident on a transmission mask, which is relay imaged to the image plane, following Fig. 108.47. A Fourier plane in the imaging system can be used for Fourier filtering. An example of such a system is a two-lens system, with lenses of identical focal length, for which Fourier filtering can be performed with a pinhole at the Fourier plane of the first lens. For the sake of simplicity, we assume an imaging system with magnification equal to 1. The electric field after the binary mask with transmission $s(x,y)$ is $E(x,y) = E_0 \times s(x,y)$, where $s(x,y)$ is either 0 (presence of light-blocking metal) or 1 (no metal) and is pixelated. The electric field at a Fourier plane of the first lens is written as $E_0 \times \tilde{s}(u,v)$, where $\tilde{s}$ is the Fourier transform of s. This field is filtered by a transmission filter p, leading to the field $E_0 \times \tilde{s}(u,v) \times p(u,v)$. The resulting field at an image plane can be written as a convolution $E' = E_0 \times s \otimes \tilde{p}$. Because the convolution with the Fourier transform of the filter $\tilde{p}$ acts as a local averaging operation on the electric field of light after the shaper, the intensity of the output field at a given point (x,y) is proportional to the square of the average value of s around this point. This is important when designing a beam shaper for a spatially coherent light source because the average transmission of the beam shaper before filtering must be designed to be equal to the square root of the target intensity transmission after filtering. The averaging operation provided by the filter in the far field is the key point in obtaining a smooth continuous intensity from a binary pixelated mask.

2. Design of a Binary Beam Shaper Using Error Diffusion

Error diffusion[14,16,17] is based on the lexicographical processing of the pixels of the mask, typically from top to bottom and left to right, following the diagrams in Fig. 108.48.

Figure 108.47

Principle of the generation of a continuous shaped intensity using a binary shaper and Fourier filtering.

(a) Shaper target transmission $t(m,n)$ (b) Shaper binary transmission $s(m,n)$

(c)
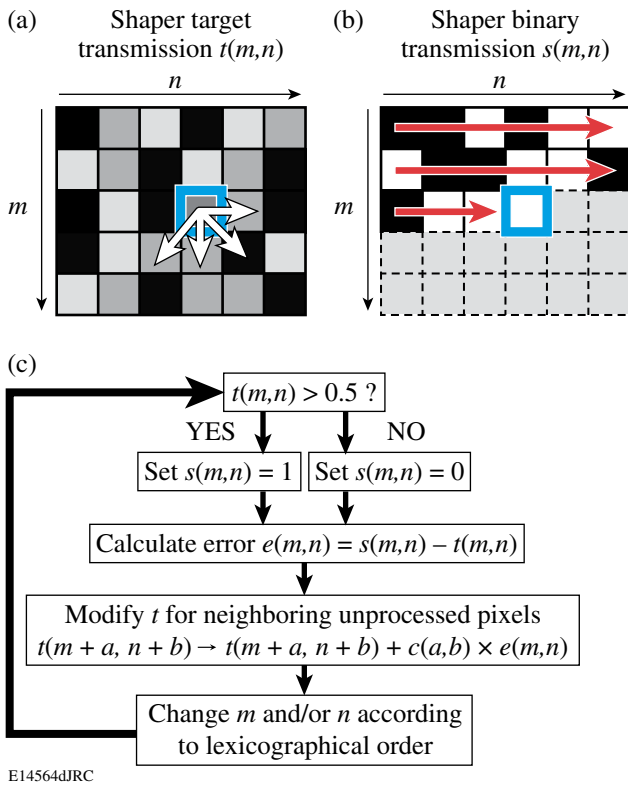
E14564dJRC

Figure 108.48

Principle of the error diffusion algorithm. (a) Representation of the target shaper transmission $t(m,n)$; (b) representation of the binary shaper transmission $s(m,n)$ being designed; (c) chart describing the design process. The thick squares on (a) and (b) represent the pixel being processed. The horizontal arrows on (b) schematize the lexicographical process over the already processed pixels. The white arrows on (a) represent the error diffusion to adjacent nonprocessed pixels.

A pixelated representation of the target transmission of the shaper, $t(m,n)$, is shown in Fig. 108.48(a), while the binary shaper being designed is shown in Fig. 108.48(b). On the latter, previously processed pixels have a transmission $s(m,n)$ equal to either 0 or 1 and are plotted in black or white, while nonprocessed pixels have been arbitrarily plotted in gray. Since the target transmission takes values in the interval [0,1] while the shaper transmission is either 0 or 1, the choice of the value of each pixel in the binary mask induces a transmission error. In error diffusion, the binary value of the pixel (m,n) is set by the information contained in the target shaper transmission $t(m,n)$, which can be modified by the choices that have been made for the mask binary value $s(m,n)$ for the pixels that have already been processed. Initially, one sets $t(m,n) = \sqrt{I(m,n)}$, where I is the sampled representation of the target intensity of the coherent source. Following the chart in Fig. 108.48(c), the choice of transmission $s(m,n)$ is made by comparing the target shaper

transmission to 0.5. If the target transmission is smaller than 0.5, $s(m,n)$ is set to 0, while, if the transmission is larger than 0.5, $s(m,n)$ is set to 1. The resulting error is "diffused" to pixels that have not yet been processed, usually neighboring pixels, to bias the binary choice for these pixels and locally compensate the transmission error. This is done by adding a fraction of the error $e(m,n) = s(m,n) - t(m,n)$ to the target transmission for these pixels, which is symbolized in Fig. 108.48(a) by white arrows pointing to these pixels. The target transmission $t(m + a, n + b)$ is then replaced by $t(m + a, n + b) + c(a,b) \times e(m,n)$ for the chosen set of integers a and b. In the initial developments of error diffusion by Floyd and Steinberg,[16] only the four neighboring pixels at coordinates $(m + 1, n - 1)$, $(m + 1, n)$, $(m + 1, n + 1)$, and $(m, n + 1)$ are used in the diffusion process (four-weights error diffusion). The results presented in this article have been obtained with such implementation, as the gain of performance when diffusing the error to a large number of neighboring pixels does not seem significant. The function c takes for value $c(1,-1) = -3/16$, $c(1,0) = -5/16$, $c(1,1) = -1/16$, and $c(0,1) = -7/16$. The algorithm then proceeds with the next pixel, following the lexicographical order.

Properties of Binary Shapers Generated with Error Diffusion

1. Error Functions for Beam-Shaping Performance

Two functions have been used to quantify beam-shaping performance. A normalized version of the rms error between the target shaped intensity and the obtained shaped intensity after filtering is

$$\varepsilon_{rms} = \sqrt{\iint_s \left[T_{obtained}(x,y) / T_{target}(x,y) - 1 \right]^2 dxdy}, \quad (1)$$

where the double integral is calculated over the region S, where the target intensity is higher than a given threshold to ensure that only relevant values are kept. The normalization ensures that the calculated error remains the same after multiplication of the target and obtained intensities by a spatially varying function. This ensures that this rms error is also a proper description of the shaping performance after amplification of the shaped beam.

Another error function of interest when dealing with shaping elements for laser applications describes the presence of local high values of the intensity because of the potential damage to optics and self-focusing,

$$\varepsilon_{peak} = \max_s \left| \frac{T_{obtained}(x,y)}{T_{target}(x,y)} - 1 \right|, \quad (2)$$

where the maximum is calculated over a region of interest (typically, the region where the beam is amplified to signifi-

cant values). This error function quantifies the magnitude of hot spots in the beam. While these two error functions are, in general, not correlated, it was found that they had similar behaviors when varying the pixel size or the parameters of the far-field filtering operation, and we therefore plot only the rms error, but quote the peak error in relevant cases.

2. Comparison of the Error Diffusion Algorithm with the Random Dither Algorithm

A simple random dither algorithm is used to emphasize the properties of the error diffusion algorithm. The random dither algorithm is one of the simplest algorithms that can be used to design binary shaping elements. It is also known as white-noise dithering because of the spectral content of the generated images.[14] While this technique has shortcomings, its simplicity makes it an ideal choice to highlight the properties and performance of the error diffusion algorithm. For the random dither algorithm, the binary transmission of each pixel is chosen by a random draw between 0 and 1. If the drawn number is smaller than the target transmission, the transmission of the pixel is set to 1, while if the drawn number is higher than the target transmission, the transmission of the pixel is set to 0. Properties of random draws ensure that this algorithm properly reproduces gray levels on average. One should note that there is no error feedback in such an algorithm.

3. Properties of the Error Diffusion Algorithm

Pixelated binary masks generated with error diffusion are highly ordered structures. Figure 108.49 displays pixelated binary distributions generated by error diffusion for target transmissions equal to 5%, 25%, and 75%. It was found that the error diffusion algorithm can reproduce gray levels very accurately. These close-ups are compared to close-ups of masks generated by the random dither algorithm to generate the same target transmission. The latter show no correlation between the presence of pixels at various locations in the mask.

To understand the binarization noise, the error diffusion and random dither algorithm were used to generate a shaping function corresponding to Fig. 108.46(b), using 10-μm pixels. The corresponding binary shaper generated by error diffusion is plotted in Fig. 108.50(a), and close-ups of the binary pixel distributions at the center and at the upper right corner are displayed in Figs. 108.50(b) and 108.50(c). A lineout of the shaped intensity plotted in Fig. 108.50(d) demonstrates the proper realization of the transmission of the shaper, including the proper transmission at the center of the beam and the high-frequency content on the edges of the beam, owing to the high resolution and proper rendition of gray levels when using error diffusion.
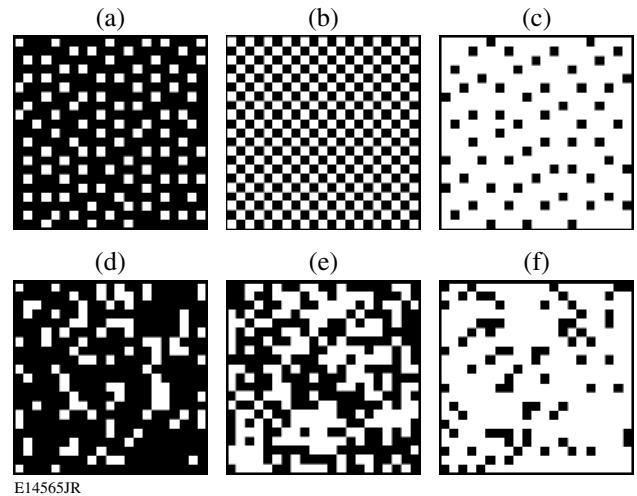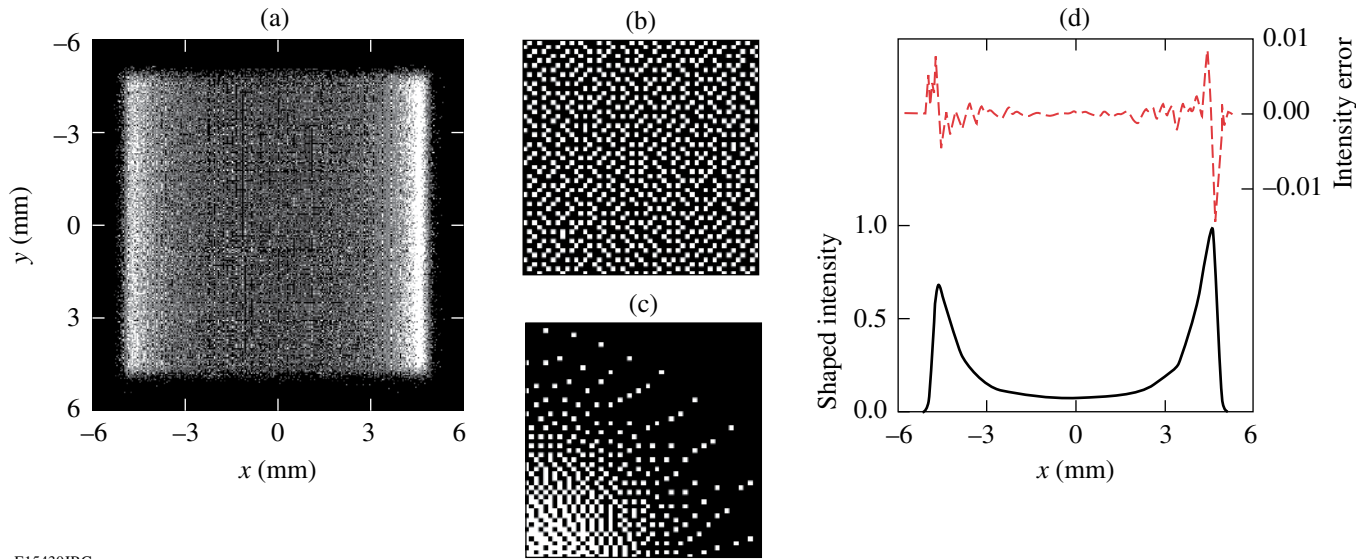

Figure 108.49
(a)–(c) Close-ups of shapers designed with error diffusion for a target-intensity transmission equal to 5%, 25%, and 75%, respectively; (d)–(f) close-ups of shapers designed with the random dither algorithm for a target-intensity transmission equal to 5%, 25%, and 75%, respectively.

This lineout corresponds to the optimal filtering in the Fourier plane, as discussed below. As can be seen, the shaped intensity varies by less than 1% around the target intensity. Intensities of the far field of the shapers generated by error diffusion and random dither are compared in Fig. 108.51, where the average of the far-field intensity in a 4-mrad interval along the y direction has been plotted on a logarithmic scale as a function of the angle in the x direction. The noise due to the binarization is pushed to high frequencies in the case of the error diffusion algorithm but is present at all frequencies in the case of the random dither algorithm—an example of the general behavior of spatially dithered masks generated with error diffusion.[17] The spectrum of the noise introduced by the binarization has no zero-frequency component and has only significant density at high frequencies, therefore the name "blue-noise dithering."[18] By comparison, the randomness of the random draw design algorithm generates a constant noise background in the far field (i.e., "white noise"). This point is particularly important for Fourier filtering because the amplitude filter in the far field (e.g., the pinhole) can effectively block the binarization noise while preserving the frequency content of the target transmission.

To demonstrate the influence of the filtering operation, the rms error is calculated as a function of the angular diameter of a circular pinhole set in the far field for a shaping element designed with error diffusion and random dither to approximate the target-shaped intensity of Fig. 108.46(b). The rms error is also calculated when propagating a field having the

target-shaped intensity. Figure 108.52(a) shows that the rms error is limited at low pinhole sizes by the propagation of the target-shaped intensity through the filtering system (i.e., the high frequencies of this intensity are blocked by the pinhole) that also constrains the rms error in the case of the binary distributions. The error increases quickly for the random dither algorithm as the pinhole size is increased, but decreases in case of error diffusion. The rms error reaches a minimum for

a given pinhole diameter for each design algorithm. The rms error is minimal for a 7-mrad pinhole in the case of error diffusion ($\varepsilon_{rms} = 0.7\%$, $\varepsilon_{peak} = 2.4\%$) and for a 3-mrad pinhole in the case of the random dither algorithm ($\varepsilon_{rms} = 7.5\%$, $\varepsilon_{peak} = 27.4\%$). The corresponding shaped intensities were used to calculate the intensity after amplification, which is expected to be functionally similar to that of Fig. 108.46(a). The three lineouts of the amplified intensity plotted in Figs. 108.53(a)

E15430JRC

Figure 108.50
(a) Binary shaper corresponding to the transmission of Fig. 108.46(b); (b) and (c): close-ups of the binary pixel distribution at the center and at the upper right corner of the beam, respectively; (d) lineout of the filtered intensity along the x direction (solid line) and lineout of the difference between the filtered intensity and the target intensity (dashed line).
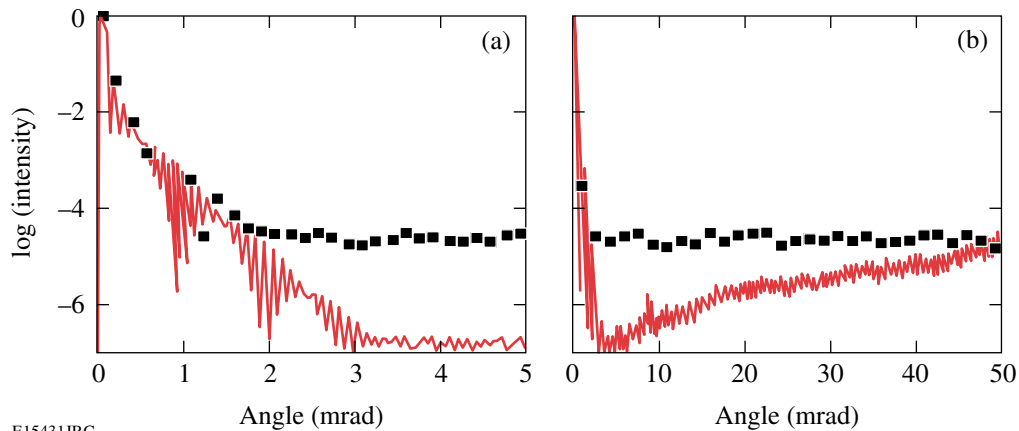
E15431JRC

Figure 108.51
Intensity of the far field of the binary beam shaper designed with the error diffusion algorithm (solid line) and the random dither algorithm (squares) for the generation of a shaped intensity of Fig. 108.46(c). The intensity is averaged over a 4-mrad angle in the y direction and plotted versus the angle in the x direction. Plots (a) and (b) cover different ranges of angles.

and 108.53(b) show that the modulations due to the shaping process are not detectable for error diffusion, but are significant for random dither.

We have also studied the effect of pixel size in the design of shapers. It is intuitive that smaller pixels lead to better resolution in the reproduction of the shaping function. This is demonstrated by plotting the rms error as a function of the pinhole diameter for the shaping function of Fig. 108.46(b) designed with error diffusion and binary shapers with 10-, 20-,

and 40-μm pixels [Fig. 108.52(b)]. Larger pixels increase the rms error, and influence the shaping performance in two ways: they generally decrease the ability to generate quickly varying functions and, in the case of a binary distribution, they imply a reduction in the number of parameters available to locally specify a gray level (for example, an area of 10-μm binary pixels has 16 times more bits of information than the same area covered with 40-μm pixels). The minimal rms error for a given pixel size is obtained for a pinhole size that decreases when the pixel size is increased. A shaper with 10-μm pixels
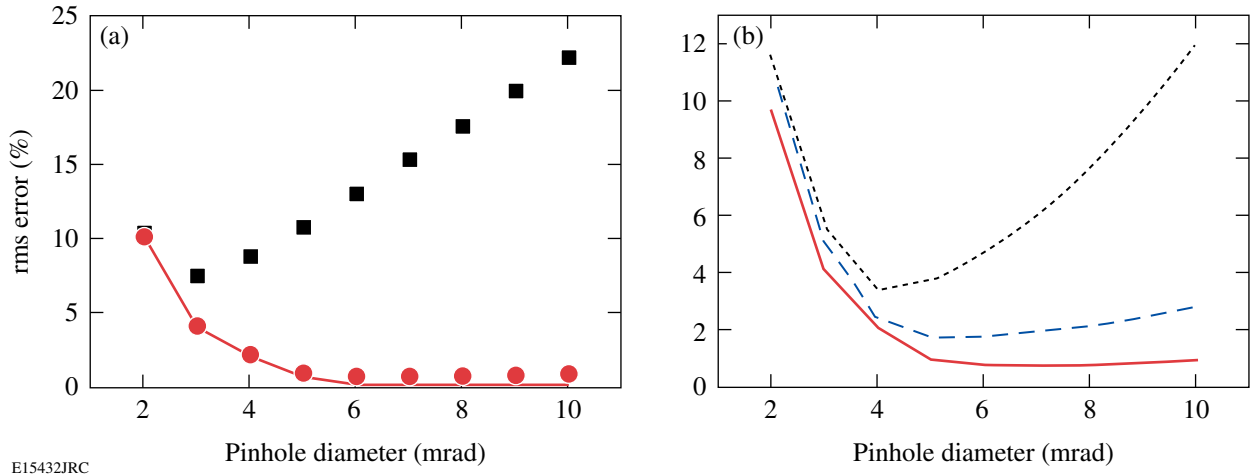

E15432JRC

Figure 108.52
(a) rms error for the realization of the shaped intensity of Fig. 108.46(b) as a function of the pinhole angular diameter in the case of the error diffusion algorithm (circles) and the random draw algorithm (squares). The solid line corresponds to the propagation of a field having the target-shaped intensity through the same filtering system. (b) rms error for the realization of the shaped intensity of Fig. 108.46(b) as a function of the pinhole angular diameter for a pixel size of 10 μm (solid line), 20 μm (dashed line), and 40 μm (dotted line) in the case of error diffusion.
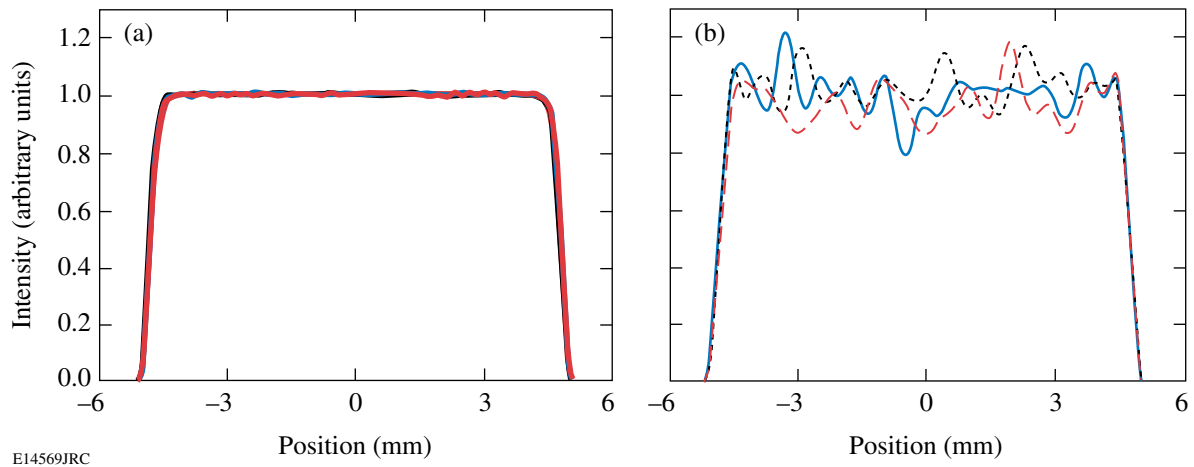

E14569JRC

Figure 108.53
Three lineouts of the simulated intensity of the shaped beam after amplification for shaping with (a) error diffusion and (b) random dither. In each case, the pixel size is 10 μm, and the pinhole size leading to the smallest rms error is used.

leads to $\varepsilon_{rms} = 0.7\%$ and $\varepsilon_{peak} = 2.4\%$ with a 7-mrad pinhole; with 20-μm pixels leads to $\varepsilon_{rms} = 1.7\%$ and $\varepsilon_{peak} = 4.3\%$ with a 5-mrad pinhole; and with 40-μm pixels leads to $\varepsilon_{rms} = 3.4\%$ and $\varepsilon_{peak} = 9\%$ with a 4-mrad pinhole.

**Effect of Feature-Size Variation
on the Shaping Performance**

Practical applications of shapers are constrained by the ability to faithfully reproduce small-scale features. A typical process for generating metal masks is based on lithography.[19] In the case of wet-etch lithography, etching can lead to a reduction in feature size, i.e., the light-blocking metal pixels are smaller than specified in the design, which leads to an increased transmission. It is important to understand the scaling of this effect, quantify it, and potentially come up with precompensation schemes.

1. Analytical Derivation

The design of shapers using error diffusion leads to highly ordered distributions of pixels, as shown in the previous section. It has been observed that shapers with isolated 100% transmission blanks [example in Fig. 108.49(a)] were obtained for target transmission smaller than 10%. Shapers with isolated 0% transmission pixels were obtained for target transmissions higher than 45% [example in Fig. 108.49(c)]. In these cases, the transmission can be predicted uniquely from the knowledge of the area of a blank (in the first case) and the area of a pixel (in the second case), these areas being scaled to the expected nominal area for these features.

In the case of isolated blanks, the intensity transmission after Fourier filtering is

$$T_{obtained} = d_{blank}^2 = \left(\frac{B \times S_{blank}}{N \times S_0} \right)^2, \qquad (3)$$

where d_{blank} is the density of blank pixels, B is the number of blank pixels in a representative area with a total number of pixels equal to N, S_{blank} is the surface of a blank pixel, and S_0 is the nominal surface of a pixel. Using the fact that $T_{target} = (B/N)^2$, one obtains the relation describing the transmission of regions with isolated blanks as

$$T_{obtained} = T_{target} \times \left(\frac{S_{blank}}{S_0} \right)^2. \qquad (4)$$

In the case of isolated pixels, the intensity transmission after Fourier filtering is

$$T_{obtained} = (1 - d_{metal})^2 = \left(1 - \frac{M \times S_{metal}}{N \times S_0} \right)^2, \qquad (5)$$

where d_{metal} is the density of metal pixels, M is the number

of metal pixels in a representative area with a total number of pixels equal to N, S_{metal} is the surface of a metal pixel, and S_0 is the surface of a pixel. Using the relation $T_{target} = \left[1 - (M/N) \right]^2$, one obtains

$$T_{obtained} = \left[\left(1 - \sqrt{T_{target}} \right) \times \frac{S_{metal}}{S_0} - 1 \right]^2. \qquad (6)$$

For transmissions between 10% and 45%, analytical derivation is not as simple. In the special case of a target transmission equal to 25%, the generated distribution of pixels is a checkerboard of metal and blank pixels [example in Fig. 108.49(b)], for which it can be seen that the transmission error can be predicted considering isolated metal pixels if the feature-size variation is due to the edge effect simulated below, i.e., using Eq. (6).

2. Simulations

A simulation was performed to quantify the impact of pixel-size mismatch on the transmission of shapers. It is assumed that the primary effect of pixel-size variation is an edge effect, i.e., a metal pixel neighboring a blank pixel is over-etched and an additional section of metal is removed from the corresponding edge. The offset is defined as the ratio of the length of metal additionally removed over the nominal size of the pixel (e.g., nominal 10-μm metal pixels losing 0.5 μm on each side correspond to a 5% offset, and an isolated metal pixel becomes a 9-μm pixel). A mask for a constant transmission T_{target} after filtering is first generated. The edge effect is simulated by increasing the transmission of every blank in the mask by n times the relative change due to the over-etching, where n corresponds to the number of neighboring metal pixels. The obtained transmission is obtained by calculating the actual transmission of the mask after this operation to get $T_{obtained}$. The transmission error is then defined as $(T_{obtained}/T_{target}) - 1$. While these simulations assume a specific process for the transmission degradation, it has been found to describe accurately our experimental results. One should note however that the formulas of Eq. (4) and Eq. (6) are valid for shapers with isolated blanks and pixels of arbitrary shape.

The transmission error is plotted in Fig. 108.54 as a function of the target transmission in the case of a 5% offset (e.g., 9-μm pixels obtained on a 10-μm grid) and a 10% offset (e.g., 8-μm pixels obtained on a 10-μm grid), with the corresponding analytical prediction calculated using the size of both the metal and blank pixels. The simulations and the analytical predictions of Eq. (4) and Eq. (6) agree well in their respective domain of validity. For over-etched metal pixels, the maximal transmission error is obtained for low target-intensity transmission smaller than 10%. The predicted transmission error at low

design transmission using the surface of a blank and Eq. (4) is, respectively, 44% and 96% for size offset equal to 5% and 10%. This error can be reduced by decreasing the offset in pixel size. While small pixels lead theoretically to better shaping capabilities, the absolute reduction in metal pixel size due to lithography is mostly independent of the pixel size, i.e., the offset becomes larger when using smaller pixels. For example, a process leading to a 10% offset error on 10-μm pixels would give only a 5% offset on 20-μm pixels. There is a trade-off between shaping capabilities and transmission error, unless some precompensation of the shaper design taking into account the feature size of the mask is performed.

E15433JR
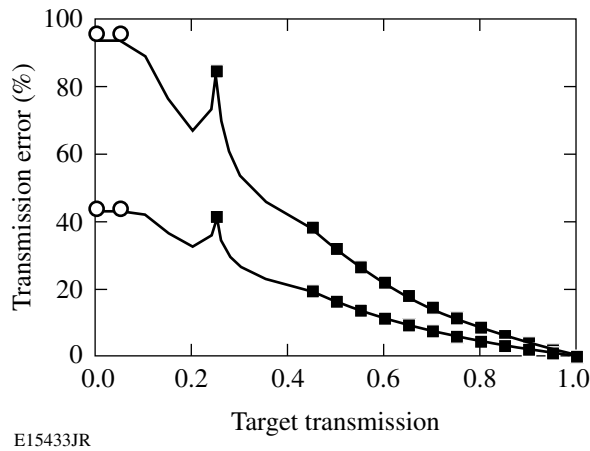
Figure 108.54

Transmission error simulated as a function of the target-intensity transmission for a pixel-size offset equal to 5% (lower curve) and 10% (upper curve). In each case, the circles correspond to the error prediction using Eq. (4) and the squares correspond to the error prediction using Eq. (6) (markers are plotted only in the domain of validity of these two equations).

3. Precompensation

Precompensation of the transmission error due to the feature size is made possible by the predictability of the transmission error. While an exact knowledge of the transmission error requires an exact knowledge of the feature sizes and shapes, one can rely on an approximate model of the pixel shape and size to precompensate the transmission by modifying the pixel density. One starts with the knowledge of the relation between design transmission and obtained transmission, written as $T_{obtained} = f(T_{design})$. It suffices to chose $T_{design} = f^{-1}(T_{target})$ to obtain $T_{obtained} = T_{target}$, where f^{-1} is the reciprocal function of f. Precompensation can be performed simply by applying the error diffusion algorithm to $f^{-1}[T_{target}(x,y)]$ instead of $T_{target}(x,y)$. In practice, the exact shape of the function f (and f^{-1}) is not known. It depends on the feature size of the generated shaper as well as the feature shape. These properties are

likely to be similar for different runs of the same fabrication process, which allows some precompensation of these effects at the design stage.

The function f calculated in the previous subsection for a 5% offset was used to precompensate the shaper design. As in the previous subsection, shapers with a target transmission ranging from 0% to 100% were generated by applying the error diffusion algorithm. The transmission obtained with these shapers was then calculated, following the previous procedure, for pixels corresponding to offsets equal to 4%, 5%, and 6%. The transmission error in the absence of precompensation for these three offsets is plotted in Fig. 108.55(a). It can be compared to the transmission error with precompensation of a 5% offset, which is plotted in Fig. 108.55(b). A significant reduction of the transmission error is obtained. As expected, the transmission error after precompensation is positive for an offset equal to 6%, approximately equal to zero for an offset of 5%, and negative for an offset equal to 4%.
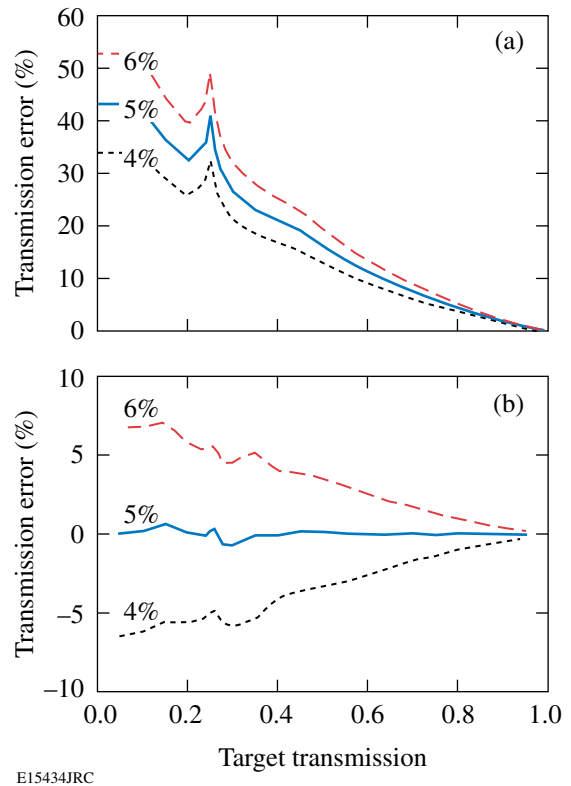

E15434JRC

Figure 108.55

Transmission error as a function of the target transmission for pixel-size offsets equal to 4% (dotted line), 5% (solid line), and 6% (dashed line) (a) without precompensation and (b) with precompensation of the pixel-size offset assuming a pixel-size offset equal to 5%.

Conclusion

The error diffusion algorithm has been studied in the context of the design of beam shapers for high-power laser applications. The high resolution and accurate reproduction of continuous shaping functions is beneficial to these applications. In particular, it has been shown that the shaped intensity has no significant hot spots, therefore decreasing the risk of damage in the laser system. The practical problem of accurate feature size reproduction has been studied in detail, and it has been shown that the transmission error can be reduced significantly by proper biasing of the target transmission before applying the design algorithm. The pixel size should be chosen by considering both the theoretical shaping capability and the influence of the practical fabrication process.

REFERENCES

1. U. Efron, *Spatial Light Modulator Technology: Materials, Devices, and Applications*, Optical Engineering, Vol. 47 (Marcel Dekker, New York, 1995).

2. I. N. Ross *et al.*, J. Opt. Soc. Am. B **19**, 2945 (2002).

3. V. Bagnoud *et al.*, Opt. Lett. **26**, 337 (2001).

4. T. Yu. Cherezova *et al.*, Appl. Opt. **40**, 6026 (2001).

5. A. J. Campillo *et al.*, Opt. Commun. **10**, 313 (1974).

6. G. Emiliani *et al.*, Appl. Opt. **28**, 2832 (1989).

7. G. Giuliani, Y. K. Park, and R. L. Byer, Opt. Lett. **5**, 491 (1980).

8. G. Dubé, Opt. Commun. **12**, 344 (1974).

9. J. M. Auerbach and V. P. Karpenko, Appl. Opt. **33**, 3179 (1994).

10. B. M. Van Wonterghem *et al.*, Appl. Opt. **36**, 4932 (1997).

11. G. H. Miller, E. I. Moses, and C. R. Wuest, Nucl. Fusion **44**, S228 (2004).

12. M. Henesian, Lawrence Livermore National Laboratory, Livermore, CA, private communication (2006).

13. J. H. Kelly, L. J. Waxer, V. Bagnoud, I. A. Begishev, J. Bromage, B. E. Kruschwitz, T. J. Kessler, S. J. Loucks, D. N. Maywar, R. L. McCrory, D. D. Meyerhofer, S. F. B. Morse, J. B. Oliver, A. L. Rigatti, A. W. Schmid, C. Stoeckl, S. Dalton, L. Folnsbee, M. J. Guardalben, R. Jungquist, J. Puth, M. J. Shoup III, D. Weiner, and J. D. Zuegel, J. Phys. IV France **133**, 75 (2006).

14. R. Ulichney, *Digital Halftoning* (MIT Press, Cambridge, MA, 1987).

15. J. Stoffel and J. Moreland, IEEE Trans. Commun. **29**, 1898 (1981).

16. R. W. Floyd and L. Steinberg, J. Soc. Inf. Disp. **17**, 75 (1976).

17. S. Weissbach and F. Wyrowski, Appl. Opt. **31**, 2518 (1992).

18. R. A. Ulichney, Proc. IEEE **76**, 56 (1988).

19. M. J. Madou, *Fundamentals of Microfabrication: The Science of Miniaturization* (CRC Press, Boca Raton, FL, 2002).

LLE's Summer High School Research Program

During the summer of 2006, 13 students from Rochester-area high schools participated in the Laboratory for Laser Energetics' Summer High School Research Program. The goal of this program is to excite a group of high school students about careers in the areas of science and technology by exposing them to research in a state-of-the-art environment. Too often, students are exposed to "research" only through classroom laboratories, which have prescribed procedures and predictable results. In LLE's summer program, the students experience many of the trials, tribulations, and rewards of scientific research. By participating in research in a real environment, the students often become more excited about careers in science and technology. In addition, LLE gains from the contributions of the many highly talented students who are attracted to the program.

The students spent most of their time working on their individual research projects with members of LLE's technical staff. The projects were related to current research activities at LLE and covered a broad range of areas of interest including computational hydrodynamics modeling, materials science, laser-fusion diagnostic development, fiber optics, database development, computational chemistry, and the computational modeling of electron, neutron, and radiation transport (see Table 108.VI).

The students attended weekly seminars on technical topics associated with LLE's research. Topics this year included laser physics, fusion, holographic optics, fiber optics, liquid crystals, atomic force microscopy, and the physics of music. The students also received safety training, learned how to give scientific presentations, and were introduced to LLE's resources, especially the computational facilities.

The program culminated on 30 August with the "High School Student Summer Research Symposium," at which the students presented the results of their research to an audience including parents, teachers, and LLE staff. The students' written reports will be made available on the LLE Web site and bound into a permanent record of their work that can be cited in scientific publications.

Two hundred and four high school students have now participated in the program since it began in 1989. This year's students were selected from approximately 60 applicants.

At the symposium, LLE presented its tenth William D. Ryan Inspirational Teacher Award to Mr. Thomas Lewis, a former earth science teacher (currently retired) at Greece Arcadia High School. This award is presented to a teacher who motivated one of the participants in LLE's Summer High School Research Program to study science, mathematics, or technology and includes a $1000 cash prize. Teachers are nominated by alumni of the summer program. Mr. Lewis was nominated by Benjamin L. Schmitt, a participant in the 2003 Summer Program, with a letter co-signed by 13 other students. "Mr. Lewis was an inspirational, monumental educator (scientific and otherwise), developing a course to be known as 'Advanced Earth Science' as a response to the Advanced Placement science program," Benjamin writes in his nomination letter. "He provided constant challenges and supplied his students with current publications and electronic media about their individual interests." His pursuit of direct student encouragement and interaction came with weekly invitations to his home for star-viewing events. Mr. Lewis "holds one of the most distinguished records in the New York State High School Science Olympiad... spending countless hours each year outside of normal school hours to lead practices, assist with studying... the construction of technical event projects. His devotion to student learning was unmatched by any other teacher or Science Olympiad coach to succeed him." Mr. Lewis announced that he would donate his $1000 award to the Science Olympiad.

Table 108.VI: High School Students and Projects—Summer 2006.

| Name	High School	Supervisor	Project Title
Deshpreet Bedi	Brighton	F. Marshall	X-Ray Diffraction Measurements of Laser-Generated Plasmas
Ryan Burakowski	Churchville-Chili	T. Kosc	PCLC Flakes for OMEGA Laser Applications
Alexandra Cok	Allendale Columbia	S. Craxton	Optimization of Polar Direct Drive Beam Profiles for Initial NIF Targets
Zuzana Culakova	Brighton	K. Marshall	Organic Coatings for Hardening of Laser Optics
Eric Dobson	Harley	J. Delettrez	Modeling Collisional Blooming and Straggling of the Electron Beam in the Fast Ignition Scenario
Elizabeth Gregg	Naples Central	S. Mott/ J. Zuegel	Development of a Test Apparatus for the Optimization of Fiber Splicing
Daniel Gresh	Wheatland-Chili	R. Kidder	Implementing a Knowledge Database for Scientific Control Systems
Matt Heavner	Fairport	C. Stoeckl	Realtime Focal Spot Characterization
Sean Lourette	Fairport	C. Stoeckl	Neutron Transport Calculations Using Monte-Carlo Methods
Ben Matthews	York Central	D. Lonobile/ G. Brent	Precision Flashlamp Current Measurement—Thermal Sensitivity and Compensation Techniques
Ryan Menezes	Webster Schroeder	D. Harding	Evaluation of Confocal Microscopy for Measurement of the Roughness of Deuterium Ice
Rui Wang	Fairport	K. Marshall	Nickel Dithiolene Systems: Computational Modeling of Spectral Properties
Nicholas Whiting	Bloomfield	R. Epstein	Dynamic Energy Grouping in Multigroup Radiation Transport Calculations

FY06 Laser Facility Report

During FY06 the OMEGA Facility conducted 1394 target shots for a variety of users. Shaped-pulse cryogenic DT implosions highlighted the development of direct-drive cryogenic capability. A total of 12 D_2 and 15 DT direct-drive cryogenic target implosions were performed (see Table 108.VII). OMEGA Availability and Experimental Effectiveness averages for FY06 were 93.3% and 95.3%, respectively (see Fig. 108.56). Highlights of other achievements for FY06 include the following:

• The first of a series of direct-drive, ignition-scaled cryogenic targets containing tritium were imploded in February 2006. LLE achieved a DOE milestone in March by imploding two layered DT cryogenic targets containing tritium. The first high-yield, direct-drive, ignition-scaled, 50% DT cryogenic implosion was achieved in June 2006—the first time that such a target was imploded on an ICF facility. OMEGA is now fully capable of fielding high-tritium-fraction cryogenic

Table 108.VII: The OMEGA target shot summary for FY06.

Laboratory	Planned Number of Target Shots	Actual Number of Target Shots	IDI NIC	DDI NIC	Total NIC	Non-NIC
LLE	724	714	201	497	698	16
LLNL	325	348	243	0	243	105
LANL	121	125	54	0	54	71
NLUF	120	122	0	0	0	122
CEA	40	49	0	0	0	49
SNL	24	30	30	0	30	0
NWET	6	6	0	0	0	6
Total	1360	1394	528	497		369
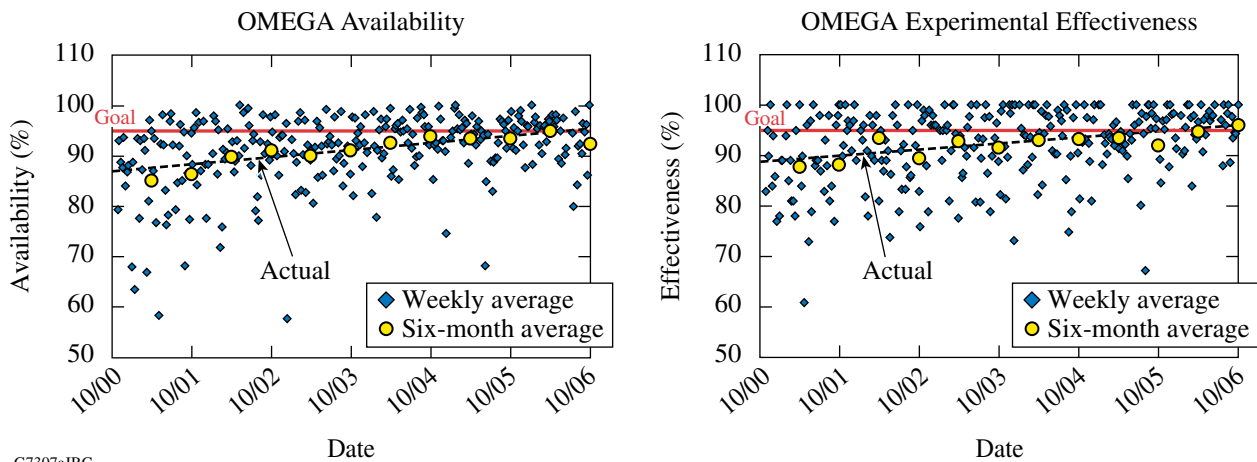
G7307aJRC

Figure 108.56
OMEGA Availability and Experimental Effectiveness data from FY01 to FY06.

targets and has the infrastructure in place to support the corresponding radiological issues.

• A full set of 42 new indirect-drive-ignition distributed phase plates (IDI DPP's) were designed and fabricated for National Ignition Campaign (NIC) experiments on OMEGA. The phase plates produce an elliptical far field (200 μm × 300 μm) at normal incidence and a nearly circular spot at the plane of the laser entrance hole (LEH) and can be oriented for use in both pent and hex configurations. Hohlraum energetics experiments using IDI DPP's were successfully conducted in August, completing a DOE milestone for the National Ignition Campaign. The primary objective of these experiments is to study the effect of laser-beam smoothing with phase plates on the radiation temperature and scattering losses of the hohlraum.

• Low-adiabat, high-contrast pulse shapes are required for OMEGA ignition-scaled cryogenic DT target experiments. Such pulse shapes are typically characterized by a narrow picket pulse on top of a low-intensity foot pulse, followed by a high-intensity drive pulse. The new front end on OMEGA—the integrated front-end source (IFES)—is a highly stable optical-pulse-generation system based on fiber amplification of an optical signal that is temporally carved from a continuous-wave fiber laser. The use of fiber-optic lasers and amplifiers and waveguide temporal modulators makes IFES ideally suited for producing reliable, stable pulse shapes. Recent experiments on OMEGA have required >100:1-contrast-ratio pulse shapes. The electrical waveform that drives the waveguide modulators to shape the pulse is produced using LLE's aperture-coupled-strip-line (ACSL) technology. The shape is designed to precompensate the temporal distortions in the laser due to amplifier gain saturation and nonlinear conversion in the frequency-conversion crystals (FCC's). Figure 108.57 shows (on a logarithmic scale) the design template and the measured ultraviolet laser pulse produced on target by OMEGA for pulse shape LA279901P. The match between the designed and measured shapes is excellent, particularly in the following critical pulse parameters: the picket energy, the >100:1-contrast foot, and the rising edge of the drive pulse.

• A year-long project to upgrade the active-shock-breakout (ASBO) diagnostic was completed in April 2006. The upgrade
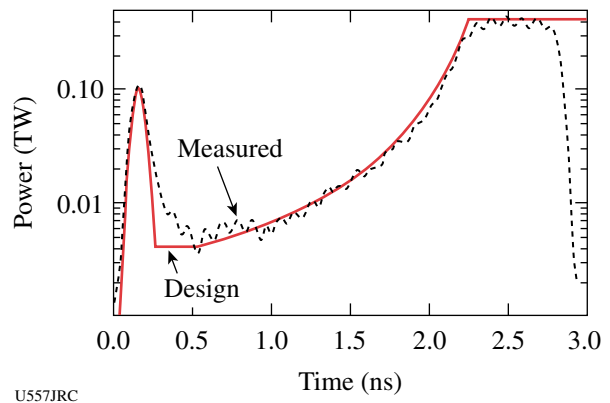

Figure 108.57
OMEGA single-beam pulse shape from low-adiabat cryogenic target implosions (shot #42966) using pulse shape LA279901P.

enables high-precision measurements and ease of operation for equation-of-state (EOS) and shock-timing experiments. Using the existing system as a baseline, the upgrade incorporates a new optical layout that uses the Rochester Optical Streak System (ROSS) streak cameras as detectors for the two velocity interferometer system for any reflector (VISAR) channels. The result is an outstanding optical device that provides excellent performance and smooth operation using the accurately calibrated ROSS cameras. Many experiments are using the new ASBO system. CCD camera data-acquisition capability for x-ray framing cameras was extended to TIM's 4 and 5 and is now available on all TIM's.

• The OMEGA EP short-pulse beam-transport tube was installed during an extended maintenance week in June 2006. The beam-transport tube connects the OMEGA EP grating compression chamber located within the OMEGA EP Target Bay to port P9 on the OMEGA target chamber. Significant structural modifications within the OMEGA target area were required to facilitate the installation of the short-pulse beam tube including target bay platform structural modifications, modifications required to facilitate access to OMEGA UV transport optics, and the addition of two Target Bay jib cranes. Facility modifications planned for FY07 include the relocation of TIM 2 from port H7 to port H3, installation of the off-axis parabola in port H7, and installation of the OMEGA EP transport mirrors on the east side of the OMEGA target chamber.

National Laser Users' Facility and External Users' Programs

During FY06, 680 target shots were taken on OMEGA for external users' experiments, accounting for 48.8% of the total OMEGA shots for the year. The external users during this year included seven collaborative teams participating in the National Laser Users' Facility (NLUF) program and many collaborative teams from the National Laboratories (LLNL, LANL, and SNL) and the Commissariat à l'Énergie Atomique (CEA) of France. Some of this work is highlighted in this section.

NLUF Program

In FY06, the Department of Energy (DOE) issued a solicitation for NLUF grants for the period of FY07–FY08. A total of 12 proposals were submitted to DOE for the NLUF FY07/08 program. An independent DOE Technical Evaluation Panel comprised of Prof. Ani Aprahamian (University of Notre Dame), Dr. Steven Batha (LANL), Dr. Ramon Leeper (SNL), Prof. Howard Milchberg (University of Maryland), and Dr. Robert Turner (LLNL) reviewed the proposals on 18 April 2006 and recommended that six of the twelve proposals receive DOE funding and shot time on OMEGA in FY07–FY08. Table 108.VIII lists the successful proposals.

FY06 NLUF Experiments

FY06 was the second of a two-year period of performance for the NLUF projects approved for the FY05–FY06 funding and OMEGA shots. Six of these NLUF projects were allotted OMEGA shot time and received a total of 122 shots on OMEGA in FY06. Some of this work is summarized in this section.

Isentropic Compression Experiments (ICE) for Measuring EOS on OMEGA
Principal Investigators: Y. M. Gupta and J. R. Asay (University of Washington)

This experimental effort is geared toward developing new areas of high-pressure research. The aim of the FY06 shots was to continue development of techniques to generate high-accuracy, quasi-isentrope, equation-of-state data. This will make possible, for the first time, "cold" stress-density loading curves for standard materials at loading rates up to ten times higher than possible with other methods in the Mbar regime. For the FY05 NLUF allocation, a platform was developed to produce high-accuracy and high-pressure stress-strain data on aluminum.[1] This was the first such data to be measured with a

Table 108.VIII: FY07–FY08 NLUF Proposals.

Principal Investigator	Affiliation	Proposal Title
R. P. Drake	University of Michigan	Experimental Astrophysics on the OMEGA Laser
R. Falcone	University of California, Berkeley	X-Ray Compton Scattering on Compressed Matter
P. Hartigan	Rice University	Laboratory Experiments on Supersonic Astrophysical Flows Interacting with Clumpy Environments
R. Jeanloz	University of California, Berkeley	Recreating Planetary Core Conditions on OMEGA—Techniques to Produce Dense States of Matter
R. Mancini	University of Nevada, Reno	Multiview Tomographic Study of OMEGA Direct-Drive Implosion Experiments
R. D. Petrasso, C. K. Li	Massachusetts Institute of Technology	Monoenergetic Proton Radiography of Laser/Plasma-Generated Fields and ICF Implosions

laser driver and was taken with ramp compression timescales more than ten times faster than had previously been possible. A stiffer response of aluminum was observed than had been previously observed at slower ramp compression experiments on the Z facility at Sandia National Laboratory. In addition, it was observed that the elastic–plastic transition is much larger than expected from previous work at Z. This points to a strong rate dependence in the material strength. The new high-strain-rate data provided by these experiments are being used to benchmark models that incorporate time dependence being developed at Washington State University (WSU).

On 26 April 2006, 14 shots were performed on isentropic compression targets. The ICE-EOS package, as shown in Fig. 108.58, consists of a Au hohlraum, a plastic reservoir followed by a vacuum gap, and a triple-stepped Ta target. Fifteen beams from the OMEGA laser at 0.35-μm wavelength, containing a combined energy of 5 kJ in a 2-ns temporally flat pulse, are focused symmetrically onto the inner walls of the Au hohlraum (1.7-mm LEH, 2.2-mm diameter, 1.7-mm length). This confined high-Z geometry results in a near-blackbody distribution of thermal x rays ($T_h \sim 120$ eV) with uniform temperature gradients over a spatial region close to the diameter of the hohlraum. The hohlraum is attached to a 25-μm-thick Be foil glued to a 180-μm-thick, 12% Br-doped polystyrene foil ($C_8H_6Br_2$). The x-ray field within the hohlraum launches an ablatively driven shock through the foil. The initial region of planarity is expected to approach the diameter of the halfraum and can extend over millimeters. The Bromine dopant absorbs high-energy Au M-band x rays (~2 to 5 keV) generated within the hohlraum, which otherwise could preheat the Ta step sample. After breakout from the rear-surface shock, heating and momentum cause the Br-CH to dissociate and unload across a 600-μm vacuum gap. Transit across the vacuum gap causes the mass-density gradients along the target axis to relax as a function of distance from the original Br-CH/vacuum-gap interface. The unloading Br-CH monotonically loads up against the Ta sample, and the imparted momentum launches a ramp stress wave through the material. The temporal profile of the compression wave may be shaped by varying the size of the vacuum gap, the density of the reservoir, or the temperature within the hohlraum. In the FY06 experiments the main targets consisted of 25/40/55/70 μm Ta or W. A significant change in the target design from the previous campaigns in FY05 was the inclusion of a Be ablator and 1-μm CH liner on the inner wall of the Au hohlraum. The purpose of this modification was to keep the hohlraum open for ~80 ns to facilitate future on-axis radiography experiments that would diagnose material properties (e.g., material strength) during compression. In this context an "open" hohlraum means no on-axis, line-of-sight Au content that would

serve to absorb the flash x-ray photons used for radiography. Be has a high-ablation velocity, and its inclusion (1) increases the x-ray ablative shock pressure into the sample for a given input laser energy and (2) serves to fill the holhraum rapidly and thus acts as a filler, which delays the on-axis stagnation of the cylindrically converging Au holhraum material. The 1-μm-CH liner serves to further tamp the hohlraum collapse. The primary goal of the FY06 NLUF shots was to use this planar drive to extract a single-shot series of equation-of-state (EOS) data for Ta and W up to peak pressures in excess of 1 Mbar.
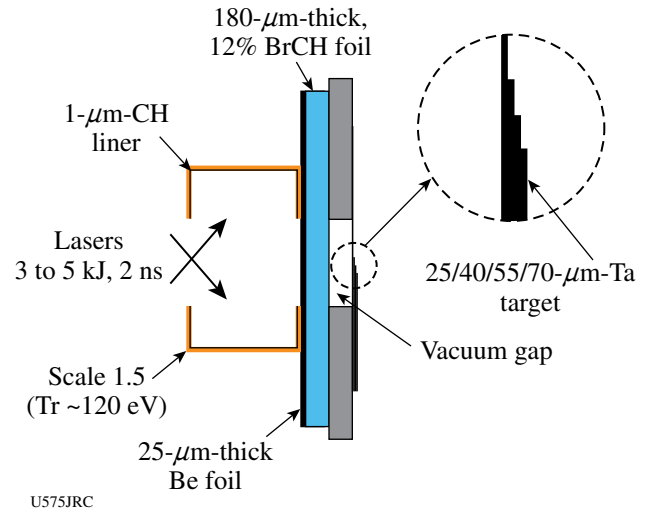

Figure 108.58
Schematic of ICE–EOS target package. The inclusion of a Be ablator and a 1-mm CH liner material serves to keep the hohlraum open for ~100 ns, as was verified in a separate radiography campaign.

The time history of the Ta/vacuum interface acceleration is recorded with a line-imaging velocity interferometer [velocity interferometry system for any reflector (VISAR)] with two channels set at different sensitivities. The time-resolved fringe movement recorded by a streak camera is linearly proportional to the velocity of the reflecting surface, which in this case is the Ta/vacuum interface. This allows an accurate measurement of the free-surface velocity as a function of time. The streak camera output of the VISAR for the target conditions described in Fig. 108.58 is shown in Fig. 108.59. The recently upgraded LLE VISAR provides a greater target field of view than had previously been possible, thereby allowing the use of four separate steps on a single shot for the first time, which ultimately increases the accuracy of the equation-of-state measurement.

The VISAR image provides spatial resolution at the target plane over ~800 μm and temporal resolution of the interferometer fringe displacement over a 30-ns time window. A planar
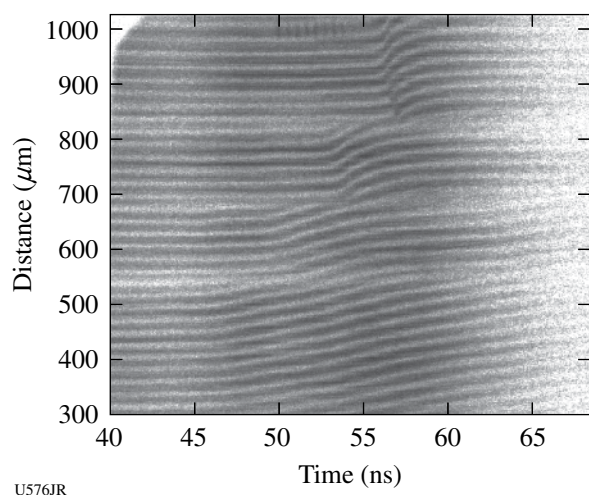
U576JR

Figure 108.59
VISAR streak record for target conditions described in Fig. 108.58.

drive was observed across the field of view with smooth ramp unloading from the 25-, 40-, 55-, and 70-μm-Ta samples at progressively later times. The velocity sensitivity (set by the resolving element within the VISAR) is 0.995 km s^{-1} fringe shift^{-1}. Using Fourier analysis and after deconvolving the data for temporal and spatial distortions within the streak camera, the time-resolved free-surface velocity (U_{FS}) profile for each Ta thickness (Fig. 108.60) can be extracted. There is a very pronounced elastic–plastic precursor wave on all steps. An

U577JRC
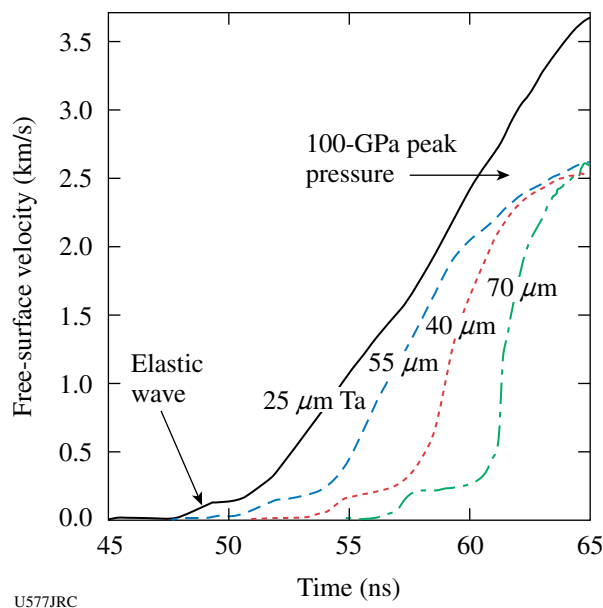
Figure 108.60
Free-surface velocity profile deduced from the data in Fig. 108.59.

increase in this elastic–plastic wave as a function of Ta thickness/ramp rise time is observed. This is an important observation that points to a rate dependence in the material response. Analysis of this data is ongoing.

Using the iterative analysis technique described by Rothman *et al.*,[2] the free-surface velocity profiles in Fig. 108.60 can be used to generate a path through stress-density space up to 1 Mbar (Ref. 1). In future experiments techniques will be developed to shape the pressure profile of the ramp compression wave by using graded density reservoir materials.[3] This will increase the shock-up distance within the target, which in turn will facilitate larger step heights resulting in lower error bars. In addition, the use of graded density reservoirs is expected to increase the accessible peak pressure on OMEGA to greater than 4 Mbar.

Laser–Plasma Interactions in High-Energy-Density Plasmas
Principal Investigator: H. Baldis (University of California, Davis)

High-temperature hohlraums (HTH) are designed to reach high radiation temperatures by coupling a maximum amount of laser energy into a small target in a short time. These 400- to 800-μm-diam gold cylinders fill rapidly with hot plasma during irradiation with multiple beams in 1-ns laser pulses. The high-Z plasmas are dense, (electron density n_e/n_c ~ 0.1 to 0.4), hot (electron temperature T_e ~ 10 keV), and bathed in a high-temperature radiation field (radiation temperature T_{rad} ~ 300 eV). Here the critical density n_c equals 9×10^{21}/cm^3. The laser beams heating this plasma are intense (~10^{15} to 10^{17} W/cm^2). The coupling of the laser to the plasma is a rich regime for laser–plasma interaction (LPI) physics. The LPI mechanisms in this study include beam deflection and forward scattering. To understand the LPI mechanisms, the plasma parameters must be known. An L-band spectrometer is used to measure the electron temperature. A ride-along experiment is to develop the x-radiation emitted by the thin back wall of the half-hohlraum into a thermal radiation source.

Figure 108.61 shows the experimental setup. About twenty laser beams in three cone angles are incident into a 600-μm-diam, 660-μm-long half-hohlraum. The side walls of the hohlraum are gold, usually 20 μm thick. The back wall is thin, ~1 μm of gold or 1 μm of gold overcoated with 1 μm of parylene. The high- and intermediate-angle beams are focused at the center of the laser entrance hole (LEH), but the low-angle beams are focused ~250 to 400 μm in front of the LEH to avoid hitting the back wall. An LPI probe beam is incident almost normal to the hohlraum axis and aimed to an interaction region,

which is the plasma that is 200 μm in front of the LEH. The transmission and forward scatter of this beam are measured with the temporally and spectrally resolved spectrometers and calorimeters in the full-aperture backscatter (FABS) diagnostic. Because of the laser-beam configuration on the OMEGA laser, one can use FABS to measure the forward-scattered light from opposing beams. If the beam is deflected, it falls onto the NBI plate. A time-averaged image of this deflection is recorded by the NBI camera. The L-band spectrometer views the plasma in the LEH region. The x-radiation emitted by the thin back wall can be used to heat a physics target. To characterize this source, the heating of a witness placed ~400 μm outside the back wall (Fig. 108.61) was measured.

Beam deflection is measured with the NBI plate. Figure 108.62 shows images of the NBI plate as a function of LPI

Figure 108.61
Experimental setup of a hot hohlraum experiment.

probe-beam intensity for two independent interaction beams. As the intensity increases, the beam deflection increases (the cross marks the center of the beam). The LPI beam is "bent" by the plasma flowing out of the target. Beam deflection occurs when the ponderomotively induced density depressions in the plasma move downstream and carry the light refracted into them. The images from NBI 25 and NBI 30 correspond to interaction beams B46 and B61, traversing the plasma at angles 31° and 9°, respectively, with respect to the normal to the axis of symmetry of the hohlraum. The beam deflections at 5×10^{15}W/cm^2 are approximately 15° and 7.2°, respectively. This is the first observation of beam deflection as a function of laser intensity for different optical paths along the plasma.

Understanding the measured LPI mechanisms depends on knowing the plasma parameters. Radiation-hydrodynamics codes are used to predict the plasma conditions. These must be benchmarked by measurements of n_e and T_e. In highly charged gold, the $3d \rightarrow 2p$ transitions of individual ionization states are separated by about 40 eV. If these lines can be resolved, the spectrum gives the distribution of the ionization states of gold. This, combined with models that predict the ionization state as a function of electron temperature, would give T_e.

The L-band spectrometer is designed to measure the $3d \rightarrow 2p$ transitions in gold with high resolution. It is a transmission crystal spectrometer mounted to a single-strip framing camera. It captures a single-time and space-resolved, high-resolution spectrum. Figure 108.63(a) shows a measured spectrum. There is a group of lines, peaking at 10,100 eV, with half-width of about 250 eV. Simulated spectra [Fig. 108.63(b)] from the nonlocal thermodynamic equilibrium (NLTE) code *FLYCHK* (for $\langle Z \rangle$ as a function of electron temperature) and *FLYSPEC* (for spectral lines) show similar features: a group of lines about 200 eV wide. The centroid moves to higher x-ray energy with higher electron temperature. A comparison of the data with simulation shows the measured electron temperature is ~7 to 8 keV.
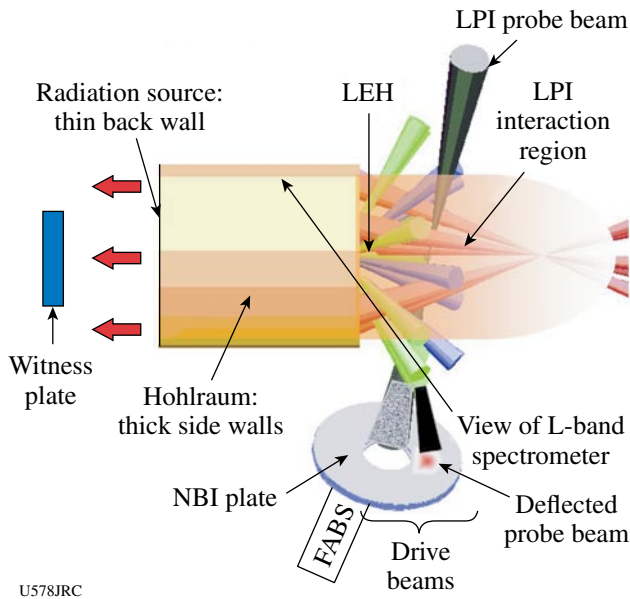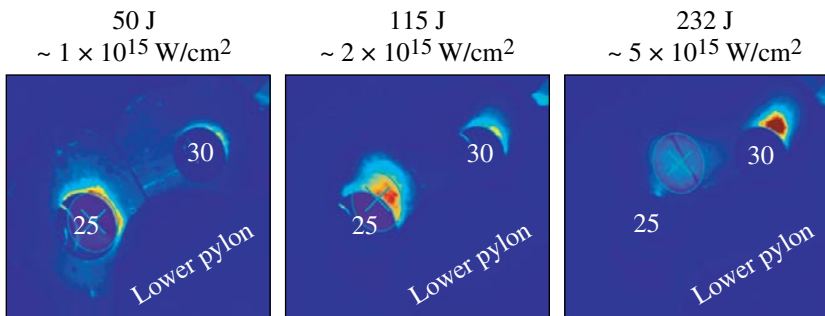
50 J
~ 1 × 10^{15} W/cm^2

115 J
~ 2 × 10^{15} W/cm^2

232 J
~ 5 × 10^{15} W/cm^2

Figure 108.62
Images of NBI plates show beam deflection as a function of LPI probe-beam intensity.
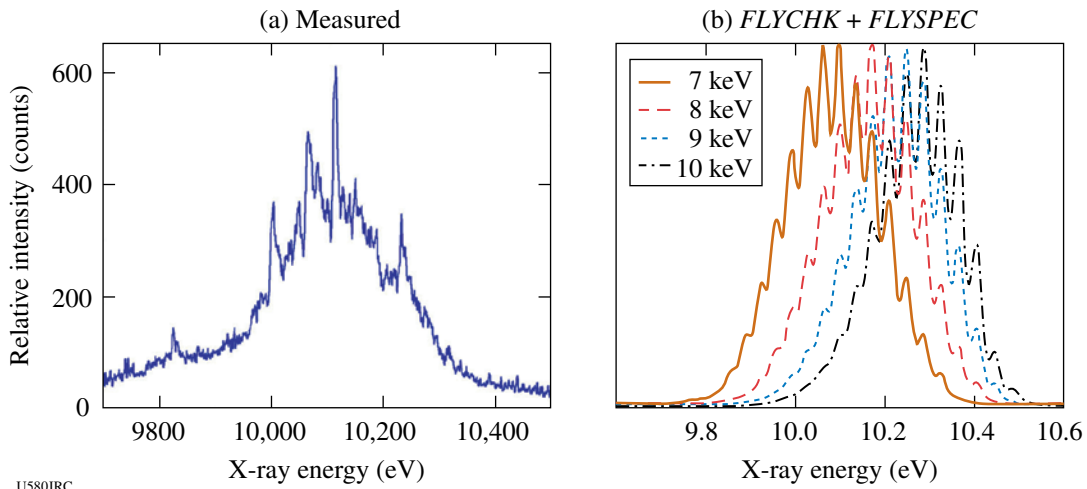
Figure 108.63
(a) L-band spectrometer measurement of $3d \rightarrow 2p$ transitions in Au. (b) Simulated spectra using the code *FLYCHK*.

Measured stimulated Brillouin forward scattering (SBFS) is shown in Fig. 108.64. The SBFS confirms the time at which the plasma reached the interaction region, by the transition from 3ω laser light to SBFS. The absence of 3ω light after 1 ns may indicate that the nonlinear beam deflection has shifted the beam toward the NBI plate, with the light missing the collecting lens. It is possible that the SBFS is *not* deflected because of its lower intensity.

The use of the back wall as a radiation source is demonstrated by using it to heat a Cr witness plate. The arrangement for the HTH half-hohlraum with a witness plate is shown in Fig. 108.65. Figure 108.65(a) shows a schematic of the target. The witness plate (WP) is mounted ~400 μm from the back wall, at an 11° tilt to the back wall so that the imaging diagnostic views the WP edge-on. The WP is a thin chromium foil
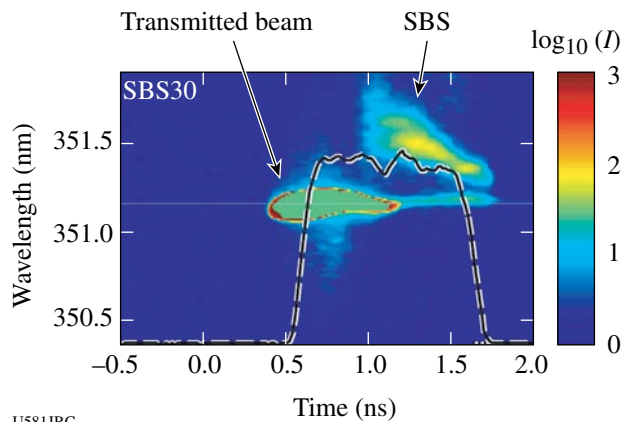

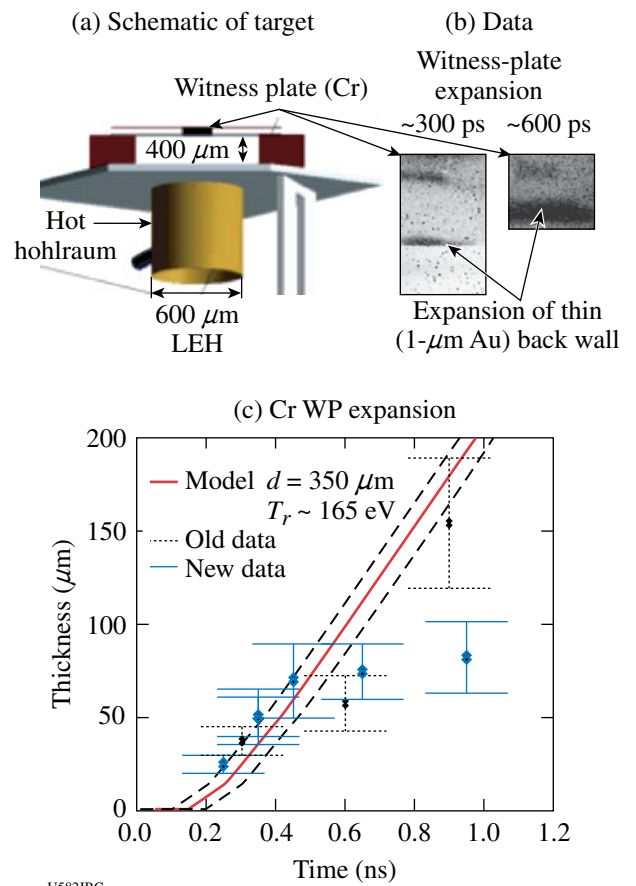Figure 108.64
Streak camera image showing forward SBS.

Figure 108.65
New radiation source: the thin back wall of an HTH half-hohlraum is used to heat a witness plate (WP). (a) The sketch of the target shows a WP mounted ~300 μm from the back wall at an 11° angle so it is viewed edge-on by the OMEGA diagnostic. (b) The data show a WP glowing after it has been heated by the back wall (also glowing). (c) The measured expansion of the Cr WP.

sandwiched in plastic (1 μm on each side). Figure 108.65(b) shows the heated WP at two different times. Since these were taken on two different shots, the distance of the WP from the back wall is slightly different; however, the WP is clearly expanding as it is heated. Figure 108.65(c) shows the measured width of the WP as a function of time from several shots on several different days. The solid line is the predicted expansion from a radiation–hydrodynamic simulation, assuming the WP is heated solely by radiation from the back wall. The data are consistent with the simulation, which predicts the radiation temperature in the plate to be ~165 eV.

The following additional measurements of plasma parameters in the LPI region have been performed: (a) the M-shell spectra of gold, (b) Raman backscatter, and (c) 2ω and 4ω Thomson scattering. These data are still being analyzed.

Experimental Astrophysics on the OMEGA Laser

Principal Investigator: R. P. Drake (University of Michigan)
Co-investigators: B. A. Remington, H. F. Robey, S. G. Glendinning, D. D. Ryutov, M. Herrmann, A. R. Miles, A. J. MacKinnon, B. E. Blue, and J. F. Hansen (LLNL); M. Koenig (LULI, Ecole Polytechnique, France); D. Arnett (University of Arizona); R. Rosner and T. Plewa (University of Chicago); J. Stone (Princeton University); S. Bouquet (CEA, France); J. P. Knauer and T. R. Boehly (LLE); Y. Zhang and J. Glimm (SUNY Stony Brook)

The OMEGA laser can address important issues in astrophysics because, through laser ablation, it can produce pressures of tens of Mbars over areas of square millimeters. Two such issues are the contribution of hydrodynamic instabilities to the structure in supernovae and the dynamics of radiative shock waves. After successfully creating collapsed radiative shock structures in both argon and xenon gas, an experiment was performed to Thomson-scatter light from the 4ω beam off of a shock front in argon gas.

In the experiment, ten smoothed beams of the OMEGA laser irradiate a 20-μm beryllium disk with UV light at an irradiance of ~5×10^{14} W/cm^2 for 1 ns. This launches the disk via ablation pressure at a high velocity into a 600-μm-diam, 6-mm-long polyimide tube filled with 1.1 atm (0.001 g/cm^3) of argon gas. This target had openings covered with 3000-Å polyimide facing the 4ω probe beam and the UV spectrometer and streak camera in TIM-2. The scattering volume was 3.7 mm from the initial drive disk position. The 4ω probe beam fired in a 2-ns pulse at 200 J, with a best-focus spot size of 100 μm. The target axis for this experiment was parallel to the probed ion-acoustic waves.

Figure 108.66 shows spectral data from the first experiments to obtain Thomson-scattering data from a shock front. The signal lasted 300 ps, starting at 20.1 ns after the drive beams turned on. Before that, the signal was from the tail end of a destroyer beam blasting off the polyimide cover facing the collection diagnostic in TIM-2. The spectrum of the scattered light and a fit to the data are shown in Fig. 108.67. The overall spectrum is shifted in frequency by a Doppler shift, implying that the flow velocity of the shocked fluid is 110 km/s. Fits to the spectrum using the kinetic theory of Thomson scattering, combined with an evaluation of the average charge using an "average atom" model, give an ion temperature of 300 eV, an electron temperature of 250 eV, and an average charge of 13.7. These are sensible values for the argon near the shock front.

Astrophysical Jets and HED Laboratory Astrophysics
Principal Investigator: P. Hartigan (Rice University)

A variety of objects in the universe are surrounded by accreting disks of matter, and most of these systems drive highly collimated supersonic jets out the poles of these disks. Examples include jets from young stars, planetary nebulae, x-ray binaries, and black holes at the centers of active galaxies. The goal of this
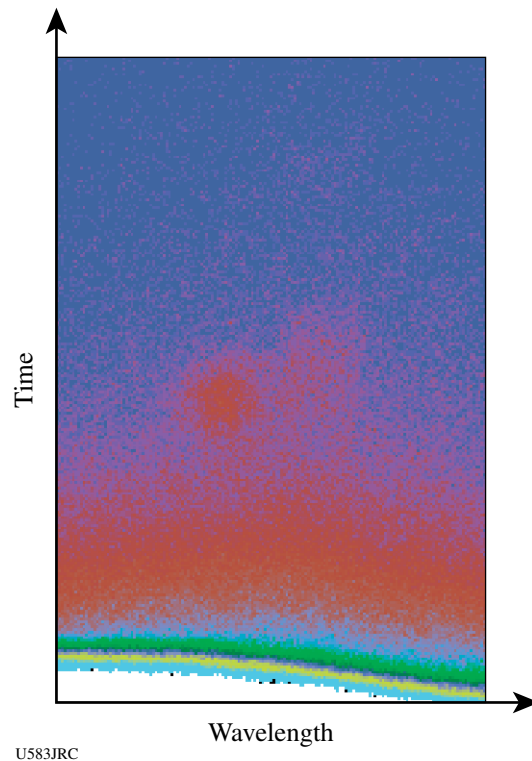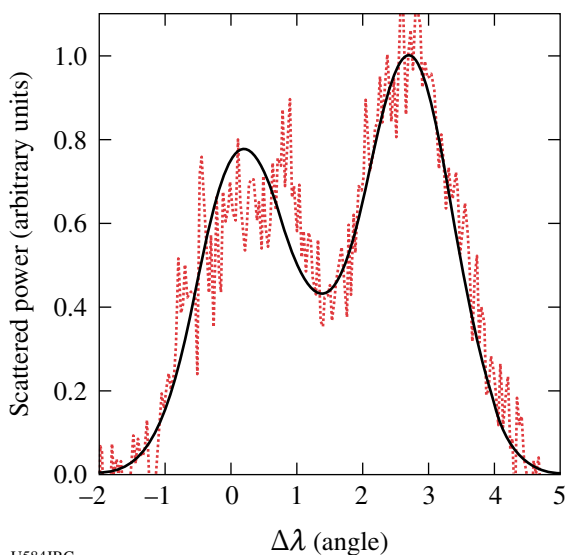

U583JRC

Figure 108.66
Streak camera data showing Thomson-scattered-light spectral evolution for collapsed radiative shock.

Figure 108.67
Thomson-scattered spectrum and fit to the data for Fig. 108.66.

project is to create laboratory analogs of the jet phenomenon in the laboratory and follow what happens when such a jet interacts with an obstacle in the flow as it is observed to do in many astrophysical situations. An astrophysics fluid dynamics code (*AstroBEAR*) and the *RAGE* code at Los Alamos are both used to help design the experiment and interpret the results.

In the past year, two shot days were allotted for the project, and both succeeded in producing excellent images of shocks in the jet and the ball as the latter was being destroyed and entrained by the flow. The targets consisted of a dense ball embedded at various offset distances (impact parameters) from the axis of the jet. The data set now includes a continuous range of impact parameters and times so we can follow the process as a function of these two variables. Sample images from the experiment are shown in the Fig. 108.68. Astrophysical observations of a deflected jet are scheduled for the end of November, and we will be comparing the new spectra from that effort with numerical datacubes of the *RAGE* and *AstroBEAR* simulations of the laser experiments to improve our understanding of the dynamics of these flows.

Recreating Planetary Core Conditions on OMEGA
Principal Investigator: R. Jeanloz (University of California, Berkeley)

Significant technical as well as scientific breakthroughs in the NLUF high-pressure experiments on planetary fluids were made this past year. The approach that is used involves driving a laser-induced shock wave through a sample already precompressed in a diamond-anvil cell (Fig. 108.69). This combines the benefits of static and dynamic methods of high-pressure experiments, allowing the final pressure–volume–temperature (P–V–T) state of the sample to be tuned across a broad range of thermodynamic conditions (Fig. 108.70). In fact, much-higher compressions, thus more-extreme interatomic interactions, are achieved through this approach than through traditional shock-wave (Hugoniot) measurements.

One of the major technical accomplishments of this program has been the significant improvement of the understanding of
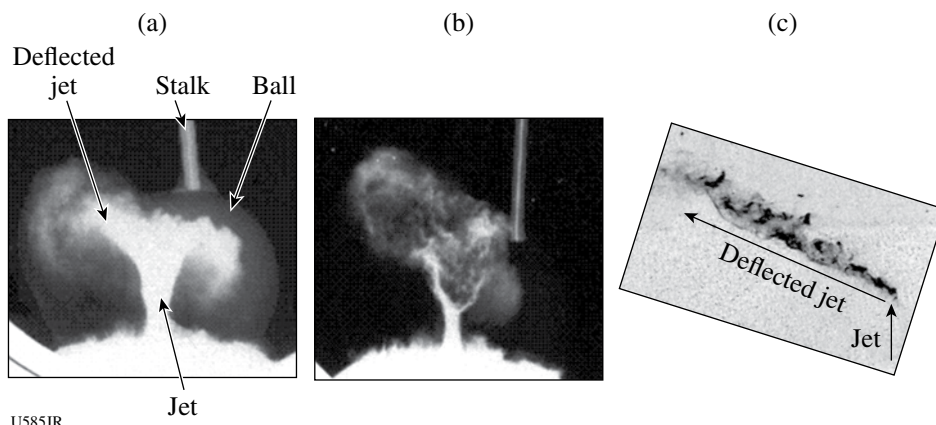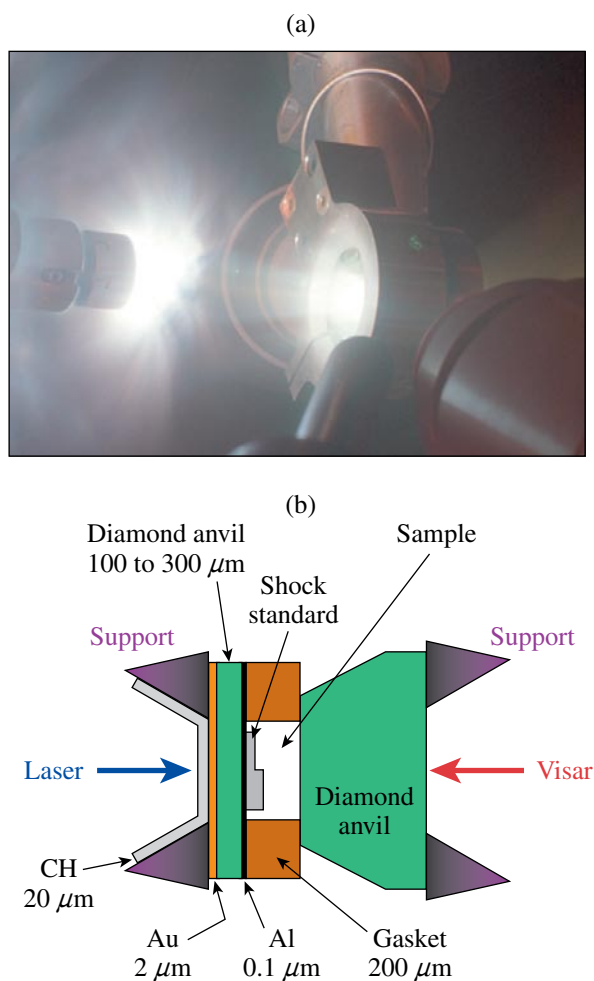

Figure 108.68
Deflected jets in the laboratory and in the universe. (a) OMEGA image of a jet deflecting from a ball located 300 μm from the axis of the jet, at 150 ns, taken with an Fe backlighter. Shocks are clearly visible in the ball and ahead of the deflected jet, which is starting to fragment. (b) Same as (a) with a 350-μm offset at 200 ns and a Zn backlighter. (c) Hubble Space Telescope image of the deflected jet HH 110. The jet emerges from a young star off the bottom of the image and deflects off an opaque dark cloud of gas and dust.

the interferometry records obtained from the shock experiments (Fig. 108.71). Despite the use of antireflection coatings, the components in these experiments generate residual reflections that cause "ghost fringes" to appear in the VISAR records. This source of noise is now understood, to the point that the "ghost fringes" serve as internal calibrants for the records and a joint inversion of the records can be performed to obtain far better velocity resolution than previously thought possible.

In addition to equation-of-state measurements, one of the key measurements obtained from the VISAR records is the optical reflectivity of the shock front: it is possible to determine whether one is looking through the shock front or off its surface

(a)

(b)

U586JRC

Figure 108.69
Photograph of (a) a loaded diamond cell subjected to laser-shock compression and (b) schematic cross section of the diamond cell. The diamond anvil of the entry (drive-laser) side must be thin in order to minimize attenuation of the shock front before it enters the sample. Diagnostics include velocity interferometry (using VISAR) as well as pyrometry (not shown).

by the way the velocity fringes. The reflectivity at optical wavelengths can be converted to an equivalent of electrical conductivity, allowing us to determine the competing P–T conditions under which helium becomes metallic (Fig. 108.72). This is important because the metallization conditions for helium, far more extreme than those for hydrogen, determine the depths at which hydrogen and helium—the primary constituents of giant planets—can behave as metallic alloys. Without such alloying, it is expected that helium separates from the much lighter hydrogen, and the gravitational energy released by this "differentiation" process is thought to be a major source of heat and internal evolution of giant-planetary interiors. Indeed, experiments now underway will allow the documentation of the enhanced reflectivity of hydrogen + helium mixtures (Fig. 108.73), promising to offer significant new constraints on models of planetary evolution and origins.
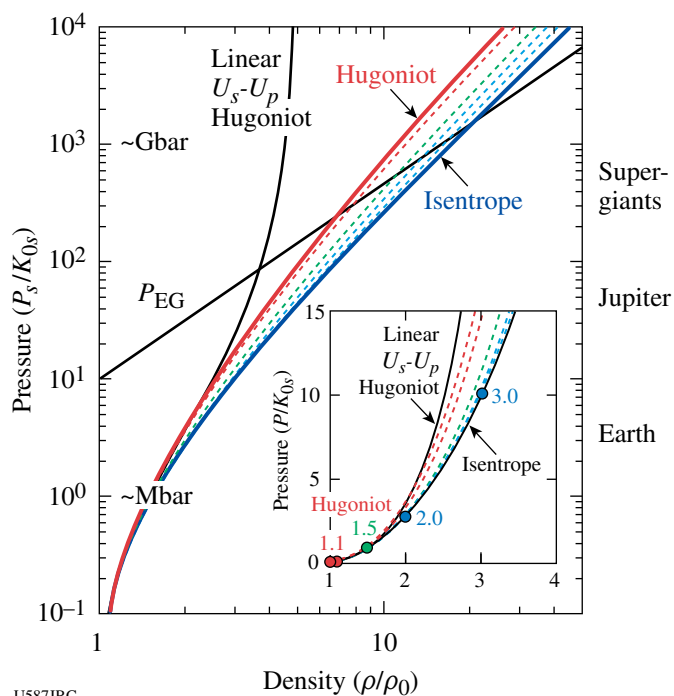

U587JRC

Figure 108.70
Pressure–density (P–ρ) equations of state, normalized by the zero-pressure bulk modulus (K) and density illustrating the range of conditions that can be achieved between the single-shock Hugoniot and isentrope as a function of precompression by factors of 1.1, 1.5, 2.0, and 3.0 (see inset), all calculated from the Birch–Murnaghan[4] and Mie–Grüneisen[5] approaches assuming $K'_0 = 4$, a Grüneisen parameter varying as γ/ρ = constant, and $\gamma_0 = 1.5$ (subscripts 0 and s indicate zero-pressure and isentropic conditions, respectively). The linear shock-velocity U_s versus particle-velocity U_p relationship, and the density dependence of the ideal electron–gas pressure (P_{EG}) are shown for comparison, as are Mbar and Gbar pressures and planetary-center conditions (Earth, Jupiter, and supergiants) corresponding to a typical bulk-modulus value of 100 GPa (= 1 Mbar). The inset shows the lower-pressure range on a linear plot.
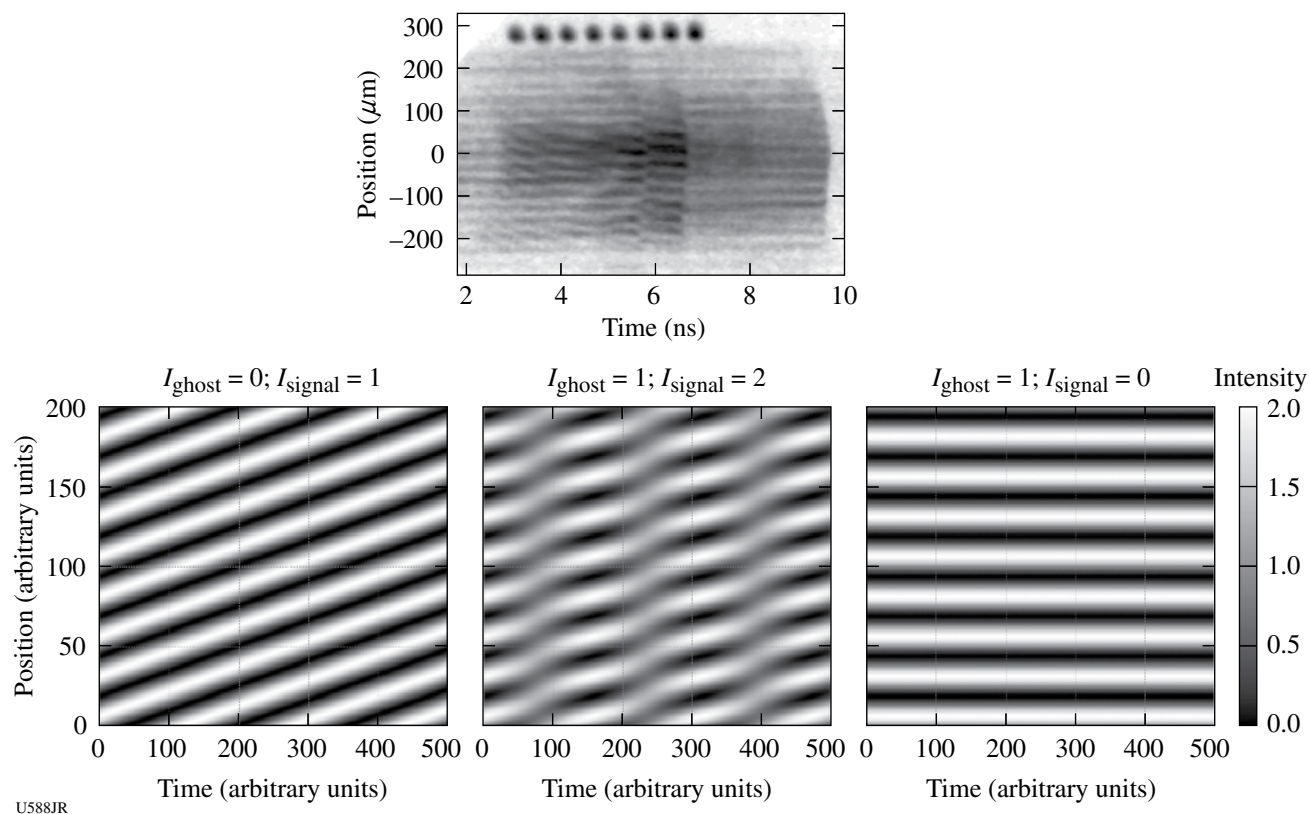
Figure 108.71

(Top) Velocity-interferometry (using VISAR) record from a laser-shock experiment on precompressed helium showing the presence of "ghost fringes" due to residual reflections from diamond and other surfaces. (Bottom) Simulations of the ghost fringes, from 100% signal (no ghost) on the left to 100% ghost (no signal) on the right; center panel shows a 2:1 intensity ratio for signal:ghost.
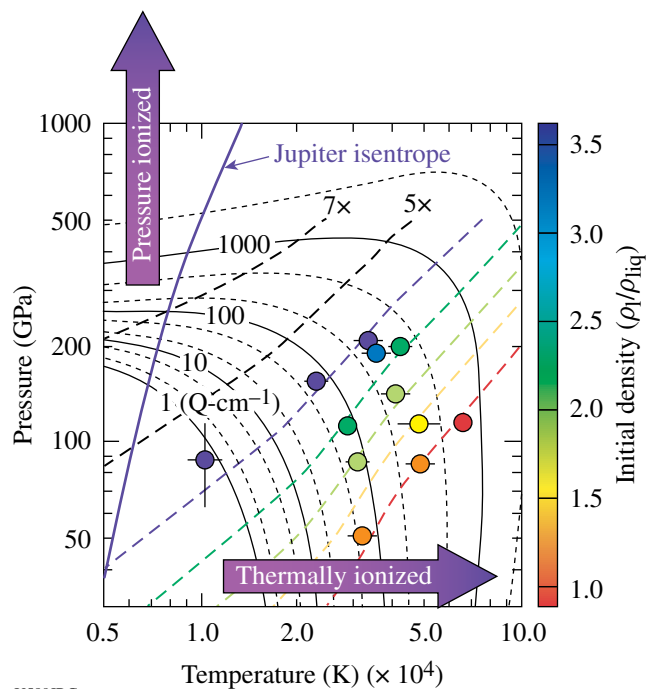
Figure 108.72

Reflectivity measurements as a function of pressure–temperature conditions achieved in helium (circles shaded according to the precompressed density ρ_1 prior to shock loading) quantified in terms of equivalent electrical conductivity (solid and dotted contours). The data clearly probe the trade-offs between pressure and temperature in causing metallization (ionization), with predicted trajectories for different amounts of precompression indicated by the dashed lines and the model temperature distribution (isentrope) inside Jupiter shown for comparison.
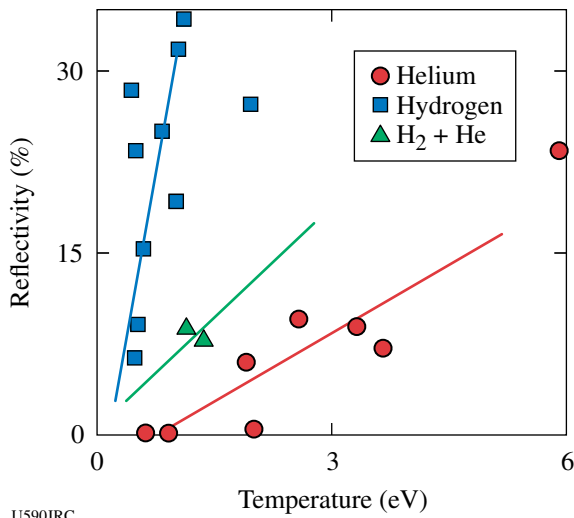
U590JRC

Figure 108.73
High-pressure reflectivity of hydrogen, helium, and hydrogen + helium mixtures under shock compression, shown as a function of Hugoniot temperature determined from pyrometry.

Three-Dimensional Study of the Spatial Structure of Direct-Drive Implosion Cores on OMEGA
Principal Investigator: R. Mancini (University of Nevada, Reno)

The objective of this project is to study the three-dimensional (3-D) structure of the temperature and density spatial profiles of OMEGA direct-drive implosion cores using data from gated narrowband x-ray core images recorded along three quasi-orthogonal directions. To this end, this experiment uses plastic shell targets filled with deuterium gas and a tracer amount of argon for spectroscopic diagnostic purposes. Three identical multimonochromatic imagers (MMI) have been designed, built, and fielded on OMEGA implosion experiments to perform observations along the lines of sight (LOS) of TIM-2, TIM-3, and TIM-4; this set of TIM's represents a quasi-orthogonal system of x-y-z Cartesian axes. The implosions were driven with 60 OMEGA beams, 23 kJ of UV energy, and a 1-ns square laser pulse. At the collapse of the implosion, the hot and dense core plasma achieved temperatures in the 1- to 1.5-keV range and electron number densities in the 1×10^{24} cm^{-3} to 2×10^{24} cm^{-3} range. X-ray K-shell line emission from the argon dopant is a suitable spectroscopy diagnostic for this temperature and density range.

Core images (recorded by MMI instruments) that are formed by a large array of 10-μm-diam pinholes and reflected off a depth-graded WB$_4$C multilayer mirror with an average bilayer thickness of 15 Å yield narrowband x-ray images in the photon energy range from 3 to 5 keV. They have a magnification of 8.5,

provide spatial resolution of approximately 10 μm, and record gated (framed) images characteristic of a 50-ps time interval. Indeed, these instruments record data with simultaneous space, time, and photon energy resolution. As an illustration of the data recorded by MMI, Figs. 108.74 and 108.75 display a time history of narrowband x-ray core images from OMEGA shot 42643 at the collapse of the implosion, based on the argon Ly$_\beta$ ($1s$ ^2S–$3p$ ^2P, $h\nu$ = 3936 eV) and He$_\beta$ ($1s^2$ ^1S–$1s2p$ ^1P, $h\nu$ = 3684 eV) line emissions. The photon energy narrowband of these images is given by the (mainly) Stark-broadening widths of the line shapes, which for the plasma conditions of these cores is 60 to 70 eV. Core dimensions are in the 60- to 100-μm range. At early times, images recorded along both quasi-orthogonal directions show cores that are large and mostly round. For later times, one LOS shows a core shape that evolves into an oval shape, while the other LOS shows an object that remains more rounded but
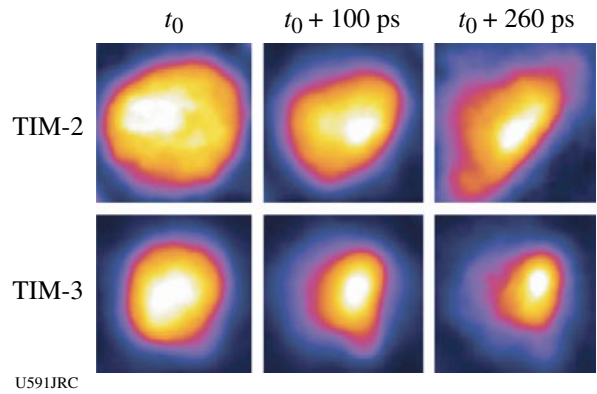

U591JRC

Figure 108.74
Gated argon Ly$_\beta$ narrowband core images recorded along two quasi-orthogonal directions on OMEGA shot 42643.
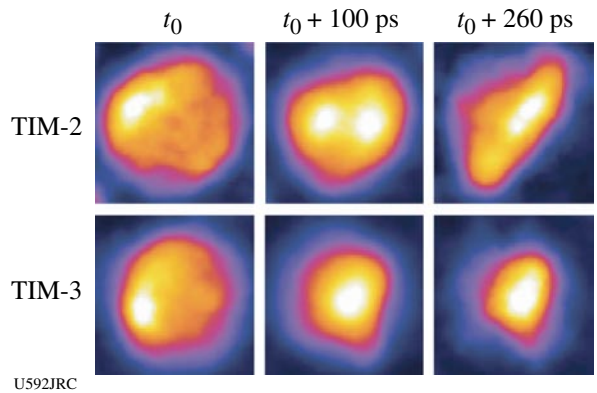

U592JRC

Figure 108.75
Gated argon He$_\beta$ narrowband core images recorded along two quasi-orthogonal directions on OMEGA shot 42643.

getting smaller. Both observations suggest the evolution of a 3-D core from rounded to ellipsoidal shapes with a well-defined orientation in space. It is also interesting to observe the regions of greatest brightness associated with the Ly_β and He_β line emissions, which depends on both temperature and density conditions in the core. Detailed spectral modeling and analysis of the emissivity and opacity of the argon x-ray emission permit a reconstruction of spatial structure of the plasma. In this connection, Fig. 108.76 displays a temperature map based on the analysis of the second frame of data (i.e., $t_0 + 100$ ps) displayed in Figs. 108.74 and 180.75. The range of values of this spatial profile is consistent with the range of temperatures extracted from the analysis of data independently recorded with streaked spectrometers in the same experiment. Several analysis methods are currently being investigated that simultaneously consider data observed along several LOS's.
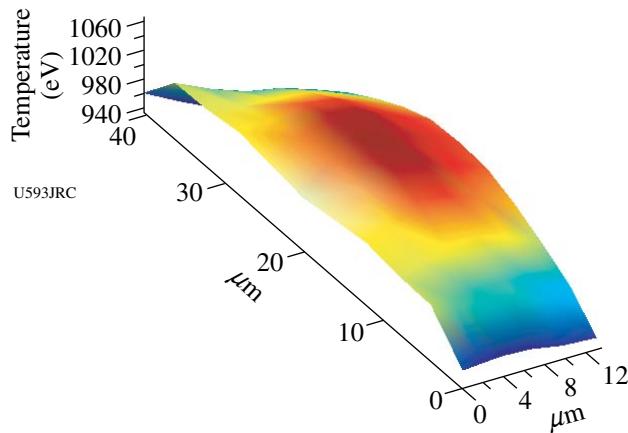

Figure 108.76
Core temperature map for OMEGA shot 42643 extracted from TIM-2 data in Figs. 108.74 and 108.75 for $t_0 + 100$ ps.

Implosion Dynamics and Symmetry from Proton Imaging, Spectrometry, and Temporal Measurements

Principal Investigators: R. D. Petrasso and C. K. Li (Massachusetts Institute of Technology)

As part of the MIT NLUF program, data was taken in an ongoing series of experiments using proton radiography to study transient E and B fields generated by the interaction of OMEGA laser beams with plastic foils. High-resolution, time-gated radiography images of a plastic foil driven by a 10^{14}-W/cm² laser implied B fields of ~0.5 MG and E fields of ~1.5×10^8 V/m. Simulations of these experiments with *LASNEX + LSP* have been performed and are in overall (though not exact) agreement with the data both for field strengths and for spatial distributions; this is the first direct experimental test of the laser-generated B-field package in *LASNEX*. The experiments also demonstrated that laser phase plates substantially reduce medium-scale chaotic field structure. The results have recently been published in *Physical Review Letters*[6] and in *Review of Scientific Instruments*.[7]

In each experiment, two plastic foils were illuminated by a single OMEGA laser beam, and a projection radiograph was made of each foil using a backlighter providing monoenergetic 14.7-MeV protons and a CR-39 area detector for image recording. One foil was perpendicular to the backlighter–detector direction, giving a face-on view of the resultant field structure, while the other foil was parallel to the backlighter–detector direction, giving a side-on view. The backlighter was formed by imploding a D^3He-filled, glass-shell capsule with 20 OMEGA laser beams (see Fig. 108.77). Since the burn duration of the D^3He implosion was short (~150 ps) relative to the 1-ns duration of the foil illumination, and the relative timing of the implosion and the foil illumination was adjustable, it was possible to record images at different times relative to the foil illumination.
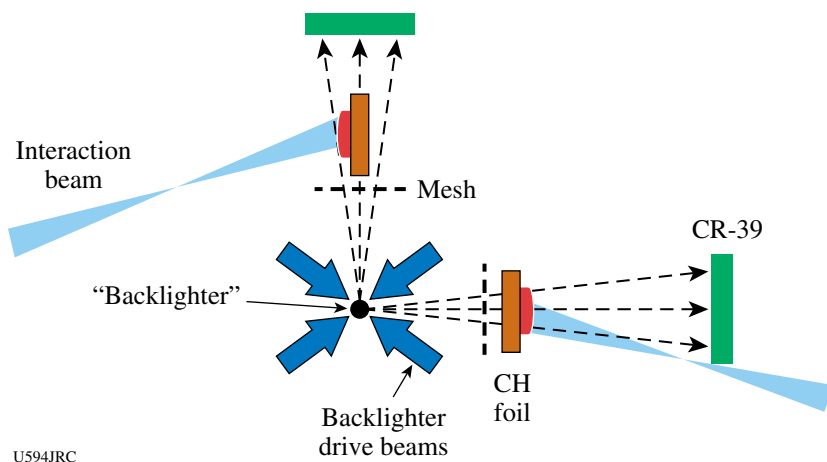

Figure 108.77
Schematic illustration of experimental setup and the physical relationship between the proton backlighter (imploded D^3He-filled capsule), mesh, CH foils, CR-39 imaging detectors, and OMEGA laser beams. The distances of components from backlighter were 0.8 cm for mesh, 1 cm for foil, and 36 cm for detector. The hole-to-hole spacing in the mesh was 150 μm.

The distortion in the mesh pattern at the detector shows how the proton trajectories were deflected through interaction with the fields generated by laser–plasma interaction at the foil. Sample images recorded at different times are shown in Fig. 108.78 (face-on) and Fig. 108.79 (side-on). These images have been analyzed in collaboration with LLNL and LLE to provide information about the time evolution of the field-induced distortion.[6,7]
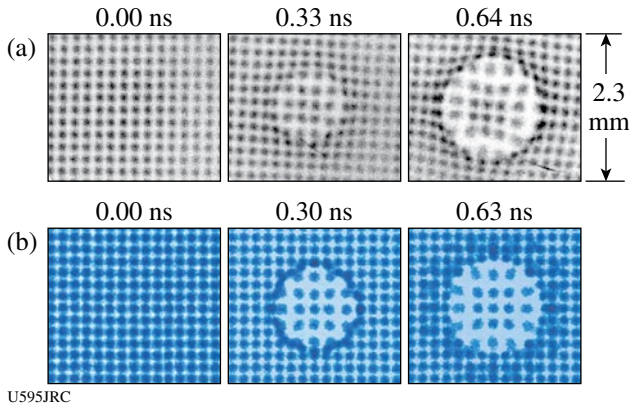

Figure 108.78

(a) Measured face-on D^{3}He proton images showing the effects of the *B* field generated by laser–plasma interactions at 0.0, 0.33, and 0.64 ns, respectively, after the interaction beam was turned on. The labeled dimensions of the image are scaled to the location of the foil. (b) Images simulated by *LASNEX + LSP* for the conditions that produced the experimental images shown in (a).
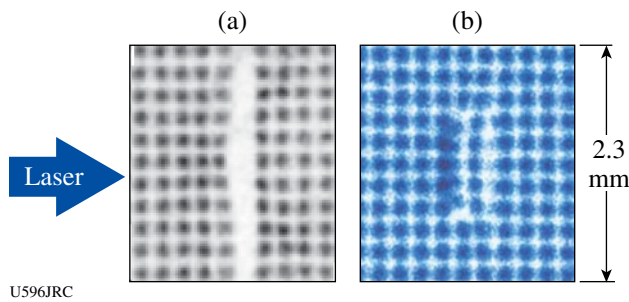

Figure 108.79

(a) Data and (b) simulation for the side-on images. The distortion in the center column of (a) resulted from the *E* field. The large separation between the two center columns of beamlets in (a) is due to attenuation by the CH foil, which is 50 μm thick but 3 mm long in the direction parallel to the proton trajectories; this effect is not seen in (b) because proton–foil interactions were not modeled in the *LSP* simulation.

FY06 LLNL OMEGA Experimental Programs

In FY06 LLNL led 354 shots on the OMEGA system. This total represents a shot rate of approximately 4% higher than nominal (340 shots scheduled for the year), an excellent achievement when one considers that LLNL's programmatic needs frequently dictated difficult reconfigurations from one day to the next, especially during split days.

National Ignition Campaign (NIC) Experiments: One of the first experiments of the year was designed to examine the direct effects of laser-heated gas on an implosion capsule within a gas-filled hohlraum. Plastic hohlraums (to minimize radiation drive) and foam witness balls were used in a NIF-foot-scale experiment. The x-ray backlighting data are shown in Fig. 108.80. Arrows point to regions where there is a departure from spherical symmetry due to pressure from the laser-heated gas that filled the hohlraum.

Several shot days were devoted to the study of collective x-ray scattering from plasmons in warm (10 to 15 eV), dense (2 to 3 × 10^{23} electrons/cm^3) matter. By fitting the data to theoretical models, the electron density is obtained from the scattered x-ray data and found to be in agreement with simulations.

Throughout FY06 a number of laser–plasma interaction experiments were carried out, some in collaboration with CEA, using a gas-filled hohlraum arranged so that one OMEGA beam (beam 30) could be used as an on-axis probe. Spatially imaged Thomson scattering and a time-resolved transmitted beam diagnostic (3ω TBD) were successfully fielded on OMEGA. Various experimental results are shown in Fig. 108.81 (electron and ion temperatures in the gas as a function of time), Fig. 108.82 (Brillouin scattering reduced as electron temperature increases), and Fig. 108.83 (Raman scattering measured as a function of density for fixed intensity). Experiments using a defocused beam with phase plates showed interaction instabilities decreasing with the average intensity, as predicted. Finally, a semiautomated mechanism for calibration of the near-backscatter plate was fielded and tested.[8]

An albedo (ratio of radiant energy emitted divided by radiant energy absorbed) experiment compared gold hohlraums and "cocktail" (mixtures of gold and uranium) 180-eV hohlraums and found, as predicted, a slight increase for the cocktail case.

In another collaboration with CEA, the OMEGA laser was used in the direct-drive configuration to illuminate spheres of gold, uranium, and a cocktail mixture to measure the conversion of laser energy into x-ray energy. Particular attention was given to obtaining detailed measurements in the 2- to 5-keV range.

An extensive series of experiments were performed for platform development, and use of that platform, for measuring the
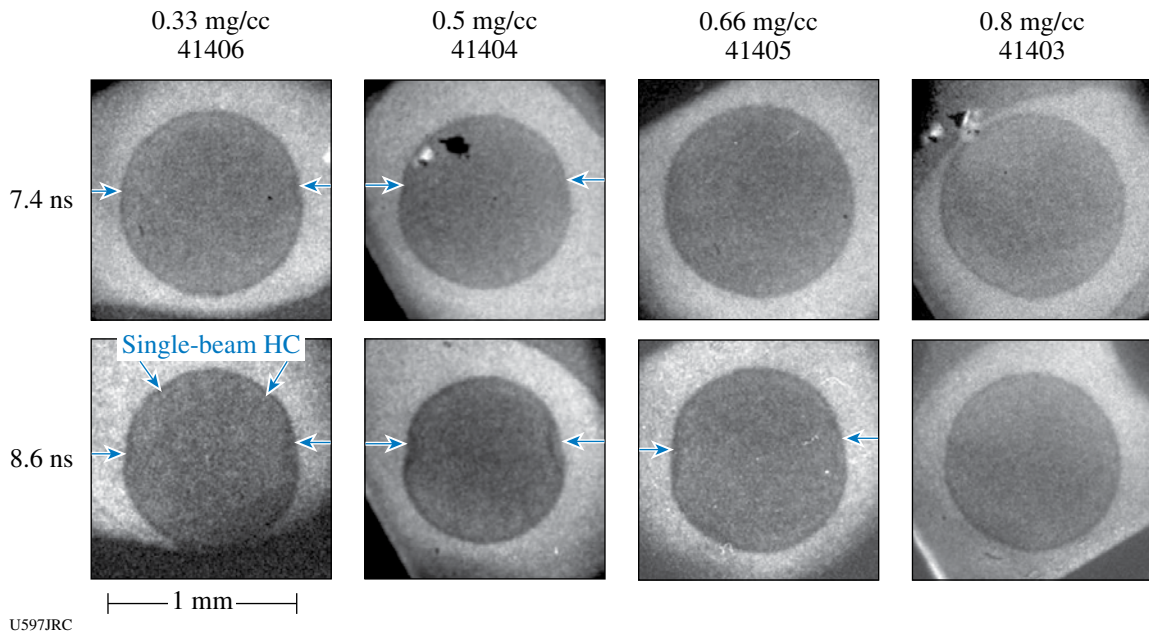
Figure 108.80
X-ray-backlit images of foam spheres, showing (arrows) effects of pressure from laser-heated hohlraum fill gas. Good backlighting foam-ball data were measured for the 0.3- to 0.8-mg/cc hohlraum fill range of interest for HC.
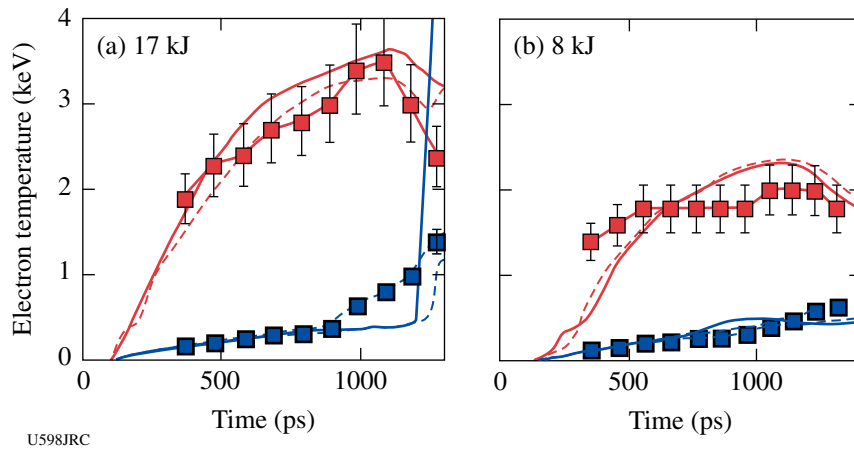

Figure 108.81
Electron temperature (open squares), ion temperature (dark squares), and simulations (solid lines) as a function of time along the laser beam path. The measured electron- and ion-temperature evolution validates the simulations of the plasma conditions along the interaction beam path.

Rayleigh–Taylor growth of ablator materials, being ablatively accelerated by x-ray drive. The planar ablator samples were mounted on the end of a one-ended hohlraum ("halfraum"). X-ray backlighting of the planar samples was used in both side-on and face-on geometry. The latter required imaging through the halfraum. Side-on images were obtained with both 2-D framing cameras and 1-D streak cameras, depending on the experiment. One goal is to be able to measure RT growth in Be from its inherent grain structure; this requires that the platform be capable of nearly 1000× growth, to increase the structure to observable size and simulate expected NIF conditions. Figure 108.84 shows face-on data for two materials, Be and diamond. The initially imposed 1-D perturbations have grown to measurable size. Figure 108.85 shows a summary of these results for diamond. Analysis and simulations are still ongoing to form a more complete understanding of the processes.
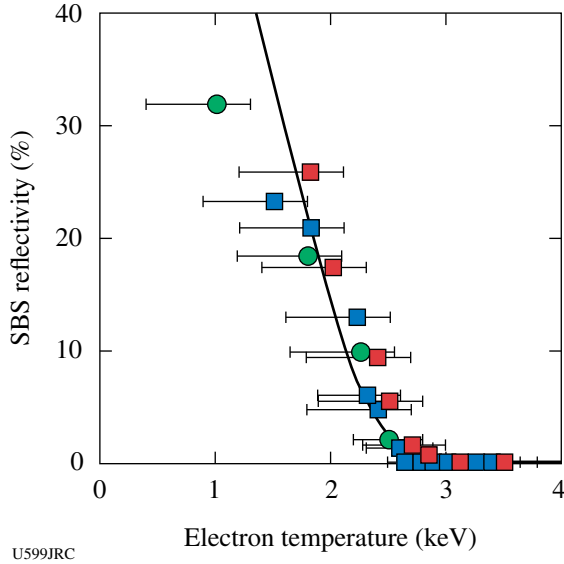

Figure 108.82
Measured SBS reflectivity (points) follows linear gain calculation (solid line) and drops with electron temperature, as predicted. Stimulated Brillouin scattering is reduced to zero for electron temperatures above 2.5 keV.
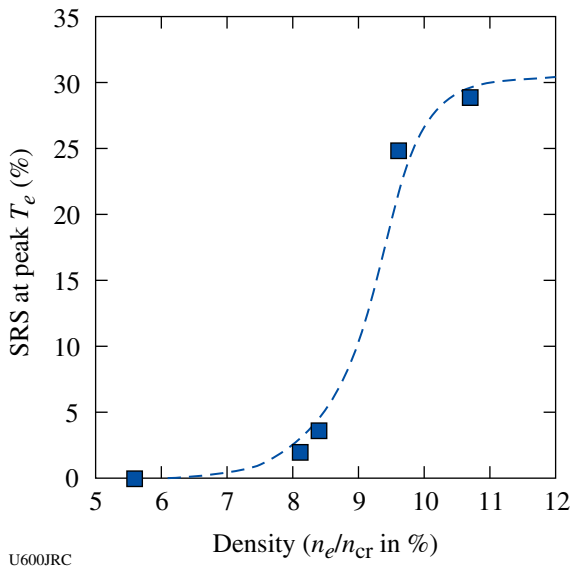

Figure 108.83
Density scaling of SRS at an intensity of 1.5×10^{15} W/cm^{-2}. Raman-scattering levels are consistent with linear gain calculations, varying with electron density for fixed laser intensity.
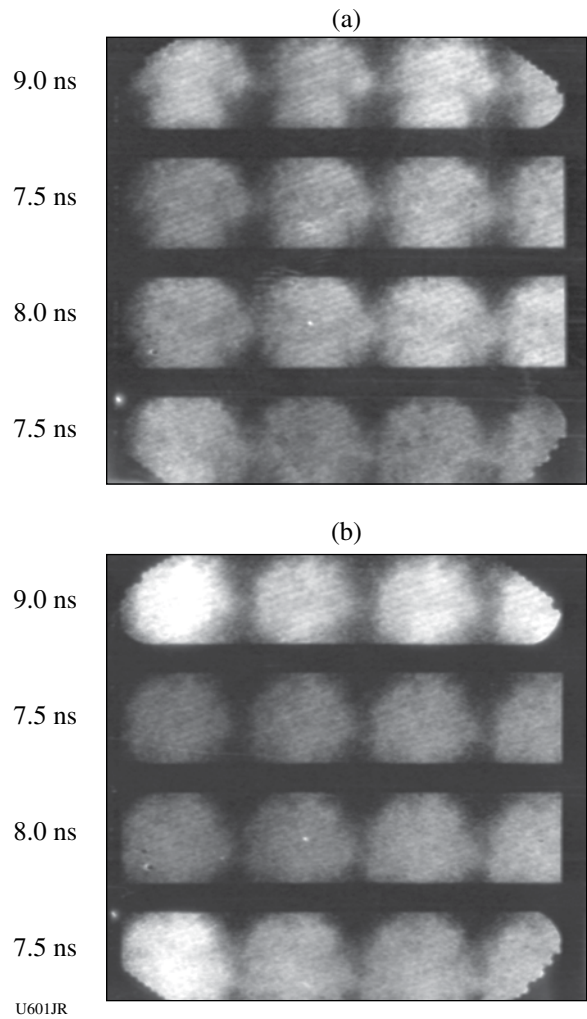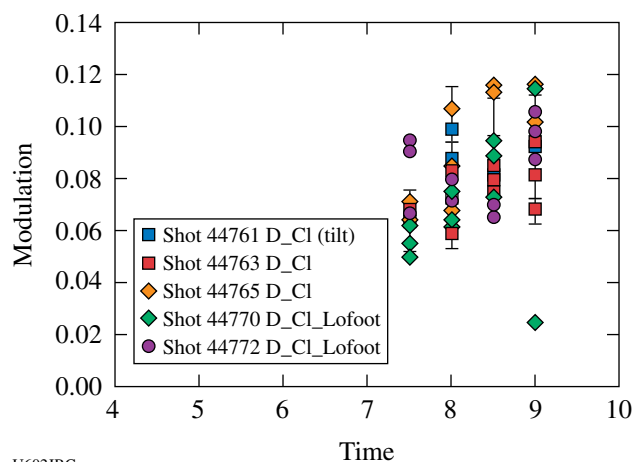

Figure 108.84
X-ray-backlit images of ablatively accelerated planar foils. Observation of large growth of 150-nm amplitude initial perturbations demonstrated (lines running diagonally lower left to upper right) for both (a) carbon (diamond) and (b) Be ablators, as expected, based on previous CH(Ge) results.
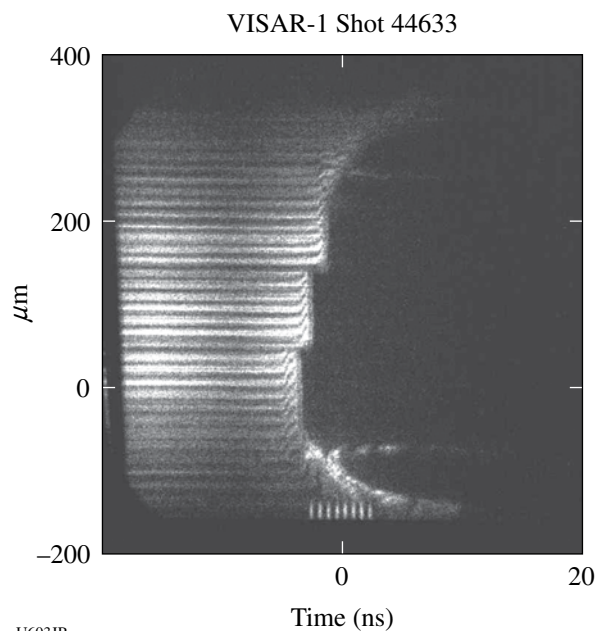
Figure 108.85
Modulation depth for diamond foils (see Fig. 108.84) for various times and laser drives.

Figure 108.86
ASBO data: shocks in Be driven by x rays from window. The abrupt turnoff of the reflected light (fringes) coincides with the time of shock breakout from the three different thicknesses of Be (thinnest at bottom).

A concern with gas-filled hohlraums is that they must, of necessity, have a window to contain the gas. Despite the fact that these windows are thin and low *Z*, they are the first objects irradiated by the laser beams, and they can generate x rays that may affect the capsule. To obtain quantitative data, Be step wedges (planar Be samples with three different thicknesses) were exposed to x rays produced by the interaction of the OMEGA laser with a thin plastic window. The resulting shock and preheating of the Be were measured with the active shock breakout (ASBO) diagnostic. An example of such data is shown in Fig. 108.86. The termination of the fringes (time runs left to right) coincides with the shock breaking out of the rear surface of the three steps (thickest step at top). Still other experiments used the ASBO, VISAR, and streaked optical pyrometer (SOP) to infer changes in the state—specifically, melting points—of Be and diamond, under varying levels of x-ray preheat and shock compression.

A series of implosion experiments modeled NIF fill tubes with a deliberately placed perturbation on the surface of the capsule. The inner layer of the capsule contained a mid-*Z* (Ti) dopant. Under certain conditions, the perturbation resulted in a hydrodynamic jet of material moving through the imploded core. This jet was detected by the x-ray emission from the Ti dopant. While this experiment looked at the effect of the tube above the capsule, another experiment ("planar fill tube"), done in collaboration with LANL, investigated the effect of the fill hole using a planar analog. Initial experiments gave promising results using foams as a stand-in for solid DT and showed a jet of the indirectly driven ablator material propagating through the hole.

One design for x-ray backlighters on the NIF looks like a peaked roof. Several OMEGA shots were carried out with this geometry to ascertain the x-ray conversion efficiency, and also the spatial uniformity, of this design. The results showed these targets capable of meeting the NIF specifications.

High-Energy-Density Science (HEDS) Experiments: Approximately one third of the LLNL OMEGA shots were for HEDS experiments.

One experiment used very small hohlraums to generate a thermal source of x rays at high photon energies, while at the same time examining the laser–plasma interaction issues associated with such targets. Figure 108.87 shows the x-ray spectra from the 10-keV region, along with model calculations for various thermal temperatures.

Late in FY06 LLNL executed a day of experiments using "double-shell" targets. This represented the culmination of extensive target fabrication work; x-ray tomographic images of the targets are shown in Fig. 108.88. The experiment used a variety of diagnostics, such as time-resolved x-ray backlighting, shown in Fig. 108.89. These data are now undergoing detailed analysis.

The nonlocal thermodynamic equilibrium (NLTE) experiments have as their goal the study and understanding of the radiative effects of high-Z (atomic number) dopants on implosions. Capsules containing deuterium, plus dopant gas, were directly driven by the OMEGA laser. Both spectroscopic x-ray and nuclear diagnostics were employed. Figure 108.90 shows the dramatic order-of-magnitude change in secondary neutrons (those arising as a result of tritium being generated in primary

Figure 108.87
Spectroscopic data (gray, shaded area) from small, high-temperature hohlraum are best fit by model calculations (*FLYCHK*) between 7 and 8 keV (between thick and thin solid curves).

nuclear fusion reactions) observed when a small amount of xenon is added. This is indicative of higher densities in the imploded fuel as a result of radiative cooling from the xenon.

Several experiments were carried out to prove the concept of an experimental platform for measuring x-ray opacities in warm, dense matter. These included the development of broadband soft-x-ray backlighters, point backlighters at higher energies, and a hohlraum drive to heat the samples to the desired conditions, along with the necessary diagnostics. These experiments will continue into FY07.

Dynamic hohlraums are directly driven, capsule-within-a-capsule targets. The idea is shown in Fig. 108.91; xenon gas within the outer capsule becomes hot and radiates, causing an x-ray-driven implosion of the inner, deuterium-containing capsule. Data obtained include x-ray-streaked images of the self-emitted x rays, multiple x-ray images, charged-particle information (collaboration with MIT), and multiple standard OMEGA neutron diagnostics. These data are currently being analyzed and compared with simulations.

We continued with our ICE (isentropic compression experiments) in FY06. Various improvements were made to targets, to increase planarity and temporal behavior of the shockless drive. Equation-of-state data were obtained for various materials.

The "shock-sphere" experiment conducted on OMEGA is an example of laboratory astrophysics. In this case, it is model-

Figure 108.88
SiO$_2$ double-shell implosions. 3-D tomography of each double-shell capsule was performed to verify that all capsules meet all required specifications.

SiO$_2$ double-shell implosions
backlit x-ray images (shot 44391)
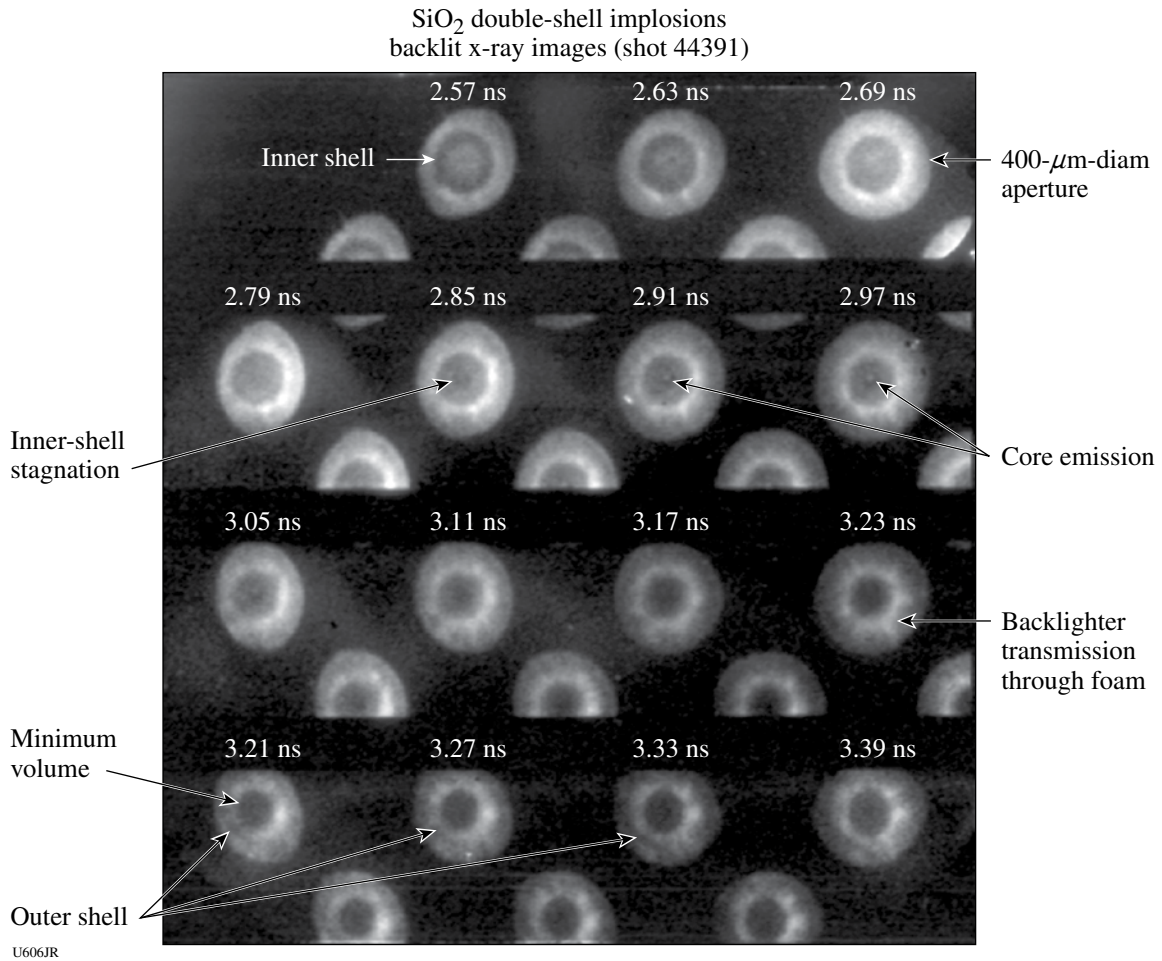
Figure 108.89
Example of backlit x-ray images obtained from double-shell experiments.
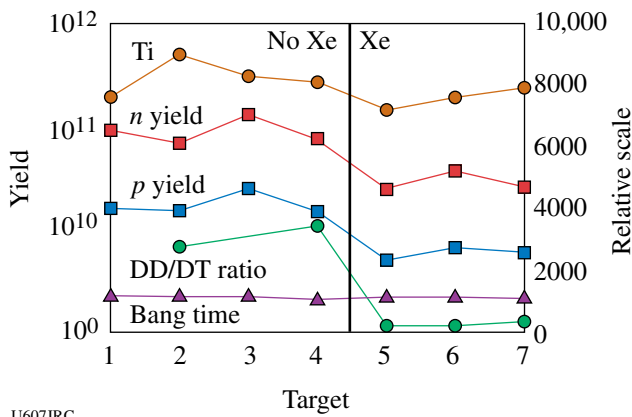
Figure 108.90
Addition of Xe has a significant impact on implosion parameters in NLTE experiments, as shown by neutron data. Note the order-of-magnitude change in DT (secondary) neutrons, due to the radiative cooling by xenon atoms.

Figure 108.91
Concept of "dynamic hohlraum;" Xe gas between shells produces x rays that ablatively implode inner shell.

ing the passage of a shock in low-density material past denser spherical objects and examining how the shock passage induces mixing of material into the interstellar medium. Figure 108.92 shows an example of the data. The laser-generated shock is moving toward the lower left, past the two spherical objects. (The grid is for diagnostic reference.) X-ray backlighting provides images at various times. On the right (at 12 ns) the shock is still visible, just to the r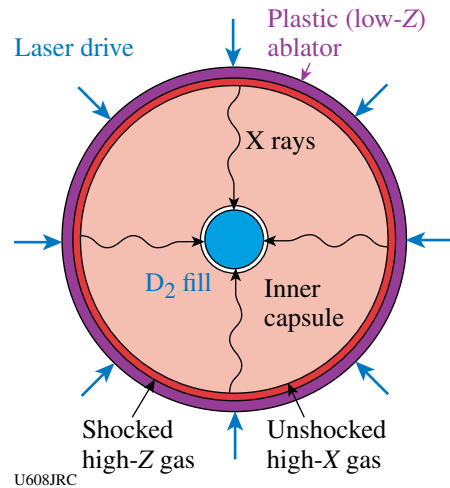ight of the spheres. These data are being used to benchmark model calculations, which will then be applied to astronomical observations for comparison.

Another experiment looked at the propagation of "jets" into a low-density background material ("DDP experiment"), again using x-ray backlighting after lengthy (15- to 35-ns) time delays. The cell size of the low-density material (a copper foam) was

varied, and the results compared to simulations. Figure 108.93 shows a schematic of the experiment and an example of the data. As the jet of material moves upward, vortices form to the left and right ("roll up"), in agreement with hydrodynamic simulations.

Finally, another collaboration (CEA, NRL, and LLNL) used OMEGA shots for x-ray source and effects experiments. Various targets were investigated for their ability to produce copious x rays in the region around 10 keV, as shown in Fig. 108.94.

FY06 LANL OMEGA Experimental Programs

Los Alamos National Laboratory (LANL) successfully fielded a range of experiments on OMEGA during FY06 studying the physics relevant to inertial confinement fusion (ICF) and high-energy-density (HED) science in support of the national
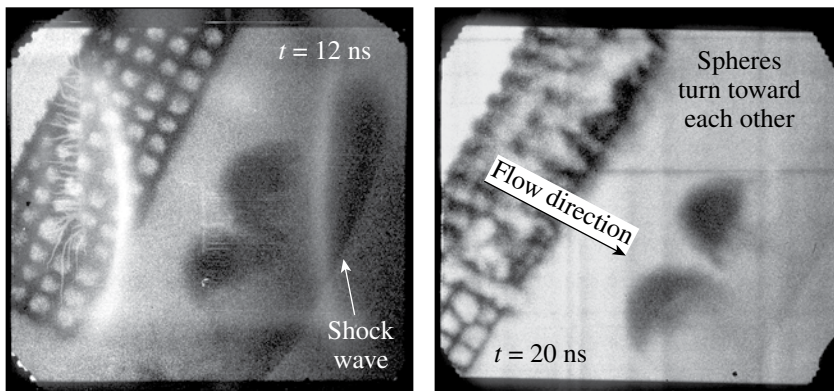
U609JR

Figure 108.92
X-ray-backlit images of shock (visible on right of the right-hand image, moving away from reference grid) and spheres imbedded in the low-density medium. Interacting clouds turn toward each other and eject material downstream after shock passage.
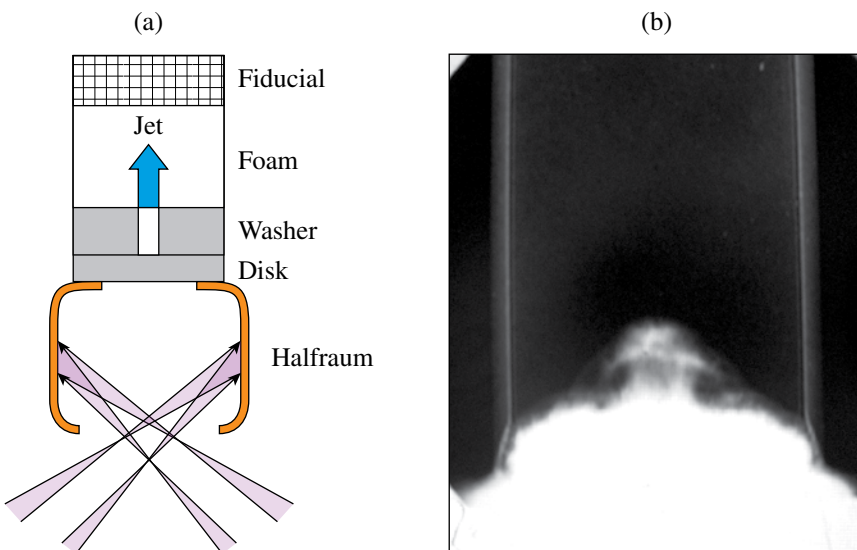
U610JRC

Figure 108.93
(a) Layout of DPP experiment (x-ray backlighting not shown, perpendicular to page through the foam). (b) Data at 15 ns. Note the classic "roll up" of the upward-moving jet.

DMX spectra indicate 80 to 170 J/sphere at 10 keV
and up to 6 kJ/sphere in the 1- to 3-keV band.
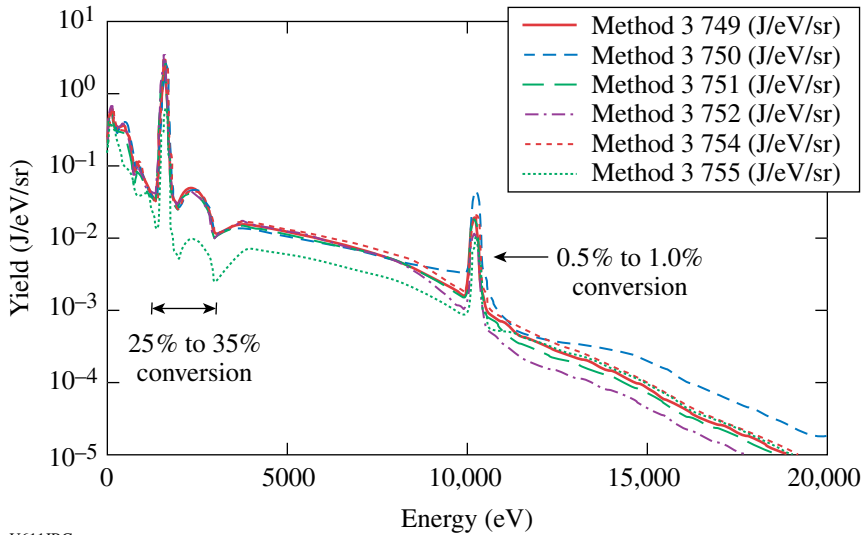
Figure 108.94
Laser and target conditions that optimize the 10-keV x-ray output have been identified.

ignition effort. Many of these experiments were focused on developing underlying physics, diagnostics, and platforms for future experiments on the National Ignition Facility (NIF). LANL conducted a total of 125 target shots on OMEGA. Collaborations with LLNL, LLE, MIT, and AWE remain an important component of LANL's program on OMEGA. With the consolidation of ignition research in the United States into the National Ignition Campaign (NIC), healthy partnerships are required to achieve success in the national scientific objectives.

Off-Hugoniot Heated Hydrodynamics: The off-Hugoniot (OH) campaign continued in FY06 with three days of experiments. High-quality data were obtained on 37 of 39 system shots. These experiments studied material dynamics under heated and shocked conditions. In ignition capsules, defects, arising from the manufacturing process, undergo significant evolution due to heating from Au M-band radiation prior to passage of the main shock. It has not been demonstrated that our hydrocodes accurately capture the physics of this interaction. The OH platform provides the means to study the complex interaction between shocks and heated material.

The OH platform utilizes a beryllium (Be) housing that is coated with a thin layer of tin (Sn). Inside the housing are layers of foam and epoxy. Thirty-three beams strike the tin and produce L-shell radiation that permeates throughout the package, heating the epoxy and foam (Fig. 108.95). A short time later, seven beams launch a strong shock into the foam. As the heated epoxy expands in the foam, the shock interaction with this system is radiographed onto Agfa-D7 film.
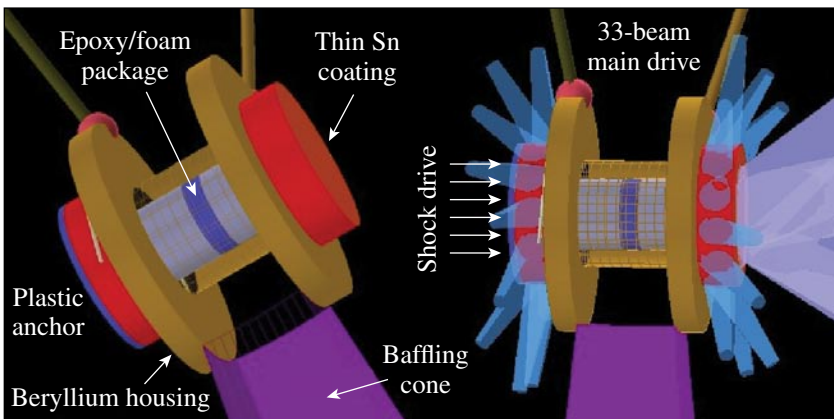
Figure 108.95
The target configuration for the off-Hugoniot experiment. A beryllium housing filled with layers of epoxy and foam is heated by exciting Sn L-shell radiation. The evolution of the epoxy expanding into the foam is imaged via radiography.

An example of the improved data quality is shown in Fig. 108.95. Data from heat-only experiments [Fig. 108.96(a)] clearly show the epo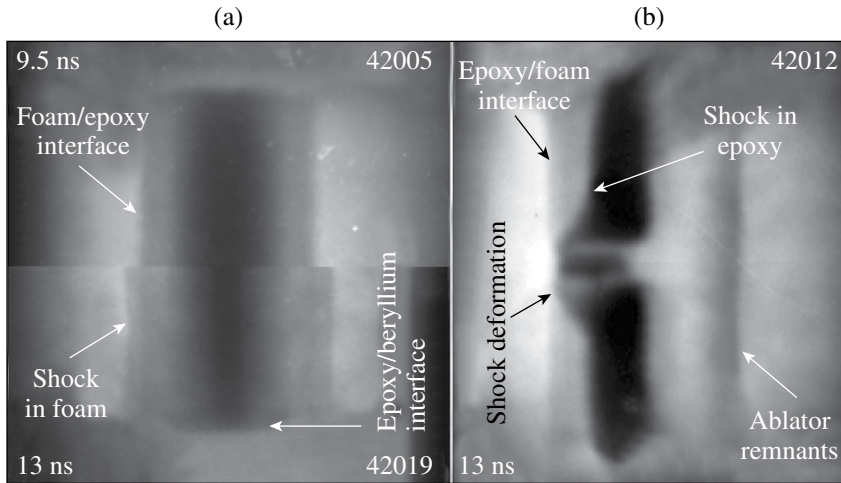xy expansion and shock in the foam. Moreover, the use of the calibrated D7 film allows complete resolution of the evolving density profiles. When a defect is heated and a strong shock is introduced [Fig. 108.96(b)], the residual density perturbations from the healing defect distort the shock front as it propagates through the epoxy. The resulting density profiles and spatial deformation of the shock front provide tight constraints for our ignition design hydrocodes like *RAGE* and *PETRA*.

Inhomogeneous Radiation Flow: Inhomogeneously mixed materials can occur in a variety of environments. Two examples are ICF capsules, where shell material mixes with the fuel and turbulent flows, and astrophysical systems, such as molecular clouds and star-forming regions, where density clumps can form. Models for the transport of radiation in inhomogenously mixed

materials exist, each differing in the statistical treatment of the material mixtures. However, there is little experimental data to test these models. The inhomogeneous radiation flow experiment aims to provide data that can be used to test different models.

Figure 108.97 shows an overview of the experiment. A laser-driven hohlraum is heated to roughly 205 eV, which generates a temperature front. The temperature front propagates through gold-loaded foam, heating it. The soft-emission (~300 eV) of the heated foam is measured to determine the position of the radiation front. Two different gold-doped foams were examined: one loading with gold particles of diameters between 0.3 and 1.0 μm and another with very fine gold particles, diameters less than 0.1 μm.

Figure 108.98 displays preliminary measurements of the temperature-front position (circles) and the simulated trajectory

(a)   (b)

9.5 ns — 42005
Foam/epoxy interface
Shock in foam
13 ns — 42019

Epoxy/foam interface
Shock in epoxy
Epoxy/beryllium interface
Shock deformation
Ablator remnants
13 ns — 42012

U613JR

Figure 108.96
(a) Radiographs of a heated-only, epoxy disk at 9.5 and 13.0 ns after the onset of heating. The deformation in the beryllium/epoxy interface and the shock formed by the epoxy expansion are both clearly visible. (b) Data from a heated and shocked 37.5-μm rectangular gap.

(2) Radiation front propagates through doped foam
(3) Radiation front tracked via soft-x-ray emission
(1) Hohlraum creates radiation front
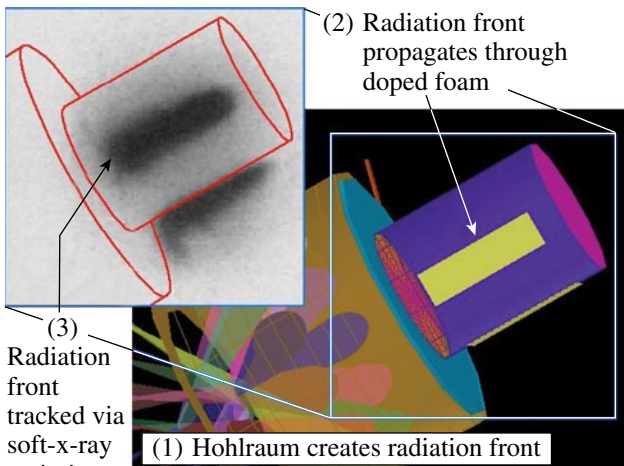
U614JRC

Figure 108.97
Sixteen beams heat a gold hohlraum that produces a radiation front that propagates through the foam. Diagnostic slits allow measurement of the front's progression.

of the temperature front (solid line). The simulation appears to be in good agreement with the data.

Beryllium Fill-Tube Defect Studies: Be shells are impermeable to gaseous and liquid DT. To fill an ICF capsule with a Be shell, a fill tube is used. The fill tube is attached to the shell through a counter-bored fill hole. Fill tubes and fill-tube holes for Be ICF capsules inject shell material into the fuel perturbing the implosion. Mixing between the shell material and the fuel cools the fuel and degrades the efficiency of the ICF capsule.

As part of the LANL/LLNL NIC effort, experiments designed to quantify the amount of Be mass ejected by the jet formed by the fill-tube hole were conducted. These experiments were performed in planar geometry due to complications of fabricating and diagnosing in spherical geometry. This experiment focused on large-aspect-ratio (depth/diameter), from 2 to 20,

holes. The experimental configuration is shown in Fig. 108.99. A hohlraum is heated to 170- to 180-eV temperature. The temperature drive ablates and shocks the 100-μm-thick Be (3% Cu–doped) ablator. The shock ejects some material down the fill-tube hole and also propagates into the Be (3% Cu–doped) washer. The shock in the washer pushes material into the hole that jets into the foam.
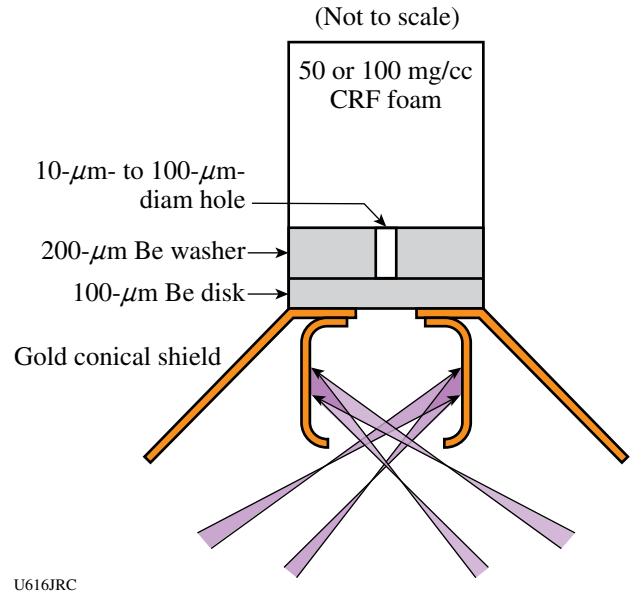
Figure 108.99
A heated gold hohlraum drives a shock into the beryllium disk, creating a jet as the Be is forced out the small hole at the bottom. The Be jet and disk are imaged from two orthogonal directions.

The mass of material jetted into the foam is measured with point-projection radiography at either 4.3 keV or 2.8 keV. Data have been obtained for jets formed by 100-, 50-, 40-, and 30-μm-diam holes. Figure 108.100 shows preliminary data of the jet formed by a 50-μm-diam fill-tube hole. The data were recorded with 4.3-keV x rays, 15 ns after the laser drive. The jet is roughly 170 μm across at the head and approximately 170 μm in length.

High-Z Shell Implosions: Two days of experiments studied the progression from non-LTE to LTE as the dopant gas concentration in a deuterium-filled capsule is increased. The presence of the high-Z dopants increases the radiation losses from the plasma, allowing the plasma to compress to a smaller volume. The physics of ignition and burn in high-Z capsules—specifically the effect of high-Z dopants on energy balance, equilibration, yield, and transport in implosions—is examined with measurements of yield, ρR, T_e, T_i, T_r, and implosion size.
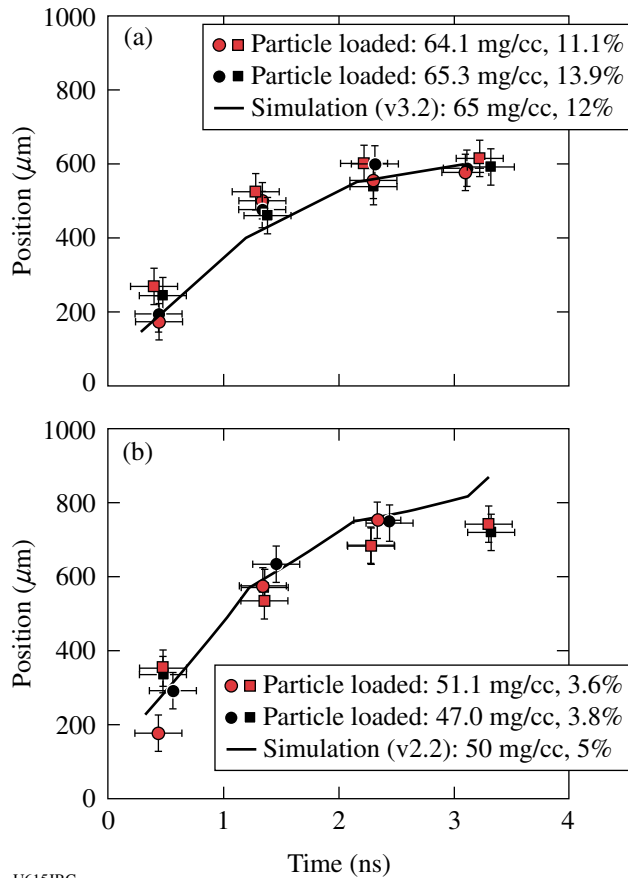

Figure 108.98
Simulations using NYM are in excellent agreement with the two cases examined: (top) 65-mg/cc foam with approximately 12% gold by weight and (bottom) 50-mg/cc foam with 5% gold by weight. [NYM simulations courtesy of M. Taylor (AWE).]

U617JR

Figure 108.100
The jet caused by a 50-μm-diam hole taken 15 ns after onset of the laser drive. Visible are the jet and the shock wave that has passed through the Be. The radiograph was obtained with 4.3-keV x rays.

These experiments used a 5-μm-thick SiO_2 spherical shell of 430-μm radius, filled with 7 atm of deuterium and 3 atm of ^3He. The ^3He allows measurement of the proton spectrum from the D^3He reaction and thus determines the target's ion temperature and ρR. Kr dopants were used as spectroscopic tracers to measure the electron temperature in the plasma from the helium lines. Variation of electron density is achieved by adjusting the Xe gas concentration. The experiments produced a wealth of data that is being used to determine how equilibrium is reached and to validate code calculations (Fig. 108.101).
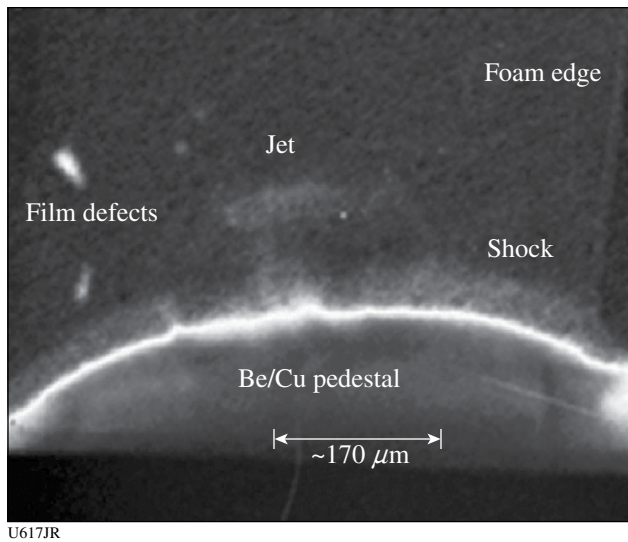
High-Z Dopant Impact in Stimulated Raman Scattering (SRS): Experiments at the Helen laser observed a clear decrease in stimulated Raman backscattered (SRS) light when a small percentage, ~1%–2%, of a high-Z dopant such as Ar or Xe was added to a CH-filled gas-bag target. This experimental observation prompted interest in the phenomenon, especially as a mitigation strategy for reducing SRS in NIF hohlraums. However, the exact physical mechanism of the high-Z dopant effects was unknown, especially the fact that only small amounts of high-Z dopant are required. Theoretical investigation of the effects of high-Z dopants on SRS at LANL found that the addition of high-Z dopants leads to beam spray of the laser via thermally enhanced forward stimulated Brillouin scattering (FSBS). This beam spray causes a reduction is SRS due to a reduction in the spatial coherence of the laser. Thermal effects due to inverse-Bremsstrahlung absorption of the laser have a Z^2 dependence, meaning that a small amount of high-Z

material, compared to the background plasma Z, can have a large effect on the thermal response.

U618JRC
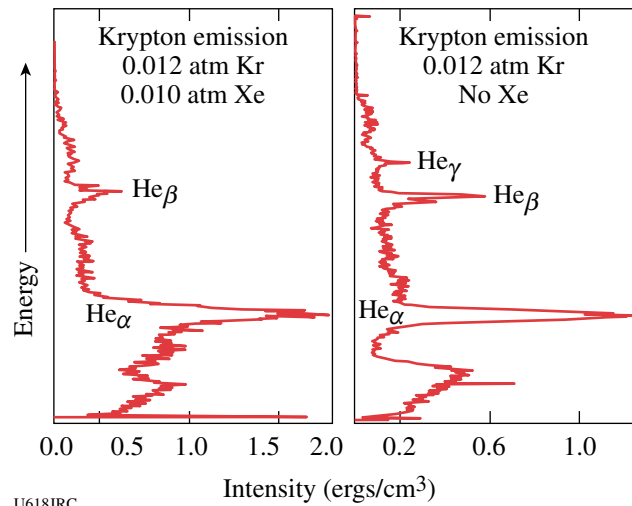
Figure 108.101
13- to 15-keV Krypton spectra of implosions doped (left) and undoped (right) with Xe. The enhanced cooling from Xe emission is observed by the reduction in He$_\gamma$ and He$_\beta$ emission of the Krypton spectra.

Through a strong collaboration by LANL, LLNL, and AWE, experiments were conducted at LLE using C_5H_{12} gas-filled hohlraum targets to validate theory. SRS was measured for various amounts of Xe dopant added to the hohlraum gas fill. As the percentage of Xe dopant exceeded ~5%, SRS from the uniform interior hohlraum plasma region decreased. Figure 108.102 shows that the SRS reflectivity at wavelengths of ~550 nm, corresponding to an electron density of n/n_c ~ 0.11, where n_c is the critical density for 351-nm light, is reduced with the addition of 8.7% Xe compared to that of 3.6% Xe early in the interaction-beam laser pulse. This is an indication that high-Z dopants may affect SRS. However, measurements of the beam spray for the transmitted beam did not change significantly between the two cases. Thus, it is inconclusive whether the effect is due to beam spray or another mechanism such as reabsorption of SRS light via inverse Bremsstrahlung. Interestingly, large amounts of SRS come from the plasma expanding from the hohlraum based on hydrodynamic simulations and the wavelength of SRS at ~520 nm corresponding to an electron density n/n_c ~ 0.06.

In FY07 experiments, the laser intensity will be lowered to values closer to the critical onset intensity for SRS. The theory predicts a stronger effect of high-Z dopants at that intensity. In addition, the SRS reflectivity from the plasma expanding from the hohlraum should be decreased based on past experiments at the NOVA laser.
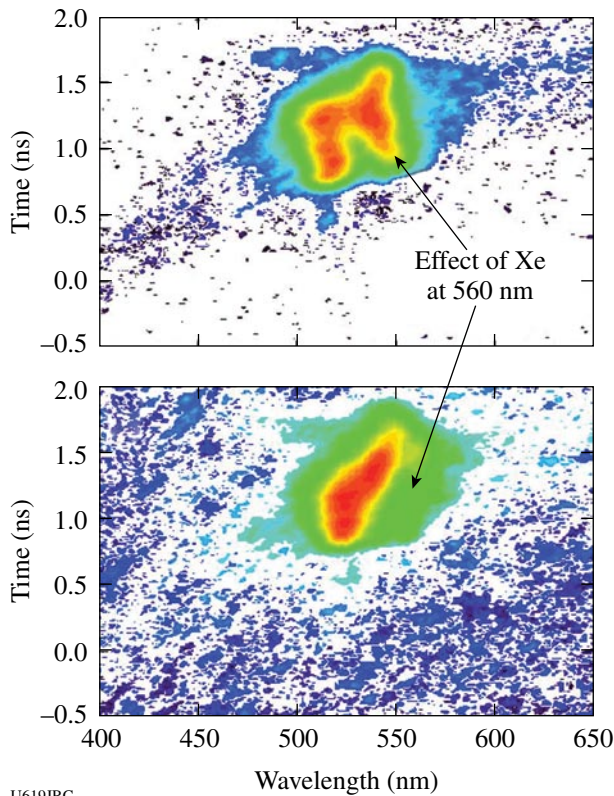
Figure 108.102

SRS spectra with (a) 3.6% and (b) 8.7% Xe dopant added to C_5H_{12} gas-filled hohlraums show a reduction in reflectivity at the interior electron density of $n/n_c \sim 0.11$ (~550 nm). However, most of the SRS reflectivity comes from the plasma expanding from the hohlraum at a lower electron density, $n/n_c \sim 0.06$ (~520 nm).

Gas Cherenkov Detector Development: The Gas Cherenkov Detector (GCD) is a collaborative effort between LANL, AWE, Photek, Inc., and NSTec to develop a fast "bang-time" diagnostic for NIF. The project benefited greatly from the multi-institutional diagnostic development efforts in FY06. Implementation of an ultrafast microchannel plate enhanced time response by a factor of 2.5 to better than 100 ps. This increased bandwidth enabled quality reaction histories of fusion burn using gammas (Fig. 108.103) to be obtained with speeds comparable to or exceeding that of the neutron temporal diagnostic (NTD). Moreover, bang-time measurements, i.e., the time of peak fusion reactivity, were achieved with a precision of 25 ps, when cross calibrated to NTD. This development should allow the gamma bang time/reaction history detector being planned for NIF to easily exceed the NIF system design requirement of 50 ps. The bang-time measurements, shown in Fig. 108.104, were obtained over a three-month period starting in May and ending with the 50/50 DT Cryo shots in July.
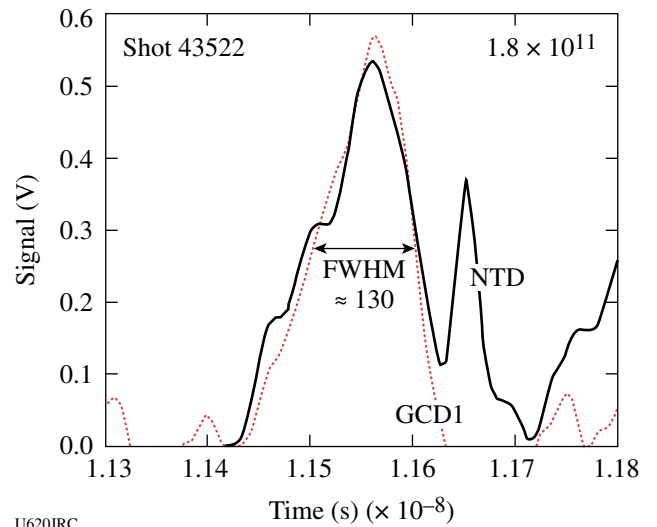
Figure 108.103

Gamma (GCD) and neutron reaction history (NTD) showing the consistency between burn history and peak neutron bang time.
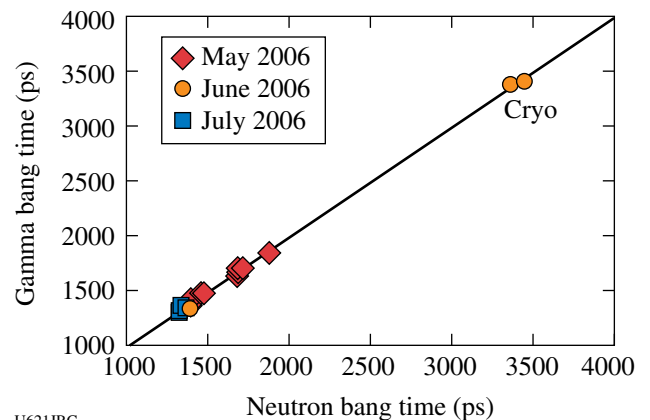
Figure 108.104

Peak-neutron-bang-time measurements of GCD and NTD are consistent over a wide time window.

FY06 Sandia National Laboratories OMEGA Experimental Programs

SNL carried out 30 shots on OMEGA in FY06 including the following experiments:

Beryllium Ablation Rate Measurements in Planar Geometry: For a successful NIF ignition experiment, the ablator mass remaining at the end of the capsule implosion must be in the range of 3%–5% of the original ablator mass. If too much of the ablator burns off, the DT fuel will be preheated and the required fuel ρR cannot be achieved with the absorbed energy of the baseline ignition capsule. If too little of the ablator mass

burns off, the peak implosion velocity will be reduced and the hot-spot energy density will not be adequate for ignition. Thus, it is imperative that the mass ablation rate be known to high precision for the entire range of hohlraum temperatures encountered in the NIF ignition pulse shape. The experimental technique for ablation rate measurements in planar geometry is illustrated in Fig. 108.105 (details in Ref. 9). Basically, ablator samples are placed over an opening on the end of a halfraum. Laser beams enter through the LEH and provide the input power required to maintain the radiation field. The Dante array of K- and L-edge filtered photocathodes views the hohlraum wall through the LEH, and a time- and spectrally resolved measurement of the hohlraum radiation field is obtained from this data. An x-ray framing camera views the interior surface of the ablator sample, and the relative x-ray re-emission of the ablator versus the Au wall is determined. The streaked x-ray imager (SXI) diagnostic views the exterior surface of the abla-tor sample. The SXI employs an imaging slit, a transmission grating, an offset slit, and a streak camera to provide a highly time-resolved streaked image of the x-ray burnthrough flux on the exterior-facing side of the sample (as shown in Fig. 108.105). The combined information from these three measurements over a series of experiments is used to determine the mass ablation rate (mg/cm^2/ns) as a function of hohlraum radiation temperature. In FY06, reduced-scale halfraums and increased SXI magnification were used to extend the ablation rate data for Be and Cu-doped Be into the 200- to 270-eV temperature range. As shown in Fig. 108.106, the measurements have been directly compared to the equivalent mass ablation rate in the baseline NIF ignition capsule calculations.[10–12]
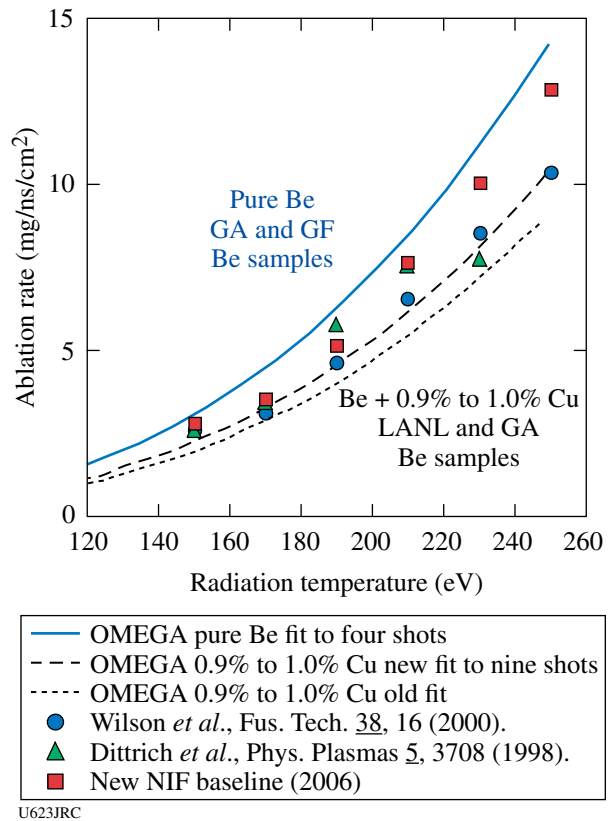
Figure 108.106
Ablation rate plotted as a function of radiation temperature from the OMEGA experiments (solid and dashed lines) and comparison to the baseline NIF capsule calculation. The range in the measured ablation rate seems to depend on view factor and spectrum as well as sample type and dopant concentration. Complete understanding of this data is work in progress.
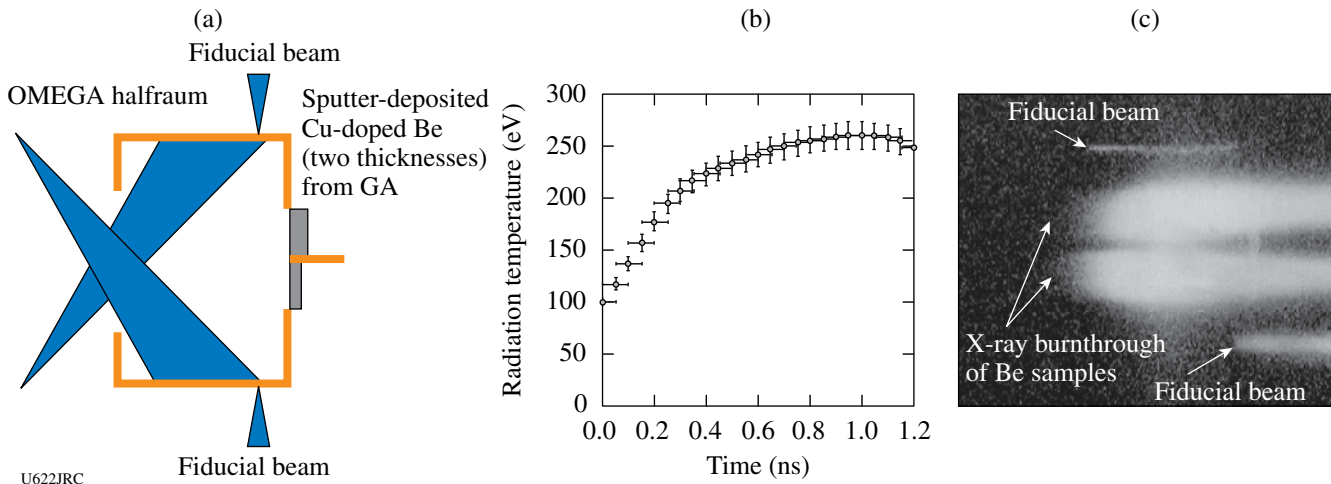
Figure 108.105
(a) Schematic of an ablation-rate measurement experiment. (b) DANTE-derived radiation temperature as a function of time. (c) Sample SXI streaked data showing burnthrough of Be samples.

Beryllium X-Ray Burnthrough and Ablation-Rate Measurements in Convergent Geometry: Since the ignition capsule's radius-time trajectory will vary with the shock-timing adjustments, it will be necessary to experimentally determine the burnthrough/no-burnthrough threshold of an imploding ablator shell and to iterate this burnthrough threshold measurement with the NIF shock-timing experiments. In FY06, SNL performed a series of experiments to develop a convergent ablation rate and burnthrough measurement technique. As illustrated in Fig. 108.107, the convergent burnthrough experiments are a logical extension of the planar ablation rate experiments. In the convergent experiments, a beryllium hemi-shell was mounted in a halfraum. The halfraum was larger than the sizes used in planar experiments, and specific beam-pointing adjustments were required to obtain acceptable capsule illumination symmetry (<±5% in flux). An important diagnostic concern was that pinhole SXI imaging (rather than

slit imaging) was required for the convergent measurement, and a new technique was developed to verify the pointing and alignment accuracy to within ±50 μm. The SXI pinhole imaging setup is illustrated in Fig. 108.108, and the alignment verification technique is illustrated in Fig. 108.109. Key features of the burnthrough and no-burnthrough SXI streaks were verified in the FY06 experiments, and a preliminary unfold of convergent ablation rate was obtained from one of the experiments. Figure 108.110 shows an example x-ray streak image illustrating the spatial and time fiducials and an overlay of computationally simulated ablation-front and implosion features.

VISAR Measurement of Hohlraum Radiation Temperature: In FY05, a new technique for time-resolved measurement of hohlraum radiation temperature was successfully tested in a series of OMEGA experiments.[13] In FY05, we performed a series of experiments to extend the measurement techniques of Ref. 13 to situations in which shaped laser pulses have been used to produce sudden increases in the hohlraum radiation field, resulting in multiple shock fronts that converge within the quartz sample. As can be seen in Fig. 108.111, the interferometer technique appears to work well for this situation. Based on FY06 results, it is conceivable that a new series of Dante-interferometer calibration shots can be used to produce empirical relationships for the situation of multiply shocked quartz.

Development of a NIF Shock-Timing Diagnostic: The x-ray flux absorbed by an indirect-drive ICF capsule consists of a combination of blackbody x rays emitted from the high-Z hohlraum walls and higher-energy (>1 keV) x rays that originate in and near the hot, low-density plasma in which the laser light is absorbed. The high-energy photons can penetrate beyond the capsule. In previous LLE/SNL/LLNL collaborative experiments,[14] we found that, as hohlraum temperatures were increased beyond 135 eV, the ASBO window was preheated and became opaque. In the first half of FY06, the approach was to position the window completely out of the
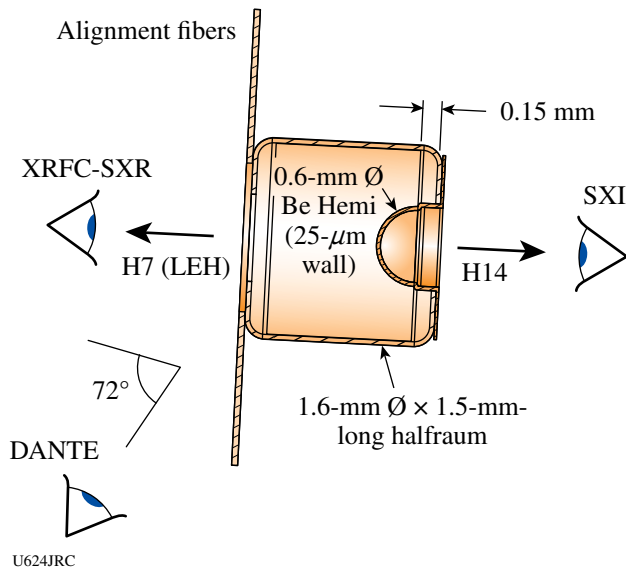
Figure 108.107
Illustration of a convergent burnthrough experiment.
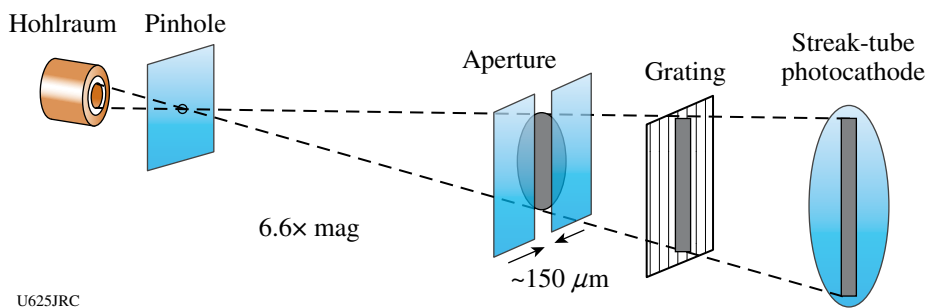
Figure 108.108
Schematic showing SXI pinhole imaging setup.

Preshot *LASNEX* simulation

Straight-
through

Ablated Be
emission

Laser fiducial

Shot 44788

Note: The top laser fiducial is above
the SXI field of view in the data

U626JRC

Straight-through slots verify
±50-μm horizonal alignment

Inside
surface
of Be
hemi

Laser fiducial

25-μm × 1650-μm
SXI field of view
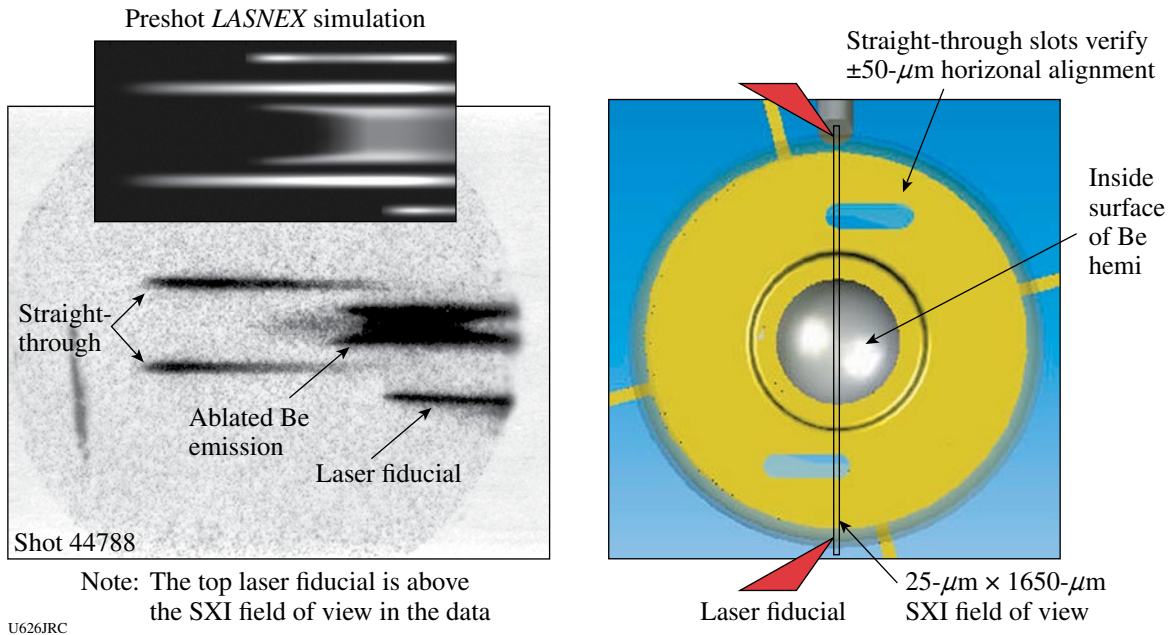
Figure 108.109
Illustration of the alignment verification technique.

OMEGA shot 44788 SXI image

Simulated SXI image
using 44788 Dante Tr

1.0
mm

Overlay
of simulated
ablation front
and stagnation

$t = 0$ ns

$t = 2.5$ ns

U627JRC
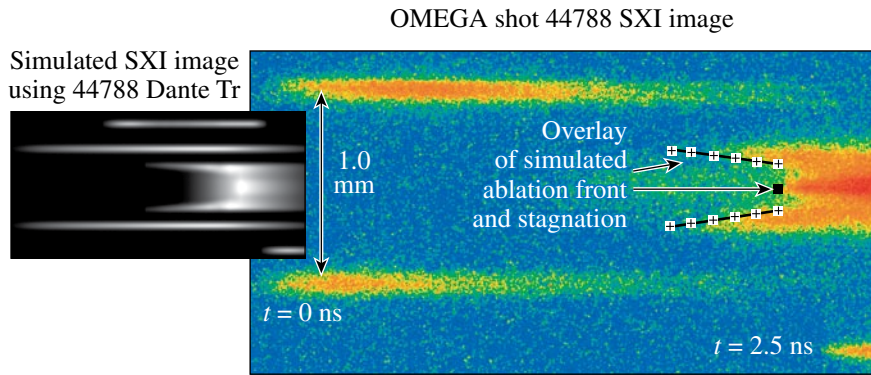
Figure 108.110
Sample SCI data (right) and simulation from a
convergent breakthrough experiment (left).

ASBO

SOP

Tr increasing   Second shock   First shock   Second shock

U628JRC

SOP lineout

First
shock

Second
shock

Normalized intensity

Time (ns)

Figure 108.111
Illustration of the VISAR technique to measure hohlraum radiation temperature.

line of sight of the laser spots in a halfraum geometry. This approach improved the situation and resulted in successful ASBO measurements for halfraum temperatures exceeding 140 eV (see Fig. 108.112). In late FY06, a series of experiments was started in which a NIF-like shock-timing geometry was tested. The first so-called "line-of-sight" hohlraum targets (Fig. 108.113) were designed and assembled at SNL. The targets worked well, but the experimental results indicated that further refinements in the design will be required for a successful shock-timing technique.
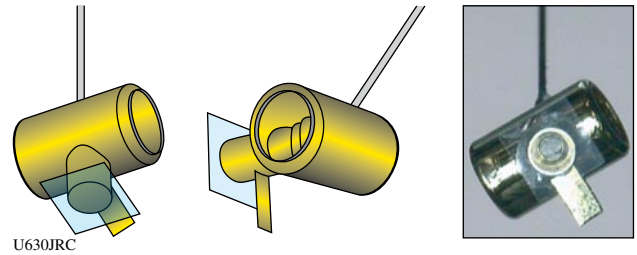
Figure 108.113
Schematic of hohlraum used to test a NIF-like shock-timing geometry.

Figure 108.112
Illustration of successful ASBO measurement in radiation fills exceeding 140 eV.

FY06 CEA OMEGA Experimental Programs

In FY06, CEA carried out 49 target shots on OMEGA on several campaigns including studies of Rayleigh–Taylor instabilities in indirect-drive targets and the implementation of high-resolution x-ray imaging. Some of this work is outlined in this section.

Rayleigh–Taylor Instabilities in Indirect Drive: Mode-Coupling Experiments: Rayleigh–Taylor instabilities in indirect drive have been investigated by CEA on OMEGA since 2002 by using a rugby wall-shaped hohlraum.[15] Rugby hohlraums are, in fact, alternative designs for pre-ignition experiments with reduced energy on LMJ,[16] and the control of symmetry in a rugby hohlraum was also one of the goals of CEA FY06 symmetry experiments. A sketch of a rugby hohlraum is shown in Fig. 108.114 together with a diagram of the experimental configuration used for the RTI experiments. The cavity is heated with 40 beams (pulse shape PS26) in a three-cone (21°, 42°, and 59°) irradiation scheme. The 21° beams propagate across the hohlraum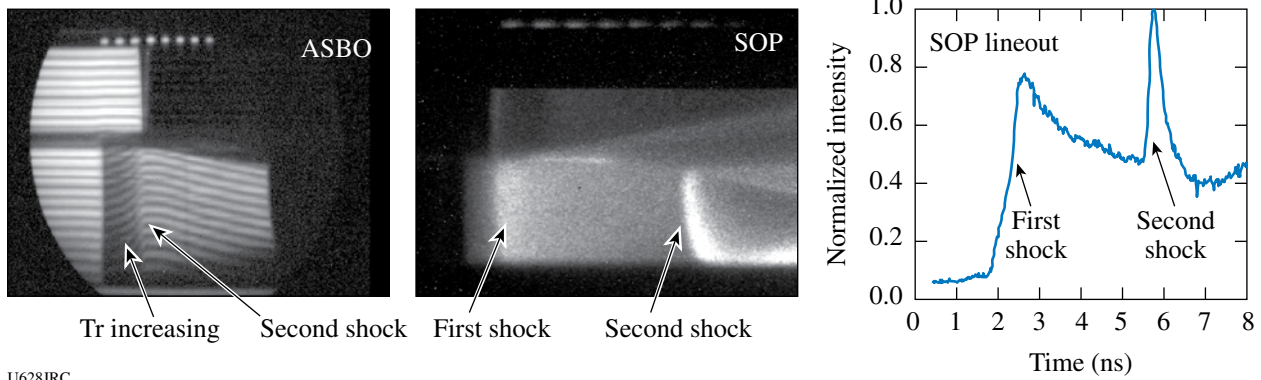 and are absorbed in the slanted part of the wall on the opposite side of the laser entrance hole. Dual-axis radiographies (side-on and face-on) are performed on each shot to measure the foil acceleration and the perturbation growth.

Previous experimental campaigns were devoted to the measurement of single-mode RT growth rate (wavelengths $\lambda =$ 50 and 70 μm) and the study of the feedout mechanism[17] in the case where the modulations were placed on the cold face [rear side, Fig. 108.114(a)] of the radiatively driven plastic foils.

The FY06 campaign focused on mode coupling with germanium-doped foils (CHGe, 2.8% in atomic weight) modulated front side with a two-mode pattern ($\lambda = 35$ and 70 μm). Depending on the relative phase between the two modes (in phase or in opposite phase), one or the other wavelength is predicted to become predominant during the growth. As illustrated in Fig. 108.115, if we compare two face-on pictures taken at the same time after t_0 ($t = 2.7$ ns), one sees clearly on the lineouts that
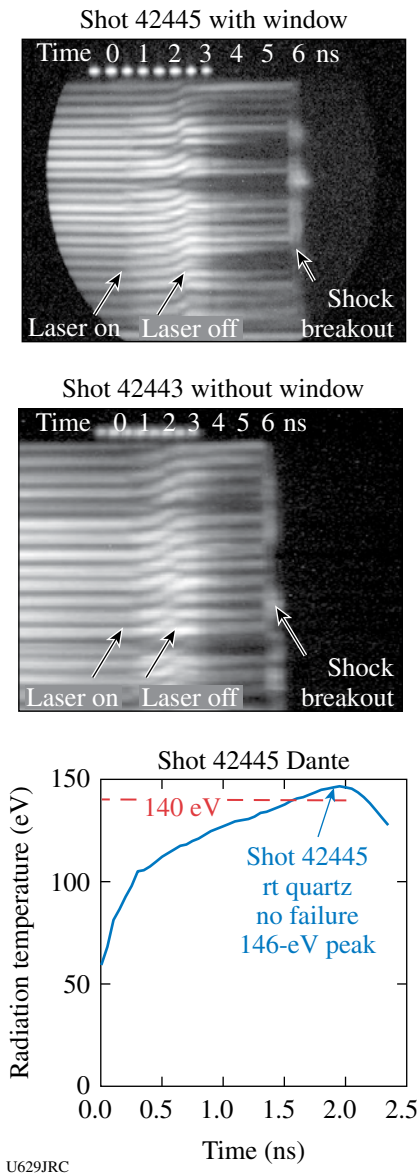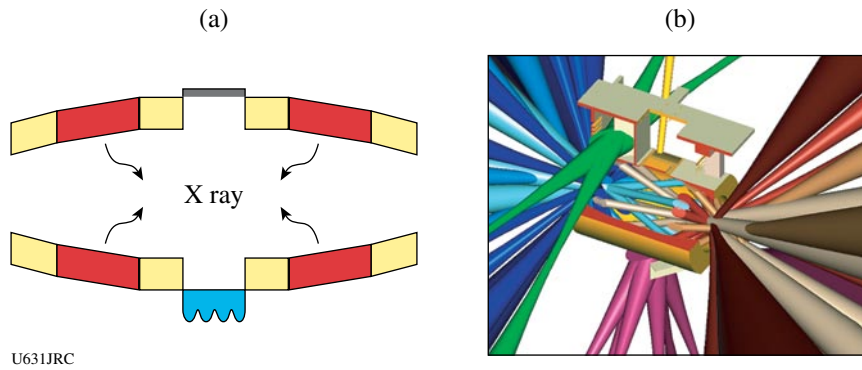
U631JRC

Figure 108.114

(a) Sketch of a rugby hohlraum. (b) Diagram of the configuration for RTI experiments. The 21° beams propagate across the cavity and are absorbed in the slanted part of the wall on the opposite side of the laser entrance hole.
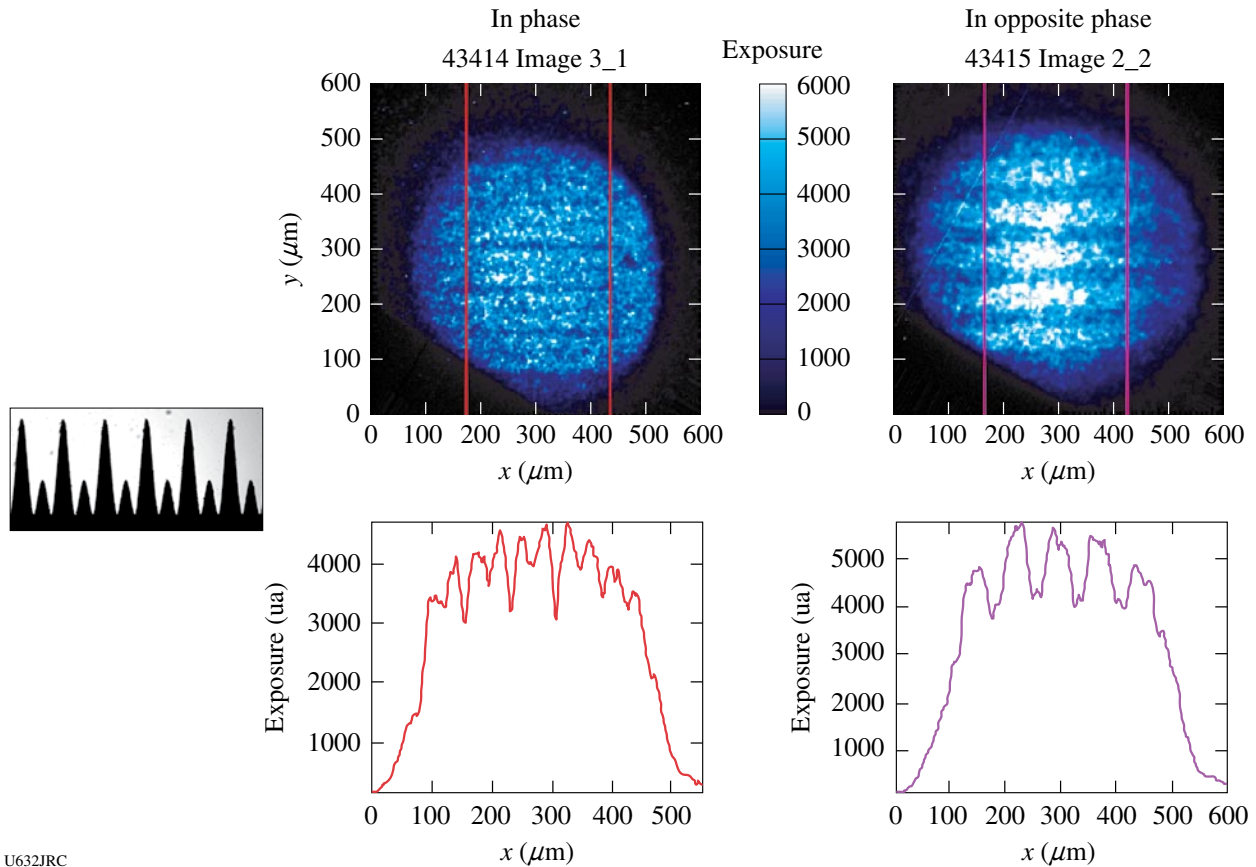
U632JRC

Figure 108.115

Lineouts across two face-on pictures taken at the same time ($t = 2.7$ ns) for the two-mode patterns ($\lambda = 35$ and 70 μm) under study. On the left, in phase pattern with the preponderant $\lambda = 35$-μm mode. On the right, the opposite phase pattern where $\lambda = 70$ μm predominates.

the $\lambda = 35$-μm mode overwhelms the $\lambda = 70$-μm mode for the in-phase case, and inversely for the opposite-phase pattern. As a consequence, the growth of the $\lambda = 35$-μm mode in the opposite-phase pattern is predicted to be delayed in time (due to a phase inversion) in comparison with a pure $\lambda = 35$-μm monomode. This trend is recovered in Fig. 108.116 on the plot showing the evolution of the optical depth versus time for both cases.

High-Resolution X-Ray Imaging (HRXI): For several years, Commissariat à l'Énergie Atomique in France (CEA/DIF Center[18]) has been developing HRXI, a high-resolution, time-resolved, x-ray imaging diagnostic. In FY06, HRXI was implemented and tested for the first time on OMEGA. HRXI combines two state-of-the-art technologies: a high-resolution x-ray microscope and a high-speed x-ray streak camera. The resulting instrument achieves a spatial and temporal resolution of ~5 μm and ~30 ps, respectively. The experimental configuration is shown in Fig. 108.117. The Wolter x-ray microscope for HRXI, used previously on Phebus experiments,[19] consists of two similar off-axis toroidal mirrors. The microscope had a focal length of 218 mm and a magnification ratio of 16. The mirrors were coated with a 30-nm Ni coating (energy cutoff ~6 keV). The microscope features an integrated visible-light alignment system enabling the simultaneous projection of two crosses in the object plane and the image plane.
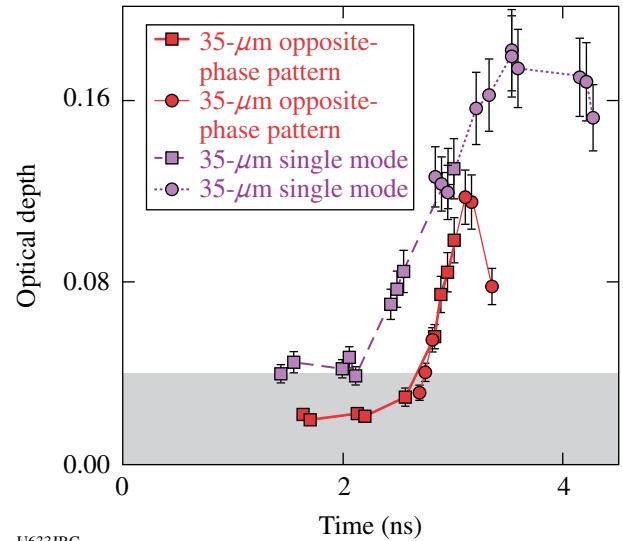
U633JRC

Figure 108.116
Growth (in optical depth) of the $\lambda = 35$-μm mode for the opposite phase pattern (solid symbols) and for a pure monomode perturbation (open symbols).
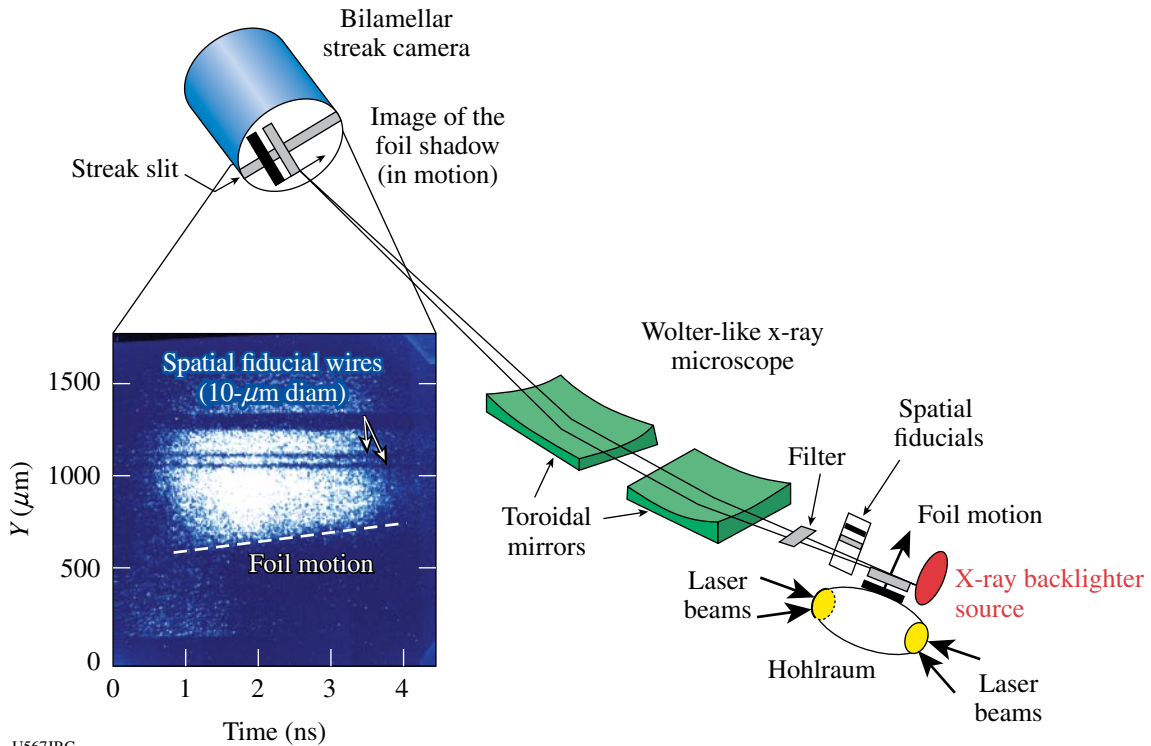
U567JRC

Figure 108.117
HRXI setup with a streaked image recorded during OMEGA shot 43418.

The streak camera includes a bilamellar-type streak tube,[20] which achieves both high temporal (30 ps) and spatial resolution (15 lp/mm). To match to the emitted x-ray backlighter spectrum used for these experiments (Ti foil emission near 4.8 keV), a transmission-mode photocathode was used with a thin CsI coating (10 nm) that was deposited on a self-sustaining CH foil of 800-nm thickness. The streak tube's P20 phosphor screen was read out with a cooled 1340×1300-pixel CCD with a 20-μm pixel size.

HRXI was sucessfully tested for the first time on OMEGA during a joint CEA/DOE-LLE campaign on 27 April 2006. For these tests, HRXI recorded the acceleration of a thin, Ge-doped CH (45-μm) foil driven by radiation from a rugby-wall–shaped hohlraum heated by 40 OMEGA beams with a 2-ns-time-duration, PS26 pulse shape. The foil was accelerated to a velocity of 60 μm/ns. The inset in Fig. 108.117 shows a streak record of the motion of this thin foil in time using a 3-ns x-ray backlighter source. Three test objects were placed close to the foil to assess the spatial resolution of the diagnostic. Two 10-μm-diam wires are clearly visible in the middle and along the streak image, leading to an actual estimated spatial resolution on the streaked image of less than 5 μm.

REFERENCES

1. R. F. Smith *et al*., "Stiff Response in Aluminum Under Ultrafast Shockless Compression up to 110 Gpa," submitted to Physical Review Letters.

2. S. D. Rothman *et al*., J. Phys. D **38**, 733 (2005).

3. R. F. Smith *et al*., "Graded-Density Reservoirs for Accessing High Pressure Low Temperature Material States," to be published in Astrophysics and Space Science.

4. R. Jeanloz, Geophys. Res. Lett. **8**, 1219 (1981).

5. M. H. Rice, R. G. McQueen, and J. M. Walsh, Solid State Phys. **6**, 1 (1958).

6. C. K. Li, F. H. Séguin, J. A. Frenje, J. R. Rygg, R. D. Petrasso, R. P. J. Town, P. A. Amendt, S. P. Hatchett, O. L. Landen, A. J. Mackinnon, P. K. Patel, V. A. Smalyuk, T. C. Sangster, and J. P. Knauer, Phys. Rev. Lett. **97**, 135003 (2006).

7. C. K. Li, F. H. Séguin, J. A. Frenje, J. R. Rygg, R. D. Petrasso, R. P. J. Town, P. A. Amendt, S. P. Hatchett, O. L. Landen, A. J. Mackinnon, P. K. Patel, V. Smalyuk, J. P. Knauer, T. C. Sangster, and C. Stoeckl, Rev. Sci. Instrum. **77**, 10E725 (2006).

8. D. H. Froula *et al*., Phys. Plasmas **13**, 052704 (2006).

9. R. E. Olson, R. J. Leeper, A. Nobile, J. A. Oertel, G. A. Chandler, K. Cochrane, S. C. Dropinski, S. Evans, S. W. Haan, J. L. Kaae, J. P. Knauer, K. Lash, L. P. Mix, A. Nikroo, G. A. Rochau, G. Rivera, C. Russell, D. Schroen, R. J. Sebring, D. L. Tanner, R. E. Turner, and R. J. Wallace, Phys. Plasmas **11**, 2778 (2003).

10. D. C. Wilson *et al*., Fusion Technol. **38**, 16 (2000).

11. T. R. Dittrich *et al*., Phys. Plasmas **5**, 3708 (1998).

12. S. W. Haan *et al*., Fusion Sci. Technol. **49**, 553 (2006).

13. R. E. Olson *et al*., Rev. Sci. Instrum. **77**, 10E523 (2006).

14. R. E. Olson, R. J. Leeper, G. A. Rochau, D. K. Bradley, P. M. Celliers, and T. R. Boehly, J. Phys. IV France **133**, 179 (2006).

15. A. Casner *et al*., J. Phys. IV France **133**, 163 (2006).

16. J. Giorla *et al*., Plasma Phys. Control. Fusion **48**, B75 (2006).

17. D. P. Smitherman *et al*., Phys. Plasmas **6**, 932 (1999).

18. J. L. Bourgade *et al*., CEA/DIF Center, Service SCEP, BP 12, Bruyères le Châtel, 91680, France.

19. Ph. Troussel *et al*., Rev. Sci. Instrum. **76**, 063707 (2005).

20. A. Mens *et al*., in *19th International Congress on High-Speed Photography and Photonics*, edited by B. Garfield and J. Rendell (SPIE, Bellingham, WA, 1990), Vol. 1358, pp. 315–328.

Publications and Conference Presentations

--- **Publications** ---

Y. V. Artemova, G. S. Bisnovatyi-Kogan, I. V. Igumenshchev, and I. D. Novikov, "Black Hole Advective Accretion Disks with Optical Depth Transition," Astrophys. J. **637**, 968 (2006).

R. Betti and C. Zhou, "High-Density and High-ρR Fuel Assembly for Fast-Ignition Inertial Confinement Fusion," Phys. Plasmas **12**, 110702 (2005).

R. Betti and C. Zhou, "Low-Adiabat Implosions for Fast-Ignition Inertial Confinement Fusion," J. Phys. IV France **133**, 379 (2006).

M. Bobeica, D. R. Harding, and R. Q. Gram, "An Experimental Method for Measuring the Response of a Target to the Thermal Environment of the Fusion Reaction Chamber," in the *Twenty-First IEEE/NPSS Symposium on Fusion Engineering 2005* (IEEE, Piscataway, NJ, 2005).

T. R. Boehly, E. Vianello, J. E. Miller, R. S. Craxton, T. J. B. Collins, V. N. Goncharov, I. V. Igumenshchev, D. D. Meyerhofer, D. G. Hicks, P. M. Celliers, and G. W. Collins, "Shock-Timing Experiments Using Double-Pulse Laser Irradiation," Phys. Plasmas **13**, 056303 (2006) (invited).

J. Bromage, J. D. Zuegel, S.-W. Bahk, D. S. Vickery, L. J. Waxer, D. Irwin, V. Bagnoud, R. Boni, M. D. Moore, R. Jungquist, and C. Stoeckl, "High-Intensity Laser Diagnostics for OMEGA EP," J. Phys. IV France **133**, 705 (2006).

J. Bunkenburg, T. J. Kessler, W. Skulski, and H. Huang, "Phase-Locked Control of Tiled-Grating Assemblies for Chirped-Pulse-Amplified Lasers Using a Mach–Zehnder Interferometer," Opt. Lett. **31**, 1561 (2006).

A. C.-A. Chen, J. U. Wallace, S. K.-H. Wei, L. Zeng, S. H. Chen, and T. N. Blanton, "Light-Emitting Organic Materials with Variable Charge Injection and Transport Properties," Chem. Mater. **18**, 204 (2006).

A. C.-A. Chen, J. U. Wallace, L. Zeng, S. K.-H. Wei, and S. H. Chen, "Novel Light-Emitting Organic Materials with Variable Electron and Hole Conductivities," in *Liquid Crystals IX*, edited by I.-C. Khoo (SPIE, Bellingham, WA, 2005), Vol. 5936-18.

D. Clay, D. Poslusny, M. Flinders, S. D. Jacobs, and R. A. Cutler, "Effect of $LiAl_5O_8$ Additions on the Sintering and Optical Transparency of LiAlON," J. Europ. Ceram. Soc. **26**, 1351 (2006).

S. W. Culligan, A. C.-A. Chen, J. U. Wallace, K. P. Klubek, C. W. Tang, and S. H. Chen, "Effect of Hole Mobility Through Emissive Layer on Temporal Stability of Blue Organic Light-Emitting Diodes," Adv. Funct. Mater. **16**, 1481 (2006).

J. E. DeGroote, A. E. Marino, J. P. Wilson, K. E. Spencer, and S. D. Jacobs, "Effects of Nanodiamond Abrasive Friability in Experimental MR Fluids with Phosphate Laser Glass LHG-8 and Other Optical Glasses," in *Optical Manufacturing and Testing VI*, edited by H. P. Stahl (SPIE, Bellingham, WA, 2005), Vol. 5869, pp. 121–132.

J. A. Delettrez, J. Myatt, P. B. Radha, C. Stoeckl, S. Skupsky, and D. D. Meyerhofer, "Hydrodynamic Simulations of Integrated Experiments Planned for the OMEGA/OMEGA EP Laser Systems," Plasma Phys. Control. Fusion **47**, B791 (2005).

D. H. Edgell, R. S. Craxton, L. M. Elasky, D. R. Harding, L. S. Iwan, R. L. Keck, L. D. Lund, S. J. Verbridge, M. D. Wittman, A. Warrick, T. Brown, and W. Seka, "Three-Dimensional Characterization of Cryogenic Target Ice Layers Using Shadowgraph Views," Fusion Sci. Technol. **49**, 616 (2006).

D. H. Edgell, W. Seka, R. S. Craxton, L. M. Elasky, D. R. Harding, R. L. Keck, L. D. Lund, and M. D. Wittman, "Characterization of Cryogenic Direct-Drive ICF Targets During Layering Studies and Just Prior to Shot Time," J. Phys. IV France **133**, 903 (2006).

E. Fess, J. Schoen, M. Bechtold, D. Mohring, and C. Bouvier, "Ultraform Finishing Process for Optical Materials," in *Optical Manufacturing and Testing VI*, edited by H. P. Stahl (SPIE, Bellingham, WA, 2005), Vol. 5869, pp. 88–93.

V. N. Goncharov, O. V. Gotchev, R. L. McCrory, P. W. McKenty, D. D. Meyerhofer, T. C. Sangster, S. Skupsky, and C. Cherfils-Clerouin, "Ablative Richtmyer–Meshkov Instability: Theory and Experimental Results," J. Phys. IV France **133**, 123 (2006).

V. N. Goncharov, O. V. Gotchev, E. Vianello, T. R. Boehly, J. P. Knauer, P. W. McKenty, P. B. Radha, S. P. Regan, T. C. Sangster, S. Skupsky, V. A. Smalyuk, R. Betti, R. L. McCrory, D. D. Meyerhofer, C. Cherfils-Clérouin, "Early Stage of Implosion in Inertial Confinement Fusion: Shock Timing and Perturbation Evolution," Phys. Plasmas **13**, 012702 (2006).

O. V. Gotchev, V. N. Goncharov, J. P. Knauer, T. R. Boehly, T. J. B. Collins, R. Epstein, P. A. Jaanimagi, and D. D. Meyerhofer, "Test of Thermal Transport Models through Dynamic Overpressure Stabilization of Ablation-Front Perturbation Growth in Laser-Driven CH Foils," Phys. Rev. Lett. **96**, 115005 (2006).

D. R. Harding, D. D. Meyerhofer, S. J. Loucks, L. D. Lund, R. Janezic, L. M. Elasky, T. H. Hinterman, D. H. Edgell, W. Seka, M. D. Wittman, R. Q. Gram, D. Jacobs-Perkins, R. Early, T. Duffy, and M. J. Bonino, "Forming Cryogenic Targets for Direct-Drive Experiments," Phys. Plasmas **13**, 056316 (2006) (invited).

D. R. Harding, T. C. Sangster, D. D. Meyerhofer, P. W. McKenty, L. D. Lund, L. Elasky, M. D. Wittman, W. Seka, S. J. Loucks, R. Janezic, T. H. Hinterman, D. H. Edgell, D. Jacobs-Perkins, and R. Q. Gram, "Producing Cryogenic Deuterium Targets for Experiments on OMEGA," Fusion Sci. Technol. **48**, 1299 (2005).

M. Haurylau, S. P. Anderson, K. L. Marshall, and P. M. Fauchet, "Electrical Modulation of Silicon-Based Two-Dimensional Photonic Bandgap Structures," Appl. Phys. Lett. **88**, 061103 (2006).

M. Haurylau, S. P. Anderson, K. L. Marshall, and P. M. Fauchet, "Electrical Tuning of Photonic-Bandgap Structures in Silicon," SPIE Newsroom, *Nanotechnology*, April 2006, http://newsroom.spie.org.

M. Haurylau, S. P. Anderson, K. L. Marshall, and P. M. Fauchet, "Electrical Tuning of Silicon-Based 2-D Photonic Bandgap Structures," in *Tuning the Optical Response of Photonic Bandgap Structures II*, edited by P. M. Fauchet and P. V. Braun (SPIE, Bellingham, WA, 2005), Vol. 5926, pp. 15–24.

I. V. Igumenshchev, "Three-Dimensional Simulations of Spherical Accretion Flows with Small-Scale Magnetic Fields," Astrophys. J. **649**, 361 (2006).

A. Jukna, I. Barboy, G. Jung, A. Abrutis, X. Li, D. Wang, and R. Sobolewski, "Electric Transport Properties of $YBa_2Cu_3O_{7-\delta}$ Thin-Film Bridges with Laser-Written Channels of Easy Vortex Motion," J. Appl. Phys. **99**, 113902 (2006).

A. Jukna, I. Barboy, G. Jung, S. S. Banerjee, Y. Myasoedov, V. Plausinaitiene, A. Abrutis, X. Li, D. Wang, and R. Sobolewski, "Laser Processed Channels of Easy Vortex Motion in $YBa_2Cu_3O_{7-\delta}$ Films," Appl. Phys. Lett. **87**, 192504 (2005).

J. Keck, J. B. Oliver, T. J. Kessler, H. Huang, J. Barone, J. Hettrick, A. L. Rigatti, T. Hoover, K. L. Marshall, A. W. Schmid, A. Kozlov, and T. Z. Kosc, "Manufacture and Development of Multilayer Diffraction Gratings," in *Laser-Induced Damage in Optical Materials: 2005*, edited by G. J. Exarhos, A. H. Guenther, K. L. Lewis, D. Ristau, M. J. Soileau, and C. J. Stolz (SPIE, Bellingham, WA, 2005), Vol. 5991, pp. 443–448.

J. H. Kelly, L. J. Waxer, V. Bagnoud, I. A. Begishev, J. Bromage, B. E. Kruschwitz, T. J. Kessler, S. J. Loucks, D. N. Maywar, R. L. McCrory, D. D. Meyerhofer, S. F. B. Morse, J. B. Oliver, A. L. Rigatti, A. W. Schmid, C. Stoeckl, S. Dalton, L. Folnsbee, M. J. Guardalben, R. Jungquist, J. Puth, M. J. Shoup III, D. Weiner, and J. D. Zuegel, "OMEGA EP: High-Energy Petawatt Capability for the OMEGA Laser Facility," J. Phys. IV France **133**, 75 (2006).

C. Kim, A. Trajkovska, J. U. Wallace, and S. H. Chen, "New Insight into Photoalignment of Liquid Crystals on Coumarin-Containing Polymer Films," Macromolecules **39**, 3817 (2006).

A. K. Knight and D. R. Harding, "Modeling Polymer Vapor Deposition: PMDA-ODA Poly(amic Acid)," Fusion Sci. Technol. **49**, 728 (2006).

A. Korneev, O. Minaeva, I. Rubtsova, I. Milostnaya, G. Chulkova, B. Voronov, K. Smirnov, V. Seleznev, G. Gol'tsman,

A. Pearlman, W. Słysz, A. Cross, P. Alvarez, A. Verevkin, R. Sobolewski, "Superconducting Single-Photon Ultrathin NbN Film Detector," Quantum Electron. **35**, 698 (2005).

B. E. Kruschwitz, R. Jungquist, J. Qiao, S. Abbey, S. E. Dean, D. N. Maywar, M. D. Moore, L. J. Waxer, and M. E. Wilson, "Large-Aperture Deformable Mirror Correction of Tiled-Grating Wavefront Error," J. Phys. IV France **133**, 645 (2006).

S. I. Kudryashov, S. D. Allen, S. Papernov, and A. W. Schmid, "Nanoscale Laser-Induced Spallation in SiO_2 Films Containing Gold Nanoparticles," Appl. Phys. B **82**, 523 (2006).

C. K. Li and R. D. Petrasso, "Energy Deposition of MeV Electrons in Compressed Target of Fast-Ignition Inertial Confinement Fusion," Phys. Plasmas **13**, 056314 (2006).

C. K. Li and R. D. Petrasso, "Stopping, Straggling, and Blooming of Directed Energetic Electrons in Hydrogenic and Arbitrary-Z Plasmas," Phys. Rev. E **73**, 016402 (2006).

S. G. Lukishova, N. Lepeshkin, R. W. Boyd, and K. L. Marshall, "Far-Field Patterns from Dye-Doped Planar-Aligned Nematic Liquid Crystals Under Nanosecond Laser Irradiation," Mol. Cryst. Liq. Cryst. **453**, 393 (2006).

S. G. Lukishova, R. P. Knox, P. Freivald, A. McNamara, R. W. Boyd, C. R. Stroud, Jr., A. W. Schmid, and K. L. Marshall, "Single-Photon Source for Quantum Information Based on Single Dye Molecule Fluorescence in Liquid Crystal Host," Mol. Cryst. Liq. Cryst. **454**, 403 (2006).

S. G. Lukishova and A. W. Schmid, "Near-Field Optical Microscopy of Defects in Cholesteric Oligomeric Liquid Crystal Films," Mol. Cryst. Liq. Cryst. **454**, 417 (2006).

J. R. Marciante and J. D. Zuegel, "High-Gain, Polarization-Preserving, Yb-Doped Fiber Amplifier for Low-Duty-Cycle Pulse Amplification," Appl. Opt. **45**, 6798 (2006).

J. A. Marozas, F. J. Marshall, R. S. Craxton, I. V. Igumenshchev, S. Skupsky, M. J. Bonino, T. J. B. Collins, R. Epstein, V. Yu. Glebov, D. Jacobs-Perkins, J. P. Knauer, R. L. McCrory, P. W. McKenty, D. D. Meyerhofer, S. G. Noyes, P. B. Radha, T. C. Sangster, W. Seka, and V. A. Smalyuk, "Polar-Direct-Drive Simulations and Experiments," Phys. Plasmas **13**, 056311 (2006) (invited).

F. J. Marshall, R. S. Craxton, M. J. Bonino, R. Epstein, V. Yu. Glebov, D. Jacobs-Perkins, J. P. Knauer, J. A. Marozas, P. W. McKenty, S. G. Noyes, P. B. Radha, W. Seka, S. Skupsky, and V. A. Smalyuk, "Polar-Direct-Drive Experiments on OMEGA," J. Phys. IV France **133**, 153 (2006).

K. L. Marshall, K. Adelsberger, B. Kolodzie, G. Mhyre, and D. W. Griffin, "A Second-Generation, Liquid Crystal Phase-Shifting Point-Diffraction Interferometer Employing Structured Substrates," in *Optical Diagnostics*, edited by L. M. Hanssen and P. V. Farrell (SPIE, Bellingham, WA, 2005), Vol. 5880, pp. 103–114.

K. L. Marshall, K. Adelsberger, G. Myhre, and D. W. Griffin, "The LCPDI: A Compact and Robust Phase-Shifting, Point-Diffraction Interferometer Based on Dye-Doped LC Technology," Mol. Cryst. Liq. Cryst. **454**, 23 (2006).

K. L. Marshall, G. Painter, K. Lotito, A. G. Noto, and P. Chang, "Transition Metal Dithiolene Near-IR Dyes and Their Applications in Liquid Crystal Devices," Mol. Cryst. Liq. Cryst. **454**, 47 (2006) (invited).

K. L. Marshall, A. Trajkovska-Petkoska, T. Z. Kosc, and S. D. Jacobs, "Polymer Cholesteric Liquid Crystal (PCLC) Flake/Fluid Host Suspensions: A Novel Electro-Optical Medium for Reflective Color Display Applications," in *EuroDisplay 2005* (Society for Information Display, San Jose, CA, 2005), pp. 552–554.

R. L. McCrory, D. D. Meyerhofer, S. J. Loucks, S. Skupsky, R. Betti, T. R. Boehly, T. J. B. Collins, R. S. Craxton, J. A. Delettrez, D. H. Edgell, R. Epstein, K. A. Fletcher, C. Freeman, J. A. Frenje, V. Yu. Glebov, V. N. Goncharov, D. R. Harding, I. V. Igumenshchev, R. L. Keck, J. D. Kilkenny, J. P. Knauer, C. K. Li, J. Marciante, J. A. Marozas, F. J. Marshall, A. V. Maximov, P. W. McKenty, S. F. B. Morse, J. Myatt, S. Padalino, R. D. Petrasso, P. B. Radha, S. P. Regan, T. C. Sangster, F. H. Séguin, W. Seka, V. A. Smalyuk, J. M. Soures, C. Stoeckl, B. Yaakobi, and J. D. Zuegel, "Progress in Direct-Drive Inertial Confinement Fusion Research at the Laboratory for Laser Energetics," J. Phys. IV France **133**, 59 (2006).

R. L. McCrory, S. P. Regan, S. J. Loucks, D. D. Meyerhofer, S. Skupsky, R. Betti, T. R. Boehly, R. S. Craxton, T. J. B. Collins, J. A. Delettrez, D. Edgell, R. Epstein, K. A. Fletcher, C. Freeman, J. A. Frenje, V. Yu. Glebov, V. N. Goncharov, D. R. Harding, I. V. Igumenshchev, R. L. Keck, J. D. Kilkenny, J. P. Knauer, C. K. Li, J. Marciante, J. A. Marozas, F. J. Marshall, A. V. Maximov, P. W. McKenty, J. Myatt, S. Padalino, R. D. Petrasso, P. B. Radha, T. C. Sangster, F. H. Séguin, W. Seka, V. A. Smalyuk, J. M. Soures, C. Stoeckl, B. Yaakobi, and J. D. Zuegel, "Direct-Drive Inertial Confinement Fusion Research

at the Laboratory for Laser Energetics: Charting the Path to Thermonuclear Ignition," Nucl. Fusion **45**, S283 (2005).

M. Mikulics, S. Wu, M. Marso, R. Adam, A. Förster, A. van der Hart, P. Kordoš, H. Lüth, and R. Sobolewski, "Ultrafast and Highly Sensitive Photodetectors With Recessed Electrodes Fabricated on Low-Temperature-Grown GaAs," IEEE Photonics Technol. Lett. **18**, 820 (2006).

A. G. Noto and K. L. Marshall, "Application of Computational Chemistry Methods to the Prediction of Chirality and Helical Twisting Power in Liquid Crystal Systems," in *Liquid Crystals IX*, edited by I.-C. Khoo (SPIE, Bellingham, WA, 2005), Vol. 5936-27.

A. V. Okishev, K. P. Dolgaleva, and J. D. Zuegel, "Experimental Optimization of Diode-Pumped Yb:GdCOB Laser Performance for Broadband Amplification at 1053 nm," in *International Conference on Lasers, Applications, and Technologies 2005: Advanced Lasers and Systems*, edited by G. Huber, V. Ya. Panchenko, and I. A. Scherbakov (SPIE, Bellingham, WA, 2006), Vol. 6054, pp. 124–127.

A. V. Okishev, R. G. Roides, I. A. Begishev, and J. D. Zuegel, "All-Solid-State, Diode-Pumped, Multiharmonic Laser System for a Timing Fiducial," in *International Conference on Lasers, Applications, and Technologies 2005: High-Power Lasers and Applications*, edited by W. L. Bohn, V. S. Golubev, A. A. Ionin, and V. Ya. Panchenko (SPIE, Bellingham, WA, 2006), Vol. 6053, pp. 141–147.

J. B. Oliver, T. J. Kessler, H. Huang, J. Keck, A. L. Rigatti, A. W. Schmid, A. Kozlov, and T. Z. Kosc, "Thin-Film Design for Multilayer Diffraction Gratings," in *Laser-Induced Damage in Optical Materials: 2005*, edited by G. J. Exarhos, A. H. Guenther, K. L. Lewis, D. Ristau, M. J. Soileau, and C. J. Stolz (SPIE, Bellingham, WA, 2005), Vol. 5991, pp. 402–408.

J. B. Oliver, A. L. Rigatti, J. D. Howe, J. Keck, J. Szczepanski, A. W. Schmid, S. Papernov, A. Kozlov, and T. Z. Kosc, "Thin-Film Polarizers for the OMEGA EP Laser System," in *Laser-Induced Damage in Optical Materials: 2005*, edited by G. J. Exarhos, A. H. Guenther, K. L. Lewis, D. Ristau, M. J. Soileau, and C. J. Stolz (SPIE, Bellingham, WA, 2005), Vol. 5991, pp. 394–401.

J. B. Oliver and D. Talbot, "Optimization of Deposition Uniformity for Large-Aperture National Ignition Facility Substrates in a Planetary Rotation System," Appl. Opt. **45**, 3097 (2006).

S. Papernov, A. W. Schmid, A. L. Rigatti, J. B. Oliver, and J. D. Howe, "Damage Behavior of HfO$_2$ Monolayer Film Containing Gold Nanoparticles as Artificial Absorbing Defects," in *Laser-Induced Damage in Optical Materials: 2005*, edited by G. J. Exarhos, A. H. Guenther, K. L. Lewis, D. Ristau, M. J. Soileau, and C. J. Stolz (SPIE, Bellingham, WA, 2005), Vol. 5991, pp. 429–435.

O. Sadot, V. A. Smalyuk, J. A. Delettrez, D. D. Meyerhofer, T. C. Sangster, R. Betti, V. N. Goncharov, and D. Shvarts, "Observation of Self-Similar Behavior of the 3D, Nonlinear Rayleigh–Taylor Instability," Phys. Rev. Lett. **95**, 265001 (2005).

F. H. Séguin, J. L. DeCiantis, J. A. Frenje, C. K. Li, J. R. Rygg, C. D. Chen, R. D. Petrasso, J. A. Delettrez, S. P. Regan, V. A. Smalyuk, V. Yu. Glebov, J. P. Knauer, F. J. Marshall, D. D. Meyerhofer, S. Roberts, T. C. Sangster, C. Stoeckl, K. Mikaelian, H. S. Park, H. F. Robey, and R. E. Tipton, "Measured Dependence of Nuclear Burn Region Size on Implosion Parameters in Inertial Confinement Fusion Experiments," Phys. Plasmas **12**, 082704 (2006).

W. T. Shmayda, S. J. Loucks, R. Janezic, T. W. Duffy, D. R. Harding, and L. D. Lund, "Tritium Operations at the Laboratory for Laser Energetics," Fusion Sci. Technol. **49**, 851 (2006).

S. Skupsky, R. S. Craxton, F. J. Marshall, R. Betti, T. J. B. Collins, R. Epstein, V. N. Goncharov, I. V. Igumenshchev, J. A. Marozas, P. W. McKenty, P. B. Radha, J. D. Kilkenny, D. D. Meyerhofer, T. C. Sangster, and R. L. McCrory, "Polar Direct Drive—Ignition at 1 MJ," J. Phys. IV France **133**, 233 (2006).

W. Słysz, M. Węgrzecki, J. Bar, P. Grabiec, M. Górska, V. Zwiller, C. Latta, P. Bohi, I. Milostnaya, O. Minaeva, A. Antipov, O. Okunev, A. Korneev, K. Smirnov, B. Voronov, N. Kaurova, G. Gol'tsman, A. Pearlman, A. Cross, I. Komissarov, A. Verevkin, and R. Sobolewski, "Fiber-Coupled Single-Photon Detectors Based on NbN Superconducting Nanostructures for Practical Quantum Cryptography and Photon-Correlation Studies," Appl. Phys. Lett. **88**, 261113 (2006).

V. A. Smalyuk, O. Sadot, R. Betti, V. N. Goncharov, J. A. Delettrez, D. D. Meyerhofer, S. P. Regan, T. C. Sangster, and D. Shvarts, "Rayleigh–Taylor Growth Measurements of Three Dimensional Modulations in a Nonlinear Regime," Phys. Plasmas **13**, 056312 (2006) (invited).

V. A. Smalyuk, O. Sadot, J. A. Delettrez, D. D. Meyerhofer, S. P. Regan, and T. C. Sangster, "Fourier-Space Nonlinear Rayleigh–

Taylor Growth Measurements of 3D Laser-Imprinted Modulations in Planar Targets," Phys. Rev. Lett. **95**, 215001 (2005).

C. Stoeckl, T. R. Boehly, J. A. Delettrez, S. P. Hatchett, J. A. Frenje, V. Yu. Glebov, C. K. Li, J. E. Miller, R. D. Petrasso, F. H. Séguin, V. A. Smalyuk, R. B. Stephens, W. Theobald, B. Yaakobi, and T. C. Sangster, "Direct-Drive Fuel-Assembly Experiments with Gas-Filled, Cone-in-Shell, Fast-Ignitor Targets on the OMEGA Laser," Plasma Phys. Control. Fusion **47**, B859 (2005).

C. Stoeckl, J. A. Delettrez, J. H. Kelly, T. J. Kessler, B. E. Kruschwitz, S. J. Loucks, R. L. McCrory, D. D. Meyerhofer, D. N. Maywar, S. F. B. Morse, J. Myatt, A. L. Rigatti, L. J. Waxer, J. D. Zuegel, and R. B. Stephens, "High-Energy Petawatt Project at the University of Rochester's Laboratory for Laser Energetics," Fusion Sci. Technol. **49**, 367 (2006).

W. Theobald, K. Akli, R. Clarke, J. A. Delettrez, R. R. Freeman, S. Glenzer, J. Green, G. Gregori, R. Heathcote, N. Izumi, J. A. King, J. A. Koch, J. Kuba, K. Lancaster, A. J. MacKinnon, M. Key, C. Mileham, J. Myatt, D. Neely, P. A. Norreys, H.-S. Park, J. Pasley, P. Patel, S. P. Regan, H. Sawada, R. Shepherd, R. Snavely, R. B. Stephens, C. Stoeckl, M. Storm, B. Zhang, and T. C. Sangster, "Hot Surface Ionic Line Emission and Cold K-Inner Shell Emission from Petawatt-Laser-Irradiated Cu Foil Targets," Phys. Plasmas **13**, 043102 (2006).

J. U. Wallace and S. H. Chen, "Simplified Scheme for Deterministic Synthesis of Chiral-Nematic Glassy Liquid Crystals," Ind. Eng. Chem. Res. **45**, 4494 (2006).

S. Wu, P. Geiser, J. Jun, J. Karpinski, J.-R. Park, and R. Sobolewski, "Long-Lived, Coherent Acoustic Phonon Oscillators in GaN Single Crystals," Appl. Phys. Lett. **88**, 041917 (2006).

L. Zheng, J. C. Lambropoulos, and A. W. Schmid, "Molecular Dynamics Study of UV-Laser-Induced Densification of Fused Silica. II. Effects of Laser Pulse Duration, Pressure, and Temperature, and Comparison with Pressure-Induced Densification," J. Non-Cryst. Solids **351**, 3271 (2005).

J. D. Zuegel, V. Bagnoud, J. Bromage, I. A. Begishev, and J. Puth, "High-Performance OPCPA Laser System," J. Phys. IV France **133**, 701 (2006).

J. D. Zuegel, S. Borneis, C. Barty, B. LeGarrec, C. Danson, N. Miyanaga, P. K. Rambo, C. LeBlanc, T. J. Kessler, A. W. Schmid, L. J. Waxer, J. H. Kelly, B. Kruschwitz, R. Jungquist, E. Moses, J. Britten, I. Jovanovic, J. Dawson, and N. Blanchot, "Laser Challenges for Fast Ignition," Fusion Sci. Technol. **49**, 453 (2006).

OMEGA External Users' Publications

S. H. Batha, J. R. Fincke, J. M. Taccetti, N. D. Delamater, G. R. Magelssen, N. E. Lanier, R. M. Hueckstaedt, K. W. Parker, S. D. Rothman, and C. J. Horsfield, "Reduced Reshock Growth in a Convergent/Divergent System: Effect of Reshock Strength," J. Phys. IV France **133**, 441 (2006).

I. Carusotto, S. X. Hu, L. A. Collins, and A. Smerzi, "Bogoliubov-Čerenkov Radiation in a Bose-Einstein Condensate Flowing Against an Obstacle," Phys. Rev. Lett. **97**, 260403 (2006).

A. Casner, G. Huser, J.-P. Jadaud, S. Liberatore, D. Galmiche, and M. Vandenboomgaerde, "Planar Rayleigh–Taylor and Feedthrough Experiments with CH(Ge) on OMEGA," J. Phys. IV France **133**, 163 (2006).

P. M. Celliers, G. W. Collins, D. G. Hicks, and J. H. Eggert, "Systematic Uncertainties in Shock-Wave Impedance-Match

Analysis and the High-Pressure Equation of State of Al," J. Appl. Phys. **98**, 113529 (2005).

K. M. Chandler, S. A. Pikuz, T. A. Shelkovenko, M. D. Mitchell, D. A. Hammer, and J. P. Knauer, "Cross Calibration of New X-Ray Films Against Direct Exposure Film from 1 to 8 keV Using the X-Pinch X-Ray Source," Rev. Sci. Instrum. **76**, 113111 (2005).

D. H. Cohen, O. L. Landen, and J. J. MacFarlane, "Numerical Modeling of Hohlraum Radiation Conditions: Spatial and Spectral Variations Due to Sample Position, Beam Pointing, and Hohlraum Geometry," Phys. Plasmas **12**, 122703 (2005).

C. G. Constantin, H. A. Baldis, M. B. Schneider, D. E. Hinkel, A. B. Langdon, W. Seka, R. Bahr, and S. Depierreux, "Laser–Plasma Interactions in High-Energy Density Plasmas," J. Phys. IV France **133**, 243 (2006).

J. Dahlburg, S. L. Allen, R. Betti, S. Knowlton, R. Maingi, G. A. Navratil, S. A. Sabbagh, J. Sheffield, J. W. Van Dam, and D. Whyte, "Characteristics and Contributions of the Three Major United States Toroidal Magnetic Fusion Facilities," J. Fusion Energy **24**, 125 (2005).

J. L. DeCiantis, F. H. Séguin, J. A. Frenje, V. Berube, M. J. Canavan, C. D. Chen, S. Kurebayashi, C. K. Li, J. R. Rygg, B. E. Schwartz, R. D. Petrasso, J. A. Delettrez, S. P. Regan, V. A. Smalyuk, J. P. Knauer, F. J. Marshall, D. D. Meyerhofer, S. Roberts, T. C. Sangster, C. Stoeckl, K. Mikaelian, H. S. Park, and H. F. Robey, "Proton Core Imaging of the Nuclear Burn in Inertial Confinement Fusion Implosions," Rev. Sci. Instrum. **77**, 043503 (2006).

E. L. Dewald, O. S. Jones, O. L. Landen, L. Suter, P. Amendt, R. E. Turner, and S. Regan, "Hard X-Ray Imaging for Measuring Laser Absorption Spatial Profiles on the National Ignition Facility," Rev. Sci. Instrum. **77**, 10E310 (2006).

L. Disdier, A. Rouyer, I. Lantuejoul, O. Landoas, J. L. Bourgade, T. C. Sangster, V. Yu. Glebov, and R. A. Lerche, "Inertial Confinement Fusion Neutron Images," Phys. Plasmas **13**, 056317 (2006).

S. N. Dixit, D. Munro, J. R. Murray, M. Nostrand, P. J. Wegner, D. Froula, C. A. Haynam, and B. J. MacGowan, "Polarization Smoothing on the National Ignition Facility," J. Phys. IV France **133**, 717 (2006).

J. M. Foster, B. H. Wilde, P. A. Rosen, R. J. R. Williams, B. E. Blue, R. F. Coker, R. P. Drake, A. Frank, P. A. Keiter, A. M. Khokhlov, J. P. Knauer, and T. S. Perry, "High-Energy-Density Laboratory Astrophysics Studies of Jets and Bow Shocks," Astrophys. J. **634**, L77 (2005).

K. B. Fournier, C. Constantin, C. A. Back, L. J. Suter, H.-K. Chung, M. C. Miller, D. H. Froula, G. Gregori, S. H. Glenzer, E. L. Dewald, and O. L. Landen, "Electron-Density Scaling of Conversion Efficiency of Laser Energy into L-Shell X-Rays," J. Quant. Spectrosc. Radiat. Trasnf. **99**, 186 (2006).

K. B. Fournier, M. Tobin, J. F. Poco, K. Bradley, S. B. Hansen, C. A. Coverdale, D. Beutler, M. Severson, E. A. Smith, and D. L. Reeder, "Absolute X-Ray Yields from Laser-Irradiated, Ge-Doped Aerogel Targets," J. Phys. IV France **133**, 449 (2006).

R. R. Freeman, K. Akli, F. Beg, R. Betti, S. Chen, D. J. Clark, P. M. Gu, G. Gregori, S. P. Hatchett, D. Hey, K. Highbarger, J. M. Hill,

N. Izumi, M. Key, J. A. King, J. A. Koch, B. Lasinski, B. Langdon, A. J. MacKinnon, D. D. Meyerhofer, N. Patel, P. Patel, J. Pasley, H. S. Park, C. Ren, R. A. Snavely, R. B. Stephens, C. Stoeckl, M. Tabak, R. Town, L. Van Woerkom, R. Weber, S. C. Wilks, and B. B. Zhang, "Overview of Recent Progress in US Fast Ignition Research," J. Phys. IV France **133**, 95 (2006).

D. H. Froula, V. Rekow, C. Sorce, K. Piston, R. Knight, S. Alvarez, R. Griffith, D. Hargrove, J. S. Ross, S. Dixit, B. Pollock, L. Divol, S. H. Glenzer, W. Armstrong, R. Bahr, K. Thorp, and G. Pien, "3ω Transmitted Beam Diagnostic at the OMEGA Laser Facility," Rev. Sci. Instrum. **77**, 10E507 (2006).

D. A. Gates, C. Kessel, J. Menard, G. Taylor, J. R. Wilson, M. G. Bell, R. E. Bell, S. Bernabei, J. Bialek, T. Biewer, W. Blanchard, J. Boedo, C. Bush, M. D. Carter, W. Choe, N. Crocker, D. S. Darrow, W. Davis, L. Delgado-Aparicio, S. Diem, J. Ferron, A. Field, J. Foley, E. D. Fredrickson, T. Gibney, R. Harvey, R. E. Hatcher, W. Heidbrink, K. Hill, J. C. Hosea, T. R. Jarboe, D. W. Johnson, R. Kaita, S. Kaye, S. Kubota, H. W. Kugel, J. Lawson, B. P. LeBlanc, K. C. Lee, F. Levinton, R. Maingi, J. Manickam, R. Maqueda, R. Marsala, D. Mastrovito, T. K. Mau, S. S. Medley, H. Meyer, D. R. Mikkelsen, D. Mueller, T. Munsat, B. A. Nelson, C. Neumeyer, N. Nishino, M. Ono, H. Park, W. Park, S. Paul, T. Peebles, M. Peng, C. Phillips, A. Pigarov, R. Pinsker, A. Ram, S. Ramakrishnan, R. Raman, D. Rasmussen, M. Redi, M. Rensink, G. Rewoldt, J. Robinson, P. Roney, L. Roquemore, E. Ruskov, P. Ryan, S. A. Sabbagh, H. Schneider, C. H. Skinner, D. R. Smith, A. Sontag, V. Soukhanovskii, T. Stevenson, D. Stotler, B. Stratton, D. Stutman, D. Swain, E. Syankowski, Y. Takase, K. Tritz, A. von Halle, M. Wade, R. White, J. Wilgen, M. Williams, W. Zhu, S. J. Zweben, R. Akers, P. Beiersdorfer, R. Betti, and T. Bigelow, "Progress Towards Steady State on NSTX," Nucl. Fusion **46**, S22 (2006).

G. Gregori, S. H. Glenzer, H.-K. Chung, D. H. Froula, R. W. Lee, N. B. Meezan, J. D. Moody, C. Niemann, O. L. Landen, B. Holst, R. Redmer, S. P. Regan, and H. Sawada, "Measurement of Carbon Ionization Balance in High-Temperature Plasma Mixtures by Temporally Resolved X-Ray Scattering," J. Quant. Spectrosc. Radiat. Transf. **99**, 225 (2006).

G. P. Grim, C. W. Barnes, P. A. Bradley, C. R. Christensen, A. Hauer, G. L. Morgan, J. A. Oertel, M. D. Wilke, D. C. Wilson, C. Barrera, S. W. Haan, B. A. Hammel, J. A. Koch, R. A. Lerche, M. J. Moran, V. L. Glebov, T. C. Sangster, J.-L. Bourgade, L. Disdier, I. Lantuejoul, and O. Landoas, "Neutron Imaging at the NIF," J. Phys. IV France **133**, 913 (2006).

H. Habara, P. A. Norreys, R. Kodama, C. Stoeckl, and V. Yu. Glebov, "Neutron Measurements and Diagnostic Developments Relevant to Fast Ignition," Fusion Sci. Technol. **49**, 517 (2006).

S. P. Hatchett, D. Clark, M. Tabak, R. E. Turner, C. Stoeckl, R. B. Stephens, H. Shiraga, and K. Tanaka, "Hydrodynamics of Conically Guided Fast Ignition Targets," Fusion Sci. Technol. **49**, 327 (2006).

J. Hecht, "A Proliferation of Petawatt Lasers," Laser Focus World **42**, 105 (2006).

D. G. Hicks, T. R. Boehly, J. H. Eggert, J. E. Miller, P. M. Celliers, and G. W. Collins, "Dissociation of Liquid Silica at High Pressures and Temperatures," Phys. Rev. Lett. **97**, 025502 (2006).

D. E. Hinkel, M. B. Schneider, B. K. Young, A. B. Langdon, E. A. Williams, M. D. Rosen, and L. J. Suter, "Creation of Hot Radiation Environments in Laser-Driven Targets," Phys. Rev. Lett. **96**, 195001 (2006).

P. A. Holstein, "Update on Ignition Studies at CEA," J. Phys. IV France **133**, 67 (2006).

M. Houry, E. Delagnes, D. Riz, B. Canaud, L. Disdier, F. Garaude, Y. Giomataris, V. Yu. Glebov, Ph. Legou, Ph. Rebourgeard, and C. Sangster, "DEMIN: A Neutron Spectrometer, Micromegas-Type, for Inertial Confinement Fusion Experiments," Nucl. Instrum. Methods Phys. Res. A **557**, 648 (2006).

S. M. Kaye, M. G. Bell, R. E. Bell, S. Bernabei, J. Bialek, T. Biewer, W. Blanchard, J. Boedo, C. Bush, M. D. Carter, W. Choe, N. Crocker, D. S. Darrow, W. Davis, L. Delgado-Aparicio, S. Diem, J. Ferron, A. Field, J. Foley, E. D. Fredrickson, D. A. Gates, T. Gibney, R. Harvey, R. E. Hatcher, W. Heidbrink, K. Hill, J. C. Hosea, T. R. Jarboe, D. W. Johnson, R. Kaita, C. Kessel, S. Kubota, H. W. Kugel, J. Lawson, B. P. LeBlanc, K. C. Lee, F. Levinton, R. Maingi, J. Manickam, R. Maqueda, R. Marsala, D. Mastovito, T. K. Mau, S. S. Medley, J. Menard, H. Meyer, D. R. Mikkelsen, D. Mueller, T. Munsat, B. A. Nelson, C. Neumeyer, N. Nishinio, M. Ono, H. Park, W. Park, S. Paul, T. Peebles, M. Peng, C. Phillips, A. Pigarov, R. Pinsker, A. Ram, S. Ramakrishnan, R. Raman, D. Rasmussen, M. Redi, M. Rensink, G. Rewoldt, J. Robinson, P. Roney, A. L. Roquemore, E. Ruskov, P. Ryan, S. A. Sabbagh, H. Schneider, C. H. Skinner, D. R. Smith, A. Sontag, V. Soukhanovskii, T. Stevenson, D. Stotler, B. Stratton,

D. Stutman, D. Swain, E. Synakowski, Y. Takase, G. Taylor, K. Tritz, A. von Halle, M. Wade, R. White, J. Wilgen, M. Williams, J. R. Wilson, W. Zhu, S. J. Zweben, R. Akers, P. Beiersdorfer, R. Betti, T. Bigelow, M. Bitter, P. Bonoli, C. Boudelle, C. S. Chang, J. Chrzanowski, C. Domier, L. Dudek, P. C. Efthimion, M. Finkenthal, E. Fredd, G. Y. Fu, A. Glasser, R. J. Goldston, N. L. Greenough, L. R. Grisham, N. Gorelenkov., L. Guazzotto, R. J. Hawryluk, J. Hogan, W. Houlberg, D. Humphreys, F. Jaeger, M. Kalish, S. Krasheninnikov, L. L. Lao, J. Lawrence, J. Leuer, D. Liu, N. C. Luhmann, E. Mazzucato, G. Oliaro, D. Pacella, R. Parsells, M. Schaffer, I. Semenov, K. C. Shaing, M. A. Shapiro, K. Shinohara, P. Sichta, X. Tang, R. Vero, D. Walker, and W. Wampler, "Progress Towards High Performance Plasmas in the National Spherical Torus Experiment (NSTX)," Nucl. Fusion **45**, S168 (2005).

M. H. Key, K. Akli, F. Beg, M. H. Chen, H.-K. Chung, R. R. Freeman, M. E. Foord, J. S. Green, P. Gu, G. Gregori, H. Habara, S. P. Hatchett, D. Hey, J. M. Hill, J. A. King, R. Kodama, J. A. Koch, K. Lancaster, B. F. Lasinski, B. Langdon, A. J. MacKinnon, C. D. Murphy, P. A. Norreys, N. Patel, P. Patel, J. Pasley, R. A. Snavely, R. B. Stephens, C. Stoeckl, M. Tabak, W. Theobald, K. Tanaka, R. Town, S. C. Wilks, T. Yabuuchi, and B. Zhang, "Study of Electron and Proton Isochoric Heating for Fast Ignition," J. Phys. IV France **133**, 371 (2006).

G. A. Kyrala, M. A. Gunderson, N. D. Delamater, D. A. Haynes, D. C. Wilson, J. A. Guzik, and K. A. Klare, "Detailed Diagnosis of a Double-Shell Collision Under Realistic Implosion Conditions," Phys. Plasmas **13**, 056306 (2006).

G. A. Kyrala, M. A. Gunderson, N. D. Delamater, D. A. Haynes, D. C. Wilson, J. A. Guzik, and K. A. Klare, "Detailed Diagnosis of Double Shell Collision Using X-Ray Radiography Under Realistic Implosion Conditions," J. Phys. IV France **133**, 147 (2006).

O. L. Landen, S. Glenzer, D. Froula, E. Dewald, L. J. Suter, M. Schneider, D. Hinkel, J. Fernandez, J. Kline, S. Goldman, D. Braun, P. Celliers, S. Moon, H. Robey, N. Lanier, G. Glendinning, B. Blue, B. Wilde, O. Jones, J. Schein, L. Divol, D. Kalantar, K. Campbell, J. Holder, J. McDonald, C. Niemann, A. Mackinnon, R. Collins, D. Bradley, J. Eggert, D. Hicks, G. Gregori, R. Kirkwood, C. Niemann, B. Young, J. Foster, F. Hansen, T. Perry, D. Munro, H. Baldis, G. Grim, R. Heeter, B. Hegelich, D. Montgomery, G. Rochau, R. Olson, R. Turner, J. Workman, R. Berger, B. Cohen, W. Kruer, B. Langdon, S. Langer, N. Meezan, H. Rose, B. Still, E. Williams, E. Dodd, J. Edwards, M.-C. Monteil, M. Stevenson, B. Thomas, R. Coker,

G. Magelssen, P. Rosen, P. Stry, D. Woods, S. Weber, S. Alvarez, G. Armstrong, R. Bahr, J.-L. Bourgade, D. Bower, J. Celeste, M. Chrisp, S. Compton, J. Cox, C. Constantin, R. Costa, J. Duncan, A. Ellis, J. Emig, C. Gautier, A. Greenwood, R. Griffith, F. Holdner, G. Holtmeier, D. Hargrove, T. James, J. Kamperschroer, J. Kimbrough, M. Landon, D. Lee, R. Malone, M. May, S. Montelongo, J. Moody, E. Ng, A. Nikitin, D. Pellinen, K. Piston, M. Poole, V. Rekow, M. Rhodes, R. Shepherd, S. Shiromizu, D. Voloshin, A. Warrick, P. Watts, F. Weber, P. Young, P. Arnold, L. Atherton, G. Bardsley, R. Bonanno, T. Borger, M. Bowers, R. Bryant, S. Buckman, S. Burkhart, F. Cooper, S. Dixit, G. Erbert, D. Eder, B. Ehrlich, B. Felker, J. Fornes, G. Frieders, S. Gardner, C. Gates, M. Gonzalez, S. Grace, T. Hall, C. Haynam, G. Heestand, M. Henesian, M. Hermann, G. Hermes, S. Huber, K. Jancaitis, S. Johnson, B. Kauffman, T. Kelleher, T. Kohut, A. E. Koniges, T. Labiak, D. Latray, A. Lee, D. Lund, S. Mahavandi, K. R. Manes, C. Marshall, J. McBride, T. McCarville, L. McGrew, J. Menapace, E. Mertens, D. Munro, J. Murray, J. Neumann, M. Newton, P. Opsahl, E. Padilla, T. Parham, G. Parrish, C. Petty, M. Polk, C. Powell, I. Reinbachs, R. Rinnert, B. Riordan, G. Ross, V. Robert, M. Tobin, S. Sailors, R. Saunders, M. Schmitt, M. Shaw, M. Singh, M. Spaeth, A. Stephens, G. Tietbohl, J. Tuck, B. Van Wonterghem, R. Vidal, P. Wegner, P. Whitman, K. Williams, K. Winward, K. Work, R. Wallace, A. Nobile, M. Bono, B. Day, J. Elliott, D. Hatch, H. Louis, R. Manzenares, D. O'Brien, P. Papin, T. Pierce, G. Rivera, J. Ruppe, D. Sandoval, D. Schmidt, L. Valdez, K. Zapata, B. MacGowan, M. Eckart, W. Hsing, P. Springer, B. Hammel, E. Moses, and G. Miller, "The First Experiments on the National Ignition Facility," J. Phys. IV France **133**, 43 (2006).

N. E. Lanier, G. R. Magelssen, S. H. Batha, J. R. Fincke, C. Horsfield, K. W. Parker, and S. D. Rothman, "Validation of the Radiation Hydrocode RAGE Against Defect-Driven Mix Experiments in a Compressible, Convergent, and Miscible Plasma System," Phys. Plasmas **13**, 042703 (2006).

C. K. Li and R. D. Petrasso, "Energy Deposition of MeV Electrons in Compressed Targets of Fast-Ignition Inertial Confinement Fusion," Phys. Plasmas **13**, 056314 (2006).

C. K. Li and R. D. Petrasso, "Stopping, Straggling, and Blooming of Directed Energetic Electrons in Hydrogenic and Arbitrary-Z Plasmas," Phys. Rev. E **73**, 016402 (2006).

C. K. Li, F. H. Séguin, J. A. Frenje, J. R. Rygg, R. D. Petrasso, R. P. J. Town, P. A. Amendt, S. P. Hatchett, O. L. Landen, A. J. Mackinnon, P. K. Patel, V. A. Smalyuk, T. C. Sangster, and

J. P. Knauer, "Measuring E and B Fields in Laser-Produced Plasmas with Monoenergetic Proton Radiography," Phys. Rev. Lett. **97**, 135003 (2006).

J. J. MacFarlane, I. E. Golovkin, R. C. Mancini, L. A. Welser, J. E. Bailey, J. A. Koch, T. A. Melhorn, G. A. Rochau, P. Wang, and P. Woodruff, "Dopant Radiative Cooling Effects in Indirect-Drive Ar-doped Capsule Implosion Experiments," Phys. Rev. E **72**, 066403 (2005).

S. W. McAlpin, R. M. Stevenson, B. R. Thomas, J. Kline, and S. Batha, "Assessing Plasma Filling in NIF Cluster Geometry," J. Phys. IV France **133**, 309 (2006).

K. Mima, T. Takeda, and "Proof-of-Principle Experiments for Fast Ignition and the Fast Ignition Realization Experiment," Fusion Sci. Technol. **49**, 358 (2006).

J. D. Moody, L. Divol, S. H. Glenzer, A. J. MacKinnon, D. H. Froula, G. Gregori, W. L. Kruer, N. B. Meezan, L. J. Suter, E. A. Williams, R. Bahr, and W. Seka, "Efficient Coupling of 527 nm Laser Beam Power to a Long Scalelength Plasma," J. Phys. IV France **133**, 321 (2006).

E. I. Moses, G. H. Miller, and R. L. Kauffman, "The ICF Status and Plans in the United States," J. Phys. IV France **133**, 9 (2006).

P. A. Norreys, K. L. Lancaster, H. Habara, J. R. Davies, J. T. Mendonca, R. J. Clarke, B. Dromey, A. Gopal, S. Karsch, R. Kodama, K. Krushelnick, S. D. Moustaizis, C. Stoeckl, M. Tatarakis, M. Tampo, N. Vakakis, M. S. Wei, and M. Zepf, "Observation of Ion Temperatures Exceeding Background Electron Temperatures in Petawatt Laser–Solid Experiments," Plasma Phys. Control. Fusion **47**, L49 (2005).

R. E. Olson, R. J. Leeper, G. A. Rochau, D. K. Bradley, P. M. Celliers, and T. R. Boehly, "Hohlraum X-Ray Deposition in Indirect-Drive ICF Ablator Materials," J. Phys. IV France **133**, 179 (2006).

H.-S. Park, D. M. Chambers, H.-K. Chung, R. J. Clarke, R. Eagleton, E. Giraldez, T. Goldsack, R. Heathcote, N. Izumi, M. H. Key, J. A. King, J. A. Koch, O. L. Landen, A. Nikroo, P. K. Patel, D. F. Price, B. A. Remington, H. F. Robey, R. A. Snavely, D. A. Steinman, R. B. Stephens, C. Stoeckl, M. Storm, M. Tabak, W. Theobald, R. P. J. Town, J. E. Wickersham, and B. B. Zhang, "High-Energy Kα Radiography Using High-Intensity, Short-Pulse Lasers," Phys. Plasmas **13**, 056309 (2006).

P. K. Patel, M. H. Key, A. J. Mackinnon, R. Berry, M. Borghesi, D. M. Chambers, H. Chen, R. Clarke, C. Damian, R. Eagleton, R. Freeman, S. Glenzer, G. Gregori, R. Heathcote, D. Hey, N. Izumi, S. Kar, J. King, A. Nikroo, A. Niles, H.-S. Park, J. Pasley, N. Patel, R. Shepherd, R. A. Snavely, D. Steinman, C. Stoeckl, M. Storm, W. Theobald, R. Town, R. Van Maren, S. C. Wilks, and B. Zhang, "Integrated Laser–Target Interaction Experiments on the RAL Petawatt Laser," Plasma Phys. Control. Fusion **47**, B83 (2005).

A. B. Reighard, R. P. Drake, K. K. Dannenberg, D. J. Kremer, M. Grosskopf, E. C. Harding, D. R. Leibrandt, S. G. Glendinning, T. S. Perry, B. A. Remington, J. Greenough, J. Knauer, T. Boehly, S. Bouquet, L. Boireau, M. Koenig, and T. Vinci, "Observation of Collapsing Radiative Shocks in Laboratory Experiments," Phys. Plasmas **13**, 082901 (2006).

P. A. Rosen, J. M. Foster, R. J. R. Williams, B. H. Wilde, R. F. Coker, B. Blue, T. S. Perry, P. Hartigan, R. P. Drake, K. Dannenberg, A. M. Khokhlov, A. Frank, and J. P. Knauer, "Laboratory-Astrophysics Jet Experiments at the OMEGA Laser Facility," J. Phys. IV France **133**, 1019 (2006).

J. R. Rygg, J. A. Frenje, C. K. Li, F. H. Séguin, R. D. Petrasso, J. A. Delettrez, V. Yu. Glebov, V. N. Goncharov, D. D. Meyerhofer, S. P. Regan, T. C. Sangster, and C. Stoeckl, "Tests of the Hydrodynamic Equivalence of Direct-Drive Implosions with Different D_2 and ^{3}He Mixtures," Phys. Plasmas **13**, 052702 (2006).

M. B. Schneider, D. E. Hinkel, B. K. Young, J. P. Holder, A. B. Langdon, H. A. Baldis, R. Bahr, D. E. Bower, H. C. Bruns, K. M. Campbell, J. R. Celeste, S. Compton, C. G. Constantin, R. L. Costa, E. L. Dewald, S. N. Dixit, M. J. Eckart, D. C. Eder, M. J. Edwards, A. D. Ellis, J. A. Emig, D. H. Froula, V. Glebov, S. H. Glenzer, D. Hargrove, C. A. Haynam, R. F. Heeter, M. A. Henesian, G. Holtmeier, D. L. James, K. S. Jancaitis, D. H. Kalantar, J. H. Kamperschroer, R. L. Kauffman, J. Kimbrough, R. Kirkwood, A. E. Koniges, O. L. Landen, M. Landon, F. D. Lee, B. J. MacGowan, A. J. Mackinnon, K. R. Manes, C. Marshall, M. J. May, J. W. McDonald, J. Menapace, S. J. Moon, E. I. Moses, D. H. Munro, J. R. Murray, C. Niemann, D. Pellinen, K. Piston, G. D. Power, V. Rekow, S. Roberts,

J. A. Ruppe, J. Schein, W. Seka, R. Shepherd, M. S. Singh, C. Sorce, P. T. Springer, C. H. Still, C. Stoeckl, L. J. Suter, G. L. Tietbohl, R. E. Turner, B. M. Van Wonterghem, R. J. Wallace, A. Warrick, P. Watts, F. Weber, P. J. Wegner, E. A. Williams, and P. E. Young, "X-Ray Flux and X-Ray Burnthrough Experiments on Reduced-Scale Targets at the NIF and OMEGA Lasers," J. Phys. IV France **133**, 1205 (2006).

J. F. Seely, C. A. Back, C. Constantin, R. W. Lee, H.-K. Chung, L. T. Hudson, C. I. Szabo, A. Henins, G. E. Holland, R. Atkin, and L. Marlin, "Krypton K-Shell X-Ray Spectra Recorded by the HENEX Spectrometer," J. Quant. Spectrosc. Radiat. Transf. **99**, 572 (2006).

R. B. Stephens, R. P. J. Snavely, Y. Aglitskii, K. U. Akli, F. Amiranoff, C. Andersen, D. Batani, S. D. Baton, T. Cowan, R. R. Freeman, J. S. Green, H. Habara, T. Hall, S. P. Hatchett, D. S. Hey, J. M. Hill, J. L. Kaae, M. H. Key, J. A. King, J. A. Koch, R. Kodama, M. Koenig, K. Krushelnick, K. L. Lancaster, A. J. MacKinnon, E. Martinolli, C. D. Murphy, M. Nakatsutsumi, P. Norreys, E. Perelli-Cippo, M. Rabec Le Gloahec, B. Remington, C. Rousseaux, J. J. Santos, F. Scianitti, C. Stoeckl, M. Tabak, K. A. Tanaka, W. Theobald, R. Town, T. Yabuuchi, and B. Zhang, "High Energy Electron Transport in Solids," J. Phys. IV France **133**, 355 (2006).

R. Tommasini, J. A. Koch, N. Izumi, L. A. Welser, R. C. Mancini, J. A. Delettrez, S. Regan, and V. Smalyuk, "Multispectral X-Ray Imaging for Core Temperature and Density Maps Retrieval in Direct Drive Implosions," Rev. Sci. Instrum. **77**, 10E303 (2006).

F.-Y. Tsai, Y.-H. Kuo, and D. R. Harding, "Properties and Structure of Vapor-Deposited Polyimide upon Electron-Beam Irradiation," J. Appl. Phys. **99**, 064910 (2006).

L. A. Welser, R. C. Mancini, J. A. Koch, N. Izumi, S. J. Louis, I. E. Golovkin, T. W. Barbee, Jr., S. W. Haan, J. A. Delettrez, F. J. Marshall, S. P. Regan, V. A. Smalyuk, D. A. Haynes, Jr., and R. W. Lee, "Multi-Objective Spectroscopic Analysis of Core Gradients: Extension from Two to Three Objectives," J. Quant. Spectrosc. Radiat. Transf. **99**, 649 (2006).

Conference Presentations

The following presentations were made at the 11th International Topical Meeting on Optics of Liquid Crystals, Sand Key, FL, 2–7 October 2005:

S. G. Lukishova, N. Lepeshkin, R. W. Boyd, and K. L. Marshall, "Feedback-Free Hexagon Pattern Formation with Liquid Crystals and Isotropic Liquids."

S. G. Lukishova and A. W. Schmid, "Near-Field Optical Microscopy of Cholesteric Oligomeric Liquid Crystal Layers."

S. G. Lukishova, A. W. Schmid, C. M. Supranowitz, A. J. McNamara, P. Freivald, R. P. Knox, R. W. Boyd, and C. R. Stroud, "Single-Photon Source for Quantum Information Based on Single Dye Molecule Fluorescence in Liquid Crystal Host."

K. L. Marshall, K. Adelsberger, G. Mhyre, and D. W. Griffith, "The LCPDI: A Compact and Robust Phase-Shifting, Point-Diffraction Interferometer Based on Dye-Doped LC Technology."

K. L. Marshall, G. Painter, K. Lotito, A. G. Noto, and P. Chang, "Transition Metal Dithiolene Near-IR Dyes and Their Applications in Liquid Crystal Devices" (invited).

———

The following presentations were made at the 47th Annual Meeting of the APS Division of Plasma Physics, Denver, CO, 24–28 October 2005:

K. Anderson and R. Betti, "2-D Simulations of Adiabat-Shaped Targets."

R. Betti and C. Zhou, "Fuel Assembly for Fast-Ignition Inertial Confinement Fusion."

R. Betti and C. Zhou, "High-Density and High-ρR-Fuel Assembly for Fast-Ignition Inertial Confinement Fusion."

T. R. Boehly, E. Vianello, J. E. Miller, R. S. Craxton, T. J B. Collins, V. N. Goncharov, I. V. Igumenshchev, D. D. Meyerhofer, D. G. Hicks, P. M. Celliers, and G. W. Collins, "Shock-Timing Experiments Using Double-Pulse Laser Irradiation" (invited).

M. J. Canavan, J. A. Frenje, R. Leiter, C. K. Li, J. R. Rygg, F. H. Séguin, R. D. Petrasso, and S. Roberts, "Characterization of a Fusion Product Source for ICF Diagnostic Development."

D. T. Casey, J. A. Frenje, C. K. Li, J. R. Rygg, F. H. Séguin, R. D. Petrasso, V. Yu. Glebov, D. D. Meyerhofer, T. C. Sangster, C. Stoeckl, S. W. Haan, S. P. Hatchett, P. A. Amendt, D. Eder, N. Izumi, O. L. Landen, R. A. Lerche, D. C. Wilson, R. Leeper, and R. E. Olson, "Design of the Shielding for the Magnetic Recoil Spectrometer (MRS) on OMEGA and the NIF Using the Neutron Transport Code TART2002."

C. D. Chen, C. K. Li, J. A. Frenje, F. H. Séguin, R. D. Petrasso, J. Myatt, and J. A. Delettrez, "Monte Carlo Simulations for Studying Hot-Electron Transport in Nondegenerate Plasmas of Arbitrary Z."

T. J. B. Collins, P. W. McKenty, P. B. Radha, V. N. Goncharov, and S. Skupsky, "Stability and Performance of a Direct-Drive, 1-MJ, Wetted-Foam Target Design."

R. S. Craxton, F. J. Marshall, M. J. Bonino, S. G. Noyes, and V. A. Smalyuk, "Radiation Transport in Saturn Targets Used for Polar Direct Drive."

J. A. Delettrez, J. Myatt, P. B. Radha, C. Stoeckl, and D. D. Meyerhofer, "Hydrodynamic Simulations of Integrated Experiments Planned for the OMEGA/OMEGA EP Laser Systems."

D. H. Edgell, R. S. Craxton, L. M. Elasky, D. R. Harding, L. S. Iwan, R. L. Keck, L. D. Lund, S. J. Verbridge, M. J. Wittman, and W. Seka, "Calibration of Cryogenic Target Optical Shadowgraphic Characterization."

R. Epstein, T. J. B. Collins, J. A. Delettrez, V. N. Goncharov, J. P. Knauer, J. A. Marozas, P. W. McKenty, P. B. Radha, and V. A. Smalyuk, "Effects of Perturbed Picket Pulses in Adiabat-Shaped Direct-Drive Implosion Experiments."

J. A. Frenje, D. T. Casey, C. K. Li, J. R. Rygg, F. H. Séguin, S. Volkmer, R. D. Petrasso, V. Yu. Glebov, D. D. Meyerhofer, T. C. Sangster, C. Stoeckl, S. W. Haan, S. P. Hatchett, P. A. Amendt, D. Eder, N. Izumi, O. L. Landen, R. A. Lerche, D. C. Wilson, R. Leeper, and O. L. Olson, "A Magnetic Recoil Spectrometer (MRS) for ρR, Yield, and T_i Measurements of Implosions on OMEGA and the NIF."

M. Ghilea, D. D. Meyerhofer, T. C. Sangster, D. Lonobile, A. Dillenbeck, R. A. Lerche, and L. Disdier, "Neutron Imaging with Bubble Chambers."

V. Yu. Glebov, T. C. Sangster, S. Roberts, M. J. Moran, and B. Davis, "Neutron Time-of-Flight Detectors Based on Vacuum Photodiodes for the NIF and LMJ."

V. N. Goncharov, G. Li, P. B. Radha, J. A. Delettrez, A. V. Maximov, and R. L. McCrory, "Electron Transport Modeling in Inertial Confinement Fusion Experiments."

O. V. Gotchev, D. D. Meyerhofer, and C. Stoeckl, "A Compact, Multiangle Electron Spectrometer for Ultra-Intense Laser–Plasma Interaction Experiments."

L. Guazzotto, R. Betti, and J. P. Freidberg, "First Results of a Linear MHD Stability Code for Axisymmetric Plasmas with Arbitrary Equilibrium Flow."

D. R. Harding, D. D. Meyerhofer, S. J. Loucks, L. D. Lund, R. Janezic, L. M. Elasky, T. H. Hinterman, D. H. Edgell, W. Seka, M. D. Wittman, R. Q. Gram, and M. J. Bonino, "Forming Smooth Cryogenic Target Layers for OMEGA Direct-Drive ICF Implosions and Prospects for Direct-Drive Targets for the NIF" (invited).

I. V. Igumenshchev, R. S. Craxton, P. W. McKenty, J. A. Marozas, and S. Skupsky, "Reduction of the Effects of Nonuniform Laser Irradiation in Polar-Direct-Drive Implosions on the NIF."

P. A. Jaanimagi, R. Boni, and D. D. Meyerhofer, "Update on the Rochester Optical Streak System."

N. Jang, J. P. Knauer, R. Betti, and D. D. Meyerhofer, "Laser Driven Magnetic Field Compression."

J. P. Knauer, K. Anderson, R. Betti, T. J. B. Collins, V. Yu. Glebov, V. N. Goncharov, F. J. Marshall, D. D. Meyerhofer, P. B. Radha, S. P. Regan, T. C. Sangster, C. Stoeckl, J. A. Frenje, C. K. Li, R. D. Petrasso, and F. H. Séguin, "Direct-Drive, Low-Adiabat ICF Implosions."

C. K. Li and R. D. Petrasso, "Stopping, Straggling and Blooming of Directed Energetic Electrons in Hydrogenic and Arbitrary-Z Plasmas" (invited).

C. K. Li, F. H. Séguin, J. R. Rygg, J. A. Frenje, R. D. Petrasso, T. C. Sangster, V. A. Smalyuk, J. A. Delettrez, J. P. Knauer, S. P. Regan, J. M. Soures, F. J. Marshall, P. W. McKenty, D. D. Meyerhofer, C. Stoeckl, R. P. J. Town, A. J. MacKinnon, P. A. Amendt, N. Izumi, and O. L. Landen, "Proton Radiography of Electromagnetic Fields Generated by Laser-Driven Plastic Foils."

D. Li and V. N. Goncharov, "Numerical Study of Temporal Density Variation Effects on Nonlinear Perturbation Evolution in Classical Rayleigh–Taylor Instability."

G. Li and V. N. Goncharov, "Effect of Ponderomotive Terms on Heat Flux in Laser-Produced Plasmas."

J. A. Marozas, F. J. Marshall, R. S. Craxton, I. V. Igumenshchev, S. Skupsky, P. B. Radha, T. J. B. Collins, R. Epstein, P. W. McKenty, M. J. Bonino, D. Jacobs-Perkins, D. D. Meyerhofer, T. C. Sangster, J. P. Knauer, V. A. Smalyuk, V. Yu. Glebov, S. G. Noyes, W. Seka, and R. L. McCrory, "Progress in Polar-Direct-Drive Simulations and Experiments" (invited).

F. J. Marshall, R. S. Craxton, M. J. Bonino, R. Epstein, V. Yu. Glebov, D. Jacobs-Perkins, J. P. Knauer, J. A. Marozas, P. W. McKenty, S. G. Noyes, P. B. Radha, W. Seka, S. Skupsky, V. A. Smalyuk, J. A. Frenje, C. K. Li, R. D. Petrasso, and F. H. Séguin, "Polar-Direct-Drive Experiments on OMEGA."

A. V. Maximov, J. Myatt, and R. W. Short, "Electron Distribution and Transport in a Laser Field in Direct-Drive ICF Plasmas."

P. W. McKenty and M. D. Wittman, "Role of Hydrogen Fractionation in ICF Ignition Target Designs."

D. D. Meyerhofer, T. C. Sangster, C. Stoeckl, S. F. B. Morse, J. H. Kelly, S. J. Loucks, and R. L. McCrory, "OMEGA EP: Status and Use Planning."

J. E. Miller, T. R. Boehly, D. D. Meyerhofer, and J. H. Eggert, "Equation-of-State Measurement in High Porosity Ta_2O_5 Foam."

J. Myatt, J. A. Delettrez, W. Theobald, C. Stoeckl, M. Storm, A. V. Maximov, R. W. Short, R. P. J. Town, and L. A. Cottrill, "Numerical Calculations of Laser-Generated MeV Electrons and Characteristic X-Ray Production in Copper Foil Targets."

R. D. Petrasso and C. K. Li, "Energy Deposition, Penetration, and Blooming of Energetic Electrons in Fast Ignition and Preheat Scenarios."

P. B. Radha, R. Betti, V. Yu. Glebov, V. N. Goncharov, J. P. Knauer, P. W. McKenty, J. A. Marozas, D. D. Meyerhofer, S. P. Regan, T. C. Sangster, and C. Stoeckl, "Two-Dimensional Simulations of Low-Adiabat Plastic-Shell Implosions on OMEGA."

S. P. Regan, J. A. Delettrez, V. Yu. Glebov, V. N. Goncharov, J. A. Marozas, F. J. Marshall, P. W. McKenty, D. D. Meyerhofer, P. B. Radha, T. C. Sangster, V. A. Smalyuk, C. Stoeckl, J. R. Rygg, J. A. Frenje, C. K. Li, R. D. Petrasso, and F. H. Séguin, "Target Performance of Direct-Drive, D_2-, D^3He-, and DT-Filled Plastic-Shell Implosions on OMEGA."

C. Ren, G. Li, and V. N. Goncharov, "Hot Electron Generation During ICF Target Compression."

J. R. Rygg, J. A. Frenje, C. K. Li, F. H. Séguin, R. D. Petrasso, J. A. Delettrez, V. Yu. Glebov, D. D. Meyerhofer, and T. C. Sangster, "Studies of Shock Convergence in ICF Implosions Using Nuclear Burn History Measurements."

O. Sadot, V. A. Smalyuk, J. A. Delettrez, D. D. Meyerhofer, T. C. Sangster, D. Shvarts, R. Betti, and V. N. Goncharov, "Measurements of Bubble Evolution in the Nonlinear Ablative Rayleigh–Taylor Instability."

T. C. Sangster, J. A. Delettrez, V. Yu. Glebov, V. N. Goncharov, D. R. Harding, J. P. Knauer, F. J. Marshall, P. W. McKenty, D. D. Meyerhofer, P. B. Radha, S. P. Regan, S. Skupsky, V. A. Smalyuk, C. Stoeckl, J. A. Frenje, C. K. Li, R. D. Petrasso, and F. H. Séguin, "Recent Cryogenic Implosion Results on OMEGA."

H. Sawada, S. P. Regan, T. R. Boehly, I. V. Igumenshchev, V. N. Goncharov, F. J. Marshall, B. Yaakobi, T. C. Sangster, D. D. Meyerhofer, G. Gregori, D. G. Hicks, S. H. Glenzer, and O. L. Landen, "Measurements of T_e and Z in Direct-Drive, Shock-Heated Planar Targets."

F. H. Séguin, J. DeCiantis, C. K. Li, J. A. Frenje, J. R. Rygg, R. D. Petrasso, S. P. Regan, J. A. Delettrez, R. Epstein, J. P. Knauer, F. J. Marshall, P. W. McKenty, D. D. Meyerhofer, S. Roberts, T. C. Sangster, V. A. Smalyuk, K. Mikaelian, H. S. Park, H. F. Robey, and R. Tipton, "Measured Nuclear Burn Region Sizes and Symmetries for Different Capsule and Drive Conditions in Direct Drive."

W. Seka, H. Baldis, J. Myatt, A. V. Maximov, R. W. Short, R. S. Craxton, R. E. Bahr, and T. C. Sangster, "Stimulated Brillouin Scattering in Plasmas Relevant to Direct-Drive Laser Fusion."

R. W. Short and J. Myatt, "Relativistic Electron Beam Micro-instabilities in the Fast-Ignition Regime."

S. Skupsky, R. S. Craxton, F. J. Marshall, R. Betti, T. J. B. Collins, R. Epstein, V. N. Goncharov, I. V. Igumenshchev, J. S. Keller, J. A. Marozas, P. W. McKenty, P. B. Radha, J. D.

Kilkenny, D. D. Meyerhofer, T. C. Sangster, and R. L. McCrory, "Polar Direct Drive on the National Ignition Facility."

V. A. Smalyuk, O. Sadot, R. Betti, V. N. Goncharov, J. A. Delettrez, D. D. Meyerhofer, S. P. Regan, T. C. Sangster, and D. Shvarts, "Rayleigh–Taylor Growth Measurements of 3-D Modulations in Nonlinear Regime" (invited).

A. Solodov, R. Betti, and J. Myatt, "Stopping of Fast Electrons in Dense Hydrogenic Plasmas."

A. Solodov, C. Ren, J. Myatt, R. Betti, and W. B. Mori, "Simulation of Weibel Electromagnetic Instability of Electron Beams in Plasma Using the Codes LSP and OSIRIS."

C. Stoeckl, T. R. Boehly, J. A. Delettrez, J. Myatt, J. E. Miller, R. B. Stephens, W. Theobald, and T. C. Sangster, "Measurements of Plasma Filling Inside a Fast-Ignitor Cone Target Using Streaked Optical Pyrometry."

S. Sublett, J. P. Knauer, I. V. Igumenshchev, A. Frank, and D. D. Meyerhofer, "Temporal Evolution of Directly Driven Hydrodynamic Jets Relevant to Astrophysics."

W. Theobald, J. E. Miller, T. R. Boehly, E. Vianello, I. V. Igumenshchev, V. N. Goncharov, A. V. Maximov, and T. C. Sangster, "Optical Measurements at Preheated Polystyrene and Aluminum Layers."

S. Volkmer, F. H. Séguin, C. K. Li, J. R. Rygg, R. D. Petrasso, T. C. Sangster, V. Yu. Glebov, D. D. Meyerhofer, and C. Stoeckl, "Improved Signal-to-Background for Neutron Spectroscopy Through Coincidence Counting of Charged-Particle Tracks in CR-39 Detectors."

C. Zhou and R. Betti, "Shock Fast Ignition of Thermonuclear Fuel with High Areal Density."

S. G. Lukishova, A. W. Schmid, R. Knox, P. Freivald, S. Schrauth, L. Bissell, R. W. Boyd, C. R. Stroud, Jr., and K. L. Marshall, "Deterministically Polarized, Room Temperature Source of Single Photons," Single-Photon Workshop 2005: Sources, Detectors, Applications and Measurement Methods, Teddington, UK, 24–26 October 2005.

The following presentations were made at Advanced Solid-State Photonics 2006, Incline Village, NV, 29 January–1 February 2006:

I. A. Begishev, V. Bagnoud, M. J. Guardalben, and J. D. Zuegel, "OPCPA Output Wavelength Tuning by Adjusting Time Delay Between Seed and Pump Pulses."

A. V. Okishev and J. D. Zuegel, "Athermal, Diode-Pumped Nd:YLF Regenerative Amplifier."

J. D. Zuegel, V. Bagoud, J. Bromage, and I. A. Begishev, "High-Performance OPCPA Laser System."

_____

K. L. Marshall, A. Trajkovska-Petkoska, T. Z. Kosc, and S. D. Jacobs, "Polymer Cholesteric Liquid Crystal (PCLC) Flake/Fluid Host Electro-Optical Suspensions: Progress Toward Flexible Reflective Displays," USDC Fifth Annual Flexible Microelectronics and Displays Conference, Phoenix, AZ, 6–9 February 2006.

_____

The following presentations were made at the 6th International Conference on High Energy Density Laboratory Astrophysics, Houston, TX, 11–14 March 2006:

S. Sublett, J. P. Knauer, I. V. Igumenshchev, A. Frank, and D. D. Meyerhofer, "Double-Pulse Laser-Driven Jets on OMEGA."

B. Yaakobi, "EXAFS Study of Shock Compression, Isentropic Compression, and Phase Transformation in Metals."

_____

W. Seka, P. Rechmann, J. D. B. Featherstone, and D. Fried, "Lasers in Hard Tissue Dentistry," Academy of Laser Dentistry Annual Conference, Tucson, AZ, 15–18 March 2006.

_____

J. Zhang and T. Y. Hsiang, "Dispersion Characteristics of Coplanar Waveguides at Subterahertz Frequencies," Progress in Electromagnetics Research Symposium, Cambridge, MA, 26–29 March 2006.

_____

S. G. Lukishova, A. W. Schmid, R. S. Knox, P. Freivald, L. Bissell, R. W. Boyd, C. R. Stroud, Jr., and K. L. Marshall, "Deterministically Polarized, Room-Temperature Source of Single Photons," Workshop on Linear Optical Quantum Information Processing, Baton Rouge, LA, 10–12 April 2006.

_____

C. Wu and D. R. Harding, "Chemical Vapor Deposition of Carbon Nanotube-Reinforced Polymer Composites," 2006 MRS Spring Meeting, San Francisco, CA, 17–21 April 2006.

_____

A. K. Knight, F.-Y. Tsai, T. N. Blanton, D. R. Harding, and S. H. Chen, "Optimizing the Vapor Deposition Method of Making Polyimide," 12th Meeting of the Symposium on Polymers for Microelectronics, Wilmington, DE, 3–5 May 2006.

_____

The following presentations were made at the 16th Topical Conference on High-Temperature Diagnostics, Williamsburg, VA, 7–11 May 2006:

V. Yu. Glebov, D. D. Meyerhofer, T. C. Sangster, C. Stoeckl, S. Roberts, C. A. Barrera, J. R. Celeste, C. J. Cerjan, L. S. Dauffy, D. C. Eder, R. L. Griffith, S. W. Haan, B. A. Hammel, S. P. Hatchett, N. Izumi, J. R. Kimbrough, J. A. Koch, O. L. Landen, R. A. Lerche, B. J. MacGowan, M. J. Moran, E. W. Ng, T. W. Phillips, P. M. Song, R. Tommassini, B. K. Young, S. E. Caldwell, G. P. Grim, S. C. Evans, J. M. Mack, T. J. Sedillo, M. D. Wilke, D. C. Wilson, C. S. Young, D. Casey, J. A. Frenje, C. K. Li, R. D. Petrasso, F. H. Séguin, J. L. Bourgade, L. Disdier, M. Houry, I. Lantejoule, O. Landoas, G. A. Chandler, G. W. Cooper, R. J. Leeper, R. E. Olson, C. L. Ruiz, M. A. Sweeney, S. P. Padalino, C. Horsfield, and B. A. Davis, "Development of Nuclear Diagnostics for the National Ignition Facility" (invited).

V. Yu. Glebov, C. Stoeckl, T. C. Sangster, C. Mileham, and R. A. Lerche, "High-Yield Bang Time Detector for the OMEGA Laser."

J. P. Knauer, F. J. Marshall, B. Yaakobi, D. Anderson, B. A. Schmitt, K. M. Chandler, S. A. Pikuz, T. A. Shelkovenko, M. D. Mitchell, and D. A. Hammer, "Response Model for Kodak Biomax-MS Film to X Rays."

F. J. Marshall, J. P. Knauer, D. Anderson, and B. A. Schmitt, "Absolute Calibration of Kodak Biomax-MS Film to X Rays in the 1.5- to 8-keV Range."

C. Stoeckl, V. Yu. Glebov, P. A. Jaanimagi, D. D. Meyerhofer, T. C. Sangster, M. Storm, S. Sublett, W. Theobald, M. H. Key, A. J. MacKinnon, P. K. Patel, D. Neely, and P. A. Norreys, "Operation of Target Diagnostics in a Petawatt Environment" (invited).

———

The following presentations were made at the Glass and Optical Materials Division Spring 2006 Meeting, Greenville, SC, 16–19 May 2006:

J. E. DeGroote, A. E. Marino, J. P. Wilson, and S. D. Jacobs, "The Role of Nanodiamond Abrasives in Optical Glass Removal with Magnetorheological Finishing (MRF)."

J. E. DeGroote, J. P. Wilson, T. M. Pfuntner, and S. D. Jacobs, "Incorporating Optical Glass Chemical Durability into a Glass Removal Model for Magnetorheological Finishing (MRF)."

———

The following presentations were made at CLEO/QELS 2006, Long Beach, CA, 21–26 May 2006:

W. R. Donaldson, D. N. Maywar, R. G. Roides, J. R. Marciante, J. H. Kelly, J. D. Zuegel, and R. L. Keck, "High-Bandwidth, Pulse-Shape Control on a Frequency-Tripled Multiterawatt Solid-State Laser."

C. Dorrer and J. D. Zuegel, "Design and Analysis of Beam Apodizers Using Error Diffusion."

S. G. Lukishova, A. W. Schmid, R. S. Knox, P. Freivald, L. Bissell, R. W. Boyd, C. R. Stroud, Jr., and K. L. Marshall, "Deterministically Polarized, Room-Temperature Source of Single Photons Based on a Single-Emitter Fluorescence in Aligned Liquid Crystal Hosts."

J. R. Marciante, W. A. Bittle, and J. D. Zuegel, "Subpicosecond Jitter from a Precision Optical Triggering and Timing System Without Active Stabilization."

———

A. K. Knight, F.-Y. Tsai, and D. R. Harding, "Using Experiments and Calculations to Analyze Gas Flow and Surface Reaction in the Vapor Deposition of a Copolymer," FLUENT 2006 CFD Summit, Monterey, CA, 22–24 May 2006.

———

The following presentations were made at the 36th Anomalous Absorption Conference, Jackson Hole, WY, 4–9 June 2006:

R. S. Craxton, F. J. Marshall, M. J. Bonino, R. Epstein, V. Yu. Glebov, J. A. Marozas, S. G. Noyes, and V. A. Smalyuk, "An Update on Polar-Direct-Drive Experiments on OMEGA."

A. V. Maximov, J. Myatt, and R. W. Short, "Transport Near Critical Density Surface in Direct-Drive ICF Plasmas."

J. Myatt, A. V. Maximov, and R. W. Short, "Laboratory Astrophysics of e^+e^- Pair-Plasma Production on OMEGA EP."

W. Seka, V. N. Goncharov, J. A. Delettrez, R. W. Short, and R. S. Craxton, "Laser Absorption in Spherical Target Experiments on OMEGA."

R. W. Short and J. Myatt, "Filamentation of Fast-Ignition Transport in Plasmas: Spatial Growth and Absolute Modes."

———

The following presentations were made at the 29th ECLIM, Madrid, Spain, 11–16 June 2006:

R. L. McCrory, "Highlights of the History of the University of Rochester's Laboratory for Laser Energetics."

R. L. McCrory, "Present and Future Research at the Laboratory for Laser Energetics."

———

R. Betti, K. Anderson, T. R. Boehly, T. J. B. Collins, R. S. Craxton, J. A. Delettrez, D. H. Edgell, R. Epstein, V. Yu. Glebov, V. N. Goncharov, D. R. Harding, R. L. Keck, J. H. Kelly, J. P. Knauer, S. J. Loucks, J. A. Marozas, F. J. Marshall, A. V. Maximov, D. N. Maywar, R. L. McCrory, P. W. McKenty, D. D. Meyerhofer, J. Myatt, P. B. Radha, S. P. Regan, C. Ren, T. C. Sangster, W. Seka, S. Skupsky, V. A. Smalyuk, J. M. Soures, C. Stoeckl, W. Theobald, B. Yaakobi, C. Zhou, J. D. Zuegel, C. K. Li, R. D. Petrasso, F. H. Séguin, and J. A. Frenje, "Progress in Hydrodynamic Theory

and Experiments for Direct-Drive and Fast-Ignition Inertial Confinement Fusion," 33rd European Physical Society Conference on Plasma Physics, Rome, Italy, 19–23 June 2006 (invited).

———

A. Melchior, T. R. Boehly, and J. E. Miller, "High-Pressure and Temperature Equation-of-State Studies Using Laser-Driven Shocks," Gordon Research Conference on High Pressure, Biddleford, ME, 25–30 June 2006.

———

W. Seka, "Overview of the LLE Effort in Support of the U.S. National HED and ICF Programs," JOWOG 37, Aldermaston, UK, 26–30 June 2006.

———

V. A. Smalyuk, R. Betti, T. R. Boehly, J. A. Delettrez, V. Yu. Glebov, V. N. Goncharov, J. P. Knauer, D. Y. Li, R. L. McCrory, D. D. Meyerhofer, P. B. Radha, S. P. Regan, T. C. Sangster, S. Skupsky, J. M. Soures, C. Stoeckl, B. Yaakobi, O. Sadot, D. Shvarts, J. A. Frenje, C. K. Li, R. D. Petrasso, and F. H. Séguin, "Experimental Studies of Nonlinear, Directly-Driven, Rayleigh–Taylor Instability on OMEGA," 10th International Workshop on the Physics of Compressible Turbulent Mixing, Paris, France, 17–21 July 2006.

———

The following presentations were made at the International Conference on Computational Science and Education, Rochester, NY, 7–10 August 2006:

J. A. Delettrez, "A Survey of the Use of Computer Technology at the Laboratory for Laser Energetics."

P. B. Radha, "Modeling Inertial Confinement Fusion Implosions Through Large-Scale Simulations."

———

The following presentations were made at Optics and Photonics 2006, San Diego, CA, 13–17 August 2006:

T. Z. Kosc, K. L. Marshall, A. Trajkovska-Petkoska, C. J. Coon, and S. D. Jacobs, "Exploring Motion Reversal in Polymer Cholesteric Liquid Crystal Devices."

N. N. Lepeshkin, S. G. Lukishova, R. W. Boyd, and K. L. Marshall, "Feedback-Free, Single-Beam Pattern Formation by Nanosecond Pulses in Dye-Doped Liquid Crystals."

K. L. Marshall, A. G. Noto, G. Painter, and N. Tabirian, "Computational Chemistry Methods for Predicting the Chiroptical Properties of Liquid Crystal Systems. II. Application to Chiral Azobenzenes."

———

The following presentations were made at the Applied Superconductivity Conference 2006, Seattle, WA, 27 August–1 September 2006:

G. N. Gol'tsman, A. Korneev, O. Minaeva, A. Antipov, A. Divochiy, N. Kaurova, B. Voronov, D. Pan, A. Cross, A. Pearlman, I. Komissarov, W. Słysz, and R. Sobolewski, "Low-Kinetic-Inductance Superconducting Single-Photon Detectors for GHz-Rate and High Quantum Efficiency Counting of Infrared Photons."

M. Khafizov, X. Li, R. Sobolewski, Y. Cui, and X. X. Xi, "Mechanisms of Light Detection by Superconducting Current-Biased MgB_2 Microbridges."

J. Kitaygorsky, I. Komissarov, A. Jukna, R. Sobolewski, O. Minaeva, N. Kaurova, A. Korneev, B. Voronov, I. Milostnaya, and G. N. Gol'tsman, "Dark Counts in Nanostructured NbN Single-Photon Detectors and Bridges."

X. Li, M. Khafizov, R. Sobolewski, Š. Chromik, V. Štrbík, M. Valerianova, and P. Odier, "Ultrafast Carrier Dynamics and Photoresponse of Hg-Ba-Ca-Cu-O Superconducting Microbridges."

———

S. P. Regan, H. Sawada, D. D. Meyerhofer, R. Epstein, V. N. Goncharov, I. V. Igumenshchev, D. Li, P. B. Radha, J. A. Delettrez, T. R. Boehly, F. J. Marshall, T. C. Sangster, V. A. Smalyuk, B. Yaakobi, S. H. Glenzer, O. L. Landen, G. Gregori, and R. C. Mancini, "Diagnosing Shock-Heated and Compressed Matter in Direct-Drive Inertial Confinement Fusion (ICF)," 12th International Workshop on Radiative Properties of Hot Dense Matter, Albufeira, Algarve, Portugal, 11–15 September 2006.

———

The following presentations were made at Boulder Damage Symposium XXXVIII, Boulder, CO, 25–27 September 2006:

B. Ashe, K. L. Marshall, C. Giacofei, A. L. Rigatti, T. J. Kessler, A. W. Schmid, J. B. Oliver, J. Keck, and A. Kozlov, "Evaluation of Cleaning Methods for Multilayer Diffraction Gratings."

S. Papernov and A. W. Schmid, "Using Gold Nanoparticles as Artificial Defects in Thin Films: What Have We Learned About Laser-Induced Damage Driven by Localized Absorbers?"

———————

The following presentations were made at ICUIL 2006, Cassis, France, 25–29 September 2006:

J. Bromage, C. Dorrer, I. A. Begishev, N. G. Usechak, and J. D. Zuegel, "Single-Shot Pulse Characterization from 0.4 to 85 ps Using Electro-Optic Shearing Interferometry."

J. Bromage, L. J. Waxer, I. A. Begishev, C. Dorrer, J. H. Kelly, and J. D. Zuegel, "Femtosecond Optimization of a Stretcher–Compressor Pair Using a Picosecond-Resolution Diagnostic."

C. Dorrer, A. Consentino, and J. D. Zuegel, "Development of High-Fluence Beam Shapers."

T. J. Kessler, J. Bunkenburg, C. Kellogg, F. Dewitt, J. Barone, L. S. Iwan, and K. McGowan, "Holographic Exposure System for Patterning Large Gratings with High Wavefront Quality and Uniform Groove Profile."

T. J. Kessler, H. Huang, and D. Weiner, "Diffractive Optics for Compensation of Axial Chromatic Aberration in a High-Energy Short-Pulse Laser."

L. J. Waxer and D. Eimerl, "Modeling the Pulse-Shape Output of OMEGA EP."

J. D. Zuegel, I. A. Begishev, W. A. Bittle, R. Boni, J. Bromage, C. Dorrer, P. A. Jaanimagi, and J. R. Marciante, "Laser and Diagnostic Technologies Developed for Integrated Pulse-Width Control on OMEGA EP."